# HYDRODYNAMIC TRANSPORT PROPERTIES OF SUSPENSIONS OF NON-BROWNIAN PROLATE SPHEROIDS

Thesis by

Ivan Lode André Maria Claeys

*In Partial Fulfillment of the Requirements*

*for the Degree of*

*Doctor of Philosophy*

California Institute of Technology

Pasadena California

-1991-

(Defended 21 May 1991)

## ACKNOWLEDGEMENTS

Writing the acknowledgements in one's thesis is like putting a period at the end of a sentence. It marks a pause, a moment to look back before one starts something new. I have a lot to think back about. Memories abound; a lot happened in those four and a half years spent at Caltech. My gratitude goes to all who made my stay enjoyable. I cannot possibly name them all, but would like to say a special "thanks" to a few of them here.

The course of my graduate studies has been somewhat peculiar, in that I have two research advisors, Prof. J.F. Brady and Prof. F.H. Arnold. Each has taught me much, in different ways. They have helped me over the hurdles of my research and shared the thrills of it. Their doors were always open for me to come in and talk, and I have really enjoyed these conversations. They provided guidance at times, a sympathetic ear at others. Thank you both for your openness. Through our discussions, you have catalyzed many evolutions within me that will shape my future.

Quite a few students and post-docs have shared my office, and their company has made many days and evenings more enjoyable. As I held on to that office —with a view of the mountains on smog-free days— I commuted daily up and down the stairs to the computer room. There, too, I have had many stimulating conversations, many refreshing laughs and a bit of small talk when we got tired of staring at the terminals. Thanks for all of this to all past and present members of the "Brady group."

Also, thank you to my parents for encouraging me in everything that I attempted and providing me with as many opportunities in life as one can wish for. I thoroughly enjoyed your visits to California and the good times that we shared then. Thanks to my parents-in-law, too, for their trust and for always caring.

Last but most importantly, a special thank you to Mariana for always being near me. Your liveliness, love and care fill my days with sunshine. You have so often shown, especially in these last months, what a wonderful wife you are.

## ABSTRACT

The methodology of "Stokesian dynamics," an efficient and accurate simulation technique for suspensions of spheres, is extended to non-spherical particles. The model system consists of rigid, non-Brownian prolate spheroids suspended in an incompressible Newtonian fluid at zero Reynolds number. The method is applied to calculate the hydrodynamic transport properties of unbounded dispersions of ellipsoids. Both "random" configurations and very orderly arrangements of particles are considered in order to probe the relation between the microstructure of the suspension and its macroscopically observable properties.

The simulation method is based on a microstructurally detailed description of the two-phase system and explicitly takes into account hydrodynamic interactions between the particles. Non-local singularity solutions for ellipsoids in Stokes flow are combined with Faxén laws using pair-wise additivity of velocities to construct a far-field approximation to the mobility tensor. The convergence problems associated with the long-ranged nature of viscous interactions at zero Reynolds number are handled using O'Brien's renormalization procedure. The Ewald summation technique is applied to accelerate the evaluation of the lattice sums generated by the periodic boundary conditions. Lubrication stresses between almost touching spheroids are added in a pair-wise manner to the mobility inverse. All the two-body resistance functions which diverge as the surface separation vanishes are computed to $O(\epsilon^0)$, with $\epsilon$ the gap width, so that the singular behavior of the lubrication interactions is captured correctly for arbitrary relative orientations and relative motions of the particles.

The method is first illustrated for a finite number of particles in an unbounded fluid domain, and shown to be accurate and efficient. It is then applied to crystalline geometries of spheroids over the full concentration range from 0 to closest packing

(74% by volume). The dependence of the hydrodynamic transport properties (sedimentation rate, diffusion coefficient, stress/rate-of-strain relation, permeability and hindered diffusivity) on the density of the dispersion, the aspect ratio of the particles and the lattice type is investigated. Equilibrium structures of hard ellipsoids generated by a Monte Carlo procedure are also considered. The high frequency limit of the hydrodynamic transport properties is computed and compared to the results for crystalline configurations, and to available experimental measurements. A discontinuous jump in some suspension properties is observed at the isotropic to nematic transition.

As a prelude to dynamic simulations, the compatibility of unit cells with pure straining flows is examined. It is demonstrated that no self-reproducing lattices exist in axisymmetric extensional flows, but a set of compatible basis vectors is derived. Planar straining fields on the other hand possess an infinite number of strain-periodic lattices.

# TABLE OF CONTENTS

# Chapter I
# Introduction

The unifying theme of this dissertation is the numerical simulation of hydrodynamic interactions between elongated particles in viscous fluids. This research was stimulated in part by the growing industrial and commercial importance of composite materials and of liquid crystals, and in part by experiments on the hindered rotational diffusion of molecules trapped in gels (Claeys, 1988; Claeys & Arnold, 1989). The enormous impact of fibre reinforced composites on the technological scene of the last decades was driven by the constantly increasing demands on the performance of materials. Plastics gradually supplant metals in the automotive world, and replace wood and brick in the construction business. Very often, a fine dispersion of fibres is imbedded in the polymeric matrix in order to improve the quality of the hybrid material. The transport properties in particular, such as the heat conductivity or the electrical resistance, can be dramatically affected by the addition of a tiny volume fraction of filamentous material. In a suspension, the rate of momentum transport also jumps by orders of magnitude due to the presence of rod-like particles. This is obviously of great concern during the fabrication of fibre-reinforced composites, as these are often processed as dispersions of solid particles in a liquid. Although the influence of slender inclusions on the macroscopic properties of compound materials is beginning to be understood quantitatively at semi-dilute concentrations, the validity of analytical approaches is usually limited to unrealistically high aspect ratios because they rely on a slowly converging asymptotic expansion in the logarithm of the inverse aspect ratio (Batchelor, 1971; Dinh & Armstrong, 1984; Shaqfeh, 1988; Fredrickson & Shaqfeh, 1989; Shaqfeh & Fredrickson, 1990). In other cases, their usefulness is hampered by the crude approximation of the particle geometry as a "shish-kebab" (Fesciyan & Dahler, 1982; Muthukumar & Edwards, 1983).

In this work, we study the rheological properties of dispersions of ellipsoids in a liquid by numerical simulation. We start from a microstructurally detailed description of the system as a heterogeneous mixture of elongated solid particles in a bath of fluid, and "scale up" to calculate the observable, macroscopic characteristics of the two-phase composite. Hydrodynamic interactions between the fibres are taken into account rigorously. It is shown that computer modeling can increase our insight in the connection between the properties of the suspension and its geometric features (such as the orientation distribution and the degree of translational order). Furthermore, by visualizing the evolution of the microstructure under imposed deformations, the interdependency of topology and rheology will become more clear. Although we have not yet performed dynamic simulations on infinite suspensions, our work paves the way for such studies. Since the positioning of the fibres in a composite greatly affects its properties—heat conduction may be favored in the direction of alignment of the threads, for instance—and because this microstructure is determined under dynamic (flowing) conditions, the rheological properties of rod suspensions need to be understood before major advances can be made in the application of fibre composites to new and existing technologies. Theoretical investigations of this issue are just emerging and restricted to very dilute dispersions.† Dynamic simulations offer a valuable alternative.

Solid-liquid suspensions also occur in a variety of other circumstances, and the methods developed in this work pertain to most of them. The "particles" may be sub-micron sized such as the molecular constituents of liquid crystals (which are generally composed of elongated rigid polymers in a suitable solvent), or quite large, such as the splinters in the slurries generated during the production of paper from pulp. In all instances, hydrodynamic interactions play a dominant role in determining the macroscopic behavior, and these are the focus of the present study. If the rods are fixed rather than moving with the fluid, the approach described

† We are aware of current research by A. Szeri & L.G. Leal on that subject.

in the thesis allows one to evaluate the properties of fibrous media (specifically, the permeability and the hindered diffusion coefficients). This work is therefore also relevant to the study of filters and membranes. It may also help quantify the contributions from viscous effects in gel chromatography and electrophoresis. The accent, however, lies on the development and validation of the simulation technique. Most applications are left for future work. We do, however, report on the hydrodynamic transport properties of crystalline configurations and equilibrium structures of prolate spheroids (Ch. IV).

Several key model assumptions are made throughout the dissertation. The particles are rigid non-Brownian prolate spheroids unless stated otherwise (except in Ch. II). Their dynamics are taken to be representative, at least qualitatively, of most rod-like objects, but their axisymmetry simplifies the mathematical analysis considerably. The suspending fluid is incompressible and Newtonian, and sufficiently viscous for inertial effects to be negligible on the length scale of the particle (i.e., the Reynolds number, based on the dimensions of the fibres, approaches zero). The usual "no-slip" boundary condition is assumed at the contact surface between the liquid and the spheroids. We further suppose that the characteristic rate of deformation is sufficiently slow for the motion to be quasi-stationary. Finally, solid boundaries are absent in the simulation; we either imagine a few particles in a vast liquid domain, or a dispersion of infinite extent. This is a significant restriction, because wall effects are believed to be important in many practical situations. However, our simulations, by focussing on the "bulk" properties, in effect analyze the proper constitutive equation for the composite material. Particle slip at the walls, and wall induced alignment, if real, can then be incorporated in continuum models as boundary conditions.

The chapters are arranged in order of increasing complexity. The lubrication interactions between two isolated particles are analyzed first. Chapter III then describes the dynamics of a finite number of spheroids in an unbounded Stokes flow. We extend the method to suspensions containing infinitely many particles in Ch. IV,

but report data for the short-time limit of the hydrodynamic transport properties only. Some aspects regarding dynamic simulations of unbounded dispersions are then addressed in the last chapter. The complexity of the particle shape, on the contrary, lessens as one progresses through this work. The formulae of Ch. II are derived for arbitrary surfaces (the only restriction being that they cannot touch at more than one point when brought into contact). Chapters III and IV concern prolate spheroids, or, in some sections, triaxial ellipsoids. The final chapter makes abstraction of the particles and considers them as points —a few results for spheres are also quoted.

The very large and localized stresses experienced by almost touching particles in relative motion dominate the rheological behavior of dense dispersions. These so-called lubrication interactions cause the stress response to a straining field to diverge as the maximum packing fraction is attained, and dramatically reduce the mobility of particles at high concentrations. In flowing suspensions, they prevent particles from overlapping and provide the connectivity needed for efficient stress transfer via particle clusters. Because of their importance, Ch. II is dedicated exclusively to the study of lubrication interactions. Expressions are derived to $O(\epsilon^0)$ for the force, torque and stresslet exerted by two close rigid surfaces of arbitrary shape in arbitrary relative motion. (The symbol $\epsilon$ represents the minimum separation between the surfaces. The stresslet, which is defined in the next chapter, is germane to the viscosity of suspensions (see §4.5).) The formulae given in Ch. II relate the first two moments of the stress density on the particle surfaces to their relative velocities and to the externally imposed rate-of-strain. They suffice to construct the grand resistance tensor for any system of two almost touching bodies. They capture all the singular components of the stress at contact. In particular, we show that forces and torques that diverge logarithmically with decreasing surface separation can arise due to curvature of more than second order.

Chapter III describes the simulation method for a finite number of prolate spheroids in an unbounded fluid. The fundamental concepts of Stokesian dynam-

ics (Brady & Bossis, 1988) are introduced, and the theoretical framework of the technique is rigorously defined. The general procedure is then applied to ellipsoids; the construction of the grand mobility tensor is thoroughly explained in the special case of prolate spheroids. An efficient algorithm for the accurate determination of the points of closest approach of two ellipsoids at arbitrary separations and at any relative orientation is sketched, and its advantages for the calculation of lubrication interactions is emphasized. To conclude the chapter, we illustrate the importance of hydrodynamic interactions by means of a few examples. Comparisons with other numerical techniques for Stokes flow show that our approach is both accurate and efficient.

The procedure developed in Ch. III is adapted for unbounded dispersions in Ch. IV. The difficulties associated with the long-ranged nature of hydrodynamic interactions at zero Reynolds number are clarified, and a renormalization technique due to O'Brien (1979) is used to obtain an absolutely convergent formulation of the solution. Numerical aspects of the simulation method, which become quite intricate for infinite systems, are discussed in a separate section. The practical implementation of the Ewald summation technique in particular is examined in detail. We then report simulation data for the short-time limit of the hydrodynamic transport properties (sedimentation rates, self-diffusivities, viscosity, permeability and hindered diffusion coefficients) for two classes of dispersions: crystalline configurations, characterized by perfect order, and equilibrium structures, which are random at low densities, but become nematic at higher volume fractions (in agreement with thermodynamic predictions (Onsager, 1949) and molecular dynamics simulations (Frenkel *et al.*, 1985)). The variation of the macroscopic characteristics of the suspension with concentration, their dependence on the aspect ratio of the particles, and the influence of the dispersion microstructure on the properties are systematically investigated and discussed. The results are compared with experimental measurements available in the literature. The long-time limit of the transport properties is not calculated, since it can only be accessed by dynamic simulations, in which the

microstructure of the dispersion evolves under action of the imposed velocity field. This type of study has not yet been performed for dispersions of infinite extent.

The last chapter deals with unit cells suited for dynamic simulations of unbounded dispersions. We first define a standard shape for the simulation box which facilitates geometric operations such as the search for nearest neighbors. The kinematic compatibility of unit cells with pure straining flows is examined next. An infinite family of admissible basis vectors is found for planar extension. For uniaxial stretching flows, we demonstrate the non-existence of self-reproducing lattices. Using a theorem from the geometry of numbers, we are able, however, to deduce a unit cell which accepts the maximum packing fraction of spheres tolerable under these flow conditions. The issue of strain periodicity in general three-dimensional pure straining flows is also resolved. The implications for dynamic simulations are briefly discussed.

## References

Batchelor, G.K. (1971) The stress generated in a non-dilute suspension of elongated particles by pure straining motion, *J. Fluid Mech.* **46**, 813-829.

Brady, J.F. & Bossis, G. (1988) Stokesian dynamics, *Ann. Rev. Fluid Mech.* **20**, 111-157.

Claeys, I.L. (1988) *Experimental and numerical study of molecular rotational diffusion in gel-like media.* M.S. thesis, California Institute of Technology, 40 pp.

Claeys, I.L. & Arnold, F.H. (1989) Nuclear magnetic relaxation study of hindered rotational diffusion in gels, *A.I.Ch.E. Journal* **35**, 335-337.

Dinh, S.M. & Armstrong, R.C. (1984) A rheological equation of state for semiconcentrated fiber suspensions, *J. Rheol.* **28**, 207-227.

Fesciyan, S. & Dahler, J.S. (1982) Screened hydrodynamic interactions in a semidilute solution of rodlike macromolecules, *Macromol.* **15**, 517-520.

Fredrickson, G.H. & Shaqfeh, E.S.G. (1989) Heat and mass transport in composites of aligned slender fibers, *Phys. Fluids A***1**, 3-20.

Frenkel, D., Mulder, B.M. & McTague, J.P. (1984) Phase diagram of a system of hard ellipsoids, *Phys. Rev. Lett.* **52**, 287-290.

Muthukumar, M. & Edwards, S.F. (1983) Screening of hydrodynamic interaction in a solution of rodlike macromolecules, *Macromol.* **16**, 1475-1478.

O'Brien, R.W. (1979) A method for the calculation of the effective transport properties of suspensions of interacting particles, *J. Fluid Mech.* **91**, 17-39.

Onsager, L. (1949) The effects of shape on the interaction of colloidal particles, *Ann. N.Y. Acad. Sci.* **51**, 627-659.

Shaqfeh, E.S.G. (1988) A non local theory for the heat transport in composites containing highly conducting fibrous inclusions, *Phys. Fluids* **31**, 2405-2425.

Shaqfeh, E.S.G. & Fredrickson, G.H. (1990) The hydrodynamic stress in a suspension of rods, *Phys. Fluids A***2**, 7-24.

# Chapter II
# Grand resistance tensor for two arbitrary almost touching particles

## 2.1 Introduction

The large pressure produced in the thin fluid layer between a rotating shaft and its bearing allow it to support heavy loads. This common application illustrates the importance of lubrication forces, which occur whenever two immersed surfaces near contact are in relative motion. It is a well-known result of low-Reynolds-number hydrodynamics that the force required to push these two surfaces together diverges as the surface separation becomes vanishingly small. Thus, two particles subject to finite attractive forces cannot, in theory, come into contact. In practice, surface roughness, the compressibility of the solid surfaces or of the fluid, and other considerations play a role when the gap width reaches extremely small dimensions, but nonetheless, lubrication theory is a very useful continuum-mechanical approximation to the fluid forces influencing relative motion. Also, as alluded to in Ch. I, lubrication stresses dominate the rheological response of concentrated suspensions and dramatically affect their dynamics.

Lubrication theory is essentially an asymptotic method for flow problems involving very narrow channels. The results are usually expressed as expansions in the smallest dimension of the flow domain. In this chapter, the dominant terms, to $O(1)$, are calculated for the forces, torques and stresslets exerted by two surfaces moving in close proximity of each other. The formulae are presented in the framework of low-Reynolds-number hydrodynamics, where the linearity of the governing equations implies the existence of a so-called mobility tensor relating the particle velocities to their stress moments. This tensor, which depends on the instantaneous configuration of the system only, is symmetric and positive definite (Brenner, 1963).

Its inverse, relating the stress moments to the velocities, is called the resistance tensor. Its symmetry properties are often referred to as Lorentz' reciprocal theorem (*cf.* Appendix B).

For the purpose of accurate and efficient computer simulations of many-body low-Reynolds-number flow problems, the method known as Stokesian dynamics (Brady & Bossis, 1988; see also Ch. III) extends the formalism of the resistance and mobility tensors to include the effects of an imposed linear flow field. The expanded tensor is called the "grand" resistance tensor. The good agreement between experiment and numerical data obtained by Stokesian dynamics for the hydrodynamic transport properties of hard-sphere dispersions (Phillips *et al.*, 1988) confirms that the method not only captures the essential physics, but is also quantitatively accurate for volume fractions ranging from the dilute limit up to very high packing densities (Ladd, 1990). The importance of lubrication interactions is demonstrated by the fact that suppressing them in the computation results in a failure to reproduce experimental data at moderate and high concentrations. Phillips *et al.* (1988) also showed that including higher order moments in the multipole expansion for the force density on the particle surfaces (see Ch. III) improves the reliability of the simulation method, but they found that a truncation at the stresslet level is satisfactory for most purposes. In order to apply the methodology of Stokesian dynamics to particulate geometries other than spheres, it is necessary to know the forces, torques and stresslets exerted by such particles when placed very near to each other in an arbitrary linear flow or when near contact and moving with respect to each other in an arbitrary fashion. The appropriate resistance factors are derived analytically in this work for any two curved surfaces near contact. The formulae are accurate to $O(1)$ in the surface separation. The contributions from an imposed straining field are included in the calculation, and stresslets, which are often omitted, are evaluated. Higher stress moments are not considered because they are seldom necessary for the evaluation of physical quantities. It should also be obvious from section 2.1.2 that they are less singular than the first two stress

moments and therefore less important.

The present analysis is a complement to the work of Cox (1974), who approximated the geometry of the almost touching surfaces by quadratics at the point of minimum separation. Cox recognized that this level of approximation is insufficient if one wishes to calculate the leading order behavior of all the forces and torques for arbitrary prescribed motions of the surfaces. He indicated that a more detailed description of the particles' shape, retaining features on a finer scale than the principal radii of curvature at the point of closest approach, is necessary to find some of the resistance factors. It is obvious that $O(1)$ contributions to the stress moments can only be computed if the entire shape of the particle is known, rather than just its local features near the point of minimum separation. However, as stated by Cox (1974), even the calculation of a few logarithmically "singular" forces requires a more complete knowledge of the surfaces' geometry. The terms "singular" and "divergent" will be used in this context to describe any quantity that becomes unbounded as the surface separation goes to zero. Cox also showed that the first order correction to the force required for motion of the bodies along their common normal is itself singular, and that its calculation requires that the surfaces be described with a greater accuracy than the one assumed by him. The present analysis has therefore been undertaken to extend Cox's results so as to correctly calculate all the divergent forces, torques, and stresslets for arbitrary relative motions of the surfaces. The singular resistance functions associated with imposed linear flows, which were not considered previously, are now derived. The approach followed in this work mirrors the approach taken by Cox (1974), and the notation is largely borrowed from his article. His results are, of course, also applicable here and they will simply be quoted to avoid redundancy.

In section 2.1.1, the problem at hand is formulated mathematically. The governing lubrication equations are derived in §2.1.2, and formulae for the stress moments sought are given in terms of rescaled variables. The sections 2.2-2.4 then discuss three separate classes of relative motion (covering all possibilities) which

give rise to different levels of singularities. For motion of the particles along their common normal (§2.2), the solution is subdivided into three parts, corresponding to an increasingly detailed description of the surfaces. The force, torque and stresslet exerted by deforming particles near contact are considered in section 2.5 in order to calculate the effects of a straining flow. Section 2.6 proceeds to construct the resistance tensor for a system of two arbitrary almost touching particles and demonstrates for a few selected elements that the results reported here satisfy Lorentz' reciprocal theorem. A comparison with published formulae for two spheres near contact is made in §2.7. These examples also illustrate some of the manipulations involved when the point of reference chosen for the stress moments and the velocity of the particle is changed. The conclusions in section 2.8 summarize the main features of this chapter.

### 2.1.1 Statement of the problem

Consider two rigid surfaces $W$ and $W'$ moving in a Newtonian fluid of viscosity $\mu$. The minimum distance $\grave{\epsilon}$ between the two walls is assumed to be small compared to the radii of curvature of the surfaces at the point of minimum separation. It is further assumed that contact would occur only at a single point if the particles were brought together in their current relative orientation. The fluid in the gap is incompressible and the Reynolds number (based on the gap width) is so small that inertial effects may be neglected. The creeping flow equations are therefore applicable. From lubrication theory, one expects very high pressures in the gap, leading to singular behavior of the stress tensor when the particles' separation becomes vanishingly small. In the present chapter, the leading terms in the expansion for small $\grave{\epsilon}$ of the hydrodynamic force, torque and stresslet acting on these surfaces are found for any prescribed motion of the particles. From these results, the resistance tensor for a system of two arbitrary bodies near contact can be constructed accurate to $O(\epsilon^0)$.

The governing equations for this problem read:

$$\grave{\mu}\nabla^2\grave{\mathbf{u}} = \nabla\grave{p}\ , \tag{2.1a}$$

$$\nabla\cdot\grave{\mathbf{u}} = 0\ . \tag{2.1b}$$

A cartesian frame of reference $(\grave{x}_1, \grave{x}_2, \grave{x}_3)$ centered on $W$ at the point of closest approach $O$ is used to describe the instantaneous geometry of the particles (Fig.2.1). The $\grave{x}_3$ axis is chosen along the line of minimum separation, i.e., normal to both surfaces, and pointing toward $W'$. The $\grave{x}_1$ and $\grave{x}_2$ axes are tangent to the surface $W$ but otherwise arbitrary. For example, they can be taken in the directions of principal curvature of the surface $W$ at $O$.

The surface $W$ can then be locally described by an equation of the form

$$\grave{x}_3 = -\frac{\grave{x}_1^2}{2\grave{R}_1} - \frac{\grave{x}_2^2}{2\grave{R}_2} - \sum_{i=0}^{3}\grave{\Gamma}_i\grave{x}_1^{3-i}\grave{x}_2^i - \sum_{i=0}^{4}\grave{\Upsilon}_i\grave{x}_1^{4-i}\grave{x}_2^i + O(\grave{r}^5)\ , \tag{2.2a}$$

with $\grave{r} = (\grave{x}_1^2 + \grave{x}_2^2)^{\frac{1}{2}}$ small. $\grave{R}_1$ and $\grave{R}_2$ are the principal radii of curvature of the surface $W$ at $O$, while the coefficients $\grave{\Gamma}_i$ and $\grave{\Upsilon}_i$ depend on the finer details of the local shape of $W$ near $O$. The labels "1" and "2" are assigned to the radii of curvature such that the set of coordinates $(\grave{x}_1, \grave{x}_2, \grave{x}_3)$ defines a right-handed frame of reference.

Similarly, one can choose a second cartesian coordinate system $(\grave{x}_1', \grave{x}_2', \grave{x}_3')$ centered at the point of closest approach $O'$ on $W'$, with the $\grave{x}_3'$ axis coincident with the $\grave{x}_3$ axis and the other two axes along the directions of the principal curvature of $W'$ at $O'$ (Fig. 2.1). The surface $W'$ is then given by

$$\grave{x}_3' = \frac{\grave{x}_1'^2}{2\grave{R}_1'} + \frac{\grave{x}_2'^2}{2\grave{R}_2'} + \sum_{i=0}^{3}\grave{\Gamma}_i'\grave{x}_1'^{3-i}\grave{x}_2'^i + \sum_{i=0}^{4}\grave{\Upsilon}_i'\grave{x}_1'^{4-i}\grave{x}_2'^i + O(\grave{r}'^5)\ , \tag{2.2b}$$

for small $\grave{r}' = (\grave{x}_1'^2 + \grave{x}_2'^2)^{\frac{1}{2}}$.

If $\phi$ is the angle between the $\grave{x}_1$ and the $\grave{x}_1'$ axes, the relation between both coordinate systems reads:

$$\grave{x}_1' = \grave{x}_1\cos\phi + \grave{x}_2\sin\phi, \qquad \grave{x}_2' = -\grave{x}_1\sin\phi + \grave{x}_2\cos\phi, \qquad \grave{x}_3' = \grave{x}_3 - \grave{\epsilon}\ . \tag{2.3}$$

Therefore, the surface $W'$ can also be written in the form:

$$\grave{x}_3 = \grave{\epsilon} + \sum_{i=0}^{2} \grave{\mathcal{B}}_i \grave{x}_1^{2-i} \grave{x}_2^i + \sum_{i=0}^{3} \grave{\beta}_i \grave{x}_1^{3-i} \grave{x}_2^i + \sum_{i=0}^{4} \grave{b}_i \grave{x}_1^{4-i} \grave{x}_2^i + O(\grave{r}^5) \ , \tag{2.4a}$$

where for example

$$\grave{\mathcal{B}}_0 = \frac{\cos^2\phi}{2\grave{R}_1'} + \frac{\sin^2\phi}{2\grave{R}_2'}, \qquad \grave{\mathcal{B}}_1 = \left(\frac{1}{\grave{R}_1'} - \frac{1}{\grave{R}_2'}\right)\sin\phi\cos\phi, \qquad \grave{\mathcal{B}}_2 = \frac{\sin^2\phi}{2\grave{R}_1'} + \frac{\cos^2\phi}{2\grave{R}_2'} \ . \tag{2.4b}$$

If the velocities of the points $O$ and $O'$ are given by $\grave{\mathbf{U}}$ and $\grave{\mathbf{U}}'$ respectively, and the angular velocities of the surfaces $W$ and $W'$ are $\grave{\mathbf{\Omega}}$ and $\grave{\mathbf{\Omega}}'$ respectively, the no-slip boundary conditions for this problem may be written as

$$\grave{\mathbf{u}} = \grave{\mathbf{U}} + \grave{\mathbf{\Omega}} \wedge \grave{\mathbf{r}}_W \qquad \text{on } W, \tag{2.5a}$$

with, of course, $\grave{\mathbf{r}}_W = (\grave{x}_1, \grave{x}_2, \grave{x}_{3W})$, $\grave{x}_{3W}$ being given by (2.2a). Similarly,

$$\grave{\mathbf{u}} = \grave{\mathbf{U}}' + \grave{\mathbf{\Omega}}' \wedge \grave{\mathbf{r}}_{W'}' \qquad \text{on } W', \tag{2.5b}$$

where $\grave{\mathbf{r}}_{W'}' = (\grave{x}_1, \grave{x}_2, \grave{x}_{3W'} - \grave{\epsilon})$, $\grave{x}_{3W'}$ now being given by (2.4).

The variables are non-dimensionalized using the scaling typical of viscous flow:

$$\grave{\mathbf{r}} = \grave{R}_c \mathbf{r} \ , \qquad \grave{\mathbf{u}} = \grave{U}_c \mathbf{u} \ , \qquad \grave{p} = \frac{\grave{\mu}\grave{U}_c}{\grave{R}_c} p \ , \tag{2.6}$$

with $\grave{R}_c^{-1} = (\grave{R}_1^{-1} + \grave{R}_2^{-1} + \grave{R}_1'^{-1} + \grave{R}_2'^{-1})/4$, and the characteristic velocity $\grave{U}_c = \left(|\grave{\mathbf{\Omega}} - \grave{\mathbf{\Omega}}'|\grave{R}_c + |\grave{\mathbf{U}} - \grave{\mathbf{U}}'|\right)/2$. Of course, other dimensional variables such as $\grave{x}_i$, $\grave{R}_1$, $\grave{\Upsilon}_i$, etc., must be made dimensionless accordingly and are denoted by the corresponding symbols without accent. In particular, the non-dimensional gap width $\epsilon$ is defined by $\epsilon = \grave{\epsilon}/\grave{R}_c$.

### 2.1.2 Method of solution

As usual for this type of geometry, the lubrication hypothesis is invoked, and the velocity and pressure fields $(\mathbf{u}, p)$ are expanded in terms of the small parameter $\epsilon$.

In the inner region, the coordinates need to be stretched depending on the gap width. The correct scaling is derived by Cox (1974). From the expressions (2.2a) and (2.4) for the surfaces, one easily obtains

$$\tilde{x}_1 = \epsilon^{-\frac{1}{2}} x_1 \ , \qquad \tilde{x}_2 = \epsilon^{-\frac{1}{2}} x_2 \ , \qquad \tilde{x}_3 = \epsilon^{-1} x_3 \ , \tag{2.7a}$$

and from the equations of motion, it follows that

$$\tilde{u}_1 = \epsilon^{(1/2-k)} u_1 \ , \qquad \tilde{u}_2 = \epsilon^{(1/2-k)} u_2 \ , \qquad \tilde{u}_3 = \epsilon^{-k} u_3 \ , \qquad \tilde{p} = \epsilon^{(2-k)} p \ . \tag{2.7b}$$

The exponent "$k$" is a constant to be determined from the boundary conditions (see below). The surfaces $W$ and $W'$ are now respectively given by:

$$\tilde{x}_3 = -\frac{\tilde{x}_1^2}{2R_1} - \frac{\tilde{x}_2^2}{2R_2} - \epsilon^{1/2} \sum_{i=0}^{3} \Gamma_i \tilde{x}_1^{3-i} \tilde{x}_2^i - \epsilon \sum_{i=0}^{4} \Upsilon_i \tilde{x}_1^{4-i} \tilde{x}_2^i + O(\epsilon^{3/2} \tilde{r}^5) \ , \tag{2.8a}$$

$$\tilde{x}_3 = 1 + \sum_{i=0}^{2} \mathcal{B}_i \tilde{x}_1^{2-i} \tilde{x}_2^i + \epsilon^{1/2} \sum_{i=0}^{3} \beta_i \tilde{x}_1^{3-i} \tilde{x}_2^i + \epsilon \sum_{i=0}^{4} b_i \tilde{x}_1^{4-i} \tilde{x}_2^i + O(\epsilon^{3/2} \tilde{r}^5) \ . \tag{2.8b}$$

In order to cast the boundary conditions into a more convenient form, a set of non-orthogonal curvilinear coordinates defined by

$$\bar{x}_1 = \tilde{x}_1, \qquad \bar{x}_2 = \tilde{x}_2, \qquad \bar{x}_3 = \tilde{x}_3 + \frac{\tilde{x}_1^2}{2R_1} + \frac{\tilde{x}_2^2}{2R_2} + \epsilon^{1/2} \sum_{i=0}^{3} \Gamma_i \tilde{x}_1^{3-i} \tilde{x}_2^i + \epsilon \sum_{i=0}^{4} \Upsilon_i \tilde{x}_1^{4-i} \tilde{x}_2^i \tag{2.9}$$

is used to square-up the geometry. The walls $W$ and $W'$ are then described by:

$$\bar{x}_3 = O(\epsilon^{3/2} \bar{r}^5) \qquad \text{on } W, \tag{2.10a}$$

and

$$\begin{aligned} \bar{x}_3 = 1 &+ \Big(\mathcal{B}_0 + 1/(2R_1)\Big) \bar{x}_1^2 + \mathcal{B}_1 \bar{x}_1 \bar{x}_2 + \Big(\mathcal{B}_2 + 1/(2R_2)\Big) \bar{x}_2^2 \\ &+ \epsilon^{1/2} \sum_{i=0}^{3} (\beta_i + \Gamma_i) \bar{x}_1^{3-i} \bar{x}_2^i + \epsilon \sum_{i=0}^{4} (b_i + \Upsilon_i) \bar{x}_1^{4-i} \bar{x}_2^i + O(\epsilon^{3/2} \bar{r}^5) \\ = h_z(\bar{x}_1, \bar{x}_2) &+ \epsilon^{1/2} h_h(\bar{x}_1, \bar{x}_2) + \epsilon h_\epsilon(\bar{x}_1, \bar{x}_2) + O(\epsilon^{3/2} \bar{r}^5) \qquad \text{on } W'. \end{aligned} \tag{2.10b}$$

In this new coordinate system, the Stokes equations of motion take the following form, accurate to $O(\epsilon)$:†

$$\frac{\partial^2\tilde{u}_1}{\partial\bar{x}_3^2}+\epsilon\Bigg\{\frac{\partial^2\tilde{u}_1}{\partial\bar{x}_1^2}+\frac{\partial^2\tilde{u}_1}{\partial\bar{x}_2^2}+\frac{2\bar{x}_1}{R_1}\frac{\partial^2\tilde{u}_1}{\partial\bar{x}_1\partial\bar{x}_3}+\frac{2\bar{x}_2}{R_2}\frac{\partial^2\tilde{u}_1}{\partial\bar{x}_2\partial\bar{x}_3}$$
$$+\Big(\frac{1}{R_1}+\frac{1}{R_2}\Big)\frac{\partial\tilde{u}_1}{\partial\bar{x}_3}+\Big(\frac{\bar{x}_1^2}{R_1^2}+\frac{\bar{x}_2^2}{R_2^2}\Big)\frac{\partial^2\tilde{u}_1}{\partial\bar{x}_3^2}\Bigg\} \tag{2.11a}$$
$$=\frac{\partial\tilde{p}}{\partial\bar{x}_1}+\frac{\bar{x}_1}{R_1}\frac{\partial\tilde{p}}{\partial\bar{x}_3}+\epsilon^{\frac{1}{2}}\sum_{i=0}^{2}(3-i)\Gamma_i\bar{x}_1^{2-i}\bar{x}_2^i\frac{\partial\tilde{p}}{\partial\bar{x}_3}+\epsilon\sum_{i=0}^{3}(4-i)\Upsilon_i\bar{x}_1^{3-i}\bar{x}_2^i\frac{\partial\tilde{p}}{\partial\bar{x}_3}\ ,$$

$$\frac{\partial^2\tilde{u}_2}{\partial\bar{x}_3^2}+\epsilon\Bigg\{\frac{\partial^2\tilde{u}_2}{\partial\bar{x}_1^2}+\frac{\partial^2\tilde{u}_2}{\partial\bar{x}_2^2}+\frac{2\bar{x}_1}{R_1}\frac{\partial^2\tilde{u}_2}{\partial\bar{x}_1\partial\bar{x}_3}+\frac{2\bar{x}_2}{R_2}\frac{\partial^2\tilde{u}_2}{\partial\bar{x}_2\partial\bar{x}_3}$$
$$+\Big(\frac{1}{R_1}+\frac{1}{R_2}\Big)\frac{\partial\tilde{u}_2}{\partial\bar{x}_3}+\Big(\frac{\bar{x}_1^2}{R_1^2}+\frac{\bar{x}_2^2}{R_2^2}\Big)\frac{\partial^2\tilde{u}_2}{\partial\bar{x}_3^2}\Bigg\} \tag{2.11b}$$
$$=\frac{\partial\tilde{p}}{\partial\bar{x}_2}+\frac{\bar{x}_2}{R_2}\frac{\partial\tilde{p}}{\partial\bar{x}_3}+\epsilon^{\frac{1}{2}}\sum_{i=1}^{3}i\Gamma_i\bar{x}_1^{3-i}\bar{x}_2^{i-1}\frac{\partial\tilde{p}}{\partial\bar{x}_3}+\epsilon\sum_{i=1}^{4}i\Upsilon_i\bar{x}_1^{4-i}\bar{x}_2^{i-1}\frac{\partial\tilde{p}}{\partial\bar{x}_3}\ ,$$

$$\epsilon\frac{\partial^2\tilde{u}_3}{\partial\bar{x}_3^2}=\frac{\partial\tilde{p}}{\partial\bar{x}_3}\ , \tag{2.11c}$$

and the continuity equation becomes

$$\frac{\partial\tilde{u}_1}{\partial\bar{x}_1}+\frac{\partial\tilde{u}_2}{\partial\bar{x}_2}+\frac{\partial\tilde{u}_3}{\partial\bar{x}_3}+\frac{\bar{x}_1}{R_1}\frac{\partial\tilde{u}_1}{\partial\bar{x}_3}+\frac{\bar{x}_2}{R_2}\frac{\partial\tilde{u}_2}{\partial\bar{x}_3}+\epsilon^{1/2}\Bigg\{\sum_{i=0}^{2}(3-i)\Gamma_i\bar{x}_1^{2-i}\bar{x}_2^i\frac{\partial\tilde{u}_1}{\partial\bar{x}_3} \tag{2.11d}$$
$$+\sum_{i=1}^{3}i\Gamma_i\bar{x}_1^{3-i}\bar{x}_2^{i-1}\frac{\partial\tilde{u}_2}{\partial\bar{x}_3}\Bigg\}+\epsilon\Bigg\{\sum_{i=0}^{3}(4-i)\Upsilon_i\bar{x}_1^{3-i}\bar{x}_2^i\frac{\partial\tilde{u}_1}{\partial\bar{x}_3}+\sum_{i=1}^{4}i\Upsilon_i\bar{x}_1^{4-i}\bar{x}_2^{i-1}\frac{\partial\tilde{u}_2}{\partial\bar{x}_3}\Bigg\}=0\ .$$

This set of equations is solved for $\mathbf{u}$ and $p$ using an expansion of the form

$$\mathbf{u}=\mathbf{u}_z+\epsilon^{1/2}\mathbf{u}_h+\epsilon\mathbf{u}_\epsilon+\ldots \qquad \text{and} \qquad p=p_z+\epsilon^{1/2}p_h+\epsilon p_\epsilon+\ldots \tag{2.12}$$

† It is also possible to work with the formalism of covariant and contravariant components; this is not necessary, however, and the method employed here follows the original work by Cox (1974) more closely. Note also that the velocity vector $\mathbf{u}$ is still projected onto the Cartesian set of coordinates $(\tilde{x}_1,\tilde{x}_2,\tilde{x}_3)$ even though one works in the curvilinear frame $(\bar{x}_1,\bar{x}_2,\bar{x}_3)$.

The rescaled and non-dimensionalized boundary conditions (2.5) applicable at the surface $W$ now read:

$$u_1 = \epsilon^{-k+\frac{1}{2}}\left\{U_1 - \epsilon^{\frac{1}{2}}\Omega_3\bar{x}_2 - \epsilon\Omega_2\left\{\frac{\bar{x}_1^2}{2R_1} + \frac{\bar{x}_2^2}{2R_2} + \epsilon^{\frac{1}{2}}\sum_{i=0}^{3}\Gamma_i\bar{x}_1^{3-i}\bar{x}_2^i + \epsilon\sum_{i=0}^{4}\Upsilon_i\bar{x}_1^{4-i}\bar{x}_2^i\right\}\right\}, \tag{2.13a}$$

$$u_2 = \epsilon^{-k+\frac{1}{2}}\left\{U_2 + \epsilon^{\frac{1}{2}}\Omega_3\bar{x}_1 + \epsilon\Omega_1\left\{\frac{\bar{x}_1^2}{2R_1} + \frac{\bar{x}_2^2}{2R_2} + \epsilon^{\frac{1}{2}}\sum_{i=0}^{3}\Gamma_i\bar{x}_1^{3-i}\bar{x}_2^i + \epsilon\sum_{i=0}^{4}\Upsilon_i\bar{x}_1^{4-i}\bar{x}_2^i\right\}\right\}, \tag{2.13b}$$

$$u_3 = \epsilon^{-k}\left\{U_3 + \epsilon^{1/2}(\Omega_1\bar{x}_2 - \Omega_2\bar{x}_1)\right\}, \tag{2.13c}$$

and, at the surface $W'$:

$$u_1 = \epsilon^{-k+\frac{1}{2}}\left\{U_1' - \epsilon^{\frac{1}{2}}\Omega_3'\bar{x}_2 - \epsilon\Omega_2'\Big(h_z(\bar{x}_1,\bar{x}_2) - 1 + \epsilon^{\frac{1}{2}}h_h(\bar{x}_1,\bar{x}_2) + \epsilon h_\epsilon(\bar{x}_1,\bar{x}_2)\Big)\right\}, \tag{2.14a}$$

$$u_2 = \epsilon^{-k+\frac{1}{2}}\left\{U_2' + \epsilon^{\frac{1}{2}}\Omega_3'\bar{x}_1 + \epsilon\Omega_1'\Big(h_z(\bar{x}_1,\bar{x}_2) - 1 + \epsilon^{\frac{1}{2}}h_h(\bar{x}_1,\bar{x}_2) + \epsilon h_\epsilon(\bar{x}_1,\bar{x}_2)\Big)\right\}, \tag{2.14b}$$

$$u_3 = \epsilon^{-k}\left\{U_3' + \epsilon^{1/2}(\Omega_1'\bar{x}_2 - \Omega_2'\bar{x}_1)\right\}. \tag{2.14c}$$

From the linearity of the creeping flow equations and of the boundary conditions, it can be seen that the problem at hand can be subdivided into three distinct cases characterized by different values of "$k$" and corresponding to different non-zero components of the prescribed motions of the walls $W$ and $W'$. The flow resulting from $U_3$ and/or $U_3'$ requires $k = 0$, as should be obvious from (2.13c) and (2.14c). It will be discussed first, and will be referred to as a "direct approach" of the surfaces. Second, $k = 1/2$ for non-zero values of $U_1, U_2, U_1', U_2', \Omega_1, \Omega_2, \Omega_1'$ or $\Omega_2'$. This represents a tangential or rolling motion of the surfaces. Finally, if $\Omega_3$ or $\Omega_3'$ differ from zero (i.e., the particles rotate around their common normal), $k = 1$ gives the correct scaling.

Before proceeding with the solution of the problem, the expressions for the dimensionless force, torque and stresslet on the wall $W$ should be considered. Let

$\mathbf{n}$ be the unit normal to the surface $W$, pointing into the fluid, so that the force $\mathbf{F}$, the torque $\mathbf{T}$ and the stresslet $\mathbf{S}$ exerted by the particle on the fluid about the point $O$ are defined as

$$\mathbf{F} = -\int_W \boldsymbol{\sigma}\cdot \mathrm{d}\mathbf{W} \ , \qquad \mathbf{T} = -\int_W \mathbf{r}_w \wedge \boldsymbol{\sigma}\cdot \mathrm{d}\mathbf{W} \ , \tag{2.15a}$$

$$\mathbf{S} = -\frac{1}{2}\int_W \Big(\mathbf{r}_w\boldsymbol{\sigma} + (\boldsymbol{\sigma}\mathbf{r}_w)^T - \frac{2}{3}\mathbf{I}\mathbf{r}_w\cdot\boldsymbol{\sigma}\Big)\cdot \mathrm{d}\mathbf{W} \ , \tag{2.15b}$$

with $\mathrm{d}\mathbf{W} = \mathbf{n}\mathrm{d}W$ an infinitesimal surface element of the wall $W$ and the stress

$$\boldsymbol{\sigma} = -p\mathbf{I} + \nabla\mathbf{u} + \nabla\mathbf{u}^T \ . \tag{2.16}$$

The unit normal $\mathbf{n}$ is given by

$$\mathbf{n} = \frac{\nabla f_w}{|\nabla f_w|} \ , \tag{2.17a}$$

where $f_w(\mathbf{x}) = 0$ defines the surface $W$. It is apparent from (2.2a) that, to $O(r^4)$,

$$\nabla f_w = \Big[\frac{x_1}{R_1} + \sum_{i=0}^{2}\Gamma_i(3-i)x_1^{2-i}x_2^i + \sum_{i=0}^{3}\Upsilon_i(4-i)x_1^{3-i}x_2^i\Big]\mathbf{e}_1 \tag{2.17b}$$

$$+ \Big[\frac{x_2}{R_2} + \sum_{i=1}^{3} i\Gamma_i x_1^{3-i}x_2^{i-1} + \sum_{i=1}^{4} i\Upsilon_i x_1^{4-i}x_2^{i-1}\Big]\mathbf{e}_2 + \mathbf{e}_3 \ .$$

Here, $\mathbf{e}_1, \mathbf{e}_2$ and $\mathbf{e}_3$ are the unit base vectors corresponding to the coordinates $x_1, x_2$ and $x_3$ respectively.† The elementary surface area $\mathrm{d}W$ can be deduced by noting that $\mathbf{e}_3\cdot\mathrm{d}\mathbf{W} = \mathrm{d}x_1\mathrm{d}x_2$. Hence $\mathrm{d}W = \mathrm{d}x_1\mathrm{d}x_2/\mathbf{n}\cdot\mathbf{e_3} = |\nabla f_w|\mathrm{d}x_1\mathrm{d}x_2$.

The lubrication equations are valid only in a small domain $\Sigma_\varepsilon$ around the point of closest approach, where the gap is very narrow. Let this region be determined by requiring that the distance between the two surfaces must be smaller than some quantity $\epsilon + \varepsilon^2$ in $\Sigma_\varepsilon$ (the parameter $\varepsilon$ is independent of $\epsilon$). In terms of inner variables, the boundary of $\Sigma_\varepsilon$ thus becomes

$$h_z(\tilde{x}_1, \tilde{x}_2) = 1 + \epsilon^{-1}\varepsilon^2 \ . \tag{2.18}$$

† $\mathbf{e}_1$ and $\mathbf{e}_2$ are also the base vectors corresponding to the coordinates $\bar{x}_1$ and $\bar{x}_2$. The base vector associated with $\bar{x}_3$ is a combination of $\mathbf{e}_1, \mathbf{e}_2$ and $\mathbf{e}_3$. The reciprocal base vector corresponding to $\bar{x}_3$, however, is $\mathbf{e}_3$.

Since $\varepsilon$ is independent of $\epsilon$, it suffices to evaluate (2.15) over $\Sigma_\varepsilon$ to obtain the singular behavior of the force, torque and stresslet as $\epsilon \to 0$. The rest of the wall will give at most an $O(1)$ contribution.

The integrals over $\Sigma_\varepsilon$ can best be evaluated by expressing all quantities in inner variables: $\mathbf{r}_w = \epsilon^{\frac{1}{2}}\tilde{x}_1\mathbf{e}_1 + \epsilon^{\frac{1}{2}}\tilde{x}_2\mathbf{e}_2 + \epsilon\tilde{x}_{3w}\mathbf{e}_3$, where $\tilde{x}_{3w}$ is given by (2.8a), and similarly, $\mathrm{d}\mathbf{W} = \epsilon\mathbf{n}\mathrm{d}\tilde{x}_1\mathrm{d}\tilde{x}_2/\mathbf{n}\cdot\mathbf{e_3}$. Expanding $|\nabla f_w|$ in half-integral powers of $\epsilon$, one obtains

$$\mathbf{n} = \mathbf{e}_3 + \epsilon^{\frac{1}{2}}\Big\{\frac{\tilde{x}_1}{R_1}\mathbf{e}_1 + \frac{\tilde{x}_2}{R_2}\mathbf{e}_2\Big\} \tag{2.19}$$

$$+ \epsilon\Big\{\mathbf{e}_1\sum_{i=0}^{2}\Gamma_i(3-i)\tilde{x}_1^{2-i}\tilde{x}_2^i + \mathbf{e}_2\sum_{i=1}^{3}i\Gamma_i\tilde{x}_1^{3-i}\tilde{x}_2^{i-1} - \frac{\mathbf{e}_3}{2}\Big(\frac{\tilde{x}_1^2}{R_1^2} + \frac{\tilde{x}_2^2}{R_2^2}\Big)\Big\} + O(\epsilon^{\frac{3}{2}})\ .$$

The area of the elementary surface element $\mathrm{d}W$ then turns out to be

$$\mathrm{d}W = \epsilon\mathrm{d}\widetilde{W} = \epsilon\Big[1 + \frac{\epsilon}{2}\Big(\frac{\tilde{x}_1^2}{R_1^2} + \frac{\tilde{x}_2^2}{R_2^2}\Big)\Big]\,\mathrm{d}\tilde{x}_1\,\mathrm{d}\tilde{x}_2 + O(\epsilon^3)\ . \tag{2.20}$$

The components of the stress tensor are

$$\boldsymbol{\sigma}_{ii} = \epsilon^{k-2}\Big\{-\tilde{p} + 2\epsilon\frac{\partial\tilde{u}_i}{\partial\tilde{x}_i}\Big\} \qquad \text{for } i = 1, 2 \text{ or } 3\ , \tag{2.21a}$$

$$\boldsymbol{\sigma}_{12} = \boldsymbol{\sigma}_{21} = \epsilon^{k-1}\Big\{\frac{\partial\tilde{u}_1}{\partial\tilde{x}_2} + \frac{\partial\tilde{u}_2}{\partial\tilde{x}_1}\Big\}\ , \tag{2.21b}$$

$$\boldsymbol{\sigma}_{23} = \boldsymbol{\sigma}_{32} = \epsilon^{k-\frac{3}{2}}\Big\{\frac{\partial\tilde{u}_2}{\partial\tilde{x}_3} + \epsilon\frac{\partial\tilde{u}_3}{\partial\tilde{x}_2}\Big\}\ , \tag{2.21c}$$

$$\boldsymbol{\sigma}_{13} = \boldsymbol{\sigma}_{31} = \epsilon^{k-\frac{3}{2}}\Big\{\frac{\partial\tilde{u}_1}{\partial\tilde{x}_3} + \epsilon\frac{\partial\tilde{u}_3}{\partial\tilde{x}_1}\Big\}\ . \tag{2.21d}$$

Using rescaled variables, the leading terms of the expansions for the force, torque and stresslet exerted by the surface $W$ on the surrounding fluid then read, to $O(1)$†,

$$F_1 = -\int_{\Sigma_\varepsilon}\mathbf{e}_1\cdot\boldsymbol{\sigma}\cdot\mathrm{d}\mathbf{W} = \epsilon^{k-\frac{1}{2}}\int_{\Sigma_\varepsilon}\Big[\frac{\tilde{x}_1}{R_1}\tilde{p}_z - \frac{\partial\tilde{u}_{z1}}{\partial\tilde{x}_3}\Big]\,\mathrm{d}\tilde{x}_1\,\mathrm{d}\tilde{x}_2 \tag{2.22a}$$

$$+ \epsilon^k\int_{\Sigma_\varepsilon}\Big[\frac{\tilde{x}_1}{R_1}\tilde{p}_h - \frac{\partial\tilde{u}_{h1}}{\partial\tilde{x}_3} + \sum_{i=0}^{2}\Gamma_i(3-i)\tilde{x}_1^{2-i}\tilde{x}_2^i\tilde{p}_z\Big]\,\mathrm{d}\tilde{x}_1\,\mathrm{d}\tilde{x}_2$$

† The $O(1)$ error arises from neglecting that part of the surface not included in $\Sigma_\varepsilon$. For $k > 0$, some of the terms written in the expressions (2.22) are therefore superfluous, being negligibly small compared to the $O(1)$ error term.

$$F_2 = -\int_{\Sigma_\epsilon} \mathbf{e}_2 \cdot \boldsymbol{\sigma} \cdot \mathrm{d}\mathbf{W} = \epsilon^{k-\frac{1}{2}} \int_{\Sigma_\epsilon} \Big[\frac{\tilde{x}_2}{R_2}\tilde{p}_z - \frac{\partial \tilde{u}_{z2}}{\partial \tilde{x}_3}\Big]\,\mathrm{d}\tilde{x}_1\,\mathrm{d}\tilde{x}_2 \tag{2.22b}$$

$$+ \epsilon^k \int_{\Sigma_\epsilon} \Big[\frac{\tilde{x}_2}{R_2}\tilde{p}_h - \frac{\partial \tilde{u}_{h2}}{\partial \tilde{x}_3} + \sum_{i=1}^{3} i\Gamma_i x_1^{3-i}\tilde{x}_2^{i-1}\tilde{p}_z\Big]\,\mathrm{d}\tilde{x}_1\,\mathrm{d}\tilde{x}_2$$

$$F_3 = \epsilon^{k-1}\int_{\Sigma_\epsilon} \tilde{p}_z\,\mathrm{d}\tilde{x}_1\,\mathrm{d}\tilde{x}_2 + \epsilon^{k-\frac{1}{2}}\int_{\Sigma_\epsilon} \tilde{p}_h\,\mathrm{d}\tilde{x}_1\,\mathrm{d}\tilde{x}_2 \tag{2.22c}$$

$$+ \epsilon^k \int_{\Sigma_\epsilon} \Big[\tilde{p}_\epsilon - 2\frac{\partial \tilde{u}_{z3}}{\partial \tilde{x}_3} - \frac{\tilde{x}_1}{R_1}\frac{\partial \tilde{u}_{z1}}{\partial \tilde{x}_3} - \frac{\tilde{x}_2}{R_2}\frac{\partial \tilde{u}_{z2}}{\partial \tilde{x}_3}\Big]\,\mathrm{d}\tilde{x}_1\,\mathrm{d}\tilde{x}_2$$

$$T_1 = \epsilon^{k-\frac{1}{2}}\int_{\Sigma_\epsilon} \tilde{x}_2\tilde{p}_z\,\mathrm{d}\tilde{x}_1\,\mathrm{d}\tilde{x}_2 + \epsilon^k \int_{\Sigma_\epsilon} \tilde{x}_2\tilde{p}_h\,\mathrm{d}\tilde{x}_1\,\mathrm{d}\tilde{x}_2 \tag{2.23a}$$

$$T_2 = -\epsilon^{k-\frac{1}{2}}\int_{\Sigma_\epsilon} \tilde{x}_1\tilde{p}_z\,\mathrm{d}\tilde{x}_1\,\mathrm{d}\tilde{x}_2 - \epsilon^k \int_{\Sigma_\epsilon} \tilde{x}_1\tilde{p}_h\,\mathrm{d}\tilde{x}_1\,\mathrm{d}\tilde{x}_2 \tag{2.23b}$$

$$T_3 = \epsilon^k \int_{\Sigma_\epsilon} \Big[\Big(\frac{1}{R_2} - \frac{1}{R_1}\Big)\tilde{x}_1\tilde{x}_2\tilde{p}_z + \tilde{x}_2\frac{\partial \tilde{u}_{z1}}{\partial \tilde{x}_3} - \tilde{x}_1\frac{\partial \tilde{u}_{z2}}{\partial \tilde{x}_3}\Big]\,\mathrm{d}\tilde{x}_1\,\mathrm{d}\tilde{x}_2 \tag{2.23c}$$

$$S_{11} = \epsilon^k \int_{\Sigma_\epsilon} \Big[\frac{\tilde{x}_1^2}{R_1}\tilde{p}_z - \tilde{x}_1\frac{\partial \tilde{u}_{z1}}{\partial \tilde{x}_3} - \frac{1}{3}\Big\{\Big(\frac{\tilde{x}_1^2}{2R_1} + \frac{\tilde{x}_2^2}{2R_2}\Big)\tilde{p}_z - \Big(\tilde{x}_1\frac{\partial \tilde{u}_{z1}}{\partial \tilde{x}_3} + \tilde{x}_2\frac{\partial \tilde{u}_{z2}}{\partial \tilde{x}_3}\Big)\Big\}\Big]\,\mathrm{d}\tilde{x}_1\,\mathrm{d}\tilde{x}_2 \tag{2.24a}$$

$$S_{22} = \epsilon^k \int_{\Sigma_\epsilon} \Big[\frac{\tilde{x}_2^2}{R_2}\tilde{p}_z - \tilde{x}_2\frac{\partial \tilde{u}_{z2}}{\partial \tilde{x}_3} - \frac{1}{3}\Big\{\Big(\frac{\tilde{x}_1^2}{2R_1} + \frac{\tilde{x}_2^2}{2R_2}\Big)\tilde{p}_z - \Big(\tilde{x}_1\frac{\partial \tilde{u}_{z1}}{\partial \tilde{x}_3} + \tilde{x}_2\frac{\partial \tilde{u}_{z2}}{\partial \tilde{x}_3}\Big)\Big\}\Big]\,\mathrm{d}\tilde{x}_1\,\mathrm{d}\tilde{x}_2 \tag{2.24b}$$

$$S_{33} = \epsilon^k \int_{\Sigma_\epsilon} \Big[-\Big(\frac{\tilde{x}_1^2}{2R_1} + \frac{\tilde{x}_2^2}{2R_2}\Big)\tilde{p}_z - \frac{1}{3}\Big\{\Big(\frac{\tilde{x}_1^2}{2R_1} + \frac{\tilde{x}_2^2}{2R_2}\Big)\tilde{p}_z - \Big(\tilde{x}_1\frac{\partial \tilde{u}_{z1}}{\partial \tilde{x}_3} + \tilde{x}_2\frac{\partial \tilde{u}_{z2}}{\partial \tilde{x}_3}\Big)\Big\}\Big]\,\mathrm{d}\tilde{x}_1\,\mathrm{d}\tilde{x}_2 \tag{2.24c}$$

$$S_{12} = S_{21} = \frac{\epsilon^k}{2}\int_{\Sigma_\epsilon} \Big[\Big(\frac{1}{R_1} + \frac{1}{R_2}\Big)\tilde{x}_1\tilde{x}_2\tilde{p}_z - \tilde{x}_1\frac{\partial \tilde{u}_{z2}}{\partial \tilde{x}_3} - \tilde{x}_2\frac{\partial \tilde{u}_{z1}}{\partial \tilde{x}_3}\Big]\,\mathrm{d}\tilde{x}_1\,\mathrm{d}\tilde{x}_2 \tag{2.24d}$$

$$S_{13} = S_{31} = -T_2/2 \qquad (2.24e) \qquad\qquad S_{23} = S_{32} = T_1/2\,. \tag{2.24f}$$

It follows from (2.24e) that, to $O(1)$, the (1,3) components of the symmetric and antisymmetric parts of the first moment about $O$ of the stress density on the particle surface $W$ are equal. Indeed, in the domain where the lubrication approximations hold, the distance $(\mathbf{r}_W)_3$ is $O(\epsilon^{1/2})$ compared to $(\mathbf{r}_W)_1$, as are the force components in the direction of $\mathbf{e}_1$ compared to those along $\mathbf{e}_3$. Hence the (3,1) component of the first moment about $O$ of the stress density is $O(\epsilon)$ compared to the (1,3) component,

and the relation (2.24e) between $S_{13}$ and $T_2$ follows. A similar reasoning applies to (2.24f).

The only difficulty remaining is the calculation of $p_z, p_h, p_\epsilon, \mathbf{u}_z$ and $\mathbf{u}_h$ for arbitrary prescribed motions of the walls $W$ and $W'$.

## 2.2 Direct approach of the surfaces

### 2.2.1 Leading order problem — Cox's solution (1974)

The leading order problem has been solved by Cox (1974). We shall only outline the major steps here. From (2.11), the equations for $\mathbf{u}_z$ reduce to:

$$\frac{\partial^2 \tilde{u}_{z1}}{\partial \bar{x}_3^2} = \frac{\partial \tilde{p}_z}{\partial \bar{x}_1} + \frac{\bar{x}_1}{R_1}\frac{\partial \tilde{p}_z}{\partial \bar{x}_3} , \qquad \frac{\partial^2 \tilde{u}_{z2}}{\partial \bar{x}_3^2} = \frac{\partial \tilde{p}_z}{\partial \bar{x}_2} + \frac{\bar{x}_2}{R_2}\frac{\partial \tilde{p}_z}{\partial \bar{x}_3} , \qquad \frac{\partial \tilde{p}_z}{\partial \bar{x}_3} = 0 , \quad (2.25a)$$

$$\frac{\partial \tilde{u}_{z1}}{\partial \bar{x}_1} + \frac{\partial \tilde{u}_{z2}}{\partial \bar{x}_2} + \frac{\partial \tilde{u}_{z3}}{\partial \bar{x}_3} + \frac{\bar{x}_1}{R_1}\frac{\partial \tilde{u}_{z1}}{\partial \bar{x}_3} + \frac{\bar{x}_2}{R_2}\frac{\partial \tilde{u}_{z2}}{\partial \bar{x}_3} = 0 . \quad (2.25b)$$

Taking $k = 0$, the boundary conditions on $\mathbf{u}_z$ for a direct approach of the surfaces along the $\tilde{x}_3$ axis read:

$$\tilde{u}_{z1} = \tilde{u}_{z2} = 0 , \qquad \tilde{u}_{z3} = U_3 \qquad \text{on} \quad \bar{x}_3 = 0, \quad (2.26a)$$

$$\tilde{u}_{z1} = \tilde{u}_{z2} = 0 , \qquad \tilde{u}_{z3} = U_3' \qquad \text{on} \quad \bar{x}_3 = h_z(\bar{x}_1, \bar{x}_2). \quad (2.26b)$$

By solving the equations (2.25a) in terms of the unknown pressure field, and substituting the expressions in the continuity equation (2.25b), one obtains the following Reynolds equation for the pressure $p_z$:

$$\bar{\nabla} \cdot (h_z^3 \bar{\nabla} p_z) = 12(U_3' - U_3) . \quad (2.27)$$

In this equation, as well as in the remainder of this chapter, the vectorial operator $\bar{\nabla}$ stands for

$$\bar{\nabla} = \mathbf{e}_1 \partial/\partial \bar{x}_1 + \mathbf{e}_2 \partial/\partial \bar{x}_2 . \quad (2.28)$$

In order to solve (2.27), another coordinate transformation is carried out, mapping the $(\bar{x}_1, \bar{x}_2)$ axes onto the directions of principal curvature of $h_z$ (Appendix A), so that

$$h_z = 1 + \lambda_1 \hat{x}_1^2 + \lambda_2 \hat{x}_2^2 \ . \tag{2.29}$$

It can easily be proven that $0 < \lambda_i < 2$ for any non-intersecting surfaces $W$ and $W'$ (Appendix A). The transformation from $(\bar{x}_1, \bar{x}_2)$ onto $(\hat{x}_1, \hat{x}_2)$ is orthogonal, and can thus be cast in the form

$$\begin{pmatrix} \tilde{x}_1 \\ \tilde{x}_2 \end{pmatrix} = \begin{pmatrix} \bar{x}_1 \\ \bar{x}_2 \end{pmatrix} = \begin{pmatrix} \cos\chi & \sin\chi \\ -\sin\chi & \cos\chi \end{pmatrix} \cdot \begin{pmatrix} \hat{x}_1 \\ \hat{x}_2 \end{pmatrix} \ . \tag{2.30}$$

Elliptic coordinates, defined by the relations

$$\hat{x}_1 = \hat{r}\cos\theta/\sqrt{\lambda_1} \ , \qquad \hat{x}_2 = \hat{r}\sin\theta/\sqrt{\lambda_2} \ , \tag{2.31}$$

are then introduced, yielding the following form for the lubrication equation (2.27):

$$\begin{aligned}
&(\lambda_1\cos^2\theta + \lambda_2\sin^2\theta)\hat{r}^2\frac{\partial^2\tilde{p}_z}{\partial\hat{r}^2} + 2(\lambda_2-\lambda_1)\sin\theta\cos\theta\hat{r}\frac{\partial^2\tilde{p}_z}{\partial\hat{r}\partial\theta} \\
&\quad + (\lambda_1\sin^2\theta + \lambda_2\cos^2\theta)\frac{\partial^2\tilde{p}_z}{\partial\theta^2} + (\lambda_1\sin^2\theta + \lambda_2\cos^2\theta)\hat{r}\frac{\partial\tilde{p}_z}{\partial\hat{r}} \\
&\quad + 2(\lambda_1-\lambda_2)\sin\theta\cos\theta\frac{\partial\tilde{p}_z}{\partial\theta} + \frac{6\hat{r}^3}{(1+\hat{r}^2)}(\lambda_1\cos^2\theta + \lambda_2\sin^2\theta)\frac{\partial\tilde{p}_z}{\partial\hat{r}} \\
&\quad + \frac{6\hat{r}^2}{(1+\hat{r}^2)}(\lambda_2-\lambda_1)\sin\theta\cos\theta\frac{\partial\tilde{p}_z}{\partial\theta} = 12(U_3'-U_3)\frac{\hat{r}^2}{(1+\hat{r}^2)^3} \ .
\end{aligned} \tag{2.32a}$$

The operation on the left-hand side of the previous equation will be referred to as $\mathcal{L}(\tilde{p}_z(\hat{r},\theta))$:

$$\mathcal{L}(\tilde{p}_z) = 12(U_3'-U_3)\frac{\hat{r}^2}{(1+\hat{r}^2)^3} \ . \tag{2.32b}$$

As $\hat{r} \to \infty$, the inner solution, valid in the thin gap separating the two surfaces, must match the flow-field in the "outer" region. Since the pressure $\dot{p}$ in the outer region must not diverge as $\dot{\epsilon} \to 0$, it can easily be shown that $\tilde{p}_z$ must be $O(\hat{r}^{-4})$ as $\hat{r} \to \infty$. Indeed, assume that $\tilde{p}_z$ is of order $\hat{r}^n$ for very large $\hat{r}$, then $\dot{p} = (\dot{\mu}\dot{U}_c/\dot{R}_c)\epsilon^{-2}\tilde{p}_z$ is $O(\epsilon^{-2}\hat{r}^n) = O(\epsilon^{-\frac{(n+4)}{2}}\dot{r}^n)$ as $\hat{r} \to \infty$ (but with finite $\dot{\mathbf{r}}$).

Hence $n \leq -4$ is required. Also, the solution of (2.32) must not be singular at the origin. Cox (1974) then found the solution

$$\tilde{p}_z = -3\,\frac{U_3' - U_3}{\lambda_1 + \lambda_2}\,\frac{1}{(1+\hat{r}^2)^2}\,. \tag{2.33}$$

The components of the velocity field are given by

$$\tilde{u}_{z1} = \frac{1}{2}\frac{\partial \tilde{p}_z}{\partial \bar{x}_1}\bar{x}_3(\bar{x}_3 - h_z), \qquad \tilde{u}_{z2} = \frac{1}{2}\frac{\partial \tilde{p}_z}{\partial \bar{x}_2}\bar{x}_3(\bar{x}_3 - h_z)\,, \tag{2.34a}$$

$$\tilde{u}_{z3} = \frac{1}{12}\bar{\nabla}^2\tilde{p}_z(3h_z - 2\bar{x}_3)\bar{x}_3^2 + \frac{1}{4}\bar{\nabla}\tilde{p}_z\cdot\bar{\nabla}h_z\bar{x}_3^2 + \frac{1}{2}\bar{\mathbf{x}}\cdot\boldsymbol{\mathcal{R}}^{-1}\cdot\bar{\nabla}\tilde{p}_z\bar{x}_3(h_z - \bar{x}_3) + U_3\,. \tag{2.34b}$$

Here, $\bar{\mathbf{x}} = \bar{x}_1\mathbf{e}_1 + \bar{x}_2\mathbf{e}_2$ and $\boldsymbol{\mathcal{R}} = \boldsymbol{diag}(R_1, R_2)$. Then, according to eq. (2.22)-(2.24), with $k = 0$,

$$F_1 = O(\ln\epsilon) \qquad F_2 = O(\ln\epsilon) \qquad F_3 = -3\pi\epsilon^{-1}\frac{(U_3' - U_3)}{\sqrt{\lambda_1\lambda_2}(\lambda_1 + \lambda_2)} + O(\epsilon^{-1/2}) \tag{2.35a}$$

$$T_1 = O(\ln\epsilon) \qquad\qquad T_2 = O(\ln\epsilon)$$

$$T_3 = \frac{3}{2}\pi\,\ln\epsilon\frac{(U_3' - U_3)}{\sqrt{\lambda_1\lambda_2}(\lambda_1 + \lambda_2)}\Big(\frac{1}{R_1} - \frac{1}{R_2}\Big)\Big(\frac{1}{\lambda_1} - \frac{1}{\lambda_2}\Big)\sin\chi\cos\chi + O(1) \tag{2.35b}$$

$$S_{11} = 3\pi\,\ln\epsilon\frac{(U_3' - U_3)}{\sqrt{\lambda_1\lambda_2}(\lambda_1 + \lambda_2)}\Big\{\Big(\frac{\cos^2\chi}{\lambda_1} + \frac{\sin^2\chi}{\lambda_2}\Big)\frac{1}{2R_1} - \frac{1}{12}\cos^2\chi\Big(\frac{1}{\lambda_1 R_1} + \frac{1}{\lambda_2 R_2}\Big) - \frac{1}{12}\sin^2\chi\Big(\frac{1}{\lambda_2 R_1} + \frac{1}{\lambda_1 R_2}\Big) - \frac{1}{3}\Big\} + O(1) \tag{2.35c}$$

$$S_{22} = 3\pi\,\ln\epsilon\frac{(U_3' - U_3)}{\sqrt{\lambda_1\lambda_2}(\lambda_1 + \lambda_2)}\Big\{\Big(\frac{\cos^2\chi}{\lambda_2} + \frac{\sin^2\chi}{\lambda_1}\Big)\frac{1}{2R_2} - \frac{1}{12}\cos^2\chi\Big(\frac{1}{\lambda_1 R_1} + \frac{1}{\lambda_2 R_2}\Big) - \frac{1}{12}\sin^2\chi\Big(\frac{1}{\lambda_2 R_1} + \frac{1}{\lambda_1 R_2}\Big) - \frac{1}{3}\Big\} + O(1) \tag{2.35d}$$

$$S_{33} = 3\pi\,\ln\epsilon\frac{(U_3' - U_3)}{\sqrt{\lambda_1\lambda_2}(\lambda_1 + \lambda_2)}\Big\{-\frac{1}{3}\cos^2\chi\Big(\frac{1}{\lambda_1 R_1} + \frac{1}{\lambda_2 R_2}\Big) - \frac{1}{3}\sin^2\chi\Big(\frac{1}{\lambda_2 R_1} + \frac{1}{\lambda_1 R_2}\Big) + \frac{2}{3}\Big\} + O(1) \tag{2.35e}$$

$$S_{12} = \frac{3}{4}\pi\,\ln\epsilon\frac{(U_3' - U_3)}{\sqrt{\lambda_1\lambda_2}(\lambda_1 + \lambda_2)}\Big(\frac{1}{R_1} + \frac{1}{R_2}\Big)\Big(\frac{1}{\lambda_2} - \frac{1}{\lambda_1}\Big)\sin\chi\cos\chi \tag{2.35f}$$

$$S_{23} = O(\ln\epsilon) \qquad\qquad S_{13} = O(\ln\epsilon)\,.$$

Equations (2.35a)-(2.35b) were also given by Cox (1974), who did not, however, calculate the stresslet.

### 2.2.2 Second order problem

As indicated in (2.35), the solution of the leading order problem, which amounts to a local approximation of the surface geometry by quadratics, does not suffice to calculate the dominant singular behavior of the components $F_1, F_2, T_1$ and $T_2$. Also, the correction to the result (2.35a) for $F_3$ diverges as $\epsilon \to 0$, and is thus needed since the desired level of accuracy is $O(\epsilon^0)$. It is therefore necessary to consider the next order in the hierarchy of problems generated by the asymptotic expansion (2.12). The equations (2.22)-(2.23) show that the pressure field correction $p_h$ and the velocity field correction $\mathbf{u}_h$ can indeed give singular contributions for $k = 0$. From (2.11), the equations to be solved are

$$\frac{\partial^2 \tilde{u}_{h1}}{\partial \bar{x}_3^2} = \frac{\partial \tilde{p}_h}{\partial \bar{x}_1} + \frac{\bar{x}_1}{R_1}\frac{\partial \tilde{p}_h}{\partial \bar{x}_3} + \sum_{i=0}^{2}(3-i)\Gamma_i \bar{x}_1^{2-i}\bar{x}_2^i \frac{\partial \tilde{p}_z}{\partial \bar{x}_3} \ , \tag{2.36a}$$

$$\frac{\partial^2 \tilde{u}_{h2}}{\partial \bar{x}_3^2} = \frac{\partial \tilde{p}_h}{\partial \bar{x}_2} + \frac{\bar{x}_2}{R_2}\frac{\partial \tilde{p}_h}{\partial \bar{x}_3} + \sum_{i=1}^{3} i\Gamma_i \bar{x}_1^{3-i}\bar{x}_2^{i-1} \frac{\partial \tilde{p}_z}{\partial \bar{x}_3} \ , \tag{2.36b}$$

$$\frac{\partial \tilde{p}_h}{\partial \bar{x}_3} = 0 \ , \tag{2.36c}$$

$$\frac{\partial \tilde{u}_{h1}}{\partial \bar{x}_1} + \frac{\partial \tilde{u}_{h2}}{\partial \bar{x}_2} + \frac{\partial \tilde{u}_{h3}}{\partial \bar{x}_3} + \frac{\bar{x}_1}{R_1}\frac{\partial \tilde{u}_{h1}}{\partial \bar{x}_3} + \frac{\bar{x}_2}{R_2}\frac{\partial \tilde{u}_{h2}}{\partial \bar{x}_3} + \sum_{i=0}^{2}(3-i)\Gamma_i \bar{x}_i^{2-i}\bar{x}_2^i \frac{\partial \tilde{u}_{z1}}{\partial \bar{x}_3} + \sum_{i=1}^{3} i\Gamma_i \bar{x}_1^{3-i}\bar{x}_2^{i-1}\frac{\partial \tilde{u}_{z2}}{\partial \bar{x}_3} = 0 \ , \tag{2.36d}$$

subject to the following boundary conditions on $W'$:

$$\tilde{u}_{h1} = -\frac{1}{2}\frac{\partial \tilde{p}_z}{\partial \bar{x}_1} h_z h_h, \tag{2.37a}$$

$$\tilde{u}_{h2} = -\frac{1}{2}\frac{\partial \tilde{p}_z}{\partial \bar{x}_2} h_z h_h \ , \tag{2.37b}$$

$$\tilde{u}_{h3} = -\frac{1}{2}\Big(\frac{\partial \tilde{p}_z}{\partial \bar{x}_1}\frac{\partial h_z}{\partial \bar{x}_1} + \frac{\partial \tilde{p}_z}{\partial \bar{x}_2}\frac{\partial h_z}{\partial \bar{x}_2}\Big) h_z h_h + \frac{1}{2}\Big(\frac{\bar{x}_1}{R_1}\frac{\partial \tilde{p}_z}{\partial \bar{x}_1} + \frac{\bar{x}_2}{R_2}\frac{\partial \tilde{p}_z}{\partial \bar{x}_2}\Big) h_z h_h \ . \tag{2.37c}$$

On $W$, the no-slip boundary condition simply prescribes that $\mathbf{u}_h = 0$. One proceeds following the same steps as Cox (1974) to arrive at the modified Reynolds equation

$$\bar{\nabla} \cdot \left\{ h_z^3 \bar{\nabla} \tilde{p}_h \right\} = -3\bar{\nabla} \cdot \left\{ h_z^2 h_h \bar{\nabla} \tilde{p}_z \right\} . \tag{2.38}$$

In terms of $\hat{r}$ and $\theta$, this reads:

$$\begin{aligned} \mathcal{L}(\tilde{p}_h) = 36 \frac{(U_3' - U_3)}{\lambda_1 + \lambda_2} \frac{\hat{r}^5}{(1+\hat{r}^2)^4} \Big\{ & (\lambda_2 - \lambda_1) \sin\theta \cos\theta \big[ \kappa_1 \cos^3\theta + \\ & (2\kappa_2 - 3\kappa_0) \cos^2\theta \sin\theta + (3\kappa_3 - 2\kappa_1) \sin^2\theta \cos\theta - \kappa_2 \sin^3\theta \big] \\ + \sum_{i=0}^{3} \kappa_i \cos^{3-i}\theta \sin^i\theta \Big[ & \lambda_1 \sin^2\theta + \lambda_2 \cos^2\theta + (\lambda_1 \cos^2\theta + \lambda_2 \sin^2\theta) \Big( 4 - \frac{2\hat{r}^2}{1+\hat{r}^2} \Big) \Big] \Big\} \end{aligned} \tag{2.39}$$

where the operator $\mathcal{L}$ was defined in the preceding section (2.32b), and the coefficients $\kappa_i$ are defined such that $h_h = \hat{r}^3 \sum_{i=0}^{3} \kappa_i \cos^{3-i}\theta \sin^i\theta$: if $\mathcal{K}_i$ is defined via the relation (2.30) in such a way that

$$h_h \stackrel{\text{def}}{=} \sum_{i=0}^{3} (\beta_i + \Gamma_i) \bar{x}_1^{3-i} \bar{x}_2^i = \sum_{i=0}^{3} \mathcal{K}_i \hat{x}_1^{3-i} \hat{x}_2^i , \tag{2.40}$$

then $\kappa_i$ can be derived from the simple formula $\kappa_i = \mathcal{K}_i \lambda_1^{-\frac{3-i}{2}} \lambda_2^{-\frac{i}{2}}$. The boundary conditions for the partial differential equation (2.39) are periodicity in $\theta$, boundedness at the origin, and the requirement that $\tilde{p}_h = O(\hat{r}^{-3})$ as $\hat{r} \to \infty$ at finite $\grave{\mathbf{r}}$.

In order to solve this equation, it is useful to solve the problem in the limit of large $\hat{r}$ first. Separation of variables is then possible, with a solution of the form $\tilde{p}_h = \hat{r}^{-3}\Theta(\theta)$. It is fairly straightforward to solve the remaining linear ordinary differential equation for $\Theta$. Inspired by this result, we then succeeded in solving (2.39) over the entire range of $\{\hat{r}, \theta\}$. The first order correction to the pressure field is found to be

$$\begin{aligned} \tilde{p}_h = -6 \frac{(U_3' - U_3)}{\lambda_1 + \lambda_2} \Big\{ & \sum_{i=0}^{3} \kappa_i \cos^{3-i}\theta \sin^i\theta \frac{\hat{r}^3}{(1+\hat{r}^2)^3} + \\ & \Big[ \frac{3\lambda_2\kappa_3 + \lambda_1\kappa_1}{2\lambda_1 + 3\lambda_2} \sin\theta + \frac{3\lambda_1\kappa_0 + \lambda_2\kappa_2}{3\lambda_1 + 2\lambda_2} \cos\theta \Big] \frac{\hat{r}}{(1+\hat{r}^2)^2} \Big\} \end{aligned} \tag{2.41a}$$

or equivalently,

$$\tilde{p}_h = -6\frac{(U_3' - U_3)}{\lambda_1 + \lambda_2}\left\{\frac{h_h}{h_z^3} + \frac{1}{h_z^2}\left[\frac{3\mathcal{K}_0 + \mathcal{K}_2}{3\lambda_1 + 2\lambda_2}\hat{x}_1 + \frac{3\mathcal{K}_3 + \mathcal{K}_1}{2\lambda_1 + 3\lambda_2}\hat{x}_2\right]\right\} . \tag{2.41b}$$

The velocity field can then be calculated from $\tilde{p}_h$ using equations analogous to (2.34), namely:

$$\tilde{u}_{h1} = \frac{1}{2}\left\{\frac{\partial\tilde{p}_h}{\partial\bar{x}_1}\bar{x}_3^2 - \left(\frac{\partial\tilde{p}_z}{\partial\bar{x}_1}h_h + \frac{\partial\tilde{p}_h}{\partial\bar{x}_1}h_z\right)\bar{x}_3\right\} , \tag{2.42a}$$

$$\tilde{u}_{h2} = \frac{1}{2}\left\{\frac{\partial\tilde{p}_h}{\partial\bar{x}_2}\bar{x}_3^2 - \left(\frac{\partial\tilde{p}_z}{\partial\bar{x}_2}h_h + \frac{\partial\tilde{p}_h}{\partial\bar{x}_2}h_z\right)\bar{x}_3\right\} , \tag{2.42b}$$

$$\begin{aligned}\tilde{u}_{h3} = &-\frac{1}{6}\bar{\nabla}^2\tilde{p}_h\bar{x}_3^3 + \frac{1}{4}\{h_h\bar{\nabla}^2\tilde{p}_z + \bar{\nabla}\tilde{p}_z\cdot\bar{\nabla}h_h + h_z\bar{\nabla}^2\tilde{p}_h + \bar{\nabla}\tilde{p}_h\cdot\bar{\nabla}h_z\}\bar{x}_3^2 \\ &- \frac{1}{2}\frac{\bar{x}_1}{R_1}\left\{\frac{\partial\tilde{p}_h}{\partial\bar{x}_1}\bar{x}_3^2 - \frac{\partial\tilde{p}_z}{\partial\bar{x}_1}h_h\bar{x}_3 - \frac{\partial\tilde{p}_h}{\partial\bar{x}_1}h_z\bar{x}_3\right\} - \frac{1}{2}\frac{\bar{x}_2}{R_2}\left\{\frac{\partial\tilde{p}_h}{\partial\bar{x}_2}\bar{x}_3^2 - \frac{\partial\tilde{p}_z}{\partial\bar{x}_2}h_h\bar{x}_3 - \frac{\partial\tilde{p}_h}{\partial\bar{x}_2}h_z\bar{x}_3\right\} \\ &- \frac{1}{2}\sum_{i=0}^{2}(3-i)\Gamma_i\bar{x}_1^{2-i}\bar{x}_2^i\left\{\frac{\partial\tilde{p}_z}{\partial\bar{x}_1}\bar{x}_3^2 - \frac{\partial\tilde{p}_z}{\partial\bar{x}_1}h_z\bar{x}_3\right\} - \frac{1}{2}\sum_{i=1}^{3}i\Gamma_i\bar{x}_1^{3-i}\bar{x}_2^i\left\{\frac{\partial\tilde{p}_z}{\partial\bar{x}_2}\bar{x}_3^2 - \frac{\partial\tilde{p}_z}{\partial\bar{x}_2}h_z\bar{x}_3\right\} .\end{aligned} \tag{2.42c}$$

After considerable algebraic effort, one can then calculate the contributions from the $O(\epsilon^{\frac{1}{2}})$ pressure and velocity field corrections to the force $\mathbf{F}$ and the torque $\mathbf{T}$:

$$\begin{aligned}F_1 = \frac{3}{2}\pi\ \ln\epsilon\frac{(U_3' - U_3)}{\sqrt{\lambda_1\lambda_2}(\lambda_1+\lambda_2)}\Bigg\{&\frac{(\lambda_1+2\lambda_2)\kappa_2 + (7\lambda_1+2\lambda_2)\kappa_0}{3\lambda_1+2\lambda_2}\left(\frac{3}{2}\frac{1}{\sqrt{\lambda_1}R_1} - 3\sqrt{\lambda_1}\right)\cos\chi \\ &+ \frac{(2\lambda_1+\lambda_2)\kappa_1 + (2\lambda_1+7\lambda_2)\kappa_3}{2\lambda_1+3\lambda_2}\left(\frac{3}{2}\frac{1}{\sqrt{\lambda_2}R_1} - 3\sqrt{\lambda_2}\right)\sin\chi \\ &- \lambda_1^{\frac{1}{2}}\cos\chi\frac{\kappa_2+3\kappa_0}{2} - \lambda_2^{\frac{1}{2}}\sin\chi\frac{3\kappa_3+\kappa_1}{2} + 3\Gamma_0\left(\frac{\cos^2\chi}{\lambda_1} + \frac{\sin^2\chi}{\lambda_2}\right) \\ &+ 2\Gamma_1\sin\chi\cos\chi\left(\frac{1}{\lambda_2} - \frac{1}{\lambda_1}\right) + \Gamma_2\left(\frac{\sin^2\chi}{\lambda_1} + \frac{\cos^2\chi}{\lambda_2}\right)\Bigg\} + O(1)\end{aligned} \tag{2.43a}$$

$$\begin{aligned}F_2 = \frac{3}{2}\pi\ \ln\epsilon\frac{(U_3' - U_3)}{\sqrt{\lambda_1\lambda_2}(\lambda_1+\lambda_2)}\Bigg\{&\frac{(\lambda_1+2\lambda_2)\kappa_2 + (7\lambda_1+2\lambda_2)\kappa_0}{3\lambda_1+2\lambda_2}\left(3\sqrt{\lambda_1} - \frac{3}{2}\frac{1}{\sqrt{\lambda_1}R_2}\right)\sin\chi \\ &+ \frac{(2\lambda_1+\lambda_2)\kappa_1 + (2\lambda_1+7\lambda_2)\kappa_3}{2\lambda_1+3\lambda_2}\left(\frac{3}{2}\frac{1}{\sqrt{\lambda_2}R_2} - 3\sqrt{\lambda_2}\right)\cos\chi \\ &+ \lambda_1^{\frac{1}{2}}\sin\chi\frac{\kappa_2+3\kappa_0}{2} - \lambda_2^{\frac{1}{2}}\cos\chi\frac{3\kappa_3+\kappa_1}{2} + 3\Gamma_3\left(\frac{\sin^2\chi}{\lambda_1} + \frac{\cos^2\chi}{\lambda_2}\right) \\ &+ 2\Gamma_2\sin\chi\cos\chi\left(\frac{1}{\lambda_2} - \frac{1}{\lambda_1}\right) + \Gamma_1\left(\frac{\cos^2\chi}{\lambda_1} + \frac{\sin^2\chi}{\lambda_2}\right)\Bigg\} + O(1)\end{aligned} \tag{2.43b}$$

$$T_1 = \frac{9}{4}\pi \ln\epsilon \frac{(U_3' - U_3)}{\sqrt{\lambda_1\lambda_2}(\lambda_1+\lambda_2)} \left\{ \frac{(2\lambda_1+\lambda_2)\kappa_1 + (2\lambda_1+7\lambda_2)\kappa_3}{2\lambda_1+3\lambda_2} \frac{\cos\chi}{\sqrt{\lambda_2}} \right.$$
$$\left. - \frac{(\lambda_1+2\lambda_2)\kappa_2 + (7\lambda_1+2\lambda_2)\kappa_0}{3\lambda_1+2\lambda_2} \frac{\sin\chi}{\sqrt{\lambda_1}} \right\} + O(1) \qquad (2.43c)$$

$$T_2 = -\frac{9}{4}\pi \ln\epsilon \frac{(U_3' - U_3)}{\sqrt{\lambda_1\lambda_2}(\lambda_1+\lambda_2)} \left\{ \frac{(\lambda_1+2\lambda_2)\kappa_2 + (7\lambda_1+2\lambda_2)\kappa_0}{3\lambda_1+2\lambda_2} \frac{\cos\chi}{\sqrt{\lambda_1}} \right.$$
$$\left. + \frac{(2\lambda_1+\lambda_2)\kappa_1 + (2\lambda_1+7\lambda_2)\kappa_3}{2\lambda_1+3\lambda_2} \frac{\sin\chi}{\sqrt{\lambda_2}} \right\} + O(1)\ . \qquad (2.43d)$$

The contribution to $F_3$ of the $O(\epsilon^{\frac{1}{2}})$ solution turns out to be zero, which is not surprising since this correction arises from the $O(r^3)$ features of the wall, which are antisymmetric about the origin. The $O(\ln\epsilon)$ components of the stresslet $S_{13} = S_{31}$ and $S_{23} = S_{32}$ can be obtained from the equations (2.24e) and (2.24f): $S_{13} = -T_2/2$ and $S_{23} = T_1/2$.

### 2.2.3 Third order problem

Since the error on $F_3$ is still $O(\ln\epsilon)$, and hence singular, it is necessary to solve for the second correction $\tilde{p}_\epsilon$ to the pressure field. The procedure is conceptually quite similar to the method of solution adopted in the preceding sections, but the algebra gets even more involved. The interested reader is referred to Appendix C, where some of the details of the calculation and several intermediate results have been recorded. The expression for the normal force $F_3$ that is finally derived reads, for a

direct approach of the surfaces and to $O(1)$:

$$
\begin{aligned}
F_3 = &-3\pi\epsilon^{-1}\frac{(U_3'-U_3)}{\sqrt{\lambda_1\lambda_2}(\lambda_1+\lambda_2)} - \frac{9}{4}\pi\ln\epsilon\frac{(U_3'-U_3)}{\sqrt{\lambda_1\lambda_2}(\lambda_1+\lambda_2)^2}\Big[\Big(10\lambda_1+\frac{5}{2}\lambda_2\Big)\kappa_0^2 \\
&+\Big(\frac{3}{2}\lambda_1+\lambda_2\Big)\kappa_1^2+\Big(\lambda_1+\frac{3}{2}\lambda_2\Big)\kappa_2^2+\Big(\frac{5}{2}\lambda_1+10\lambda_2\Big)\kappa_3^2+(3\lambda_1+2\lambda_2)\kappa_0\kappa_2 \\
&+(2\lambda_1+3\lambda_2)\kappa_1\kappa_3+(7\lambda_1+2\lambda_2)\kappa_0 K_1+(\lambda_1+2\lambda_2)\kappa_2 K_1+(2\lambda_1+\lambda_2)\kappa_1 K_2 \\
&+(2\lambda_1+7\lambda_2)\kappa_3 K_2+(5\lambda_1+\lambda_2)\zeta_0+(\lambda_1+\lambda_2)\zeta_2+(\lambda_1+5\lambda_2)\zeta_4\Big] \\
&+\frac{3}{2}\pi\ln\epsilon\frac{(U_3'-U_3)}{\sqrt{\lambda_1\lambda_2}(\lambda_1+\lambda_2)^2}\Big[\frac{48}{5}(\lambda_1^2+\lambda_2^2)+\frac{32}{5}\lambda_1\lambda_2-\frac{4}{\hat{R}_1}(3\lambda_1+\lambda_2) \\
&-\frac{4}{\hat{R}_2}(\lambda_1+3\lambda_2)+\frac{2}{\hat{R}_1\hat{R}_2}+\frac{\lambda_2}{\lambda_1\hat{\rho}_1^2}+\frac{\lambda_1}{\lambda_2\hat{\rho}_2^2}+\frac{3}{\hat{R}_1^2}+\frac{3}{\hat{\rho}_1^2}+\frac{3}{\hat{R}_2^2}+\frac{3}{\hat{\rho}_2^2} \\
&+\frac{1}{\hat{R}_s^2}\Big(\sqrt{\frac{\lambda_1}{\lambda_2}}+\sqrt{\frac{\lambda_2}{\lambda_1}}\Big)^2\Big]\,. \qquad (2.44)
\end{aligned}
$$

The parameters $\hat{R}_1, \hat{R}_2, \hat{R}_s, \hat{\rho}_1, \hat{\rho}_2, K_1$ and $K_2$ are defined in (C.2b), (C.4c) and (C.12c); the coefficients $\zeta_i$ can be derived from (C.12b).

At this point, all the singular components of the forces, torques and stresslets exerted by two bodies in close proximity approaching each other along their common normal (or moving away from each other along that normal) have been obtained in closed form.

## 2.3 Tangential and rolling motion of the surfaces

For this class of motions, the value of the parameter "$k$" is $1/2$. As a consequence, at all particle spacings, this type of movement contributes at most $O(1)$ to the components $S_{ii}$ ($i = 1$, 2, or 3) and $S_{12} = S_{21}$ of the stresslet and to the component $T_3$ of the torque (*cf.* (2.22)-(2.24)).

Cox (1974) formulated and solved this problem for the singular stress moments by following the same steps as in section 2.2. His results are:

$$
\begin{aligned}
F_1 = \frac{\pi\ln\epsilon}{4\sqrt{\lambda_1\lambda_2}}\Big[&\frac{\hat{Q}_1\cos\chi}{3\lambda_1+2\lambda_2}\Big(\frac{1}{R_1\lambda_1}-1\Big)+\frac{\hat{Q}_2\sin\chi}{2\lambda_1+3\lambda_2}\Big(\frac{1}{R_1\lambda_2}-1\Big) \\
&+4(U_1'-U_1)\Big]+O(1)\,, \qquad (2.45a)
\end{aligned}
$$

$$F_2 = \frac{\pi \ln \epsilon}{4\sqrt{\lambda_1 \lambda_2}} \Big[ \frac{-\hat{Q}_1 \sin\chi}{3\lambda_1 + 2\lambda_2} \Big( \frac{1}{R_2 \lambda_1} - 1 \Big) + \frac{\hat{Q}_2 \cos\chi}{2\lambda_1 + 3\lambda_2} \Big( \frac{1}{R_2 \lambda_2} - 1 \Big) + 4(U_2' - U_2) \Big] + O(1) \,, \tag{2.45b}$$

$$T_1 = \frac{\pi \ln \epsilon}{4\sqrt{\lambda_1 \lambda_2}} \Big[ \frac{-\hat{Q}_1 \sin\chi}{\lambda_1(3\lambda_1 + 2\lambda_2)} + \frac{\hat{Q}_2 \cos\chi}{\lambda_2(2\lambda_1 + 3\lambda_2)} \Big] + O(1) \,, \tag{2.45c}$$

$$T_2 = \frac{-\pi \ln \epsilon}{4\sqrt{\lambda_1 \lambda_2}} \Big[ \frac{\hat{Q}_1 \cos\chi}{\lambda_1(3\lambda_1 + 2\lambda_2)} + \frac{\hat{Q}_2 \sin\chi}{\lambda_2(2\lambda_1 + 3\lambda_2)} \Big] + O(1) \,. \tag{2.45d}$$

The dependence of the force and the torque on the relative motion of the surfaces is concealed in the factors $\hat{Q}_1$ and $\hat{Q}_2$ which are given by

$$\begin{pmatrix} \hat{Q}_1 \\ \hat{Q}_2 \end{pmatrix} = \begin{pmatrix} \cos\chi & -\sin\chi \\ \sin\chi & \cos\chi \end{pmatrix} \cdot \begin{pmatrix} \tilde{Q}_1 \\ \tilde{Q}_2 \end{pmatrix} \,, \tag{2.46a}$$

with

$$\begin{pmatrix} \tilde{Q}_1 \\ \tilde{Q}_2 \end{pmatrix} = 12 \begin{pmatrix} -(\Omega_2' - \Omega_2) + (U_1' - U_1)\Big( (2R_1)^{-1} - \mathcal{B}_0 \Big) - (U_2' - U_2)\mathcal{B}_1/2 \\ (\Omega_1' - \Omega_1) + (U_2' - U_2)\Big( (2R_2)^{-1} - \mathcal{B}_2 \Big) - (U_1' - U_1)\mathcal{B}_1/2 \end{pmatrix} . \tag{2.46b}$$

Cox (1974) did not calculate $F_3$, but showed that it was $O(\ln \epsilon)$. Actually, one does not need to calculate $F_3$, since Lorentz' reciprocal theorem predicts that the relation between $F_3$ and $U_1$ is the same as that between $F_1$ and $U_3$, and similarly for the pairs $(F_3, \Omega_1)$ and $(T_1, U_3)$. One can then immediately deduce that

$$\begin{aligned} F_3 = \frac{3}{2}\pi \ln\epsilon \frac{(U_1' - U_1)}{\sqrt{\lambda_1\lambda_2}(\lambda_1 + \lambda_2)} \Big\{ & \frac{(\lambda_1 + 2\lambda_2)\kappa_2 + (7\lambda_1 + 2\lambda_2)\kappa_0}{3\lambda_1 + 2\lambda_2} \frac{3}{2} \Big( \frac{1}{\sqrt{\lambda_1} R_1} - \sqrt{\lambda_1} \Big) \cos\chi \\ & + \frac{(2\lambda_1 + \lambda_2)\kappa_1 + (2\lambda_1 + 7\lambda_2)\kappa_3}{2\lambda_1 + 3\lambda_2} \frac{3}{2} \Big( \frac{1}{\sqrt{\lambda_2} R_1} - \sqrt{\lambda_2} \Big) \sin\chi \\ & - \lambda_1^{\frac{1}{2}} \cos\chi \frac{\kappa_2 + 3\kappa_0}{2} - \lambda_2^{\frac{1}{2}} \sin\chi \frac{3\kappa_3 + \kappa_1}{2} + 3\Gamma_0 \Big( \frac{\cos^2\chi}{\lambda_1} + \frac{\sin^2\chi}{\lambda_2} \Big) \\ & + 2\Gamma_1 \sin\chi\cos\chi \Big( \frac{1}{\lambda_2} - \frac{1}{\lambda_1} \Big) + \Gamma_2 \Big( \frac{\sin^2\chi}{\lambda_1} + \frac{\cos^2\chi}{\lambda_2} \Big) \Big\} \end{aligned}$$

$$+\frac{3}{2}\pi\ln\epsilon\frac{(U_2'-U_2)}{\sqrt{\lambda_1\lambda_2}(\lambda_1+\lambda_2)}\Big\{\frac{(\lambda_1+2\lambda_2)\kappa_2+(7\lambda_1+2\lambda_2)\kappa_0}{3\lambda_1+2\lambda_2}\frac{3}{2}\Big(\sqrt{\lambda_1}-\frac{1}{\sqrt{\lambda_1}R_2}\Big)\sin\chi$$
$$+\frac{(2\lambda_1+\lambda_2)\kappa_1+(2\lambda_1+7\lambda_2)\kappa_3}{2\lambda_1+3\lambda_2}\frac{3}{2}\Big(\frac{1}{\sqrt{\lambda_2}R_2}-\sqrt{\lambda_2}\Big)\cos\chi$$
$$+\lambda_1^{\frac{1}{2}}\sin\chi\frac{\kappa_2+3\kappa_0}{2}-\lambda_2^{\frac{1}{2}}\cos\chi\frac{3\kappa_3+\kappa_1}{2}+3\Gamma_3\Big(\frac{\sin^2\chi}{\lambda_1}+\frac{\cos^2\chi}{\lambda_2}\Big)$$
$$+2\Gamma_2\sin\chi\cos\chi\Big(\frac{1}{\lambda_2}-\frac{1}{\lambda_1}\Big)+\Gamma_1\Big(\frac{\cos^2\chi}{\lambda_1}+\frac{\sin^2\chi}{\lambda_2}\Big)\Big\}$$
$$+\frac{9}{4}\pi\ln\epsilon\frac{(\Omega_1'-\Omega_1)}{\sqrt{\lambda_1\lambda_2}(\lambda_1+\lambda_2)}\Big\{\frac{(2\lambda_1+\lambda_2)\kappa_1+(2\lambda_1+7\lambda_2)\kappa_3}{2\lambda_1+3\lambda_2}\frac{\cos\chi}{\sqrt{\lambda_2}}$$
$$-\frac{(\lambda_1+2\lambda_2)\kappa_2+(7\lambda_1+2\lambda_2)\kappa_0}{3\lambda_1+2\lambda_2}\frac{\sin\chi}{\sqrt{\lambda_1}}\Big\}$$
$$-\frac{9}{4}\pi\ln\epsilon\frac{(\Omega_2'-\Omega_2)}{\sqrt{\lambda_1\lambda_2}(\lambda_1+\lambda_2)}\Big\{\frac{(\lambda_1+2\lambda_2)\kappa_2+(7\lambda_1+2\lambda_2)\kappa_0}{3\lambda_1+2\lambda_2}\frac{\cos\chi}{\sqrt{\lambda_1}}$$
$$+\frac{(2\lambda_1+\lambda_2)\kappa_1+(2\lambda_1+7\lambda_2)\kappa_3}{2\lambda_1+3\lambda_2}\frac{\sin\chi}{\sqrt{\lambda_2}}\Big\}+O(1)\ . \qquad (2.47)$$

## 2.4 Rotational motion of the surfaces about their normal

Cox (1974) also discussed this case, for which $k=1$. From (2.22)-(2.24), it should be apparent that only $F_3$ needs to be considered here. The result obtained by Cox reads

$$F_3=\frac{3\pi\ln\epsilon}{2\sqrt{\lambda_1\lambda_2}}(\Omega_3'-\Omega_3)\Big(\frac{1}{R_1}-\frac{1}{R_2}\Big)\frac{\lambda_2-\lambda_1}{\lambda_1\lambda_2(\lambda_1+\lambda_2)}\sin\chi\cos\chi+O(1)\ . \qquad (2.48)$$

## 2.5 Particles in a straining flow

As stated in the introduction, the microstructural dynamics of any system of particles suspended in a Newtonian fluid are characterized, in the limit of zero Reynolds number, by the grand resistance tensor. For two almost touching surfaces $W$ and $W'$, it is convenient to introduce the vectors $\mathcal{U}=(\mathbf{U},\boldsymbol{\Omega})^T$ and $\mathcal{F}=(\mathbf{F},\mathbf{T})^T$ and their analogs $\mathcal{U}'$ and $\mathcal{F}'$ for the surface $W'$, and to subdivide the grand resis-

tance tensor $\mathbf{R}_G$ as shown below:

$$\begin{pmatrix} \boldsymbol{\mathcal{F}} \\ \boldsymbol{\mathcal{F}}' \\ \mathbf{S} \\ \mathbf{S}' \end{pmatrix} = \mathbf{R}_G \otimes \begin{pmatrix} \boldsymbol{\mathcal{U}} \\ \boldsymbol{\mathcal{U}}' \\ -\mathbf{E} \\ -\mathbf{E}' \end{pmatrix} = \begin{pmatrix} \mathbf{R}^{ww}_{\mathcal{FU}} & \mathbf{R}^{ww'}_{\mathcal{FU}} & \mathbf{R}^{ww}_{\mathcal{F}E} & \mathbf{R}^{ww'}_{\mathcal{F}E} \\ \mathbf{R}^{w'w}_{\mathcal{FU}} & \mathbf{R}^{w'w'}_{\mathcal{FU}} & \mathbf{R}^{w'w}_{\mathcal{F}E} & \mathbf{R}^{w'w'}_{\mathcal{F}E} \\ \mathbf{R}^{ww}_{S\mathcal{U}} & \mathbf{R}^{ww'}_{S\mathcal{U}} & \mathbf{R}^{ww}_{SE} & \mathbf{R}^{ww'}_{SE} \\ \mathbf{R}^{w'w}_{S\mathcal{U}} & \mathbf{R}^{w'w'}_{S\mathcal{U}} & \mathbf{R}^{w'w}_{SE} & \mathbf{R}^{w'w'}_{SE} \end{pmatrix} \otimes \begin{pmatrix} \boldsymbol{\mathcal{U}} \\ \boldsymbol{\mathcal{U}}' \\ -\mathbf{E} \\ -\mathbf{E}' \end{pmatrix} . \tag{2.49}$$

The symbol $\otimes$ denotes the appropriate contraction operator. $\mathbf{E} = \mathbf{E}'$ is the rate-of-strain tensor of the imposed linear flow field. The subscript and superscript notation should be fairly transparent and is further explained in the nomenclature of this chapter. The results arrived at in the previous sections suffice to calculate the coupling terms between the stress moments and the velocities of the particles, with at most an $O(1)$ inaccuracy. Evidently, from (2.49), the construction of the grand resistance tensor also requires the evaluation of the force, torque and stresslet exerted by the particles when subjected to a straining flow. For this problem to be independent of the ones discussed previously, the relative velocity of the surfaces (both translational and rotational) should be zero at the points of closest approach. Thus the rigid bodies are immobile with respect to one another, and the lubrication equations predict a non-singular net force, torque and stresslet (since the boundary conditions impose a zero velocity along all the walls). Hence any singularities in the components of the resistance tensor which link the stress moments to the rate of strain must come in pairs such that they cancel each other exactly when the *net* force, torque or stresslet (about the point of minimum separation) is calculated. Therefore it is not necessary in practice to know these singular terms. For the sake of completeness, however, and because it has been found in the case of two spherical particles that their knowledge helps to speed up the calculation of the non-singular contributions to the stresslet (Jeffrey, 1989; Jeffrey & Corless, 1988), the components of the resistance tensor for two arbitrary bodies placed near contact in a straining flow are calculated here. These results will also provide a check for internal consistency of some formulae derived in this work by means of Lorentz' reciprocal theorem.

Following Jeffrey (1989), the individual contribution of each tensor element to the total stress moment exerted by the particle can be found using lubrication theory if one considers deformable surfaces. Let the surface velocity be $\grave{\mathbf{U}}(\grave{\mathbf{x}}_W) = \grave{\mathbf{D}} \cdot \grave{\mathbf{x}}_W$ on $W$ and $\grave{\mathbf{U}}'(\grave{\mathbf{x}}'_W) = \grave{\mathbf{D}}' \cdot \grave{\mathbf{x}}'_W$ on $W'$ where $\grave{\mathbf{x}}_W$ and $\grave{\mathbf{x}}'_W$ are measured from the points $O$ and $O'$, respectively, and $\grave{\mathbf{D}}$ and $\grave{\mathbf{D}}'$ are the deformation rate tensors. Assuming that the particles are incompressible, $\grave{\mathbf{D}}$ should be traceless. For the sake of generality, no other constraints will be put on the tensor $\grave{\mathbf{D}}$. Obviously, if desired, $\grave{\mathbf{D}}$ can be separated into an antisymmetric rotation tensor and a symmetric deformation tensor $\grave{\mathbf{E}}_W$.

Expressed in rescaled variables (using (2.7)), the boundary conditions on $W$ read, correct to $O(\epsilon^{1-k})$:

$$u_1 = \epsilon^{-k+1}\left\{D_{11}\tilde{x}_1 + D_{12}\tilde{x}_2\right\}, \qquad u_2 = \epsilon^{-k+1}\left\{D_{21}\tilde{x}_1 + D_{22}\tilde{x}_2\right\}, \quad (2.50a)$$

$$u_3 = \epsilon^{-k+\frac{1}{2}}\left\{D_{31}\tilde{x}_1 + D_{32}\tilde{x}_2 + \epsilon^{\frac{1}{2}}D_{33}\tilde{x}_3\right\}. \quad (2.50b)$$

Analogous expressions can easily be written for the velocity at the wall $W'$. Three cases need to be discerned. $D_{31}, D_{32}, D'_{31}$ or $D'_{32} \neq 0$ imply that $k = 1/2$. If all these components are zero, the exponent $k$ must be chosen equal to 1, unless the only non-zero elements in $\mathbf{D}$ and $\mathbf{D}'$ are $D_{13}, D_{23}, D'_{13}$ and $D'_{23}$, in which case no singular force, torque or stresslet will arise due to the deformation, since the velocity of the boundary is then at most $O(\epsilon^{-k+\frac{3}{2}})$.

### 2.5.1 Non-zero $D_{31}$ or $D_{32}$

The problem with $k = 1/2$ is easily solved by noting that the boundary conditions are formally identical to the case of a rolling motion of the particles. Replacing $\Omega_2$ by $-D_{31}$, $\Omega'_2$ by $-D'_{31}$, $\Omega_1$ by $D_{32}$ and $\Omega'_1$ by $D'_{32}$, the results from §2.3 can thus be carried over as

$$F_1 = \frac{3\pi \ln\epsilon}{\sqrt{\lambda_1\lambda_2}}\left[\frac{(\hat{D}'_{31} - \hat{D}_{31})\cos\chi}{3\lambda_1 + 2\lambda_2}\left(\frac{1}{R_1\lambda_1} - 1\right) + \frac{(\hat{D}'_{32} - \hat{D}_{32})\sin\chi}{2\lambda_1 + 3\lambda_2}\left(\frac{1}{R_1\lambda_2} - 1\right)\right] + O(1) \quad (2.51a)$$

$$F_2 = \frac{3\pi \ln\epsilon}{\sqrt{\lambda_1\lambda_2}}\left[\frac{(\hat{D}_{31}-\hat{D}'_{31})\sin\chi}{3\lambda_1+2\lambda_2}\left(\frac{1}{R_2\lambda_1}-1\right)+\frac{(\hat{D}'_{32}-\hat{D}_{32})\cos\chi}{2\lambda_1+3\lambda_2}\left(\frac{1}{R_2\lambda_2}-1\right)\right]+O(1) \tag{2.51b}$$

$$T_1 = \frac{3\pi \ln\epsilon}{\sqrt{\lambda_1\lambda_2}}\left[\frac{-(\hat{D}'_{31}-\hat{D}_{31})\sin\chi}{\lambda_1(3\lambda_1+2\lambda_2)}+\frac{(\hat{D}'_{32}-\hat{D}_{32})\cos\chi}{\lambda_2(2\lambda_1+3\lambda_2)}\right]+O(1) \tag{2.51c}$$

$$T_2 = \frac{-3\pi \ln\epsilon}{\sqrt{\lambda_1\lambda_2}}\left[\frac{(\hat{D}'_{31}-\hat{D}_{31})\cos\chi}{\lambda_1(3\lambda_1+2\lambda_2)}+\frac{(\hat{D}'_{32}-\hat{D}_{32})\sin\chi}{\lambda_2(2\lambda_1+3\lambda_2)}\right]+O(1)\ . \tag{2.51d}$$

The variables $\hat{D}_{ij}$ are related to the components $D_{ij}$ of the displacement rate tensor $\mathbf{D}$ in the usual way,

$$\begin{pmatrix}\hat{D}'_{31}-\hat{D}_{31}\\ \hat{D}'_{32}-\hat{D}_{32}\end{pmatrix} = \begin{pmatrix}\cos\chi & -\sin\chi\\ \sin\chi & \cos\chi\end{pmatrix}\cdot\begin{pmatrix}D'_{31}-D_{31}\\ D'_{32}-D_{32}\end{pmatrix}\ . \tag{2.51e}$$

The normal force can be derived in the same manner:

$$\begin{aligned}F_3 =& \frac{9}{4}\pi\ln\epsilon\frac{(D'_{32}-D_{32})}{\sqrt{\lambda_1\lambda_2}(\lambda_1+\lambda_2)}\left\{\frac{(2\lambda_1+\lambda_2)\kappa_1+(2\lambda_1+7\lambda_2)\kappa_3}{2\lambda_1+3\lambda_2}\frac{\cos\chi}{\sqrt{\lambda_2}}\right.\\ &\left.-\frac{(\lambda_1+2\lambda_2)\kappa_2+(7\lambda_1+2\lambda_2)\kappa_0}{3\lambda_1+2\lambda_2}\frac{\sin\chi}{\sqrt{\lambda_1}}\right\}\\ &+\frac{9}{4}\pi\ln\epsilon\frac{(D'_{31}-D_{31})}{\sqrt{\lambda_1\lambda_2}(\lambda_1+\lambda_2)}\left\{\frac{(\lambda_1+2\lambda_2)\kappa_2+(7\lambda_1+2\lambda_2)\kappa_0}{3\lambda_1+2\lambda_2}\frac{\cos\chi}{\sqrt{\lambda_1}}\right.\\ &\left.+\frac{(2\lambda_1+\lambda_2)\kappa_1+(2\lambda_1+7\lambda_2)\kappa_3}{2\lambda_1+3\lambda_2}\frac{\sin\chi}{\sqrt{\lambda_2}}\right\}+O(1)\ .\end{aligned} \tag{2.51f}$$

As always, the relations $S_{13}=S_{31}=-T_2/2$ and $S_{23}=S_{32}=T_1/2$ (2.24e-f) hold.

### 2.5.2 $D_{31}$ and $D_{32}$ equal to zero

The governing equations are identical to (2.25):

$$\frac{\partial^2\tilde{u}_{z1}}{\partial\bar{x}_3^2}=\frac{\partial\tilde{p}_z}{\partial\bar{x}_1}+\frac{\bar{x}_1}{R_1}\frac{\partial\tilde{p}_z}{\partial\bar{x}_3}\ ,\qquad \frac{\partial^2\tilde{u}_{z2}}{\partial\bar{x}_3^2}=\frac{\partial\tilde{p}_z}{\partial\bar{x}_2}+\frac{\bar{x}_2}{R_2}\frac{\partial\tilde{p}_z}{\partial\bar{x}_3}\ ,\qquad \frac{\partial\tilde{p}_z}{\partial\bar{x}_3}=0\ , \tag{2.52a}$$

$$\frac{\partial\tilde{u}_{z1}}{\partial\bar{x}_1}+\frac{\partial\tilde{u}_{z2}}{\partial\bar{x}_2}+\frac{\partial\tilde{u}_{z3}}{\partial\bar{x}_3}+\frac{\bar{x}_1}{R_1}\frac{\partial\tilde{u}_{z1}}{\partial\bar{x}_3}+\frac{\bar{x}_2}{R_2}\frac{\partial\tilde{u}_{z2}}{\partial\bar{x}_3}=0\ . \tag{2.52b}$$

The no-slip boundary conditions, however, now imply that (note that $k=1$), on $\bar{x}_3=0$:

$$\tilde{u}_{z1}=D_{11}\tilde{x}_1+D_{12}\tilde{x}_2\ ,\qquad \tilde{u}_{z2}=D_{21}\tilde{x}_1+D_{22}\tilde{x}_2\ ,$$

$$\tilde{u}_{z3}=D_{33}\tilde{x}_3\ , \tag{2.53a}$$

while on $\bar{x}_3 = h_z(\bar{x}_1, \bar{x}_2)$:

$$\tilde{u}_{z1} = D'_{11}\tilde{x}_1 + D'_{12}\tilde{x}_2 \ , \qquad \tilde{u}_{z2} = D'_{21}\tilde{x}_1 + D'_{22}\tilde{x}_2 \ ,$$
$$\tilde{u}_{z3} = D'_{33}(\tilde{x}_3 - 1) \ . \tag{2.53b}$$

The steps leading to the solution of a set of equations such as (2.25) are outlined by Cox (1974). The following differential equation for $\tilde{p}_z$ is readily arrived at:

$$\begin{aligned}
\bar{\nabla}\cdot(h_z^3\bar{\nabla}\tilde{p}_z) &= 12D'_{33}(h_z - 1) + 12(D_{11} + D_{22})h_z + 6(\Delta_{11} + \Delta_{22})h_z \qquad (2.54)\\
&- 12\Delta_{33}\Big\{\Big(\frac{\cos^2\chi}{2R_1} + \frac{\sin^2\chi}{2R_2}\Big)\hat{x}_1^2 + \sin\chi\cos\chi\Big(\frac{1}{R_1} - \frac{1}{R_2}\Big)\hat{x}_1\hat{x}_2 + \Big(\frac{\sin^2\chi}{2R_1} + \frac{\cos^2\chi}{2R_2}\Big)\hat{x}_2^2\Big\}\\
&- 6\Big((\Delta_{11}\cos\chi - \Delta_{12}\sin\chi)\hat{x}_1 + (\Delta_{11}\sin\chi + \Delta_{12}\cos\chi)\hat{x}_2\Big)\Big(\cos\chi\frac{\partial h_z}{\partial\hat{x}_1} + \sin\chi\frac{\partial h_z}{\partial\hat{x}_2}\Big)\\
&- 6\Big((\Delta_{21}\cos\chi - \Delta_{22}\sin\chi)\hat{x}_1 + (\Delta_{21}\sin\chi + \Delta_{22}\cos\chi)\hat{x}_2\Big)\Big(-\sin\chi\frac{\partial h_z}{\partial\hat{x}_1} + \cos\chi\frac{\partial h_z}{\partial\hat{x}_2}\Big)\\
&+ 12\Big((\Delta_{11}\cos\chi - \Delta_{12}\sin\chi)\hat{x}_1 + (\Delta_{11}\sin\chi + \Delta_{12}\cos\chi)\hat{x}_2\Big)\frac{\hat{x}_1\cos\chi + \hat{x}_2\sin\chi}{R_1}\\
&+ 12\Big((\Delta_{21}\cos\chi - \Delta_{22}\sin\chi)\hat{x}_1 + (\Delta_{21}\sin\chi + \Delta_{22}\cos\chi)\hat{x}_2\Big)\frac{-\hat{x}_1\sin\chi + \hat{x}_2\cos\chi}{R_2} \ ,
\end{aligned}$$

where the shorthand notation $\Delta_{ij} = D'_{ij} - D_{ij}$ has been introduced. The boundary conditions for this p.d.e. are most easily expressed in terms of the cylindrical coordinates $(\hat{r}, \theta)$. The solution must be periodic in $\theta$, bounded at the origin, and must satisfy $\tilde{p}_z = O(\hat{r}^{-2})$ for large $\hat{r}$ at finite $\hat{r}$. Since $k = 1$ for this problem, only the $F_3$ component can display singular behavior as $\epsilon \to 0$ (see (2.22 - 2.24)). From the discussion in §2.2.3 (especially eq. (C.8) and following), it should be apparent that it suffices to solve the previous p.d.e. in the limit $\hat{r} \to \infty$ to capture the singular nature of the normal force. For large $\hat{r}$, a separation of variables is possible. A

solution of the form $\tilde{p}_z = \hat{r}^{-2}\Theta(\theta)$ exists, where $\Theta(\theta)$ must satisfy:

$$
\begin{aligned}
&(\lambda_1 \sin^2\theta + \lambda_2 \cos^2\theta)\frac{d^2\Theta}{d\theta^2} - \big((6\lambda_1 + 2\lambda_2)\cos^2\theta + (2\lambda_1 + 6\lambda_2)\sin^2\theta\big)\Theta = \\
&\quad - 12\Delta_{33}\Big\{\big(\frac{\cos^2\chi}{2R_1} + \frac{\sin^2\chi}{2R_2}\big)\frac{\cos^2\theta}{\lambda_1} + \big(\frac{1}{R_1} - \frac{1}{R_2}\big)\sin\chi\cos\chi\frac{\sin\theta\cos\theta}{\sqrt{\lambda_1\lambda_2}} \\
&\quad + \big(\frac{\sin^2\chi}{2R_1} + \frac{\cos^2\chi}{2R_2}\big)\frac{\sin^2\theta}{\lambda_2}\Big\} + 6(\Delta_{11} + \Delta_{22}) \\
&\quad - 12\Big(\Delta_{11}\cos^2\chi - (\Delta_{12} + \Delta_{21})\sin\chi\cos\chi + \Delta_{22}\sin^2\chi\Big)\cos^2\theta \\
&\quad - 12\Big(\Delta_{11}\sin^2\chi + (\Delta_{12} + \Delta_{21})\sin\chi\cos\chi + \Delta_{22}\cos^2\chi\Big)\sin^2\theta \\
&\quad - 12\Big\{\Delta_{12}\big(\sqrt{\frac{\lambda_1}{\lambda_2}}\cos^2\chi - \sqrt{\frac{\lambda_2}{\lambda_1}}\sin^2\chi\big) + \Delta_{21}\big(\sqrt{\frac{\lambda_2}{\lambda_1}}\cos^2\chi - \sqrt{\frac{\lambda_1}{\lambda_2}}\sin^2\chi\big)\Big\}\sin\theta\cos\theta \\
&\quad + 12\Big[\Delta_{11}\frac{\cos^2\chi}{R_1} + \Delta_{22}\frac{\sin^2\chi}{R_2} + \sin\chi\cos\chi\big(\frac{\Delta_{12}}{R_1} + \frac{\Delta_{21}}{R_2}\big)\Big]\frac{\cos^2\theta}{\lambda_1} \\
&\quad + 12\Big[\Delta_{11}\frac{\sin^2\chi}{R_1} + \Delta_{22}\frac{\cos^2\chi}{R_2} + \sin\chi\cos\chi\big(\frac{\Delta_{12}}{R_1} + \frac{\Delta_{21}}{R_2}\big)\Big]\frac{\sin^2\theta}{\lambda_2} \qquad (2.55) \\
&\quad + 12\Big[\big(2\frac{\Delta_{11}}{R_1} - \frac{\Delta_{22}}{R_2}\big)\sin\chi\cos\chi + (\cos^2\chi - \sin^2\chi)\big(\frac{\Delta_{12}}{R_1} + \frac{\Delta_{21}}{R_2}\big)\Big]\frac{\sin\theta\cos\theta}{\sqrt{\lambda_1\lambda_2}} \\
&\quad - 12(\Delta_{11} + \Delta_{22})\Big(\sqrt{\frac{\lambda_1}{\lambda_2}} + \sqrt{\frac{\lambda_2}{\lambda_1}}\Big)\sin\chi\cos\chi\sin\theta\cos\theta + 12(D_{11} + D_{22} + D'_{33})\ .
\end{aligned}
$$

Using the tracelessness of $\mathbf{D}'$, the last term can be written as $-12(\Delta_{11} + \Delta_{22})$. The solution of (2.55) is of the form $\Theta(\theta) = \sum_{i=0}^{2} \xi_i \cos^{2-i}\theta \sin^i\theta$. Since $\Theta(\theta)$ has to be integrated from 0 to $2\pi$ in order to evaluate $F_3$, only the coefficients $\xi_0$ and $\xi_2$ need to be calculated. (The term in $\xi_1$ yields zero.) After some straightforward algebra, one gets the following result:

$$
\begin{aligned}
F_3 = \int_{\Sigma_\epsilon} \tilde{p}_z \,\mathrm{d}\tilde{x}_1 \mathrm{d}\tilde{x}_2 + O(\epsilon^0) &= (\lambda_1\lambda_2)^{-\frac{1}{2}} \int_{\delta}^{\epsilon^{1/2}\varepsilon} \hat{r}^{-1}\,\mathrm{d}\hat{r} \int_0^{2\pi} \Theta(\theta)\,\mathrm{d}\theta + g(\delta) + O(\epsilon^0) = \\
&\frac{3\pi\ln\epsilon}{2\sqrt{\lambda_1\lambda_2}(\lambda_1+\lambda_2)}\Big\{-\Delta_{33}\Big[\frac{1}{2R_1}\big(\frac{\cos^2\chi}{\lambda_1} + \frac{\sin^2\chi}{\lambda_2}\big) + \frac{1}{2R_2}\big(\frac{\sin^2\chi}{\lambda_1} + \frac{\cos^2\chi}{\lambda_2}\big)\Big] \\
&\quad + \frac{\Delta_{11}}{R_1}\Big(\frac{\cos^2\chi}{\lambda_1} + \frac{\sin^2\chi}{\lambda_2}\Big) + \frac{\Delta_{22}}{R_2}\Big(\frac{\cos^2\chi}{\lambda_2} + \frac{\sin^2\chi}{\lambda_1}\Big) \qquad (2.56) \\
&\quad + \sin\chi\cos\chi\Big(\frac{\Delta_{12}}{R_1} + \frac{\Delta_{21}}{R_2}\Big)\Big(\frac{1}{\lambda_2} - \frac{1}{\lambda_1}\Big) - 2(\Delta_{11} + \Delta_{22})\Big\} + O(\epsilon^0).
\end{aligned}
$$

### 2.5.3 Rigid particles in a straining flow

The tensorial relation between $\mathbf{F}$ and $\mathbf{E}_W$ is the same as between $\mathbf{F}$ and the opposite of the imposed rate of strain $\mathbf{E}$ (Jeffrey, 1989). Hence according to (2.56), the (3,3,3) component of the subtensor linking the force $\mathbf{F}$ to the rate of strain $-\mathbf{E}$ in the grand resistance tensor is given by

$$(\mathbf{R}_{FE}^{WW})_{333} = \frac{3\pi \ln \epsilon}{2\sqrt{\lambda_1\lambda_2}(\lambda_1+\lambda_2)}\left[\frac{1}{2R_1}\left(\frac{\cos^2\chi}{\lambda_1}+\frac{\sin^2\chi}{\lambda_2}\right)+\frac{1}{2R_2}\left(\frac{\sin^2\chi}{\lambda_1}+\frac{\cos^2\chi}{\lambda_2}\right)\right.$$
$$\left.+\frac{1}{3}\left\{\frac{1}{2R_1}\left(\frac{\cos^2\chi}{\lambda_1}+\frac{\sin^2\chi}{\lambda_2}\right)+\frac{1}{2R_2}\left(\frac{\cos^2\chi}{\lambda_2}+\frac{\sin^2\chi}{\lambda_1}\right)-4\right\}\right]. \quad (2.57)$$

The tracelessness of $\mathbf{E}$ has been used to confer the same property to $\mathbf{R}_{FE}^{WW}$, following the usual convention (Kim & Mifflin, 1985). It is now easy to see that the result (2.57) and equation (2.35e) satisfy the symmetry relation $(\mathbf{R}_{FE}^{WW})_{ijk} = (\mathbf{R}_{SU}^{WW})_{jki}$ predicted for any $i,j,k$ by Lorentz' reciprocal theorem for the case $i=j=k=3$. Also, since

$$\frac{\Delta_{12}}{R_1}+\frac{\Delta_{21}}{R_2} = \left(\frac{E'_{w12}+E'_{w21}}{2} - \frac{E_{w12}+E_{w21}}{2}\right)\left(\frac{1}{R_1}+\frac{1}{R_2}\right)+(\Omega_3-\Omega'_3)\left(\frac{1}{R_1}-\frac{1}{R_2}\right), \quad (2.58)$$

the tensor elements $(\mathbf{R}_{FE}^{WW})_{312} = (\mathbf{R}_{FE}^{WW})_{321}$ are found to be:

$$(\mathbf{R}_{FE}^{WW})_{312} = \frac{-3\pi \ln \epsilon}{4\sqrt{\lambda_1\lambda_2}(\lambda_1+\lambda_2)} \sin\chi\cos\chi\left(\frac{1}{R_1}+\frac{1}{R_2}\right)\left(\frac{1}{\lambda_2}-\frac{1}{\lambda_1}\right), \quad (2.59)$$

which agrees with (2.35f). One can also easily recover the result of §2.4 for the dependence of $F_3$ on $\Omega_3$.

Note also that since the formulae derived in this section only involve the difference in the deformation rates of $W$ and $W'$, the tensors $\mathbf{R}_{\mathcal{F}E}^{WW} = -\mathbf{R}_{\mathcal{F}E}^{WW'}$ and $\mathbf{R}_{SE}^{WW} = -\mathbf{R}_{SE}^{WW'}$. Hence the net forces, torques and stresslets exerted by immobile surfaces near contact in a straining flow are at most $O(1) = O(\epsilon^0)$, as discussed at the beginning of §2.5.

## 2.6 Resistance tensor for two particles near contact

### 2.6.1 Structure of the resistance tensor in the lubrication limit

The general structure of the grand resistance tensor for any two particles in a low-Reynolds-number linear flow is given by (2.49). However, in the special case of almost touching particles, the results of the lubrication analysis only depend on the *relative* motion $(\mathcal{U} - \mathcal{U}')$ of the two surfaces at their point of closest approach and the general formulation (in the absence of an imposed rate of strain),

$$\begin{pmatrix} \mathcal{F} \\ \mathcal{F}' \end{pmatrix} = \begin{pmatrix} \mathbf{F} \\ \mathbf{T} \\ \mathbf{F}' \\ \mathbf{T}' \end{pmatrix} = \mathbf{R} \cdot \begin{pmatrix} \mathbf{U} \\ \mathbf{\Omega} \\ \mathbf{U}' \\ \mathbf{\Omega}' \end{pmatrix} = \mathbf{R} \cdot \begin{pmatrix} \mathcal{U} \\ \mathcal{U}' \end{pmatrix} , \tag{2.60a}$$

must satisfy

$$\mathbf{R} = \begin{pmatrix} \mathbf{R}_L & -\mathbf{R}_L \\ -\mathbf{R}'_L & \mathbf{R}'_L \end{pmatrix} , \tag{2.60b}$$

with $\mathbf{R}_L$ and $\mathbf{R}'_L$ $6 \times 6$ subtensors. In addition, Lorentz' reciprocal theorem states that $\mathbf{R}$ should be symmetric, hence it requires that $\mathbf{R}_L = \mathbf{R}'^T_L$ and that $\mathbf{R}_L = \mathbf{R}^T_L$. Therefore,

$$\mathbf{R} = \begin{pmatrix} \mathbf{R}_L & -\mathbf{R}_L \\ -\mathbf{R}_L & \mathbf{R}_L \end{pmatrix} , \tag{2.60c}$$

with $\mathbf{R}_L = \mathbf{R}^T_L$.

### 2.6.2 Agreement with Lorentz' theorem

In some of the preceding sections [e.g., eq. (2.47)], explicit use of Lorentz' theorem has been made in order to avoid lengthy and error-prone calculations. In many other cases, however, the reciprocal theorem provides a check for internal consistency. In §2.5.3, it has been shown that $(\mathbf{R}^{WW}_{FE})_{3ij} = (\mathbf{R}^{WW}_{SU})_{ij3}$ for the pairs $(i, j) = (3,3)$ and (1,2). It is very easy to prove the same relation for the sets of indices (1,1) and (2,2). The formula for $F_3$ given in §2.5.1 can also be shown to fulfill the requirements set by Lorentz' theorem, but since this equation was derived from (2.47), this is a circular argument. In this section, the reciprocal theorem is shown to be satisfied by a few additional sets of resistance factors derived in this work. Other examples can be found readily, but may require more algebra.

*2.6.2.1.* $(\mathbf{R}^{WW'}_{F\Omega})_{33}$ *and* $(\mathbf{R}^{W'W}_{TU})_{33}$

By applying Lorentz' theorem to the result quoted in §2.4 we obtain the relation

$$T_3' = \frac{3\pi \ln \epsilon}{2\sqrt{\lambda_1\lambda_2}}(U_3 - U_3')\Big(\frac{1}{R_1} - \frac{1}{R_2}\Big)\frac{\lambda_2 - \lambda_1}{\lambda_1\lambda_2(\lambda_1 + \lambda_2)}\sin\chi\cos\chi + O(1)\ . \qquad (2.61)$$

Note from (2.35b) that this implies $T_3 = -T_3' + O(1)$. Indeed, conservation of linear and angular momentum implies that for any finite values of $\boldsymbol{\mathcal{U}}$,$\boldsymbol{\mathcal{U}}'$ and $\mathbf{E}$, the singular parts of $\boldsymbol{\mathcal{F}}$ and $\boldsymbol{\mathcal{F}}'$ must satisfy $\boldsymbol{\mathcal{F}} = -\boldsymbol{\mathcal{F}}'$, because the total (combined) force on the particles cannot be singular as $\epsilon \to 0$.

It is also possible, rather than deriving (2.61) from Lorentz' theorem, to apply (2.35b) directly to the surface $W'$. The relevant frame of reference is then given by the set of coordinates $(x_1', x_2', x_3')$. Therefore, the angle $\chi$ between the $\hat{x}_1$ axis and the $x_1$ axis has to be replaced by the angle $\chi + \phi$ between the $\hat{x}_1$ axis and the $x_1'$ axis (Fig. 2.1). Also, since the outward normal now points in the opposite sense of the $x_3'$ axis, the right hand side of (2.35b) is "off" by a minus sign,† i.e.,

$$T_3' = -\frac{3}{2}\pi\ \ln\epsilon\frac{(U_3 - U_3')}{\sqrt{\lambda_1\lambda_2}(\lambda_1 + \lambda_2)}\Big(\frac{1}{R_2'} - \frac{1}{R_1'}\Big)\Big(\frac{1}{\lambda_2} - \frac{1}{\lambda_1}\Big)\sin(\chi+\phi)\cos(\chi+\phi) + O(1)\ . \qquad (2.62)$$

---

† A more careful, but also more elaborate and less insightful, proof of this change of sign requires the introduction of a set of coordinates $(x_1^*, x_2^*, x_3^*)$, centered at $O'$. The $x_3^*$ axis points in the direction of the outward normal to $W'$ at $O'$ and hence runs antiparallel to the $x_3$ and $x_3'$ axes. The $x_1^*$ and $x_2^*$ axes are chosen along the local directions of principal curvature of $W'$ such that the set $(x_1^*, x_2^*, x_3^*)$ forms a right handed coordinate system. A logical choice is $x_1^* = x_2'$ and $x_2^* = x_1'$. This set of coordinates is the equivalent on $W'$ of the frame defined by $(x_1, x_2, x_3)$ on $W$. In order to convert the formulae obtained in the previous sections to this new coordinate system, yet another set of coordinates $(\hat{x}_1^*, \hat{x}_2^*, \hat{x}_3^*)$ needs to be introduced, with $\hat{x}_3^* = x_3^*$, $\hat{x}_1^* = \hat{x}_2$, and $\hat{x}_2^* = \hat{x}_1$. The angle between $\hat{x}_1^*$ and $x_1^*$ is $-(\chi + \phi)$. Taking these transformations into account, and applying them to (2.35b), one arrives at the formula (2.62).

The expressions (2.61) and (2.62) can only agree if

$$\Big(\frac{1}{R_1}-\frac{1}{R_2}\Big)\sin\chi\cos\chi=-\Big(\frac{1}{R_1'}-\frac{1}{R_2'}\Big)\sin(\chi+\phi)\cos(\chi+\phi)+O(1)\,. \qquad (2.63)$$

This simple relation is proven in Appendix A.

*2.6.2.2.* $(\mathbf{R}_{T\Omega}^{ww'})_{11}$ *and* $(\mathbf{R}_{T\Omega}^{w'w})_{11}$

It is easy to derive the following components of the resistance tensor from the expressions (2.45c) and (2.45d):

$$(\mathbf{R}_{T\Omega}^{ww'})_{11}=\frac{3\pi\ln\epsilon}{\sqrt{\lambda_1\lambda_2}}\Big[\frac{\sin^2\chi}{\lambda_1(3\lambda_1+2\lambda_2)}+\frac{\cos^2\chi}{\lambda_2(2\lambda_1+3\lambda_2)}\Big]\,, \qquad (2.64a)$$

$$(\mathbf{R}_{T\Omega}^{ww'})_{12}=(\mathbf{R}_{T\Omega}^{ww'})_{21}=\frac{3\pi\ln\epsilon}{\sqrt{\lambda_1\lambda_2}}\sin\chi\cos\chi\Big[\frac{1}{\lambda_1(3\lambda_1+2\lambda_2)}-\frac{1}{\lambda_2(2\lambda_1+3\lambda_2)}\Big]\,, \qquad (2.64b)$$

$$(\mathbf{R}_{T\Omega}^{ww'})_{22}=\frac{3\pi\ln\epsilon}{\sqrt{\lambda_1\lambda_2}}\Big[\frac{\cos^2\chi}{\lambda_1(3\lambda_1+2\lambda_2)}+\frac{\sin^2\chi}{\lambda_2(2\lambda_1+3\lambda_2)}\Big]\,. \qquad (2.64c)$$

These equalities are valid to $O(\epsilon^0)$. The equation (2.64b) shows that the predicted symmetry of $\mathbf{R}_L$ is not violated. Lorentz' reciprocal theorem demands that $(\mathbf{R}_{T\Omega}^{ww'})_{11}=(\mathbf{R}_{T\Omega}^{w'w})_{11}$. However, by applying (2.64a) directly to $W'$ in the frame $(x_1^*,x_2^*,x_3^*)$ [see preceding footnote or eq. (2.66)], the following expression is arrived at:

$$(\mathbf{R}_{T\Omega}^{w'w})_{11}^{**}=\frac{3\pi\ln\epsilon}{\sqrt{\lambda_1\lambda_2}}\Big[\frac{\sin^2(\chi+\phi)}{\lambda_2(3\lambda_2+2\lambda_1)}+\frac{\cos^2(\chi+\phi)}{\lambda_1(2\lambda_2+3\lambda_1)}\Big]\,. \qquad (2.65)$$

Use has been made of the fact that $\lambda_1^*=\lambda_2$ and $\lambda_2^*=\lambda_1$. In order to verify (2.65), one calculates $(\mathbf{R}_{T\Omega}^{w'w})_{11}^{**}$ from the expressions (2.45) derived in the frame $(x_1,x_2,x_3)$ by applying the transformation

$$\begin{pmatrix}x_1^*\\x_2^*\\x_3^*\end{pmatrix}=\begin{pmatrix}-\sin\phi&\cos\phi&0\\\cos\phi&\sin\phi&0\\0&0&-1\end{pmatrix}\cdot\begin{pmatrix}x_1\\x_2\\x_3\end{pmatrix}=\mathbf{A}\cdot\begin{pmatrix}x_1\\x_2\\x_3\end{pmatrix} \qquad (2.66)$$

to the components of the torque $\mathbf{T}'$ and of the angular velocity $\mathbf{\Omega}$. (The boldface characters in the next two equations stand for the matrix representations of the

corresponding tensors in the relevant coordinate systems, rather than for the tensors themselves):

$$\mathbf{T}' = \mathbf{A}^T \cdot \mathbf{T}'^* = \mathbf{R}^{W'W}_{T\,\Omega} \cdot \boldsymbol{\Omega} = \mathbf{R}^{W'W}_{T\,\Omega} \cdot \mathbf{A}^T \cdot \boldsymbol{\Omega}^* \ , \tag{2.67a}$$

where the superscript * denotes that the frame of reference used is $(x_1^*, x_2^*, x_3^*)$. But since $\mathbf{T}'^* = (\mathbf{R}^{W'W}_{T\,\Omega})^{**} \cdot \boldsymbol{\Omega}^*$, the two resistance tensors must be related by

$$(\mathbf{R}^{W'W}_{T\,\Omega})^{**} = \mathbf{A} \cdot \mathbf{R}^{W'W}_{T\,\Omega} \cdot \mathbf{A}^T \ . \tag{2.67b}$$

In particular, the $\mathbf{e}_1^*\mathbf{e}_1^*$ component can be computed as

$$(\mathbf{R}^{W'W}_{T\Omega})^{**}_{11} = \sin^2\phi(\mathbf{R}^{W'W}_{T\,\Omega})_{11} - \sin\phi\cos\phi\left[(\mathbf{R}^{W'W}_{T\,\Omega})_{12} + (\mathbf{R}^{W'W}_{T\,\Omega})_{21}\right] + \cos^2\phi(\mathbf{R}^{W'W}_{T\,\Omega})_{22} \ . \tag{2.67c}$$

This relation is easily verified using the formulae above.

## 2.7 Application to two spheres near contact

The use of the results derived above will be illustrated for two almost touching spherical objects. Cox (1974) calculated the first term in the asymptotic expansion of most, but not all, of the resistance functions for this system. The present results now make it possible to construct the resistance tensor accurate to $O(\epsilon^0)$ for any two surfaces near contact. In the special case of two spheres, the expressions can be compared with Jeffrey's calculations (Jeffrey, 1982; Jeffrey & Corless, 1988; Corless & Jeffrey, 1988; Jeffrey, 1989).

The gap width between the two spheres, expressed in terms of rescaled variables, is given by

$$h = 1 + \frac{1}{2}\Big(\frac{1}{R} + \frac{1}{R'}\Big)r^2 + \frac{\epsilon}{8}\Big(\frac{1}{R^3} + \frac{1}{R'^3}\Big)r^4 \ , \tag{2.68a}$$

where $R = R_1 = R_2$ and $R' = R'_1 = R'_2$ are the radii of the spheres with surface $W$ and $W'$ respectively. All the other symbols retain the meaning of the preceding sections. Obviously, $\lambda_1 = \lambda_2 = \lambda = (R^{-1} + R'^{-1})/2$, $\kappa_i = 0$ for all i, and

$$\zeta_0 = \frac{1}{2}\zeta_2 = \zeta_4 = \frac{1}{4\lambda}\Big(\frac{1}{R^2} - \frac{1}{RR'} + \frac{1}{R'^2}\Big) \ . \tag{2.68b}$$

### 2.7.1 $(\mathbf{R}_{FU}^{WW})_{33}$ and $(\mathbf{R}_{FU}^{WW'})_{33}$

As a first example, the normal force exerted by the surface $W$ when the particles move along their line of centers can be calculated. Using (2.44), it is immediately deduced after some simplification, that

$$F_3 = -\frac{3\pi}{2\epsilon}\frac{(U_3' - U_3)}{\lambda^2} + \frac{3}{20}\pi \ln\epsilon \frac{(U_3' - U_3)}{\lambda^3}\Big(\frac{1}{R^2} + \frac{7}{RR'} + \frac{1}{R'^2}\Big) \,. \tag{2.69}$$

This result agrees with the expression given by Jeffrey (1982).

### 2.7.2 $(\mathbf{R}_{S\Omega}^{WW})_{132}$ and $(\mathbf{R}_{S\,\Omega}^{W'W})_{132}$

The next example to be discussed concerns the stresslets exerted by both spheres on the surrounding fluid when one of the particles rotates about an axis perpendicular to the line of centers and the other sphere is kept stationary. The rotation axis, which passes through the geometric center of the spinning sphere, defines the direction of the $x_2$ axis. From the definition of the stresslet, (2.15b), it is straightforward to derive that a change of origin from a point $B$ to a point $A$ transforms $\mathbf{S}$ according to the rule

$$\mathbf{S}^A = \mathbf{S}^B - \frac{1}{2}\{\mathbf{r}_{AB}\mathbf{F} + \mathbf{F}\mathbf{r}_{AB}\} + \frac{1}{3}(\mathbf{F}\cdot\mathbf{r}_{AB})\mathbf{I} \,, \tag{2.70}$$

where $\mathbf{r}_{AB}$ is the vector linking $B$ to $A$, and $\mathbf{S}^A$ is the stresslet at $A$. (In the preceding sections, $\mathbf{S} = \mathbf{S}^O$.) Also, for rigid bodies, the velocities at $A$ and at $B$ are related as follows:

$$\mathbf{U}^A = \mathbf{U}^B + \mathbf{\Omega}\wedge\mathbf{r}_{AB} \,. \tag{2.71}$$

The stresslet component $S_{13}^C$ exerted by the sphere of radius $R$ at its geometric center $C$ when it rotates with angular velocity $\Omega_2\mathbf{e}_2$ in the vicinity of a stationary sphere of radius $R'$ can then be calculated using the expressions derived in this work:

$$\begin{aligned} S_{13}^C &= S_{13}^O + \frac{R}{2}F_1 \\ &= \Big[(\mathbf{R}_{S\Omega}^{WW})_{132} + \frac{R}{2}(\mathbf{R}_{F\Omega}^{WW})_{12} + R(\mathbf{R}_{SU}^{WW})_{131} + \frac{R^2}{2}(\mathbf{R}_{FU}^{WW})_{11}\Big]\Omega_2 \,. \end{aligned} \tag{2.72}$$

We omitted the superscript "$O$" on all the resistance tensors, since this has been the default point of reference throughout this chapter. On the surface, at $O$, where the coordinate $(\mathbf{r}_W)_3$ is $O(\epsilon^{1/2})$ compared to the radial distance $\left[(\mathbf{r}_W)_1^2 + (\mathbf{r}_W)_2^2\right]^{1/2}$, the relations (2.24e) and (2.24f) hold so that $(\mathbf{R}^{WW}_{S\Omega})_{132} = -\frac{1}{2}(\mathbf{R}^{WW}_{T\Omega})_{22}$ and $(\mathbf{R}^{WW}_{SU})_{131} = -\frac{1}{2}(\mathbf{R}^{WW}_{TU})_{21}$. Also, from Lorentz' reciprocal theorem, $(\mathbf{R}^{WW}_{F\Omega})_{12} = (\mathbf{R}^{WW}_{TU})_{21}$. Therefore (2.72) is equivalent to

$$\mathbf{S}^C_{13} = \left\{-\frac{1}{2}(\mathbf{R}^{WW}_{T\Omega})_{22} + \frac{R^2}{2}(\mathbf{R}^{WW}_{FU})_{11}\right\}\Omega_2 \ . \tag{2.73}$$

The resistance functions in the previous formula can be evaluated from (2.45). A little algebra yields, with $\varrho = R'/R$,

$$S^C_{13} = -\frac{4}{5}\pi \ln\epsilon \frac{R^3}{(1+\varrho)^2}(2\varrho - \varrho^2)\Omega_2 \ , \tag{2.74}$$

which is identical up to $O(1)$ to the result reported by Corless and Jeffrey (1988). Note also that all the other components of $\mathbf{S}^C$, save $S^C_{31} = S^C_{13}$, should be at most $O(1)$ from symmetry considerations. This can easily be verified using the relevant resistance functions (2.45) applied to two spherical bodies.

The relations (2.45) can also be used to calculate the stresslet on the stationary particle. In this case,

$$\begin{aligned} S'^{C'}_{13} &= S'^{O'}_{13} - \frac{R'}{2}F'_1 \qquad (2.75)\\ &= \left[(\mathbf{R}^{W'W}_{S\Omega})_{132} - \frac{R'}{2}(\mathbf{R}^{W'W}_{F\Omega})_{12} + R(\mathbf{R}^{W'W}_{SU})_{131} - \frac{RR'}{2}(\mathbf{R}^{W'W}_{FU})_{11}\right]\Omega_2 \\ &= \left[-\frac{1}{2}(\mathbf{R}^{W'W}_{T\Omega})_{22} - \frac{R'}{2}(\mathbf{R}^{WW'}_{TU})_{21} - \frac{R}{2}(\mathbf{R}^{W'W}_{TU})_{21} - \frac{RR'}{2}(\mathbf{R}^{W'W}_{FU})_{11}\right]\Omega_2 \\ &= \left[-\frac{1}{2}(\mathbf{R}^{WW'}_{T\Omega})_{22} - \frac{R'}{2}(\mathbf{R}^{WW'}_{TU})_{21} - \frac{R}{2}(\mathbf{R}^{WW'}_{TU})_{21} - \frac{RR'}{2}(\mathbf{R}^{WW'}_{FU})_{11}\right]\Omega_2 \ . \end{aligned}$$

The last step exploits the fact that only relative particle motions matter in the lubrication approximation so that

$$(\mathbf{R}^{W'W}_{TU})_{21} = (\mathbf{R}^{WW'}_{F\Omega})_{12} = -(\mathbf{R}^{WW}_{F\Omega})_{12} = -(\mathbf{R}^{WW}_{TU})_{21} = (\mathbf{R}^{WW'}_{TU})_{21} \ . \tag{2.76}$$

The application of (2.45) in the special case of two spheres near contact, and some simple algebraic manipulations, then reproduce Corless and Jeffrey's results (1988), i.e.,

$$S_{13}^{\prime C^{\prime}} = -\frac{2}{5}\pi \ln \epsilon \, (R+R^{\prime})^3 \left\{ \frac{7\varrho^2+\varrho^3}{(1+\varrho)^5} \right\} \Omega_2 \ . \tag{2.77}$$

Other known results for two almost touching spheres (Jeffrey, 1989; Jeffrey & Corless, 1988) can be recovered through analogous calculations.

## 2.8 Conclusions

The grand resistance tensor for two nearly touching walls can now be constructed accurate to $O(\epsilon^0)$, where $\epsilon$ is the minimum separation between the surfaces, non-dimensionalized by the harmonic mean of the principal radii of curvature at the points of closest approach. The formulae needed are given in (2.35), (2.43), (2.44), (2.45), (2.48), (2.51), (2.56) and (2.24e-f), and occasional use of Lorentz' reciprocal theorem to find resistance factors which were not calculated explicitly. The only restriction placed on the walls is that contact would occur at a single point if the surfaces were forced to touch in their present orientation. Any two convex shapes satisfy this criterion. This work extends Cox's analysis (1974) of the forces for two bodies near contact by including stresslets in the calculation, by considering the effect of an imposed rate of strain, and by evaluating the stress moments arising due to surface curvature of more than second order. Most notably, it has been shown that the $O(r^3)$ and $O(r^4)$ features of the particle shapes can give rise to logarithmically singular forces and torques as $\epsilon \to 0$. Since it is not possible with lubrication theory alone to determine the $O(1)$ corrections to the resistance tensor, this study has reached the limits of attainable accuracy based on this asymptotic method. Note however that the singular behavior of the derivatives of the resistance functions with respect to position is not yet fully characterized, as $O\big(\epsilon \ln(\epsilon)\big)$ contributions to the stress moments were not estimated. Since the magnitude of the Brownian displacements of suspended particles depends on the divergence of $\mathbf{R}_{FU}^{-1}$

(Brady & Bossis, 1988), these quantities are of interest in suspension rheology. They could, in principle, be obtained by carrying out the analysis to higher order, but the algebra becomes quite complicated even in the case of spheres (Jeffrey & Corless, 1988; Corless & Jeffrey, 1988; Jeffrey, 1989). We did not attempt their calculation for arbitrary surface shapes.

# APPENDIX A

## The relation between $\lambda_1, \lambda_2$ and $\chi$, and the geometry of the problem

Finding the transformation matrix mapping the $(\bar{x}_1, \bar{x}_2)$ coordinate system onto the set $(\hat{x}_1, \hat{x}_2)$ requires the solution of a simple eigenvalue problem. The equation for the gap width $h_z$ can be written in the form

$$h_z = 1 + (\bar{x}_1\ \bar{x}_2) \cdot \mathbf{C} \cdot (\bar{x}_1\ \bar{x}_2)^T \ . \tag{A.1}$$

The characteristic matrix $\mathbf{C}$ is defined as

$$\mathbf{C} = \begin{pmatrix} (2R_1)^{-1} + \mathcal{B}_0 & \mathcal{B}_1/2 \\ \mathcal{B}_1/2 & (2R_2)^{-1} + \mathcal{B}_2 \end{pmatrix} \ . \tag{A.2}$$

Let $\hat{\mathbf{e}}_1$ and $\hat{\mathbf{e}}_2$ be the unit eigenvectors of $\mathbf{C}$ corresponding to the eigenvalues $\lambda_1$ and $\lambda_2$ and consider the orthonormal matrix $\mathbf{Y} = (\hat{\mathbf{e}}_1\ \hat{\mathbf{e}}_2)$. By definition then $\mathbf{C} \cdot \mathbf{Y} = \mathbf{Y} \cdot \boldsymbol{diag}(\lambda_1, \lambda_2)$ and the transformation $(\bar{x}_1, \bar{x}_2)^T = \mathbf{Y} \cdot (\hat{x}_1, \hat{x}_2)^T$ achieves the desired simplification,

$$h_z - 1 = (\bar{x}_1\ \bar{x}_2) \cdot \mathbf{C} \cdot (\bar{x}_1, \bar{x}_2)^T = (\hat{x}_1\ \hat{x}_2) \cdot \boldsymbol{diag}(\lambda_1, \lambda_2) \cdot (\hat{x}_1, \hat{x}_2)^T = \lambda_1 \hat{x}_1^2 + \lambda_2 \hat{x}_2^2 \ . \tag{A.3}$$

Thus $\mathbf{Y}$ can be associated with the transformation matrix in (2.30). Solving the characteristic equation $\det(\mathbf{C} - \lambda_i \mathbf{I}) = 0$ gives the following roots:

$$\lambda_i = \frac{1}{4}\Big\{ \frac{1}{R_1} + \frac{1}{R_2} + \frac{1}{R_1'} + \frac{1}{R_2'} \pm \sqrt{\mathcal{D}} \Big\} \ , \tag{A.4}$$

where the discriminant $\mathcal{D}$ is given by

$$\mathcal{D} = \Big( \frac{1}{R_1} - \frac{1}{R_2} \Big)^2 + \Big( \frac{1}{R_1'} - \frac{1}{R_2'} \Big)^2 + 2 \cos 2\phi \Big( \frac{1}{R_1} - \frac{1}{R_2} \Big) \Big( \frac{1}{R_1'} - \frac{1}{R_2'} \Big) \ . \tag{A.5}$$

Since the surfaces are non-intersecting, $\mathbf{C}$ is positive definite and $\lambda_i > 0$. This implies that $\mathcal{D} < (R_1^{-1} + R_2^{-1} + R_1'^{-1} + R_2'^{-1})^2$. If one recalls that distances are

non-dimensionalized using $\grave{R}_c^{-1} = (\grave{R}_1^{-1} + \grave{R}_2^{-1} + \grave{R}_1'^{-1} + \grave{R}_2'^{-1})/4$, it is clear that $0 < \lambda_i < 2$.

The relation between the eigenvectors $\hat{\mathbf{e}}_1$ and $\hat{\mathbf{e}}_2$ and the angle $\chi$ defined in (2.30) leads to:

$$\tan\chi = \frac{(R_1^{-1} - R_2^{-1}) + \cos 2\phi(R_1'^{-1} - R_2'^{-1}) + \sqrt{\mathcal{D}}}{\sin 2\phi(R_1'^{-1} - R_2'^{-1})} , \tag{A.6}$$

from which it is easy to derive using trigonometric identities that

$$\left(\frac{1}{R_1} - \frac{1}{R_2}\right)\sin\chi\cos\chi = -\left(\frac{1}{R_1'} - \frac{1}{R_2'}\right)\sin(\chi+\phi)\cos(\chi+\phi) . \tag{A.7}$$

# APPENDIX B

## Implications of Lorentz' reciprocal theorem

Let $\mathbf{u}$ be the velocity field and $\boldsymbol{\sigma} = -\mathbf{I}p + \nabla\mathbf{u} + (\nabla\mathbf{u})^T$ be the pressure field corresponding to any flow satisfying the Stokes equations

$$\nabla p = \nabla^2\mathbf{u} \qquad \text{and} \qquad \nabla\cdot\mathbf{u} = 0\ , \tag{B.1}$$

and let $(\mathbf{u}', \boldsymbol{\sigma}')$ characterize any other fluid motion conforming to (B.1). Then the reciprocal theorem, originally due to Lorentz, demands that (Brenner 1963)

$$\int_{\mathcal{S}} \mathrm{d}\boldsymbol{\mathcal{S}}\cdot\boldsymbol{\sigma}\cdot\mathbf{u}' = \int_{\mathcal{S}} \mathrm{d}\boldsymbol{\mathcal{S}}\cdot\boldsymbol{\sigma}'\cdot\mathbf{u}\ , \tag{B.2}$$

in which $\mathcal{S}$ is any closed surface drawn in the fluid. The result (B.2) imposes symmetry requirements on the resistance tensor of an arbitrary isolated particle (Brenner, 1963; Brenner, 1964; Hinch, 1972). Lorentz' theorem also determines the symmetry properties of the $N$-body resistance tensor in systems of $N$ particles.

Consider, for example, the two flow cases depicted in Figure 2.2. The velocity field $\mathbf{u}$ and the associated stress field $\boldsymbol{\sigma}$ arise from the translation of a particle $W$ with velocity $\mathbf{U}$, keeping particle $W'$ stationary. The fields $\mathbf{u}'$ and $\boldsymbol{\sigma}'$ are caused by spinning particle $W'$ at an angular velocity $\boldsymbol{\Omega}'$, while fixing particle $W$. Let $\mathcal{S}$ consist of the particle surfaces, and of a shell $Z$ of very large radius $R_Z$ chosen such that $Z$ surrounds both bodies. When applying the reciprocal theorem, the contribution of the outer sphere $Z$ vanishes, since $\boldsymbol{\sigma}\cdot\mathbf{u}'$ and $\boldsymbol{\sigma}'\cdot\mathbf{u}$ are at most $O(R_Z^{-3})$ as $R_Z \to \infty$, while the surface is $O(R_Z^2)$ (Brenner, 1963). Using the no-slip boundary condition at the particles' surface, we obtain the relation

$$\int_{W'} \mathrm{d}\mathbf{W}'\cdot\boldsymbol{\sigma}\cdot(\boldsymbol{\Omega}'\wedge\mathbf{r}) = \int_{W} \mathrm{d}\mathbf{W}\cdot\boldsymbol{\sigma}'\cdot\mathbf{U}\ , \tag{B.3}$$

which can be rearranged as

$$\boldsymbol{\Omega}'\cdot\Big(\int_{W'} \mathbf{r}\wedge\boldsymbol{\sigma}\cdot\mathrm{d}\mathbf{W}'\Big) = \mathbf{U}\cdot\int_{W} \mathrm{d}\mathbf{W}\cdot\boldsymbol{\sigma}'\ . \tag{B.4}$$

The integral on the left hand side is the hydrodynamic torque experienced by particle $W'$ under action of the translating particle $W$. It depends linearly on $\mathbf{U}$ in the limit of zero Reynolds number, when (B.1) apply. Hence

$$-\int_{W'} \mathbf{r} \wedge \boldsymbol{\sigma} \cdot \mathrm{d}\mathbf{W}' = \mathbf{R}_{TU}^{W'W} \cdot \mathbf{U} \ , \tag{B.5}$$

with $\mathbf{R}_{TU}^{W'W}$ a part of the grand resistance tensor for this two-body system. Similarly,

$$-\int_{W} \mathrm{d}\mathbf{W} \cdot \boldsymbol{\sigma}' = \mathbf{R}_{F\Omega}^{WW'} \cdot \boldsymbol{\Omega}' \tag{B.6}$$

is the force experienced by particle $W$ due to the rotation of its companion $W'$. The reciprocal theorem predicts that

$$\boldsymbol{\Omega}' \cdot \mathbf{R}_{TU}^{W'W} \cdot \mathbf{U} = \mathbf{U} \cdot \mathbf{R}_{F\Omega}^{WW'} \cdot \boldsymbol{\Omega}' \ . \tag{B.7}$$

Since $\boldsymbol{\Omega}'$ and $\mathbf{U}$ are arbitrary, this implies that

$$\mathbf{R}_{TU}^{W'W} = (\mathbf{R}_{F\Omega}^{WW'})^T \ . \tag{B.8}$$

A series of similar expressions can be derived to show that the $N$-body resistance tensor is symmetric.

# APPENDIX C

## Solution of the third order problem for a direct approach of the surfaces (complement of §2.2.3)

From (2.11), the equations describing the flow are:

$$\frac{\partial^2 \tilde{u}_{\epsilon 1}}{\partial \bar{x}_3^2}+\left\{ \frac{\partial^2 \tilde{u}_{z1}}{\partial \bar{x}_1^2} + \frac{\partial^2 \tilde{u}_{z1}}{\partial \bar{x}_2^2} + \frac{2\bar{x}_1}{R_1}\frac{\partial^2 \tilde{u}_{z1}}{\partial \bar{x}_1 \partial \bar{x}_3} + \frac{2\bar{x}_2}{R_2}\frac{\partial^2 \tilde{u}_{z1}}{\partial \bar{x}_2 \partial \bar{x}_3} + \left(\frac{1}{R_1}+\frac{1}{R_2}\right)\frac{\partial \tilde{u}_{z1}}{\partial \bar{x}_3} + \left(\frac{\bar{x}_1^2}{R_1^2}+\frac{\bar{x}_2^2}{R_2^2}\right)\frac{\partial^2 \tilde{u}_{z1}}{\partial \bar{x}_3^2}\right\} \tag{C.1a}$$

$$= \frac{\partial \tilde{p}_\epsilon}{\partial \bar{x}_1} + \frac{\bar{x}_1}{R_1}\frac{\partial \tilde{p}_\epsilon}{\partial \bar{x}_3} + \sum_{i=0}^{2}(3-i)\Gamma_i \bar{x}_1^{2-i}\bar{x}_2^i \frac{\partial \tilde{p}_h}{\partial \bar{x}_3} + \sum_{i=0}^{3}(4-i)\Upsilon_i \bar{x}_1^{3-i}\bar{x}_2^i \frac{\partial \tilde{p}_z}{\partial \bar{x}_3} ,$$

$$\frac{\partial^2 \tilde{u}_{\epsilon 2}}{\partial \bar{x}_3^2}+\left\{ \frac{\partial^2 \tilde{u}_{z2}}{\partial \bar{x}_1^2} + \frac{\partial^2 \tilde{u}_{z2}}{\partial \bar{x}_2^2} + \frac{2\bar{x}_1}{R_1}\frac{\partial^2 \tilde{u}_{z2}}{\partial \bar{x}_1 \partial \bar{x}_3} + \frac{2\bar{x}_2}{R_2}\frac{\partial^2 \tilde{u}_{z2}}{\partial \bar{x}_2 \partial \bar{x}_3} + \left(\frac{1}{R_1}+\frac{1}{R_2}\right)\frac{\partial \tilde{u}_{z2}}{\partial \bar{x}_3} + \left(\frac{\bar{x}_1^2}{R_1^2}+\frac{\bar{x}_2^2}{R_2^2}\right)\frac{\partial^2 \tilde{u}_{z2}}{\partial \bar{x}_3^2}\right\} \tag{C.1b}$$

$$= \frac{\partial \tilde{p}_\epsilon}{\partial \bar{x}_2} + \frac{\bar{x}_2}{R_2}\frac{\partial \tilde{p}_\epsilon}{\partial \bar{x}_3} + \sum_{i=1}^{3} i\Gamma_i \bar{x}_1^{3-i}\bar{x}_2^{i-1} \frac{\partial \tilde{p}_h}{\partial \bar{x}_3} + \sum_{i=1}^{4} i\Upsilon_i \bar{x}_1^{4-i}\bar{x}_2^{i-1} \frac{\partial \tilde{p}_z}{\partial \bar{x}_3} ,$$

$$\frac{\partial^2 \tilde{u}_{z3}}{\partial \bar{x}_3^2} = \frac{\partial \tilde{p}_\epsilon}{\partial \bar{x}_3} , \tag{C.1c}$$

$$\frac{\partial \tilde{u}_{\epsilon 1}}{\partial \bar{x}_1} + \frac{\partial \tilde{u}_{\epsilon 2}}{\partial \bar{x}_2} + \frac{\partial \tilde{u}_{\epsilon 3}}{\partial \bar{x}_3} + \frac{\bar{x}_1}{R_1}\frac{\partial \tilde{u}_{\epsilon 1}}{\partial \bar{x}_3} + \frac{\bar{x}_2}{R_2}\frac{\partial \tilde{u}_{\epsilon 2}}{\partial \bar{x}_3} + \sum_{i=0}^{2}(3-i)\Gamma_i \bar{x}_1^{2-i}\bar{x}_2^i \frac{\partial \tilde{u}_{h1}}{\partial \bar{x}_3} \tag{C.1d}$$

$$+ \sum_{i=1}^{3} i\Gamma_i \bar{x}_1^{3-i}\bar{x}_2^{i-1} \frac{\partial \tilde{u}_{h2}}{\partial \bar{x}_3} + \sum_{i=0}^{3}(4-i)\Upsilon_i \bar{x}_1^{3-i}\bar{x}_2^i \frac{\partial \tilde{u}_{z1}}{\partial \bar{x}_3} + \sum_{i=1}^{4} i\Upsilon_i \bar{x}_1^{4-i}\bar{x}_2^{i-1} \frac{\partial \tilde{u}_{z2}}{\partial \bar{x}_3} = 0 .$$

Although the expressions become extremely unwieldy, the procedure for solving these coupled equations is identical to that followed at the two lower levels of approximation. First, $\tilde{p}_\epsilon$ can be calculated, up to an unknown function $\Pi(\bar{x}_1, \bar{x}_2)$, by integration of (C.1c). Making use of the result (2.34b), it is straightforward to

obtain that

$$\begin{aligned}\tilde{p}_\epsilon =& 3\frac{(U_3' - U_3)}{\lambda_1+\lambda_2}\Bigg\{ \frac{-2(\lambda_1+\lambda_2)}{(1+\hat{r}^2)^3}\bar{x}_3^2 + \frac{12\hat{r}^2}{(1+\hat{r}^2)^4}(\lambda_1\cos^2\theta + \lambda_2\sin^2\theta)\bar{x}_3^2 \\ &+ \frac{2(\lambda_1+\lambda_2)}{(1+\hat{r}^2)^2}\bar{x}_3 - \frac{8\hat{r}^2}{(1+\hat{r}^2)^3}(\lambda_1\cos^2\theta + \lambda_2\sin^2\theta)\bar{x}_3 \\ &- \frac{4\hat{r}^2}{(1+\hat{r}^2)^3}\left[\frac{\cos^2\theta}{\hat{R}_1} + \frac{\sin^2\theta}{\hat{R}_2} + \left(\sqrt{\frac{\lambda_1}{\lambda_2}} + \sqrt{\frac{\lambda_2}{\lambda_1}}\right)\frac{\sin\theta\cos\theta}{\hat{R}_s}\right]\bar{x}_3 \qquad \text{(C.2a)} \\ &+ \frac{2\hat{r}^2}{(1+\hat{r}^2)^2}\left[\frac{\cos^2\theta}{\hat{R}_1} + \frac{\sin^2\theta}{\hat{R}_2} + \left(\sqrt{\frac{\lambda_1}{\lambda_2}} + \sqrt{\frac{\lambda_2}{\lambda_1}}\right)\frac{\sin\theta\cos\theta}{\hat{R}_s}\right] + \Pi(\hat{r},\theta)\Bigg\} ,\end{aligned}$$

where the variables $\hat{R}_1, \hat{R}_2$ and $\hat{R}_s$ have been introduced so that:

$$\frac{1}{\hat{R}_1} = \frac{\cos^2\chi}{R_1} + \frac{\sin^2\chi}{R_2} , \qquad \frac{1}{\hat{R}_2} = \frac{\sin^2\chi}{R_1} + \frac{\cos^2\chi}{R_2} ,$$
$$\frac{1}{\hat{R}_s} = \left(\frac{1}{R_1} - \frac{1}{R_2}\right)\sin\chi\cos\chi . \qquad \text{(C.2b)}$$

The velocity components $\tilde{u}_{\epsilon 1}$ and $\tilde{u}_{\epsilon 2}$ can then be written in terms of $\Pi$ by integrating (C.1a) and (C.1b). It is convenient for this purpose to define $\hat{u}_{\epsilon 1}$ and $\hat{u}_{\epsilon 2}$ in analogy with eq. (2.30), i.e.,

$$\begin{pmatrix}\hat{u}_{\epsilon 1}\\ \hat{u}_{\epsilon 2}\end{pmatrix} = \begin{pmatrix}\cos\chi & -\sin\chi\\ \sin\chi & \cos\chi\end{pmatrix}\cdot\begin{pmatrix}\tilde{u}_{\epsilon 1}\\ \tilde{u}_{\epsilon 2}\end{pmatrix} , \qquad \text{(C.3)}$$

and to express the equations in terms of $\hat{x}_1$ and $\hat{x}_2$:

$$\begin{aligned}&\frac{\partial^2\hat{u}_{\epsilon 1}}{\partial\bar{x}_3^2} + \Bigg\{\frac{\partial^2\hat{u}_{z1}}{\partial\hat{x}_1^2} + \frac{\partial^2\hat{u}_{z1}}{\partial\hat{x}_2^2} + \frac{2\hat{x}_1}{\hat{R}_1}\frac{\partial^2\hat{u}_{z1}}{\partial\hat{x}_1\partial\bar{x}_3} + \frac{2\hat{x}_2}{\hat{R}_2}\frac{\partial^2\hat{u}_{z1}}{\partial\hat{x}_2\partial\bar{x}_3} + \left(\frac{1}{\hat{R}_1}+\frac{1}{\hat{R}_2}\right)\frac{\partial\hat{u}_{z1}}{\partial\bar{x}_3} \\ &\quad + \frac{2}{\hat{R}_s}\left(\hat{x}_2\frac{\partial^2\hat{u}_{z1}}{\partial\hat{x}_1\partial\bar{x}_3} + \hat{x}_1\frac{\partial^2\hat{u}_{z1}}{\partial\hat{x}_2\partial\bar{x}_3}\right) + \left(\frac{\hat{x}_1^2}{\hat{\rho}_1^2} + \frac{2}{\hat{\rho}_s}\hat{x}_1\hat{x}_2 + \frac{\hat{x}_2^2}{\hat{\rho}_2^2}\right)\frac{\partial^2\hat{u}_{z1}}{\partial\bar{x}_3^2}\Bigg\} \\ &\quad = \frac{\partial\tilde{p}_\epsilon}{\partial\hat{x}_1} + \frac{\hat{x}_1}{\hat{R}_1}\frac{\partial\tilde{p}_\epsilon}{\partial\bar{x}_3} + \frac{\hat{x}_2}{\hat{R}_s}\frac{\partial\tilde{p}_z}{\partial\bar{x}_3} , \qquad \text{(C.4a)}\end{aligned}$$

$$\begin{aligned}&\frac{\partial^2\hat{u}_{\epsilon 2}}{\partial\bar{x}_3^2} + \Bigg\{\frac{\partial^2\hat{u}_{z2}}{\partial\hat{x}_1^2} + \frac{\partial^2\hat{u}_{z2}}{\partial\hat{x}_2^2} + \frac{2\hat{x}_1}{\hat{R}_1}\frac{\partial^2\hat{u}_{z2}}{\partial\hat{x}_1\partial\bar{x}_3} + \frac{2\hat{x}_2}{\hat{R}_2}\frac{\partial^2\hat{u}_{z2}}{\partial\hat{x}_2\partial\bar{x}_3} + \left(\frac{1}{\hat{R}_1}+\frac{1}{\hat{R}_2}\right)\frac{\partial\hat{u}_{z2}}{\partial\bar{x}_3} \\ &\quad + \frac{2}{\hat{R}_s}\left(\hat{x}_2\frac{\partial^2\hat{u}_{z2}}{\partial\hat{x}_1\partial\bar{x}_3} + \hat{x}_1\frac{\partial^2\hat{u}_{z2}}{\partial\hat{x}_2\partial\bar{x}_3}\right) + \left(\frac{\hat{x}_1^2}{\hat{\rho}_1^2} + \frac{2}{\hat{\rho}_s}\hat{x}_1\hat{x}_2 + \frac{\hat{x}_2^2}{\hat{\rho}_2^2}\right)\frac{\partial^2\hat{u}_{z2}}{\partial\bar{x}_3^2}\Bigg\} \\ &\quad = \frac{\partial\tilde{p}_\epsilon}{\partial\hat{x}_2} + \frac{\hat{x}_2}{\hat{R}_2}\frac{\partial\tilde{p}_\epsilon}{\partial\bar{x}_3} + \frac{\hat{x}_1}{\hat{R}_s}\frac{\partial\tilde{p}_z}{\partial\bar{x}_3} , \qquad \text{(C.4b)}\end{aligned}$$

In these equations, it has been taken into account that $\partial\tilde{p}_z/\partial\bar{x}_3 = 0$ and likewise that $\partial\tilde{p}_h/\partial\bar{x}_3 = 0$. The quantities $\hat{\rho}_1, \hat{\rho}_2$ and $\hat{\rho}_s$ are chosen to satisfy

$$\frac{1}{\hat{\rho}_1^2} = \frac{\cos^2\chi}{R_1^2} + \frac{\sin^2\chi}{R_2^2}\,, \qquad \frac{1}{\hat{\rho}_2^2} = \frac{\sin^2\chi}{R_1^2} + \frac{\cos^2\chi}{R_2^2}\,,$$
$$\frac{1}{\hat{\rho}_s} = \Big(\frac{1}{R_1^2} - \frac{1}{R_2^2}\Big)\sin\chi\cos\chi\,. \tag{C.4c}$$

The boundary conditions for these equations can easily be shown to be $\hat{\mathbf{u}}_\epsilon = 0$ on $W$ and

$$\hat{\mathbf{u}}_\epsilon = -\frac{1}{2}h_\epsilon h_z\bar{\boldsymbol{\nabla}}\tilde{p}_z - \frac{1}{2}h_h h_z\bar{\boldsymbol{\nabla}}\tilde{p}_h \tag{C.5}$$

on $W'$. The solution of these equations is quite simple but long. The expressions for $\hat{\mathbf{u}}_\epsilon$ can then be inserted into (C.1d), which then needs to be integrated with respect to $\bar{x}_3$. The no-slip condition at the wall $W$ requires that $\tilde{u}_{\epsilon 3}$ vanishes there, and on $W'$, it reduces to the following constraint:

$$\begin{aligned}\tilde{u}_{\epsilon 3} = &-\frac{1}{4}h_z h_h^2\bar{\nabla}^2\tilde{p}_z - \frac{1}{4}(h_h^2 + 2h_z h_\epsilon)\bar{\nabla}p_z\cdot\bar{\nabla}h_z + \frac{h_z}{2}\bar{\mathbf{x}}\cdot\boldsymbol{\mathcal{R}}^{-1}\cdot\big(h_\epsilon\bar{\nabla}\tilde{p}_z + h_h\bar{\nabla}\tilde{p}_h\big)\\ &- \frac{1}{2}h_z h_h\big(\bar{\nabla}\tilde{p}_z\cdot\bar{\nabla}h_h + \bar{\nabla}\tilde{p}_h\cdot\bar{\nabla}h_z\big) + \frac{1}{2}h_z h_h\frac{\partial\tilde{p}_z}{\partial\bar{x}_1}\sum_{i=0}^{2}(3-i)\Gamma_i\bar{x}_1^{2-i}\bar{x}_2^i\\ &+ \frac{1}{2}h_z h_h\frac{\partial\tilde{p}_z}{\partial\bar{x}_2}\sum_{i=1}^{3}i\Gamma_i\bar{x}_1^{3-i}\bar{x}_2^{i-1}\,.\end{aligned} \tag{C.6}$$

After more tedious algebra, the desired equation for $\Pi(\hat{r},\theta)$ is obtained:

$$\bar{\nabla}\cdot\big\{h_z^3\bar{\nabla}\Pi\big\} = \frac{-(\lambda_1+\lambda_2)}{(U_3'-U_3)}\bar{\nabla}\cdot\big\{h_z^2h_\epsilon\bar{\nabla}\tilde{p}_z + h_zh_h^2\bar{\nabla}\tilde{p}_z + h_z^2h_h\bar{\nabla}\tilde{p}_h\big\} + \frac{(1+\hat{r}^2)^3}{\hat{r}^2}\mathcal{N}(\hat{r},\theta) \tag{C.7a}$$

or equivalently,

$$\mathcal{L}(\Pi) = \frac{-(\lambda_1+\lambda_2)}{(U_3'-U_3)}\frac{\hat{r}^2}{(1+\hat{r}^2)^3}\bar{\nabla}\cdot\big\{h_z^2h_\epsilon\bar{\nabla}\tilde{p}_z + h_zh_h^2\bar{\nabla}\tilde{p}_z + h_z^2h_h\bar{\nabla}\tilde{p}_h\big\} + \mathcal{N}(\hat{r},\theta)\,, \tag{C.7b}$$

where the function $\mathcal{N}(\hat{r},\theta)$ stands for

$$\mathcal{N}(\hat{r},\theta)=\frac{4}{5}\frac{\hat{r}^2}{(1+\hat{r}^2)^2}(3\lambda_1^2+2\lambda_1\lambda_2+3\lambda_2^2)+\frac{\hat{r}^4}{(1+\hat{r}^2)^3}\Big\{-8\Big(\frac{\lambda_1}{\hat{R}_2}\sin^2\theta+\frac{\lambda_2}{\hat{R}_1}\cos^2\theta\Big)$$
$$+\frac{56}{5}(3\lambda_1^2\cos^2\theta+\lambda_1\lambda_2+3\lambda_2^2\sin^2\theta)-4\Big(\frac{\lambda_1}{\hat{R}_2}+\frac{\lambda_2}{\hat{R}_1}\Big)-48\Big(\frac{\lambda_1}{\hat{R}_1}\cos^2\theta+\frac{\lambda_2}{\hat{R}_2}\sin^2\theta\Big)$$
$$+12\Big[\cos^2\theta\Big(\frac{1}{\hat{R}_1^2}+\frac{1}{\hat{\rho}_1^2}\Big)+\sin^2\theta\Big(\frac{1}{\hat{R}_2^2}+\frac{1}{\hat{\rho}_2^2}\Big)\Big]+4\Big(\frac{1}{\hat{R}_1\hat{R}_2}+\frac{\lambda_2\cos^2\theta}{\lambda_1\hat{\rho}_1^2}+\frac{\lambda_1\sin^2\theta}{\lambda_2\hat{\rho}_2^2}\Big)$$
$$+8\frac{\sin\theta\cos\theta}{\hat{R}_s}\Big[\frac{1}{\hat{R}_1}\Big(2\sqrt{\frac{\lambda_1}{\lambda_2}}+\sqrt{\frac{\lambda_2}{\lambda_1}}\Big)+\frac{1}{\hat{R}_2}\Big(\sqrt{\frac{\lambda_1}{\lambda_2}}+2\sqrt{\frac{\lambda_2}{\lambda_1}}\Big)\Big]+32\frac{\sin\theta\cos\theta}{\hat{\rho}_s}\Big(\sqrt{\frac{\lambda_1}{\lambda_2}}+\sqrt{\frac{\lambda_2}{\lambda_1}}\Big)$$
$$+\frac{4}{R_s^2}\Big(\sqrt{\frac{\lambda_1}{\lambda_2}}+\sqrt{\frac{\lambda_2}{\lambda_1}}\Big)\Big(\sqrt{\frac{\lambda_1}{\lambda_2}}\sin^2\theta+\sqrt{\frac{\lambda_2}{\lambda_1}}\cos^2\theta\Big)+16\sqrt{\lambda_1\lambda_2}\frac{\sin\theta\cos\theta}{\hat{R}_s}\Big\}\,. \qquad \text{(C.7c)}$$

As before, the solution of this p.d.e. is subject to the conditions of boundedness at the origin, periodicity in the parameter $\theta$ and the requirement that $\Pi(\hat{r},\theta)=O(\hat{r}^{-2})$ as $\hat{r}\to\infty$ at finite $\hat{r}$. It is very simple to prove that the solution for large $\hat{r}$ can be decomposed into an angle-dependent part $\Theta(\theta)$ and a distance dependent factor, which proves to be simply $\hat{r}^{-2}$. In other words,

$$\Pi(\hat{r},\theta)\to\hat{r}^{-2}\Theta(\theta) \qquad \text{as } \hat{r}\to\infty\,. \qquad \text{(C.8)}$$

To calculate $F_3$, it is necessary to evaluate $\int_{\Sigma_\epsilon}\tilde{p}_\epsilon\,\mathrm{d}\,\widetilde{W}$. From (C.2), bearing in mind that the wall $W$ is described by $\bar{x}_3=O(\epsilon^{3/2}\hat{r}^5)$, it is easy to see that

$$\int_{\Sigma_\epsilon}\tilde{p}_\epsilon\,\mathrm{d}\,\widetilde{W}=3\frac{(U_3'-U_3)}{\lambda_1+\lambda_2}\Big\{\int_0^{2\pi}\int_0^{\epsilon^{-1/2}\varepsilon}\Pi(\hat{r},\theta)\frac{\hat{r}\,\mathrm{d}\hat{r}\,\mathrm{d}\theta}{\sqrt{\lambda_1\lambda_2}} \qquad \text{(C.9a)}$$
$$+\int_0^{2\pi}\int_0^{\epsilon^{-1/2}\varepsilon}\frac{2\hat{r}^2}{(1+\hat{r}^2)^2}\Big[\frac{\cos^2\theta}{\hat{R}_1}+\frac{\sin^2\theta}{\hat{R}_2}+\Big(\sqrt{\frac{\lambda_1}{\lambda_2}}+\sqrt{\frac{\lambda_2}{\lambda_1}}\Big)\frac{\sin\theta\cos\theta}{\hat{R}_s}\Big]\frac{\hat{r}\,\mathrm{d}\hat{r}\,\mathrm{d}\theta}{\sqrt{\lambda_1\lambda_2}}\Big\}$$
$$=3\frac{(U_3'-U_3)}{\sqrt{\lambda_1\lambda_2}(\lambda_1+\lambda_2)}\Big\{-\pi\ln\epsilon\Big(\frac{1}{\hat{R}_1}+\frac{1}{\hat{R}_2}\Big)+\int_\delta^{\epsilon^{1/2}\varepsilon}\hat{r}^{-1}\,\mathrm{d}\hat{r}\int_0^{2\pi}\Theta(\theta)\,\mathrm{d}\theta+g(\delta)\Big\}\,,$$

where $\delta$ is chosen such that (C.8) holds for $\hat{r}>\delta$, and $g(\delta)$ is given by:

$$g(\delta)=\int_0^{\delta}\int_0^{2\pi}\Pi(\hat{r},\theta)\hat{r}\,\mathrm{d}\hat{r}\,\mathrm{d}\theta\,. \qquad \text{(C.9b)}$$

Although the exact form of the pressure contribution $\Pi(\hat{r},\theta)$ is unknown, the fact that it is bounded everywhere is sufficient to state that $g(\delta)$ has a finite value for all gap widths. Since the integral over $\Sigma_\epsilon$ is independent of the exact choice of $\delta$, the $\ln\delta$ term from the first integral on the right-hand side of (C.9a) must be balanced exactly by $g(\delta)$. Hence one can discard the lower bound of the integral in the calculation, and lump the error with the $O(1)$ uncertainty on the force $F_3$. Note that the upper bound of the integral over $\hat{r}$ yields a logarithmically singular contribution to $F_3$ for small $\epsilon$. To find the coefficient of this $O(\ln\epsilon)$ term, $\Theta(\theta)$ must be integrated over a unit circle. Now for $\Pi = \hat{r}^{-2}\Theta$, the operator $\mathcal{L}(\Pi)$ can be factorized as $\mathcal{L}(\Pi) = \hat{r}^{-2}\mathcal{L}_\theta(\Theta)$ with

$$\mathcal{L}_\theta(\Theta) = (\lambda_1 \sin^2\theta + \lambda_2 \cos^2\theta)\frac{\partial^2\Theta}{\partial\theta^2} - 2\big\{(\lambda_1 + 3\lambda_2)\sin^2\theta + (3\lambda_1 + \lambda_2)\cos^2\theta\big\}\Theta\ . \tag{C.10}$$

Direct integration of $\mathcal{L}(\Pi)$ over $\theta$ from 0 to $2\pi$ in the limit of $\hat{r}\to\infty$ (after multiplication by $\hat{r}^2$) thus yields

$$\int_0^{2\pi}\mathcal{L}_\theta(\Theta)\,\mathrm{d}\theta = \tag{C.11a}$$

$$= \int_0^{2\pi}\left\{(\lambda_1 \sin^2\theta + \lambda_2 \cos^2\theta)\frac{\partial^2\Theta}{\partial\theta^2} - 2\big\{(\lambda_1 + 3\lambda_2)\sin^2\theta + (3\lambda_1 + \lambda_2)\cos^2\theta\big\}\Theta\right\}\mathrm{d}\theta$$

$$= 2(\lambda_1 - \lambda_2)\int_0^{2\pi}(\cos^2\theta - \sin^2\theta)\Theta\,\mathrm{d}\theta - 2\int_0^{2\pi}\big\{(\lambda_1 + 3\lambda_2)\sin^2\theta + (3\lambda_1 + \lambda_2)\cos^2\theta\big\}\Theta\,\mathrm{d}\theta\ .$$

To arrive at this simplification, two integrations by parts have been carried out on the first term of the operator $\mathcal{L}_\theta$. Mere algebra then yields the simple formula

$$\int_0^{2\pi}\mathcal{L}_\theta(\Theta)\,\mathrm{d}\theta = -4(\lambda_1 + \lambda_2)\int_0^{2\pi}\Theta\,\mathrm{d}\theta\ . \tag{C.11b}$$

This result implies that (C.7) need not be solved, since it is known from (C.9) that integrating over the angular variable $\theta$ at large values of $\hat{r}$ suffices to obtain the singular contributions of $\tilde{p}_\epsilon$ to the normal force $F_3$. Substituting the expressions for

$\tilde{p}_z, \tilde{p}_h, h_z, h_h$ and $h_\epsilon$ in the right-hand side of (C.7b), the integration yields that

$$4(\lambda_1+\lambda_2)\int_0^{2\pi}\Theta\,\mathrm{d}\theta = 6\pi\Big[(10\lambda_1+\frac{5}{2}\lambda_2)\kappa_0^2+(\frac{3}{2}\lambda_1+\lambda_2)\kappa_1^2+(\lambda_1+\frac{3}{2}\lambda_2)\kappa_2^2$$
$$+(\frac{5}{2}\lambda_1+10\lambda_2)\kappa_3^2+(3\lambda_1+2\lambda_2)\kappa_0\kappa_2+(2\lambda_1+3\lambda_2)\kappa_1\kappa_3+$$
$$(7\lambda_1+2\lambda_2)\kappa_0K_1+(\lambda_1+2\lambda_2)\kappa_2K_1+(2\lambda_1+\lambda_2)\kappa_1K_2+(2\lambda_1+7\lambda_2)\kappa_3K_2+$$
$$(5\lambda_1+\lambda_2)\zeta_0+(\lambda_1+\lambda_2)\zeta_2+(\lambda_1+5\lambda_2)\zeta_4\Big]+\pi\Big[-\frac{192}{5}(\lambda_1^2+\lambda_2^2)-\frac{128}{5}\lambda_1\lambda_2$$
$$+\frac{16}{\hat{R}_1}(3\lambda_1+\lambda_2)+\frac{16}{\hat{R}_2}(\lambda_1+3\lambda_2)-4(\frac{2}{\hat{R}_1\hat{R}_2}+\frac{\lambda_1}{\lambda_2\hat{\rho}_1^2}+\frac{\lambda_2}{\lambda_1\hat{\rho}_2^2})$$
$$-12(\frac{1}{\hat{R}_1^2}+\frac{1}{\hat{\rho}_1^2}+\frac{1}{\hat{R}_2^2}+\frac{1}{\hat{\rho}_2^2})-\frac{4}{\hat{R}_s^2}(\sqrt{\frac{\lambda_1}{\lambda_2}}+\sqrt{\frac{\lambda_2}{\lambda_1}})^2\Big]\,, \qquad \text{(C.12a)}$$

where the coefficients $\zeta_i$ are defined by the requirement that

$$h_\epsilon \stackrel{\text{def}}{=} \sum_{i=0}^{4}(b_i+\Upsilon_i)\bar{x}_1^{4-i}\bar{x}_2^i = \hat{r}^4\sum_{i=0}^{4}\zeta_i\cos^{4-i}\theta\sin^i\theta\,, \qquad \text{(C.12b)}$$

and the notation $K_1$ and $K_2$ has been introduced for the following:

$$K_1 = \frac{3\lambda_1\kappa_0+\lambda_2\kappa_2}{3\lambda_1+2\lambda_2} \qquad \text{and} \qquad K_2 = \frac{3\lambda_2\kappa_3+\lambda_1\kappa_1}{2\lambda_1+3\lambda_2}\,. \qquad \text{(C.12c)}$$

Noting from (2.34) that on the surface $W$ given by $\bar{x}_3 = O(\epsilon^{3/2})$,

$$2\frac{\partial\tilde{u}_{z3}}{\partial\tilde{x}_3} = h_z\,\bar{\mathbf{x}}\cdot\boldsymbol{\mathcal{R}}^{-1}\cdot\bar{\boldsymbol{\nabla}}\tilde{p}_z\,. \qquad \text{(C.13a)}$$

while also, for $i=1$ or $i=2$,

$$-\frac{\partial\tilde{u}_{zi}}{\partial\tilde{x}_3} = \frac{1}{2}h_z\frac{\partial\tilde{p}_z}{\partial\tilde{x}_i}\,, \qquad \text{(C.13b)}$$

it is possible to rewrite the expression for the $O(\ln\epsilon)$ correction to the force $F_3$ in terms of $(\hat{x}_1,\hat{x}_2)$ as

$$\int_{\Sigma_\epsilon}\Big[\tilde{p}_\epsilon-2\frac{\partial\tilde{u}_{z3}}{\partial\tilde{x}_3}-\frac{\tilde{x}_1}{R_1}\frac{\partial\tilde{u}_{z1}}{\partial\tilde{x}_3}-\frac{\tilde{x}_2}{R_2}\frac{\partial\tilde{u}_{z2}}{\partial\tilde{x}_3}\Big]\,\mathrm{d}\tilde{x}_1\,\mathrm{d}\tilde{x}_2 = \int_{\Sigma_\epsilon}\Big[\tilde{p}_\epsilon-\frac{1}{2}h_z\bar{\mathbf{x}}\cdot\boldsymbol{\mathcal{R}}^{-1}\cdot\bar{\boldsymbol{\nabla}}\tilde{p}_z\Big]\,\mathrm{d}\tilde{x}_1\,\mathrm{d}\tilde{x}_2 =$$
$$=\int_{\Sigma_\epsilon}\Big[\tilde{p}_\epsilon-\frac{1}{2}h_z(\frac{\hat{x}_1}{\hat{R}_1}\frac{\partial\tilde{p}_z}{\partial\hat{x}_1}+\frac{\hat{x}_2}{\hat{R}_2}\frac{\partial\tilde{p}_z}{\partial\hat{x}_2})-\frac{1}{2}\frac{h_z}{\hat{R}_s}(\hat{x}_1\frac{\partial\tilde{p}_z}{\partial\hat{x}_2}+\hat{x}_2\frac{\partial\tilde{p}_z}{\partial\hat{x}_1})\Big]\,\mathrm{d}\hat{x}_1\,\mathrm{d}\hat{x}_2\,. \qquad \text{(C.14)}$$

When this integral is evaluated, and the result (2.35a) is taken into consideration, the expression for the normal force $F_3$ for a direct approach of the surfaces becomes, to $O(\epsilon^0)$,

$$
\begin{aligned}
F_3 = & -3\pi\epsilon^{-1}\frac{(U_3'-U_3)}{\sqrt{\lambda_1\lambda_2}(\lambda_1+\lambda_2)} - \frac{9}{4}\pi\ln\epsilon\frac{(U_3'-U_3)}{\sqrt{\lambda_1\lambda_2}(\lambda_1+\lambda_2)^2}\Big[\Big(10\lambda_1+\frac{5}{2}\lambda_2\Big)\kappa_0^2 \\
& + \Big(\frac{3}{2}\lambda_1+\lambda_2\Big)\kappa_1^2 + \Big(\lambda_1+\frac{3}{2}\lambda_2\Big)\kappa_2^2 + \Big(\frac{5}{2}\lambda_1+10\lambda_2\Big)\kappa_3^2 + (3\lambda_1+2\lambda_2)\kappa_0\kappa_2 \\
& + (2\lambda_1+3\lambda_2)\kappa_1\kappa_3 + (7\lambda_1+2\lambda_2)\kappa_0 K_1 + (\lambda_1+2\lambda_2)\kappa_2 K_1 + (2\lambda_1+\lambda_2)\kappa_1 K_2 \\
& + (2\lambda_1+7\lambda_2)\kappa_3 K_2 + (5\lambda_1+\lambda_2)\zeta_0 + (\lambda_1+\lambda_2)\zeta_2 + (\lambda_1+5\lambda_2)\zeta_4\Big] \\
& + \frac{3}{2}\pi\ln\epsilon\frac{(U_3'-U_3)}{\sqrt{\lambda_1\lambda_2}(\lambda_1+\lambda_2)^2}\Big[\frac{48}{5}(\lambda_1^2+\lambda_2^2) + \frac{32}{5}\lambda_1\lambda_2 - \frac{4}{\hat{R}_1}(3\lambda_1+\lambda_2) \\
& - \frac{4}{\hat{R}_2}(\lambda_1+3\lambda_2) + \frac{2}{\hat{R}_1\hat{R}_2} + \frac{\lambda_2}{\lambda_1\hat{\rho}_1^2} + \frac{\lambda_1}{\lambda_2\hat{\rho}_2^2} + \frac{3}{\hat{R}_1^2} + \frac{3}{\hat{\rho}_1^2} + \frac{3}{\hat{R}_2^2} + \frac{3}{\hat{\rho}_2^2} \\
& + \frac{1}{\hat{R}_s^2}\Big(\sqrt{\frac{\lambda_1}{\lambda_2}}+\sqrt{\frac{\lambda_2}{\lambda_1}}\Big)^2\Big]\,, \qquad \text{(C.15)}
\end{aligned}
$$

which is (2.44) reported in §2.2.3.

## References

Brady, J.F. & Bossis, G. (1988) Stokesian dynamics, *Ann. Rev. Fluid Mech.* **20**, 111-157.

Brenner, H. (1963) The Stokes resistance of an arbitrary particle, *Chem. Eng. Sci.* **18**, 1-25.

Brenner, H. (1964) The Stokes resistance of an arbitrary particle–IV. Arbitrary fields of flow, *Chem. Eng. Sci.* **19**, 703-727.

Corless, R.M. & Jeffrey, D.J. (1988) Stress moments of nearly touching spheres in low-Reynolds-number flow, *Z. Angew. Math. Phys.* **39**, 874-884.

Cox, R.G. (1974) The motion of suspended particles almost in contact, *Int. J. Multiphase Flow* **1**, 343-371.

Hinch, E.J. (1972) Note on the symmetries of certain material tensors for a particle in Stokes flow, *J. Fluid. Mech.* **54**, 423-425.

Jeffrey, D.J. (1982) Low-Reynolds-number flow between converging spheres, *Mathematika* **29**, 58-66.

Jeffrey, D.J. (1989) Stresslets resistance functions for low-Reynolds-number flow using deforming spheres, *J. Appl. Math. Phys.* **40**, 163-171.

Jeffrey, D.J. & Corless, R.M. (1988) Forces and stresslets for the axisymmetric motion of nearly touching unequal spheres, *PhysicoChemical Hydrodynamics* **10**, 461-470.

Kim, S. & Mifflin, R.T. (1985) The resistance and mobility functions of two equal spheres in low-Reynolds number flow, *Phys. Fluids* **28**, 2033-2045.

Ladd, A.J.C. (1990) Hydrodynamic transport coefficients of random dispersions of hard spheres, *J. Chem. Phys.* **93**, 3484-3494.

Phillips, R.J., Brady, J.F. & Bossis, G. (1988) Hydrodynamic transport properties of hard-sphere dispersions . I. Suspensions of freely mobile particles, *Phys. Fluids* **31**, 3462-3472.

Phillips, R.J., Brady, J.F. & Bossis, G. (1988) Hydrodynamic transport properties of hard-sphere dispersions II. Porous media, *Phys. Fluids* **31**, 3473-3479.

## Nomenclature of Chapter II

A nomenclature section is included in this chapter because the notation is quite involved, as the length of the list of variables will attest. This compilation may also help those who wish to apply the lubrication formulae without going through their derivation. We have tried to keep the symbols consistent throughout the dissertation. However, it would be impractical to never deviate from the conventions used in this chapter in the remainder of the thesis. We mention in particular, that $\mathcal{R}$ will subsequently denote the true $N$-particle grand resistance tensor (as opposed to its numerical approximation $\mathbf{R}$) and that $\boldsymbol{\delta}$ will stand for the idemfactor.

*Roman*

$\mathbf{A}$ : transformation matrix mapping the principal coordinate system $(x_1, x_2, x_3)$ of $W$ onto the principal frame of $W'$, given by the set $(x_1^*, x_2^*, x_3^*)$

$b_i$ : coefficients of the fourth order terms in the local approximation of $W'$ about $O'$ (expressed in the system of principal axes of $W$) [$\mathrm{m}^{-3}$]

$\mathcal{B}_i$ : coefficients of the second order terms in the local approximation of $W'$ about $O'$ (expressed in the system of principal axes of $W$) [$\mathrm{m}^{-1}$]

$C$ : geometric center of the particle

$\mathbf{C}$ : characteristic matrix for the quadratic $h_z - 1$

$\mathbf{D}$ : displacement rate tensor [$\mathrm{s}^{-1}$]

$\mathcal{D}$ : discriminant defined in Appendix A

$\mathbf{e}_i$ : unit base vector

$\mathbf{E}$ : rate-of-strain tensor [$\mathrm{s}^{-1}$]

$\mathbf{E}_w$ : deformation tensor [$\mathrm{s}^{-1}$]

$\mathbf{F}$ : force exerted by the particle on the fluid [N]

$\boldsymbol{\mathcal{F}}$ : generalized force vector (force and torque exerted by the particle on the fluid)

$f_w$ : function of position defining the surface $W$

$h$ : term in the expansion of the rescaled dimensionless gap width in powers of $\epsilon^{\frac{1}{2}}$

$\mathbf{I}$ : identity tensor

$i,j$ : dummy indices

$k$ : exponent of $\epsilon$ determining the scaling appropriate for the boundary conditions

$\mathcal{K}_i$ : coefficient of $\hat{x}_1^{3-i}\hat{x}_2^i$ in the expression for $h_h$

$K_i$ : linear combination of the $\mathcal{K}_i$ defined in Appendix C

$\mathcal{L}$ : operator acting on a function of $(\hat{r},\theta)$

$\mathcal{L}_\theta$ : operator acting on a function of $\theta$

$\mathcal{N}$ : function of $(\hat{r},\theta)$ defined in Appendix C

$O$ : point of closest approach on the particle

$p$ : pressure field [Pa]

$Q_i$ : factors arising in the solution of the problem for tangential or rolling motions of the surfaces (§2.3)

$r$ : radial distance from $O$ [m]

$\mathbf{r}_{AB}$ : vector linking point $B$ to point $A$ in space [m]

$R_i$ : principal radius of curvature of $W$ at $O$ [m]

$\hat{R}_i$ : linear combinations of the principal radii of curvature $R_i$ defined in Appendix C

$\boldsymbol{\mathcal{R}}$ : diagonal matrix consisting of the principal radii of curvature $R_i$

$\grave{R}_c$ : characteristic length scale [m]

$\mathbf{R}$ : resistance tensor for the system of two nearly touching particles [units depend on component considered]

$R_Z$ : radius of the spherical shell $Z$ considered in Appendix B [m]

$\mathbf{S}$ : stresslet exerted by the particle on the fluid at the point of closest approach [N.m]

$\mathcal{S}$ : composite surface considered in Appendix B in order to apply Lorentz' reciprocal theorem to a system of two particles ; $\mathcal{S} = Z \cup W \cup W'$

$\mathbf{T}$ : torque exerted by the particle on the fluid at the point of closest approach [N.m]

$\mathbf{u}$ : fluid velocity [m/s]

$\mathbf{U}$ : translational velocity of the surface at the point of closest approach [m/s]

$\mathcal{U}$ : generalized velocity (translational and rotational velocities) of the surface at the point of closest approach

$U_c$ : characteristic velocity [m/s]

$W$ : surface of the particle

$\mathrm{d}\mathbf{W}$ : infinitesimal surface element of the particle [$\mathrm{m}^2$]

$x_i$ : coordinate in physical space [m]

$\bar{\mathbf{x}} = \bar{x}_1\mathbf{e}_1 + \bar{x}_2\mathbf{e}_2$

$\mathbf{Y}$ : transformation matrix mapping $(\bar{x}_1, \bar{x}_2)^T$ onto $(\hat{x}_1, \hat{x}_2)^T$

$Z$ : spherical surface of very large radius considered in Appendix B

*Greek*

$\beta_i$ : coefficients of the third order terms in the local approximation of $W'$ about $O'$ (expressed in the system of principal axes of $W$) [$\mathrm{m}^{-2}$]

$\Gamma_i$ : coefficients of the third order terms in the approximation of $W$ about $O$ [$\mathrm{m}^{-2}$]

$\delta$ : small dimensionless distance in the $(x_1, x_2)$ plane

$\Delta_{ij} = D'_{ij} - D_{ij}$

$\epsilon$ : minimal gap width [m]

$\varepsilon$ : small dimensionless distance measured in the $\mathbf{e}_3$ direction

$\zeta_i$ : coefficient of $\hat{r}^4 \cos^{4-i}\theta \sin^i\theta$ in the expression for $h_\epsilon$

$\Theta$ : function of the angular variable $\theta$ only

$\theta$ : angular variable in the elliptic coordinate system defined in §2.2.1

$\kappa_i$ : coefficient of $\hat{r}^3 \cos^{3-i}\theta \sin^i\theta$ in the expression for $h_h$

$\lambda_i$ : coefficients of the second order terms in the expansion of $h_z$ around the point $O$ [$(2\lambda_i)^{-1}$ is a non-dimensionalized principal radius of curvature of surfaces of constant $h_z$]

$\grave{\mu}$ : fluid viscosity [Pa.s]

$\xi_i$ : coefficient of $\cos^{2-i}\theta \sin^i\theta$ in the expression for $\Theta(\theta)$ in §2.5

$\Pi$ : term in the expression for $\tilde{p}_\epsilon$, Appendix C

$\varrho$ : ratio of the sphere radii $R'/R$

$\hat{\rho}_i$ : functions of $R_1^2$ and $R_2^2$ defined in Appendix C

$\boldsymbol{\sigma}$ : stress tensor [Pa]

$\Sigma_\varepsilon$ : region around the point of closest approach where the lubrication approximations are valid

$\Upsilon_i$ : coefficients of the fourth order terms in the approximation of $W$ about $O$ [$\mathrm{m}^{-3}$]

$\phi$ : angle between the principal axes of $W$ and $W'$

$\chi$ : angle between the principal axes of $h_z$ and $W$

$\boldsymbol{\Omega}$ : angular velocity of the surface [$\mathrm{s}^{-1}$]

*Subscripts*

1, 2 : (for tensorial quantities) denote projections of the subscribed tensor onto coordinate axes which are tangent to the surfaces at their point of minimum separation

3 : (for tensorial quantities) denotes a projection of the subscribed vector onto the coordinate axis lying along the normal common to both surfaces at their point of minimum separation

$c$ : indicates that this quantity is chosen as the "characteristic" measure for this variable

$FE, \mathcal{FU}, \mathcal{FE}, \mathcal{SU}, SE$ (subscripts for various resistance tensors) : the subscripts indicate which quantities are linked by the subscribed tensor; $\mathbf{R}_{SE}$, for example, relates the stresslet $\mathbf{S}$ to the applied rate of strain $\mathbf{E}$

$h$ : the subscribed variable is the first correction to the leading order term in the asymptotic expansion of this quantity for small $\epsilon^{1/2}$

$L$ : the lubrication approximations have been invoked to calculate this variable

$w, w'$ : lying on surface $W$, $W'$ respectively

$z$ : the subscribed variable is the lowest order term in the asymptotic expansion of this quantity for small $\epsilon^{1/2}$

$\epsilon$ : the subscribed variable is the third order term in the asymptotic expansion of this quantity for small $\epsilon^{1/2}$

*Superscripts*

$A$, $B$ : denotes that the origin, or the reference point, is $A$ or $B$ respectively

$'$ : for variables concerning surface $W'$ in particular

$*$ : for components along the $x_1^*, x_2^*$ or $x_3^*$ axes, i.e., for projections onto the principal frame of reference of $W'$

$ww, ww', w'w, w'w'$ (for resistance tensors) : indicate that the superscribed tensor relates a quantity concerning the surface $W$ to another quantity associated with the surface $W$ (or $W/W'$, $W'/W$ and $W'/W'$ respectively). The ordering of the subscripts dictates the sequence in which the superscripts are written; for instance, $\mathbf{R}_{S\mathcal{U}}^{ww'}$ links the stresslet exerted on the fluid by the wall $W$ to the translational/rotational velocity $\mathcal{U}'$ of $W'$ at $O'$.

$\grave{}$ : denotes that the variable has dimensions (the corresponding non-dimensionalized variable has the same symbol, without accent)

$\tilde{}$ : indicates that the variable is non-dimensionalized and rescaled according to (2.7)

$\bar{}$ : indicates that the coordinates of the position vector are given in the non-orthogonal frame defined by the transformation (2.9)

$\hat{}$ : indicates that the axes "1" and "2" of the frame of reference lie in the directions of principal curvature of the surface $h_z$ = constant

*Operations*

$det(\ )$ : takes the determinant of the matrix between the parentheses

$\boldsymbol{diag}(i_1, i_2, ..., i_n)$ : forms a $n \times n$ diagonal matrix with $i_1, i_2, ..., i_n$ on the diagonal

$^T$ : transpose of the superscribed tensor; $\mathbf{A}^T$ performs a right transpose of the tensor $\mathbf{A}$ (the last two indices of the matricial representation of $\mathbf{A}$ are reversed); $^T\mathbf{A}$ indicates a left transpose (the two first indices are exchanged).

$\nabla$ : nabla operator [$\mathrm{m}^{-1}$]

$\bar{\nabla} = \mathbf{e}_1 \partial/\partial\bar{x}_1 + \mathbf{e}_2 \partial/\partial\bar{x}_2$ ; two-dimensional nabla operator

$\cdot$ : scalar (dot) multiplication of vectors

$\wedge$ : vectorial (cross) multiplication of vectors

$\otimes$ : contraction of tensors; it can denote the scalar multiplication "$\cdot$" or the nested "double-dot" product ":" depending on circumstances

*Abbreviations*

o.d.e. : ordinary differential equation

p.d.e. : partial differential equation

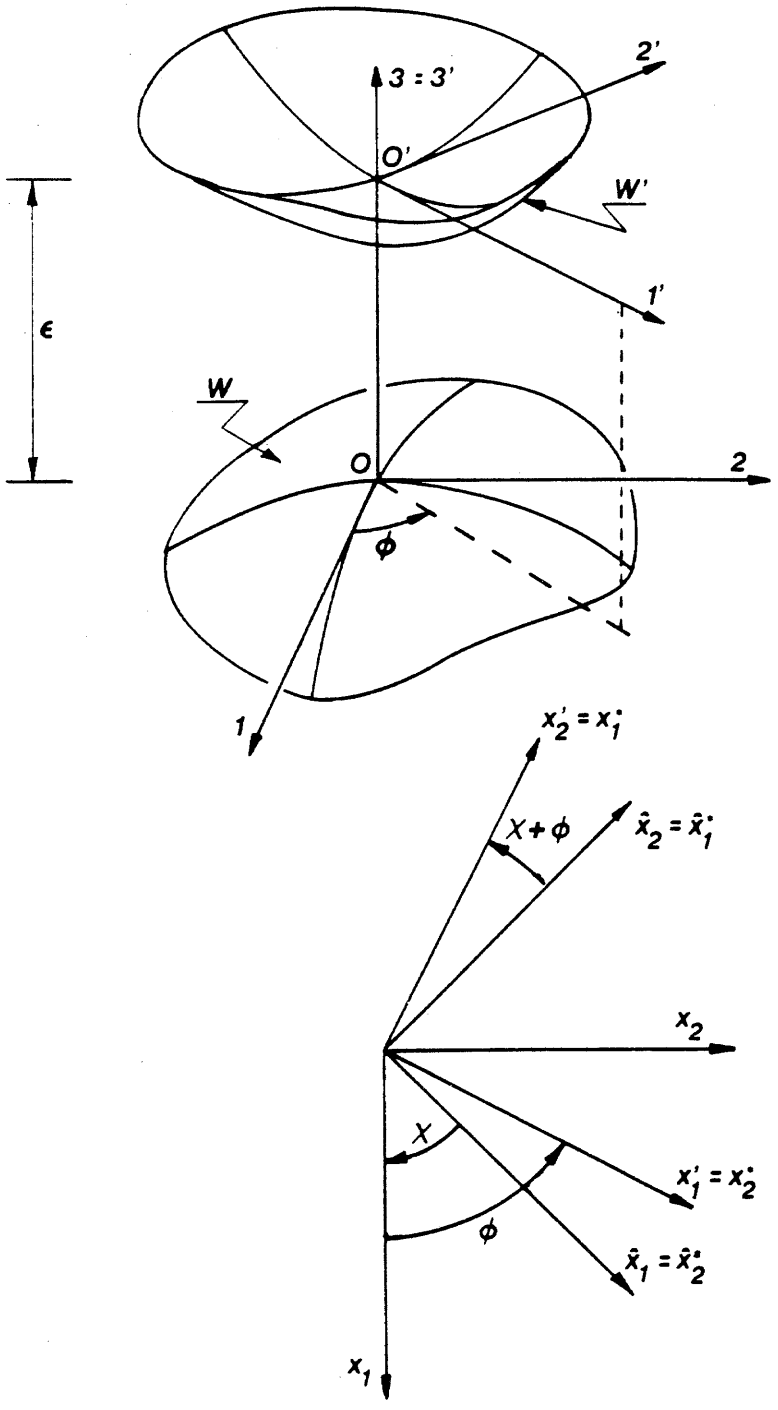


**Fig.2.1**: Coordinate systems used in this chapter

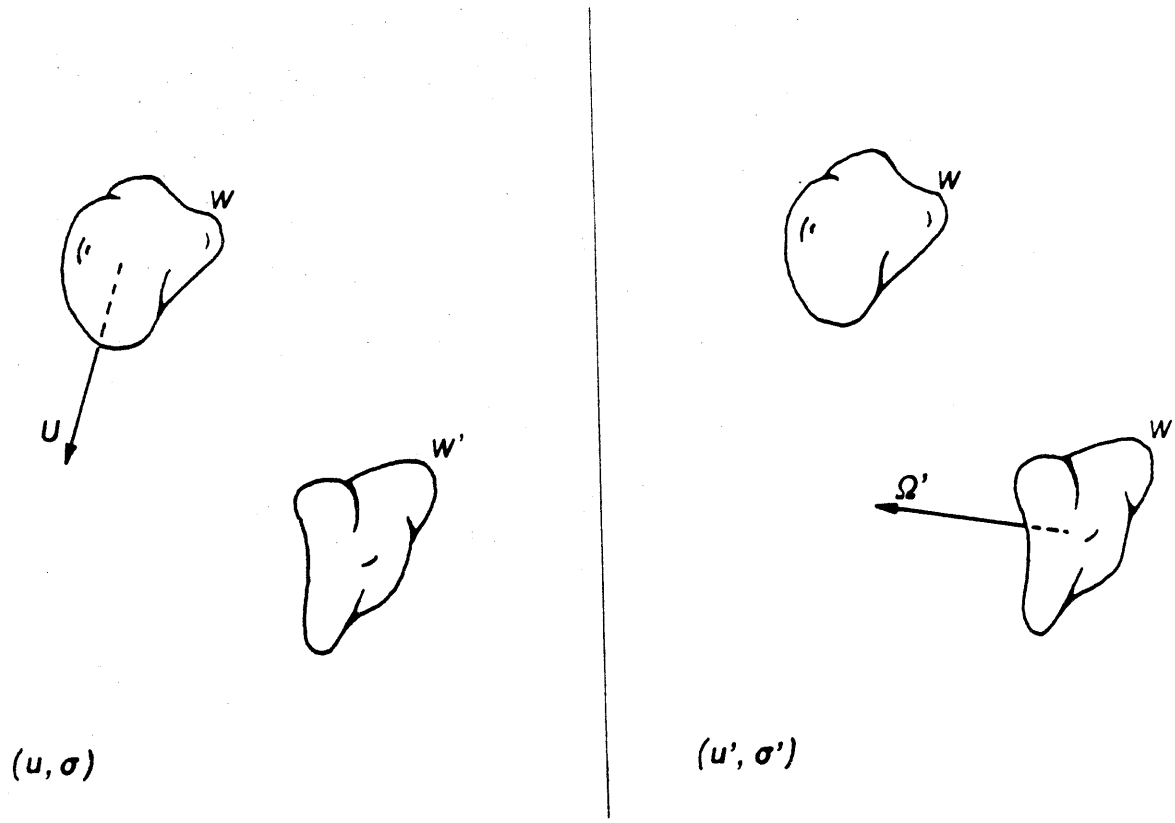


**Fig. 2.2**: Geometry of the problem considered in Appendix B.

# Chapter III
# Stokesian dynamics for a finite number of non-Brownian prolate spheroids

## 3.1 Introduction

The motion of small particles in viscous fluids is relevant to fields as disparate as chemical engineering, biology, soil mechanics, geophysics, materials science and the microelectronics industry (Happel & Brenner, 1973; Kim & Lawrence, 1988). It pertains to the locomotion of microorganisms, the transport of blood cells in arteries, and the diffusional approach of substrates to enzymes. More traditionally, low-Reynolds-number hydrodynamics have been used to analyze the processing of slurries, colloids and composites. If some of the particles are fixed, the results apply to petroleum recovery in porous rocks, or to the monitoring and control of particulate contaminants in cleanroom environments. Suspension rheology is also at the core of active efforts in constitutive equation modeling for polymeric and liquid crystalline solutions.

In many cases, the particles are distinctly non-spherical, and their anisometric shape is a fundamental characteristic of the problem at hand. Typically, the departure from sphericity influences the global properties of the fluid-particles system in any of three major ways. Equilibrium Monte-Carlo studies (Frenkel & Mulder, 1985; Frenkel, 1988) have shown that the phase-diagram of fluids of anisotropic hard bodies of revolution differs qualitatively from that for spheres, with the appearance of orientationally ordered structures in concentrated samples, even for particles with moderate aspect ratios. These structural changes due solely to packing considerations affect all macroscopic properties of the solvent-particles composite. In effect, the anisotropy of the microscopic constituent is imparted to the entire dispersion. In general, the microscale anisotropy reflects on the suspension average properties

whenever a preferred direction of alignment for the particles exists (due to extensional components in the flow for example). Additionally, under non-equilibrium conditions, orientation is no longer a dead degree of freedom and particle rotations cause non-trivial changes in the instantaneous microstructure and this in turn reflects on the suspension properties. For example, the tumbling of spheroids in shear flow (Jeffery, 1922) induces periodic variations in the local stress response (Ivanov *et al.*, 1982). Finally, suspensions of anisometric particles often behave quite differently from suspensions of spheres because the solid inclusions interact hydrodynamically much more strongly than spheres do at the same volume fraction. This effect is most pronounced for elongated particles, and semi-dilute fibre suspensions for example display extremely high extensional viscosities as a result of these "screening" interactions (Batchelor, 1971; Shaqfeh & Fredrickson, 1990; Mewis & Metzner, 1974). This tremendous increase in the resistance of fluids to stretch by the addition of a minuscule amount of fibrous material is of great technological importance, and is one of the factors that prompted us to study ovary particle shapes rather than planetary.

Much is known at present about the motion of single, rigid particles in creeping flow. This knowledge is directly applicable to the analysis of dilute suspensions, in which each particle is effectively isolated. The behavior of more concentrated dispersions, however, remains a challenge for rheologists. For spherical particles, dynamic microstructural simulations have provided valuable insight into the flow behavior of suspensions up to very high particle densities (Brady & Bossis, 1988; Phung & Brady, 1991). Similar attempts for dispersions of elongated particles however, have thus far neglected hydrodynamic interactions, modeling the suspension as a gas of impenetrable needles, and incorporating solvent effects in an ad hoc manner (Bitsanis *et al.*, 1988, 1990). As mentioned previously, hydrodynamic interactions have been shown to be immensely important, especially for rod-like particles (Batchelor, 1971). The numerical difficulties experienced with continuum descriptions of fibre suspensions in the semi-dilute concentration regime and near solid boundaries also

reflect the importance of viscous interactions and the difficulty in treating them adequately (Rosenberg *et al.*, 1990). The need exists, clearly, for a hydrodynamically rigorous simulation method for dispersions of elongated particles. In addition, very few numerical and theoretical investigations are available to date in the literature on the rheology of suspensions of thick rods, with moderate aspect ratios. Asymptotic theories for fibre dispersions usually employ the so-called weak expansion in inverse powers of the logarithm of the aspect ratio, and their predictive value is thus limited to extremely slender bodies. This is unfortunate since most particles and macromolecules of practical importance have eccentricities intermediate between spheres and very slender rods.

We present herein a new simulation method for suspensions of prolate spheroids of arbitrary aspect ratio, which accurately accounts for hydrodynamic interactions, including many-body effects. It is similar in concept to the successful simulation technique for dispersions of spheres known as Stokesian dynamics. Only systems consisting of a finite number of particles are considered here first in order to demonstrate the essence of the new approach and its advantages. These simple systems also serve to highlight the effect of viscous interactions, which are harder to distill from simulations of infinite suspensions. Two-body dynamics are also interesting in their own right. For instance, they determine the tendency of rods sedimenting through highly porous fixed beds to line up in the direction of gravity (Shaqfeh & Koch, 1990). The next chapter discusses the extension of our method to unbounded suspensions and illustrates its effectiveness with selected results on the transport properties of uniformly aligned and equilibrium hard-ellipsoid structures. The model suspension consists of rigid non-Brownian prolate spheroids interacting hydrodynamically in a Newtonian, incompressible fluid at zero Reynolds number (based on the largest particle dimension). Since the body is axisymmetric, this is the simplest geometry retaining the essential novel feature of interest: orientability. It encompasses the sphere at one end of the spectrum and slender round-ended rods at the other.

As the inertia of particles up to several hundredths of a millimeter in size can often be neglected relative to viscous retardation in common liquids, the equations governing fluid motion in suspension rheology are usually taken to be the Stokes equations:

$$\nabla p = \mu \nabla^2 \mathbf{u} \tag{3.1a}$$

$$\nabla \cdot \mathbf{u} = 0 \ . \tag{3.1b}$$

($\mu$ represents the viscosity of the suspending fluid; $\mathbf{u}$ is the velocity field, and $p$ the associated pressure.) Even though the creeping flow equations (3.1a-b) are linear, very few analytical solutions are known which satisfy the no-slip boundary condition on two or more immersed particle surfaces. The most notable exception is the solution in terms of bipolar coordinates for two spheres traveling with equal velocity along the line joining their geometrical centres (Stimson & Jeffery, 1926). The method of reflections (Happel & Brenner, 1973) exploits the linearity of the Stokes equations to generate an iterative sequence of solutions of ever increasing accuracy for problems involving two bodies in an unbounded fluid, provided the disturbance velocity due to each particle separately is known. This technique is not easily amenable to situations where three or more particles interact simultaneously (Kynch, 1959). Based on an elaborate formulation in terms of ellipsoidal harmonics, Wakiya (1965) derived an analytical expression for the sedimentation rate of two widely separated spheroids. However, his results assume that the distance between the particles greatly exceeds their largest dimension, and the intricacy of the algebra required forbid the application of his method to include more particles. Many numerical techniques for Stokes flow problems have therefore been developed (Weinbaum *et al.*, 1990). We shall focus on their utility for suspensions of prolate spheroids. Finite difference or finite element schemes will not be discussed as they are not generally applicable to unconfined Stokes flow problems, where velocity disturbances decay so slowly that an immense region would need to be discretized. Instead, solutions for the particulate dynamics are sought, which do not require

determining the entire flow field.

The first class of methods is based on a discretization of the boundary integral equation (Ladyzhenskaya, 1963), which writes the velocity at any point $\mathbf{x}$ of the (bounded) flow domain in terms of the force density and fluid motion at the boundary $\partial V$:

$$\mathbf{u}(\mathbf{x}) = \frac{-1}{8\pi\mu}\int_{\partial V}\mathbf{J}(\mathbf{x}-\mathbf{y})\cdot\boldsymbol{\sigma}(\mathbf{y})\cdot\mathrm{d}\mathbf{A}_\mathbf{y} + \frac{3}{4\pi}\int_{\partial V}\frac{(\mathbf{x}-\mathbf{y})(\mathbf{x}-\mathbf{y})(\mathbf{x}-\mathbf{y})}{|\mathbf{x}-\mathbf{y}|^5} : \mathbf{u}(\mathbf{y})\mathrm{d}\mathbf{A}_\mathbf{y}\ , \tag{3.2}$$

with

$$\boldsymbol{\sigma} = -p\boldsymbol{\delta} + \mu(\nabla\mathbf{u} + {}^T\nabla\mathbf{u})\ . \tag{3.3}$$

The stress tensor $\boldsymbol{\sigma}$ is evaluated at $\mathbf{y}$ on the boundary. $\mathrm{d}\mathbf{A}_\mathbf{y}$ is an elementary surface element of $\partial V$, pointing into the control volume $V$; the subscript $\mathbf{y}$ indicates that the integration is carried out with respect to the vector $\mathbf{y}$. The first integral therefore represents the disturbance produced by a surface distribution of point forces with strength $\boldsymbol{\sigma}\cdot\mathrm{d}\mathbf{A}_\mathbf{y}$. Their effect propagates with the Oseen tensor

$$\mathbf{J}(\mathbf{r}) = \frac{\boldsymbol{\delta}}{|\mathbf{r}|} + \frac{\mathbf{rr}}{|\mathbf{r}|^3}\ . \tag{3.4}$$

A straightforward application of the divergence theorem shows that the second term on the right hand side of (3.2) vanishes for rigid particles for any $\mathbf{x}$ in the flow domain.

In essence, boundary element methods evaluate (3.2) at $\partial V$, apply the appropriate boundary conditions and solve the resulting Fredholm integral equation by discretizing the surface. Coincidentally, the first article exposing a numerical application of this technique considered Stokes flow past spheroids (Youngren & Acrivos, 1975). As many as 64 surface patches were needed to determine the torque exerted by simple shear flow on the particles to an accuracy of 1% or better. Although the programming aspects have become more refined since, this work illustrates the high computational cost of the technique. Since point forces are distributed on the

surface of the particles, evaluating (3.2) at the boundary generates singular integrals. Moreover, a very fine mesh is necessary to capture large stress gradients in the flow, such as may occur between almost touching particles in relative motion. More effective numerical approaches, collectively known as multipole techniques, are now available for a wide class of creeping flow problems, restricting the use of the boundary element method to systems with deformable interfaces or complicated geometries.

The oldest of these techniques is the multipole collocation method (Gluckman *et al.*, 1971). It has mostly been applied to the motion of two or three spheres (Hassonjee *et al.*, 1988), and to axisymmetric flows past chains of ellipsoids (Gluckman *et al.*, 1971; Liao & Krueger, 1980). It is best suited for problems involving a finite number of identical particles positioned in a very symmetric arrangement. Basically, stress singularities are located at the centre of the particles, and their strength is determined by simultaneously satisfying the no-slip condition on all spheroids on a number of judiciously chosen rings on their surface. Since all unknown coefficients are found collectively as the solution of one matrix equation, many-body effects are incorporated. Surface-averaged properties such as the drag can be calculated quite accurately using this technique. However, as the particle separation decreases, many terms must be retained in Lamb's fundamental solution (Lamb, 1932), on which the method is based. Also, as recognized by Hassonjee *et al.* (1988), the computer memory and computation time requirements are rather large, and compare unfavorably with the needs of Stokesian dynamics (see §3.2). Although the "multipoles" were described merely as "multilobular disturbances" originally (Gluckman *et al.*, 1971), Weinbaum *et al.* (1990) have shown for spheres that they correspond to moments of the stress density on the particle surface, i.e., to the Stokeslet, rotlet, stresslet, quadrupole and octupole of the multipole moment method (*vide infra*). This suggests an inherent deficiency in the multipole collocation technique for non-spherical particles, since even an isolated ellipsoid creates a disturbance which can be correctly reproduced only by an infinite series of Stokes

singularities at its geometric centre (Brenner, 1964 b).

By allowing the singularities to be distributed within the particle however (rather than restricting their location to the middle), Chwang & Wu (1975) constructed exact solutions for isolated spheroids in linear ambient flows using only low-order singularities such as Stokeslets and doublets, rotlets, and stresslets and octupoles. Their singularity representation, reminiscent of the slender body theory pioneered by Batchelor (1970), is much more convenient for numerical purposes than the grantedly more compact symbolic operator formalism of Brenner & Haber (1983) (see also Brenner, 1966), which, in effect, places an infinite series of disturbances at the centre of the particle, just as in the multipole collocation technique. Chwang & Wu's result, on the other hand, states that a single spheroid in a uniform velocity field behaves hydrodynamically as a line of Stokeslets (i.e., point forces) of constant magnitude, with potential doublets distributed with a parabolic density profile to correct for the finite body thickness. This inspired Barta & Liron (1988) to calculate hydrodynamic interactions between slender objects by determining the Stokeslet distribution along their axes which best satisfies the no-slip condition. Their procedure, unfortunately, does not allow the forces on the particles to be specified, and is limited to thread-like bodies. Kim (1985 a) furnished a very elegant proof of the functional equivalence between Faxén laws and the singularity representation of disturbance velocities for rigid particles in Stokes flow. [Kim & Lu (1987) extended their theorem to include fluid-fluid boundaries.] He then used Chwang & Wu's formulation for spheroids (1974, 1975) in conjunction with the method of reflections to examine the sedimentation of two identical spheroids in an unbounded fluid (Kim, 1985 b). Since the formulation is exact in the absence of interactions (unlike the multipole collocation approach for non-spherical bodies), better accuracy is expected for the same number of unknown multipoles, even though many iterations may be necessary. Kim carried the calculations out to the second reflection, but lost convergence at small separations.

The multipole collocation and the multipole moment methods are similar in

many ways and have been blended in a few hybrid approaches. Indeed, for spheres, as pointed out, there exists a one-to-one correspondence between the disturbances of the collocation technique and the stress moment propagators of the moment expansion. Yet this second scheme is substantially more efficient and typically introduces fewer unknowns. It also very readily accommodates periodic boundary conditions to simulate suspensions of infinite extent. The multipole-moment technique expands the contribution of the surface stresses on each particle in the boundary integral equation (3.2) into moments about the particle centre. The zeroth moment singles out the effect of the total force. The first moment has antisymmetric and symmetric components. The former corresponds to the net torque experienced by the particle; the latter is identified as the stresslet. Higher moments yield the quadrupole, octupole, hexadecupole, etc. This series is truncated at the level appropriate for the accuracy desired. The motion of each submerged object is then determined from Faxén formulae, with the velocity field given by the moments expansion of (3.2). This method lies at the core of Stokesian dynamics (Brady & Bossis, 1988; Brady *et al.*, 1988) and of the technique presented herein, and will therefore be explained in greater detail in §3.2. It converges particularly rapidly for suspension viscosities and self-diffusion coefficients; more terms are needed to determine sedimentation rates and permeabilities (Ladd, 1990). In all cases the number of moments necessary to achieve quantitative accuracy increases with solid volume fraction. The only application to non-spherical particles of a variant of the multipole moment method of which we are aware, is the recent work by Yoon & Kim (1990), in which up to 4 moments are retained to describe the dynamics of pairs of spheroids. Instead of relying on Faxén relations, a least squares collocation technique is used to calculate the strength of the unknown multipoles from the no-slip boundary conditions.

Stokesian dynamics is generally accepted as being the most cost-efficient numerical simulation technique for suspensions of spherical particles. It combines the multipole moment method with lubrication formulae to remedy the inadequacy of the moments expansion when particles are nearly touching. It is therefore accurate

over the full concentration range, from very dilute to nearly maximum packing. In addition, the method very consistently preserves any symmetry inherent to the system by making explicit use of Lorentz' reciprocal theorem (see Ch. II, App. B) in order to improve both its numerical efficiency and its robustness. Since our approach for prolate spheroids essentially adopts the same strategy, we discuss Stokesian dynamics in the next section. Section 3.3 then details how far-field interactions are calculated (i.e., the multipole moment method for our system), and near-field aspects are tackled in §3.4. The accuracy and efficiency of the method is illustrated by means of several examples in §3.5. We summarize our main findings in the concluding section.

## 3.2 Stokesian dynamics for a finite number of particles

Three major problems stand in the way of quantitative numerical simulations of non-dilute hard-body dispersions. The first stems from the long-ranged character of hydrodynamic interactions in Stokes flow: in an unbounded fluid, the velocity disturbance due to a Stokeslet decays with distance as $r^{-1}$ (*cf.* the Oseen tensor (3.4)). Such a slow dissipation of forcing actions results in non-convergent expressions when the effects of a large (infinite) number of particles subject to a net force such as gravity are summed to calculate collective properties such as the sedimentation rate. This problem, however, is not severe for finite clusters, and therefore not applicable here. Let us simply mention that it can be dealt with appropriately by "renormalizing" the interactions, i.e., subtracting the mean-field effects (O'Brien, 1979). The success of this approach has been demonstrated for suspensions of spheres (Brady *et al.*, 1988) and we shall explain how to implement it for prolate spheroids in the next chapter. A related, second difficulty is the importance of many-body effects. The motion of two particles in a fluid is affected by the presence of a third through direct hydrodynamic interactions of each particle with it, but also because the velocity disturbance of the pair is reflected on the third object's surface and thereby altered. Thus, unfortunately, the solution of the three-body problem cannot be obtained by

summing three two-body systems. Yet pair-wise additivity can be used intelligently to reproduce the dynamics of many spheres adequately. (As Stokesian dynamics exploits such a scheme, we shall come back to this later.) The third difficulty in suspension rheology lies in the very strong and localized interactions between nearly touching immersed surfaces in relative motion. These stresses, which diverge as the separation vanishes and so in theory prevent particles from ever touching (until the gap width reaches molecular dimensions at which the continuum description breaks down), can only be captured by retaining an infinite number of multipoles in the collocation and moments schemes explained in the introduction, or by an extremely fine discretization near the points of closest approach for the boundary integral method. Many researchers therefore resort to artificial repulsive potentials between particles to prevent them from overlapping during dynamic simulations. Yet analytical formulae are known for any two convex particles for the force, torque and stresslet generated at sufficiently close separations by these so-called lubrication interactions (see Ch. II). Stokesian dynamics takes advantage of these expressions and, consequently, is accurate even at very high packing densities when these interactions dominate, causing the other methods described in the introduction to fail.

Two basic problem formulations exist in suspension mechanics. In the mobility version, the velocities (both translational and rotational) of the particles are sought, given the ambient flow field and the forces and torques acting on each body. The converse, finding the forces and torques required to impose a desired particulate motion in an external flow, is referred to as the resistance formulation. The governing equations (3.1) are solved subject to no-slip boundary conditions

$$\mathbf{u}(\mathbf{x}) = \mathbf{U}_p + (\mathbf{x} - \mathbf{x}_p) \wedge \mathbf{\Omega}_p \ , \qquad \mathbf{x} \in A_p \tag{3.5}$$

on the surface $A_p$ of each particle (labeled by integers $p$ from 1 to $N$). $\mathbf{\Omega}_p$ denotes the body's angular velocity, and $\mathbf{U}_p$ is the translational velocity of its locator point $\mathbf{x}_p$ (usually its centre of hydrodynamic stress (Brenner, 1963)). Far away from the

cluster, the imposed linear flow $\mathbf{u}_\infty$ with uniform velocity $\mathbf{U}_\infty$, vorticity $\boldsymbol{\Omega}_\infty$, and rate of strain $\mathbf{E}_\infty$ must be recovered:

$$\mathbf{u}(\mathbf{x}) \to \mathbf{u}_\infty(\mathbf{x}) = \mathbf{U}_\infty + \mathbf{x} \wedge \boldsymbol{\Omega}_\infty + \mathbf{E}_\infty \cdot \mathbf{x} \ , \qquad |\mathbf{x}| \to \infty \ . \tag{3.6}$$

Owing to the linearity of the boundary conditions and of the Stokes equations, the forces and torques exerted by the particles on the fluid are related through tensors to their velocities and angular velocities relative to the undisturbed flow and to the imposed rate of strain. For instance, the force $\mathbf{F}_p$ on particle $p$ may be found as:

$$\mathbf{F}_p = \sum_{q=1}^{N} \boldsymbol{\mathcal{R}}_{FU}^{pq} \cdot \left(\mathbf{U}_q - \mathbf{u}_\infty(\mathbf{x}_q)\right) + \sum_{q=1}^{N} \boldsymbol{\mathcal{R}}_{F\Omega}^{pq} \cdot \left(\boldsymbol{\Omega}_q - \boldsymbol{\Omega}_\infty\right) - \sum_{q=1}^{N} \boldsymbol{\mathcal{R}}_{FE}^{pq} : \mathbf{E}_\infty \ . \tag{3.7}$$

The resistance tensor $\boldsymbol{\mathcal{R}}_{FU}^{pq}$ gives the force experienced by particle $p$ due to a translation of $q$, holding all objects other than $q$ fixed. (Its evaluation therefore requires the solution of an $N$-body problem). The meaning of all other quantities in (3.7) should be clear. Since the Stokes equations are memoryless, and since the dependence of $\mathbf{F}_p$ on the particulate motion and on the ambient flow have been factored out, all resistance tensors are purely geometric quantities; except for their scaling with the solvent viscosity $\mu$, they depend only on the configuration of the particles at that instant. Relations such as (3.7) may be written down for the torques as well. Grouping the forces and torques of all particles into a vector $\boldsymbol{\mathcal{F}}$ of length $6N$, their translational and angular velocities into $\boldsymbol{\mathcal{U}}$, and the undisturbed fluid velocity and vorticity at their locator points into $\boldsymbol{\mathcal{U}}_\infty$, we may write the resistance problem as:

$$\boldsymbol{\mathcal{F}} = \boldsymbol{\mathcal{R}}_{\mathcal{FU}} \cdot \left(\boldsymbol{\mathcal{U}} - \boldsymbol{\mathcal{U}}_\infty\right) - \boldsymbol{\mathcal{R}}_{\mathcal{F}E} : \mathbf{E}_\infty \ . \tag{3.8}$$

The mobility problem is not only conceptually, but also mathematically its inverse:

$$\boldsymbol{\mathcal{U}} = \boldsymbol{\mathcal{U}}_\infty + \boldsymbol{\mathcal{R}}_{\mathcal{FU}}^{-1} \cdot \boldsymbol{\mathcal{F}} + \boldsymbol{\mathcal{R}}_{\mathcal{FU}}^{-1} \cdot \boldsymbol{\mathcal{R}}_{\mathcal{F}E} : \mathbf{E}_\infty \ . \tag{3.9}$$

(The existence of $\boldsymbol{\mathcal{R}}_{\mathcal{FU}}^{-1}$ is guaranteed since resistance tensors are positive definite by virtue of the dissipative nature of viscous flow (Happel & Brenner, 1973).) Mazur &

van Saarloos (1982) tackled the complete $N$-body mobility problem for spheres using a Fourier space multipole expansion technique. They calculated the velocity functions as series in inverse powers of the particle spacing up to $O(r^{-7})$, with $r$ the centre-to-centre distance. They also proved that $n$-body effects enter the mobility problem at $O(r^{5-3n})$. In contrast, third-body reflections contribute terms of $O(r^{-2})$ to the resistance formulae.

Pair-wise additive schemes construct the resistance tensors, or their inverse, by considering all pairs of particles successively and calculating their interactions as if all other bodies were absent. In effect, in the resistance formulation, the $\mathcal{R}^{pq}$ (see (3.7)) are evaluated as two-body characteristics rather than properties depending on the configuration of all $N$ particles. Mazur & van Saarloos's findings (1982) indicate that the pair-wise mobility formulation is more accurate than additivity of forces (the resistance version), since the first many-body effects are of $O(r^{-4})$ as opposed to $O(r^{-2})$. In essence, any pair of particles senses the presence of other objects less when these are freely suspended than when they are fixed in space. Moreover, the series expansion in $r^{-1}$ for the mobility functions converges much more rapidly than the series for the resistance or friction tensors (Felderhof, 1977). Thus pair-wise additivity of velocities is preferable to additivity of forces. Lubrication forces however, are only preserved in the resistance approach. (The tensor $\mathcal{R}^{pq}_{FU}$ for two touching particles $p$ and $q$ is singular, and therefore dominates the behavior. In contrast, its inverse vanishes, and its effect will be swamped by that of all other particles in any scheme using pair-wise additivity of velocities, leading to particle overlap (Bossis & Brady, 1984).) These observations lie at the heart of the method called Stokesian dynamics (Durlofsky *et al.*, 1987). The $N$-body mobility tensor is first approximated using the more accurate pair-wise additivity of velocities. It is then inverted to yield a "far-field" estimate of the resistance tensor, to which lubrication stresses are added using the two-body resistance functions. This procedure is elucidated further below.

The boundary integral equation (3.2) can be applied to a finite cluster of parti-

cles in an unbounded domain by confining the system to a very large imaginary envelope. Order-of-magnitude arguments demonstrate that both integrals in (3.2), when performed over the virtual shell surrounding the control volume, yield zero. (One needs to know that the disturbance velocity $\mathbf{u} - \mathbf{u}_\infty$ decays at least as $O(|\mathbf{x}|^{-1})$). As mentioned earlier, rigid particles do not contribute to the second term on the right hand side of (3.2) either. Thus, for finite clusters of solid (inelastic) particles, the boundary integral equation reduces to:

$$\mathbf{u}(\mathbf{x}) - \mathbf{u}_\infty(\mathbf{x}) = -\frac{1}{8\pi\mu} \sum_{q=1}^{N} \int_{A_q} \mathbf{J}(\mathbf{x}-\mathbf{y}) \cdot \boldsymbol{\sigma}(\mathbf{y}) \cdot \mathrm{d}\mathbf{A}_\mathbf{y} \ . \tag{3.10}$$

Following the example for spheres given in Durlofsky *et al.* (1987), the integrated surface force density in (3.10) is expanded in moments about the particle locator points $\mathbf{x}_q$ to yield

$$\begin{aligned}\mathbf{u}(\mathbf{x}) - \mathbf{u}_\infty(\mathbf{x}) &= \frac{-1}{8\pi\mu} \sum_{q=1}^{N} \int_{A_q} \sum_{m=0}^{\infty} \frac{1}{m!} \overbrace{(\mathbf{y}-\mathbf{x}_q)}^{\times m} \odot^m \{ \overbrace{\boldsymbol{\nabla}_\mathbf{y}}^{\times m} \mathbf{J}(\mathbf{x}-\mathbf{y}) \}|_{\mathbf{y}=\mathbf{x}_q} \cdot \boldsymbol{\sigma}(\mathbf{y}) \cdot \mathrm{d}\mathbf{A}_\mathbf{y} \\ &= \frac{-1}{8\pi\mu} \sum_{q=1}^{N} \sum_{m=0}^{\infty} \frac{1}{m!} \int_{A_q} \mathbf{n} \cdot \boldsymbol{\sigma} \overbrace{[\mathbf{y}-\mathbf{x}_q]}^{\times m} \, \mathrm{d}A_\mathbf{y} \odot^{m+1} \overbrace{\boldsymbol{\nabla}_\mathbf{z}}^{\times m} \mathbf{J}(\mathbf{x}-\mathbf{z})|_{\mathbf{z}=\mathbf{x}_q} \ . \end{aligned} \tag{3.11a}$$

We have introduced the notations $\overbrace{\mathbf{x}}^{\times m}$ for the direct product of $m$ tensors $\mathbf{x}$, and $\odot^m$ for the $m$-fold contraction operator (for which we adopt the "nesting" convention; see, for example, Chapman & Cowling (1970)). We also decomposed $\mathrm{d}\mathbf{A} = \mathbf{n}\,\mathrm{d}A$, with $\mathbf{n}$ the unit outward normal to the surface $A$. Per definition, the $m^{\text{th}}$ multipole moment of particle $q$ is a tensor of rank $m+1$ given by

$$\mathbf{P}_q^{(m)} = -\frac{1}{m!} \int_{A_q} \mathbf{n} \cdot \boldsymbol{\sigma} \overbrace{[\mathbf{y}-\mathbf{x}_q]}^{\times m} \mathrm{d}A_\mathbf{y} \ . \tag{3.12a}$$

Hence (3.11) can be written as

$$\mathbf{u}(\mathbf{x}) - \mathbf{u}_\infty(\mathbf{x}) = \frac{1}{8\pi\mu} \sum_{q=1}^{N} \sum_{m=0}^{\infty} \mathbf{P}_q^{(m)} \odot^{m+1} \overbrace{\boldsymbol{\nabla}_{\mathbf{x}_q}}^{\times m} \mathbf{J}(\mathbf{x}-\mathbf{x}_q) \ . \tag{3.11b}$$

The monopole or zeroth moment of the stress corresponds to the net force exerted by the particle on the fluid:

$$\mathbf{P}_q^{(0)} = \mathbf{F}_q = -\int_{A_q} \boldsymbol{\sigma} \cdot \mathrm{d}\mathbf{A} \ . \tag{3.12b}$$

The dipole or first moment can be decomposed into a symmetric and an antisymmetric part. The antisymmetric component is related to the total torque by:

$$\mathbf{T}_q = -\int_{A_q} (\mathbf{y} - \mathbf{x}_q) \wedge \boldsymbol{\sigma} \cdot \mathrm{d}\mathbf{A}_\mathbf{y} = \boldsymbol{\varepsilon} : \mathbf{P}_q^{(1)} \ . \tag{3.12c}$$

The symmetric part is essentially the stresslet $\mathbf{S}$ (which is made traceless using $\nabla \cdot \mathbf{J} = 0$, a consequence of continuity):

$$\begin{aligned} \mathbf{S}_q &= -\int_{A_q} \frac{1}{2}\big[\mathbf{n} \cdot \boldsymbol{\sigma}\{\mathbf{y} - \mathbf{x}_q\} + (\mathbf{y} - \mathbf{x}_q)\boldsymbol{\sigma} \cdot \mathbf{n}\big] - \frac{1}{3}\boldsymbol{\delta}\big[\mathbf{n} \cdot \boldsymbol{\sigma} \cdot (\mathbf{y} - \mathbf{x}_q)\big]\, \mathrm{d}A_\mathbf{y} \\ &= \frac{1}{2}\big[\mathbf{P}_q^{(1)} + {}^T\mathbf{P}_q^{(1)}\big] - \frac{1}{3}\boldsymbol{\delta}\boldsymbol{\delta} : \mathbf{P}_q^{(1)} \ . \end{aligned} \tag{3.12d}$$

In any physical situation, the force and torque are the only stress moments which can be specified externally. Higher multipoles are induced – they result from interactions with the flow and with other particles. They do, however, often have components proportional to moments of lower order. For instance, the quadrupole of a sphere of radius $a_q$ can be contracted to recover the force (apart from a multiplicative constant reflecting the geometry). Namely, $\mathbf{P}_q^{(2)} : \boldsymbol{\delta} = \frac{1}{2}a_q^2\mathbf{P}_q^{(0)}$. The irreducible spherical‡ quadrupole can then be constructed as $\mathbf{P}_q^{(2)} - \frac{1}{6}a_q^2\mathbf{F}_q\boldsymbol{\delta} = \mathbf{I}_q^{(2)}$. For spheres then $\mathbf{P}_q^{(2)} = \mathbf{I}_q^{(2)} + \frac{1}{6}a_q^2\mathbf{I}_q^{(0)}\boldsymbol{\delta}$, from which we see that the summand in (3.11b) with $m = 2$ generates a term proportional to the force $\mathbf{F}_q$. In order to group all the contributions from the force, torque, etc., we rewrite (3.11b) using the irreducible multipoles $\mathbf{I}$:

$$\mathbf{u}(\mathbf{x}) - \mathbf{u}_\infty(\mathbf{x}) = \frac{1}{8\pi\mu}\sum_{q=1}^{N}\sum_{m=0}^{\infty} \mathbf{I}_q^{(m)} \odot^{m+1} \hat{\boldsymbol{\mathcal{L}}}_q^{(m)}\big\{\mathbf{J}(\mathbf{x} - \mathbf{x}_q)\big\} \ , \tag{3.13}$$

‡ Unfortunately, it is not clear how to build a basis set of irreducible moments for particles of arbitrary shape. Ellipsoidal particles are treated in §3.3.

where $\hat{\mathcal{L}}_q^{(m)}$ is a linear operator, specific for the geometry of particle $q$, which raises the rank of its tensorial argument by $m$. For spheres for example,

$$\begin{aligned}
\hat{\mathcal{L}}_q^{(0)} &= 1 + \frac{a_q^2}{6}\nabla^2 + \ldots \\
\hat{\mathcal{L}}_q^{(1)} &= (1 + \frac{a_q^2}{10}\nabla^2 + \ldots)\nabla \\
\hat{\mathcal{L}}_q^{(2)} &= (1 + \frac{a_q^2}{14}\nabla^2 + \ldots)(\nabla\nabla - \frac{1}{3}\nabla^2\boldsymbol{\delta}) \ ,
\end{aligned} \tag{3.13'}$$

where we have transferred the tracelessness of $\mathbf{I}_q^{(2)}$ to $\hat{\mathcal{L}}_q^{(2)}$, which is otherwise defined by (3.13) only to within the addition of an arbitrary isotropic operator. Equation (3.13) indicates the meaning of $\hat{\mathcal{L}}_q^{(m)}\{\mathbf{J}(\mathbf{x}-\mathbf{x}_q)\}$: it is the singularity representation of the velocity disturbance due to an irreducible multipole of order $m$ acting on particle $q$. In practice, the expansion (3.13) is truncated after a suitable number of moments $M_q$.

The algorithm of Stokesian dynamics proposed by Durlofsky *et al.* (1987) then calls for the application of Faxén formulae to the flow field (3.13) in order to determine the particle motions. Generalized Faxén laws relate the stress moments on particles to the ambient flow field $\mathbf{u}_\infty + \mathbf{u}'$ in which they are immersed. Symbolically,

$$\begin{aligned}
\mathbf{F}_p &= \hat{\boldsymbol{\Lambda}}_p^{(0)} \cdot \{\mathbf{U}_p + \boldsymbol{\Omega}_p \wedge (\mathbf{x} - \mathbf{x}_p) - \mathbf{u}_\infty(\mathbf{x}) - \mathbf{u}'(\mathbf{x})\}|_{\mathbf{x}=\mathbf{x}_p} \ , \\
\mathbf{T}_p &= \hat{\boldsymbol{\Lambda}}_p^{(1a)} \cdot \{\mathbf{U}_p + \boldsymbol{\Omega}_p \wedge (\mathbf{x} - \mathbf{x}_p) - \mathbf{u}_\infty(\mathbf{x}) - \mathbf{u}'(\mathbf{x})\}|_{\mathbf{x}=\mathbf{x}_p} \ , \\
\mathbf{S}_p &= \hat{\boldsymbol{\Lambda}}_p^{(1s)} \cdot \{\mathbf{U}_p + \boldsymbol{\Omega}_p \wedge (\mathbf{x} - \mathbf{x}_p) - \mathbf{u}_\infty(\mathbf{x}) - \mathbf{u}'(\mathbf{x})\}|_{\mathbf{x}=\mathbf{x}_p} \ , \\
\mathbf{I}_p^{(2)} &= \hat{\boldsymbol{\Lambda}}_p^{(2)} \cdot \{\mathbf{U}_p + \boldsymbol{\Omega}_p \wedge (\mathbf{x} - \mathbf{x}_p) - \mathbf{u}_\infty(\mathbf{x}) - \mathbf{u}'(\mathbf{x})\}|_{\mathbf{x}=\mathbf{x}_p} \ ,
\end{aligned} \tag{3.14}$$

and so on. In the context of Stokesian dynamics, $\mathbf{u}'$ is the disturbance velocity caused by all particles other than $p$. For spheres, Faxén relations are well known

and read:‡

$$
\begin{aligned}
\hat{\boldsymbol{\Lambda}}_p^{(0)} &= 6\pi a_p \mu (1 + \frac{a_p^2}{6}\nabla^2)\boldsymbol{\delta} \ , \\
-\hat{\boldsymbol{\Lambda}}_p^{(1a)} &= 4\pi a_p^3 \mu \nabla \cdot \boldsymbol{\varepsilon} \ , \\
\hat{\boldsymbol{\Lambda}}_p^{(1s)} &= \frac{20}{3}\pi a_p^3 \mu (1 + \frac{a_p^2}{10}\nabla^2)\tfrac{1}{2}(\nabla\boldsymbol{\delta} + {}^T\nabla\boldsymbol{\delta}) \ , \\
\hat{\boldsymbol{\Lambda}}_p^{(2)} &= 6\pi a_p^5 \mu [\boldsymbol{B}^{(3,3)}]^{-1} \odot^3 (1 + \frac{a_p^2}{14}\nabla^2)[\nabla\nabla - \frac{1}{3}\nabla^2\boldsymbol{\delta}]\boldsymbol{\delta} \ .
\end{aligned}
\tag{3.14'}
$$

($[\boldsymbol{B}^{(3,3)}]^{-1}$ is defined in Mazur & van Saarloos (1982); *cf.* their equation (F.9).)

The concise and insightful theorem by Kim (1985 a) helps to clarify the connection between the operators $\hat{\boldsymbol{\mathcal{L}}}_p^{(m)}$ and $\hat{\boldsymbol{\Lambda}}_p^{(m)}$. Brenner (1964 b) and Brenner and Haber (1983) also showed in principle how to calculate $\hat{\boldsymbol{\Lambda}}_p^{(m)}$ with $m = 0$ or 1 for arbitrary particle shapes. Their approach is straightforward to generalize to higher values of $m$ (Rallison, 1978). If $\mathbf{u}' = 0$ in (3.14), one must recover the resistance functions for an isolated particle in an unbounded linear flow, which can be written as tensors (Brenner, 1963, 1964 a). In general therefore, (3.15)

$$
\begin{aligned}
\mathbf{F}_p &= \mathbf{K}_{FU}^p \cdot \big(\mathbf{U}_p - \mathbf{u}_\infty(\mathbf{x}_p)\big) + \mathbf{K}_{F\Omega}^p \cdot \big(\boldsymbol{\Omega}_p - \boldsymbol{\Omega}_\infty\big) - \mathbf{K}_{FE}^p : \mathbf{E}_\infty - \hat{\boldsymbol{\Lambda}}_p^{(0)} \cdot \mathbf{u}'(\mathbf{x})|_{\mathbf{x}=\mathbf{x}_p} \ , \\
\mathbf{T}_p &= \mathbf{K}_{TU}^p \cdot \big(\mathbf{U}_p - \mathbf{u}_\infty(\mathbf{x}_p)\big) + \mathbf{K}_{T\Omega}^p \cdot \big(\boldsymbol{\Omega}_p - \boldsymbol{\Omega}_\infty\big) - \mathbf{K}_{TE}^p : \mathbf{E}_\infty - \hat{\boldsymbol{\Lambda}}_p^{(1a)} \cdot \mathbf{u}'(\mathbf{x})|_{\mathbf{x}=\mathbf{x}_p} \ , \\
\mathbf{S}_p &= \mathbf{K}_{SU}^p \cdot \big(\mathbf{U}_p - \mathbf{u}_\infty(\mathbf{x}_p)\big) + \mathbf{K}_{S\Omega}^p \cdot \big(\boldsymbol{\Omega}_p - \boldsymbol{\Omega}_\infty\big) - \mathbf{K}_{SE}^p : \mathbf{E}_\infty - \hat{\boldsymbol{\Lambda}}_p^{(1s)} \cdot \mathbf{u}'(\mathbf{x})|_{\mathbf{x}=\mathbf{x}_p} \ ,
\end{aligned}
$$

etc. The tensors $\mathbf{K}^p$ are similar to $\boldsymbol{\mathcal{R}}^{pp}$ in (3.7), but $\mathbf{K}^p$ is a property of particle $p$ alone; the calculation of $\boldsymbol{\mathcal{R}}^{pp}$ on the other hand, demands that the zero-velocity (no-slip) boundary condition be satisfied at the surface of all other objects in the flow domain. Energy dissipation arguments (Happel & Brenner, 1973) guarantee

‡ Alternatively, and more consistently, the second and third relations in (3.14) can be combined as $\mathbf{I}_p^{(1)} = \hat{\boldsymbol{\Lambda}}_p^{(1)} \cdot \big\{\mathbf{U}_p + \boldsymbol{\Omega}_p \wedge (\mathbf{x} - \mathbf{x}_p) - \mathbf{u}_\infty(\mathbf{x}) - \mathbf{u}'(\mathbf{x})\big\}|_{\mathbf{x}=\mathbf{x}_p}$ with $\hat{\boldsymbol{\Lambda}}_p^{(1)} = \frac{4}{3}\pi a_p^3 \mu (1 + \frac{a_p^2}{10}\nabla^2)[4\nabla\boldsymbol{\delta} + {}^T\nabla\boldsymbol{\delta}] = 6\pi a_p^3 \mu [\boldsymbol{B}^{(2,2)}]^{-1} : (1 + \frac{a_p^2}{10}\nabla^2)\nabla\boldsymbol{\delta}$ for spheres. $\boldsymbol{B}^{(2,2)}$ is given in Mazur & van Saarloos, *cf.* their equation (4.16).

that the set of three relations in (3.15) can be inverted:

$$\begin{aligned}
\mathbf{U}_p - \mathbf{u}_\infty(\mathbf{x}_p) =& \boldsymbol{\mathcal{K}}^p_{UF} \cdot \mathbf{F}_p + \boldsymbol{\mathcal{K}}^p_{UT} \cdot \mathbf{T}_p + \boldsymbol{\mathcal{K}}^p_{US} : \mathbf{S}_p - \hat{\boldsymbol{\ell}}^{(0)}_p \cdot \mathbf{u}'(\mathbf{x})|_{\mathbf{x}=\mathbf{x}_p} \,, \\
\boldsymbol{\Omega}_p - \boldsymbol{\Omega}_\infty =& \boldsymbol{\mathcal{K}}^p_{\Omega F} \cdot \mathbf{F}_p + \boldsymbol{\mathcal{K}}^p_{\Omega T} \cdot \mathbf{T}_p + \boldsymbol{\mathcal{K}}^p_{\Omega S} : \mathbf{S}_p - \hat{\boldsymbol{\ell}}^{(1a)}_p \cdot \mathbf{u}'(\mathbf{x})|_{\mathbf{x}=\mathbf{x}_p} \,, \quad (3.16a) \\
-\mathbf{E}_\infty =& \boldsymbol{\mathcal{K}}^p_{EF} \cdot \mathbf{F}_p + \boldsymbol{\mathcal{K}}^p_{ET} \cdot \mathbf{T}_p + \boldsymbol{\mathcal{K}}^p_{ES} : \mathbf{S}_p - \hat{\boldsymbol{\ell}}^{(1s)}_p \cdot \mathbf{u}'(\mathbf{x})|_{\mathbf{x}=\mathbf{x}_p} \,.
\end{aligned}$$

These expressions are then inserted into the Faxén law for the quadrupole,

$$\begin{aligned}
\mathbf{I}^{(2)}_p &= \mathbf{K}^p_{QU} \cdot \left(\mathbf{U}_p - \mathbf{u}_\infty(\mathbf{x}_p)\right) + \mathbf{K}^p_{Q\Omega} \cdot \left(\boldsymbol{\Omega}_p - \boldsymbol{\Omega}_\infty\right) - \mathbf{K}^p_{QE} : \mathbf{E}_\infty - \hat{\boldsymbol{\Lambda}}^{(2)}_p \cdot \mathbf{u}'(\mathbf{x})|_{\mathbf{x}=\mathbf{x}_p} \\
&= (\mathbf{K}^p_{QU} \cdot \boldsymbol{\mathcal{K}}^p_{UF} + \mathbf{K}^p_{Q\Omega} \cdot \boldsymbol{\mathcal{K}}^p_{\Omega F} + \mathbf{K}^p_{QE} : \boldsymbol{\mathcal{K}}^p_{EF}) \cdot \mathbf{F}_p + \ldots - \hat{\boldsymbol{\ell}}^{(2)}_p \cdot \mathbf{u}'(\mathbf{x})|_{\mathbf{x}=\mathbf{x}_p} \,, \quad (3.16b)
\end{aligned}$$

for the octupole, and all higher moments up to $\mathbf{I}^{(M_p)}_p$. When the result (3.13) for $\mathbf{u}'$ (with the restriction $q \neq p$, and truncated after $m = M_q$) is inserted into the set (3.16a-b), one obtains an approximation to the $N$-body grand mobility tensor. Physically, the disturbance field due to each particle $q$ is described by means of a series of irreducible singularities $\mathbf{I}^{(m)}_q, m = 0, 1, ..., M_q$; the motion of particle $p$ is then found as the superposition of its responses to each disturbance separately, whence the phrase "pair-wise additivity of velocities." This formulation is exact if $\forall q,\ M_q \to \infty$. In matrix notation, we construct $\boldsymbol{\mathcal{M}}$, with

$$\begin{pmatrix} \boldsymbol{\mathcal{U}} - \boldsymbol{\mathcal{U}}_\infty \\ -\boldsymbol{E}_\infty \\ 0 \end{pmatrix} = \boldsymbol{\mathcal{M}} \otimes \begin{pmatrix} \boldsymbol{\mathcal{F}} \\ \boldsymbol{S} \\ \boldsymbol{H} \end{pmatrix} = \begin{pmatrix} \boldsymbol{\mathcal{M}}_{\mathcal{U}\mathcal{F}} & \boldsymbol{\mathcal{M}}_{\mathcal{U}S} & \boldsymbol{\mathcal{M}}_{\mathcal{U}H} \\ \boldsymbol{\mathcal{M}}_{EF} & \boldsymbol{\mathcal{M}}_{ES} & \boldsymbol{\mathcal{M}}_{EH} \\ \boldsymbol{\mathcal{M}}_{\mathcal{H}F} & \boldsymbol{\mathcal{M}}_{\mathcal{H}S} & \boldsymbol{\mathcal{M}}_{\mathcal{H}H} \end{pmatrix} \otimes \begin{pmatrix} \boldsymbol{\mathcal{F}} \\ \boldsymbol{S} \\ \boldsymbol{H} \end{pmatrix} \,. \qquad (3.17)$$

The operator $\otimes$ signifies the appropriate contraction. The vectors $\boldsymbol{\mathcal{U}}$ and $\boldsymbol{\mathcal{F}}$ were defined previously (see (3.8)). The stresslets on all $N$ particles are stringed in $\boldsymbol{S}$, and $\boldsymbol{E}_\infty$ contains the rate of strain at the locator points. $\boldsymbol{H}$ stands for all higher multipoles, i.e., for $\mathbf{I}^{(m)}_q$ with $m > 1$ and $q = 1, 2, ..., N$. The tensor $\boldsymbol{\mathcal{M}}$ is, strictly speaking, of infinite dimension.

Since the last elements on the left-hand side are zero for undeformable particles in a linear impressed flow, this system can be recast into

$$\begin{pmatrix} \boldsymbol{\mathcal{U}} - \boldsymbol{\mathcal{U}}_\infty \\ -\boldsymbol{E}_\infty \end{pmatrix} = \widetilde{\boldsymbol{\mathcal{M}}} \otimes \begin{pmatrix} \boldsymbol{\mathcal{F}} \\ \boldsymbol{S} \end{pmatrix} = \begin{pmatrix} \widetilde{\boldsymbol{\mathcal{M}}}_{\mathcal{U}\mathcal{F}} & \widetilde{\boldsymbol{\mathcal{M}}}_{\mathcal{U}S} \\ \widetilde{\boldsymbol{\mathcal{M}}}_{EF} & \widetilde{\boldsymbol{\mathcal{M}}}_{ES} \end{pmatrix} \otimes \begin{pmatrix} \boldsymbol{\mathcal{F}} \\ \boldsymbol{S} \end{pmatrix} \,, \qquad (3.18)$$

where, for instance, $\widetilde{\mathcal{M}}_{us} = \mathcal{M}_{us} - \mathcal{M}_{uH} \otimes \mathcal{M}_{\mathcal{H}H}^{-1} \otimes \mathcal{M}_{\mathcal{H}S}$. Inverting the relation (3.18) to find $\mathcal{F}$ yields (3.8), which is to say that $\mathcal{R}_{\mathcal{F}\mathcal{U}}$ is the $6N \times 6N$ principal minor of $\widetilde{\mathcal{M}}^{-1}$ (or of $\mathcal{M}^{-1}$ for that matter), i.e., $\mathcal{R}_{\mathcal{F}\mathcal{U}}^{-1} = \widetilde{\mathcal{M}}_{u\mathcal{F}} - \widetilde{\mathcal{M}}_{us} : \widetilde{\mathcal{M}}_{ES}^{-1} : \widetilde{\mathcal{M}}_{EF}$. In practice, this relation is only approximate since the multipole moment expansion (3.13) is truncated. However, as shown by Durlofsky *et al.* (1987) and by Mazur (1982), the matrix inversion process sums all the reflected interactions between all moments retained during the construction of the mobility tensor by the pair-wise additive scheme explained above. Hence, the inverse $\mathbf{R}$ of $\mathbf{M}$ (which is the finite-dimensional approximation to $\mathcal{M}$) contains many-body effects, and is therefore a better estimate of $\mathcal{R}$ than what would have been obtained by pairwise additivity of forces. In particular, the mobility invert reproduces the screening characteristic of porous media (Durlofsky & Brady, 1987).

As explained earlier, however, $\mathbf{M}^{-1}$ still lacks the strong resistance interactions occurring between very close particles. Following the methodology of Stokesian dynamics (Durlofsky *et al.*, 1987), the stress moments due to lubrication are added in a pair-wise additive manner to the mobility invert. [All the resistance functions which diverge as the separation between the surfaces vanishes are known asymptotically to $O(\epsilon^0)$, with $\epsilon$ the width of the gap between the particles (Claeys & Brady, 1989; Ch. II).] Some multipole reflections between nearly touching objects may be included in both $\mathbf{M}^{-1}$ and the lubrication tensor, and must therefore be subtracted in a corrective step. In summary,

$$\mathcal{R} \simeq \mathbf{R} = \mathbf{M}^{-1} + \mathcal{R}_{lub} - \mathcal{R}_{corr} \ . \tag{3.19}$$

This approximation $\mathbf{R}$ to the true $N$-body resistance tensor $\mathcal{R}$ preserves lubrication interactions and captures the essence of many-body effects.

Dynamic simulations require one to solve

$$\begin{pmatrix} \mathcal{F} \\ \mathcal{S} \end{pmatrix} = \widetilde{\mathbf{R}} \otimes \begin{pmatrix} \mathcal{U} - \mathcal{U}_\infty \\ -\mathcal{E}_\infty \end{pmatrix} \tag{3.20}$$

for the velocities $\boldsymbol{\mathcal{U}}$ and integrate the trajectories over a small time-step to find the evolution of the particle configuration. The resistance tensor is then constructed anew with the updated particle locations. The dynamics associated with Brownian motion are well understood (Ermak & McCammon, 1978) and can be incorporated rigorously in the framework of the technique. (This is explained for spherical particles in Brady & Bossis (1988). The thermal motions of prolate spheroids can be treated in a similar fashion.)

In most applications of Stokesian dynamics to dispersions of hard spheres (Brady & Bossis, 1988; Phillips *et al.*, 1988 a-b; Bossis & Brady, 1989), the multipole moment expansion (3.13) has been truncated at $M_q = 1$. A mean-field estimate of the quadrupolar effect has sometimes been included also. Those simulations produce results in excellent agreement with experimental data. In the next sections, we present the first extension of the technique to non-spherical particles, namely prolate spheroids.

### 3.3 Far-field estimate of the resistance tensor

The far-field estimate of the resistance tensor is the many-body approximation to $\boldsymbol{\mathcal{R}}$ obtained by inverting the grand mobility tensor $\mathbf{M}$. The previous section outlines how to construct $\mathbf{M}$ by combining the Faxén relations for the particles with the irreducible multipole expansion (3.13) of the fluid velocity disturbance due to their presence in the flow. Although our work primarily concerns prolate spheroids, some of the results reported in this section are presented for arbitrary ellipsoids. It is not difficult to take the limit for ovary ellipsoids of revolution if so desired.

For a generic ellipsoid $p$ centered at $\mathbf{x}_p$ and with surface $A_p$ such that

$$\mathbf{x} \in A_p \iff \mathbf{A}_p^{-1} : (\mathbf{x} - \mathbf{x}_p)(\mathbf{x} - \mathbf{x}_p) = 1 \,, \tag{3.21}$$

with $\mathbf{A}_p$ a positive-definite symmetric tensor of rank two, we show in Appendix D that the disturbance velocity field can be decomposed into contributions from irre-

ducible multipoles $\mathbf{I}_p^{(m)}$ as follows:

$$\mathbf{u}(\mathbf{x}) - \mathbf{u}_\emptyset(\mathbf{x}) = \frac{1}{8\pi\mu} \sum_{m=0}^{\infty} \mathbf{I}_p^{(m)} \odot^{m+1} (2m+1)!! \Big[ \Big(\frac{1}{D_p}\frac{\mathrm{d}}{\mathrm{d}D_p}\Big)^m \frac{\sinh D_p}{D_p} \Big] \overbrace{\nabla_{\mathbf{x}_p}}^{\times m} \mathbf{J}(\mathbf{x}-\mathbf{x}_p) \,. \tag{3.22}$$

The velocity field $\mathbf{u}_\emptyset$ is the undisturbed flow as it would be in the absence of the particle. The scalar operator $D_p = \sqrt{D_p^2}$, with

$$D_p^2 = \mathbf{A}_p : \nabla\nabla = \sum_{i=1}^{3} a_i^2 \mathbf{e}_i\mathbf{e}_i : \nabla\nabla = \sum_{i=1}^{3} a_i^2 \frac{\partial^2}{\partial x_i^2} \,, \tag{3.23}$$

where we have defined an orthogonal coordinate system $(x_1, x_2, x_3)$ using the eigenvectors $\mathbf{e}_i$ of $\mathbf{A}_p$. These lie along the principal axes of the ellipsoid, and we shall assume that they have been labeled such that $a_1 \geq a_2 \geq a_3$. As usual, $(\sinh D_p)/D_p$ must be interpreted as its infinite series representation (with $D_p^4 = D_p^2(D_p^2)$, etc.) and $(2m+1)!! = (2m+1)!/(2^m m!)$. The irreducible stress moments $\mathbf{I}_p^{(m)}$ are defined for ellipsoids so that contractions of any two of its last $m$ indices with the dyadic $\mathbf{A}_p^{-1}$ yield zero (*cf.* Appendix D).

Faxén laws for the stress moments $\mathbf{P}_p^{(m)}$ were derived by Kim & Arunachalam (1987). At the two lowest orders, their results can be cast in the form:

$$\mathbf{F}_p = \mathbf{P}_p^{(0)} = \mathbf{I}_p^{(0)} = \mathbf{K}_{FU}^p \cdot \mathbf{U}_p - \mathbf{K}_{FU}^p \cdot \Big[ \Big(\frac{\sinh D_p}{D_p}\Big) \mathbf{u}_\emptyset(\mathbf{x}) \Big] \Big|_{\mathbf{x}=\mathbf{x}_p} \,, \tag{3.24a}$$

$$\mathbf{P}_p^{(1)} = \mathbf{I}_p^{(1)} = \mathbf{Z}^p : \boldsymbol{\varepsilon} \cdot \boldsymbol{\Omega}_p - \mathbf{Z}^p : \Big[ 3 \Big( \frac{1}{D_p}\frac{\mathrm{d}}{\mathrm{d}D_p}\frac{\sinh D_p}{D_p} \Big) \nabla \mathbf{u}_\emptyset(\mathbf{x}) \Big] \Big|_{\mathbf{x}=\mathbf{x}_p} \tag{3.24b}$$

The polyadics $\mathbf{K}_{FU}^p$ and $\mathbf{Z}^p$ can be expressed in terms of elliptic integrals depending only on the body's dimensions (Brenner, 1966; Rallison, 1978; Brenner & Haber, 1983). It is now easy, at least conceptually, to build the grand mobility tensor for a system of arbitrary ellipsoids by combining the irreducible expansion for the velocity disturbance (3.22) with the resistance functions (3.24). [Since only the Faxén laws for the force, torque and stresslet are known for arbitrary ellipsoids, the mobility tensor can readily be constructed if one truncates the multipole expansion after the

first moment. Kim & Arunachalam (1987) elucidate the procedure for calculating Faxén relations for higher stress moments if additional terms need to be retained.] The $\mathbf{M}_{UF}^{pq}$ tensor for example, which links the translational velocity of particle $p$ to the force exerted on the fluid by ellipsoid $q$, can be written as (for $p \neq q$):

$$\mathbf{M}_{UF}^{pq} = \frac{1}{8\pi\mu}\left(\frac{\sinh D_p}{D_p}\right)\left(\frac{\sinh D_q}{D_q}\right)\mathbf{J}(\mathbf{x}_p - \mathbf{x}_q) \; . \tag{3.25}$$

An alternative, non-local description of the particle's interactions with the flow-field exists. Kim (1985 a) showed that the Faxén relations for a prolate spheroid can be expressed as integrals of the velocity field $\mathbf{u}_\emptyset$ and of its gradients over a line segment along the spheroidal symmetry axis, connecting the foci at $\mathbf{x}_p \pm c_p \mathbf{d}_p$. His results (for the force, torque and stresslet only) read:‡

$$\begin{aligned}
\mathbf{F} &= 16\pi\mu c\{\alpha_1 \mathbf{dd} + \alpha_2(\boldsymbol{\delta} - \mathbf{dd})\} \cdot \mathbf{U} \qquad (3.26a)\\
&\quad - 8\pi\mu\{\alpha_1 \mathbf{dd} + \alpha_2(\boldsymbol{\delta} - \mathbf{dd})\} \cdot \int_{-c}^{c} \left\{1 + (c^2 - \xi^2)\frac{(1-e^2)}{4e^2}\nabla^2\right\}\mathbf{u}_\emptyset(\boldsymbol{\xi})\,\mathrm{d}\xi \; ,\\
\mathbf{T} &= \frac{32}{3}\pi\mu c^3\{\gamma \mathbf{dd} + \gamma'(\boldsymbol{\delta} - \mathbf{dd})\} \cdot \boldsymbol{\Omega}\\
&\quad - 4\pi\mu\{\gamma \mathbf{dd} + \gamma'(\boldsymbol{\delta} - \mathbf{dd})\} \cdot \int_{-c}^{c} (c^2 - \xi^2)\nabla \wedge \mathbf{u}_\emptyset(\boldsymbol{\xi})\,\mathrm{d}\xi \qquad (3.26b)\\
&\quad - 8\pi\mu\alpha_1 \mathbf{d} \wedge \int_{-c}^{c} (c^2 - \xi^2)\left\{1 + (c^2 - \xi^2)\frac{(1-e^2)}{8e^2}\nabla^2\right\}\mathbf{d} \cdot \mathbf{e}_\emptyset(\boldsymbol{\xi})\,\mathrm{d}\xi \; ,\\
S_{ij} &= 8\pi\mu\left\{\frac{\alpha_5}{2}\left(d_i d_j - \frac{1}{3}\delta_{ij}\right)\left(d_k d_l - \frac{1}{3}\delta_{kl}\right)\right.\\
&\quad + \frac{\alpha^*}{4}(d_i\delta_{jk}d_l + d_i\delta_{jl}d_k + \delta_{il}d_j d_k + \delta_{ik}d_j d_l - 4d_i d_j d_k d_l)\\
&\quad + \frac{\alpha_4}{2}(\delta_{ik}\delta_{jl} + \delta_{il}\delta_{jk} - \delta_{ij}\delta_{kl} + d_i d_j \delta_{kl} + \delta_{ij} d_k d_l \qquad (3.26c)\\
&\quad \left. - d_i\delta_{jl}d_k - \delta_{ik}d_j d_l - d_i\delta_{jk}d_l - \delta_{il}d_j d_k + d_i d_j d_k d_l)\right\} \cdot\\
&\qquad \cdot \int_{-c}^{c} (c^2 - \xi^2)\left\{1 + (c^2 - \xi^2)\frac{(1-e^2)}{8e^2}\nabla^2\right\}\left[\mathbf{e}_\emptyset(\boldsymbol{\xi})\right]_{kl}\mathrm{d}\xi\\
&\quad - 2\pi\mu\alpha_1(d_i\varepsilon_{jkl}d_l + d_j\varepsilon_{ikl}d_l)\int_{-c}^{c} (c^2 - \xi^2)\left\{\nabla \wedge \mathbf{u}_\emptyset(\boldsymbol{\xi}) - 2\boldsymbol{\Omega}\right\}_k \mathrm{d}\xi \; .
\end{aligned}$$

‡ Kim & Arunachalam (1987) later generalized these formulae to any multipole moment $\mathbf{P}_p^{(m)}$ for arbitrary ellipsoids.

(All variables, except $\mu$, are proper to particle $p$. We suppressed the subscript $p$ on $\mathbf{F}, \mathbf{T}, \mathbf{S}, \mathbf{U}, \mathbf{d}, \mathbf{\Omega}, \alpha, \gamma, c$ and $e$ for the sake of clarity. The implicit summation convention for repeated indices is adopted in (3.26c).) The unit vector $\mathbf{d_p}$ (for director) lies along the spheroidal axis; $\mathbf{U}_p$ and $\mathbf{\Omega}_p$ are the translational and angular velocities of the particle at its locator point $\mathbf{x}_p$. The notation $\mathbf{e}_\emptyset$ is shorthand for $\frac{1}{2}(\nabla \mathbf{u}_\emptyset + {}^T\nabla \mathbf{u}_\emptyset)$, and $\boldsymbol{\xi}$ stands for $\mathbf{x}_p + \xi \mathbf{d}_p$. All the remaining parameters depend only on the geometry of the body: $c$ is the distance between the geometric centre and the foci of the generating ellipse; $e = c/a$ is called the eccentricity, with $a$ the length of the major semi-axis; $\alpha$ and $\gamma$ are functions of $e$, defined in Kim (1985 a) (see also Chwang & Wu (1974, 1975), and App. J). In essence, $\alpha_5$ dominates during axisymmetric extension about the spheroidal axis, $\alpha^*$ characterizes the stress response to simple shear flows for which the velocity gradient lies along $\mathbf{d}_p$, and $\alpha_4$ gives the particle's stress contribution when the plane of shear is perpendicular to the director.

The two formulations (3.24) and (3.26) are of course compatible, since one can show for any tensor $\mathbf{X}(\mathbf{x})$ that (Kim & Arunachalam, 1987)

$$\left(\frac{1}{D}\frac{\partial}{\partial D}\right)^m \frac{\sinh D}{D}\mathbf{X}(\mathbf{x})|_{\mathbf{x}=\mathbf{x}_p} = \tag{3.27a}$$

$$\frac{1}{2\pi c_E c'_E}\frac{1}{(2m-1)!!}\iint_E q^{2m-1}(\mathbf{x}')\left\{1 + \frac{a_3^2 q^2}{4m+2}\nabla^2\right\}\mathbf{X}(\mathbf{x}')\,\mathrm{d}A_{\mathbf{x}'} \ .$$

The domain of integration $E$ is the elliptical disk confocal to the particle surface $A_p$ :

$$\mathbf{x} \in E \iff q^2(\mathbf{x}) = 1 - \frac{\left[(\mathbf{x}-\mathbf{x}_p)\cdot\mathbf{e}_1\right]^2}{c_E^2} - \frac{\left[(\mathbf{x}-\mathbf{x}_p)\cdot\mathbf{e}_2\right]^2}{c_E'^2} > 0 \tag{3.27b}$$

with $c_E^2 = a_1^2 - a_3^2$ and $c_E'^2 = a_2^2 - a_3^2$ . For a prolate spheroid, with $a_2 = a_3$ and $\mathbf{e}_1 = \mathbf{d}$, the fundamental ellipse degenerates into a line with length $2c_E = 2c$, and (3.27a) takes the form:

$$\left(\frac{1}{D}\frac{\partial}{\partial D}\right)^m \frac{\sinh D}{D}\mathbf{X}(\mathbf{x})|_{\mathbf{x}=\mathbf{x}_p} \tag{3.27c}$$

$$= \frac{1}{2c}\int_{-c}^{c}\frac{1}{2^m m!}\left(1-\frac{\xi^2}{c^2}\right)^m\left\{1 + \frac{a_3^2}{4m+4}\left(1-\frac{\xi^2}{c^2}\right)\nabla^2\right\}\mathbf{X}(\mathbf{x}_p + \xi\mathbf{d}_p)\,\mathrm{d}\xi \ .$$

Note that $a_3^2/c^2 = (1-e^2)/e^2$ and compare (3.27c) with (3.26).

The identity (3.27a) can be used in conjunction with the irreducible expansion (3.22) to get the disturbance velocity as:

$$\mathbf{u}(\mathbf{x}) - \mathbf{u}_\emptyset(\mathbf{x}) = \tag{3.28}$$
$$\frac{1}{8\pi\mu}\sum_{m=0}^{\infty}\mathbf{I}_p^{(m)}\odot^{m+1}\frac{2m+1}{2\pi c_E c_E'}\iint_E q^{2m-1}(\mathbf{x}')\Big\{1+\frac{a_3^2q^2}{4m+2}\nabla^2\Big\}\overbrace{\nabla_{\mathbf{x}'}}^{\times m}\mathbf{J}(\mathbf{x}-\mathbf{x}')\,\mathrm{d}A_{\mathbf{x}'}\ .$$

This is consistent with the singularity representation of Chwang & Wu (1974, 1975), who constructed exact solutions of the Stokes equations for isolated prolate spheroids suspended in linear flows using uniform, parabolic and biquadratic distribution of singularities along the particle's major axis.

We now have all the elements necessary to build the grand mobility tensor, but the Faxén laws (3.26) need to be inverted. It is trivial to obtain:

$$\begin{aligned}\mathbf{U} - \mathbf{u}_\infty(\mathbf{x}_p) =& \frac{1}{16\pi\mu c}\{\alpha_1^{-1}\mathbf{dd} + \alpha_2^{-1}(\boldsymbol{\delta}-\mathbf{dd})\}\cdot\mathbf{F} \\ &+ \frac{1}{2c}\int_{-c}^{c}\Big\{1+(c^2-\xi^2)\frac{(1-e^2)}{4e^2}\nabla^2\Big\}\mathbf{u}'(\boldsymbol{\xi})\,\mathrm{d}\xi\ ,\end{aligned} \tag{3.29a}$$

where we have extracted the contribution from the impressed flow $\mathbf{u}_\infty$ (see (3.6)), and introduced $\mathbf{u}' = \mathbf{u}_\emptyset - \mathbf{u}_\infty$. (In Stokesian dynamics, $\mathbf{u}'$ typically represents the disturbance velocity due to all particles other than $p$.) The relations (3.26b-c) for $\boldsymbol{\Omega} - \boldsymbol{\Omega}_\infty$ and $-\mathbf{E}_\infty$, however, are coupled. This reflects the fact that a spheroid tumbles in a extensional flow (unless its axis is aligned with a principal direction of the rate of strain). [From a mathematical standpoint, this coupling results from the somewhat artificial distinction between the antisymmetric and symmetric parts of the velocity gradient.] The expressions (3.26b-c) must therefore be inverted together. After a bit of algebra (Claeys, 1988), one arrives at the following mobility

functions for prolate spheroids:

$$\boldsymbol{\omega}-\boldsymbol{\Omega}_\infty=\frac{3}{32\pi\mu c^3}\left\{\gamma^{-1}\mathbf{dd}+\left[\gamma'^{-1}-\frac{e^2/(2-e^2)}{\left(\frac{2-e^2}{e^2}\alpha^*+\alpha_1\right)}\right](\boldsymbol{\delta}-\mathbf{dd})\right\}\cdot\mathbf{T}$$
$$+\frac{3}{32\pi\mu c^3}\frac{1}{\left(\frac{2-e^2}{e^2}\alpha^*+\alpha_1\right)}(\mathbf{d}\wedge\mathbf{S}\cdot\mathbf{d}-\mathbf{d}\cdot\mathbf{S}\wedge\mathbf{d}) \tag{3.29b}$$
$$+\frac{3}{8c^3}\int_{-c}^{c}(c^2-\xi^2)\nabla\wedge\mathbf{u}'(\boldsymbol{\xi})\,\mathrm{d}\xi\ ,$$

and

$$-(\mathbf{E}_\infty)_{ij}=\frac{-3}{32\pi\mu c^3}\left\{\frac{9}{2\alpha_5}(d_id_j-\frac{1}{3}\delta_{ij})(d_kd_l-\frac{1}{3}\delta_{kl})\right.$$
$$+\frac{1}{\left(\alpha^*+\frac{e^2}{2-e^2}\alpha_1\right)}(d_i\delta_{jk}d_l+d_i\delta_{jl}d_k+\delta_{il}d_jd_k+\delta_{ik}d_jd_l-4d_id_jd_kd_l)$$
$$+\frac{1}{2\alpha_4}(\delta_{ik}\delta_{jl}+\delta_{il}\delta_{jk}-\delta_{ij}\delta_{kl}+d_id_j\delta_{kl}+\delta_{ij}d_kd_l \tag{3.29c}$$
$$\left.-d_i\delta_{jl}d_k-\delta_{ik}d_jd_l-d_i\delta_{jk}d_l-\delta_{il}d_jd_k+d_id_jd_kd_l)\right\}S_{kl}$$
$$+\frac{3}{4c^3}\int_{-c}^{c}(c^2-\xi^2)\left\{1+(c^2-\xi^2)\frac{(1-e^2)}{8e^2}\nabla^2\right\}e'_{ij}(\boldsymbol{\xi})\,\mathrm{d}\xi$$
$$-\frac{3}{32\pi\mu c^3}\frac{1}{\left(\frac{2-e^2}{e^2}\alpha^*+\alpha_1\right)}(\mathbf{dd}\wedge\mathbf{T}-\mathbf{T}\wedge\mathbf{dd})_{ij}\ .$$

As before, $\mathbf{e}'=\frac{1}{2}(\boldsymbol{\nabla}\mathbf{u}'+{}^T\boldsymbol{\nabla}\mathbf{u}')$. It may be useful to point out that $e^2/(2-e^2)=(r_p^2-1)/(r_p^2+1)$, with $r_p$ the aspect ratio of the particle ($r_p>1$ for prolate bodies).

From the linearity of the creeping flow equations, $\mathbf{u}'$ may be constructed by superposing the contributions (3.28) of each particle separately. Truncating the expansion after the first moment (experience with Stokesian dynamics for spheres indicates that retaining the effects of the force, torque and stresslet is sufficient for most purposes), we rewrite (3.28) explicitly for prolate spheroids:

$$\mathbf{u}'(\mathbf{x})=\frac{1}{16\pi\mu c}\mathbf{F}_q\cdot\int_{-c}^{c}\left\{1+(c^2-\xi^2)\frac{(1-e^2)}{4e^2}\nabla^2\right\}\mathbf{J}(\mathbf{x}-\boldsymbol{\xi})\,\mathrm{d}\xi$$
$$-\frac{3}{64\pi\mu c^3}\mathbf{T}_q\cdot\int_{-c}^{c}(c^2-\xi^2)\boldsymbol{\nabla}_\mathbf{x}\wedge\mathbf{J}(\mathbf{x}-\boldsymbol{\xi})\,\mathrm{d}\xi \tag{3.30}$$
$$-\frac{3}{32\pi\mu c^3}\mathbf{S}_q:\int_{-c}^{c}(c^2-\xi^2)\left\{1+(c^2-\xi^2)\frac{(1-e^2)}{8e^2}\nabla^2\right\}\tfrac{1}{2}(\boldsymbol{\nabla}_\mathbf{x}+{}^T\boldsymbol{\nabla}_\mathbf{x})\mathbf{J}(\mathbf{x}-\boldsymbol{\xi})\,\mathrm{d}\xi\ .$$

The grand mobility tensor for a system of $N$ prolate spheroids can be constructed at the level of forces, torques and stresslets by summing the disturbances (3.30) over all particles $q \neq p$, inserting the result into the mobility functions (3.29), and repeating this for all spheroids $p$. [The inclusion of higher moments is straighforward provided their Faxén laws are first determined.] The contribution of a force $\mathbf{F}_2$ exerted by particle "2" to the translational velocity $\mathbf{U}_1$ of spheroid "1", for example, is given by:

$$\mathbf{U}_1 = \frac{1}{32\pi\mu c_1 c_2} \int_{-c_1}^{c_1} \left[ \left\{ 1 + (c_1^2 - \xi_1^2) \frac{(1-e_1^2)}{4e_1^2} \nabla^2 \right\} \right. \tag{3.31}$$
$$\left. \int_{-c_2}^{c_2} \left\{ 1 + (c_2^2 - \xi_2^2) \frac{(1-e_2^2)}{4e_2^2} \nabla^2 \right\} \mathbf{J}(\boldsymbol{\xi}_1 - \boldsymbol{\xi}_2) \right] d\xi_2 \, d\xi_1 \cdot \mathbf{F}_2 \; .$$

In contrast to (3.25), this non-local description of the interactions between spheroids only involves the Oseen tensor and its second derivative (recall that $\nabla^4 \mathbf{J} = 0$). Equation (3.31) shows that the rods behave hydrodynamically as if they were line distributions of point forces and potential doublets –no higher multipoles are needed for the $\mathbf{M}_{UF}^{pq}$-coupling. This is a definite advantage over the symbolic representation (3.25) since multipoles of higher order generate more complex flow disturbances and have stronger singularities at their origin. Indeed, we have found the formulation (3.25) to be totally unsatisfactory for numerical purposes in cases where the centre-to-centre separation of the particles is comparable to the sum of their major semi-axes (i.e., when the spheres circumscribing the spheroids penetrate). In (3.25), mobility elements are calculated as infinite alternating series with very poor convergence properties at small distances. (The amplitude of the terms grows exponentially before decreasing to zero, implying that no systematic improvement in the accuracy of $\mathbf{M}_{UF}^{pq}$ can be achieved by retaining more terms in the series representation of $\sinh D_p / D_p$, unless a sufficient number has been calculated already. The limited precision of modern-day computers very often resulted in the loss of all significant digits before convergence could be expected in theory.) The non-local description (3.31) is far more robust, although the kernel can be sharply peaked

or rapidly varying for nearly touching particles. Adaptive integration techniques (Piessens *et al.*, 1983) handle these numerical difficulties very nicely. The mobility tensor $\mathbf{M}$ obtained in this way can be inverted using a Cholesky decomposition algorithm (see for example Perry & Green, 1984) since $\mathbf{M}$ is positive definite, a consequence of viscous dissipation, and also symmetric from Lorentz' reciprocal theorem (Happel & Brenner, 1973).

The computation of each element of the mobility tensor (except the self-terms $\mathbf{M}^{pp}$) requires a double integration over the particle axes. Using cylindrical coordinates centered at the origin of spheroid "2" with the azimuthal axis along $\mathbf{d}_2$, the first integration in (3.31) can be carried out analytically. The result is most conveniently expressed in terms of the coefficients $B_{m,n}(\mathbf{x})$, which Chwang & Wu (1975) introduced as:

$$B_{m,n}(\mathbf{x}) = \int_{-c_2}^{c_2} \frac{\xi^n}{|\mathbf{x} - \boldsymbol{\xi}|^m} \, \mathrm{d}\xi \; . \tag{3.32}$$

For instance, defining a right-handed orthonormal frame of reference $(\mathbf{d}_2, \mathbf{e}_r, \mathbf{e}_\theta)$ such that $\mathbf{x} - \mathbf{x}_2 = x_d \mathbf{d}_2 + r\mathbf{e}_r$, we find

$$\begin{aligned} \int_{-c_2}^{c_2} \mathbf{J}(\mathbf{x} - \boldsymbol{\xi}_2) \, \mathrm{d}\xi_2 = {} & (2B_{1,0} - r^2 B_{3,0}) \mathbf{d}_2 \mathbf{d}_2 + (x_d B_{3,0} - B_{3,1}) r (\mathbf{d}_2 \mathbf{e}_r + \mathbf{e}_r \mathbf{d}_2) \\ & + (B_{1,0} + r^2 B_{3,0}) \mathbf{e}_r \mathbf{e}_r + B_{1,0} \mathbf{e}_\theta \mathbf{e}_\theta \; . \end{aligned} \tag{3.33}$$

Note that $\mathbf{x} = \boldsymbol{\xi}_1$ in (3.31). Therefore, $\mathbf{e}_r$ and $\mathbf{e}_\theta$ are functions of $\xi_1$, whose variation must be taken into account during the subsequent integration along the axis of spheroid "1."

Closed form expressions for $B_{m,n}(\mathbf{x})$ in terms of elementary functions are known for arbitrary integer values of $m$ and $n$, and recurrence formulae for $n > 1$ (Chwang & Wu, 1975; Claeys, 1988) make their use especially suited for computer programming. Taking advantage of identities relating derivatives of $B_{m,n}(\mathbf{x})$ (Claeys, 1988), and after some tedious but straightforward algebra, all the mobility coefficients for particles "1" and "2" can be written as integrals along the symmetry axis of either ellipsoid in the form $\mu^{-1} \int_{-c_1}^{c_1} f_M\big(\{B_{m,n}(\boldsymbol{\xi}_1)\}\big) \, \mathrm{d}\xi_1$, where $f_M\big(\{B_{m,n}\}\big)$

is a linear function of the set of $B_{m,n}(\mathbf{x})$ involving $c_1, c_2, e_1$ and $e_2$ as parameters. This integral is then evaluated numerically (Claeys, 1988; Claeys, 1991).

## 3.4 Addition of lubrication effects

As explained in §3.2, lubrication stresses arising from the relative motion of nearly touching particles in the fluid are added in a pairwise manner to the mobility invert. Unlike the far-field hydrodynamic interactions, lubrication is essentially a two-body problem dominated by the flow in the small and narrow gap region separating the close surfaces. Hence pair-wise additive schemes should be successful. The construction of the resistance tensor for two objects near contact involves two steps. At first, the points of closest approach must be determined. This then specifies the local geometry in the thin gap, from which the friction functions can be calculated. In Chapter II, we derived formulae for all stress moments which diverge as the surface separation $\epsilon$ vanishes; i.e., the resistance tensor is known to $O(\epsilon^0)$ for arbitrary objects (with mathematically smooth boundaries which would touch at a single point when brought into contact along their common normal without altering their orientation—all convex particles satisfy these conditions). The $O(1) = O(\epsilon^0)$ corrections to these expressions require the solution of the "outer" flow, which is quite complex and depends on the exact relative orientation of the particles (characterized by 4 independent parameters for axisymmetric bodies). Although they can be found using a collocation or finite elements method for example, even the task of tabulating them is foreboding.

Since the points of minimum separation $\mathbf{z}_p$ and $\mathbf{z}_q$ on particles $p$ and $q$ must be determined over and over during dynamic simulations, it is imperative to develop an efficient and accurate algorithm devoted to this goal. Precision is important since even rather good approximations to the points of closest approach can give poor estimates of the gap width $\epsilon$, with which the resistance functions scale (Fig. 3.1a). In addition, in the acicular limit, the principal radii of curvature, which also largely determine the magnitude of the stress response, change very rapidly near the tip

of the rod (Fig. 3.1b). Thus the algorithm must converge very quickly to the exact location of $\mathbf{z}_p$ and $\mathbf{z}_q$. The method we have devised is based on the observation that the normal to the surface $A_p$ at $\mathbf{z}_p$ coincides with the normal to $A_q$ at $\mathbf{z}_q$ (but is antiparallel to it). We also exploit the following property of ellipses:† the sum of the distances from any point $\mathbf{x}$ of the ellipse to the foci is constant. The surface $A_p$ of a prolate spheroid centered at the origin is thus correctly represented by

$$\mathbf{x} \in A_p \iff f_p(\mathbf{x}) = |\mathbf{x} - \mathbf{c}_p| + |\mathbf{x} + \mathbf{c}_p| = 2a_p \ . \tag{3.34}$$

Its foci are at $\pm\mathbf{c}_p$, and $a_p$ is the length of the major semi-axis. The normal to the surface at $\mathbf{x}$ can thus be written as

$$\nabla f_p = \frac{\mathbf{x} - \mathbf{c}_p}{|\mathbf{x} - \mathbf{c}_p|} + \frac{\mathbf{x} + \mathbf{c}_p}{|\mathbf{x} + \mathbf{c}_p|} \ . \tag{3.35}$$

That is, the normal bisects the lines joining $\mathbf{x}$ to $\pm\mathbf{c}_p$. As a consequence, all the normals to $A_p$ intersect the spheroidal axis betwen the foci. The normal common to $A_p$ and $A_q$ must therefore cross the symmetry axes of both particles, and $\mathbf{z}_p$ and $\mathbf{z}_q$ are the points where it penetrates their surfaces. The outline of our algorithm is thus as follows (Fig. 3.2):

1. Find the intersection $\boldsymbol{\chi}_p^{(k)}$ of the normal to $A_p$ at $\mathbf{z}_p^{(k)}$ with the spheroidal axis. Repeat for particle $q$.
2. Find the intersections $\mathbf{z}_p^{(k+1)}$ and $\mathbf{z}_q^{(k+1)}$ of the line joining $\boldsymbol{\chi}_p^{(k)}$ to $\boldsymbol{\chi}_q^{(k)}$ with the surfaces $A_p$ and $A_q$.
3. Convergence check. (For instance, are the normals at $\mathbf{z}_p^{(k+1)}$ and at $\mathbf{z}_q^{(k+1)}$ nearly antiparallel ?). Iterate 1.-3. if necessary.

The first guesses $\mathbf{z}_p^{(0)}$ and $\mathbf{z}_q^{(0)}$ must belong to the surfaces, but no other restrictions are placed on their accuracy, and one always finds $\lim_{k\to\infty} \mathbf{z}_p^{(k)} = \mathbf{z}_p$. This method has several advantages over alternatives. In the spherical limit, it corresponds to

† This property is often used by landscapers, who draw ellipses in the soil by pulling taut a rope attached to two pins hammered in the ground.

joining the centres of the particles, the most obvious way to find $\mathbf{z}_p$ and $\mathbf{z}_q$ in that case. In general, we have reduced the dimensionality of the search domain from 4 (two curved boundaries) to 2 (two line segments). This obviously speeds up the convergence. Also, all schemes scanning the surfaces of the particles slow down dramatically as they near the points of closest approach, since the step size usually scales with $|\mathbf{z}_p^{(k)} - \mathbf{z}_q^{(k)}|$ in some fashion. (In our method, on the other hand, the step size is set by $|\boldsymbol{\chi}_p^{(k)} - \boldsymbol{\chi}_q^{(k)}| >> |\mathbf{z}_p^{(k)} - \mathbf{z}_q^{(k)}|$.) Finally, this algorithm is guaranteed to have a real solution at each iteration. By contrast, many other methods which "shoot" from one surface to the other, may occasionally "miss", especially if the first estimates were poor, or if one of the points of closest approach is very near the tip of a slender ellipsoid. We note that this method also detects the points of maximum penetration in the case of overlapping spheroids (as long as the line segment $[\mathbf{x}_p - \mathbf{c}_p, \mathbf{x}_p + \mathbf{c}_p]$ is exterior to $A_q$), and that its concept can be extended to arbitrary ellipsoids (in which case $\boldsymbol{\chi}_p^{(k)}$ belongs to the elliptic disk confocal with $A_p$).

The local geometry near the points of closest approach may readily be found by expanding $f_p$ (see (3.34)) in a Taylor series about $\mathbf{z}_p$. We then apply the formulae of Chapter II to build the resistance tensor to $O(1)$ for each pair of particles near contact (i.e., for each set of spheroids for which the surface-to-surface separation, normalized by the harmonic mean of the local radii of curvature, is smaller than a prescribed threshold). This information is then added to $\mathbf{M}^{-1}$ to obtain $\mathbf{R}$ (see (3.19)). At this level of accuracy, the correction term $\boldsymbol{R}_{corr}$ is irrelevant, since it would only contribute to the unknown $O(\epsilon^0)$ part of the lubrication stresses.

## 3.5 Selected examples of simulations for a finite number of prolate spheroids interacting hydrodynamically in a viscous fluid

### 3.5.1 Numerical aspects

Using the method outlined in the preceding sections, we carried out a variety of simulations for systems involving a finite number of prolate spheroids in an unbounded

Newtonian incompressible fluid. Because of numerical rather than conceptual limitations, we restricted the range of aspect ratios from $1 + 2 \times 10^{-6}$ to about 50. The lower bound is so close to the spherical case that it can hardly be called a limitation. It springs from difficulties in computing the coefficients $\alpha$ and $\gamma$ in the expressions for the self-terms $\mathbf{M}^{pp}$ (see (3.26) and App. J), and could easily be removed. The most efficient way of dealing with spheres, however, is to take their shape explicitly into account, and replace the line distribution of singularities used here (even though the line segment becomes infinitesimally short) by the appropriate combination of point forces, doublets and other multipoles at the sphere's centre (as done in Stokesian dynamics up till now (Durlofsky *et al.*, 1987)). This is trivial to do. The upper bound $r_p \simeq 50$ comes from more subtle numerical aspects. The major difficulty in the acicular limit is the smallness of the radii of curvature near the tip of the slender body. Since lubrication interactions only set in at surface separations small compared to that dimension, extremely close encounters between particles can occur before they experience any repulsion. The time-step in dynamic simulations is mostly determined by the requirement that there would be (virtually) no particle overlap; when the superficial separations are so small, demands on the computer time become prohibitively large. This problem is by nature inexistent for static simulations (in which the evolution of the configuration is not tracked), so that one can then study fibres with much larger aspect ratios. [Few natural or man-made materials, however, consist of straight rigid fibres of very high aspect ratio; such slender bodies either bend or break (Salinas & Pittman, 1981).]

Particle paths are integrated using a fourth order Adams-Bashford formula (Abramowitz & Stegun, 1970). The time step is chosen suitably small to make errors due to the time integration insignificant. The mobility tensor was usually formed and inverted for each new configuration, since far-field interactions dominate the dynamics of most applications involving only a few spheroids. For more concentrated systems, considerable savings in computer time may be achieved by updating the mobility tensor less frequently than the lubrication interactions. (The

gross features of the $N$-body configuration, which determine $\mathbf{M}$, vary slowly on the time scale of the trajectory calculation, which is set by the requirement that typical displacements do not exceed the smallest gap width between particle surfaces.) Optimal use was made of Lorentz' reciprocal theorem for the construction of $\mathbf{M}$. To minimize the number of required operations even further, we exploited the interesting identities (see Appendix E):

$$\mathbf{M}^{pq}_{UT} = \tfrac{1}{2}\boldsymbol{\varepsilon} \cdot (\boldsymbol{\delta} : \mathbf{M}^{pq}_{US}) \,, \tag{3.36a}$$

$$[\mathbf{M}^{pq}_{\Omega T}]_{ij} = -[\mathbf{M}^{pq}_{ES}]_{iklj}\boldsymbol{\delta}_{kl} + \tfrac{1}{2}[\mathbf{M}^{pq}_{ES}]_{mkln}\boldsymbol{\delta}_{kl}\boldsymbol{\delta}_{mn}\boldsymbol{\delta}_{ij} \,, \tag{3.36b}$$

$$\mathbf{M}^{pq}_{\Omega S} = \boldsymbol{\varepsilon} \cdot \mathbf{M}^{pq}_{\Omega T} + (\boldsymbol{\varepsilon} \cdot \mathbf{M}^{pq}_{\Omega T})^T \,. \tag{3.36c}$$

These hold for ellipsoids regardless of whether $p = q$. From these relations, it can be seen that only the couplings $\mathbf{M}_{UF}$, $\mathbf{M}_{US}$ and $\mathbf{M}_{ES}$ need to be evaluated for each pair of particles to build the grand mobility tensor $\mathbf{M}$. Taking maximal advantage of the tracelessness of $\mathbf{E}$ and $\mathbf{S}$, and of the symmetry of $\mathbf{M}_{UF}$ (see (3.31)) and of $\mathbf{M}_{ES}$, this reduces the number of unknown independent mobility functions to 36 per pair of particles. (For the selfterms, only 21 are needed since $\mathbf{M}^{pp}_{US} = 0$ for spheroids.)

The identities (3.36) also imply the following, previously apparently undiscovered relations between the coefficients $\alpha$ and $\gamma$ defined by Chwang & Wu (1974, 1975) (see also Kim, 1985 a):

$$\gamma^{-1} = \tfrac{1}{2}\alpha_5^{-1} - \alpha_4^{-1} \,, \tag{3.37a}$$

$$\gamma'^{-1} - \gamma^{-1} = \frac{e^2}{2-e^2}\left(\alpha_4^{-1} - \tfrac{3}{2}\alpha_5^{-1}\right) \,, \tag{3.37b}$$

$$\alpha_4^{-1} - \tfrac{3}{2}\alpha_5^{-1} = \frac{2}{(2-e^2)\alpha^* + e^2\alpha_1} \,. \tag{3.37c}$$

The symmetry elements in some of the illustrative examples given below (mirror symmetry about a plane, planar configuration...) can also be used to reduce the number of unknowns and speed up the computations. This was done in a few cases, but most simulations were performed using a general version of the code capable of handling fully three-dimensional particle conformations and polydisperse samples.

The symmetry inherent to the method (mostly through Lorentz' reciprocal theorem) makes it very robust, and we never noticed any violations of the symmetry imposed by the initial conditions in any of our simulations.

Because of the strong coupling between the torque and the rate of strain ($\mathbf{M}_{TE}^{pq}$ is non-zero even for $p = q$), it does not make sense for spheroids to consider an "F-T"-method as proposed by Durlofsky *et al.* (1987). They found that useful results could be obtained for spheres (in the absence of extensional components in the impressed flow), by retaining only the couplings between the force and torque on the particles, and their translational and rotational velocities. They recognized, however, that they owed this success to the fact that all stresslets are induced in such circumstances. This is no longer true for ellipsoidal particles, because a single spheroid in a vorticity flow experiences strain. It is therefore necessary to keep the symmetric as well as the antisymmetric part of the first moment of the stress density on the particle surface, i.e., one must use the full "F-T-S"-method of Durlofsky *et al.* (1987).

To test the accuracy of our method, we checked our results against those obtained by other researchers using various numerical techniques (*vide infra*). We also verified for a large number of multiparticle configurations that the grand resistance tensor that we calculate in the limit of zero eccentricity matches the one found using the version of Stokesian dynamics dedicated to spheres. All calculations were performed on a Sun4/360 workstation and typically required at most a few seconds of CPU time. The duration of dynamic simulations such as those presented in sections 3.5.4 and 3.5.5 depends on the number of particles and their aspect ratio. Few of the examples given here however, were generated in more than 10 minutes. The program is written in FORTRAN (Claeys, 1991).

### 3.5.2 Axisymmetric flow past chains of spheroids

Gluckman *et al.* (1971) introduced the multipole collocation method to calculate the drag on equidistant identical spheroids, all lined up along one line, and moving

with uniform velocity. We list in table 3.1 the force necessary for this motion in the case of ellipsoids of aspect ratio 2 and 5 for various separations, and note excellent agreement with all published results. The accuracy of our results matches that achieved by Gluckman *et al.* using 3 or more "multilobular disturbances" emanating from the centre of each particle, and is always within less than 1% of their converged results. Our data for chains of up to 15 particles long also are indistinguishable from their results (data not shown), except in the case of 7 touching spheroids with $r_p = 5$, where we calculated drags approximately 5% smaller than those deduced from their Figure 11.

*Table* 3.1: Drag on two prolate spheroids moving with equal velocity **U** along their line of centres.

| $r_p$ | $\lvert\mathbf{x}_p - \mathbf{x}_q\rvert/(2a)$ | $\lvert\mathbf{F}\rvert/(8\pi a\mu\lvert\mathbf{U}\rvert)$ | $\lvert\mathbf{F}\rvert/\lvert\mathbf{F}_{\text{ref}}\rvert$ |
|---|---|---|---|
| 2 | 1.0001 | 0.31483 | .9945 |
| 2 | 2 | 0.36788 | .9998 |
| 2 | 3 | 0.39216 | 1.000 |
| 2 | 16 | 0.43908 | 1.000 |
| 5 | 1.0001 | 0.20423 | .9938 |
| 5 | 2 | 0.23512 | 1.000 |
| 5 | 3 | 0.24546 | 1.000 |

The first column ($r_p$) gives the aspect ratio of the particles; $\mathbf{F}_{\text{ref}}$ is the final result given with five significant digits in Gluckman *et al.* (1971). The smallest separation considered is 1.0001 instead of 1 because the resistance tensor is singular when the surfaces touch.

The efficiency of the multipole collocation technique was later tested by Liao & Krueger (1980) for ellipsoids of different size and aspect ratio. They calculated the force on a small sphere touching the nose of a large prolate spheroid of aspect ratio 10 as a function of the relative volume of the two bodies, which are assumed to move at the same speed in the direction of the spheroid's axis. As shown in Fig. 3.3,

we find that the sphere experiences a minimal force when it is slightly ahead of the ellipsoid, rather than against it. This peculiar behavior is reminiscent of the results of Cooley & O'Neill (1969), who calculated the resistance of two unequal spheres moving at the same velocity along their line of centres as a function of their separation (using the analytical solution for this problem due to Stimson & Jeffery (1926)). They found that, for sufficiently dissimilar radii, the drag on the large sphere first decreases with increasing distance between the particles, goes through a minimum and then monotonically ascends to its asymptotic value at large separations. It is possible that an analogous phenomenon occurs here. The harmonic mean radius of curvature at the pole of the spheroid is $b^2/a$, with $b$ the dimension of the minor semi-axis. For a spheroid of unit half-length and aspect ratio 10, this equals .01, which is considerably smaller than the radius of the spheres considered in this analysis (see Table 3.2). For reference, the volume of a sphere of radius $R_s = a/100$ is only $10^{-4}$ times that of the ellipsoid. Thus it can be argued that, in a local sense, the spheroid looks like a smaller object than the sphere, strengthening the analogy with the work of Cooley & O'Neill (1969). In Table 3.2, we compare the calculated minimum drag on the sphere to the collocation results for touching particles (Liao & Krueger, 1980). Our computations systematically predict a higher force, and the agreement gets worse as the relative size of the two bodies departs more from unity. Liao & Krueger remarked that the drag calculated using the multipole collocation technique monotonically approached a plateau value from below as the stick boundary condition was satisfied at more points on the large spheroid, but they fixed the number of collocation points on the small particle at 4, relying on earlier studies for touching spheres. In some respects, however, as pointed out above, the tip of the ellipsoid resembles an object smaller than the sphere presumed small in the analysis. Thus it may have been necessary to represent the sphere by more multipoles, and the truncation after the fourth term may have caused an underestimation of the true drag force. In the same light, it is certain that our method would be more accurate if contributions from the quadrupole, octupole

and higher moments were retained.

*Table* 3.2: Drag on a small sphere preceding a spheroid of aspect ratio 10 moving at the same velocity.

| $V_1/V_2$ | $R_s/a$ | $\lvert\mathbf{F}_1\rvert$ | $\lvert\mathbf{F}_2\rvert$ | $\lvert\mathbf{F}_2\rvert/\lvert\mathbf{F}_S\rvert$ | $r_m/a$ |
|---|---|---|---|---|---|
| 1 | .2154 | 0.1565 | 0.1255 | 1.04 | 0.2 |
| 10 | .1000 | 0.1766 | .050894 | 1.10 | 0.14 |
| 100 | .0464 | 0.1880 | .020192 | 1.25 | 0.09 |
| 1000 | .0215 | 0.1937 | .007779 | 1.38 | 0.06 |

The spheroid and the sphere move with equal velocity $U$ in the direction of the rod's axis. The first two columns determine the relative size of the particles, as a ratio of volumes ($V_1/V_2$, where the subscript "1" denotes the spheroid), or in terms of the radius of the sphere $R_s$ relative to the major semi-axis $a$ of the spheroid. The forces $\mathbf{F}_1$ and $\mathbf{F}_2$ are scaled by $8\pi a\mu U$. They are evaluated when the clearance between both bodies is $r_m$, chosen such that the drag $\mathbf{F}_2$ on the sphere is minimal. $\mathbf{F}_S$ is the value reported by Liao & Krueger (1980) for the force on the sphere when both particles are touching.

### 3.5.3 Drag on two acicular spheroids

Instead of adopting the distribution of singularities suggested by the Faxén laws, Barta & Liron (1988) determined the optimal density of Stokeslets along the symmetry axis of the spheroids as part of the solution procedure, by equating the disturbance velocity at the particle's surface to the imposed rigid body motion. Since they collapse the surface stress density onto a line, yet neglect singularities more complex than point forces, they cannot fully capture effects arising from the finite thickness of the rods. In particular, it is uncertain that a distribution of Stokeslets confined between the foci of the spheroid can correctly represent the flow field in the immediate vicinity of the particles' surface, as they assume. For two parallel ellipsoids in an unbounded fluid, the drag was calculated at various separations for synchronous motions along the axes ($\mathbf{U}_1 = \mathbf{U}_2 \parallel \mathbf{d}_1 \parallel \mathbf{d}_2$), along the line

of centres, and perpendicular to the plane defined by the directors of the particles. We repeated the analysis and obtained the results of Table 3.3. They agree quite reasonably with the forces calculated by Barta & Liron (1988). As was to be expected, the largest deviations occur in situations when hydrodynamic interactions are most pronounced, i.e., for motion in the direction of the line of centres, and at the smallest separations. In those cases, the optimal Stokeslet distribution calculated by Barta and Liron deviated significantly from the uniform density profile predicted for isolated particles by Chwang & Wu (1974, 1975), but only by about 20% at most. It is worth mentioning that Barta & Liron need to solve for a new singularity distribution for each prescribed motion, while Stokesian dynamics solves all mobility problems simultaneously for a given geometry. Our method also captured the small rotation induced by the motion of the spheroids parallel to the direction in which they point (data not shown).

*Table* 3.3: Drag on two spheroids of aspect ratio 100 placed side by side.

| $d/a$ | $\lvert\mathbf{F}_b\rvert$ | | $\lvert\mathbf{F}_n\rvert$ | | $\lvert\mathbf{F}_d\rvert$ | |
|---|---|---|---|---|---|---|
| .25 | .1168 | (1.30) | .1300 | (1.12) | .08009 | (1.10) |
| 1 | .1382 | (1.07) | .1510 | (1.021) | .09413 | (1.012) |
| 2 | .1497 | (1.024) | .1597 | (1.006) | .09885 | (1.003) |
| 4 | .1593 | (1.007) | .1655 | (1.002) | .10151 | (1.001) |
| 6 | .1632 | (1.003) | .1677 | (1.001) | .10240 | (1.000) |

In all cases the velocities $\mathbf{U}_1 = \mathbf{U}_2 = \mathbf{U}$. All forces have been non-dimensionalized by $8\pi a\mu|\mathbf{U}|$. The distance $d$ is measured between the centres of the particles. $|\mathbf{F}_b|$ is the drag for motion along the line of centres, $|\mathbf{F}_n|$ for movement perpendicular to the plane in which the spheroidal axes lie, and $|\mathbf{F}_d|$ is the force for $\mathbf{U}_\parallel \; \mathbf{d}_1 \parallel \mathbf{d}_2$. The entries in parentheses give the ratio of the drag calculated by Stokesian dynamics to the data found in Barta & Liron (1988).

### 3.5.4 Sedimentation of spheroids

The motion of two spheroids sedimenting side by side is intriguing since "peri-

odic" orbits appear for certain initial conditions (Kim, 1985 b). Hydrodynamic interactions then cause the particles' directors to rotate past $\pi/2$ radians, at which point the trajectory —projected onto a plane perpendicular to gravity— is reversed (Fig. 3.4b). At larger separations, the viscous interactions are weaker, and the bodies simply drift apart (Fig. 3.4a). Similar effects had been observed for highly symmetric arrangements of spheres (Durlofsky *et al.*, 1987); four spheres placed at the corners of a square in the vertical plane, for example, fall in a viscous fluid following a pattern in which the top spheres first move inward and faster than the ones on the bottom, eventually overtaking these to form a new square which is the mirror image of the original configuration. This scenario is repeated *ad infinitum* in the absence of external perturbations.

One can generate many "repeating" configurations of spheroids by positioning the particles' centres at the corners of a regular polygon at right angles with gravity $\mathbf{g}$, with their directors all parallel to $\mathbf{g}$ (or all at the same angle with gravity, such that the spheroidal axes lie on the envelope of a circular cone). The periodic trajectories described by the ellipsoids in the $(R/a) - \theta$-plane are shown for a few collections of spheroids of aspect ratio 2 in Fig. 3.5. ($R$ is the centre-to-centre distance between nearest neighbors and $\theta$ the azimuthal angle.) The time $t_P$ necessary for the original configuration to be reproduced decreases at first with the number of spheroids in the system, as expected because of the more numerous hydrodynamic interactions (Table 3.4). However, as the arrangement becomes more circular, the effects of the two nearest neighbors balance each other progressively more (the induced torques are nearly antiparallel) and the distance between spheroids diametrically opposed grows, weakening their interaction. As a result, we observe a minimum in $t_P$ at $N = 5$ for spheroids released at the corners of regular polygons of side $2a$. If we fix the diameter of the polygon instead, we still observe a minimum ($t'_P$, Table 3.4), now due to the strong mutual hindrance of the tumbling spheroids as they are nearly close packed. It is coincidental that both minima occur for pentagons. Note that, even though the period of similitude $t_P$ is shorter for $N = 5$

than for $N = 4$, the particles travel farther in one cycle when they are arranged in a pentagon. This is due, of course, to the fact that the drag decreases with $N$, causing them to fall faster.

*Table* 3.4: Period of similitude of highly symmetric configurations of sedimenting spheroids.

| $N$ | $t_P$ | $z(t_P)$ | $t'_P$ | $z(t'_P)$ |
|---|---|---|---|---|
| 2 | 32.4 | 76.1 | 33.6 | 78.7 |
| 3 | 11.3 | 33.2 | 8.48 | 26.5 |
| 4 | 9.51 | 31.4 | 5.13 | 20.1 |
| 5 | 9.24 | 32.9 | 3.88 | 18.5 |
| 6 | 9.40 | 35.3 | 5.95 | 32.6 |
| 8 | 10.1 | 41.1 | | |
| 10 | 11.1 | 47.5 | | |

This table reports some characteristics of the trajectories of $N$ identical sedimenting spheroids released parallel to gravity at the corners of regular polygons of side $2a$ (columns $t_P$ and $z$) or of diameter $2.02a$ (columns $t'_P$ and $z'$). The period of similitude $t_P$ (or $t'_P$) is defined as the minimum time elapsed between two instants at which the configuration of the spheroids is the same, except for a uniform translation by $z(t_P)$ along the direction of gravity. (A spheroid pointing "up" is considered equivalent to one pointing "down". If the sense of the director needs to be distinguished, the reported values of $t_P$ and $t'_P$ should be doubled, since the configuration first reverses before reassembling.) Time is non-dimensionalized by $|\mathbf{F}|/(8\pi\mu a^2)$, with $\mathbf{F}$ the force of gravity. The distance $z$ traveled by the centre of mass of the arrangement is scaled by the particle's half-length $a$.

Two horizontal spheroids placed directly atop one another, but not perfectly aligned, spin while sedimenting because, as a pair, they have a propeller-like geometry. Our simulations show that both particles rotate in the same sense and at the same rate as they fall; there is no relative motion between the two bodies. (This behavior is the only one consistent with the symmetries which the system must obey upon reversal of the direction of gravity.) The rate of rotation of the

particles for different centre-to-centre separations $R$ is plotted as a function of the angle $\psi$ inscribed between the spheroidal axes in Fig. 3.6. Similar plots for other aspect ratios display the same qualitative features, but the magnitude of the speed of gyration is lower for blunter spheroids, and the maximum in the curves shifts toward the middle ($\psi = \pi/4$). The angle $\psi_m(R/a)$ at which the tumbling is most rapid does not increase monotonically with separation $R$, but is minimal at about $\{R = .3a, \psi_m = .28\pi/2\}$ for rods of aspect ratio 10. For all aspect ratios considered, we found $\lim_{R\to\infty} \psi_m = \pi/4$. This limit is always approached from below.

The fact that the rotation rate is zero for $\psi = \pi/2$ can be proven from symmetry arguments. The (small) negative rotation rate for almost touching particles and very acute inscribed angles can be explained by the trade-off between two competing effects. Those are best brought to light by considering the equivalent resistance problem and decomposing the motion of the spheroids: in the first case, the top spheroid is moved downward, holding the other particle fixed; in the second, the lower rod is pulled away from the stationary upper rod. We then superpose both motions to reproduce the original situation. In the first case, a torque must be exerted on the moving spheroid to oppose its tendency to rotate at right angles to the lower rod. This can be understood by visualizing the fluid as being squeezed more tightly in the sharp corner formed by the rods, than in the obtuse angle complimentary to it. In the second case, the moving lower rod attempts to drag the upper rod in its wake; thus holding it stationary requires a torque in the opposite sense. The first effect is only important at very close separations, and for angles relatively far removed from $\pi/2$, and explains the negative rotation rate in Fig. 3.6. In most situations, the second contribution is the largest, and the propeller-like motion is observed.‡ As one would expect, this phenomenon is absent (or not noticeable) for spheroids of aspect ratio 2, and confined to a much smaller range

‡ We are not aware of any experiments confirming the reversal of the sense of rotation predicted here.

of $\psi$ when $r_p = 50$.

### 3.5.5 Perturbation of Jeffery orbits and migration in shear flow

A force-free isolated spheroid placed at the origin of an unbounded simple shear flow precesses about the vorticity axis with a period of $2\pi(r_p + r_p^{-1})/E$ (with $E$ the magnitude of the velocity gradient), but the particle's centre does not move (Jeffery, 1922). The rate of rotation is not uniform however, and the particle spends most of the time aligned with the flow. This swinging motion suggests that the stress response of a dilute suspension of rods in simple shear is oscillatory. Experimental evidence abounds however (Ivanov *et al.*, 1982), indicating that these fluctuations are transient, and that a well-defined, time-independent macroscopic viscosity can eventually be assigned to the dispersion. Many randomizing factors have been implicated, including polydispersity and other imperfections in the particle shape, Brownian motion, and hydrodynamic interactions (including wall effects). It is therefore instructive to examine the motion of pairs of non-Brownian, identical spheroids in shear flow to isolate the role of viscous forces.

The geometry considered consists of two ellipsoids of aspect ratio 2 which are mirror images of each other with respect to the plane of shear (Fig. 3.7). They are inclined at an angle $\pi/3$ relative to the vorticity axis, and are initially either perpendicular to the velocity gradient ($\phi_{|t=0} = 0$), or to the direction of flow ($\phi_{|t=0} = \pi/2$). Somewhat surprisingly, the particles migrate due to hydrodynamic interactions, even though the undisturbed fluid velocity at their centres is zero. When the particles start off aligned with the flow ($\phi_{|t=0} = 0$), they cycle on a closed trajectory, moving atop one another in a fashion similar to the jaws of a nutcracker. The composite centre of mass follows an 8-shaped loop in the plane of shear in the clockwise direction (Fig. 3.8); the rods meanwhile, "open" and "close," making the most acute angle with the vorticity axis when they reach the top and the bottom of the figure "8." This motion can be rationalized more easily perhaps by picturing dumbbells instead of spheroids. Initially, the simple shear exerts a torque on the particles, causing them to spin. It experiences less resistance from the ends of the

rods which are close together (the hinge of the nutcracker) however, than from the poles which are farther apart. (In the same manner, the combined drag on two nearly touching spheres is less than twice the force felt by an isolated particle.) The effect of this imbalance is a net displacement of the rods in the same direction as the "hinge." If the spheroids are initially at right angles to the fluid velocity, their interactions result in a finite translation in the flow direction during each period of rotation. At the inflection point in the orbit of the centre of mass (Fig. 3.8), the particles are perpendicular to the velocity gradient ($\phi = 0$) and the inscribed angle between their axes is minimal. Note that the behavior is very similar to the former case, $\phi_{|t=0} = 0$, except that, when $\phi = 0$ here, the centroid lies on a streamline with non-zero velocity. Lubrication interactions are, on average, less important in the second case, and the motion perpendicular to the plane of shear is consequently much less pronounced. The period of rotation is 15.66 for rods initially at right angles to the flow and 15.53 when $\phi_{|t=0} = 0$. (Time is non-dimensionalized by the magnitude of the velocity gradient.) For comparison, it is 15.71 for an isolated spheroid of aspect ratio 2. The slight decrease can be understood since the pair of ellipsoids effectively acts as a body with a lower aspect ratio.

## 3.6 Concluding remarks

The examples of the preceding section demonstrate the effectiveness and accuracy of the moment expansion technique that we have developed for Stokes flow problems involving interacting spheroids. Because it is analogous in spirit to the established simulation method for spheres (Brady & Bossis, 1988), we also use the name "Stokesian dynamics" to describe this new technique. In fact, we have shown in §3.2 that the fundamental concepts of Stokesian dynamics can be stated in very general terms, and thereby hinted that its methodology can be valuable for a much wider class of body geometries than ellipsoids only. We discussed its application to prolate spheroids in particular in §3.3 and §3.4, and have shown that our approach compares quite favorably with other numerical methods.

Although many relevant problems can be addressed by considering the interactions between only a few particles, the usefulness of the technique introduced in this chapter would be increased manifold if it were applicable to systems containing a very large (infinite) number of particles. Most importantly, this would make it a valuable tool in suspension rheology, and enable one to study the flow properties of slurries, the permeability of fibrous media, or the diffusion coefficients within liquid crystalline domains for instance. The extension of the method to unbounded dispersions constitutes the topic of the next chapter.

# APPENDIX D

## Irreducible expansion for the disturbance velocity of an ellipsoid

We define the surface $A$ of an arbitrary ellipsoid by specifying that

$$\mathbf{x} \in A \iff \mathbf{A}^{-1} : \mathbf{x}\mathbf{x} = 1 \ , \tag{D.1}$$

with $\mathbf{A}$ any positive-definite symmetric second rank tensor. Without loss of generality, we have set the origin $\mathbf{x} = 0$ at the geometric centre of the particle. It is apparent from (D.1) and the definition (3.12) of the multipole moments

$$\mathbf{P}^{(m)} = -\frac{1}{m!} \int_A \mathbf{n} \cdot \boldsymbol{\sigma} \overbrace{\mathbf{x}}^{\times m} \mathrm{d}A_{\mathbf{x}} \tag{D.2}$$

that any contraction of $\mathbf{P}^{(m)}$ by $\mathbf{A}^{-1}$ in any two of its last $m$ indices yields $\mathbf{P}^{(m-2)}$ (apart from a multiplicative constant). Resorting to index notation,

$$\left[\mathbf{P}^{(m)}\right]_{i_0 i_1 i_2 \ldots i_m} \left[\mathbf{A}^{-1}\right]_{i_k i_l} = \frac{1}{m(m-1)} \left[\mathbf{P}^{(m-2)}\right]_{i_0 i_{j_1} i_{j_2} \ldots i_{j_{m-2}}} \tag{D.3}$$

with $\quad 1 \leq k < l \leq m \quad$ and $\quad \forall p \in [1, m]$: $\{j_{p-1} < j_p$ and $k \neq j_p \neq l\}$.

We therefore define the irreducible moment $\mathbf{I}^{(m)}$ for an ellipsoid such that all similar contractions give zero:

$$\mathbf{I}^{(m)} = -\frac{1}{m!} \int_A \mathbf{n} \cdot \boldsymbol{\sigma} \overbrace{\mathbf{x}}^{\times m} \mathrm{d}A_{\mathbf{x}} \ . \tag{D.4a}$$

For instance,

$$\mathbf{I}^{(0)} = \mathbf{P}^{(0)} = \mathbf{F} \ , \tag{D.4b}$$

$$\mathbf{I}^{(1)} = \mathbf{P}^{(1)} = \mathbf{S} - \tfrac{1}{2}\boldsymbol{\varepsilon} \cdot \mathbf{T} + \tfrac{1}{3}\mathbf{P}^{(1)} : \boldsymbol{\delta}\boldsymbol{\delta} \ , \tag{D.4c}$$

$$\mathbf{I}^{(2)} = -\frac{1}{2} \int_A \mathbf{n} \cdot \boldsymbol{\sigma} \left[\mathbf{x}\mathbf{x} - \tfrac{1}{3}\mathbf{A}\right] \mathrm{d}A_{\mathbf{x}} = \mathbf{P}^{(2)} - \tfrac{1}{6}\mathbf{P}^{(0)}\mathbf{A} \ . \tag{D.4d}$$

We now prove by induction that

$$\overbrace{\mathbf{x}}^{\times m} = \sum_{j=0}^{\lfloor m/2 \rfloor} \frac{(2m-4j+1)!!}{(2m-2j+1)!!} \wp\Big( \overbrace{\mathbf{x}}^{\times(m-2j)} \overbrace{\mathbf{A}}^{\times j} \Big) \tag{D.5a}$$

or, equivalently, for $m > 1$,

$$\widehat{\mathbf{x}}^{\times m} = \overbrace{\mathbf{x}}^{\times m} - \sum_{j=1}^{\lfloor m/2 \rfloor} \frac{(2m-4j+1)!!}{(2m-2j+1)!!} \wp\Big( \overbrace{\mathbf{x}}^{\times(m-2j)} \overbrace{\mathbf{A}}^{\times j} \Big) \; . \tag{D.5b}$$

The notation $\lfloor x \rfloor$ means the largest integer value smaller or equal to $x$. As can be inferred from (D.4), $\widehat{\mathbf{x}}^{\times m}$ stands for the irreducible core of $\overbrace{\mathbf{x}}^{\times m}$, which has the property that all possible contractions by the dyadic $\mathbf{A}^{-1}$ give zero. [Alternatively, (D.5b) can be seen as its definition, in which case we must prove its irreducibility with respect to contractions by $\mathbf{A}^{-1}$.] The operation $\wp(\mathbf{X})$, with $\mathbf{X}$ a tensor of rank $m$, sums all distinguishable tensors which can be constructed from $\mathbf{X}$ by permuting its indices. For instance,

$$\wp(\mathbf{xxyy}) = \mathbf{xxyy} + \mathbf{xyxy} + \mathbf{xyyx} + \mathbf{yxxy} + \mathbf{yxyx} + \mathbf{yyxx} \; . \tag{D.6}$$

It is an easy combinatorial problem to show that $(2j+k)!/(k!\,2^j j!)$ different permutations of the indices of $\widehat{\mathbf{x}}^{\times k} \overbrace{\mathbf{A}}^{\times j}$ exist. Of these,

- $(2j+k-2)!/\big(k!\,2^{j-1}(j-1)!\big)$ begin with $\mathbf{A}$. They are contracted to $3\wp\big(\widehat{\mathbf{x}}^{\times k} \overbrace{\mathbf{A}}^{\times(j-1)}\big)$ by a double-dot multiplication with $\mathbf{A}^{-1}$.
- $(2j+k-2)!/\big(k!\,2^{j-2}(j-2)!\big)$ begin with two indices belonging to different $\mathbf{A}$'s, like $[\mathbf{X}]_{ijkl} = [\mathbf{A}]_{ik}[\mathbf{A}]_{jl}$. These permutations yield $2(j-1)\wp\big(\widehat{\mathbf{x}}^{\times k} \overbrace{\mathbf{A}}^{\times(j-1)}\big)$.
- $2(2j+k-2)!/\big((k-1)!\,2^{j-1}(j-1)!\big)$ have the same first two indices as either $\mathbf{xA}$ or $\mathbf{A}\mathbf{x}^T$, and condense onto $2k\,\wp\big(\widehat{\mathbf{x}}^{\times k} \overbrace{\mathbf{A}}^{\times(j-1)}\big)$.
- $(2j+k-2)!/\big((k-2)!\,2^j j!\big)$ begin with the first two indices of $\widehat{\mathbf{x}}^{\times k}$ and are contracted to zero by definition.

Therefore,

$$\mathbf{A}^{-1} : \wp\big(\widehat{\mathbf{x}}^{\times k} \overbrace{\mathbf{A}}^{\times j}\big) = (2k+2j+1)\wp\big(\widehat{\mathbf{x}}^{\times k} \overbrace{\mathbf{A}}^{\times(j-1)}\big) \; . \tag{D.7}$$

We now condense both sides of the relation (D.5b) with $\mathbf{A}^{-1}$, and use $\mathbf{A}^{-1} : \mathbf{x}\mathbf{x} = 1$ to get:

$$\mathbf{A}^{-1} : \overbrace{\mathbf{x}}^{\times m} = \overbrace{\mathbf{x}}^{\times(m-2)} - \sum_{j=1}^{\lfloor m/2 \rfloor} \frac{(2m-4j+1)!!}{(2m-2j-1)!!} \wp\Big( \overbrace{\mathbf{x}}^{\times(m-2j)} \overbrace{\mathbf{A}}^{\times(j-1)} \Big) , \tag{D.8}$$

which is zero by induction from (D.5a) (*Q.E.D.*). Obviously, the proof does not depend on which two indices of $\overbrace{\mathbf{x}}^{\times m}$ are condensed, and all multiple contractions of $\overbrace{\mathbf{x}}^{\times m}$ by permutations of $\overbrace{\mathbf{A}^{-1}}^{\times j}$ (with $0 < j \leq \lfloor m/2 \rfloor$) will also yield zero. Finally, it is trivial to show that the premise (D.5a) holds for $m = 0$ and $m = 1$, since $\overbrace{\mathbf{x}}^{\times 0} = 1$ and $\overbrace{\mathbf{x}}^{\times 1} = \mathbf{x}$, which are both irreducible. This completes the proof of (D.5a).

We now prove the following preposition for any sufficiently smooth tensorial function $\mathbf{X}(\mathbf{x})$:

$$\mathbf{X}(\mathbf{x}) = \sum_{m=0}^{\infty} \frac{(2m+1)!!}{m!} \overbrace{\mathbf{x}}^{\times m} \odot^m \left[ \left( \frac{1}{D} \frac{\mathrm{d}}{\mathrm{d}D} \right)^m \frac{\sinh D}{D} \right] \overbrace{\nabla}^{\times m} \mathbf{X}(\mathbf{y})|_{\mathbf{y}=0} . \tag{D.9}$$

We begin with the Taylor series expansion for $\mathbf{X}$ about $\mathbf{x} = 0$:

$$\mathbf{X}(\mathbf{x}) = \sum_{m=0}^{\infty} \frac{1}{m!} \overbrace{\mathbf{x}}^{\times m} \odot^m \overbrace{\nabla}^{\times m} \mathbf{X}(\mathbf{y})|_{\mathbf{y}=0} . \tag{D.10}$$

We then apply (D.5a) to expand $\overbrace{\mathbf{x}}^{\times m}$, and use

$$\wp\Big( \overbrace{\mathbf{x}}^{\times(m-2j)} \overbrace{\mathbf{A}}^{\times j} \Big) \odot^m \overbrace{\nabla}^{\times m} = \frac{m!}{(m-2j)!\, 2^j j!} \overbrace{\mathbf{x}}^{\times(m-2j)} \odot^{m-2j} \overbrace{\nabla}^{\times(m-2j)} D^{2j} , \tag{D.11}$$

(with $D^2 = \mathbf{A} : \nabla\nabla$ as defined in (3.23)), to get

$$\mathbf{X}(\mathbf{x}) = \sum_{m=0}^{\infty} \sum_{j=0}^{\lfloor m/2 \rfloor} \frac{(2m-4j+1)!!}{(2m-2j+1)!!} \frac{1}{(m-2j)!\, 2^j j!} \times \tag{D.12}$$

$$\overbrace{\mathbf{x}}^{\times(m-2j)} \odot^{m-2j} D^{2j} \overbrace{\nabla}^{\times(m-2j)} \mathbf{X}(\mathbf{y})|_{\mathbf{y}=0} .$$

After changing the running index from $m$ to $n = m - 2j$, we find

$$\mathbf{X}(\mathbf{x}) = \sum_{n=0}^{\infty} \frac{(2n+1)!!}{n!} \overset{\times n}{\widehat{\mathbf{x}}} \odot^n \sum_{j=0}^{\infty} \frac{1}{(2n+2j+1)!!\, 2^j j!} D^{2j} \overbrace{\nabla}^{\times n} \mathbf{X}(\mathbf{y})|_{\mathbf{y}=0} \ , \quad \text{(D.13)}$$

which is equivalent to (D.9).

Finally, we now derive the irreducible expansion of the disturbance velocity of an arbitrary ellipsoid in Stokes flow. According to the boundary integral equation (3.10) (Ladyzhenskaya, 1963), the disturbance velocity due to the presence of any rigid particle in a flow $\mathbf{u}_\emptyset$ may be written as

$$\mathbf{u}(\mathbf{x}) - \mathbf{u}_\emptyset(\mathbf{x}) = -\frac{1}{8\pi\mu} \int_A \mathbf{J}(\mathbf{x}-\mathbf{y}) \cdot \boldsymbol{\sigma}(\mathbf{y}) \cdot \mathrm{d}\mathbf{A}_\mathbf{y} \ . \quad \text{(D.14)}$$

Introduction of the identity (D.9) with $\mathbf{X} = \mathbf{J}$ into (D.14) yields

$$\mathbf{u}(\mathbf{x}) - \mathbf{u}_\emptyset(\mathbf{x}) = \quad \text{(D.15)}$$

$$\frac{-1}{8\pi\mu} \sum_{m=0}^{\infty} \frac{(2m+1)!!}{m!} \int_A \mathbf{n} \cdot \boldsymbol{\sigma} \overset{\times m}{\widehat{\mathbf{y}}} \ \mathrm{d}A_\mathbf{y} \odot^{m+1} \left[ \left( \frac{1}{D} \frac{\mathrm{d}}{\mathrm{d}D} \right)^m \frac{\sinh D}{D} \right] \overbrace{\nabla_\mathbf{z}}^{\times m} \mathbf{J}(\mathbf{x}-\mathbf{z})|_{\mathbf{z}=0} \ ,$$

which is identical to (3.22).

# APPENDIX E

## Relations between the mobility tensors of hydrodynamically interacting ellipsoids

It should not be surprising that a relation linking $\mathbf{M}_{UT}$ to $\mathbf{M}_{US}$ exists: both tensors couple the velocity of one particle to the first moment of the force density on another body. Equation (3.36) then shows that enough information is contained in the coupling to the symmetric part of the stress multipole (i.e., the stresslet $\mathbf{S}$) to deduce the mobility response due to the antisymmetric half (the torque $\mathbf{T}$). We explore the origin of this relation here.

From the definitions (3.12) of the torque and stresslet exterted by a particle $q$, and of its first multipole $\mathbf{P}_q^{(1)}$, we get

$$\mathbf{T}_q = \boldsymbol{\varepsilon} : \mathbf{P}_q^{(1)} \qquad \text{and} \qquad \mathbf{S}_q = \left[\tfrac{1}{2}(\widehat{\boldsymbol{\delta\delta}} + \breve{\boldsymbol{\delta\delta}}) - \tfrac{1}{3}\boldsymbol{\delta\delta}\right] : \mathbf{P}_q^{(1)} = \boldsymbol{\varsigma} : \mathbf{P}_q^{(1)} \ , \tag{E.1}$$

where we introduced the notations

$$(\widehat{\boldsymbol{\delta\delta}})_{ijkl} = \boldsymbol{\delta}_{ik}\boldsymbol{\delta}_{jl} \qquad \text{and} \qquad (\breve{\boldsymbol{\delta\delta}})_{ijkl} = \boldsymbol{\delta}_{il}\boldsymbol{\delta}_{jk} \ . \tag{E.2}$$

Inversely,

$$\mathbf{P}_q^{(1)} = \mathbf{S}_q - \frac{1}{2}\boldsymbol{\varepsilon} \cdot \mathbf{T}_q + \frac{1}{3}\int_{A_q} [\mathbf{y} - \mathbf{x}_q] \cdot \boldsymbol{\sigma} \cdot \mathrm{d}\mathbf{A}_y \boldsymbol{\delta} \ . \tag{E.3}$$

The last term on the right hand side is inconsequential in incompressible media, and will not be considered further. We now introduce the mobility tensor $\mathbf{M}_{01}$ which couples the $0^{\text{th}}$ gradient of the particle velocity (relative to the ambient flow) to the $1^{\text{st}}$ moment of the force density on the particle surface. By definition then, if we ignore the contribution to the translational motion of particle $p$ of all objects other than $q$ and of all stress multipoles other than $\mathbf{P}_q^{(1)}$, we have

$$\mathbf{U}_p - \mathbf{u}_\emptyset = \mathbf{M}_{01}^{pq} : \mathbf{P}_q^{(1)} = \mathbf{M}_{01}^{pq} : \mathbf{S}_q - \tfrac{1}{2}\mathbf{M}_{01}^{pq} : \boldsymbol{\varepsilon} \cdot \mathbf{T}_q \ . \tag{E.4}$$

We can clearly identify the more familiar tensors $\mathbf{M}_{UT}$ and $\mathbf{M}_{US}$ as

$$\mathbf{M}_{UT}^{pq} = -\tfrac{1}{2}\mathbf{M}_{01}^{pq} : \boldsymbol{\varepsilon} \qquad \text{and} \qquad \mathbf{M}_{US}^{pq} = \mathbf{M}_{01}^{pq} : \boldsymbol{\varsigma} \ . \tag{E.5}$$

Note that $\mathbf{M}_{US}$ is defined as being symmetric and traceless in its last two indices, since it is otherwise indeterminate (Kim & Mifflin, 1985; Brenner, 1964 a). To convert $\mathbf{M}_{01}$ into $\mathbf{M}_{US}$, we thus need to multiply it by $\varsigma$ (see (E.1)).

We shall derive the relations (3.36) for ellipsoids in what follows, but conjecture that they hold for a wider class of body geometries. Indeed, our proof hinges mostly on the existence of singularity solutions to describe the dynamics of the particles in Stokes flow, and these certainly are not limited to ellipsoids (Chwang & Wu, 1974; 1975). We shall sometimes hint how to generalize our reasoning, but leave the details of a formal theorem up to the interested reader.

We explained in §3.3 how to construct the mobility coefficients by combining the disturbance velocity and the Faxén relations for the particles. In the case of ellipsoids, the non-local representation (Kim, 1986) clearly shows that each element of the mobility tensor can be written as a linear functional of the Oseen tensor and higher singularities. For instance,

$$\begin{aligned}\mathbf{M}_{UF}^{pq} = & \frac{1}{32\pi^3\mu c_{E_p}c'_{E_p}c_{E_q}c'_{E_q}}\iint_{E_p}\iint_{E_q} q_p^{-1}(\mathbf{x})\left\{1+\frac{a_{3p}^2q_p^2}{2}\nabla^2\right\} \\ & q_q^{-1}(\mathbf{x}')\left\{1+\frac{a_{3q}^2q_q^2}{2}\nabla^2\right\}\mathbf{J}(\mathbf{x}-\mathbf{x}')\,\mathrm{d}A_p\,\mathrm{d}A_q \qquad \text{(E.6)} \\ = & \mathcal{O}_{00}(\mathbf{J})\ ,\end{aligned}$$

with $\mathbf{x}\in E_p$ and $\mathbf{x}'\in E_q$. All other symbols have been introduced in §3.3, except the operator $\mathcal{O}_{00}$ which is defined, for an arbitrary tensorial function $\mathbf{X}$ of the separation vector $\mathbf{x}-\mathbf{x}'$, as

$$\begin{aligned}&\mathcal{O}_{00}(\mathbf{X}) = \qquad \text{(E.6b)} \\ &\frac{1}{32\pi^3\mu c_{E_p}c'_{E_p}c_{E_q}c'_{E_q}}\iint_{E_p}\iint_{E_q} q_p^{-1}q_q^{-1}\left\{1+\frac{1}{2}(a_{3p}^2q_p^2+a_{3q}^2q_q^2)\nabla^2\right\}\mathbf{X}\,\mathrm{d}A_p\,\mathrm{d}A_q\ .\end{aligned}$$

In general, it follows from Appendix D (see also Kim & Arunachalam, 1987) that the mobility interaction between the $m^{\text{th}}$ gradient of the velocity at the particle locator point and the $n^{\text{th}}$ irreducible stress multipole is a linear functional of an appropriate transpose of $\overbrace{\nabla}^{m+n}\mathbf{J}$. In particular, the coupling between the translational

velocity $\mathbf{U}_p - \mathbf{u}_\emptyset(\mathbf{x}_p)$ and the first moment of the force density $\mathbf{I}_q^{(1)}$ involves ${}^T\boldsymbol{\nabla}\mathbf{J}$ only. (This is not necessarily so; counterexamples can be found among the class of bodies with screw-symmetry.) Note also that $\mathbf{I}_q^{(1)} = \mathbf{P}_q^{(1)}$ for ellipsoids, so that the equations (E.1)-(E.5) still hold in terms of the irreducible multipole.

One can now write the Oseen tensor $\mathbf{J}(r)$ as $(\nabla^2\boldsymbol{\delta} - \boldsymbol{\nabla}\boldsymbol{\nabla})r$, an identity first used by Beenakker (1986) to facilitate the application of the Ewald summation to hydrodynamic interactions in periodic suspensions. This brings out the symmetry which we exploit to derive the relations (3.36):

$$\mathbf{M}_{01} = \mathcal{O}_{01}({}^T\boldsymbol{\nabla}\mathbf{J}) = \mathcal{O}_{01}\big((\nabla^2{}^T\boldsymbol{\nabla}\boldsymbol{\delta} - \boldsymbol{\nabla}\boldsymbol{\nabla}\boldsymbol{\nabla})r\big) \ . \tag{E.7}$$

Since $\mathcal{O}_{01}$ consists of linear non-tensorial operations only (such as integration and differentiation with respect to a coordinate, multiplication by a scalar function of position, etc.), the contractions given by (E.5) commute with the operator and

$$\mathbf{M}_{US} = \mathcal{O}_{01}\big(({}^T\boldsymbol{\nabla}\mathbf{J}) : \boldsymbol{\varsigma}\big) = \mathcal{O}_{01}\big((\tfrac{1}{2}\nabla^2[\boldsymbol{\delta}\boldsymbol{\nabla}^T + \boldsymbol{\delta}\boldsymbol{\nabla}] - \boldsymbol{\nabla}\boldsymbol{\nabla}\boldsymbol{\nabla})r\big) \tag{E.8a}$$

$$\mathbf{M}_{UT} = -\frac{1}{2}\mathcal{O}_{01}\big(({}^T\boldsymbol{\nabla}\mathbf{J}) : \boldsymbol{\varepsilon}\big) = \frac{1}{2}\mathcal{O}_{01}\big((\nabla^2\boldsymbol{\nabla}\cdot\boldsymbol{\varepsilon})r\big) \ . \tag{E.8b}$$

For $p \neq q$, relation (3.36a) now follows as an identity, since

$$\boldsymbol{\delta} : \mathbf{M}_{US} = \boldsymbol{\delta} : \mathcal{O}_{01}\big(({}^T\boldsymbol{\nabla}\mathbf{J}) : \boldsymbol{\varsigma}\big) = \mathcal{O}_{01}\big(\boldsymbol{\delta} : ({}^T\boldsymbol{\nabla}\mathbf{J}) : \boldsymbol{\varsigma}\big) = \mathcal{O}_{01}(\nabla^2\boldsymbol{\nabla}r) \ . \tag{E.9}$$

The other two equations in this set can be derived in a similar fashion, but concern couplings between the first gradient of the particle velocity and the first irreducible stress moment. They thus involve a scalar linear functional $\mathcal{O}_{11}$ instead of $\mathcal{O}_{01}$, but the reasoning is the same.

For $p = q$, the validity of these relations is most easily demonstrated by checking the identities (3.37). It is then easy to verify (3.36) from the expressions (3.29b-c) for the mobility tensors $\mathbf{M}_{\Omega T}^{pp}$, $\mathbf{M}_{\Omega S}^{pp}$ and $\mathbf{M}_{ES}^{pp}$. The relation between $\mathbf{M}_{US}^{pq}$ and $\mathbf{M}_{UT}^{pq}$ becomes trivial since both tensors are zero for $p = q$.

## References

Abramowitz, M. & Stegun I.A. (1970) Handbook of mathematical functions, Dover Publications, Inc., New York.

Barta, E. & Liron, N. (1988) Slender body interactions for low Reynolds numbers –Part II: Body-body interactions, *SIAM J. Appl. Math.* **48**, 1262-1280.

Batchelor, G.K. (1970) Slender-body theory for particles of arbitrary cross-section in Stokes flow, *J. Fluid Mech.* **44**, 419-440.

Batchelor, G.K. (1971) The stress generated in a non-dilute suspension of elongated particles by pure straining motion, *J. Fluid Mech.* **46**, 813-829.

Beenakker, C.W.J. (1986) Ewald sum of the Rotne-Prager tensor, *J. Chem. Phys.* **85**, 1581-1582.

Bitsanis, I., Davis, H.T. & Tirell, M. (1988) Brownian dynamics of nondilute solutions of rodlike polymers 1. Low concentrations, *Macromolecules* **21**, 2824-2835.

Bitsanis, I., Davis, H.T. & Tirell, M. (1990) Brownian dynamics of nondilute solutions of rodlike polymers 2. High concentrations, *Macromolecules* **23**, 1157-1165.

Bossis, G. & Brady, J.F. (1984) Dynamic simulation of sheared suspensions. I. General method, *J. Chem. Phys.* **80**, 5141-5154.

Bossis, G. & Brady, J.F. (1989) The rheology of Brownian suspensions, *J. Chem. Phys.* **91**, 1866-1874.

Brady, J.F. & Bossis, G. (1988) Stokesian dynamics, *Ann. Rev. Fluid Mech.* **20**, 111-157.

Brady, J.F., Phillips, R.J., Lester, J.C. & Bossis, G. (1988) Dynamic simulation of hydrodynamically interacting suspensions, *J. Fluid Mech.* **195**, 257-280.

Brenner, H. (1963) The Stokes resistance of an arbitrary particle, *Chem. Eng. Sci.* **18**, 1-25.

Brenner, H. (1964 a) The Stokes resistance of an arbitrary particle –III. Shear fields, *Chem. Eng. Sci.* **19**, 631-651.

Brenner, H. (1964 b) The Stokes resistance of an arbitrary particle –IV. Arbitrary fields of flow, *Chem. Eng. Sci.* **19**, 703-727.

Brenner, H. (1966) The Stokes resistance of an arbitrary particle –V. Symbolic operator representation of intrinsic resistance, *Chem. Eng. Sci.* **21**, 97-109.

Brenner, H. & Haber, S. (1983) Symbolic operator representation of generalized Faxén relations, *PhysicoChem. Hydrodyn.* **4**, 271-278.

Chapman, S. & Cowling, T.G. (1970) *The Mathematical Theory of Non-Uniform Gases*, 3rd edn., Cambridge University Press, Cambridge.

Chwang, A.T. & Wu, T.Y. (1974) Hydromechanics of low-Reynolds-number flow, Part 1: Rotation of axisymmetric prolate bodies, *J. Fluid Mech.* **63**, 607-622.

Chwang, A.T. & Wu, T.Y. (1975) Hydromechanics of low-Reynolds-number flow, Part 2: Singularity method for Stokes flows, *J. Fluid Mech.* **67**, 787-815.

Claeys, I.L. (1988) *Experimental and numerical study of molecular rotational diffusion in gel-like media*, M.S. thesis, California Institute of Technology, 40 pp.

Claeys, I.L. & Brady, J.F. (1989) Lubrication singularities of the resistance tensor for two arbitrary particles, *PhysicoChem. Hydrodyn.* **11**, 261-293.

Claeys, I.L. (1991) *SDPS, a package of subroutines to simulate systems of hydrodynamically interacting prolate spheroids*, FORTRAN program, California Institute of Technology 210-41.

Cooley, M.D.A. & O'Neill, M.E. (1969) On the slow motion of two spheres in contact along their line of centers through a viscous fluid, *Proc. Camb. Phil. Soc.* **66**, 407-415.

Durlofsky, L. & Brady, J.F. (1987) Analysis of the Brinkman equation as a model for flow in porous media, *Phys. Fluids* **30**, 3329-3341.

Durlofsky, L., Brady, J.F. & Bossis, G. (1987) Dynamic simulation of hydrodynamically interacting particles, *J. Fluid Mech.* **180**, 21-49.

Ermak, D.L. & McCammon, J.A. (1978) Brownian dynamics with hydrodynamic interactions, *J. Chem. Phys.* **69**, 1352-1360.

Felderhof, B.U. (1977) Hydrodynamic interactions between two spheres, *Physica* **89A**, 373-384.

Frenkel, D. (1988) Structure of hard-core models for liquid crystals, *J. Phys. Chem.* **92**, 3280-3284.

Frenkel, D. & Mulder, B.M. (1985) The hard ellipsoid-of-revolution fluid I. Monte-Carlo simulations, *Mol. Phys.* **55**, 1171-1192.

Gluckman, M.J., Pfeffer, R. & Weinbaum, S. (1971) A new technique for treating multiparticle slow viscous flow: axisymmetric flow past spheres and spheroids, *J. Fluid Mech.* **50**, 705-740.

Happel, J. & Brenner, H. (1973) *Low Reynolds Number Hydrodynamics*, 2nd edn., Martinus Nijhoff, Dordrecht.

Hassonjee, Q., Ganatos, P. & Pfeffer, R. (1988) A strong-interaction theory for the motion of arbitrary three-dimensional clusters of spherical particles at low Reynolds number, *J. Fluid Mech.* **197**, 1-37.

Ivanov, Y., Van de Ven, T.G.M. & Mason, S.G. (1982) Damped oscillations in the viscosity of suspensions of rigid rods. I. Monomodal suspensions, *J. Rheol.* **26**, 213-230.

Jeffery, G.B. (1922) The motion of ellipsoidal particles immersed in a viscous fluid, *Proc. Roy. Soc. Lond. A***102**, 161-179.

Kim, S. (1985 a) A note on Faxén laws for nonspherical particles, *Int. J. Multiphase Flow* **11**, 713-719.

Kim, S. (1985 b) Sedimentation of two arbitrarily oriented spheroids in a viscous fluid, *Int. J. Multiphase Flow* **11**, 699-712.

Kim, S. (1986) Singularity solutions for ellipsoids in low-Reynolds-number flows: with application to the calculation of hydrodynamic interactions in suspensions of ellipsoids, *Int. J. Multiph. Flow* **12**, 469-491.

Kim, S. & Arunachalam, P.V. (1987) The general solution for an ellipsoid in low-Reynolds-number flow, *J. Fluid Mech.* **178**, 535-547.

Kim, S. & Lawrence, C.J. (1988) Suspension mechanics for particle contamination control, *Chem. Eng. Sci.* **43**, 991-1016.

Kim, S. & Lu, S.Y. (1987) The functional similarity between Faxén relations and singularity solutions for fluid-fluid, fluid-solid and solid-solid dispersions, *Int. J. Multiphase Flow* **13**, 837-844.

Kim, S. & Mifflin, R.T. (1985) The resistance and mobility functions for two equal spheres in low-Reynolds-number flow, *Phys. Fluids* **28**, 2033-2045.

Kynch, G.J. (1959) The slow motion of two or more spheres through a viscous fluid, *J. Fluid Mech.* **5**, 193-208.

Ladd, A.J.C. (1990) Hydrodynamic transport coefficients of random dispersions of hard spheres, *J. Chem. Phys.* **93**, 3484-3494.

Ladyzhenskaya, O.A. (1963) *The Mathematical Theory of Viscous Incompressible Flow*, Gordon and Breach, New York/London, Chapter 3.

Lamb, H. (1932) *Hydrodynamics*, 6th edn., Cambridge University Press, Cambridge.

Liao, W.H. & Krueger, D.A. (1980) Multipole expansion calculation of slow viscous flow about spheroids of different sizes, *J. Fluid Mech.* **96**, 223-241.

Mazur, P. (1982) On the motion and Brownian motion of $n$ spheres in a viscous fluid, *Physica* **110A**, 128-146.

Mazur, P. & van Saarloos, W. (1982) Many-sphere hydrodynamic interactions and mobilities in a suspension, *Physica* **115A**, 21-57.

Mewis, J. & Metzner, A.B. (1974) The rheological properties of suspensions of fibres in Newtonian fluids subjected to extensional deformations, *J. Fluid Mech.* **62**,

593-600.

O'Brien, R.W. (1979) A method for the calculation of the effective transport properties of suspensions of interacting particles, *J. Fluid Mech.* **91**, 17-39.

Perry, R.H. & Green, D.W. (1984) *Perry's Chemical Engineer's Handbook*, 6th edn., McGraw-Hill Book Co., New York, Section 2.

Phillips, R.J., Brady, J.F. & Bossis, G. (1988 a) Hydrodynamic transport properties of hard-sphere dispersions. I. Suspensions of freely mobile particles, *Phys. Fluids* **31**, 3462-3472.

Phillips, R.J., Brady, J.F. & Bossis, G. (1988 b) Hydrodynamic transport properties of hard-sphere dispersions. II. Porous media, *Phys. Fluids* **31**, 3473-3479.

Piessens, R., de Doncker-Kapenga, E., Uberhuber, C.W. & Kahaner, D.K. (1983) *QUADPACK, A Subroutine Package for Automatic Integration*, Springer-Verlag, Berlin.

Phung, T. & Brady, J.F. (1991) manuscript in preparation.

Rallison, J.M. (1978) Note on the Faxén relations for a particle in Stokes flow, *J. Fluid Mech.* **88**, 529-533.

Rosenberg, J., Denn, M. & Keunings, R. (1990) Simulation of non-recirculating flows of dilute fiber suspensions, *J. Non-Newt. Fluid Mech.* **37**, 317-345.

Salinas, A. & Pittman, J.F.T. (1981) Bending and breaking fibers in sheared suspensions, *Polym. Eng. Sci.* **21**, 23-31.

Shaqfeh, E.S.G. & Fredrickson, G.H. (1990) The hydrodynamic stress in a suspension of rods, *Phys. Fluids A***2**, 7-24.

Shaqfeh, E.S.G. & Koch, D.L. (1988) The combined effect of hydrodynamic interactions and Brownian motion on the orientation of particles flowing through fixed beds, *Phys. Fluids* **31**, 2769-2780.

Stimson, M. & Jeffery, G.B. (1926) The motion of two spheres in a viscous fluid, *Proc. Roy. Soc. Lond. A***111**, 110-116.

Wakiya, S. (1965) Mutual interactions of two spheroids sedimenting in a viscous fluid, *J. Phys. Soc. Japan* **20**, 1502-1514.

Weinbaum, S., Ganatos, P. & Yan, Z.Y. (1990) Numerical multipole and boundary integral techniques in Stokes flow, *Ann. Rev. Fluid Mech.* **22**, 275-316.

Yoon, B.J. & Kim, S. (1990) A boundary collocation method for the motion of two spheroids in Stokes flow: hydrodynamic and colloidal interactions, *Int. J. Multiphase Flow* **16**, 639-649.

Youngren, G.K. & Acrivos, A. (1975) Stokes flow past a particle of arbitrary shape: a numerical method of solution, *J. Fluid Mech.* **69**, 377-403.

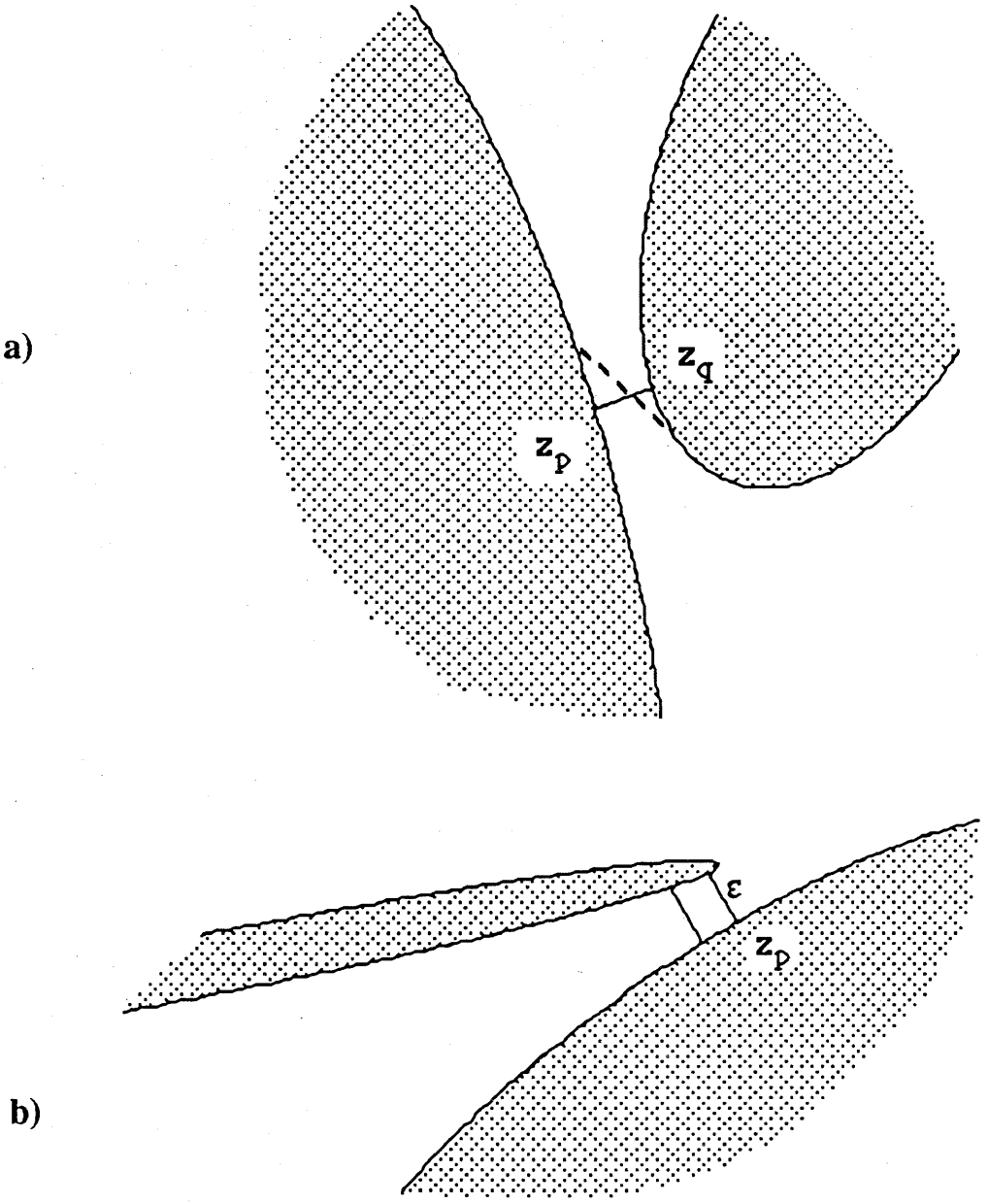


**Fig. 3.1**: Sensitivity of the lubrication parameters to local features of the geometry.
**a)** Although the points of closest approach are well approximated (on the scale of the particles), the estimate of the minimum separation ε is poor.
**b)** ε is estimated accurately, but the principal radii of curvature are incorrect.

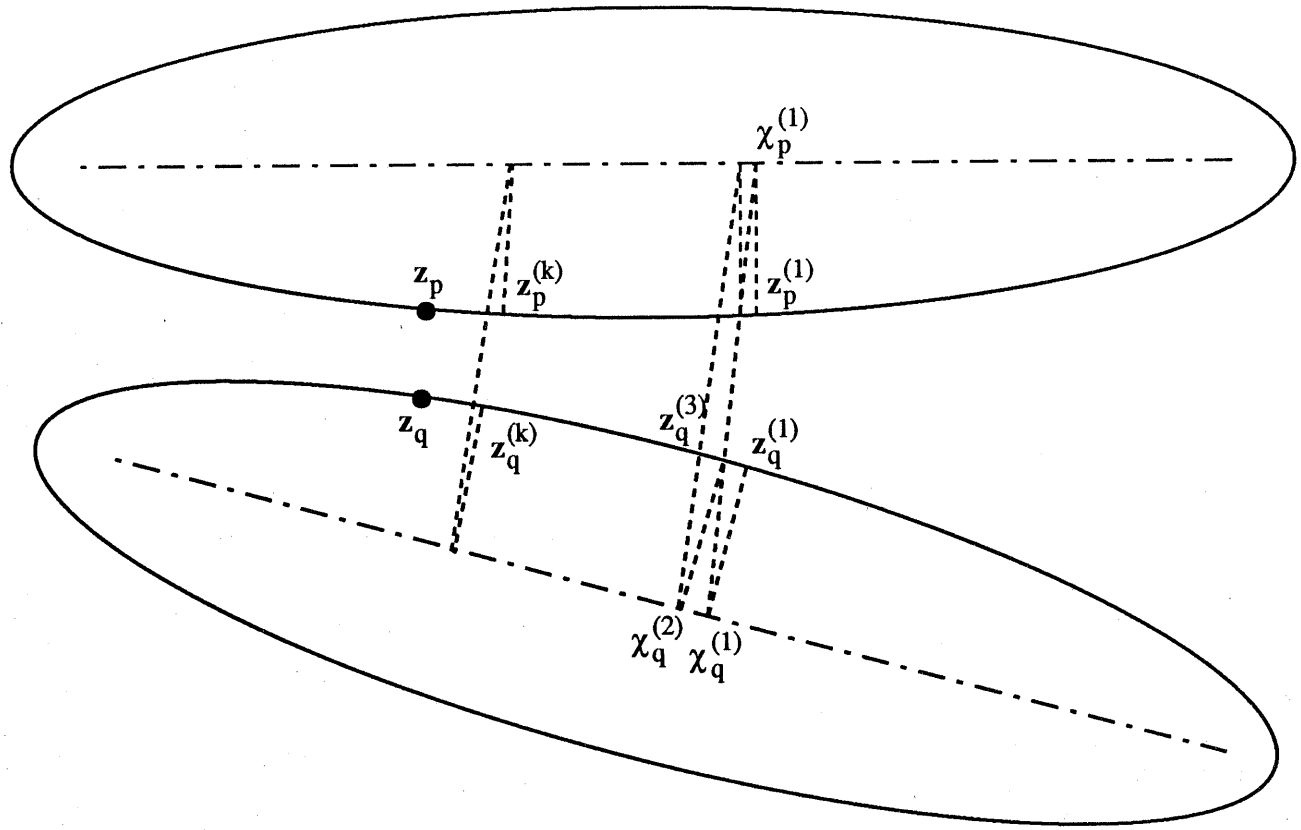


**Fig. 3.2**: Illustration of the algorithm to find the points of closest approach on two prolate spheroids.

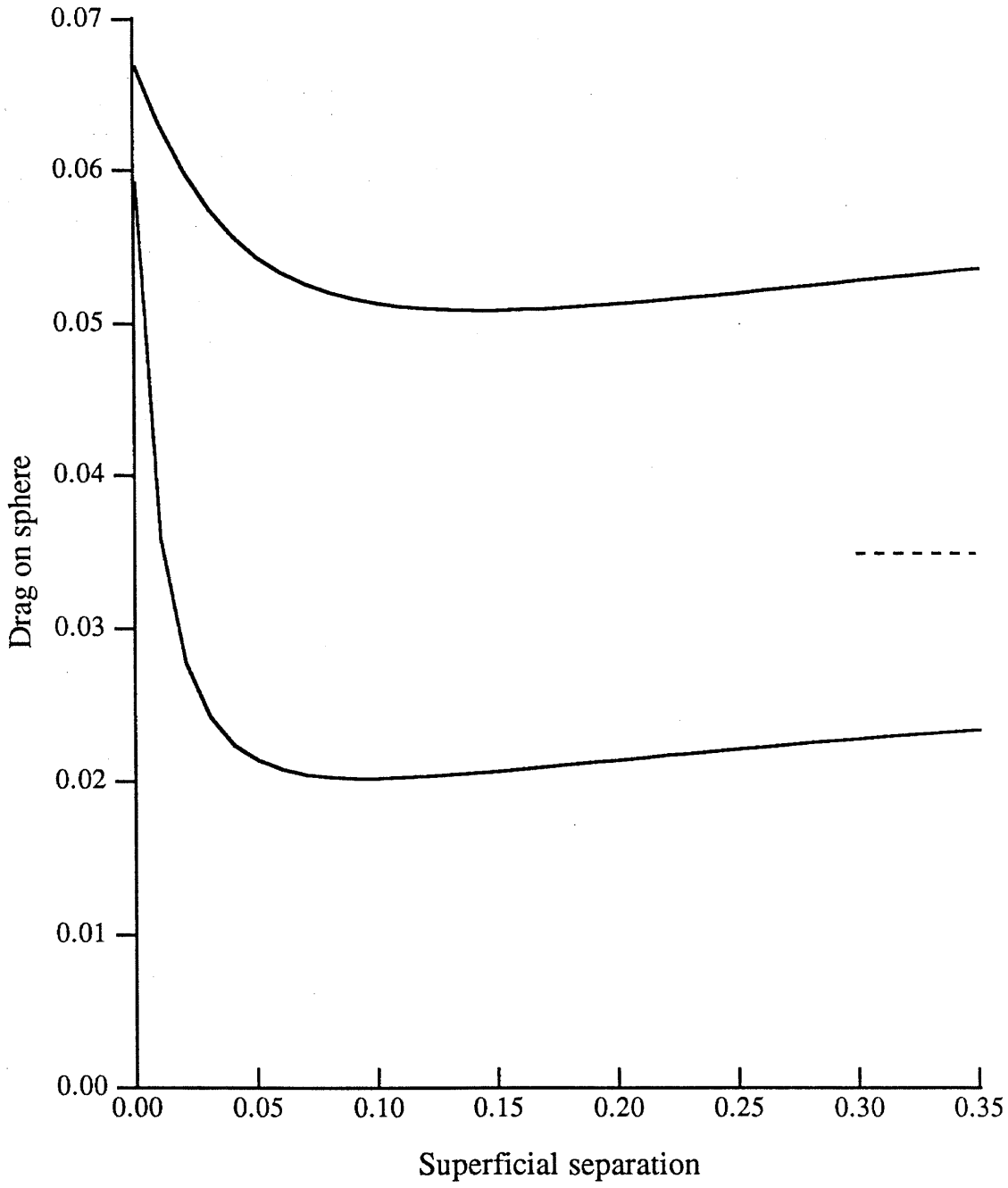


**Fig.3.3**: Drag on a small sphere placed at the tip of a spheroid of aspect ratio 10 moving at the same speed.

The drag is non dimensionalized by $8\pi\mu aU$. Distances scale with the half-length "a" of the spheroid. The radius of the sphere equals 0.0464 for the bottom curve, and is 0.1 for the other. The drag which the sphere of radius 0.0464 would experience in the absence of the large particle is indicated by the dashed line. The asymptote for the other sphere lies at 0.075. See text for details.

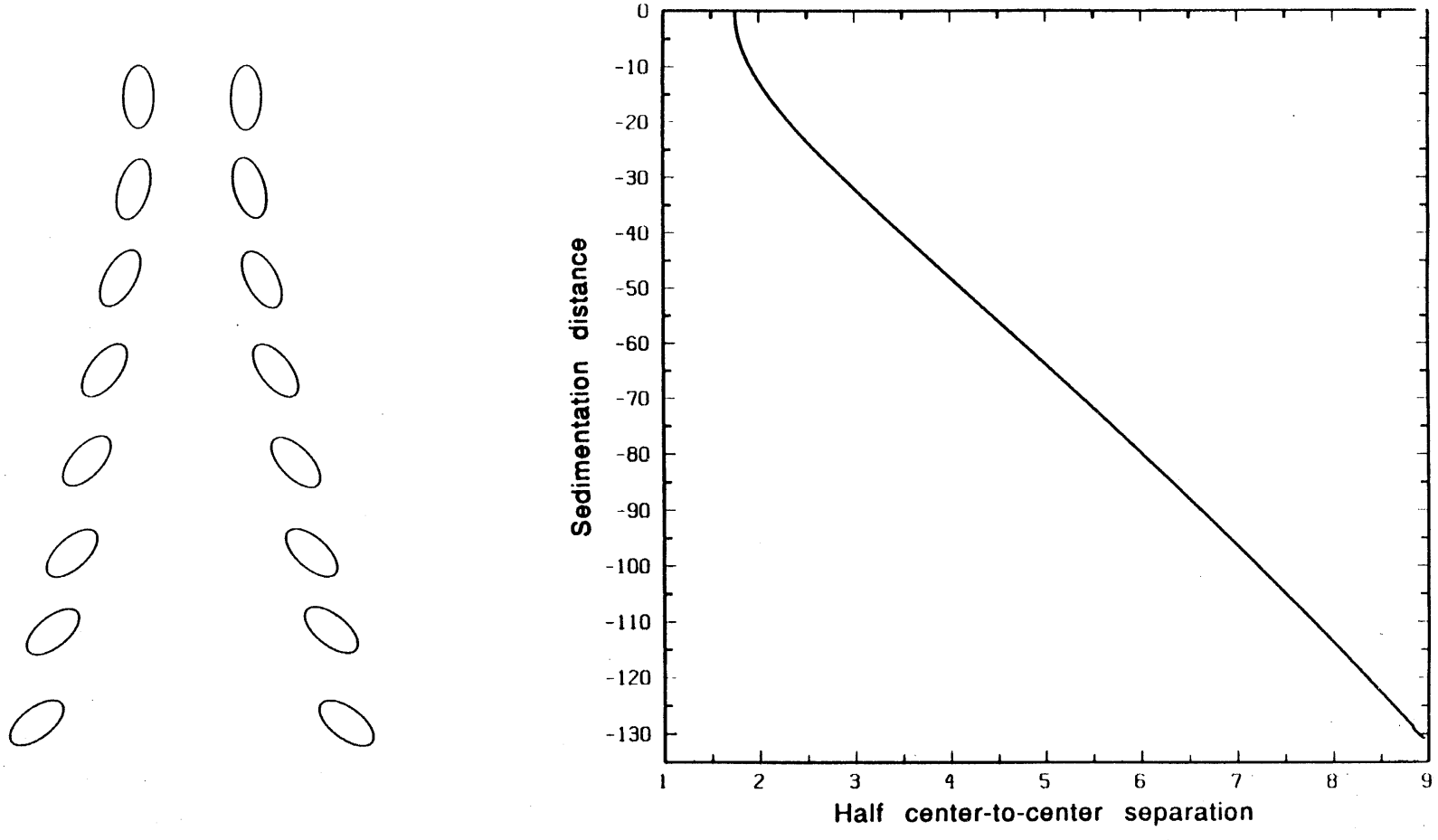


**Fig. 3.4 a**: Sedimentation of two prolate spheroids of aspect ratio 2 at an initial centre-to-centre separation of 3.5.
The particles are released side by side and aligned with the direction of gravity. The sketch on the left represents snapshots of the spheroids taken at equal time intervals. The vertical distance has been scaled down in this illustration.

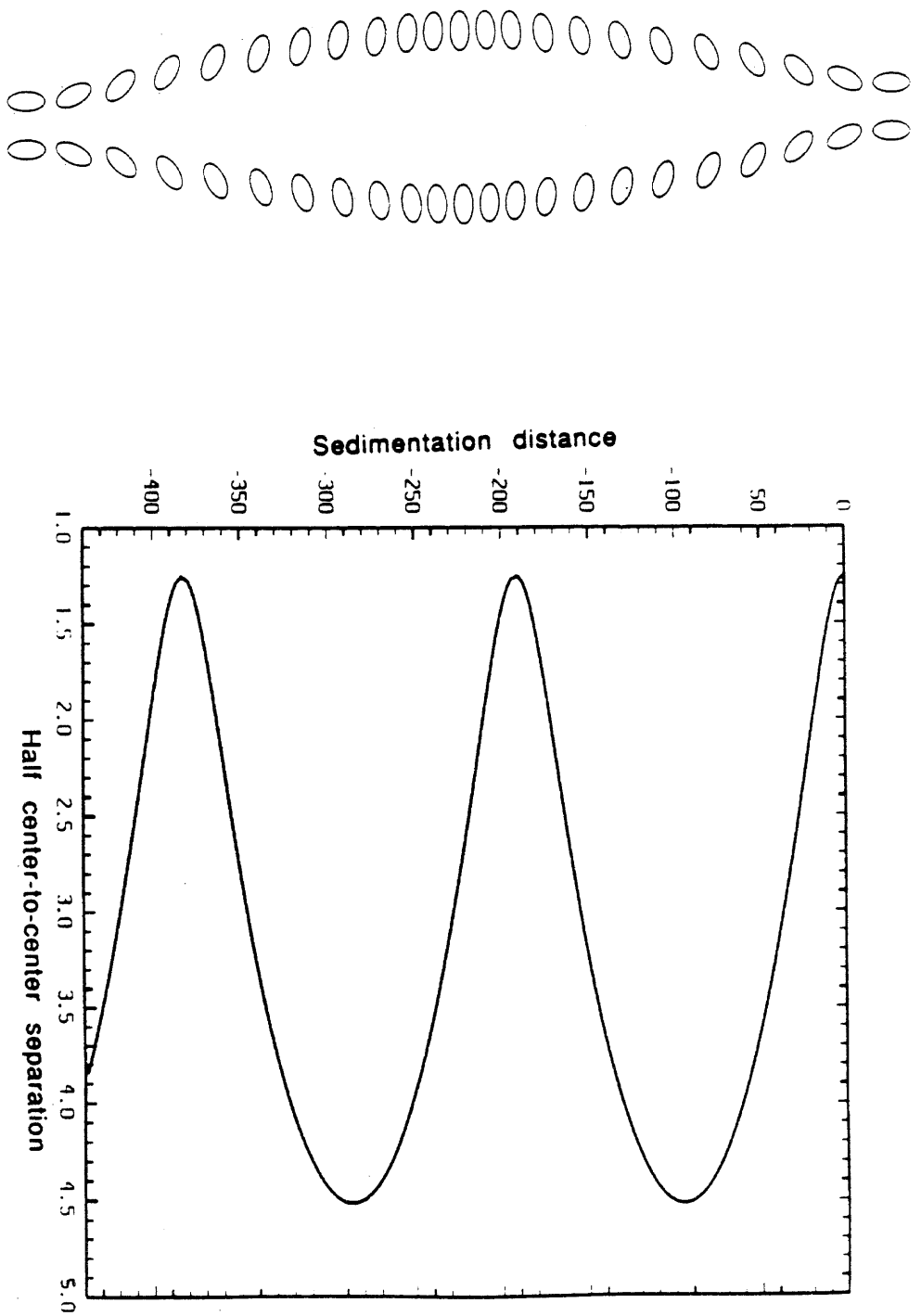


**Fig. 3.4 b**: Sedimentation of two prolate spheroids of aspect ratio 2 at an initial centre-to-centre separation of 2.5. See caption of Fig. 3.4.a.

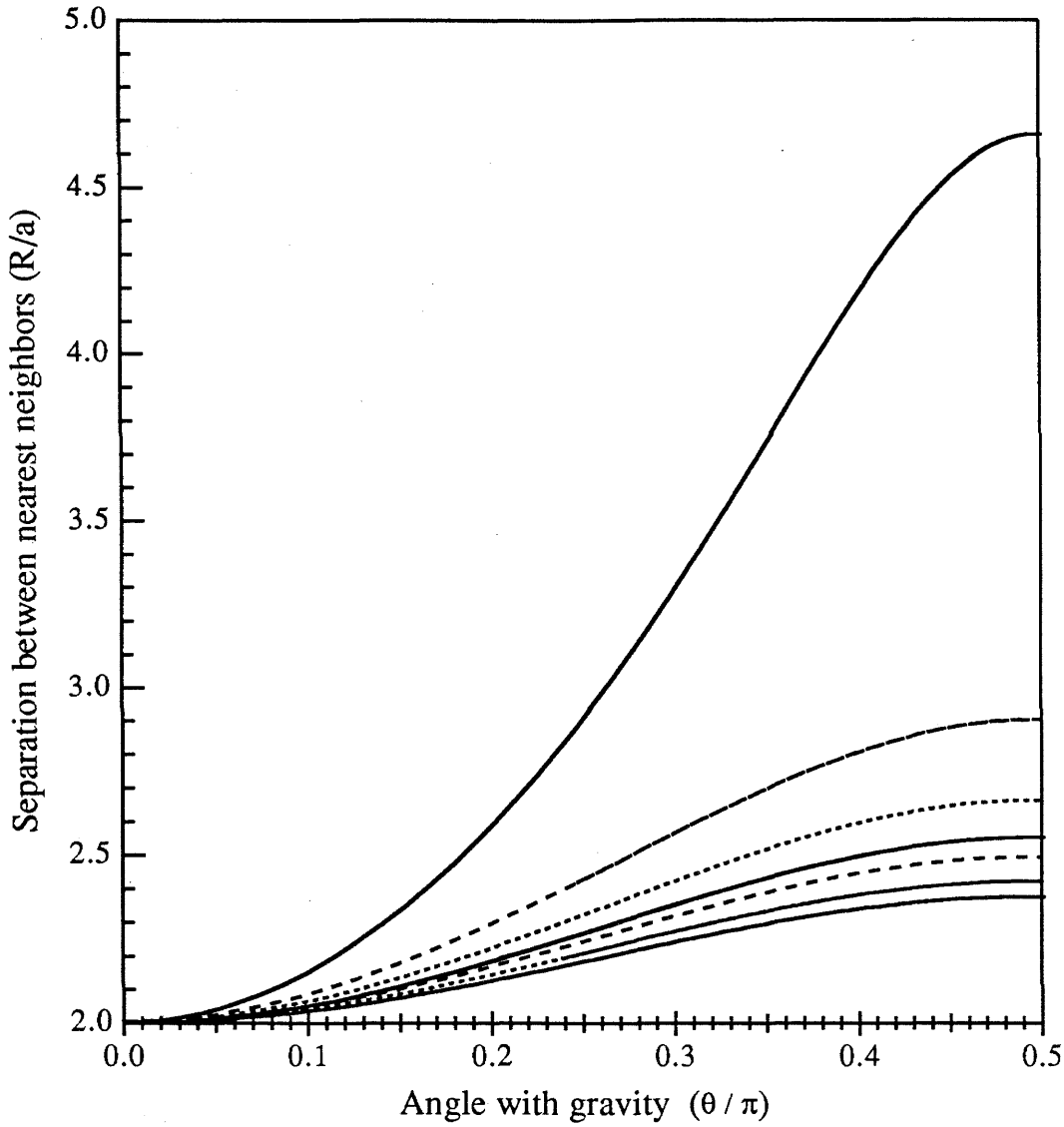


**Fig.3.5**: Periodic centre-of-mass trajectories of spheroids with aspect ratio 2 sedimenting at the corners of regular polygons.
From top to bottom, N=2 (line); N=3 (equilateral triangle); N=4 (square); N=5 (pentagon); N=6 (hexagon); N=8 (octagon); N=10 (decagon).
All curves are symmetric about $\theta = \pi / 2$.
The spheroids are initially separated by R = 2a, with "a" the particle half-length, and aligned with gravity ($\theta = 0$).

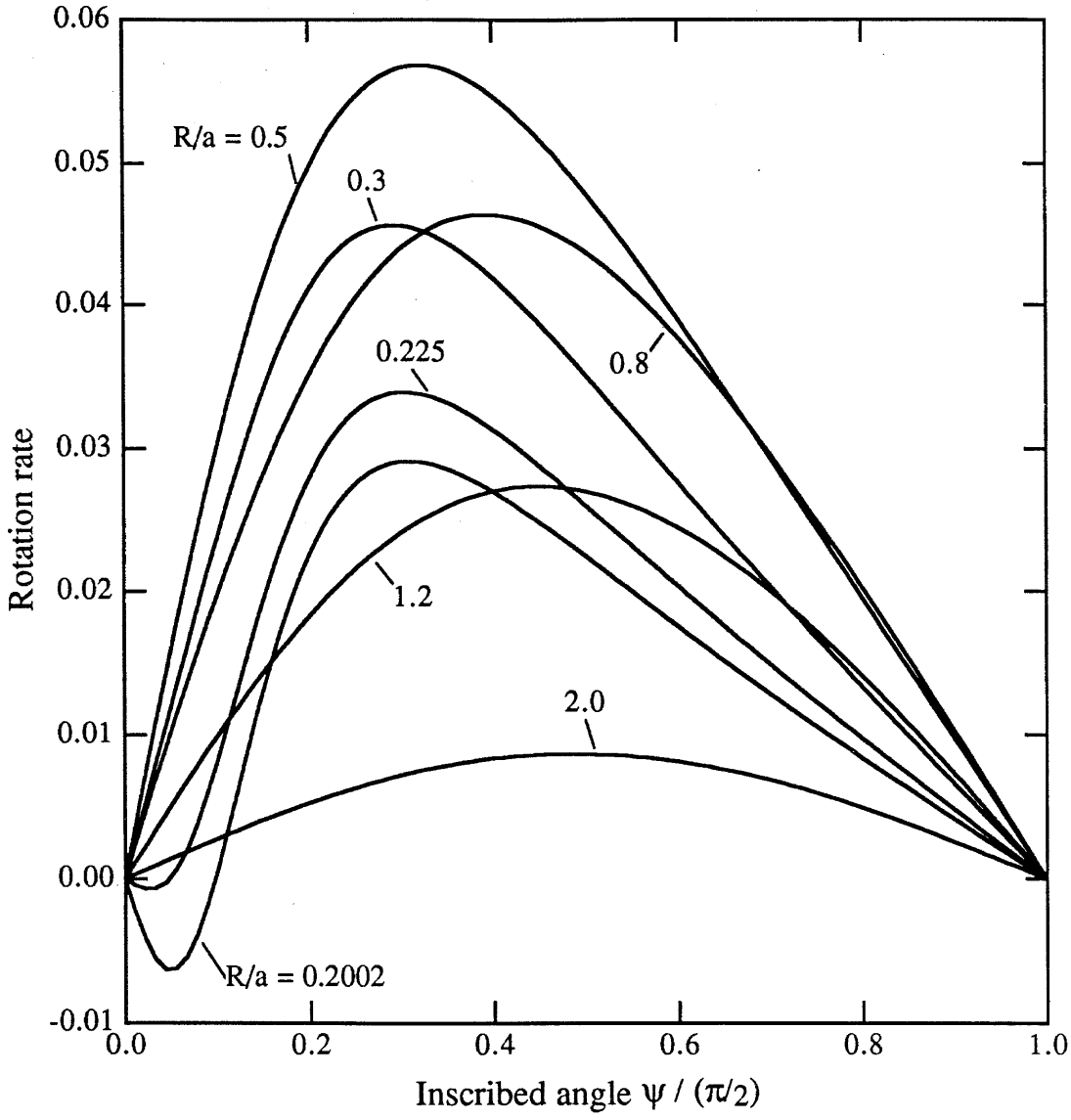


**Fig.3.6**: Rate of rotation of two spheroids of aspect ratio 10 sedimenting atop one another .
The distance R/a is the centre-to-centre separation.
The speed of gyration is non-dimensionalized by $8\pi\mu a^2 / |\mathbf{F}_g|$, with $\mathbf{F}_g$ the force of gravity.

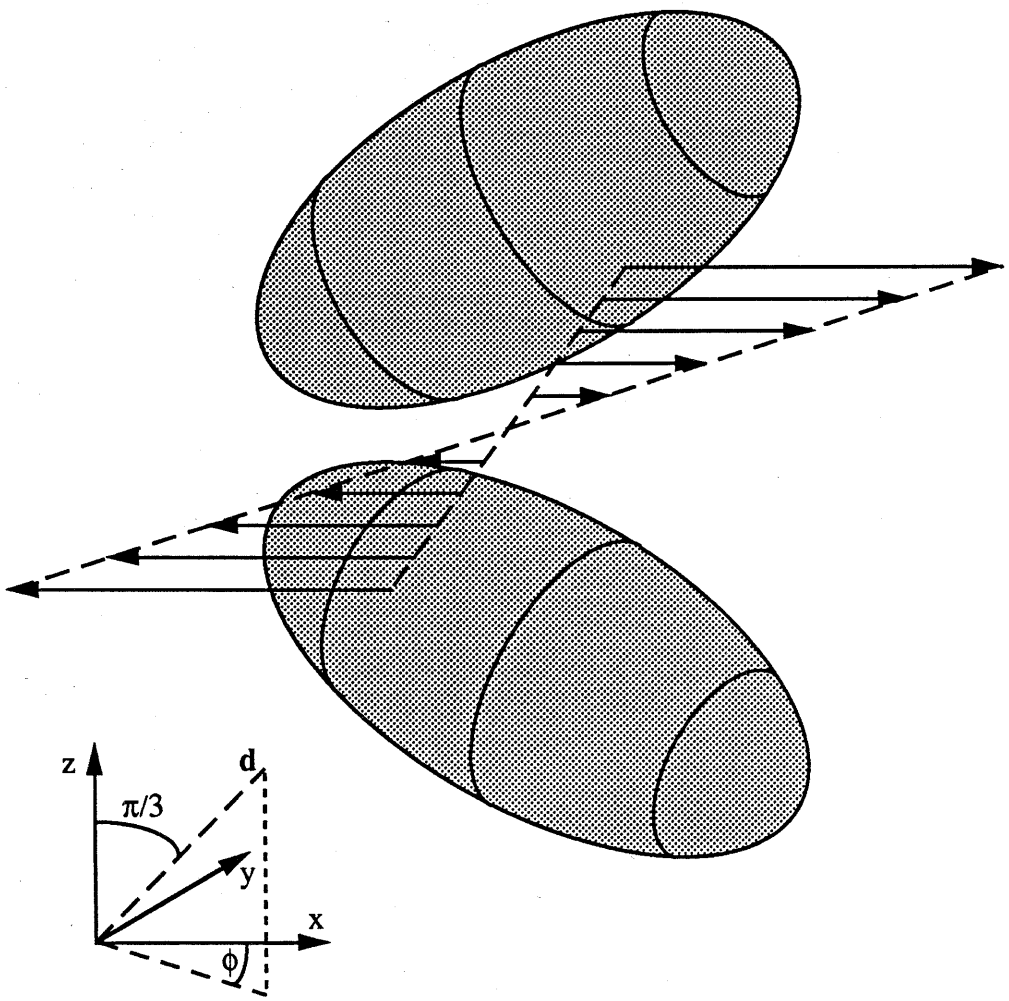


**Fig. 3.7**: Geometry considered in Fig. 3.8.
The vector **d** indicates the orientation of the particles. z lies along the vorticity of the shear field, and x is the direction of the flow. The angle $\phi$ is measured from x.

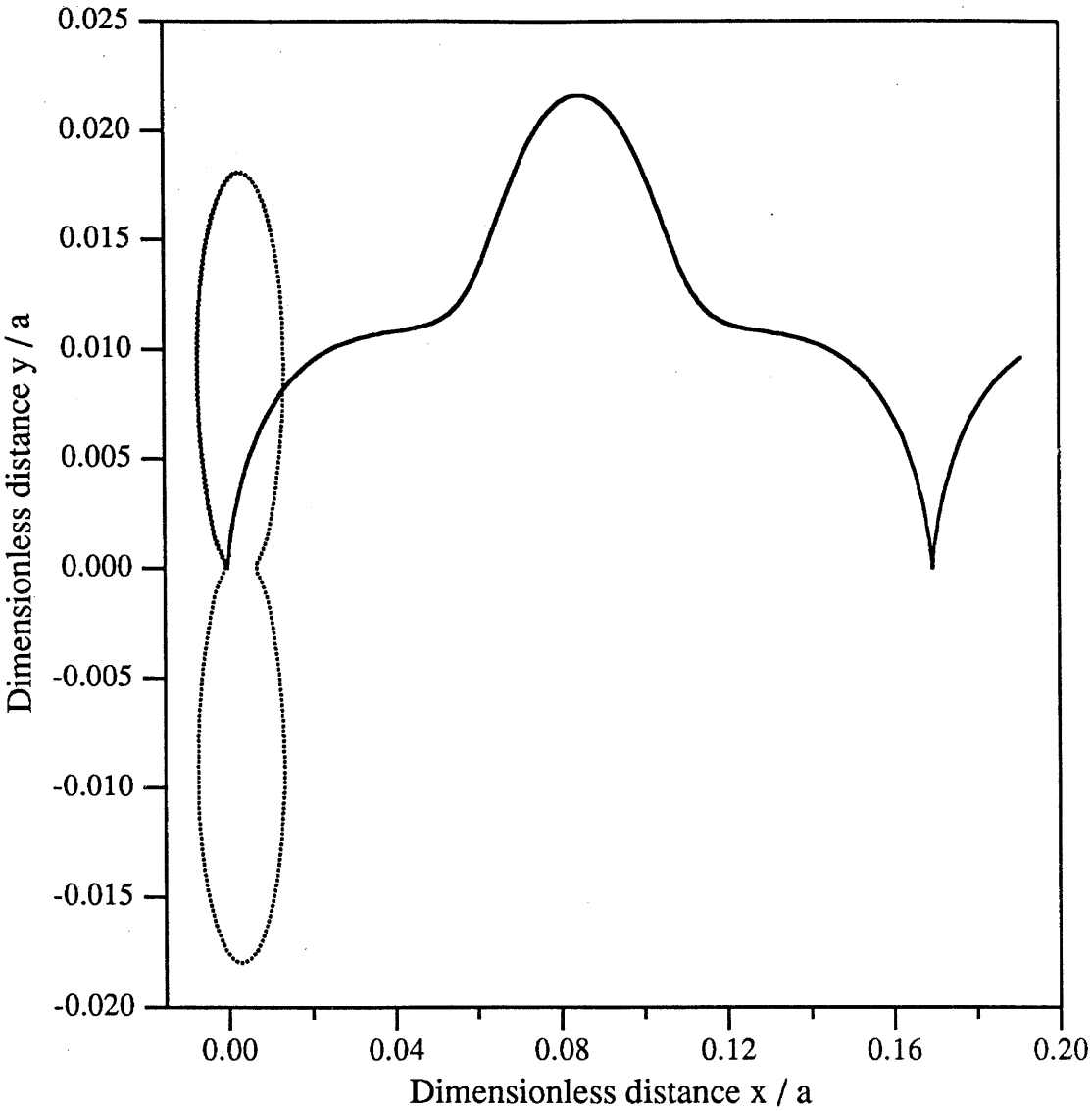


**Fig.3.8**: Shear induced migration of two spheroids of aspect ratio 2. The abcissa, x/a, denotes a displacement in the direction of the undisturbed streamlines. The ordinate, y/a, measures distances traveled in the plane of shear, perpendicular to the flow.

The closed orbit (dotted line) is described if $\phi = 0$ initially.

For $\phi = \pi / 2$, the open trajectory (solid line) is followed.

# Chapter IV
# Stokesian dynamics for unbounded dispersions of prolate spheroids

## 4.1 Introduction

Fluid-particle systems in which the solid phase consists of elongated objects occur in all areas of science and engineering. Suspensions of rods are essential intermediates in many production processes, ranging from the fabrication of fibre-reinforced composites to the manufacture of paper from pulp. The permeability of filters and fibrous membranes depends, apart from specific physico-chemical factors, on the pressure drop across a fixed bed of fibres. The electrophoretic mobility of biopolymers in a gel is greatly influenced by steric and viscous interactions between the macromolecule and the fibrous network through which it moves. The molecular constituents of all liquid crystals are elongated, and self-diffusion in those anisotropic fluids is of great interest from both a practical and scientific standpoint. In all cases, from a rheologist's point of view, the physical system consists of a fluid in which non-spherical particles are suspended. In this chapter, we propose to calculate the hydrodynamic transport properties of such dispersions by extending the ideas set forth in Ch. III to systems consisting of infinitely many particles. The approach is akin in concept to the simulation technique for unbounded suspensions of spheres known as "Stokesian dynamics" (Brady & Bossis, 1988; Brady *et al.*, 1988).

Rod dispersions are of particular interest because they can display radically different transport properties than the solvent, even at concentrations of solid matter so low that most other characteristics of the sample are unaltered. In the semi-dilute concentration regime especially (defined as the range of volume fractions $\phi$ such that $r_p^{-2} < \phi \ll r_p^{-1}$, with $r_p$ a characteristic length-to-breadth ratio for the

particles), hydrodynamic interactions between the rods totally dominate the rheological response of the suspension, even if only minute quantities of fibers are present ($\phi \ll 1$). The incommensurate increase of the extensional viscosity of fluids upon addition of minuscule amounts of dispersed fibrous material (Mewis & Metzner, 1974; Pittman & Bayram, 1990) is the most vivid illustration thereof. This dramatic enhancement of the resistance to stretch is typical for rod suspensions, and is not observed when the particles are spherical or disk-like. It is of tremendous relevance for the processing of fiber dispersions, and is the hydrodynamic analogue of the large directional increase in heat transport or electrical conductivity which can be achieved in fiber composites. The origin of these phenomena is now well understood (Batchelor, 1971), and can be traced back to the observation that rods which transmit energy, current or stress very effectively, influence the transport of these quantities over regions much larger than their own volume. In fact, while the concentration of the fibres scales with the length $L$ of the particles (for a given cross-sectional area), the domain over which their presence is felt grows with the cube of the length (Batchelor, 1971; Shaqfeh & Fredrickson, 1990). Long, slender particles therefore affect the macroscopic properties far more than would be expected from their concentration, and increases of the Trouton viscosity by orders of magnitude can be attained by adding just fractions of a percent of rods to the suspension (provided the rods are slender enough, so that $\phi {r_p}^2 = O(1)$, i.e., the suspension is semi-dilute).

Although the fundamental elements determining the hydrodynamic behavior of rod suspensions begin to be understood, many benefits can still be reaped from microstructurally detailed simulations such as the ones we propose. In a certain sense, the computer is the ideal tool for non-invasive experimentation. Our method enables us to investigate the effects of aspect ratio and concentration, and even to study polydisperse samples (spheroids of varying dimension and/or shape). More importantly, numerical simulations allow one to turn on and off interactions at will, permitting an in-depth analysis of the interplay between the various forces

in the system (hydrodynamic, gravitational, Brownian, colloidal, etc.). They often give one the opportunity to test hypotheses in the most direct and convenient way possible (which is not always accessible experimentally). Wall effects are absent (or can be included if desired). One exerts absolute control over the microstructure of the suspension, and can impose perfect order if desired, an idealization unachievable otherwise. Alternatively, the configuration may be allowed to evolve with the flow, in which case computer simulations generate precise snapshots of the microstructure, revealing geometric characteristics such as clusters and flow-induced alignment. This information provides the link between the topology of the dispersion and its macroscopic properties. Experience with Stokesian dynamics for spheres has taught that numerical simulations help increase our insight into the dynamics of suspensions, and contribute much to our understanding of their rheology. Computer simulations, of course, have their limitations. They always make use of an idealized model of reality, and, by necessity, only incorporate the physics which are understood. Constraints on the computer time usually imply a trade-off between rigor and feasibility. Wall effects are replaced by artifacts due to boundary conditions. Yet we are convinced that numerical simulations remain a very powerful tool of investigation, and there exists a wide body of literature to back this claim. Moreover, most analytical theories on fibre dispersions are asymptotic, and hold only in the limit of very slender inclusions. No information is given about the behavior of moderately elongated particles, of aspect ratio intermediate between the sphere and the line. Indeed, many theoretical treatments (Batchelor, 1971; Shaqfeh & Fredrickson, 1990) employ a very slowly converging series expansion in the inverse of the logarithm of the aspect ratio, so that corrections can only be neglected in principle for extremely anisotropic fibres (with $r_p \geq O(10^6)$ or so). Few natural or man-made materials, however, consist of straight rigid fibres of very high aspect ratio; such slender bodies either bend or break (Salinas & Pittman, 1981). Slurries commonly contain particles which are distinctly non-spherical, but they usually resemble short rods rather than fibres. Similarly, the shape of many

proteins is well approximated by ellipsoids, but their length-to-width ratio seldom exceeds five or six. Our simulation method accurately describes the rheology of these slightly elongated, fat bodies.

The model system we consider consists of prolate ellipsoids of revolution suspended in a Newtonian fluid. This class of particle shapes includes the sphere at one end of the spectrum, and the line segment (i.e., an infinitely slender rod) at the other. The method can accommodate heterogeneous populations of spheroids, accepting polydispersity in both size and aspect ratio. The Reynolds number, based on the largest particle dimension in the dispersion, is assumed to be vanishingly small, so that the dynamics of the fluid phase are adequately described by the quasi-stationary creeping flow equations:

$$\boldsymbol{\nabla} p = \mu \nabla^2 \mathbf{u} \ , \tag{4.1a}$$

$$\boldsymbol{\nabla} \cdot \mathbf{u} = 0 \ . \tag{4.1b}$$

The vector field $\mathbf{u}$ represents the fluid velocity, $p$ is the associated pressure and $\mu$ the viscosity of the liquid in the absence of particles. The adoption of the Stokes equations (4.1) implies that inertial effects are negligible compared to viscous retardation on the length scale of the particles. The spheroids are, however, large enough to neglect the effects of Brownian motion. No-slip boundary conditions hold at the surfaces $A_p$ of the particles, which are considered to be undeformable:

$$\mathbf{u}(\mathbf{x}) = \mathbf{U}_p + (\mathbf{x} - \mathbf{x}_p) \wedge \boldsymbol{\Omega}_p \ , \qquad \text{for} \quad \mathbf{x} \in A_p \ . \tag{4.2}$$

The translational and angular velocities $\mathbf{U}_p$ and $\boldsymbol{\Omega}_p$ of particle $p$ fully characterize its motion. $\mathbf{U}_p$ is evaluated at the locator point $\mathbf{x}_p$ of the spheroid (chosen to be its geometric centre).

Unbounded, statistically homogeneous suspensions are modeled by periodically replicating a suitable number ($N$) of spheroids in space. Denoting the fluid phase by $V$ and its boundary by $\partial V$ (= the union of all the particle surfaces $A_p$) we thus

require, $\forall \mathbf{z} \in \mathcal{Z}^3$:

$$\mathbf{x} \in \partial V \iff \mathbf{x} + \boldsymbol{x}_{\{\mathbf{z}\}} \in \partial V \ , \qquad \text{with} \quad \boldsymbol{x}_{\{\mathbf{z}\}} = \mathbf{B} \cdot \mathbf{z} \ . \tag{4.3}$$

$\mathcal{Z}^3$ denotes the space of all ordered sets of 3 integers; hence $\mathbf{z}$ contains three integer coordinates. The columns of the $3 \times 3$ constant matrix $\mathbf{B}$ make up the basis vectors $\mathbf{b}_i$ $(i = 1, 2, 3)$ used to reproduce the $N$ reference spheroids periodically in space. The ensemble $\mathcal{L}$ of all possible points $\boldsymbol{x}_{\{\mathbf{z}\}}$ therefore defines a lattice. In essence, (4.3) states that the microstructure is invariant with respect to translations along any of the basis vectors $\mathbf{b}_i$ of the lattice $\mathcal{L}$. The only restriction placed on the basis vectors is that they should be compatible with the mutual impenetrability of the particles. They should, of course, also be linearly independent and form a complete basis set for the three-dimensional Euclidean space. If dynamic simulations need to be performed, some care should also be taken to ensure that the chosen lattice is compatible with the kinematics of the imposed motion. In particular, the basis vectors must retain a finite length at all times under the deformation, as well as, in principle, for $t \to \infty$. In the absence of boundaries, it would be inconsistent in a statistically homogeneous dispersion to consider any imposed flow other than those characterized by a constant (position independent) velocity gradient $\boldsymbol{\nabla}\mathbf{u} = \mathbf{G}$ (which may be zero). Since the lattice must deform affinely with the flow, the most general rate of deformation of the unit cell is defined by

$$\dot{\mathbf{B}} = \mathbf{G} \cdot \mathbf{B} \ , \tag{4.4}$$

with $\mathbf{G}$ an arbitrary, possibly time-dependent, traceless second rank tensor. (The trace $\mathbf{G} : \boldsymbol{\delta} = 0$ as a consequence of incompressibility.) The tools of the geometry of numbers (Gruber & Lekkerkerker, 1987) can be employed to investigate the existence of lattices compatible with isochoric time-independent linear deformations (i.e., $\dot{\mathbf{G}} = 0$ in (4.4)) (Adler, 1985; see also Ch. V). In these studies, appropriate sets of basis vectors $\mathbf{B}$ were derived for all two-dimensional flows, as well as for uniaxial extension (even though no strain-periodic lattices exist in this case (Chapter V;

Reinelt & Kraynik, 1990)). No universal procedure is available yet to find unit cells compatible with more general, fully three-dimensional flows, even though some examples are known.

The simulation method outlined hereafter is general, and can be applied for dynamic calculations. We shall, however, only present results in which the time evolution of the microstructure under influence of the flow is not followed. Hence we shall not be concerned with the compatibility of our lattices with any imposed deformation. Instead, the hydrodynamic transport properties are computed for a few chosen, representative configurations. As we shall explain in section 4.5 (see also Brady & Bossis, 1988), all the transport properties (sedimentation rates, self-diffusivities, hindered diffusion coefficients, viscosity and permeability tensors) can be calculated simultaneously by Stokesian dynamics. Results are reported for two types of microstructures in this work. In §4.6, we discuss crystalline geometries, characterized by perfect translational and orientational order. The entire dispersion is usually constructed using only one particle per unit cell. In a second part, §4.7, the transport properties of equilibrium hard-ellipsoid structures are calculated. They are averaged over several configurations generated by a Monte-Carlo procedure. Quite interestingly, we tracked the concentration dependence of several properties across the thermodynamic isotropic-to-nematic boundary for a few systems. As is to be expected from a first-order phase transition, a discontinuous jump occurs at that point.

The method proposed here is essentially a multipole moment technique for Stokes flow (Weinbaum *et al.*, 1990). The basic ideas were laid down in Ch. III, and the present chapter mostly concerns the adaptations needed for suspensions of infinite extent. It is now well documented (Batchelor, 1972; Brady *et al.*, 1988) that the slow decay of velocity disturbances in creeping flow lead to severely non-convergent expressions for many transport properties in an infinite suspension, unless the interactions are properly renormalized and the appropriate "backflow" integrals are subtracted from the results obtained by a simple-minded superposition of effects.

In the next section, we shall discuss the application of O'Brien's method (1979) to correct these aphysical convergence problems. We shall then give a brief overview of the methodology of Stokesian dynamics for prolate spheroids (but refer to the preceding chapter for details), and discuss the application of the Ewald summation technique (Ewald, 1921; Beenakker, 1986) to accelerate the convergence of the calculations. Sections 4.6 and 4.7 are illustrations of the method, and we close in §4.8 with a few comments about present and future work.

## 4.2 A convergent formulation of hydrodynamic interactions in unbounded dispersions

The Green's function for the governing equations (4.1) is called the Oseen tensor **J** (Ladyzhenskaya, 1963):

$$\mathbf{J}(\mathbf{x}) = \frac{\boldsymbol{\delta}}{r} + \frac{\mathbf{xx}}{r^3} \ , \tag{4.5}$$

with $r = |\mathbf{x}|$. According to (4.5), the velocity response at $\mathbf{x}$ due to a point force $\mathbf{f}$ at the origin is $\mathbf{u}(\mathbf{x}) = \mathbf{J} \cdot \mathbf{f}/8\pi\mu$. At zero Reynolds number, velocity disturbances thus decay inversely proportionally with distance in an unbounded Newtonian fluid of viscosity $\mu$. Hence a simple-minded calculation of the sedimentation rate of an infinite collection of particles by superposing the contributions of all bodies (since each of them acts as a point force to a first approximation) diverges as $R_\Gamma^2$, with $R_\Gamma$ a characteristic size of the macroscopic system. The origin of these convergence difficulties is now well understood, and several procedures have been devised for overcoming them (Batchelor, 1972; Batchelor & Green, 1972; Jeffrey, 1973; Hinch, 1977; O'Brien, 1979). O'Brien's method is most conveniently adapted to microstructurally detailed numerical simulations, since it does not rely on preaveraging the interactions to obtain well-posed, absolutely convergent expressions for the transport properties. Since the technique is well-documented (O'Brien, 1979; Brady *et al.*, 1988), we shall only briefly review the main lines of its reasoning here.

It starts by applying the boundary integral equation (Ladyzhenskaya, 1963) to the portion of a statistically homogeneous suspension delimited in thought by a

mathematical surface $\Gamma'$ lying entirely within the fluid:

$$\mathbf{u}(\mathbf{x}) = -\frac{1}{8\pi\mu}\sum_{p=1}^{N}\int_{A_p}\mathbf{J}(\mathbf{x}-\mathbf{y})\cdot\boldsymbol{\sigma}(\mathbf{y})\cdot\mathrm{d}\mathbf{A}_\mathbf{y} \tag{4.6}$$

$$-\frac{1}{8\pi\mu}\int_{\Gamma'}\mathbf{J}(\mathbf{x}-\mathbf{y})\cdot\boldsymbol{\sigma}(\mathbf{y})\cdot\mathrm{d}\mathbf{A}_\mathbf{y} - \frac{1}{8\pi\mu}\int_{\Gamma'}\mathbf{K}(\mathbf{x}-\mathbf{y}):\mathbf{u}(\mathbf{y})\mathrm{d}\mathbf{A}_\mathbf{y}\ .$$

The sum represents the effect of the $N$ particles included in the fluid domain, while the last two integrals give the contributions of the stress density $\boldsymbol{\sigma}$ and the velocity $\mathbf{u}$ at the surrounding surface $\Gamma'$. The infinitesimal vector $\mathrm{d}\mathbf{A}_\mathbf{y} = \mathbf{n}\mathrm{d}A_\mathbf{y}$ is an elementary surface patch with normal $\mathbf{n}$ pointing into the control volume $V$ containing the $N$ particles; the subscript $\mathbf{y}$ indicates that the integration is carried out with respect to the vector $\mathbf{y} \in \partial V$. The stress tensor

$$\boldsymbol{\sigma} = -p\boldsymbol{\delta} + \mu(\boldsymbol{\nabla}\mathbf{u} + {}^T\boldsymbol{\nabla}\mathbf{u})\ , \tag{4.7}$$

and

$$\mathbf{K} = -3\frac{\mathbf{xxx}}{r^5} = \frac{1}{2}(\boldsymbol{\nabla}\mathbf{J} + {}^T\boldsymbol{\nabla}\mathbf{J}) - \frac{\boldsymbol{\delta}\mathbf{x}}{r^3}\ . \tag{4.8}$$

Equation (4.6) is exact for rigid particles. If $\Gamma'$ is taken to be very large, so that $|\mathbf{x}-\mathbf{y}| \gg \ell$ for $\mathbf{y} \in \Gamma'$, with $\ell$ a characteristic separation between the particle centres, one may replace $\Gamma'$ by a smooth surface $\Gamma$ which cuts through both fluid and solid phases, and express the last two integrals in (4.6) in terms of suspension averaged values of $\boldsymbol{\sigma}$ and $\mathbf{u}$:

$$\int_{\Gamma'}\mathbf{J}(\mathbf{x}-\mathbf{y})\cdot\boldsymbol{\sigma}(\mathbf{y})\cdot\mathbf{n}'\,\mathrm{d}A'_\mathbf{y} + \int_{\Gamma'}\mathbf{K}(\mathbf{x}-\mathbf{y}):\mathbf{u}(\mathbf{y})\mathrm{d}\mathbf{A}'_\mathbf{y} = \tag{4.9}$$

$$\int_{\Gamma}\{\langle\boldsymbol{\sigma}\rangle:\mathbf{n}\mathbf{J} - n_\phi\langle\mathbf{Q}'\rangle\odot^3\mathbf{n}\boldsymbol{\nabla}_\mathbf{y}\mathbf{J}\}\,\mathrm{d}A_\mathbf{y} + \int_{\Gamma}\mathbf{K}:<\mathbf{u}>\mathrm{d}\mathbf{A}_\mathbf{y}\ .$$

We introduced $n_\phi$ for the number density of particles, and the notation $\odot^m$ for the $m$-fold nested contraction operator. The vector $\mathbf{n}$ is the normal to the smoothed surface $\Gamma$. The mean quadrupole $\mathbf{Q}'$ arises as a contribution from the "slices" of particles between the surfaces $\Gamma'$ and $\Gamma$ (Glendinning & Russel, 1982). It is defined as the second moment of the force density on the particle surface

$$\mathbf{Q}'_p = -\frac{1}{2}\int_{A_p}\mathbf{n}_p\cdot\boldsymbol{\sigma}[\mathbf{y}-\mathbf{x}_p][\mathbf{y}-\mathbf{x}_p]\mathrm{d}A_\mathbf{y}\ . \tag{4.10a}$$

By use of the divergence theorem, (4.9) can be converted into a volume integral of average forces

$$\mathbf{F}_p = -\int_{A_p} \boldsymbol{\sigma} \cdot \mathrm{d}\mathbf{A} \ , \tag{4.10b}$$

torques

$$\mathbf{T}_p = -\int_{A_p} (\mathbf{y} - \mathbf{x}_p) \wedge \boldsymbol{\sigma} \cdot \mathrm{d}\mathbf{A}_\mathbf{y} \ , \tag{4.10c}$$

stresslets

$$\mathbf{S}_p = -\int_{A_p} \frac{1}{2}\left[\mathbf{n}\cdot\boldsymbol{\sigma}\{\mathbf{y}-\mathbf{x}_p\} + \{\mathbf{y}-\mathbf{x}_p\}\boldsymbol{\sigma}\cdot\mathbf{n}\right] - \frac{1}{3}\boldsymbol{\delta}\left[\mathbf{n}\cdot\boldsymbol{\sigma}\cdot(\mathbf{y}-\mathbf{x}_p)\right] \mathrm{d}A_\mathbf{y} \ , \tag{4.10d}$$

and quadrupoles $\mathbf{Q}'_p$ (Brady *et al.*, 1988). Taking care to isolate the singularity at $\mathbf{x}$ by surrounding it by an infinitesimal shell enclosing a volume of fluid $V_\epsilon$, one then transforms (4.6) into

$$\mathbf{u}(\mathbf{x}) - \langle \mathbf{u}(\mathbf{x}) \rangle = \frac{2n_\phi}{15\mu}\left[2\langle \mathbf{Q}' : \boldsymbol{\delta} \rangle - \langle \boldsymbol{\delta} : \mathbf{Q}' \rangle\right] - \frac{1}{8\pi\mu}\sum_{p=1}^{N}\int_{A_p} \mathbf{J}\cdot\boldsymbol{\sigma}\cdot\mathrm{d}\mathbf{A}_\mathbf{y} \tag{4.11}$$

$$- \frac{n_\phi}{8\pi\mu}\int_{V-V_\epsilon} \{\langle \mathbf{F} \rangle \cdot \mathbf{J} + \langle \mathbf{T} \rangle \cdot \mathbf{R} + \langle \mathbf{S} \rangle : \mathbf{K} + \langle \mathbf{Q}' \rangle \odot^3 \boldsymbol{\nabla}\boldsymbol{\nabla}\mathbf{J}\} \, \mathrm{d}V_\mathbf{y} \ .$$

The tensor $\mathbf{R} = \frac{1}{2}\boldsymbol{\epsilon} : \boldsymbol{\nabla}\mathbf{J}$ is the propagator for a point torque (or rotlet) in Stokes flow. The limit as $V_\epsilon \to 0$ is implied in the second integral of (4.11). Although this is irrelevant for the first three terms in the kernel, it is necessary to exclude $\mathbf{x}$ from the integration domain in the calculation of the contribution from the average quadrupole, since the finite effect of this singularity at $\mathbf{x}$ is accounted for explicitly by the first term on the right hand side of the equation. One can now let the dimensions of the surface $\Gamma$ become larger and larger, since the expression (4.11) for the velocity at a point $\mathbf{x}$ in the suspension is absolutely convergent. Indeed, it is easy to see that the contribution of the $N$ particles cancels, in an average sense, the volume integral. Note that the velocity enters the formulation only relative to the flow field imposed on the dispersion. Equation (4.11) is thus expressed in a frame which moves and deforms so that the net volumetric flux through any surface

fixed in it is zero. Physically, the first term in the volume integral thus represents the backflow of fluid relative to these axes, driven by the pressure gradient which balances the excess average force $\langle \mathbf{F} \rangle$ exerted by the particles. By analogy, we shall refer to all the contributions from the volume integral as the "backflow."

The motion of the particles may then be related to the fluid velocity $\mathbf{u}$ given in (4.11) by means of Faxén relations. As explained in Ch. III (eq. (3.24a); see also Brenner, 1966), an ambient field $\mathbf{u}$ causes a force-free ellipsoid whose surface is defined by $\mathbf{A}_p^{-1} : (\mathbf{x} - \mathbf{x}_p)(\mathbf{x} - \mathbf{x}_p) = 1$ ($\mathbf{A}_p$ is a positive definite second rank tensor) to translate with a velocity $\mathbf{U}_p$ given by:

$$\mathbf{U}_p = \frac{\sinh D_p}{D_p} \mathbf{u}(\mathbf{x}_p) \tag{4.12a}$$

$$\text{with} \quad D_p = \sqrt{D_p^2} \qquad \text{and} \quad D_p^2 = \mathbf{A}_p : \nabla\nabla \; . \tag{4.12b}$$

As usual, $\sinh D_p / D_p$ stands for its series expansion, and $D_p^4 \mathbf{u} = D_p^2 (D_p^2 \mathbf{u})$, etc. By applying this formula to (4.11), and accounting for the force $\mathbf{F}_p$ acting on the particle, we obtain an absolutely convergent expression for the translational velocity of ellipsoids in a statistically homogeneous unbounded suspension (Appendix F):

$$\begin{aligned} \mathbf{U}_p - \langle \mathbf{u}(\mathbf{x}_p) \rangle = \frac{2 n_\phi}{15 \mu} \Big[ & 2 \langle \mathbf{Q} : \boldsymbol{\delta} \rangle - \langle \boldsymbol{\delta} : \mathbf{Q} \rangle + \frac{1}{3} (\mathbf{A}_p : \boldsymbol{\delta}) \langle \mathbf{F} \rangle - \frac{1}{6} \mathbf{A}_p \cdot \langle \mathbf{F} \rangle \\ & + \frac{1}{3} \langle (\mathbf{A} : \boldsymbol{\delta}) \mathbf{F} \rangle - \frac{1}{6} \langle \mathbf{A} \cdot \mathbf{F} \rangle \Big] + \mathbf{K}_{UF}^p \cdot \mathbf{F}_p - \frac{1}{8 \pi \mu} \sum_{q \neq p} \int_{A_q} \frac{\sinh D_p}{D_p} \mathbf{J} \cdot \boldsymbol{\sigma} \cdot \mathrm{d}\mathbf{A} \\ & - \frac{n_\phi}{8 \pi \mu} \int_{V - V_\epsilon} \Big\{ \big(1 + \frac{1}{6} D_p^2\big) \langle \mathbf{F} \rangle \cdot \mathbf{J} + \frac{1}{6} \langle \mathbf{F} \rangle \cdot \mathbf{J} \\ & + \langle \mathbf{T} \rangle \cdot \mathbf{R} + \langle \mathbf{S} \rangle : \mathbf{K} + \langle \mathbf{Q} \rangle \odot^3 \nabla\nabla \mathbf{J} \Big\} \, \mathrm{d}V \; . \end{aligned} \tag{4.13}$$

We expressed (4.13) in terms of the irreducible ellipsoidal quadrupole $\mathbf{Q} = \mathbf{Q}' - \frac{1}{6} \mathbf{F}\mathbf{A}$ (Appendix D), and neglected contributions which decay as $O(|\mathbf{x} - \mathbf{y}|^{-4})$ in the volume integral. The dyadic $\mathbf{K}_{UF}^p$ relates the velocity of the spheroid to the force it exerts on the fluid, and is a well-known material constant (Brenner, 1964). Expressions analogous to (4.13) can be obtained for the angular velocity relative to

the vorticity of the imposed flow and the (zero) rate of deformation relative to the impressed rate of strain. A similar derivation is also possible for $\nabla\nabla\mathbf{u}_{|\mathbf{x}_p}$ (the velocity counterpart of the quadrupole), but, as explained in Brady *et al.* (1988), this is only marginally necessary since all irreducible second moments are induced by particle interactions and are therefore of small amplitude. Expressions for higher multipoles are convergent even without applying O'Brien's method and do not need to be considered.

As mentioned in the introduction to this chapter, we approximate the microstructure of an unbounded, statistically homogeneous suspension by periodically replicating $N$ spheroids in space. It was demonstrated by Brady *et al.* (1988) that the application of the Ewald summation technique to construct the grand resistance tensor for such spatially periodic dispersions correctly accounts for hydrodynamic interactions, and yields an expression which corresponds term by term with the "renormalized" formulation obtained using O'Brien's ideas. In periodic dispersions obeying (4.3), particle interactions can thus be computed as sums over the lattice $\mathcal{L}$. Their evaluation is dramatically accelerated by an ingenious technique due to Ewald (1921). In essence, the slowly converging lattice sum is replaced by two complementary summations: one consists of terms which decay rapidly with distance, ensuring a speedy convergence; the other is Fourier transformed and calculated in reciprocal space. Nijboer & DeWette (1957) describe judicious ways to split the original lattice sum so that exponential rates of convergence are achieved for summands which decay only algebraically with distance. The first application of this method to the Oseen tensor (4.5) is due to Beenakker (1986). Brady *et al.* (1988) extended his approach and lifted the restriction $\langle\mathbf{F}\rangle = 0$ that he had placed on his derivation. We refer to their papers for details concerning this technique (see also the next section).

## 4.3 Stokesian dynamics methodology for unbounded suspensions of prolate spheroids

The linearity of the Stokes equations guarantees the existence of a "grand resistance

tensor" $\mathcal{R}$ connecting the moments of the stress density on the particle surfaces (i.e., the force, torque, stresslet and higher multipoles) to the motion of the particles relative to the fluid. We chose to truncate the multipole expansion after the first two moments, so that 11 unknowns are associated with each particle. These typically are the three components of the velocity, the three components of the rotation rate, and the five independent elements of the stresslet (a symmetric, traceless second rank tensor, see (4.10d)). Therefore, $\mathcal{R}$ is an $11N \times 11N$ tensor so that

$$\begin{pmatrix} \boldsymbol{F} \\ \boldsymbol{T} \\ \boldsymbol{S} \end{pmatrix} = \mathcal{R} \otimes \begin{pmatrix} \boldsymbol{U} - \boldsymbol{U}_\infty \\ \boldsymbol{\Omega} - \boldsymbol{\Omega}_\infty \\ -\boldsymbol{E}_\infty \end{pmatrix} = \begin{pmatrix} \boldsymbol{R}_{FU} & \boldsymbol{R}_{TU} & \boldsymbol{R}_{SU} \\ \boldsymbol{R}_{F\Omega} & \boldsymbol{R}_{T\Omega} & \boldsymbol{R}_{S\Omega} \\ \boldsymbol{R}_{FE} & \boldsymbol{R}_{TE} & \boldsymbol{R}_{SE} \end{pmatrix} \otimes \begin{pmatrix} \boldsymbol{U} - \boldsymbol{U}_\infty \\ \boldsymbol{\Omega} - \boldsymbol{\Omega}_\infty \\ -\boldsymbol{E}_\infty \end{pmatrix} . \quad (4.14)$$

The operator $\otimes$ signifies the appropriate contraction. The vectors of length $3N$ $\boldsymbol{U}, \boldsymbol{\Omega}, \boldsymbol{F}$, and $\boldsymbol{T}$ , and the $3N \times 3$ matrix $\boldsymbol{S}$ group the translational and angular velocities of all $N$ particles, and the forces, torques and stresslets that they exert respectively. Similarly, the undisturbed ambient fluid velocity, vorticity and rate of strain at the geometric centres of the spheroids are lumped into $\boldsymbol{U}_\infty, \boldsymbol{\Omega}_\infty$ and $\boldsymbol{E}_\infty$. Standard arguments in zero-Reynolds-number hydrodynamics (Happel & Brenner, 1973) show that $\mathcal{R}$ is positive-definite and symmetric. More importantly, it is a purely geometric quantity, fully determined by the instantaneous configuration (and shape) of the particles. The greatest asset of Stokesian dynamics is its efficient and accurate algorithm to approximate this resistance tensor. The method was first developed for suspensions of spheres (Durlofsky *et al.*, 1987), and we showed in the preceding chapter how it can be applied to a finite number of prolate spheroids. We now extend the approach to unbounded dispersions.

The first step in the procedure consists in forming the grand mobility tensor $\mathrm{M} = \mathcal{R}^{-1}$:

$$\begin{pmatrix} \boldsymbol{U} - \boldsymbol{U}_\infty \\ \boldsymbol{\Omega} - \boldsymbol{\Omega}_\infty \\ -\boldsymbol{E}_\infty \end{pmatrix} = \mathrm{M} \otimes \begin{pmatrix} \boldsymbol{F} \\ \boldsymbol{T} \\ \boldsymbol{S} \end{pmatrix} = \begin{pmatrix} \boldsymbol{M}_{UF} & \boldsymbol{M}_{UT} & \boldsymbol{M}_{US} \\ \boldsymbol{M}_{\Omega F} & \boldsymbol{M}_{\Omega T} & \boldsymbol{M}_{\Omega S} \\ \boldsymbol{M}_{EF} & \boldsymbol{M}_{ET} & \boldsymbol{M}_{ES} \end{pmatrix} \otimes \begin{pmatrix} \boldsymbol{F} \\ \boldsymbol{T} \\ \boldsymbol{S} \end{pmatrix} . \quad (4.15)$$

We explained previously (Ch. III) how to construct M for a finite number of spheroids by combining the singularity representation for the disturbance veloc-

ity (Chwang & Wu, 1974, 1975) with the non-local formulation of the Faxén laws derived from the work of Kim (1985). The $\mathbf{M}_{UF}^{pq}$-coupling, for instance, which links the translational velocity of particle $p$ to the force exerted by $q$, can be written as:

$$\mathbf{M}_{UF}^{pq} = \frac{1}{32\pi\mu c_p c_q} \int_{-c_p}^{c_p} \{1 + (c_p^2 - \xi_p^2)\frac{1-e_p^2}{4e_p^2}\nabla_p^2\} \int_{-c_q}^{c_q} \{1 + (c_q^2 - \xi_q^2)\frac{1-e_q^2}{4e_q^2}\nabla_q^2\}\mathbf{J}(\boldsymbol{\xi}_p - \boldsymbol{\xi}_q)\,\mathrm{d}\xi_q\,\mathrm{d}\xi_p \ . \tag{4.16a}$$

The geometry of the spheroids is characterized by the distance $c_q$ from their centre to the foci of the generating ellipse, and by their eccentricity $e_q$, defined as $c_q/a_q = \sqrt{(1 - b_q^2/a_q^2)}$, with $a_q$ and $b_q$ the lengths of the major and minor semi-axes respectively. The vector $\boldsymbol{\xi}_q = \mathbf{x}_q + \xi_q \mathbf{d}_q$, with $\mathbf{d}_q$ the unit vector along the axis of the particle. One sees from (4.16a) that, as far as $\mathbf{M}_{UF}$ is concerned, each spheroid is equivalent to a line of stokeslets with uniform density, supplemented by potential dipoles, $\nabla^2\mathbf{J}$, distributed between the foci according to a parabolic density profile. As for spheres, these quadrupolar pieces reflect the finite cross-section of the particle. As an alternative to (4.16a), a symbolic operator representation for the mobility elements can be used to get:

$$\mathbf{M}_{UF}^{pq} = \frac{1}{8\pi\mu}\frac{\sinh D_p}{D_p}\frac{\sinh D_q}{D_q}\mathbf{J}(\mathbf{x}_p - \mathbf{x}_q) \ . \tag{4.16b}$$

The operator $D_p$ has been defined in (4.12b), which reduces to $D_p^2 = c_p^2[(\mathbf{d}_p \cdot \nabla)^2 + (1 - e_p^2)/e_p^2\nabla^2]$ for axisymmetric spheroids. The non-local description (4.16a) and the infinite operator series (4.16b) are fully equivalent (eq. (3.27); Kim, 1986; Kim & Arunachalam, 1987). The former, however, is to be preferred for numerical evaluation, except when the particles $p$ and $q$ are very distant (see §4.4). The entire grand mobility tensor $\mathbf{M}$ is built up of similar double integrals.

For unbounded systems, the grand mobility tensor becomes, in principle, of infinite dimension. Periodic structures, however, in which the configuration of $N$ chosen spheroids is replicated on a lattice, are amenable to a simpler treatment,

provided all "images" of a given particle are subject to the same force and torque‡ (i.e., $\forall\{z\}$, $\mathbf{F}_{p+\{z\}} = \mathbf{F}_p$ with $\mathbf{F}_{p+\{z\}}$ the force exerted by the particle at $\mathbf{x}_p + \boldsymbol{x}_{\{z\}}$, and a similar condition on $\mathbf{T}_p$.) In these circumstances, the dynamics of the entire dispersion may be described by a $N \times N$ mobility tensor $\widetilde{\mathbf{M}}$.

To calculate $\widetilde{\mathbf{M}}^{pq}_{UF}$ for such a periodic system, consider a force-free spheroid $p$ embedded in a lattice of spheroids $q$, each exerting a force $\mathbf{F}_q$ on the fluid, which would otherwise be quiescent. The velocity of the test particle $p$ is given by (4.13) as:

$$\begin{aligned}\mathbf{U}_p =& \frac{2n_\phi}{15\mu}\Big[2\mathbf{Q}_q : \boldsymbol{\delta} - \boldsymbol{\delta} : \mathbf{Q}_q + \frac{1}{3}(\mathbf{A}_p : \boldsymbol{\delta})\mathbf{F}_q - \frac{1}{6}\mathbf{A}_p \cdot \mathbf{F}_q + \frac{1}{3}(\mathbf{A}_q : \boldsymbol{\delta})\mathbf{F}_q - \frac{1}{6}\mathbf{A}_q \cdot \mathbf{F}_q\Big] \\ & - \frac{1}{8\pi\mu}\sum_{\{z\}} \frac{\sinh D_p}{D_p} \int_{A_{q+\{z\}}} \mathbf{J} \cdot \boldsymbol{\sigma} \cdot \mathrm{d}\mathbf{A} \qquad (4.17) \\ & - \frac{n_\phi}{8\pi\mu}\int_{V-V_\epsilon} \big\{(1 + \frac{1}{6}D_p^2 + \frac{1}{6}D_q^2)\mathbf{F}_q \cdot \mathbf{J} + \mathbf{S}_q : \mathbf{K} + \mathbf{Q}_q \odot^3 \boldsymbol{\nabla}\boldsymbol{\nabla}\mathbf{J}\big\}\,\mathrm{d}V\ .\end{aligned}$$

We have assumed that no external torque acts on the particles and implicitly restrict the summation to those particles of the lattice whose centre lies in $V$. The integral of the stress density on the surfaces $A_q$ may then be expanded into irreducible moments $\mathbf{I}_q^{(m)}$ as follows (Appendix D), in order to isolate the effect of the force $\mathbf{F}_q$:

$$\begin{aligned}& -\int_{A_q} \mathbf{J}(\mathbf{x} - \mathbf{x}_q) \cdot \boldsymbol{\sigma} \cdot \mathrm{d}\mathbf{A} \qquad (4.18) \\ & \quad = \sum_{m=0}^{\infty} (2m+1)!!\mathbf{I}_q^{(m)} \odot^{m+1} \left[\Big(\frac{1}{D_q}\frac{\mathrm{d}}{\mathrm{d}D_q}\Big)^m \frac{\sinh D_q}{D_q}\right] \overbrace{\boldsymbol{\nabla}_{\mathbf{z}}}^{\times m} \mathbf{J}(\mathbf{x} - \mathbf{z})|_{\mathbf{z}=\mathbf{x}_q} \\ & \quad = \mathbf{F}_q \cdot \frac{\sinh D_q}{D_q}\mathbf{J}(\mathbf{x} - \mathbf{x}_q) + \ldots\end{aligned}$$

The irreducible ellipsoidal moment $\mathbf{I}_q^{(m)}$ is defined as the projection of the $m^{\text{th}}$ moment of the stress density on the particle surface for which all contractions by $\mathbf{A}_q^{-1}$

‡ If the problem is formulated as a resistance rather than a mobility problem, the imposed translational and angular velocities must be the same for all "images" when measured relative to the ambient flow (so that the integrity of the periodic microstructure is preserved while the lattice deforms affinely with the flow).

in any two of its last $m$ indices yields zero (Appendix D). The notation $(2m+1)!!$ is standard and stands for $(2m+1)!/(2^m m!)$ (Abramowitz & Stegun, 1970); $\overbrace{\nabla}^{\times m}$ is shorthand for the direct product of $m$ nabla operators, and the subscript $\mathbf{z}$ on $\nabla_{\mathbf{z}}$ implies that the derivative is taken with respect to $\mathbf{z}$.

Concentrating on the direct contribution of the force $\mathbf{F}_q$ to $\mathbf{U}_p$, we find

$$\widetilde{\mathbf{M}}_{UF}^{pq} = \frac{n_\phi}{45\mu}\Big[2(\mathbf{A}_p : \boldsymbol{\delta})\boldsymbol{\delta} - \mathbf{A}_p + 2(\mathbf{A}_q : \boldsymbol{\delta})\boldsymbol{\delta} - \mathbf{A}_q\Big] \tag{4.19}$$
$$+ \frac{1}{8\pi\mu}\sum_{\{z\}} \frac{\sinh D_p}{D_p}\frac{\sinh D_q}{D_q}\mathbf{J}(\mathbf{x}_p - \mathbf{x}_q - \boldsymbol{x}_{\{z\}}) - \frac{n_\phi}{8\pi\mu}\int_{V-V_\epsilon}\big(1 + \frac{1}{6}D_p^2 + \frac{1}{6}D_q^2\big)\mathbf{J}\,\mathrm{d}V\ .$$

As shown by Beenakker (1986), the lattice sum is most efficiently evaluated by noting that

$$\mathbf{J}(\mathbf{x}) = (\nabla^2\boldsymbol{\delta} - \boldsymbol{\nabla}\boldsymbol{\nabla})|\mathbf{x}| \tag{4.20}$$

and writing

$$\frac{1}{8\pi\mu}\frac{\sinh D_p}{D_p}\frac{\sinh D_q}{D_q}\mathbf{J}(\mathbf{x}_p - \mathbf{x}_q - \boldsymbol{x}_{\{z\}}) = \mathbf{M}_{UF}^{p[q+\{z\}]} = \mathbf{M}_1^{p[q+\{z\}]} + \mathbf{M}_2^{p[q+\{z\}]}\ , \tag{4.21a}$$

$$\text{with} \qquad \mathbf{M}_1^{pq} = \frac{1}{8\pi\mu}\frac{\sinh D_p}{D_p}\frac{\sinh D_q}{D_q}(\nabla^2\boldsymbol{\delta} - \boldsymbol{\nabla}\boldsymbol{\nabla})\big(r_{pq}\mathrm{erfc}(\mathcal{E}r_{pq})\big)\ , \tag{4.21b}$$

$$\text{and} \qquad \mathbf{M}_2^{pq} = \frac{1}{8\pi\mu}\frac{\sinh D_p}{D_p}\frac{\sinh D_q}{D_q}(\nabla^2\boldsymbol{\delta} - \boldsymbol{\nabla}\boldsymbol{\nabla})\big(r_{pq}\mathrm{erf}(\mathcal{E}r_{pq})\big)\ . \tag{4.21c}$$

We introduced the succinct notation $r_{pq} = |\mathbf{x}_p - \mathbf{x}_q|$. The sum of $\mathbf{M}_1^{p[q+\{z\}]}$ over all $\{z\}$ is performed in real space, while the lattice summation of $\mathbf{M}_2$ is best carried out in reciprocal space by applying the Poisson summation formula (Nijboer & de Wette, 1957) (see §4.4). The parameter $\mathcal{E}$ dictates the rate of convergence of the two sums (see §4.4). Using the Ewald technique, equation (4.19) can be converted into

$$\widetilde{\mathbf{M}}_{UF}^{pq} = \sum_{\{z\}}\mathbf{M}_1^{p[q+\{z\}]} + \frac{1}{|\mathbf{B}|}\sum_{\{\zeta\}\neq 0}\cos\Big(\mathbf{k}_{\{\zeta\}}\cdot(\mathbf{x}_p - \mathbf{x}_q)\Big)\widehat{\mathbf{M}}_2^{pq}(\mathbf{k}_{\{\zeta\}})\ , \tag{4.22}$$

where $\mathbf{k}_{\{\zeta\}} = \zeta_1\mathbf{k}_1 + \zeta_2\mathbf{k}_2 + \zeta_3\mathbf{k}_3$ are the points of the reciprocal lattice. The basis vectors $\mathbf{k}_i$ are defined such that $\mathbf{k}_i \cdot \mathbf{b}_j = 2\pi\delta_{ij}$, with $\delta_{ij}$ the Kronecker delta. $\widehat{\mathbf{M}}_2^{pq}$ is

the Fourier transform $\int \exp(-i\mathbf{k}\cdot\mathbf{r})\mathbf{M}_2(\mathbf{r})\,d\mathbf{r}$. As explained for spheres in Brady *et al.* (1988), one can show that the "backflow" volume integral and the first term on the right hand side of (4.19) (proportional to $n_\phi$) are cancelled by the limit as $\mathbf{k}_{\{\zeta\}} \to 0$ of $\widehat{\mathbf{M}}_2^{pq}(\mathbf{k}_{\{\zeta\}})$ (Appendix F). The origin of the lattice in $k$-space is thus omitted from the sum.

All the elements of the grand mobility tensor (4.15) can be constructed by performing similar lattice summations. A few numerical aspects of this procedure will be discussed in the next section. Heed is needed in the case of the hydrodynamic coupling $\widetilde{\mathbf{M}}_{UF}^{pp}$ between a particle and its own images, since the effect of the force acting on the "reference" spheroid is accounted for separately. In order not to include the self-term twice in the mobility interactions, one must therefore remove the "image" at $\mathbf{x}_p + \boldsymbol{x}_{\{0\}}$ from the lattice sum by excluding the central unit cell from the sum of $\mathbf{M}_1$ and subtracting its contribution to the summation in reciprocal space. In other words, for $p = q$, (4.22) is replaced by

$$\widetilde{\mathbf{M}}_{UF}^{pp} = \mathbf{K}_{UF}^{p} + \sum_{\{z\}\neq 0} \mathbf{M}_1^{p[p+\{z\}]} + \frac{1}{|\mathbf{B}|} \sum_{\{\zeta\}\neq 0} \widehat{\mathbf{M}}_2^{pp}(\mathbf{k}_{\{\zeta\}}) - \mathbf{M}_2^{pp}\big|_{\mathbf{r}=0} \,. \tag{4.23}$$

Symmetry arguments can be invoked to prove that there is no coupling between even derivatives of the spheroid's velocity relative to the undisturbed flow at its geometric centre, and odd moments of the stress density on its surface. Hence $\widetilde{\mathbf{M}}_{UL}^{pp}$ and $\widetilde{\mathbf{M}}_{US}^{pp}$ are identically zero (as well as $\widetilde{\mathbf{M}}_{\Omega F}^{pp}$ and $\widetilde{\mathbf{M}}_{EF}^{pp}$ by virtue of Lorentz' reciprocal theorem). This à priori knowledge helps avoid extraneous calculations during the construction of the grand mobility tensor. As shown in Appendix E, the amount of required computations can be further reduced by using the identities

$$\mathbf{M}_{UT}^{pq} = \tfrac{1}{2}\boldsymbol{\varepsilon}\cdot(\boldsymbol{\delta} : \mathbf{M}_{US}^{pq}) \,, \tag{4.24a}$$

$$[\mathbf{M}_{\Omega T}^{pq}]_{ij} = -[\mathbf{M}_{ES}^{pq}]_{iklj}\boldsymbol{\delta}_{kl} + \tfrac{1}{2}[\mathbf{M}_{ES}^{pq}]_{mkln}\boldsymbol{\delta}_{kl}\boldsymbol{\delta}_{mn}\boldsymbol{\delta}_{ij} \,, \tag{4.24b}$$

$$\mathbf{M}_{\Omega S}^{pq} = \boldsymbol{\varepsilon}\cdot\mathbf{M}_{\Omega T}^{pq} + (\boldsymbol{\varepsilon}\cdot\mathbf{M}_{\Omega T}^{pq})^T \,. \tag{4.24c}$$

Only the last two relations are also useful when $p = q$. It is clear that they hold for $\widetilde{\mathbf{M}}$ as well.

The grand mobility tensor for $N$ periodically replicated prolate spheroids is inverted to yield a "far-field" estimate of the resistance tensor $\boldsymbol{\mathcal{R}}$. Lubrication interactions between close particles are then included in a pair-wise additive manner to the inverse of the grand mobility tensor, as in the version of Stokesian dynamics for a finite number of spheroids (Ch. III):

$$\boldsymbol{\mathcal{R}} \simeq \mathbf{R} = \widetilde{\mathbf{M}}^{-1} + \mathbf{R}_{\text{lub}} \ . \tag{4.25}$$

All the resistance functions which become singular when two ellipsoids touch can be derived to $O(1)$ from Chapter II. The only caveat is that situations may now occur in which a rod is simultaneously in the vicinity of more than one image of another particle. This is merely a geometric and programmatorial complication, however, and does not add any conceptual difficulties. Also, unlike spheres, lubrication interactions between a spheroid and its own images (on a dense lattice) may result in a net torque or stresslet.

We expanded in §3.2 on the validity and accuracy of the scheme used here to approximate the grand resistance tensor, *viz.* using pair-wise additivity of velocities to form the a far-field estimate of the mobility tensor, and pair-wise additivity of forces to preserve the large, localized lubrication stresses between close pairs of particles. We shall not repeat these arguments here (see also Durlofsky *et al.*, 1987). Dynamic simulations simply solve (4.14) for the motion of the particles by balancing the hydrodynamic and external forces and torques, and integrate the trajectories (relative to the lattice which deforms affinely with the flow) to update the microstructure. Because the spheroids are non-Brownian in this work, their paths are fully deterministic. The intricacies associated with thermal motion can be addressed by the methods developed for spheres (Bossis & Brady, 1989), and form a subject for further study. Since $\widetilde{\mathbf{M}}$ is determined by the configuration of the particles, it needs, in principle, to be evaluated at each time step. This may be

deferred in some instances to maximize computer time rentability, as discussed in Durlofsky *et al.* (1987).

## 4.4 Numerical aspects of the lattice summation using the Ewald technique

A few computational details are discussed in this section to indicate how the operation intensive task of forming the mobility tensor is managed in practice. We first return to the non-local description of the mobility interactions, (4.16a)‡, and insert the representation (4.20) of the Oseen tensor **J**:

$$\mathbf{M}_{UF}^{pq} = \frac{1}{32\pi\mu c_p c_q}\int_{-c_p}^{c_p}\{1+(c_p^2-\xi_p^2)\frac{1-e_p^2}{4e_p^2}\nabla_p^2\} \qquad (4.26)$$
$$\int_{-c_q}^{c_q}\{1+(c_q^2-\xi_q^2)\frac{1-e_q^2}{4e_q^2}\nabla_q^2\}(\nabla^2\boldsymbol{\delta}-\boldsymbol{\nabla}\boldsymbol{\nabla})(r_{pq})\,\mathrm{d}\xi_q\,\mathrm{d}\xi_p\ .$$

Since the kernel in (4.26) is a function of $r_{pq}$ only, $\boldsymbol{\nabla}_p = -\boldsymbol{\nabla}_q$, and hence the operator after the first integral may be transferred to the innermost integral. To minimize the required algebra, we then simplify the expression for $\mathbf{M}_{UF}^{pq}$ by making use of the identity $\nabla^4\mathbf{J}=0$ *before* we apply the Ewald summation formula, and therefore redefine $\mathbf{M}_1^{pq}$ and $\mathbf{M}_2^{pq}$ as follows:

$$\begin{aligned}\mathbf{M}_{UF}^{pq} =& \frac{1}{32\pi\mu c_p c_q}\int_{-c_p}^{c_p}\int_{-c_q}^{c_q}\Big\{1+\Big[(c_p^2-\xi_p^2)\frac{(1-e_p^2)}{4e_p^2}\\ &+(c_q^2-\xi_q^2)\frac{(1-e_q^2)}{4e_q^2}\Big]\nabla^2\Big\}(\nabla^2\boldsymbol{\delta}-\boldsymbol{\nabla}\boldsymbol{\nabla})(r_{pq})\,d\xi_q\,d\xi_p \qquad (4.27)\\ =&\mathbf{M}_1^{pq}+\mathbf{M}_2^{pq}\ ,\end{aligned}$$

with

$$\begin{aligned}\mathbf{M}_1^{pq} =& \frac{1}{32\pi\mu c_p c_q}\int_{-c_p}^{c_p}\int_{-c_q}^{c_q}\Big\{1+\Big[(c_p^2-\xi_p^2)\frac{(1-e_p^2)}{4e_p^2}\\ &+(c_q^2-\xi_q^2)\frac{(1-e_q^2)}{4e_q^2}\Big]\nabla^2\Big\}\big(\nabla^2\boldsymbol{\delta}-\boldsymbol{\nabla}\boldsymbol{\nabla}\big)\big(r_{pq}\,\mathrm{erfc}(\mathcal{E}r_{pq})\big)\,d\xi_q\,d\xi_p\ . \qquad (4.28a)\end{aligned}$$

‡ We shall illustrate several points using the $\mathbf{M}_{UF}^{pq}$-coupling in this section, but the same principles can be applied to all elements of the grand mobility tensor.

The definition of $\mathbf{M}_2^{pq}$ simply requires that one substitutes the error function erf for erfc. The mathematical equivalence of the non-local description of interactions and of their symbolic operator representation, alluded to at the beginning of §4.3 with the expressions (4.16a) and (4.16b), can also be applied here to get

$$\mathbf{M}_1^{pq} = \frac{1}{8\pi\mu}\Big\{\frac{\sinh\Delta_p}{\Delta_p}\frac{\sinh\Delta_q}{\Delta_q} + c_p^2\frac{1-e_p^2}{2e_p^2}\Big(\frac{1}{\Delta_p}\frac{\mathrm{d}}{\mathrm{d}\Delta_p}\frac{\sinh\Delta_p}{\Delta_p}\Big)\Big(\frac{\sinh\Delta_q}{\Delta_q}\Big)\nabla^2 \quad (4.28b)$$
$$+ c_q^2\frac{1-e_q^2}{2e_q^2}\Big(\frac{\sinh\Delta_p}{\Delta_p}\Big)\Big(\frac{1}{\Delta_q}\frac{\mathrm{d}}{\mathrm{d}\Delta_q}\frac{\sinh\Delta_q}{\Delta_q}\Big)\nabla^2\Big\}\big(\nabla^2\boldsymbol{\delta} - \boldsymbol{\nabla}\boldsymbol{\nabla}\big)\big(r_{pq}\,\mathrm{erfc}(\mathcal{E}r_{pq})\big)\ ,$$

with $\Delta_p = c_p\mathbf{d}_p\cdot\boldsymbol{\nabla}_p$. Equation (4.28a) shows that $\mathbf{M}_1^{pq}$ may be calculated as a double integral over the rectangular domain $[-c_p, c_p]\times[-c_q, c_q]$. At small and moderate separations ($r_{pq} = O(c_p + c_q)$), the kernel often displays saddlepoints, with sharp peaks and deep valleys, making the cubature difficult. We found it imperative to use adaptive integration schemes (Kahaner & Rechards, 1987) in order to achieve sufficient accuracy to guarantee the positive definiteness of the numerical approximation to $\widetilde{\mathbf{M}}$. Note that this test is especially stringent, since the mobility tensor becomes increasingly ill-conditioned as the particles become more slender, reflecting the fact that fibres experience less viscous resistance than spheres as they move, and hence dissipate less energy.

The formulation (4.28b), although equivalent in principle, works poorly except at large distances. A truncation of the infinite operator series at a chosen order in $1/r_{pq}$ essentially approximates the spheroids by a set of point singularities situated at their centres: to $O(r_{pq}^{-1})$, the particles act as point forces; the first effects of their relative orientation come from including the dipoles; point quadrupoles are added next, etc. Mobility elements are then calculated according to (4.28b) as an alternating series. (Note that $\boldsymbol{\nabla}r_{pq} = (\mathbf{x}_p - \mathbf{x}_q)/r_{pq}$, and that the sign of $\frac{\mathrm{d}^{n+1}}{\mathrm{d}r^{n+1}}\frac{1}{r}$ is opposite that of $\frac{\mathrm{d}^n}{\mathrm{d}r^n}\frac{1}{r}$.) Although this series is convergent at all distances, it is inadequate for numerical purposes when the ellipsoids are close enough to "sense" each other's elongated shape, i.e., roughly speaking, when the spheres circumscribing the rods intersect. In those cases, for $r_{pq}$ small, the expansion behaves like the

Taylor series of $\exp(-r_{pq}^{-1})$ about the point at infinity: the magnitude of the terms goes through a maximum which far exceeds the numerical value of the final result, and the loss of significant digits on the computer makes the total of the addition worthless, even though the theoretical radius of convergence of the series is infinite. Hence the truncated moments expansion (4.28b) is potentially useful only at large distances $r_{pq}$, where convergence is rapid and necessitates less work than the numerical cubature of (4.28a).

Slender body theory shows that a force-free rod immersed in an axisymmetric straining flow and aligned with the principal direction of extension behaves as a line distribution of Stokeslets whose magnitude varies linearly with position (Batchelor, 1970 a). Chwang & Wu (1975), however, give an exact Stokes flow solution for the special case of spheroidal rods using a parabolic distribution of dipoles along the symmetry axis, complemented by a biquadratic profile of octupoles reflecting the finite thickness of the particle. Both results may be reconciled by partial integration, as shown below. We shall then explain the advantages of each representation for computational aims.

The singularity representation for the fluid disturbance velocity due to a stationary isolated ellipsoid in a purely extensional flow characterized by the rate-of-strain tensor $\mathbf{E}$ infinitely far away from the particle, is (Kim, 1985)

$$\mathbf{u}(\mathbf{x}) = \mathbf{E}\cdot\mathbf{x} - \frac{\alpha_1}{2}\mathbf{E} : \left[\mathbf{d}_p\mathbf{d}_p \wedge \int_{-c_p}^{c_p} (c_p^2 - \xi_p^2)\boldsymbol{\nabla}\wedge\mathbf{J}(\mathbf{x}-\boldsymbol{\xi}_p)\,\mathrm{d}\xi_p\right] \tag{4.29a}$$

$$+ \mathbf{E} : \mathbf{K}_{SE}^p : \int_{-c_p}^{c_p} (c_p^2 - \xi_p^2)\{1 + (c_p^2-\xi_p^2)\frac{1-e_p^2}{8e_p^2}\nabla^2\}\tfrac{1}{2}(\boldsymbol{\nabla} + {}^T\boldsymbol{\nabla})\mathbf{J}(\mathbf{x}-\boldsymbol{\xi}_p)\,\mathrm{d}\xi_p\ .$$

The shape specific tetradic $\mathbf{K}_{SE}^p$ and the coefficient $\alpha_1$ are known for spheroids (Appendix J; Chwang & Wu, 1975; Kim, 1985). We decompose $\boldsymbol{\nabla} = \mathbf{d}_p(\mathbf{d}_p\cdot\boldsymbol{\nabla}) + \boldsymbol{\nabla}_\perp =$

$\mathbf{d}_p \frac{\partial}{\partial \xi_p} + \nabla_\perp$ and integrate by parts:

$$\begin{aligned}\mathbf{u} = \mathbf{E}\cdot\mathbf{x} + \mathbf{E} : \mathbf{K}^p_{SE} : 2\int_{-c_p}^{c_p} \xi_p \{1 + (c_p^2 - \xi_p^2)\frac{1-e_p^2}{4e_p^2}\nabla^2\}\tfrac{1}{2}(\mathbf{d}_p\mathbf{J} + {}^T\mathbf{d}_p\mathbf{J})\,\mathrm{d}\xi_p \\ + \mathbf{E} : \mathbf{K}^p_{SE} : \int_{-c_p}^{c_p} (c_p^2 - \xi_p^2)\{1 + (c_p^2 - \xi_p^2)\frac{1-e_p^2}{8e_p^2}\nabla^2\}\tfrac{1}{2}(\nabla_\perp + {}^T\nabla_\perp)\mathbf{J}\,\mathrm{d}\xi_p \\ - \alpha_1\mathbf{E} : \left[\mathbf{d}_p\mathbf{d}_p \wedge \int_{-c_p}^{c_p} \xi_p \mathbf{d}_p \wedge \mathbf{J}\,\mathrm{d}\xi_p\right] \\ - \frac{\alpha_1}{2}\mathbf{E} : \left[\mathbf{d}_p\mathbf{d}_p \wedge \int_{-c_p}^{c_p} (c_p^2 - \xi_p^2)\nabla_\perp \wedge \mathbf{J}\,\mathrm{d}\xi_p\right].\end{aligned} \tag{4.29b}$$

In the limit $e_p \to 1$, the first and the third integrals in (4.29b) equate the effect of the spheroid with that of a linear distribution of Stokeslets, as predicted by slender body theory. Although (4.29b) is "messier" than (4.29a) (which is bad enough already!), it turns out to be useful when computing the interactions of fibres in close proximity to one another. By assigning the largest weight to the ends of the particle, this representation emphasizes the elongated nature of the rods, in contrast to the formulation (4.29a), where the density of the dipoles vanishes at the extremities. In practice therefore, we calculate the summand $\mathbf{M}_1^{pq}$ using either the infinite operator series (4.28b) when $r_{pq} \gg O(c_p + c_q)$, or the non-local singularity representation (4.28a) or its variant (4.29b), depending on circumstances, when $r_{pq} = O(c_p + c_q)$.

An alternative method for very close pairs of particles rests on the observation that (4.28a) is well approximated, for small $r_{pq} \ll 1/\mathcal{E}$, by substituting $r_{pq}$ for $r_{pq}\mathrm{erfc}(\mathcal{E}r_{pq})$. The advantage of this procedure is that the innermost integration can then be carried out analytically, as shown in Ch. III (eq. (3.33) for instance), since this amounts to calculating the interactions between these two rods as if they were isolated, without applying the Ewald technique. Only the correction due to $r_{pq}\mathrm{erf}(\mathcal{E}r_{pq})$ now requires a numerical cubature. The savings result from replacing a difficult two-dimensional integration by a simpler quadrature (in one variable) which gives the dominant contribution, plus a cubature which is much less

demanding than the original one, since it is only a corrective step, to which the global result is not very sensitive.

It will be obvious from the discussion above that summing $\mathbf{M}_1$ is a computer-intensive operation. Fortunately, the algebra is much simpler for $\mathbf{M}_2$. The sum is best carried out in reciprocal space by relying on the following identity for an arbitrary function $g$ of position (Nijboer & de Wette, 1957) :

$$\sum_{\{z\}} g(\mathbf{r}_p + \boldsymbol{x}_{\{z\}} - \mathbf{r}_q) = \frac{1}{|\mathbf{B}|} \sum_{\{\zeta\}} e^{i\mathbf{k}_{\{\zeta\}}\cdot(\mathbf{r}_p - \mathbf{r}_q)} \hat{g}(\mathbf{k}_{\{\zeta\}}) \; . \tag{4.30}$$

$\hat{g}$ is the Fourier transform of $g$. The sum on the left hand side of (4.30) runs over the lattice $\mathcal{L}$ defined by the matrix $\mathbf{B}$ (see (4.3)); the sum on the right is performed over its reciprocal lattice, with basis vectors $\mathbf{k}_i$ such that $[\mathbf{k}_1, \mathbf{k}_2, \mathbf{k}_3]^T \cdot \mathbf{B} = 2\pi\boldsymbol{\delta}$.

The Fourier transform of $\mathbf{M}_2^{pq}$ is most easily derived from (4.28b) as

$$\widehat{\mathbf{M}}_2^{pq} = \frac{1}{\mu k^4} \exp(-\frac{k^2}{4\mathcal{E}^2}) \Big(1 + \frac{k^2}{4\mathcal{E}^2} + \frac{k^4}{8\mathcal{E}^4}\Big) (k^2\boldsymbol{\delta} - \mathbf{kk}) \Big\{ \frac{\sin\hat{\Delta}_p}{\hat{\Delta}_p} \frac{\sin\hat{\Delta}_q}{\hat{\Delta}_q} \tag{4.31}$$

$$- c_p^2 \frac{1-e_p^2}{2e_p^2} \Big(\frac{1}{\hat{\Delta}_p} \frac{\mathrm{d}}{\mathrm{d}\hat{\Delta}_p} \frac{\sin\hat{\Delta}_p}{\hat{\Delta}_p}\Big) \Big(\frac{\sin\hat{\Delta}_q}{\hat{\Delta}_q}\Big) k^2 - c_q^2 \frac{1-e_q^2}{2e_q^2} \Big(\frac{1}{\hat{\Delta}_q} \frac{\mathrm{d}}{\mathrm{d}\hat{\Delta}_q} \frac{\sin\hat{\Delta}_q}{\hat{\Delta}_q}\Big) \Big(\frac{\sin\hat{\Delta}_q}{\hat{\Delta}_q}\Big) k^2 \Big\} \; .$$

$k$ stands for $|\mathbf{k}|$, and $\hat{\Delta}_p = c_p \mathbf{d}_p \cdot \mathbf{k}$. Applying (4.30) to $\mathbf{M}_2^{pq}$, and noting that $\widehat{\mathbf{M}}_2^{pq}$ is an even function of $\mathbf{k}$, we obtain

$$\sum_{\{z\}} \mathbf{M}_2^{p[q+\{z\}]} = \frac{1}{|\mathbf{B}|} \sum_{\{\zeta\}} \cos\Big(\mathbf{k}_{\{\zeta\}} \cdot (\mathbf{r}_p - \mathbf{r}_q)\Big) \widehat{\mathbf{M}}_2^{pq}(\mathbf{k}_{\{\zeta\}}) \; . \tag{4.32}$$

This was used in (4.22). The right hand side converges at an exponential rate governed by $\mathcal{E}$. Since the summand (4.31) in (4.32) is simpler to evaluate than $\mathbf{M}_1^{pq}$ (see (4.28)), it is to be expected that $\mathcal{E}$ should be chosen so that part of the lattice sum over $\mathcal{L}$ is traded for summations in reciprocal space. Indeed, the optimal value of $\mathcal{E} = \frac{\sqrt{\pi}}{\sqrt[3]{|\mathbf{B}|}} \sqrt[6]{\frac{\mathcal{N}_1}{\mathcal{N}_2}}$, with $\mathcal{N}_1, \mathcal{N}_2$ the number of computer operations needed to evaluate $\mathbf{M}_1, \widehat{\mathbf{M}}_2$ respectively at one lattice point (Appendix G). Thus $\mathcal{N}_1 > \mathcal{N}_2$ biases $\mathcal{E}$ to higher values, accelerating the convergence of the sum of $\mathbf{M}_1$ at the expense of

the summation in reciprocal space. Note that $\widehat{\mathbf{M}}_2^{pq}(0)$ is ill-defined. This singular term is not included in the calculation of the mobility elements however since it cancels the backflow integral and the contribution from $V_\epsilon$ in (4.19) (Appendix F; see also Brady *et al.*, 1988).

Our final note on numerical aspects concerns the special case $p = q$, i.e., the interactions between a spheroid and its own images. As mentioned in (4.23), the term with $\{z\} = 0$ must be excluded from the calculation of $\mathbf{M}_{UF}^{pp}$, and hence $\mathbf{M}_2^{pp}\big|_{\mathbf{r}=0}$ must be evaluated. The fastest route to the correct result is to invert the Fourier transformation:

$$\lim_{\mathbf{r}\to 0} \mathbf{M}_2^{pp} = \frac{1}{(2\pi)^3} \int \widehat{\mathbf{M}}_2^{pp} \, \mathrm{d}\mathbf{k} \; . \tag{4.33a}$$

For small $\mathcal{E}$, this can conveniently be expressed as an infinite series:

$$\lim_{\mathbf{r}\to 0} \mathbf{M}_2^{pp} = \frac{8\mathcal{E}}{\sqrt{\pi}} \sum_{n=0}^{\infty} \frac{(-1)^n}{n!} \tag{4.33b}$$
$$\frac{(2c_p\mathcal{E})^{2n}}{2n+1} \left\{ \frac{1}{2n+1} - (2c_p\mathcal{E})^2 \frac{1-e_p^2}{e_p^2} \frac{2n+5}{(2n+3)^2} \right\} \left[ (n+1)\boldsymbol{\delta} + n\mathbf{d}_p\mathbf{d}_p \right] \; .$$

For large $\mathcal{E}$, (4.33a) is written in spherical coordinates, and the azimuthal angle dependence is integrated out. The remaining cubature can easily be done numerically, since the kernel decays rapidly for large $k$.

## 4.5 Calculation of hydrodynamic transport properties via Stokesian dynamics

This section recapitulates the way hydrodynamic transport properties are evaluated in Stokesian dynamics (Brady & Bossis, 1988; Phillips *et al.*, 1988 a-b). These properties include the sedimentation rate of a dispersion, the self-diffusivities and the stress in a suspension, the hindered diffusion coefficients in porous media and the permeability of a fixed bed of particles. At the outset, let us emphasize that only the short-time limit of these properties is calculated in this work, since we do not track the evolution of the microstructure under influence of the flow. This asymptote can be accessed experimentally by dynamic light scattering or by rapid oscillatory rheometric measurements (at a frequency too high to affect the particle configuration in

the suspension); the permeability, of course, is not frequency dependent (provided the quasi-stationary Stokes equations remain valid at the frequencies of interest).

The stress in the suspension is very often the quantity of most interest to the fluid dynamicist. For non-Brownian spheroids not subject to interparticle forces, the hydrodynamic stress $\mathbf{\Sigma}$ of a suspension undergoing a shearing motion characterized by the rate of strain $\mathbf{E}_\infty$ is given by (Batchelor, 1971)

$$\mathbf{\Sigma} = -p_{\text{eff}}\boldsymbol{\delta} + 2\mu\mathbf{E}_\infty + n_\phi\langle\mathbf{S}\rangle \ . \tag{4.34}$$

The first term is an isotropic term, which is irrelevant in incompressible media. The second term represents the Newtonian fluid phase response. The final contribution to the hydrodynamic stress comes from the particles, and is proportional to the mean stresslet $\langle\mathbf{S}\rangle$, which can be calculated from (4.14) as

$$\langle\mathbf{S}\rangle = \langle\boldsymbol{R}_{SU}\cdot(\boldsymbol{\mathcal{U}}-\boldsymbol{\mathcal{U}}_\infty)-\boldsymbol{R}_{SE}:\boldsymbol{E}_\infty\rangle \tag{4.35a}$$

$$= \langle\boldsymbol{R}_{SU}\cdot\boldsymbol{R}_{\mathcal{FU}}^{-1}\cdot\boldsymbol{R}_{\mathcal{F}E}-\boldsymbol{R}_{SE}\rangle:\boldsymbol{E}_\infty \ . \tag{4.35b}$$

In going from (4.35a) to (4.35b), we have assumed that the particles are freely suspended. The vector $\boldsymbol{\mathcal{U}}$ lumps the translational and angular velocities of all particles; hence $\boldsymbol{R}_{SU}$ stands for the $5N\times 6N$ tensor in the bottom left corner of $\boldsymbol{\mathcal{R}}$ (see (4.14)) and includes both $\boldsymbol{R}_{SU}$ and $\boldsymbol{R}_{S\Omega}$. Similarly, $\boldsymbol{\mathcal{F}}$ groups the forces and the torques. The averages in the previous equations are taken over all particles, as well as over several realizations of the microstructure if applicable. The hydrodynamic stress in systems which are macroscopically isotropic is characterized by one coefficient (the effective viscosity of the medium), and additional averaging over the elements of the stress tensor $\mathbf{S}$ is possible, and recommended to obtain better statistics (since the five elements of $\mathbf{S}$ can be considered independent measures of the viscosity). In an extensive study of the multipole moment expansion technique for Stokes flow in random hard sphere dispersions, Ladd (1990) has shown that the viscosity is relatively insensitive to the number of particles used in the simulation, and that the moment expansion converges rapidly, with meaningful results when the series

is truncated at the level of stresslets (as done here), and little change beyond the octupole. Indeed, Phillips *et al.* (1988a) report excellent agreement with the experimentally measured high-frequency limit of the effective viscosity for monodisperse hard-sphere dispersions (van der Werff *et al.*, 1989) using Stokesian dynamics.

To obtain the sedimentation velocity $\mathbf{V}$ of a suspension, we consider a collection of spheroids subject to gravity. For the sake of clarity, we shall assume that the dispersion is monodisperse, in which case all forces are equal. This is a mobility problem, which is solved by inverting (4.14) to obtain

$$\langle \begin{pmatrix} \mathbf{V} \\ \mathbf{W} \end{pmatrix} \rangle = \langle \boldsymbol{R}_{\mathcal{FU}}^{-1} \cdot \begin{pmatrix} \boldsymbol{F} \\ 0 \end{pmatrix} \rangle = \langle \begin{pmatrix} \boldsymbol{R}_{FU} & \boldsymbol{R}_{F\Omega} \\ \boldsymbol{R}_{TU} & \boldsymbol{R}_{T\Omega} \end{pmatrix}^{-1} \cdot \begin{pmatrix} \boldsymbol{F} \\ 0 \end{pmatrix} \rangle , \tag{4.36}$$

or, writing out the contribution of each particle,

$$\langle \begin{pmatrix} \mathbf{V}_p \\ \mathbf{W}_p \end{pmatrix} \rangle = \langle \sum_{q=1}^{N} (\boldsymbol{R}_{\mathcal{FU}}^{-1})^{pq} \cdot \begin{pmatrix} \boldsymbol{F}_q \\ 0 \end{pmatrix} \rangle . \tag{4.37}$$

The averaging occurs over all particles $p$ in the unit cell, as well as over several realizations of the microstructure if desired. In most cases (including isotropic samples), $\mathbf{W}$ is zero because the sedimentation process does not induce non-skewed particles to rotate in a systematic sense. Special microstructures can be conceived however, which yield a non-zero average angular motion of the spheroids under the action of gravity. The collective diffusion coefficient, measuring the particle flux in response to a concentration gradient, is closely related to the sedimentation rate, and can be directly derived from it (Batchelor, 1976). Unfortunately, these properties are known to display a strong system size dependence, with the influence of periodicity decreasing very slowly (as $N^{-\frac{1}{3}}$) (Phillips *et al.*, 1988a). Ladd (1990) devised a procedure to correct for this effect, which is very effective for dispersions of spheres. He also demonstrated, however, that many force moments need to be retained in the description of the particle dynamics in order to achieve quantitative accuracy for the sedimentation rate, even if lubrication interactions are explicitly included. Since we truncate the multipole expansion after the first moment (i.e.,

we only use the force, torque and stresslet exerted by each particle), we should not expect to capture more than the leading order behavior of the sedimentation velocity.

The self-diffusion tensor of a particle can be evaluated from the Stokes-Einstein formula as

$$\langle \mathbf{D} \rangle = \mathrm{kT} \langle \left( \mathbf{R}_{\mathcal{FU}}^{-1} \right)^{pp} \rangle \ , \tag{4.38}$$

which in essence shows a direct proportionality between $\mathbf{D}$ and the velocity of a tracer subject to a force in a suspension of force-free particles. ("k" is the Boltzmann constant and "T" the absolute temperature.) In random, monodisperse systems, the averaging usually occurs over all particles and several realizations of the microstructure. In bidisperse samples, the diffusivity of one component may be of particular interest, in which case the averaging only includes this species. As noted by Phillips *et al.* (1988 a), this property also displays a strong system size dependence. Indeed, due to the spatially periodic nature of the dispersion, all images of the tracer particle are subject to a force too; hence the system *de facto* considers a simple lattice of spheroids sedimenting through $N-1$ lattices of neutrally buoyant particles. The effect of the periodically replicated force is long-ranged and introduces the $N^{-\frac{1}{3}}$ scaling. For random dispersions of hard spheres, Ladd (1990) successfully factored out this undesirable dependence by heuristically adapting the low-$n_\phi$ correction, known analytically (Hasimoto, 1959), for the increase in viscosity occurring at higher concentrations (see also Phillips *et al.*, 1988 b). He also pointed out that the moments expansion technique is very adequate to evaluate this property and converges rapidly, provided lubrication interactions are included in a pair-wise additive manner, as done here.

Hindered diffusion coefficients describe the mobility of a test particle in a fixed bed of other particles. We again rely on the Stokes-Einstein formula, which now becomes (for $\mathbf{u}_\infty = 0$, $\mathbf{F}_p \neq 0$, and $\forall q \neq p$, $\mathbf{U}_q = 0$):

$$\langle \mathbf{H}_p \rangle = \mathrm{kT} \langle \left( \mathbf{R}_{FU}^{pp} \right)^{-1} \rangle \ . \tag{4.39}$$

As for self-diffusion and viscosity, this property is expected to converge rapidly with the number of stress moments if lubrication interactions are added explicitly. Indeed, relatively few multipoles are sufficient at low concentrations, while lubrication dominates the physics at high packing fractions; since both extremes are handled well by Stokesian dynamics, deviations from the correct behavior cannot be large at intermediate densities. Note that lubrication interactions are much less pronounced in sedimenting suspensions and for permeability calculations since there is little relative motion between the particles in those cases. At high solid contents, the formulation used here (keeping only the effects of the force, torque and stresslet) is thus only qualitatively correct for these properties (Ladd, 1990). The effect of the long-ranged periodicity of the model configurations, on the other hand, is partly screened in porous media (*cf.* the analysis of the Brinkman equation by Stokesian dynamics (Durlofsky & Brady, 1987)), resulting in a weak, at most $O(N^{-1})$-dependence for the hindered diffusion coefficient (Phillips *et al.*, 1988 b).

The permeability $\mathbf{K}$ of a fibrous bed is the tensorial structural property which relates the macroscopic pressure gradient to the mean velocity of the fluid in Darcy's law:

$$\nabla p = -\mathbf{K}^{-1} \cdot \langle \mathbf{u} \rangle \ . \tag{4.40}$$

It can be evaluated by simulating a uniform flow past a collection of immobile spheroids. From an overall force balance over a representative volume of the dispersion, it is clear that $\nabla p = -n_\phi \langle \mathbf{F} \rangle$ (Brady *et al.*, 1988). Therefore the resistivity $\mathbf{K}^{-1}$ of a porous medium is given by

$$\mathbf{K}^{-1} = n_\phi \langle \sum_q \mathbf{R}_{FU}^{pq} \rangle \ . \tag{4.41}$$

As alluded to above, it is necessary at high packing fractions to retain more moments of the stress density than just the two first multipoles kept here (Ladd, 1990). The qualitative features of the concentration dependence of the permeability, however, are adequately reproduced using only 11 unknowns per particle, as done in this work.

Artifacts due to periodicity are absent provided the Brinkman screening length (which scales as $1/\sqrt{n_\phi}$) is small compared to the size of the unit cell (Phillips *et al.*, 1988 b). This condition is easily satisfied except at very low solid volume fractions.

In the remainder of this chapter, we shall apply the techniques sketched above to calculate the hydrodynamic transport properties of spheroid dispersions. Two classes of microstructures will be considered. We shall first examine perfect crystals (i.e., an extremely ordered state), and then turn our attention to equilibrium hard-ellipsoid configurations.

## 4.6. Hydrodynamic transport properties of crystalline dispersions of prolate spheroids

Hard-rod dispersions undergo a phase transition to a liquid crystalline state at high volume fractions (Onsager, 1949; Frenkel, 1987). This sudden change in the equilibrium microstructure, caused solely by excluded volume effects, dramatically alters the macroscopic characteristics of the material. Most notably, the anisotropy of the microscopic configuration imparts a directionality to most observable properties, including all hydrodynamic transport coefficients discussed in §4.5. The growing impact of liquid crystals on industrial and household technology drives many current research efforts in this area. Microstructural theories, which explain macroscopic phenomena in terms of the underlying physics at the microscale, have, in conjunction with Monte-Carlo and molecular dynamics simulations, already greatly expanded our understanding of these complex systems under equilibrium conditions (Allen *et al.*, 1989; Talbot *et al.*, 1990). Yet most of these works either consider fluids of hard convex bodies (Frenkel & Mulder, 1985; Talbot *et al.*, 1990), or neglect hydrodynamic interactions between the rods while recognizing that this significantly restricts the scope and validity of the analysis (Bitsanis *et al.*, 1988, 1990). It is tempting to use Stokesian dynamics to remedy this situation. In particular, our simulation method seems ideally suited to investigate how the rheological properties of liquid crystals depend on the concentration of the particulate phase, its microstructure, and its molecular characteristics (such as the aspect ratio and the

monodispersity).

At high concentrations, a fluid of hard spheroids spontaneously assembles into a structure devoid of translational order, but possessing a preferred direction of alignment (Frenkel *et al.*, 1984). These textures are called nematics. At higher densities still, they solidify into a crystal resembling a close-packed face-centered cubic cell of spheres stretched along the (111)-axis (see below). We shall consider idealized models of a nematic liquid in this section, characterized by perfect orientational and translational order. Near the maximum packing, their microstructure is similar to that of the frozen system of hard spheroids. These examples also serve as useful reference configurations, comparable to simple cubic lattices for spheres.

The highest packing fraction attainable for prolate spheroids on a simple cubic cell is $\pi/(6r_p^2)$, and hence is about 0.5% for rods of aspect ratio 10. It is possible, however, to achieve a density equal to the maximum for spheres, $\pi/(3\sqrt{2})$, by stretching a face-centered cubic cell of spheres in any direction by a factor equal to the aspect ratio of the spheroids. This transformation maps a sphere onto an ellipsoid without altering the volume fraction of the crystal. To preserve as many symmetry elements in the lattice as possible, we chose the direction of stretch to be perpendicular to the hexagonally packed stacks, i.e., along the (111)-diagonal of the original cubic cell (Fig. 4.1). This guarantees the simplest possible form for the tensorial properties of the crystal. We shall refer to the direction of stretch, which coincides with the orientation of the spheroids, as the $z$-axis. The system thus possesses 6-fold symmetry about $z$. Based on the invariance of the microstructure under rotations by $\pi/3$ in the $xy$-plane, and under reflections about the origin, one can show for instance that the fourth rank tensor which relates the stress to the rate of strain only has 3 independent components. (Using only the tracelessness of $\mathbf{S}$ and $\mathbf{E}$, and the symmetry of $\mathbf{R}_{SE}$, one cannot reduce the number of coefficients further than 15. For comparison, 4 coefficients are needed if the lattice is stretched in the (001) direction, and only 2 for face-centered cubic cells (Nunan & Keller, 1984).) In addition, a distortion along (111) generates a structure which resembles

the configuration into which fluids of hard ellipsoids solidify at high densities. It is thus physically realizable in this sense.

In order to study dispersions at concentrations different from the maximum, an algorithm must be devised to expand the lattice. The most simple-minded approach, an isotropic dilatation, soon results in very uninteresting structures consisting of hexagonally packed sheets of spheroids separated by large gaps filled with fluid. This is a consequence, of course, of the marked shape anisotropy of the unit cell at the highest volume fraction. In order to preserve a "space-filling" configuration even at low concentrations, we decided to expand the lattice in such a way that the surface-to-surface separation between nearest neighbors is the same in all directions.‡ Although this definition is somewhat arbitrary, it offers an unambiguous way of constructing an "isotropically compact" structure with full three-dimensional character. This has the added benefit that the geometry reduces to a face-centered *cubic* geometry at infinite dilution, independently of the aspect ratio of the particles. We shall call this type of crystalline geometry "expanded face centered," or *efc* for short.

The entire crystal can be built using only one spheroid per unit cell. This has obvious computational advantages, since the time savings associated with using the minimal number of particles far outweighs the cost of having a denser lattice over which to perform the Ewald summation. Unfortunately, this also impoverishes the information content of the simulations; indeed, because the forcing is periodic, the problem formulations for the self-diffusivity, the hindered diffusion coefficient and the sedimentation rate become identical, and no meaningful results can be obtained for $\mathbf{D}$ nor $\mathbf{H}$ unless more particles are included in the unit cell. Nevertheless, because

‡ The geometric problem of determining the correct amount of stretch along the three basis vectors in order to maintain the surface separation equal within the hexagonally packed layers and between neighbors in adjacent layers, reduces to a non-linear equation in one variable which can be solved iteratively (Appendix H).

of its efficiency, we used the most elementary module, containing a single spheroid, for most of the results reported here. Note that the basis vectors of the unit cell are non-orthogonal and of different lengths, but the resulting geometric complications are relatively straightforward to overcome.

### 4.6.1 Sedimentation rates

The sedimentation rates for an *efc*-lattice of spheroids of aspect ratio 6, normalized by their value at infinite dilution, are displayed in Fig. 4.2, alongside their rotational counterparts (i.e., the rotation rates due to uniformly applied torques). From symmetry considerations, all particles fall at the same speed, and there is no coupling between translation and rotation (i.e., $\mathbf{W} = 0$ in (4.36)). Motions along the direction of alignment are also decoupled from motions perpendicular to it. Furthermore, as pointed out earlier, the crystal possesses a 6-fold axis of symmetry and thus is isotropic in the $xy$-plane. Therefore, 4 components suffice to characterize the $6 \times 6$ sedimentation tensor (or collective diffusion tensor): $V_{\parallel}^{\mathrm{tr}}, V_{\perp}^{\mathrm{tr}}, V_{\parallel}^{\mathrm{ro}}$, and $V_{\perp}^{\mathrm{ro}}$. (The rotational "sedimentation rate" $V_{\parallel}^{\mathrm{ro}}$ represents the angular velocity of the particles resulting from a uniformly applied torque parallel to their axes; $V_{\perp}^{\mathrm{ro}}$ is defined in a similar fashion.) The most striking feature perhaps of Fig. 4.2 is the peculiar concentration dependence of the collective rotational mobility perpendicular to the rod axis. A very shallow minimum at an extremely dilute volume fraction ($V_{\perp}^{\mathrm{ro}}$ reaches 0.99933 at $\phi = 0.00035$) is followed by a pronounced maximum exceeding 1 at about 21% solids by volume. The initial drop is due to the increased effective viscosity of the suspension. The subsequent rise can be understood by reference to Fig. 4.3, where we sketch how viscous interactions between the rods reinforce the particles' rotation, in a manner similar to the drag reduction experienced by two spheres when they fall as a doublet rather than as two isolated balls. At higher concentrations, however, the hexagonally packed stacks of spheroids become interpenetrating, and actively counteract each other, causing the collective rotational diffusivity $V_{\perp}^{\mathrm{ro}}$ to drop again. A schematic drawing similar to Fig. 4.3 will show that hydrodynamic

interactions always act to retard the motion in the case of $V_{\|}^{\mathrm{ro}}$, which therefore decreases monotonically with increasing volume fraction. The translational sedimentation rates $V^{\mathrm{tr}}$ also fall off with concentration, as expected intuitively, because the strong backflow dominates the analogous cooperative effect of hydrodynamic interactions. The slight upward bend in $V^{\mathrm{tr}}$ at high packing densities is associated with the neglect of multipoles higher than the torque and the stresslet, and should be disregarded. (Similar aphysical behavior has been noted in simulations of concentrated samples of spheres if the mean field quadrupole was not included in the formulation, as is the case here.)

Symmetry arguments demonstrate why lubrication stresses affect $V^{\mathrm{ro}}$, but not $V^{\mathrm{tr}}$. This is true for every microstructure which can be constructed using a single particle per unit cell. The abruptness of the drop at about 28.5% is artificial, and merely a consequence of our lack of knowledge concerning the $O(\epsilon^0)$ correction to the lubrication formulae of Claeys & Brady (1989). This $O(1)$ constant provides the smooth transition from the "far-field" behavior to the "near-field," singular resistance behavior as the surface separation $\epsilon$ between two particles decreases. Without it, lubrication interactions must be allowed to "kick in" at a certain threshold separation $\epsilon_{\mathrm{max}}$, set at 1 in these simulations. (This distance is non-dimensionalized by the harmonic mean of the radii of curvature at the points of closest approach.) The effect is quite dramatic for crystals because lubrication stresses set in at the same concentration for all particles. No discontinuity is noticeable for more random configurations, since the contribution of lubrication stresses to macroscopic properties is smeared out by averaging over the particles in that case (*cf.* the results of §4.7). Moreover, the threshold $\epsilon_{\mathrm{max}}$, which is somewhat arbitrary, was set at an unusually high value here for illustrative purposes. We typically chose $\epsilon_{\mathrm{max}} = 0.08$, which is more consistent with the assumption underlying lubrication theory that $\epsilon \ll 1$. In the remainder of this section on crystalline geometries, we shall actually suppress lubrication effects altogether ($\epsilon_{\mathrm{max}} = 0$).

For a suspension of spheres of radius $a$ arranged on a simple cubic lattice of

volume fraction $\phi$, Hasimoto (1959) calculated that

$$V^{\mathrm{tr}} = 1 - 1.74\phi^{\frac{1}{3}} \ , \tag{4.42}$$

where the sedimentation velocity has been scaled by $|\mathbf{F}|/6\pi a\mu$. The collective translational mobilities $V^{\mathrm{tr}}$ of spheroids on an *efc*-lattice do not, however, decrease quite linearly with the cube root of the concentration, although this dependence is approached asymptotically (Fig. 4.4). This deviation is explained by the fact that the lattices do not remain perfectly self-similar when they are compressed, because they are constructed so that the superficial separation between the spheroids is uniform in 3 non-planar directions (*vide supra*).

The sedimentation rate $V_{\perp}^{\mathrm{tr}}$ drops faster with concentration than $V_{\parallel}^{\mathrm{tr}}$ for all aspect ratios examined. The decline steepens slightly as the eccentricity of the spheroids increases. The maximum in $V_{\perp}^{\mathrm{ro}}$ also becomes higher, reaching more than 10 for $r_p = 24$ at $\phi \simeq 0.21$.

### 4.6.2 Hindered diffusivities

As explained earlier, the evaluation of hindered diffusion coefficients requires the use of more than one particle per unit cell. Figure 4.5 shows the hindered diffusivities for translation and for rotation perpendicular to the rod axis in an *efc*-lattice of spheroids of aspect ratio 6 obtained using 1, 4, 8, 16 and 32 ellipsoids per unit cell. In the last case, one particle is subject to a force (or torque, respectively), and the remaining 31 are held still. The set of data with $N = 1$ reproduces the sedimentation rates. For both translational and rotary motion, the number dependence is rather mild, and the results for 32 particles are not much different from the ones for $N = 16$. The rotational mobility $H^{\mathrm{ro}} < V^{\mathrm{ro}}$, because the cooperative hydrodynamic interactions giving rise to the maximum in the $\phi$-dependence of $V_{\perp}^{\mathrm{ro}}$ are screened by the intervening stationary particles. For the translational motion, $H^{\mathrm{tr}} > V^{\mathrm{tr}}$ because the backflow of fluid, driven by the pressure gradient balancing the forces acting on the particles, weakens (from a macroscopic momentum balance), becoming zero as $N \to \infty$.

### 4.6.3 Relation between the stress and the rate of strain

By applying the transformations for which the *efc*-lattice is invariant (a rotation by $\pi/3$ about the $z$-axis, for instance), exploiting the tracelessness and symmetry of the stresslet $\mathbf{S}$ and of the rate-of-strain tensor $\mathbf{E}$, and making optimal use of the implications of Lorentz' reciprocal theorem (Hinch, 1972), it is easy to demonstrate that $\mathbf{R}_{\mathcal{SU}} \cdot \mathbf{R}_{\mathcal{FU}}^{-1} \cdot \mathbf{R}_{\mathcal{FE}} - \mathbf{R}_{\mathcal{SE}}$, which we shall denote by $\mathbf{R}_{\Sigma E}$ (see (4.35)), must have the following structure:

$$\begin{aligned}\mathbf{R}_{\Sigma E} = 8\pi a^3 \mu \Big\{ & 3\eta_T \Big(\mathbf{dd} - \tfrac{1}{3}\boldsymbol{\delta}\Big)\Big(\mathbf{dd} - \tfrac{1}{3}\boldsymbol{\delta}\Big) \\ & + \eta_\perp (\mathbf{d}\boldsymbol{\delta}\mathbf{d} + {}^T\mathbf{d}\boldsymbol{\delta}\mathbf{d} + \mathbf{d}\boldsymbol{\delta}\mathbf{d}^T + {}^T\mathbf{d}\boldsymbol{\delta}\mathbf{d}^T - 4\mathbf{dddd}) \\ & + \eta_\parallel (\breve{\boldsymbol{\delta}}\breve{\boldsymbol{\delta}} + \widehat{\boldsymbol{\delta}}\widehat{\boldsymbol{\delta}} - \boldsymbol{\delta}\boldsymbol{\delta} + \mathbf{dd}\boldsymbol{\delta} + \boldsymbol{\delta}\mathbf{dd} + \mathbf{dddd} - \mathbf{d}\boldsymbol{\delta}\mathbf{d} - {}^T\mathbf{d}\boldsymbol{\delta}\mathbf{d} - \mathbf{d}\boldsymbol{\delta}\mathbf{d}^T - {}^T\mathbf{d}\boldsymbol{\delta}\mathbf{d}^T) \Big\} .\end{aligned} \tag{4.43}$$

The unit vector $\mathbf{d}$ indicates the orientation of the rods, and lies along the $z$-axis. The non-standard notations $\widehat{\boldsymbol{\delta}\boldsymbol{\delta}}$ and $\breve{\boldsymbol{\delta}}\breve{\boldsymbol{\delta}}$ mean

$$(\breve{\boldsymbol{\delta}}\breve{\boldsymbol{\delta}})_{ijkl} = \delta_{il}\delta_{jk} \qquad \text{and} \qquad (\widehat{\boldsymbol{\delta}\boldsymbol{\delta}})_{ijkl} = \delta_{ik}\delta_{jl} \; . \tag{4.44}$$

To within at least 5 significant digits, the tensor $\mathbf{R}_{\Sigma E}$ calculated for an *efc*-lattice using Stokesian dynamics conformed to (4.43). For isotropic suspensions, the three coefficients $\eta_T, \eta_\perp$ and $\eta_\parallel$ are equal to the scaled single particle contribution $\eta$ to the effective viscosity [i.e., $\mathbf{R}_{\Sigma E} = 8\pi a^3 \mu\eta(\breve{\boldsymbol{\delta}}\breve{\boldsymbol{\delta}} + \widehat{\boldsymbol{\delta}}\widehat{\boldsymbol{\delta}} - \frac{2}{3}\boldsymbol{\delta}\boldsymbol{\delta})$ so that $\mu_{\text{eff}} = \mu(1 + 8\pi a^3 n_\phi \eta)$ $= \mu(1 + 6r_p^2 \phi\eta)$]. For dispersions which possess cylindrical symmetry about $\mathbf{d}$ (such as *efc*-lattices of spheroids), $\eta_T$ gives the resistance to uniaxial extension in the direction of $\mathbf{d}$, $\eta_\perp$ indicates the stress in response to simple shearing flows with a velocity gradient parallel to $\mathbf{d}$, and $\eta_\parallel$ corresponds to the apparent viscosity during simple shear (or hyperbolic straining) in a plane perpendicular to $\mathbf{d}$ (Fig. 4.6).

At infinite dilution, (4.43) reduces to the expression for the stresslet exerted by an isolated freely mobile spheroid in a purely extensional flow. Using the symbols of Chwang & Wu (1975) (see also Kim (1986) and App. J), we can derive the limiting forms of $\eta_T, \eta_\perp$ and $\eta_\parallel$ for very slender rods as

$$\eta_T \overset{n_\phi \to 0}{\longrightarrow} -\tfrac{2}{9} e^3 \alpha_5 \overset{e \to 1}{\longrightarrow} (18 \log(2r_p) - 27)^{-1} + O(r_p^{-2}) \tag{4.45a}$$

$$\eta_\perp \overset{n_\phi \to 0}{\longrightarrow} \tfrac{1}{3}e^3\left(\gamma^* \tfrac{e^2}{2-e^2} - \alpha^*\right) \overset{e \to 1}{\longrightarrow} \tfrac{1}{3}r_p^{-2} + O(r_p^{-4}) \qquad (4.45b)$$

$$\eta_\parallel \overset{n_\phi \to 0}{\longrightarrow} -\tfrac{2}{3}e^3\alpha_4 \overset{e \to 1}{\longrightarrow} \tfrac{1}{3}r_p^{-2} + O(r_p^{-4}) \,, \qquad (4.45c)$$

with $r_p^{-2} = 1 - e^2$. These asymptotic forms for the coefficients $\eta$ (in the double limit $n_\phi \to 0$ and $r_p \to \infty$) are accurate over a remarkably wide range of aspect ratios (Kim, 1986). Fig. 4.7 shows that they also provide rather good estimates of $\eta_\perp$ and $\eta_\parallel$ even for quite concentrated systems, since the apparent viscosity is well fitted by the line $\mu_{\text{app}} = \mu(1 + 2\phi)$ for $\phi$ up to about 10% if $r_p \geq 4$.‡ Note that this expression for $\mu_{\text{app}}$ is only valid for flows which do not have extensional components in the direction of the rod axis (i.e., $\mathbf{E}^\infty : \mathbf{dd} = 0$) since $\eta_T$ contributes otherwise. The coefficients $\eta_\parallel$ and $\eta_\perp$ are indistinguishable on the plot, but a comparison of the numerical values teaches that $\eta_\parallel < \eta_\perp$ at low concentrations, and vice-versa at high volume fractions.

A look at $\mu_{\text{ext}}$ in Fig. 4.8 reveals a richer dependence on concentration and aspect ratio. The dramatic augmentation of the extensional viscosity which can be achieved by adding less than 1000 ppm of fibrous material to the dispersion is obviously of tremendous practical importance. Note also the strong effect of the aspect ratio on the resistance of the suspension to stretch. For comparison, the extensional viscosity of an *fcc*-lattice of spheres has also been drawn, together with the expansion to $O(\phi^{10/3})$ due to Zuzovsky *et al.* (1983). The deviation of the simulation results from this theoretical prediction at the higher volume fractions is real, as supported by the exact calculations of Nunan & Keller (1984), with which our data agree very well. The asymptotic formulae obtained from (4.45a), $\mu_{\text{ext}} = \mu(1 - 12r_p^2\phi\alpha_5)$, have also been penciled in for spheroids of aspect ratio 4, 16, and 300. This brings to bare that dispersions containing 0.1% by volume of short rods may be called dilute, but that hydrodynamic interactions cause significant deviations from dilute suspension behavior for spheroids of aspect ratio 300

‡ Similarly, it has been noted by others that the Einstein correction to the viscosity of a suspension of spheres, $\mu_{\text{eff}} = \mu(1 + \frac{5}{2}\phi)$, holds well up to 10% by volume.

at the same concentration. Indeed, as first suggested by Batchelor (1971), the relevant measure of concentration for a fibrous dispersion is $n_\phi a^3$ in problems for which hydrodynamic interactions are relevant. This is roughly the volume "fraction" of the spheres which circumscribe the rods (the apostrophes emphasizing that this fraction may exceed unity). For instance, it is about 20 for the 0.1% dispersion of spheroids of aspect ratio 300 cited above. In 1990, Shaqfeh & Fredrickson calculated the hydrodynamic stress in a suspension of rods by evaluating the first and dominant term in a diagrammatic series representing multiple scattering events of the momentum propagator in the fibrous dispersion. Their rigorous treatment confirms Batchelor's main findings, and extends them to arbitrary orientation distributions. (Batchelor restricted his analysis to dispersions of parallel fibres.) The analysis rests, however, on the assumption that the locations of the centres of the particles are uncorrelated. Nevertheless, it is instructive to examine our numerical results in the light of their theory. We have therefore recast the data as shown in Fig. 4.9, where we plot the inverse of the stresslet component $\mathbf{S} : \mathbf{dd}$ for uniaxial extension about the $z$-axis of an *efc*-lattice, versus the logarithm of the volume fraction. (By definition, see (4.43), the ordinate is equal to $(8\pi a^3 \mu \eta_T)^{-1} = \left[(\mu_{\text{ext}}/\mu - 1)/n_\phi\right]^{-1}$.) For aligned identical slender ellipsoids of revolution, Shaqfeh & Fredrickson (1990) obtained

$$\frac{\mu_{\text{ext}}}{\mu} - 1 = \frac{8\pi a^3 n_\phi}{3\ln(1/\phi)}\Big(1 - \frac{\ln\ln(1/\phi)}{\ln(1/\phi)} - \frac{1.4389}{\ln(1/\phi)}\Big) + O\Big(\frac{n_\phi a^3}{\ln^3(1/\phi)}\Big)\,. \qquad (4.46)$$

They also proved that the inverse dependence on $\ln(\phi)$ in this expression is intimately related to the occurence of hydrodynamic screening in suspensions of rods, as intuitively hypothesized by Batchelor (1971). Screening is a phenomenon well understood in porous media (Brinkman, 1947), where the immobile particles actively resist the motion induced by a point force placed anywhere in the sample, thus causing its disturbance to decay faster with distance $r$ than the $r^{-1}$-dependence usually observed in Stokes flow. Hydrodynamic screening in dispersions of *freely suspended* rods, on the other hand, is a relatively new concept, and has led to some

confusion. The diagrammatic technique used to sum hydrodynamic interactions between fibres (Shaqfeh & Fredrickson, 1990) clearly demonstrates, however, that the Fourier components of incident velocity fields with a wavelength of $o(a)$ are effectively screened by force-free rods. Physically, the rigid bodies oppose any disturbance which changes direction over distances much shorter than their largest dimension. It is well known that the screening length $\zeta$ (i.e., the characteristic length scale for the decay of velocity disturbances) varies as $\phi^{-\frac{1}{2}}$ in random dispersions, but that it is shorter ranged, of $O(\phi^{-\frac{1}{3}})$, for simple lattices. This also holds in fibrous suspensions, and Shaqfeh & Fredrickson (1990) report for random dispersions of rods that $\zeta \sim (n_\phi a)^{-\frac{1}{2}}$. To account for the difference between the screening lengths in ordered and disordered dispersions, we naively rescale (4.46), which was derived using the assumption that the positions of the rods are uncorrelated, by a factor 2/3. This is obviously *ad hoc*, since there is no reason to believe that the second and third terms in the expansion (4.46) should scale like the first. Yet we take the remarkably good agreement with our simulation results noted in Fig. 4.9 to indicate that this reasoning is at least qualitatively correct. The transition from a regime in which the mean stresslet is independent of volume fraction (as it should be for dilute systems) to a concentration range where $\mathbf{S} : \mathbf{dd} \sim (\ln(1/\phi))^{-1}$ is clearly apparent and is consistent with the idea of screening. Quite fortuitously, the break point in Fig. 4.9 corresponds almost exactly to $\frac{4\pi}{3} n_\phi a^3 = O(1)$, as predicted by theory.

### 4.6.4 Dependence on the crystal geometry

One may wonder how representative the properties of an *efc*-lattice are for other crystal geometries. The fact that the maximum packing attainable for slender bodies depends so critically on the arrangement, hints that the microstructure matters much more for spheroids than for spheres. For instance, we noted earlier that simple cubic lattices cannot take up more impenetrable spheroids than $\frac{\pi}{6r_p^2}$, while *efc* structures accept as much as $\frac{\pi}{3\sqrt{2}}$. This is a considerable difference even for moderate aspect ratios. In contrast, body-centered cubic cells of spheres may be filled

up to $\frac{\sqrt{3}\pi}{8}$, which is not very different from the densest (face-centered or hexagonally close packed) structure. We explained in the introduction of this section how to construct close packed crystals of spheroids of arbitrary shape by stretching the corresponding unit cell for spheres by a factor equal to the aspect ratio, and stressed that this transformation does not affect the packing fraction. We also showed that an isotropic dilution of this dense microstructure results in uninteresting "two-dimensional" configurations as a result of the anisotropy of the unit cell at maximum packing, and introduced the alternative procedure of expanding the lattice by keeping the surface-to-surface separation between nearest neighbors the same in 3 non-planar directions. This guarantees that the dispersion possesses as much "three dimensional character" as is compatible with the chosen concentration. We apply this technique to 4 types of microstructures in what follows to investigate the impact of the detailed crystal geometry on the macroscopic properties. One lattice will also be expanded isotropically in order to judge the effect of the dilatation technique on the transport coefficients of ordered configurations. We shall primarily focus our discussion on the relation between the stress and the rate of strain because of its primary interest in the rheology of rod dispersions. Furthermore, this characteristic can be estimated reliably with Stokesian dynamics (keeping only the effects of the force, torque and stresslet exerted by the spheroids on the fluid), and is relatively insensitive to the number of particles used in the unit cell (Phillips *et al.*, 1988 a; Ladd, 1990).

Three of the five lattices considered here (Fig. 4.10) are obtained by distorting elementary modules of spheres, namely:

- ◇ the *efc*-structure of the previous section, with maximum packing $\frac{\pi}{3\sqrt{2}}$, gotten by stretching a face-centered unit cell of spheres along (111),
- ◇ the *ebc*-configuration, constructed by expanding the same lattice along (001). This obviously has the same maximum density as the *efc*-variant. For $r_p = 1$, both reduce to the face-centered cubic geometry, and are indistinguishable.

(They then become descriptions of the same packing in two different frames of reference.) Note that the *ebc*-crystal can be thought of as a staggered arrangement of spheroids placed on a square grid, just as the *efc*-lattice consists of interlocking stacks of particles distributed on a hexagonal mesh. In this sense, it is related to the body-centered crystal of spheres, hence the acronym *ebc*.‡

◇ the *esc*-structure, obtained from a simple cubic cell of spheres by stretching it along (001). This geometry resembles the *ebc*-lattice, but the stacks of spheroids are now facing each other instead of being offset by half a mesh size for a tighter packing. The gap width between the layers (i.e., the distance between the poles of two ellipsoids in adjacent stacks) is equal to the smallest surface-to-surface separation within the sheets, consistent with the convention used throughout this section (except for the *isc*-structure discussed below). The maximum density of this crystal is $\pi/6$.

A fourth crystal is built so as to bear the same relation to the *efc*-lattice as the *esc*-configuration *vis-à-vis* the *ebc*-lattice:

---

‡ A quick drawing will convince the reader that the "standard" *fcc*-lattice is actually a body-centered crystal in which the surface-to-surface separation between nearest neighbors in the "xy"-plane (i.e., on the square mesh making up the face-centered motif) is equal to the distance between adjacent spheres with different "z"-coordinates (i.e., in successive layers). In the classical definition of a *bcc*-structure, on the other hand, the spheres are farther apart in the direction of the edges of the cube [(100), (010) and (001)] than along its diagonals [(111), etc.]. In order to dilute a *bcc*-crystal according to the rules developed in this work, a diamond-shaped basis pattern must be adopted with an inscribed angle of $\arccos(1/3)$ (Appendix H). The only symmetry element of this grid is a rotation by $\pi$. This implies that 6 coefficients are needed to fully characterize $\mathbf{R}_{\Sigma E}$ for a lattice of spheroids derived from a body-centered cubic cell. In contrast, because square arrays are invariant for rotations by $\frac{\pi}{2}$, 4 independent constants suffice for *ebc*-crystals as defined here.

◇ in the *smc*-structure, honeycomb layers of spheroids are stacked directly on top of one another in a manner similar to the square arrays of particles in the *esc*-configuration. This packing is somewhat less efficient than that achieved in the *efc* and *ebc* crystals, and accommodates at most $\pi/(3\sqrt{3})$. The abbreviation *smc* was chosen because this geometry is reminiscent in a crude way of the molecular arrangement in a smectic A (a liquid crystalline phase characterized by a two-dimensional ordering of the molecular centres of mass in planes perpendicular to the direction of alignment of their directors).

The fifth and last structure to be defined is

◇ the *isc*-crystal, which is identical to the *esc*-configuration when the particles touch (i.e., it is a stretched simple cubic cell at closest packing), but is then expanded to lower volume fractions by dilating isotropically, instead of respecting the usual convention which stipulates that the surface-to-surface separation is the same in at least three non-planar directions.

In order to accentuate the differences in the stress response of the various crystals, the data are presented in terms of the average stresslet $\eta$ per particle (appropriately non-dimensionalized) rather than the apparent viscosity. As shown in the previous subsection, these quantities are related by $\mu_{\text{app}} = \mu(1 + 6r_p^2\phi\eta)$. Although we shall use the symbols $\eta_T, \eta_\parallel$ and $\eta_\perp$ to denote the flow conditions illustrated in Fig. 4.6, the tensor $\mathbf{R}_{\Sigma E}$ does not in general have the form (4.43). Figure 4.11 summarizes our findings for dispersions of spheroids of aspect ratio 8. The coefficient $\eta_\perp$ is obviously the least sensitive to the detailed features of the crystal geometry. A closer look reveals however, that the microstructures with the smallest $\eta_\perp$ at a given volume fraction (i.e., the lattices which offer the least resistance to shear flows having a velocity gradient parallel to the direction of alignment, see Fig. 4.6) display the highest extensional viscosity (i.e., the largest $\eta_T$). In fact, the ordering of the lattices according to $\eta_\perp$ is exactly the reverse of the order obtained using $\eta_T$. This correlation is not surprising since both coefficients are associated with flows straining the spheroids in a plane containing their axes.

The staggered configurations (*ebc* and *efc*) display the largest $\eta_\perp$ (Fig. 4.11a). This reflects the steric hindrance to rotation brought about by interlacing the stacks of spheroids. This reduced orientational freedom (confirmed by comparing the "sedimentation rates" $V_\perp^{ro}$ of the various crystals (data not shown)) increases the stress response of the dispersion to any shearing flow which induces a rotation in a plane containing **d**. This phenomenon is proper to non-spherical particles, for which a strong coupling exists between the stress and the rotation rate (i.e., $\mathbf{R}_{s\Omega} \neq 0$). Indeed, a close inspection of the grand mobility tensor clearly demonstrates that the origin of the larger $\eta_\perp$ for staggered configurations resides in the larger $\mathbf{M}_{\Omega S}$ for these systems. This effect is more pronounced for the *ebc*-lattice than for the *efc*-geometry because each particle has 8 out-of-plane neighbors which hinder its rotation in the former crystal (and 4 in-the-plane neighbors which reinforce its motion), as opposed to 6 out-of-plane neighbors and 6 in the same layer for the *efc*-lattice. Finally, the *isc*-geometry, which leaves the largest gaps between the layers, clearly has the lowest $\eta_\perp$, in accordance with the arguments above.

Despite the aforementioned correlation between $\eta_\perp$ and $\eta_T$, the physical mechanism responsible for the decreased extensional viscosity in staggered lattices cannot be traced to the coupling between the rotation rate and the stress ($\mathbf{M}_{\Omega S}$), since this is irrelevant for uniaxial extension. (This can best be seen by observing that the spheroid does not reorient when the principal direction of strain coincides with its axis.) Instead, the stronger resistance to axisymmetric extension of the *smc* and *esc*-configurations is directly related to a reduction of the diagonal elements of $\mathbf{M}_{ES}$ compared to their values for *efc* and *ebc*-lattices at the same volume fraction. Physically, this arises because the secondary flow generated by spheroids when they oppose the elongational deformation, more strongly affects the vicinal spheroids when these are perfectly aligned with them, than when they are slightly to the side. The analysis by Shaqfeh & Fredrickson (1990) and the qualitative argument justifying the cell model used by Batchelor (1971) to calculate the extensional viscosity of a suspension of uniformly aligned rods emphasize the importance of the smallest

distance between the fibres (measured perpendicular to the particles' axes, and not between their geometric centres), since this is the length scale for hydrodynamic screening. This is the least for *isc*-crystals, which have to compensate for the loose stacking of the layers by packing the spheroids more tightly within the sheets. This lattice correspondingly has the highest $\eta_T$.

The response of the dispersions to simple shear in the $xy$-plane, finally, depends mostly on the shortest distance between the fibres along the principal directions of the strain (i.e., the compressional and extensional axes of the flow). These distances are listed in table 4.1 for all lattices at $\phi = 0.1$, and can be seen to correlate well with $\eta_{\parallel}$. For crystals with hexagonal rather than square symmetry in the plane of shear, the separation given is the centre-to-centre distance between nearest neighbors. The spacing of the particles, averaged along both the compressional and extensional axes of the shear, will certainly be larger for these configurations, which explains why the *efc* and the *smc*-lattices display lower apparent shear viscosities than suggested by the distances of Table 4.1.

*Table* 4.1: Shortest centre-to-centre distance along the principal directions of strain of a simple shear flow in the plane perpendicular to the axis of the particles for several crystal geometries at $\phi = 0.1$ ($r_p = 8$).

| | efc | smc | esc | esc | ebc | ebc | isc | isc |
|---|---|---|---|---|---|---|---|---|
| $\vartheta$ | $\frac{\pi}{12}$ | $\frac{\pi}{12}$ | $\frac{\pi}{4}$ | 0 | $\frac{\pi}{4}$ | 0 | $\frac{\pi}{4}$ | 0 |
| $\eta_{\parallel}(\times 10^3)$ | 5.99 | 6.06 | 7.57 | 5.03 | 7.08 | 5.06 | 9.41 | 5.07 |
| $r/a$ | .592 | .569 | .535 | .757 | .570 | .806 | .429 | .606 |

$r/a$ is the shortest distance between the centres of the spheroids for the given configuration, measured at $\frac{\pi}{4}$ or $\frac{3}{4}\pi$ relative to the direction of flow in the plane of shear (i.e., along the compressional and extensional axes of the straining field). As always, $a$ denotes the particle half-length. The angle $\vartheta = 0$ if the undisturbed velocity lies along the shortest basis vector of the lattice (Fig. 4.10). See also Fig. 4.11.

### 4.6.5 Comparison of spheroids with strings of beads

One of the major advantages of the simulation technique is that it only uses 11 unknowns per particle, yet claims to reproduce hydrodynamic interactions between the rods quite well. In order to check how adequately Stokesian dynamics represents the effect of the spheroids on the flow, we compared the properties of a crystal of spheroids with those of a lattice of spheres rigidly connected into strings. Since each bead of the arrangement has 11 degrees of freedom associated with it, this representation of an "elongated" body captures more stress moments than only the total force, torque and stresslet exerted by the composite object on the fluid. We then constructed a "smectic" crystal of strings by placing arrays of 19 aligned spheres on hexagonal grids, and stacking these sheets directly on top of one another. We then calculated the properties of this lattice using a version of Stokesian dynamics dedicated to spherical particles (and verified the results with our program in the limit of zero eccentricity). The single string contribution $\eta_T$ to the extensional viscosity is given by the solid line in Fig. 4.12. We then matched this component of the stresslet for the string of beads at infinite dilution to that exerted by two isolated spheroids, one having the same length as the composite rod (20 sphere diameters), but a different aspect ratio ($r_p = 11.4$), the other having the same aspect ratio ($r_p = 20$), but a longer axis ($a = 21.93R$, with $R$ the radius of the spheres). Both spheroids are displayed in the insert of Fig. 4.12. The properties of *smc*-crystals of these spheroids were then computed using Stokesian dynamics. Since the two ellipsoids are considerably more voluminous than the string of beads (even the slender spheroid takes up about 40% more room), it is important to compare $\eta_T$ at the same number density of rods, rather than at equal packing fractions. One can then see from Fig. 4.12 that the data for the lines of spheres lie in between those for the lattices of spheroids. At each concentration, there therefore exists an ellipsoid whose geometry approximates that of the string of beads, and which has the same extensional viscosity at infinite dilution and at the chosen number density. More importantly, the version of Stokesian dynamics which truncates the moments

expansion of the stress density after the first two terms (keeping only the effect of the force, torque and stresslet) seems at the very least to capture the qualitative features of the concentration dependence of the transport properties for crystals of rod-like objects. This represents a considerable computational advantage, since only 11 unknowns describe the spheroids in this example, as opposed to 209 for the string of 19 spheres. As the time required to carry out the matrix inversion (which yields $\widetilde{\mathbf{M}}^{-1} \simeq \mathbf{R}$; see (4.25)) grows with the cube of the number of unknowns, this is very significant. Figure 4.12 also shows that the results for the spheroids agree quite well with each other when plotted *vs.* the actual volume fraction too, and that the calculations were carried out to nearly close packing, even though the corresponding density of spheres was only moderate ($\sim 15\%$). In other words, at the point where the upper curve crosses the data for the string of beads in Fig. 4.12, the spheroids are nearly touching and lubrication stresses, if they would be accounted for, would undoubtedly increase the extensional viscosity above that of the line of spheres. The agreement thus remains very good up to the highest possible density.

## 4.7 Hydrodynamic transport properties of equilibrium hard-spheroid dispersions

As shown in the previous section (§4.6.3 especially), a fibre influences the hydrodynamics of the suspension over a fluid volume of $O(a^3)$, with $a$ the particle half-length. Thus, $n_\phi a^3$ is the relevant measure of concentration for all hydrodynamic transport properties (as well as for the thermal conductivity (Shaqfeh, 1988) and the dielectric constant, by mathematical analogy (see Bonnecaze, 1991)). The density, on the other hand, scales with $n_\phi a^3/r_p^2$. For spheroids of aspect ratio 10, these scales differ by two orders of magnitude. It is therefore conceivable that a sample with an extremely low volume fraction is relatively concentrated as far as viscous interactions are concerned, with characteristics differing radically from those of isolated particles. Furthermore, the excluded volume of rods varies as $a^3/r_p$, a scaling intermediate between that of hydrodynamic effects and that of the volume actually occupied by

the fibre. At least three concentration regimes can thus be distinguished in dispersions of hard rods (Doi & Edwards, 1986): dilute systems ($n_\phi a^3 \ll 1$) in which the spheroids are essentially isolated, semi-dilute samples ($1 < n_\phi a^3 < r_p$), where hydrodynamic interactions are dominant, and concentrated rod dispersions ($n_\phi a^3 > r_p$) with noticeable excluded volume effects. The transition from dilute to semi-dilute can be thought of as the onset of entanglements; i.e., the separation between the fibres becomes smaller than their largest dimension. We already saw that this leads to hydrodynamic screening in the semi-dilute region. The concomitant reduction in the rods' motional freedom (as observed by the drop in the long-time rotational diffusivity for instance) is often graphically explained in terms of a "caging" effect (Doi & Edwards, 1986). The crossover from semi-dilute to concentrated dispersions is even more dramatic in a sense, since the microstructure changes appearance, with the formation of liquid crystalline domains. This phase transition is accompanied by discontinuities in the macroscopic properties of the suspension. In particular, the system is no longer isotropic. (The hallmark of liquid crystalline phases is long-ranged molecular orientational order. This confers a directional dependence to all tensorial observables, such as diffusivities, stress/rate-of-strain relations, permeability, conductivity, refractive index, etc.)

In this section, we report on numerical simulations tracking the properties of suspensions of hard spheroids as a function of the solid content. The effect of hydrodynamic interactions is always visible as a deviation from the single-particle behavior. Any non-linearity in the concentration dependence betrays the importance of viscous interactions. In some instances, we shall also detect the isotropic-to-nematic transition. ("Nematic" is the liquid crystalline phase favored thermodynamically by systems of hard spheroids at sufficiently high densities.) Although external fields –either electromagnetic (for susceptible particles) or mechanical (an imposed continuous deformation for example)– can induce orientational order, in effect lowering the isotropic-to-nematic boundary (Thirumalai, 1986; See *et al.*, 1990), we shall focus on equilibrium microstructures only in this work. The effect of the flow on

the configuration of the particles is not accounted for. As explained in §4.6, this amounts to calculating the short-time or high-frequency limit of the transport properties. The microstructures may be thought of as being representative of Brownian dispersions (at zero Péclet number), even though the spheroids in our simulations are not subject to thermal motion and Brownian stresses are not computed.

We pointed out in the previous paragraph that the excluded volume due to the presence of a rod exceeds its actual volume by a factor proportional to the aspect ratio. This implies that it is much harder to generate an "isotropic" configuration of rods than a random assemblage of spheres at the same volume fraction. The equilibrium hard-ellipsoid configurations discussed in this section were generated by a Monte-Carlo method (the energy function being infinite whenever two particles overlap, and indifferent to particle location and orientation otherwise). The spheroids were initially placed on an *efc*-lattice at the desired concentration. The unit cell was made "as cubic as possible" within the constraint of the imposed number of particles by taking optimal combinations of the elementary basis vectors of the lattice (i.e., of the vectors joining nearest neighbors in the crystal). For example, a run with 48 particles might start with 3 layers of 16 spheroids arranged on a $4 \times 4$ grid, or with 2 sheets of 24 rods in 4 rows of 6, depending on the relative size of the elementary basis vectors of the lattice. (For very concentrated systems of highly elongated particles, the distance between the stacks of spheroids is so much larger than the separation within each layer, that the "best" building block for the initial *efc*-lattice may very well be one 6 by 8 hexagonal pattern of spheroids.) A box shape standardization algorithm (discussed in Ch. V) guarantees that all angles inscribed between the edges of the unit cell lie between $\frac{\pi}{3}$ and $\frac{2\pi}{3}$, thus preventing the accidental use of very skewed modules which would complicate the geometric analyses, and might bias the particle configuration. This places absolutely no restriction on the type of microstructures that can be examined. The particles are then subject to random translational and rotational displacements in the manner proposed by Frenkel & Mulder (1985), rejecting all moves which cause spheroids

to overlap. The "quick" Perram-Wertheim criterion (Perram & Wertheim, 1985; Allen *et al.*, 1989) was used to screen most of the potentially offending pairs, followed by the more elaborate test for overlap due to Vieillard-Baron (1970) if the first check was inconclusive. (The six conditions satisfied by non-intersecting spheroids were derived by Vieillard-Baron for identical particles only, but the analysis leading to his equations can be adapted for unlike ellipsoids, resulting in a set of six similar criteria.) The Monte-Carlo procedure can be proven to sample configuration space evenly (Metropolis *et al*, 1953), producing representative snapshots of the equilibrium microstructures of hard-particle dispersions. We double-checked our method by verifying that the centres of mass of the spheroids wander diffusively as a function of the number of random displacements. We also found that hard-sphere suspensions generated in the same manner possess radial distribution functions in excellent agreement with the Percus-Yevick equation (Smith & Henderson, 1970; Perry & Throop, 1972; Verlet & Weis, 1972), except of course for the effects of periodicity. The values of the transport coefficients given below are averages over at least 6 to 8 different realizations of each dispersion of spheroids (at every concentration and for each aspect ratio). Only monodisperse samples were considered.

Before diving into the results, let us pause for a moment and consider the geometric problem of placing $N$ spheroids inside the unit cell. Orientational order spontaneously appears in the samples at concentrations such that $n_{\phi_c} a^3/r_p \simeq 1$ (Doi & Edwards, 1986). The scaling with inverse aspect ratio obviously follows from the fact that excluded volume is the driving force for the thermodynamic transition to liquid crystalline states. Nematics are thus formed at lower volume fractions for slender fibers than for short rods, since the critical concentration $\phi_c = n_{\phi_c} 4\pi a^3/3r_p^2 = O(4\pi/3r_p)$, a decreasing function of aspect ratio. On the other hand, it is advisable to work with unit cells which are large enough to accommodate the spheroids in any orientation they may choose, so as not to bias the resulting microstructure by the shape and size of the periodic building block. It

follows that its volume $V_{\text{cell}} \geq O(8a^3)$. Hence the number of particles needed to simulate dispersions in the transition region from isotropic to liquid crystalline is $N = O(n_{\phi_c} V_{\text{cell}}) = O(8r_p)$. The inversion of the grand mobility matrix to get a far-field approximate to the resistance tensor (as required by the algorithm of Stokesian dynamics (§4.3)) is an $O(N^3)$ operation,‡ and evaluating the mobility interactions is a costly $O(N^2)$ step (see §4.4). It is therefore computationally advantageous to examine spheroids of moderate aspect ratio if we are primarily interested in the behavior near the phase boundary. Note that hydrodynamic interactions, on the other hand, change the character of the response at $n_\phi = O(a^{-3})$, and can therefore be studied using $N = O(8)$, a very manageable number, and independent of aspect ratio. A second incentive to restrict the simulations to moderate aspect ratios (even though most theories have been developed in the limit $r_p \to \infty$, as mentioned in the introduction) was touched upon in §4.4 when we explained that $\mathbf{M}$ gets increasingly ill-conditioned as the particles become more slender, making the computations more critically sensitive to numerical inaccuracies. In view of these arguments, we concentrated most of our efforts (and available share of CPU-time) to the study of dispersions of hard ellipsoids of aspect ratio 6. However, the method was found to work well even at the highest aspect ratio considered ($r_p = 100$).

### 4.7.1 Diffusivities

The diffusion tensor of an isolated axisymmetric rod is fully determined by 4 coefficients, which characterize its translational and rotary mobilities for motions parallel and perpendicular to the centreline. In an arbitrary dispersion however, each fibre's environment is locally anisotropic and this simple structure for the diffusivity tensor is lost for each particle individually. By virtue of Lorentz' reciprocal theorem (which in this case is equivalent to an Onsager relation), the diffusivity tensor is still symmetric and hence can be diagonalized. Its eigenvectors, however, do not necessarily

‡ Methods are presently evaluated to reduce this step to an $O(N^2)$ operation by taking advantage of *à priori* knowledge about the relative strength of interactions.

coincide with the principal axes of the ellipsoid, and so the eigenvalues cannot be associated with diffusion either parallel or perpendicular to the rod. In many cases, interactions with immersed objects nearby will actually produce a coupling between translations and rotations, so that the eigenvectors represent a complex concerted motion involving some tumbling with each displacement. On a global, macroscopic scale however, the microstructure of an isotropic suspension is homogeneous and the particles do not diffuse in any preferred direction on average; there also isn't any systematic correlation between centre-of-mass motions and reorientations. From a macroscopic perspective, the translational and rotational transport processes can each be described by a single scalar. Yet we can define an average self-diffusivity parallel to the rod axis, $D_{\parallel}^{\mathrm{tr}}$, as the mean projection of the diffusion tensor of each rod onto its director. With the Stokes-Einstein relation (see (4.38)), we thus set:

$$\langle D_{\parallel}^{\mathrm{tr}} \rangle = \mathrm{kT} \langle \left( \mathbf{R}_{\mathcal{FU}}^{-1} \right)_{UF}^{pp} : \mathbf{d}_p \mathbf{d}_p \rangle \ , \tag{4.47a}$$

and, for motions perpendicular to the fibre,

$$\langle D_{\perp}^{\mathrm{tr}} \rangle = \tfrac{1}{2} \mathrm{kT} \langle \left( \mathbf{R}_{\mathcal{FU}}^{-1} \right)_{UF}^{pp} : (\boldsymbol{\delta} - \mathbf{d}_p \mathbf{d}_p) \rangle \ . \tag{4.47b}$$

The rotational analogues obviously use the $\Omega L$ (bottom-right) portion of $\left( \mathbf{R}_{\mathcal{FU}}^{-1} \right)^{pp}$. For an infinitely dilute monodisperse random dispersion, these definitions agree with the single particle characteristics.

Figure 4.13 shows for equilibrium dispersions of spheroids of aspect ratio 6 that rotational diffusivities decrease less rapidly with concentration than their translational counterparts. This was to be expected since the disturbance velocity for a tumbling particle decays faster with distance than that due to a translating body. At a given concentration, motions perpendicular to the rod axis are also affected more significantly by hydrodynamic interactions than motions parallel to it. This is in tune with intuition, since they displace more fluid, creating a stronger flow field which is opposed by the surrounding particles. In essence, this expresses the notion that the "hardest" motions in an unbounded fluid (characterized by the

smallest value of the diffusivity) are also most sensitive to increases in the viscous resistance of the medium due to the presence of obstacles. Upon freezing of the microstructure to calculate hindered diffusion coefficients, this effect is accentuated and the sharpest drops are noted for $H_{\perp}^{\mathrm{tr}}$ and $H_{\perp}^{\mathrm{ro}}$. This may seem to agree with the basic assumption of reptation theory (de Gennes, 1971; Doi & Edwards, 1986), but it must be emphasized that only the short-time limits of the transport properties are calculated here. The reduction in the mobility is due solely to hydrodynamic interactions, not to the "caging" effect on which reptation theory is founded. Steric hindrance only enters the simulation through lubrication stresses, for the given instantaneous configuration of the particles. In addition, it is apparent that the assumption that $H_{\parallel}^{\mathrm{tr}}$ remains equal to its free solution value (independent of concentration) is unwarranted, since it has already decreased to half that number in a dispersion containing 10% by volume of solid material.

The system of $\sim 50$ periodically replicated prolate spheroids of aspect ratio 6 considered here undergoes a phase transition to a nematic crystal (with a long-ranged orientational order) at a concentration of about 30%.‡ This (imperfect) alignment of the rods does not greatly influence the mobility of the particles, however, and only the translational self-diffusivities seem to increase slightly at the phase boundary. The upward shift is indicative of the tube dilatation associated with the ordering of the fibres (Doi & Edwards, 1986). Although not nearly as spectacular, it is reminiscent of the jump and maximum observed for the density variation of $D_{\parallel}^{\mathrm{tr}}$ in molecular dynamics simulations of fluids of hard ellipsoids past

‡ The volume fraction at the transition lies slightly below the phase boundary found by Monte-Carlo methods for fluids of hard ellipsoids (Frenkel & Mulder, 1985; Allen (1990) reports $\phi_c \simeq 0.36$ for $r_p = 5$). This lowering of the critical concentration is presumably a weak periodicity effect, enhanced by the relatively small size of the periodic box. For comparison, several hundred particles were used in the Monte Carlo and molecular dynamics studies.

the isotropic-to-nematic transition (Allen, 1990). That work, of course, neglected all viscous interactions and assumed free-flight dynamics between collisions. The influence of the order parameter on the motional freedom of the particles may be analogous in both systems, however.

Just as in the previous section (see Fig. 4.5), the translational self-diffusivity of the spheroids in equilibrium dispersions increases with the number of particles per unit cell because the backflow generated by the periodically replicated unit force diminishes. The effect of $N$ on the rotary diffusion is less pronounced, and masked by the statistical uncertainty (Fig.4.13 and Table 4.2). The dependence on $N$ is also weaker in fibrous media, because the fixed network tends to screen the disturbance velocities, as explained in §4.5.

*Table* 4.2: Effect of the number of particles $N$ per unit cell on the calculated diffusivities of equilibrium dispersions of spheroids of aspect ratio 6 at $\phi = 0.15$.

| $N$ | $D_\perp^{\mathrm{tr}}$ | $D_\parallel^{\mathrm{tr}}$ | $D_\perp^{\mathrm{ro}}$ | $D_\parallel^{\mathrm{ro}}$ |
|---|---|---|---|---|
| 25 | 1.35 | 2.27 | 4.82 | 49.3 |
| 30 | 1.56 | 2.48 | 5.06 | 49.9 |
| 50 | 1.59 | 2.53 | 5.00 | 48.7 |
| 60 | 1.61 | 2.55 | 4.98 | 48.7 |
| 64 | 1.71 | 2.68 | 5.10 | 49.9 |
| $N$ | $H_\perp^{\mathrm{tr}}$ | $H_\parallel^{\mathrm{tr}}$ | $H_\perp^{\mathrm{ro}}$ | $H_\parallel^{\mathrm{ro}}$ |
| 25 | .822 | 1.67 | 3.22 | 47.2 |
| 30 | 1.02 | 1.87 | 3.86 | 47.7 |
| 50 | .977 | 1.84 | 3.75 | 46.3 |
| 60 | .982 | 1.83 | 3.72 | 46.2 |

See also Fig.4.13. The transport coefficients are made dimensionless by $\mathrm{kT}/(8\pi\mu a^n)$, with $n = 1$ for the translational components and $n = 2$ for the rotary motions. For comparison, the corresponding

diffusivities at infinite dilution are $D_{\perp}^{\mathrm{tr}} = 2.991$, $D_{\parallel}^{\mathrm{tr}} = 4.069$, $D_{\perp}^{\mathrm{ro}} = 5.939$, $D_{\parallel}^{\mathrm{ro}} = 51.67$; in this limit, the hindered mobilities are equal to the self-diffusion coefficients.

For very dilute isotropic dispersions of identical spheroids, one may write unequivocally that the laboratory frame diffusion tensor $\langle \mathbf{D} \rangle = D_{\parallel}^{\mathrm{tr}} \langle \mathbf{dd} \rangle + D_{\perp}^{\mathrm{tr}} \langle \boldsymbol{\delta} - \mathbf{dd} \rangle = \left( \frac{1}{3} D_{\parallel}^{\mathrm{tr}} + \frac{2}{3} D_{\perp}^{\mathrm{tr}} \right) \boldsymbol{\delta}$. Although $\langle \mathbf{D} \rangle \neq \langle D_{\parallel}^{\mathrm{tr}} \rangle \langle \mathbf{dd} \rangle + \langle D_{\perp}^{\mathrm{tr}} \rangle \langle \boldsymbol{\delta} - \mathbf{dd} \rangle$ in general, we have verified numerically that this relation holds well for isotropic suspensions up to the transition to the nematic state. Thus the variation of $\mathbf{D} \simeq (\frac{1}{3} D_{\parallel}^{\mathrm{tr}} + \frac{2}{3} D_{\perp}^{\mathrm{tr}}) \boldsymbol{\delta}$ with volume fraction can easily be deduced from Fig. 4.13.

Several functional forms have been proposed for the $\phi$-dependence of the translational diffusion coefficients. A simple exponential decline often fits the data reasonably well over a fairly wide range of densities (White & Dorion, 1961), but stretched exponential decays are more commonly used (Wheeler *et al.*, 1987; Phillies, 1987), in part because they afford a greater flexibility. A semi-logarithmic plot of our results also reveals a span of volume fraction for which the decrease is approximately exponential, but an extrapolation to $\phi = 0$ from this region grossly underestimates the diffusivity at infinite dilution (not shown). By contrast, the law set forth by Cuckier (1984) on semi-heuristic grounds for the diffusivity of a sphere in a network of fibres, namely

$$H_{\big|\phi}^{\mathrm{tr}} = H_{\big|\phi=0}^{\mathrm{tr}} \exp(-\kappa \phi^{1/2}) \,, \tag{4.48}$$

gives quite a satisfactory fit for the hindered translational mobility in a dispersion of spheroids (Fig. 4.14). (The coefficient $\kappa$ depends on the component considered and the shape of the particles.) Since fibrous beds can be described by a Brinkman equation (Spielman & Goren, 1968), the observed dependence on $\phi^{1/2}$ can be interpreted as a manifestation of hydrodynamic screening. Indeed, Cuckier's derivation of (4.48) relied on the concept of a screening length proportional to $\phi^{-1/2}$. The results of Fig. 4.14 thus confirm that our simulation technique adequately captures the many-body effects responsible for screening in fibrous media, as advertised in §3.2 (see also Durlofsky & Brady, 1987). The influence of the particle shape on the

degree of retardation (i.e., on $\kappa$ in (4.48)) is investigated in Fig. 4.15. Concentration has been expressed as $r_p^2\phi = n_\phi \frac{4\pi}{3} a^3$. For rods of the same length, this may be thought of as the number density of spheroids. Alternatively, the abcissa can be interpreted as a count of the particles which interact hydrodynamically with the diffusing ellipsoid since, as repeatedly mentioned earlier, $a^3$ is the relevant scaling for transport properties in dispersions of fibres and hence $\frac{4\pi}{3}a^3$, the "volume of the circumscribing sphere," is a measure of the flow domain over which the presence of the fibre is felt. We have chosen to illustrate the effect of the particles' eccentricity by means of the hindered translational diffusivity perpendicular to the rod axis, but the main characteristics of Fig. 4.15 are the same for all mobility coefficients. At a given number density, one notes from Fig. 4.15 that the most slender spheroids hinder each other's motion the least. In other words, hydrodynamic interactions between two rods of fixed length $a$ at a set centre-to-centre separation are weakest for the most slender particles. This should be clear intuitively since they occupy the least space and displace the smallest amount of fluid as they move. Note however that in terms of volume fractions, the trend is opposite, with the steepest drop in $H_\perp^{\mathrm{tr}}$ (relative to the value at infinite dilution) being noted for the most elongated fibres. Indeed, at $n_\phi \frac{4\pi}{3} a^3 = 10$, the dispersion of spheroids of aspect ratio 6 contains 28% solid material, compared to 0.1% for the rod suspension with $r_p = 100$. Also, the diffusivity of ellipsoids of aspect ratio 20 has dropped by half at $\phi = 0.025$, but it takes twice this concentration to reach a similar decrease in a suspension of rods with length-to-width ratio 6.

Recall from §4.5 that the influence of the number of particles $N$ per unit cell decays quite slowly, as $N^{-1/3}$, for the self-diffusivities. The data displayed in Fig. 4.13 have not been corrected for this periodicity effect, and hence do not represent the thermodynamic limit. As stated in §4.5, the procedure proposed to extrapolate to $N \to \infty$ (Phillips *et al.*, 1988 a; Ladd, 1990) subtracts the contribution of the periodically replicated images cosedimenting with the diffusive tracer. This effect is known asymptotically for dilute arrangements of spheres on a cubic lattice (Hasi-

moto, 1959), but not for ellipsoids. Indeed, the numerical factor multiplying the $O(\phi^{1/3})$ correction then not only depends on the shape of the unit cell (which is not cubic in general), but also on the orientation of the spheroidal axis relative to the basis vectors. We can, however, estimate‡ the magnitude of the periodicity effect from our computations on $efc$-lattices and adjust the data of Fig. 4.13 according to the expression

$$D^{\rm tr}_{\{\phi_0;N\to\infty\}} = D^{\rm tr}_{\{\phi_0;N_0\}} + \left(D^{\rm tr}_{\{\phi\to 0\}} - V^{\rm tr}_{\{\phi=\phi_0/N_0;efc\}}\right)\frac{\mu(\phi_0/N_0)}{\mu(\phi_0)} \ . \qquad (4.49)$$

$\phi_0$ is the concentration of interest, and $N_0$ the number of particles in the simulation cell. The sedimentation rate $V$ is understood to be that of an $efc$-crystal with density $\phi_0/N_0$, corresponding to the volume fraction of the images of the diffusing spheroid. As explained by Ladd (1990), the factor $\mu(\phi_0/N_0)/\mu(\phi_0)$ is introduced because the $N_0 - 1$ intervening particles attenuate the periodicity effect without altering its functional form (i.e., the images of the diffusive tracer sediment in a medium of higher effective viscosity than a dispersion with concentration $\phi_0/N_0$). Figure 4.16 shows that the adjustment is substantial, especially at the lowest volume fractions (reflecting the dependence on $\phi^{1/3}$), and that the spread on the data obtained with different values of $N$ is reduced by the correction formula (4.49) (see also Table 4.3). Figure 4.16 also strongly suggests that the steep decline of $D^{\rm tr}$ with $\phi$ noted for dilute dispersions in Fig. 4.13 merely reflects the periodicity of the microstructure introduced by the boundary conditions, and is absent in truly random systems. Indeed, the extrapolated values of $D^{\rm tr}$ decrease approximately linearly with concentration, as observed experimentally for spheres (Ottewill &

‡ The configuration of the periodically replicated images of the diffusing ellipsoid does not in general constitute an $efc$-crystal, even though it forms a subset of the $efc$-lattice chosen to position the $N_0$ particles prior to the Monte-Carlo randomization. The sedimentation rate of the $efc$-structures used in the corrective formula (4.49) should thus be interpreted merely as a representative collective mobility of crystalline dispersions of spheroids with concentration $\phi_0/N_0$.

Williams, 1987; Pusey & van Megen, 1983; van Megen & Underwood, 1989; see also Phillip *et al.*, 1988a), and does not depend as critically on $\phi$ as the short-time hindered diffusivity (see (4.48)). The variance reported for the self-diffusivities in Fig. 4.16 is representative for all the transport properties and reflects the actual spread on the individual mobilities as a result of the differing local environments experienced by each particle. The average values themselves are reproducible to within two significant figures (or within 5% in some cases), a much tighter bound than that suggested by the error bars.

*Table* 4.3: Corrected values of the translational self-diffusion coefficient of equilibrium dispersions of spheroids ($r_p = 6$).

| $N_0$ | $\phi_0$ | $D^{\mathrm{tr}}_{\mid N=N_0}$ | $D^{\mathrm{tr}}_{\mid N\to\infty}$ |
|---|---|---|---|
| 0.05 | 30 | 2.31 | 3.049 |
| 0.05 | 50 | 2.42 | 3.047 |
| 0.15 | 25 | 1.66 | 2.45 |
| 0.15 | 30 | 1.87 | 2.61 |
| 0.15 | 50 | 1.90 | 2.53 |
| 0.15 | 60 | 1.92 | 2.52 |
| 0.15 | 64 | 2.03 | 2.62 |

Formula (4.49) was used to extrapolate the simulation results to the thermodynamic limit $N \to \infty$ at a fixed concentration $\phi_0$.

Within the scatter of the data in Fig. 4.13b, the rotational self-diffusivities, for which periodicity effects are much less pronounced, depend linearly on concentration. This behavior was also observed in suspensions of hard spheres upon suppression of lubrication interactions (Phillips *et al.*, 1988 b). Note that lubrication effects are relatively weak in our simulations, since the dispersions are not at all close-packed. Moreover, recall that the minimum separation between the rods must be smaller than their shortest dimension, i.e., $o(a/r_p)$, in order for the asymptotic formulae of Claeys & Brady (1989), which we use here for lack of better

information,‡ to apply. Hence, in an arbitrary microstructure, only very few pairs of particles are ever close enough to experience lubrication forces.

### 4.7.2 Resistivity of fibrous media

The permeability of fibrous packings —in preparative chromatographic columns for instance, or as support for catalysts in special reactors— is of great concern in the chemical and related industries, since it ultimately determines the flow rate achievable with a given pump, and hence the throughput and productivity of the installation. The pressure drop across filters and membranes is equally important in other processes. As explained in §4.5, Stokesian dynamics offers a way to calculate these quantities at virtually no extra cost along with the diffusivities discussed in the previous subsection and the rheological properties of suspensions (examined below). Figure 4.17 depicts some simulation data on the resistivity of equilibrium dispersions of spheroids. The mean pressure gradient over the fixed bed of fibres increases with the packing density, as expected. Since a straightforward superposition of single-rod contributions would yield a linear variation with $\phi$, the curvature in Fig. 4.17 must result from hydrodynamic interactions, which cause the dependence on concentration to steepen. Hence randomly stacking the rods amplifies their resistive response. This can be rationalized by noting that the streamlines through staggered configurations of fibres become more tortuous as the density of obstacles increases, resulting in dissipation rates which grow faster than linearly with concentration.

Although isolated slender fibres offer less viscous resistance to flow than thick rods, the pressure drop across a bed of particles of high aspect ratio is larger than that across a medium consisting of fatter spheroids at the same volumetric concen-

‡ The $O(\epsilon^0)$ correction to these formulae, with $\epsilon$ the non-dimensionalized gap width between the nearly touching surfaces, is unknown. Some of the implications of this shortcoming were explained in Ch. III. The errors it introduces are not severe at any but the most dense packing fractions.

tration (Fig. 4.17). This, of course, is a consequence of the higher number density of ellipsoids in the former case.

The dashed lines in Fig. 4.17 show the equivalent pressure gradients, $n_\phi F$, calculated for spheroids of aspect ratio 6 from the mean component of the force along the rod's axis ($n_\phi\langle F_\parallel\rangle$, lower curve) and perpendicular to it ($n_\phi\langle F_\perp\rangle$, upper bound). The net resistivity of isotropic dispersions lies between the two extremes, albeit somewhat closer to the highest limit (as might be expected from the approximate relation $\mathbf{K}^{-1}\simeq n_\phi\{\langle F_\parallel\rangle\langle\mathbf{dd}\rangle + \langle F_\perp\rangle(\boldsymbol{\delta} - \langle\mathbf{dd}\rangle)\}$, which in this case becomes $\mathbf{K}^{-1}\simeq n_\phi(\frac{1}{3}\langle F_\parallel\rangle + \frac{2}{3}\langle F_\perp\rangle)\boldsymbol{\delta}$. The permeability $\mathbf{K}$ was defined in (4.40).) Also noted at concentrations above the isotropic-to-nematic transition are the pressure drops for flow in the direction of alignment and at right angles to it. These values differ from the bounds because the ordering of the rods in the nematic phase is imperfect. It is easy to understand why structural deviations from ideality affect the permeability in the direction of the fibres the most, since any misalignment raises the pressure gradient in this case. The resistance to cross-flows, on the other hand, is relatively indifferent to disorder in the plane perpendicular to the stream vector. The phase change at ~30% also influences the bounds on the pressure gradient (the dashed curves of Fig. 4.17) inasmuch as the spread between them widens considerably more rapidly with increasing concentration past the phase boundary. This behavior follows from the definition of $\langle F_\parallel\rangle$ and $\langle F_\perp\rangle$ as $\langle\sum_q \mathbf{R}_{FU}^{pq} : \mathbf{d}_p\mathbf{d}_p\rangle$ and $\langle\sum_q \mathbf{R}_{FU}^{pq} : (\boldsymbol{\delta} - \mathbf{d}_p\mathbf{d}_p)\rangle$ respectively (see also (4.41)). In isotropic dispersions, the fibres are arbitrarily oriented, and the influence of the rods $q$ on the force exerted by $p$ is statistically uncorrelated. In nematics, $\mathbf{d}_q$ and $\mathbf{d}_p$ are nearly aligned and all the spheroids of the dispersion act consistently on the resistance of particle $p$. Hence the difference between flows parallel and perpendicular to the fibre axis are accentuated in the liquid crystalline phase, and the bounds diverge.

### 4.7.3 Viscosity and stress/rate-of-strain relations

If the fibres are force-free rather than immobile, the rheology of the suspension is of interest. In disordered dispersions, for which all rod orientations are equally

probable, the stress response to a rate of strain is Newtonian and can be characterized by one scalar, the effective viscosity. This quantity is plotted in Fig. 4.18 for equilibrium microstructures of spheroids with aspect ratio ranging from 3 to 50. The values reported are means of the particle stresslets over several realizations at each concentration. Typical simulations used 50 to 64 particles per unit cell. In addition, the 6 pertinent components of $\langle \mathbf{R}_{\Sigma E} \rangle = \langle \mathbf{R}_{su} \cdot \mathbf{R}_{\mathcal{F}u}^{-1} \cdot \mathbf{R}_{\mathcal{F}E} - \mathbf{R}_{sE} \rangle$ were also averaged as independent measures of the viscosity.‡ The disproportionate enhancement of the viscosity by the addition of a few fibres to the medium (notice the steep slope of the concentration dependence for $r_p = 50$ in Fig. 4.18) is explained by the fact that there are always some rods in an isotropic suspension which lie along the principal axes of extension of the flow. These components of the straining field are then very effectively counteracted by the rigid, unstretchable rods, generating the large stress response (*cf.* the discussion of Fig. 4.8 in §4.6.3 for crystalline geometries, and the theoretical analyses of the hydrodynamic stress in suspensions of rods by Shaqfeh & Fredrickson (1990)). The contribution of the fibres to the resistance of the suspension increases with the aspect ratio of the particles (Fig. 4.18), but the enhancement is not quite as dramatic as for *efc*-lattices (Fig. 4.8). In the regular, perfectly aligned arrays of Fig. 4.8, the effectivity of slender spheroids in raising the extensional viscosity could be attributed almost exclusively to their high

‡ These components give the responses to each of the five independent elements of the rate-of-strain tensor and correspond to the "diagonal" of $\langle \mathbf{R}_{\Sigma E} \rangle$. The sixth non-zero constituent of this tensor, which expresses a coupling between the stress and the rate of strain in mutually orthogonal directions, was found to be subject to a much greater statistical uncertainty than the other components, and was sometimes not included in the averaging process (if deemed unreliable based on its variance). The other, "irrelevant" elements of $\langle \mathbf{R}_{\Sigma E} \rangle$ were usually at least ten times smaller than the diagonal terms, and their error estimate was always more than their average value, indicating that they would indeed converge to zero as $N \to \infty$.

number density in the dispersion. Indeed, $n_\phi$ grows as $r_p^2$ (at equal volume fraction), while the average stresslet per particle, $\eta_T$, is relatively independent of the particle shape as a first approximation (see (4.45a)). The coefficients $\eta_\parallel$ and $\eta_\perp$ on the other hand, which describe the resistance of the suspension to other types of flow (see Fig. 4.6), decrease roughly as $r_p^{-2}$, thus cancelling the effect of the number density on the macroscopic shear stress (see (4.45b-c) and Fig. 4.7). In an isotropic suspension, the rods are arbitrarily oriented with respect to the principal axes of the rate of strain and consequently the single-particle contribution $\eta$ to the effective viscosity—recall that $\mu_{\text{eff}} = \mu(1 + 8\pi a^3 n_\phi \eta)$—is a mix of $\eta_T, \eta_\parallel$, and $\eta_\perp$.† Thus $(\mu_{\text{eff}}/\mu - 1)$ does not quite increase with the square of the aspect ratio at a given $\phi$, unless $\eta_T \gg \eta_\parallel + \eta_\perp$, i.e., the fibres are very slender. The data in Fig. 4.18 support this assertion, since the relative increase in the effective viscosity is larger from $r_p = 10$ to $r_p = 20$ than from $r_p = 3$ to $r_p = 6$ at any given concentration, even though neither increase is even close to a quadrupling. This is also illustrated in Fig. 4.19, where the particles' contribution to the effective viscosity is plotted

† We consider the coefficients $\eta_T, \eta_\parallel$, and $\eta_\perp$ as distinct here, yet argued in §4.6.3 that they all become equal for isotropic dispersions. This apparent contradiction stems from a different interpretation of the defining relation (4.43). Earlier, we took $\mathbf{d}$ to mean the average orientation vector in the dispersion, i.e., $\langle \mathbf{d} \rangle$. (Alternatively, it is the axis of cylindrical symmetry of the microstructure.) The coefficients $\eta_T$, $\eta_\perp$ and $\eta_\parallel$ therefore represented the average stresslet in the dispersion due to flows having the particular orientation relative to $\langle \mathbf{d} \rangle$ shown in Fig. 4.6. Now, $\mathbf{d}$ denotes the actual direction of the spheroidal axis, and the relation (4.43) must be averaged to obtain the macroscopic response. Since $\langle \mathbf{dd} \rangle = \langle \mathbf{d} \rangle \langle \mathbf{d} \rangle$ etc. for *efc*-crystals, the two interpretations were equivalent in §4.6. For isotropic suspensions, however, the former option suggests that $\eta_T = \eta_\perp = \eta_\parallel = \eta$, while the latter yields $\eta = \frac{1}{5}\eta_T + \frac{2}{5}\eta_\parallel + \frac{2}{5}\eta_\perp$. The asymptotes (4.45) implicitly assume the second meaning for the coefficients.

*vs.* the number density of particles. For rods of very high aspect ratio, the curves should almost collapse since their stresslet is then dominated by $\eta_T$, which depends only weakly on $r_p$ (namely as $\log^{-1}(r_p)$ to a first approximation for dilute systems of very slender fibres). We see a much stronger dependence on the shape of the spheroids in Fig. 4.19, reflecting the non-negligible effect of $\eta_\parallel$ and $\eta_\perp$ on the rheology of these dispersions. Although the curves in this figure seem perfectly straight, the linear plot of Fig. 4.18 clearly show a slight upward bend, indicating modest deviations from dilute suspension behavior. Figure 4.20 more explicitly demonstrates that our simulations capture the nascent semi-dilute concentration regime at the highest volume fractions. Somewhat surprisingly, the dispersion containing 1% rods of aspect ratio 50 still responds hydrodynamically as if it were dilute, even though $n_\phi \frac{4\pi}{3} a^3 = 25$. Examining the rheological properties of more concentrated systems for this aspect ratio would require the use of a prohibitively large number of particles per unit cell. (The density of a suspension with 64 spheroids of $r_p = 50$ in a periodic box of side $2a$ is 0.0134. Any increase of the volume fraction beyond this value at fixed $N$ violates the constraint that the smallest box dimension must be larger than the particle length.) Also drawn in Fig. 4.20 is the theoretical prediction of Shaqfeh & Fredrickson (1990) for the hydrodynamic stress in semi-dilute suspensions of slender rods. Our data are consistent with their result, but do not support it conclusively either. We note, however, a definite transition from a dilute concentration range, where the stresslet is independent of the volume fraction, to a semi-dilute regime, in which the particle's resistance grows with $\phi$.

We mentioned earlier that equilibrium dispersions of hard spheroids with aspect ratio 6 undergo a phase transition to a liquid crystalline state above 30% by volume. Fig. 4.21 demonstrates that the accompanying structural change causes an abrupt increase in the extensional viscosity (assuming the principal direction of strain lies along the director of the nematic phase). This is easily explained by the fact that all particles are now oriented (on average) so as to oppose the attempted stretch most effectively. (The small graph appended to Fig. 4.21 shows $\langle P_2(\mathbf{d}_p \cdot \mathbf{d}_q) \rangle$

as a function of density, with $P_2(x)$ the second order Legendre polynomial. The average runs over all pairs of rods in the unit cell. For an isotropic orientation distribution, $\langle P_2 \rangle = 0$, and $\langle P_2 \rangle = 1$ if all rods are perfectly aligned. The transition to a nematic phase is clearly visible.) The jump, however, is not nearly as large as might have been expected from a comparison with the extensional viscosity of *efc*-lattices (dashed line in Fig. 4.21). In order to test the hypothesis that this was due to the incomplete alignment of the rods, we also calculated the rheological properties of a few dispersions of parallel spheroids whose centres of mass were statistically uncorrelated, thus isolating the effect of orientational disorder. The results shown in Fig. 4.21 prove that translational mixing alone accounts for a large fraction of the difference in the extensional viscosities of nematics and *efc*-lattices, possibly because of the disruption of the very regular columnar structures typical of the latter geometry. The partial misalignment of the spheroidal axes in the liquid crystalline phase however ($\langle P_2 \rangle \simeq 0.55$ at $\phi = 0.33$), is the dominant cause for the lower Trouton viscosity of equilibrium configurations compared to that of arrangements of parallel rods. Also included in Fig. 4.21 for illustrative purposes is the effect of lubrication interactions on the calculated viscosity. It is seen to be modest, increasing monotonically with density as expected.

Milliken *et al.* (1989) measured the effective viscosity of isotropic rod suspensions by falling ball rheometry. Unlike more traditional rheometric techniques, this method offers the advantage that the microstructure of the dispersion may not be significantly perturbed by the measurement. Thus the orientation distribution of the rods remains essentially at its initial state during the experiment (Powell *et al.*, 1989). The effective viscosities are calculated from the sedimentation rate of a spherical probe through the dispersion (Milliken *et al.*, 1989). Data are reported up to a concentration of 5% in Fig. 4.18 for isotropic dispersions of polymethyl methacrylate (PMMA) rods of aspect ratio 19.83, and rayon fibres of aspect ratio 18.5. Although Milliken *et al.* (1989) claim a very good agreement with dilute suspension theory (Brenner, 1974; Haber & Brenner, 1984), our simulation results

appear to underestimate $\mu_{\text{eff}}$ by a factor of almost 2. Since the particles used in the study were cylindrical, an equivalent spheroidal shape must be assumed to make the comparison meaningful. Traditionally, the effective aspect ratio is defined as the elongation of a spheroid with the same period of rotation in simple shear flow as the rod. Using the formula for slender blunt-ended bodies given by Brenner (1974), one easily finds $r_{\text{eq}} = 14.2$ for the PMMA sample, and $r_{\text{eq}} = 13.5$ for the rayon fibres. The particle dimension can also be adjusted to improve the fit. We determine the length of the major semi-axis by matching the stresslet of the cylindrical rods to that of the equivalent spheroids at infinite dilution. By means of the material constants tabulated in the above mentioned reference (Brenner, 1974), one calculates a small correction, $(a_{\text{eq}}/a_{\text{rod}})^3 = 1.11$ for both test particles. As shown in Fig. 4.18, these refinements do not significantly reduce the discrepancies between simulation and experiment, since the data seem to lie closer to the curve for $r_p = 20$ than along $r_{\text{eq}} = 14$. Even at the lowest volume fraction for which measurements were made, the agreement is unsatisfactory. How can this be reconciled with the fact that we equated the stresslets of the particles and of the equivalent spheroids at infinite dilution, and why do Milliken *et al.* (1989) find a much better agreement with theory (their Fig. 5) than we can offer? Milliken *et al.* use the expression for the intrinsic viscosity $[\eta] = (\mu_{\text{eff}}/\mu - 1)/\phi$ from the work by Haber & Brenner (1984) on dilute monodisperse suspensions of centrosymmetric particles at small rotary Péclet number (i.e., under the assumption that the disorienting effect of Brownian motion overwhelms the tendency for alignment due to the imposed rate of strain):

$$[\eta] = \frac{1}{3}(Q_1 + Q_2 + Q_3) + (q_1 + q_2 + q_3) - \frac{5}{6}\frac{N_T^2}{{}^rK_T} \; . \tag{4.50}$$

All the symbols on the right hand side are purely geometric material constants which, for spheroids, are functions of the aspect ratio only (see Haber & Brenner (1984) for their definition). In their derivation of (4.50), Haber & Brenner (1984) emphasize that the last term arises from two contributions to the stress at steady state:

1. the mismatch between the angular velocity of the particle and the local vorticity of the flow, and
2. the Brownian couple tending to restore the orientation distribution to a fully random state, annihilating the perturbation introduced by the straining field.

For axisymmetric bodies, in the limit of strong Brownian motion, these two effects cancel each other identically ($N_T = 0$). This indicates that they are of comparable magnitude, and hence that it is inconsistent (at steady state and for small Péclet numbers) to neglect one and retain the other. In essence, if a rod is easily rotated by the flow (and therefore alleviates the stress by "yielding" to the straining field), its motion will create an anisotropic orientation distribution which, in turn, generates a Brownian stress. In our simulations, only the hydrodynamic contributions to the stress are evaluated; the Brownian part is not,‡ but for the isotropic microstructures considered here, this is exactly zero, and the entire stress in the dispersion is hydrodynamic (in the absence of interparticle forces). Bear in mind that these configurations were obtained by a Monte-Carlo technique, and that their orientation distribution is not a solution of the evolution equation in the presence of an imposed flow field, in contrast to the underlying assumption of (4.50). Alternatively, we calculate the properties of isotropic suspensions of non-Brownian rods, i.e., in the limit of infinite Péclet number, for which (4.50) does not hold. Indeed, our simulation results are in very good agreement with dilute suspension theory, provided that one recognizes that all orientations are equally probable, identically, and hence that the Brownian contribution to the viscosity is zero. Equation (4.50)

‡ The expression for the Brownian stress involves the divergence of a combination of $N$-particle resistance tensors, $\nabla \cdot [\mathbf{R}_{SU} \cdot \mathbf{R}_{FU}^{-1}]$ (Brady & Bossis, 1988; Bossis & Brady 1989), and its evaluation is intrinsically a computationally expensive operation. This problem, and other complications associated with thermal motion form a subject for further study.

then becomes

$$[\eta] = \frac{1}{3}(Q_1 + Q_2 + Q_3) + (q_1 + q_2 + q_3) - \frac{5}{6}\left(\frac{N_1^2}{{}^rK_1} + \frac{N_2^2}{{}^rK_2} + \frac{N_3^2}{{}^rK_3}\right), \qquad (4.51)$$

as first calculated by Batchelor (1970 b) for dilute suspensions of triaxial ellipsoids (see also Haber & Brenner (1984), their equation [8.8]). (One can also use Brenner's equation [4.25] (Brenner, 1974), since it does not assume steady state and is correct for any orientation distribution function, whether or not it satisfies the appropriate stationary convection-diffusion equation in orientation space.) The excellent fit of the data of Milliken *et al.* (1989) by equation (4.50) is misleading because it suggests that their experiments measure both the hydrodynamic and the Brownian stress in the suspension, even though the rotary Péclet number $Pe \gg 1.9 \times 10^9$ for the centimer-sized rods which they use. The authors recognized this and state that "the effect of Brownian forces was negligible." Yet they rely on (4.50) for comparison with theory, arguing erroneously that this formula should apply for random dispersions of axisymmetric particles, whether this randomness is caused by Brownian motion or by "whatever means" (Powell, 1991). This is untrue, and in using (4.50) rather than (4.51) they neglect a contribution from the hydrodynamic forces to the effective viscosity. Hence the excellent agreement noted by Milliken *et al.* (1989) must be called fortuitous. Powell *et al.* (1989) report data for millimeter-sized rods of aspect ratio 10 using falling ball rheometry, and find that eq. (4.50) overestimates the viscosity, in accord with our expectations. Although the authors blame the deviation on the use of slender body theory in the derivation of (4.50), it is clear that the Brownian contribution to the stress, which is included in (4.50), should be negligible in their experimental system as well as in that of Milliken *et al.* (1989). As shown in Fig. 4.18, however, their viscosity measurements (performed at $\phi = 0.05$ only) also yielded values higher than those predicted by our simulations on equilibrium hard-rod dispersions. (The equivalent aspect ratio of their cylindrical particles is 8.2.)

A possible explanation for the discrepancy between the experimental results

and the (correct) theory assumes that the perturbation, however slight, of the original microstructure by the falling ball is important and contributes substantially to the measured viscosity (as testified by the significant difference between simulation and experiment in Fig. 4.18). As shown in Fig. 4.21, an alignment of the particles, even if incomplete, can cause a sizable increase in the extensional resistance of the dispersion, i.e., in $\eta_T$. Both theory (Shaqfeh & Fredrickson, 1990) and simulation (*vide supra*) indicate that this component of the stresslet dominates the effective viscosity for sufficiently slender bodies. A partial ordering of the rods during the measurement, as suggested by simulations using boundary elements methods† (Phan-Thien & Graham, 1991; Phan-Thien *et al.*, 1991), may therefore lead to an overestimation of $[\eta]$. The extensional components of the velocity disturbance generated by the falling sphere (which acts as a point force to a first approximation) bring about this partial orientational order in the dispersion (Fig. 4.22). Additionally, the mechanism that lead Koch & Shaqfeh (1989) to propose that sedimenting suspensions of spheroids are unstable, could cause an increase of the particle density in the vicinity of the falling ball. In essence, the rods immediately above the sphere experience a straining field which aligns them in the main direction of the flow, and hence they are carried along by the fluid more readily than the fibres below the sphere, which are oriented perpendicular to gravity by the velocity field (Fig. 4.22). This results in a crowding of the particles near the sedimenting ball, with a concomitant increase in its drag (and therefore in the apparent viscosity). Milliken *et al.* (1989) have shown, however, that the dependence of the sedimentation rate on the diameter of the container can be factored out by using Faxén's correction, derived for a Newtonian fluid (Bohlin, 1960). Hence, they argued, the suspension can be characterized by a scalar viscosity, and its microstructure must

† Although the constitutive equation assumed by Phan-Thien & Graham (1991) for the fibre suspension is somewhat *ad hoc*, their simulation should capture qualitative features such as flow-induced alignment.

be isotropic. It is not clear whether the inducement of a preferred rod orientation by the falling ball would suffice to explain the magnitude of the discrepancy between the measurements and our data, nor why Faxén's correction would then apply, but it seems the most plausible hypothesis.‡

It should be clear that steady state experiments at low Péclet numbers cannot dissociate the Brownian component of the stress from the hydrodynamic contributions. In order to isolate the latter, one must thus resort to transient measurements of the viscosity, which probe the dispersion while it is still fully isotropic. (Equivalently, low-amplitude high-frequency oscillatory rheometry can be used.) Since the hydrodynamic stress is independent of the Péclet number for a given microstructure, and *à fortiori* for isotropic samples, the issue whether the dispersion is Brownian or not should be of no concern for measurements of the suspension viscosity at the inception of shear flow. A set of such experiments was performed by Bibbo *et al.* (1985) on nylon fibres of aspect ratio 16.7 and 22.7 ($r_{\mathrm{eq}} = 12.3$ and 15.9 respectively). Their data are superposed on the simulation results in Fig. 4.19. Also shown are the same values, adjusted for the cylindrical shape of the particles (as above). Although the scatter in the measurements is quite large, the agreement is reasonable, and most of the experimental points fall between the curves for $r_p = 10$ and for $r_p = 20$. The reliability of the data for the high aspect ratio particles, however, is somewhat questionable due the small gap width of the rheometer compared

‡ It is unlikely that the excellent agreement of the measured intrinsic viscosities with the formula (4.50) signifies that Brownian forces play a role in the experiments of Milliken *et al.* (1989) because the PMMA particles were more than 3 cm in length. Yet a Brownian contribution to the effective viscosity would also explain the cubic dependence on density noted by Milliken *et al.* (1989) above $\phi = 0.125$, since reptation theory for rigid Brownian rods predicts a similar variation of the stress with volume fraction in the semi-dilute concentration range (Doi & Edwards, 1986).

to the length of the 5 mm fibres (Powell, 1991).

## 4.8 A look ahead

The study of the crystalline configurations and equilibrium structures of hard ellipsoids reported here is certainly worthwhile, and has clearly illustrated the importance of controlling the microstructure in order to achieve desired macroscopic properties. Yet the most exciting research, we believe, still lies ahead, when the method developed in this chapter will be applied for dynamic simulations, so that phenomena such as flow induced alignment and possibly the dynamic creation of liquid crystalline domains can be observed and investigated. The intimate connection between microstructure and flow type, absent in the "static" simulations discussed in this chapter, will then become of great interest. As explained in Ch. I, both facets of the problem —the relation between the microstructure and the macroscopic properties on the one hand, and the interplay of dynamics and geometry on the other— must be addressed in order to understand the behavior of flowing fibre suspensions. Although some improvement in the computational efficiency of our program is still required to make time-integrated simulations of unbounded dispersions practical, these numerical difficulties will soon be overcome, opening the door for many interesting applications. The prospect of simulating suspensions of rod-like particles under extensional flows seems especially attractive since the spheroids should then achieve a steady state orientation distribution. Some aspects concerning the compatibility of simulation cells with these straining flows will therefore be addressed in the next chapter.

# APPENDIX F

## Convergent formulation of particle velocities in unbounded dispersions of ellipsoids

In this appendix, we shall first derive (4.13), an absolutely convergent expression for the translational velocity of a tracer ellipsoid in an unbounded, statistically homogeneous suspension of hydrodynamically interacting particles. Next, we shall discuss the correspondence between this formulation (based on O'Brien's method (1979)) and the Ewald summed mobility coefficients (4.22) for periodic dispersions of ellipsoids. In particular, we demonstrate that the origin must be omitted from the lattice sum performed in Fourier space in order to capture the contributions arising from the "backflow" integral in (4.13).

O'Brien's "renormalization" technique (1979) has been applied previously to surmount the convergence difficulties associated with the long-ranged nature of hydrodynamic interactions in Stokes flow (Glendinning & Russel, 1982; Brady *et al.*, 1988). The result, equation (4.11), is an absolutely convergent expression for the fluid velocity everywhere in the dispersion, involving the difference between the cumulative effect of all particles (labeled 1 through $N$) and an integral contribution representing the "backflow" of fluid in response to a non-vanishing average force, torque, stresslet or quadrupole exerted by the solid inclusions:

$$\mathbf{u}(\mathbf{x}) - \langle \mathbf{u}(\mathbf{x}) \rangle = \frac{2n_\phi}{15\mu} \left[ 2\langle \mathbf{Q}' : \boldsymbol{\delta} \rangle - \langle \boldsymbol{\delta} : \mathbf{Q}' \rangle \right] - \frac{1}{8\pi\mu} \sum_{q=1}^{N} \int_{A_q} \mathbf{J} \cdot \boldsymbol{\sigma} \cdot \mathrm{d}\mathbf{A} \qquad \text{(F.1)}$$

$$- \frac{n_\phi}{8\pi\mu} \int_{V-V_\epsilon} \{ \langle \mathbf{F} \rangle \cdot \mathbf{J} + \langle \mathbf{T} \rangle \cdot \mathbf{R} + \langle \mathbf{S} \rangle : \mathbf{K} + \langle \mathbf{Q}' \rangle \odot^3 \boldsymbol{\nabla}\boldsymbol{\nabla}\mathbf{J} \} \, \mathrm{d}V \, .$$

The derivation of this equation has been sketched in §4.2. A more complete discussion of O'Brien's method and its application to hydrodynamically interacting suspensions can be found in Brady *et al.* (1988). We now relate the velocity $\mathbf{U}_p$ of an ellipsoid placed in the dispersion to the ambient fluid velocity $\mathbf{u}_\emptyset$, which includes any externally imposed flow as well as the disturbances due to all other particles in

the suspension. Hence $\mathbf{u}_\emptyset$ is given by (F.1), with the caveat that $p$ must be excluded from the sum. Brenner (1966) has shown that

$$\mathbf{U}_p = \frac{\sinh D_p}{D_p}\mathbf{u}_\emptyset(\mathbf{x}_p) \ , \tag{F.2a}$$

$$\text{with} \quad D_p = \sqrt{D_p^2} \qquad \text{and} \quad D_p^2 = \mathbf{A}_p : \boldsymbol{\nabla\nabla} \ . \tag{F.2b}$$

The symmetric positive definite second rank tensor $\mathbf{A}_p$ characterizes the surface $A_p$ of the ellipsoid: $\mathbf{x} \in A_p \iff \mathbf{A}_p^{-1} : (\mathbf{x}-\mathbf{x}_p)(\mathbf{x}-\mathbf{x}_p) = 1$, with $\mathbf{x}_p$ the centre of the particle. The easiest way to derive the desired expression (4.13) for $\mathbf{U}_p$ is simply to apply (F.2a) to (F.1). In an unbounded statistically homogeneous dispersion, $\langle\mathbf{u}\rangle$ is either constant or a linear function of position. Hence, since $D^2$ is a linear combination of second derivatives with respect to particle location (see (F.2b)), $D^2\langle\mathbf{u}\rangle = 0$, and

$$\frac{\sinh D_p}{D_p}\langle\mathbf{u}\rangle = \sum_{n=0}^{\infty}\frac{1}{(2n+1)!}D^{2n}\langle\mathbf{u}\rangle = (1+\frac{1}{6}D^2+\frac{1}{120}D^4+...)\langle\mathbf{u}\rangle = \langle\mathbf{u}\rangle \ . \tag{F.3}$$

Also, from the definition (4.10a) of the second moment of the force density $\mathbf{Q}'_q$,

$$\mathbf{Q}'_q = -\frac{1}{2}\int_{A_q}\mathbf{n}_q\cdot\boldsymbol{\sigma}[\mathbf{y}-\mathbf{x}_q][\mathbf{y}-\mathbf{x}_q]\mathrm{d}A_\mathbf{y} \ , \tag{F.4}$$

it follows that

$$(\nabla_{\mathbf{x}_p})_i(\nabla_{\mathbf{x}_p})_j\Big(\langle\mathbf{Q}'\rangle_{|\mathbf{x}=\mathbf{x}_p}\Big)_{klm} = \frac{1}{2}\langle\mathbf{F}\rangle_k\boldsymbol{\delta}_{il}\boldsymbol{\delta}_{jm}+\frac{1}{2}\langle\mathbf{F}\rangle_k\boldsymbol{\delta}_{im}\boldsymbol{\delta}_{jl} \ . \tag{F.5}$$

Therefore $$D_p^2\big(\langle\mathbf{Q}':\boldsymbol{\delta}\rangle\big) = \mathbf{A}_p:\boldsymbol{\nabla\nabla}\big(\langle\mathbf{Q}':\boldsymbol{\delta}\rangle\big) = \big(\mathbf{A}_p:\boldsymbol{\delta}\big)\langle\mathbf{F}\rangle \tag{F.6a}$$

and $$D_p^2\big(\langle\boldsymbol{\delta}:\mathbf{Q}'\rangle\big) = \mathbf{A}_p:\boldsymbol{\nabla\nabla}\big(\boldsymbol{\delta}:\langle\mathbf{Q}'\rangle\big) = \mathbf{A}_p\cdot\langle\mathbf{F}\rangle \ . \tag{F.6a}$$

All higher derivatives (in particular $D^{2m}$ with $m>1$) give zero. The quadrupole $\mathbf{Q}'$ as defined above is not irreducible (Appendix D). We isolate the part which scales with the force and introduce $\mathbf{I}^{(2)} = \mathbf{Q} = \mathbf{Q}' - \frac{1}{6}\mathbf{F}\mathbf{A}$ to find

$$\begin{aligned}
&\frac{\sinh D_p}{D_p}\big[2\langle\mathbf{Q}':\boldsymbol{\delta}\rangle - \langle\boldsymbol{\delta}:\mathbf{Q}'\rangle\big] \\
&\quad = \big[2\langle\mathbf{Q}':\boldsymbol{\delta}\rangle - \langle\boldsymbol{\delta}:\mathbf{Q}'\rangle\big] + \frac{1}{3}\big(\mathbf{A}_p:\boldsymbol{\delta}\big)\langle\mathbf{F}\rangle - \frac{1}{6}\mathbf{A}_p\cdot\langle\mathbf{F}\rangle \\
&\quad = \big[2\langle\mathbf{Q}:\boldsymbol{\delta}\rangle - \langle\boldsymbol{\delta}:\mathbf{Q}\rangle\big] + \frac{1}{3}\big(\mathbf{A}_p:\boldsymbol{\delta}\big)\langle\mathbf{F}\rangle + \frac{1}{3}\langle(\mathbf{A}:\boldsymbol{\delta})\mathbf{F}\rangle \\
&\qquad - \frac{1}{6}\mathbf{A}_p\cdot\langle\mathbf{F}\rangle - \frac{1}{6}\langle\mathbf{A}\cdot\mathbf{F}\rangle \ .
\end{aligned} \tag{F.7}$$

The transition to irreducible moments also converts the term $\langle \mathbf{Q}' \rangle \odot^3 \boldsymbol{\nabla}\boldsymbol{\nabla}\mathbf{J}$ in the last integral of (F.1) into $\langle \mathbf{Q} \rangle \odot^3 \boldsymbol{\nabla}\boldsymbol{\nabla}\mathbf{J} + \frac{1}{6}\langle D^2\mathbf{F} \rangle \cdot \mathbf{J}$. Combining the information above, we now calculate the motion of an ellipsoid $p$ in the flow field (F.1) as

$$\begin{aligned}
\mathbf{U}_p - \langle \mathbf{u}(\mathbf{x}_p) \rangle = \mathbf{K}^p_{UF} \cdot \mathbf{F}_p + \frac{2n_\phi}{15\mu} \Big[ & 2\langle \mathbf{Q} : \boldsymbol{\delta} \rangle - \langle \boldsymbol{\delta} : \mathbf{Q} \rangle + \frac{1}{3}(\mathbf{A}_p : \boldsymbol{\delta})\langle \mathbf{F} \rangle \\
& - \frac{1}{6}\mathbf{A}_p \cdot \langle \mathbf{F} \rangle + \frac{1}{3}\langle (\mathbf{A} : \boldsymbol{\delta})\mathbf{F} \rangle - \frac{1}{6}\langle \mathbf{A} \cdot \mathbf{F} \rangle \Big] - \frac{1}{8\pi\mu} \sum_{q \neq p}^{N} \int_{A_q} \frac{\sinh D_p}{D_p} \mathbf{J} \cdot \boldsymbol{\sigma} \cdot \mathrm{d}\mathbf{A} \\
& - \frac{n_\phi}{8\pi\mu} \int_{V - V_\epsilon} \Big\{ \big(1 + \frac{1}{6}D_p^2\big)\langle \mathbf{F} \rangle \cdot \mathbf{J} + \frac{1}{6}\langle D^2\mathbf{F} \rangle \cdot \mathbf{J} \\
& \qquad + \langle \mathbf{T} \rangle \cdot \mathbf{R} + \langle \mathbf{S} \rangle : \mathbf{K} + \langle \mathbf{Q} \rangle \odot^3 \boldsymbol{\nabla}\boldsymbol{\nabla}\mathbf{J} \Big\} \, \mathrm{d}V \, .
\end{aligned} \tag{F.8}$$

Owing to the linearity of the Stokes equations (4.1), one may simply superimpose the effect of any external force to which the particle may be subject (such as gravitation) on the translation due to the flow pattern in the dispersion. This explains the first contribution on the right hand side of (F.8). Terms which decay as $O(|\mathbf{x}_p - \mathbf{y}|^{-4})$, with $\mathbf{y}$ a generic position vector within $V - V_\epsilon$, have been suppressed in the "backflow" integral for consistency. In the derivation of (F.1) (§4.2), it is clear that this piece arises from applying the divergence theorem to the contribution of a smooth surface $\Gamma$ encircling a large portion of the dispersion around the particle $p$. Returning to the original formulation, it is evident that effects of $O(|\mathbf{x}_p - \mathbf{y}|^{-3})$ may be neglected as the surface $\Gamma$ recedes to infinity. We therefore omit them in (F.8).

Equation (F.8) is absolutely convergent as the number of particles $N$ grows unbounded (at a fixed average concentration $N/V$) because their contribution is offset by the backflow; mathematically, the difference between the sum and the integral in (F.8) remains finite. Using an analogous procedure, similar expressions can be derived for the angular velocity of an ellipsoid in an infinite dispersion and for its (zero) rate of deformation relative to the imposed rate of strain.

The application of (F.8) to the motion of a force free ellipsoid $p$ through a

lattice of particles $q$ yields

$$\mathbf{U}_p = \frac{2n_\phi}{15\mu}\Big[2\mathbf{Q}_q : \boldsymbol{\delta} - \boldsymbol{\delta} : \mathbf{Q}_q + \frac{1}{3}(\mathbf{A}_p : \boldsymbol{\delta})\mathbf{F}_q - \frac{1}{6}\mathbf{A}_p \cdot \mathbf{F}_q + \frac{1}{3}(\mathbf{A}_q : \boldsymbol{\delta})\mathbf{F}_q - \frac{1}{6}\mathbf{A}_q \cdot \mathbf{F}_q\Big]$$
$$- \frac{1}{8\pi\mu}\sum_{\{z\}} \frac{\sinh D_p}{D_p} \int_{A_{q+\{z\}}} \mathbf{J} \cdot \boldsymbol{\sigma} \cdot \mathrm{d}\mathbf{A} \qquad \text{(F.9)}$$
$$- \frac{n_\phi}{8\pi\mu}\int_{V-V_\epsilon} \big\{(1 + \frac{1}{6}D_p^2 + \frac{1}{6}D_q^2)\mathbf{F}_q \cdot \mathbf{J} + \mathbf{T}_q \cdot \mathbf{R} + \mathbf{S}_q : \mathbf{K} + \mathbf{Q}_q \odot^3 \boldsymbol{\nabla}\boldsymbol{\nabla}\mathbf{J}\big\}\,\mathrm{d}V\ .$$

The sum over all $\boldsymbol{x}_{\{z\}}$ (see (4.3)) is most rapidly evaluated using Ewald's technique (Ewald, 1921; see also §4.4). Beenakker (1986) was the first to apply this method to the Oseen tensor $\mathbf{J}$, but imposed the restriction $\mathbf{F}_q = \langle \mathbf{F} \rangle = 0$ in order to eliminate the singular contribution of the origin in the summation over reciprocal space. As pointed out later by Brady *et al.* (1988) this constraint is artificial and unnecessary, since the omitted term is cancelled exactly by the other contributions from $\mathbf{F}_q$ in (F.9) (i.e., ultimately, by the "backflow" of fluid in response to the pressure gradient balancing the non-zero average force exerted by the particles $q$). We shall prove this explicitly for spheroids in what follows.

The Ewald summation of the mobility coupling $\widetilde{\mathbf{M}}_{UF}^{pq}$ between two ellipsoids $p$ and $q$ is discussed in sections 4.3 and 4.4. We shall now warrant the omission of $\mathbf{k} = 0$ from the lattice sum of $\widehat{\mathbf{M}}_2^{pq}$ in the expression for $\widetilde{\mathbf{M}}_{UF}^{pq}$ given in (4.22). The Fourier transform $\widehat{\mathbf{M}}_2^{pq}$ of $\mathbf{M}_2^{pq}$ is (see (4.31)):

$$\widehat{\mathbf{M}}_2^{pq} = \frac{1}{\mu k^4}\exp(-\frac{k^2}{4\mathcal{E}^2})\Big(1 + \frac{k^2}{4\mathcal{E}^2} + \frac{k^4}{8\mathcal{E}^4}\Big)(k^2\boldsymbol{\delta} - \mathbf{kk})\Big\{\frac{\sin\hat{\Delta}_p}{\hat{\Delta}_p}\frac{\sin\hat{\Delta}_q}{\hat{\Delta}_q} \qquad \text{(F.10)}$$
$$+ c_p^2\frac{1-e_p^2}{2e_p^2}\Big(\frac{1}{\hat{\Delta}_p}\frac{\mathrm{d}}{\mathrm{d}\hat{\Delta}_p}\frac{\sin\hat{\Delta}_p}{\hat{\Delta}_p}\Big)\Big(\frac{\sin\hat{\Delta}_q}{\hat{\Delta}_q}\Big)k^2 + c_q^2\frac{1-e_q^2}{2e_q^2}\Big(\frac{1}{\hat{\Delta}_q}\frac{\mathrm{d}}{\mathrm{d}\hat{\Delta}_q}\frac{\sin\hat{\Delta}_q}{\hat{\Delta}_q}\Big)\Big(\frac{\sin\hat{\Delta}_q}{\hat{\Delta}_q}\Big)k^2\Big\}$$

where $k = |\mathbf{k}|$ and $\hat{\Delta}_q = c_q\mathbf{d}_q \cdot \mathbf{k}$. As we are interested in the limit of small $k$, we expand the various functions in (F.10) into Taylor series about the origin. A little algebra yields

$$\lim_{\mathbf{k}\to 0}\widehat{\mathbf{M}}_2^{pq} = \frac{1}{\mu k^2}(1 + O(k^4))(\boldsymbol{\delta} - \mathbf{e_k e_k})\Big\{1 - \frac{1}{6}\big[c_p^2(\mathbf{d}_p \cdot \mathbf{k})^2 + c_q^2(\mathbf{d}_q \cdot \mathbf{k})^2\big]$$
$$- c_p^2\frac{1-e_p^2}{6e_p^2}k^2 - c_q^2\frac{1-e_q^2}{6e_q^2}k^2 + O(k^4)\Big\}\ . \qquad \text{(F.11)}$$

The unit vector $\mathbf{e_k} = \mathbf{k}/k$. Recognizing that $\lim_{\mathbf{k}\to 0} \mathbf{e_k}\mathbf{e_k} = \frac{1}{3}\boldsymbol{\delta}$ and similarly that $\lim_{\mathbf{k}\to 0} \mathbf{e_k}\mathbf{e_k}\mathbf{e_k}\mathbf{e_k} = \frac{1}{15}(\boldsymbol{\delta\delta} + \breve{\boldsymbol{\delta\delta}} + \widehat{\widehat{\boldsymbol{\delta\delta}}})$, with $\breve{\boldsymbol{\delta\delta}}$ and $\widehat{\widehat{\boldsymbol{\delta\delta}}}$ defined by (4.44), the expression (F.11) is easily evaluated as

$$\lim_{\mathbf{k}\to 0} \widehat{\mathbf{M}}_2^{pq} = \frac{1}{\mu}\Big\{ \frac{1}{k^2}(\boldsymbol{\delta} - \mathbf{e_k}\mathbf{e_k}) - \frac{c_p^2}{45}(2\boldsymbol{\delta} - \mathbf{d}_p\mathbf{d}_p) - \frac{c_q^2}{45}(2\boldsymbol{\delta} - \mathbf{d}_q\mathbf{d}_q) - \frac{c_p^2}{9}\frac{(1-e_p^2)}{e_p^2}\boldsymbol{\delta} - \frac{c_q^2}{9}\frac{(1-e_q^2)}{e_q^2}\boldsymbol{\delta}\Big\}\,, \tag{F.12}$$

which can be rearranged into

$$\begin{aligned}\lim_{\mathbf{k}\to 0} \widehat{\mathbf{M}}_2^{pq} =& \frac{1}{\mu}\Big\{ \frac{1}{k^2}(\boldsymbol{\delta} - \mathbf{e_k}\mathbf{e_k}) + \frac{c_p^2}{45}\mathbf{d}_p\mathbf{d}_p + \frac{c_p^2}{45}\frac{1-e_p^2}{e_p^2}\boldsymbol{\delta} + \frac{c_q^2}{45}\mathbf{d}_q\mathbf{d}_q + \frac{c_q^2}{45}\frac{1-e_q^2}{e_q^2}\boldsymbol{\delta} \\ & - \frac{2}{45}c_p^2\frac{3-2e_p^2}{e_p^2}\boldsymbol{\delta} - \frac{2}{45}c_q^2\frac{3-2e_q^2}{e_q^2}\boldsymbol{\delta}\Big\} \qquad\qquad (F.13)\\ =& \frac{1}{\mu}\Big\{ \frac{1}{k^2}(\boldsymbol{\delta} - \mathbf{e_k}\mathbf{e_k}) + \frac{1}{45}\mathbf{A}_p + \frac{1}{45}\mathbf{A}_q - \frac{2}{45}(\mathbf{A}_p : \boldsymbol{\delta})\boldsymbol{\delta} - \frac{2}{45}(\mathbf{A}_q : \boldsymbol{\delta})\boldsymbol{\delta}\Big\}\end{aligned}$$

The last step uses the definition of $\mathbf{A}_q = a_q^2\mathbf{d}_q\mathbf{d}_q + b_q^2(\boldsymbol{\delta} - \mathbf{d}_q\mathbf{d}_q) = (c_q/e_q)^2\mathbf{d}_q\mathbf{d}_q + c_q^2(1-e_q^2)/e_q^2\,(\boldsymbol{\delta} - \mathbf{d}_q\mathbf{d}_q)$.

From (F.9), the contribution of the force $\mathbf{F}_q$ to the translational velocity of particle $p$ can be written as

$$\begin{aligned}\widetilde{\mathbf{M}}_{UF}^{pq} =& \frac{n_\phi}{45\mu}\big[2(\mathbf{A}_p : \boldsymbol{\delta})\boldsymbol{\delta} - \mathbf{A}_p + 2(\mathbf{A}_q : \boldsymbol{\delta})\boldsymbol{\delta} - \mathbf{A}_q\big] \qquad\qquad (F.14)\\ &+ \frac{1}{8\pi\mu}\sum_{\{z\}} \frac{\sinh D_p}{D_p}\frac{\sinh D_q}{D_q}\mathbf{J}(\mathbf{x}_p - \mathbf{x}_q - \boldsymbol{x}_{\{z\}}) - \frac{n_\phi}{8\pi\mu}\int_{V-V_\epsilon}\big(1 + \frac{1}{6}D_p^2 + \frac{1}{6}D_q^2\big)\mathbf{J}\,\mathrm{d}V\,.\end{aligned}$$

In (4.22), on the other hand, we claimed that

$$\widetilde{\mathbf{M}}_{UF}^{pq} = \sum_{\{z\}} \mathbf{M}_1^{p[q+\{z\}]} + \frac{1}{|\mathbf{B}|}\sum_{\{\zeta\}\neq 0} \cos\Big(\mathbf{k}_{\{\zeta\}}\cdot(\mathbf{x}_p - \mathbf{x}_q)\Big)\widehat{\mathbf{M}}_2^{pq}(\mathbf{k}_{\{\zeta\}})\,. \tag{F.15}$$

By construction (see also (4.30)),

$$\begin{aligned}&\frac{1}{8\pi\mu}\sum_{\{z\}} \frac{\sinh D_p}{D_p}\frac{\sinh D_q}{D_q}\mathbf{J}(\mathbf{x}_p - \mathbf{x}_q - \boldsymbol{x}_{\{z\}}) = \qquad\qquad (F.16)\\ &\qquad \sum_{\{z\}} \mathbf{M}_1^{p[q+\{z\}]} + \frac{1}{|\mathbf{B}|}\sum_{\{\zeta\}} \cos\Big(\mathbf{k}_{\{\zeta\}}\cdot(\mathbf{x}_p - \mathbf{x}_q)\Big)\widehat{\mathbf{M}}_2^{pq}(\mathbf{k}_{\{\zeta\}})\,.\end{aligned}$$

Hence we must demonstrate that the contribution to the second sum from $\{\zeta\} = 0$ accounts for the remaining terms in (F.14). It is easily shown that

$$\int_V \mathbf{J}\,\mathrm{d}V = \lim_{\mathbf{k}\to 0} \hat{\mathbf{J}}(\mathbf{k}) = \lim_{\mathbf{k}\to 0} \frac{8\pi}{k^2}(\boldsymbol{\delta} - \mathbf{e_k}\mathbf{e_k}) \;, \tag{F.17a}$$

(Brady *et al.*, 1988), and that‡

$$\int_{V-V_\epsilon} \nabla\nabla\mathbf{J}\,\mathrm{d}V = 0 \;. \tag{F.17b}$$

The first term in (F.13) therefore cancels the backflow integral of (F.14). (Note that $n_\phi = 1/|\mathbf{B}|$.) The rest is trivial by comparison of (F.13) and (F.14).

Along the same lines, one can find a one-to-one correspondence between all other Ewald-summed mobility interactions ($\widetilde{\mathbf{M}}_{UT}, \widetilde{\mathbf{M}}_{UQ}, \widetilde{\mathbf{M}}_{ES}$, etc.), and each of the terms in O'Brien's absolutely convergent expressions for the translational and angular velocities of the particles in a dispersion, and for the rate of strain at their locator points. The origin of the reciprocal lattice must be omitted in each case. In a sense, the agreement with O'Brien's results validates the Ewald technique for the evaluation of the conditionally convergent sums occurring in the rheology of suspensions at zero Reynolds number.

‡ It is essential to exclude $V_\epsilon$ from the volume of integration; the singularity would give a finite contribution, but this has been accounted for explicitly in (F.14). Integrating over a domain containing the point disturbance would count its effect twice.

# APPENDIX G

## Optimal value of the convergence parameter $\mathcal{E}$ in the Ewald summation

In an effort to estimate the cohesive energy of ionic crystals, Ewald (1921) developed a numerical technique designed to accelerate the calculation of slowly converging lattice sums by splitting them into two complimentary parts, one of which contains terms which decay rapidly with distance‡ (exponentially or faster), and the other being easily evaluated, after Fourier transformation, by means of the Poisson summation formula (4.30). (See Nijboer & De Wette, 1957, for a very lucid presentation of this method.) We explained in §4.3 how to apply this procedure to $\widetilde{\mathbf{M}}_{UF}^{pq}$ in order to calculate the mobility interactions between an ellipsoid $p$ and a lattice of spheroids $q$ (see (4.21)†), and introduced a parameter $\mathcal{E}$ controlling the relative rate of convergence of the sums in real and in reciprocal space. Beenakker (1986), in the first application of the Ewald summation technique to hydrodynamic interactions, recommended that $\mathcal{E} = \sqrt{\pi}/\sqrt[3]{|\mathbf{B}|}$ for optimal convergence in the case of a simple cubic lattice. ($|\mathbf{B}|$ is the volume of the elementary unit cell). We commented in §4.4 that it is favorable in some instances to deviate from this suggestion if the

‡ The concept "distance" is appropriately defined here as $(z_1^2 + z_2^2 + z_3^2)^{1/2}$, with $\{z_i\}$ the integer coordinates of the lattice points (see (4.3)).

† The formulation (4.21) is not the only way to apply Ewald's ideas, and perhaps not the most straightforward one either. Breaking up the sum after the mobility interaction between each pair of particles has been evaluated, however, seems impractical since one would then have to calculate the Fourier transform of $\mathbf{M}_{UF}^{pq}(r_{pq})\,\mathrm{erf}(\mathcal{E}r_{pq})$, a formidable task considering that $\mathbf{M}_{UF}^{pq}(r_{pq})$ is known only as a double integral too complex to be worked out in closed form (*cf.* equation (4.16a)). The use of an auxiliary function different from the error function does not alleviate the difficulty.

computational cost of evaluating the summand is considerably different before and after Fourier transformation. We shall now substantiate this assertion.

Ewald's technique converts the original triply infinite sum (see (4.19)) into two other lattice sums:

$$\widetilde{\mathbf{M}}_{UF}^{pq} = \sum_{\{z\}} \mathbf{M}_1^{p[q+\{z\}]} + \frac{1}{|\mathbf{B}|} \sum_{\{\zeta\}\neq 0} \cos\Big(\mathbf{k}_{\{\zeta\}} \cdot (\mathbf{x}_p - \mathbf{x}_q)\Big) \widehat{\mathbf{M}}_2^{pq}(\mathbf{k}_{\{\zeta\}}) \,. \qquad \text{(G.1)}$$

These are truncated in practice after a number of terms appropriate for the accuracy demanded. In order to estimate $\widetilde{\mathbf{M}}_{UF}^{pq}$ within the specified tolerance in the minimal amount of time, the truncation error should be equal for both sums. (This intuitive argument can be justified formally by using Lagrange multipliers to incorporate the constraint on accuracy explicitly in the optimization scheme below.) Assuming a cutoff distance $R$ for the sum over $\mathbf{M}_1$, such that all terms with $r_{\{z\}} = |\mathbf{x}_q + \boldsymbol{x}_{\{z\}} - \mathbf{x}_p| > R$ are neglected, and introducing a similar radius $K$ for the sum in reciprocal space, we estimate the truncation errors $\varepsilon_1, \varepsilon_2$ as:

$$\varepsilon_1 = \sum_{r_{\{z\}}>R} \mathbf{M}_1^{p[q+\{z\}]} \sim n_1 \int_R^\infty \frac{1}{r} \mathrm{erfc}(\mathcal{E}r) r^2 \,\mathrm{d}r \sim n_1 \int_R^\infty \frac{1}{\mathcal{E}} \exp(-\mathcal{E}^2 r^2)\,\mathrm{d}r$$

$$\sim \frac{n_1}{\mathcal{E}^2} \mathrm{erfc}(\mathcal{E}R) \sim \frac{n_1}{\mathcal{E}^3 R} e^{-\mathcal{E}^2 R^2} \,, \qquad \text{(G.2a)}$$

$$\varepsilon_2 = \frac{1}{|\mathbf{B}|} \sum_{k_{\{\zeta\}}>K} \widehat{\mathbf{M}}_2^{pq} \sim \frac{n_2}{|\mathbf{B}|} \int_K^\infty \frac{1}{k^2} \exp(-\frac{k^2}{4\mathcal{E}^2}) k^2 \,\mathrm{d}k$$

$$\sim \frac{n_2}{|\mathbf{B}|} 2\mathcal{E}\,\mathrm{erfc}\Big(\frac{K}{2\mathcal{E}}\Big) \sim \frac{n_2}{|\mathbf{B}|} \frac{4\mathcal{E}^2}{K} e^{-K^2/(4\mathcal{E}^2)} \,, \qquad \text{(G.2b)}$$

with $n_1, n_2$ the number density of lattice points in real and reciprocal space respectively. These scalings are intended as order of magnitude estimates only and are based on (4.21b), (4.31) and the asymptotic expansion of the "erf" function (Abramowitz & Stegun, 1970). To get $\varepsilon_1 \simeq \varepsilon_2$, we set $K = 2\mathcal{E}^2 R$ (subject to verification later on that $n_1/\mathcal{E}^3 = (|\mathbf{B}|\mathcal{E}^3)^{-1} = O(1)$). Also note that, for a predetermined accuracy $\varepsilon$, the cutoff distance $R$ is inversely proportional to $\mathcal{E}$, while $K$ grows linearly with it.

We now need to optimize $\mathcal{E}$ to minimize the required computation time. Let $\mathcal{N}_1$ be the number of arithmetic operations required to calculate $\mathbf{M}_1^{pq}$ at one lattice point (i.e., for one image of the spheroid $q$), and denote by $\mathcal{N}_2$ the equivalent number for one term in the series over reciprocal space. The CPU cost $C$ will scale as

$$C \propto \mathcal{N}_1 \frac{4\pi}{3} R^3 n_1 + \mathcal{N}_2 \frac{4\pi}{3} K^3 n_2 \ . \tag{G.3}$$

Setting $\mathrm{d}C/\mathrm{d}\mathcal{E} = 0$, we find with a little algebra that

$$\mathcal{E}_{\mathrm{opt}}^6 = \frac{1}{8} \frac{\mathcal{N}_1 n_1}{\mathcal{N}_2 n_2} \ . \tag{G.4}$$

Per definition, $n_1 = (|\mathbf{B}|)^{-1}$ and $n_2 = |\mathbf{B}|/(8\pi^3)$ (see (4.22)) whence

$$\mathcal{E}_{\mathrm{opt}}^6 = \frac{\pi^3}{|\mathbf{B}|^2} \frac{\mathcal{N}_1}{\mathcal{N}_2} \ , \tag{G.5}$$

which is the result quoted in §4.4. For $\mathcal{N}_1 \sim \mathcal{N}_2$ (as in the case of sphere-sphere interactions), we recover Beenakker's result (1986). This is true independently of the lattice type, provided that the series are truncated at a cutoff distance $R$ (or $K$) rather than at a specified number of "shells", as is often done for convenience (i.e., one retains all terms in the sum over $\mathbf{M}_1^{pq}$ for which $|z_i| < z_{\max}$ with $i = 1, 2$ and 3). Both approaches are different in general, but almost equivalent for cubic unit cells. Even though $\mathcal{E} \sim \sqrt[6]{\mathcal{N}_1/\mathcal{N}_2}$, a relatively weak dependence, the CPU cost was found in practice to be influenced rather strongly by the choice of $\mathcal{E}$, justifying the need for this analysis.

# APPENDIX H

## Basis vectors and symmetry properties of crystalline configurations of spheroids

Each advance in scientific research, whether a novel experimental technique, a new numerical method or the extension of an existing theory, must be tested against established results in order to ascertain its validity. In every field, benchmarks are available which help determine the accuracy of the proposed improvement and its efficiency in comparison with the procedures it attempts to replace, mimic or supplement. In the (theoretical) rheology of suspensions, one such standard is the concentration dependence of the hydrodynamic transport properties of face-centered cubic lattices of spheres (Zick & Homsy, 1982; Zuzovsky *et al.*, 1983; Nunan & Keller, 1984; Brady *et al.*, 1988; Ladd, 1988). We propose that the regular arrays of prolate spheroids discussed in §4.6, in particular the *efc*-crystal, can serve a similar purpose for dispersions of elongated particles. Their geometry is unambiguously defined, and among the simplest which accept the maximum‡ packing fraction $\frac{\pi}{3\sqrt{2}}$ while retaining a fully three dimensional character at lower concentrations (see §4.6 in that regard). Their high degree of symmetry allows general predictions to be made concerning their properties and may make them amenable to some kind of analytical treatment against which present and future simulations can be tested for consistency. (The calculation of the dielectric constant of a regular array of prolate

‡ This statement has not yet been mathematically proven. Even for spheres, it has not been demonstrated rigorously in three dimensions that the maximum volumetric concentration compatible with the mutual impenetrability of the particles is $\frac{\pi}{3\sqrt{2}}$, the density of a close packed face-centered lattice (Gruber & Lekkerkerker, 1987), but this is generally accepted. The problem is even more complex for prolate spheroids, as there is an additional degree of freedom associated with each particle, yet the same maximum packing fraction is usually assumed (Frenkel & Mulder, 1985).

spheroids (Lam, 1990) offers hope that the advent of new mathematical tools will soon allow a closed-form expression for the extensional viscosity of *efc*-crystals to be derived, for instance.) We therefore consider it appropriate to carefully characterize these lattices here, and to discuss some of their properties.

The close-stacked *efc*-lattice is derived from a face-centered crystal of touching spheres by stretching it by a factor equal to the aspect ratio in a direction perpendicular to the hexagonally packed planes (i.e., along the (111)-diagonal of the cubic cell). This transformation maps spheres onto ellipsoids without altering the volume fraction of the array. We shall refer to the direction in which the spheroids point (which is also the direction of stretch) as the $\mathbf{e}_3$-axis, and introduce an orthonormal Cartesian coordinate system $(\mathbf{e}_1, \mathbf{e}_2, \mathbf{e}_3)$, with origin at the core of a particle, such that $\mathbf{e}_1$ lies along a line of centres (Fig. 4.23a). Non-dimensionalizing distances by the length $a$ of the major semi-axis of the spheroids, the matrix $\mathbf{B}$ defining the lattice (see (4.3)) can be chosen as

$$\mathbf{B} = \begin{pmatrix} 2/r_p & 1/r_p & 0 \\ 0 & \sqrt{3}/r_p & \frac{2}{3}\sqrt{3}/r_p \\ 0 & 0 & 2\sqrt{2/3} \end{pmatrix} . \tag{H.1}$$

The three columns of $\mathbf{B}$ form a set of basis vectors $\{\mathbf{b}_1, \mathbf{b}_2, \mathbf{b}_3\}$ for the crystal. The unit cell defined by (H.1) contains only one particle, but more can be included by taking appropriate integer linear combination of the $\mathbf{b}_i$ to construct a new module. This yields a different description of the crystal, and does not affect the system itself in any way, of course. The volume of a spheroid is $\frac{4\pi}{3}/r_p^2$, and that of the unit cell, $|\mathbf{B}| = 4\sqrt{2}/r_p^2$, giving a packing fraction $\phi = \pi/(3\sqrt{2})$, the theoretical regular close-packed limit for dispersions of ellipsoids.

In order to study "face-centered" suspensions at concentrations other than the maximum, we proposed in §4.6 to expand the crystal from closest packing in such a way that the minimum surface-to-surface separation $\delta$ between nearest neighbors is the same in three non-planar directions. This procedure maintains the "three-dimensional" character of the dispersion at all volume fractions, and is taken as

the definition of an *efc*-lattice. The most obvious alternative, an isotropic dilation of the crystal, preserves the anisotropy present in the unit cell at closest packing, i.e., $\mathbf{b}_3 \cdot \mathbf{e}_3 / \mathbf{b}_1 \cdot \mathbf{e}_1 = \sqrt{\frac{2}{3}} r_p$. For slender particles, this rapidly degenerates into rather uninteresting "two-dimensional" structures consisting of sheets of hexagonally packed spheroids, separated by wide gaps of fluid. *Efc*-crystals, on the other hand, converge to face-centered *cubic* lattices at infinite dilution, independent of the aspect ratio of the particles. For a chosen $\delta$, the appropriate expansion factors $h_i$ in each of the three directions $\mathbf{e}_i$ can be determined as follows. It is easy to see from the hexagonal pattern in the $\mathbf{e}_1\,\mathbf{e}_2$ plane (Fig. 4.23a) that

$$\delta = (h_1 - 1)2/r_p \tag{H.2}$$

and that $h_1 = h_2$. To find $h_3$, imagine a cross-section of the dispersion along the $\mathbf{e}_2\,\mathbf{e}_3$ plane, and isolate for consideration two neighboring particles in adjacent hexagonal layers (Fig. 4.23b). Label the midpoint of the line joining their centres $\mathbf{m} = h_2/(\sqrt{3}r_p)\mathbf{e}_2 + \sqrt{2/3}h_3\mathbf{e}_3$, and call $\mathbf{z}$ the point of closest approach on the spheroid at the origin. Since $\mathbf{z}$ belongs to the surface of the ellipsoid, we know that

$$(\mathbf{z} \cdot \mathbf{e}_3)^2 + r_p^2 |\mathbf{z} \wedge \mathbf{e}_3|^2 = 1 \; . \tag{H.3}$$

The normal at that point is parallel to $(\mathbf{z} \cdot \mathbf{e}_3)\mathbf{e}_3 + r_p^2[\mathbf{z} - (\mathbf{z} \cdot \mathbf{e}_3)\mathbf{e}_3]$, which equals $(\mathbf{z} \cdot \mathbf{e}_3)\mathbf{e}_3 + r_p^2(\mathbf{z} \cdot \mathbf{e}_2)\mathbf{e}_2$ since $\mathbf{z}$ lies in the $\mathbf{e}_2\,\mathbf{e}_3$ plane. By symmetry, it must pass through $\mathbf{m}$. Hence, letting $\mathbf{z} \cdot \mathbf{e}_3 = z_3$ and $\mathbf{z} \cdot \mathbf{e}_2 = z_2$,

$$\frac{(\mathbf{m} - \mathbf{z}) \cdot \mathbf{e}_3}{(\mathbf{m} - \mathbf{z}) \cdot \mathbf{e}_2} = \frac{\sqrt{2/3}h_3 - z_3}{h_2/(\sqrt{3}r_p) - z_2} = \frac{z_3}{r_p^2 z_2} \; . \tag{H.4}$$

The shortest distance between the ellipsoids is measured along this normal, so that also

$$\frac{\delta^2}{4} = \left(\sqrt{\frac{2}{3}}h_3 - z_3\right)^2 + \left(\frac{h_2}{\sqrt{3}r_p} - z_2\right)^2 \; . \tag{H.5}$$

Squaring (H.4) and eliminating $z_3$ using (H.3), we obtain, after a little rearrangement of (H.5), that

$$\frac{1}{4}\frac{\delta^2 z_2^2}{\left(h_2/(\sqrt{3}r_p) - z_2\right)^2} = \frac{1}{r_p^4} + \frac{r_p^2 - 1}{r_p^2} z_2^2 \; . \tag{H.6}$$

The right hand side has a slope of less than 1 when plotted as a function of $z_2^2$, and hence (H.6) can be used to generate a stable iterative scheme for $z_2$ as $\lim_{k\to\infty} z_2^{(k)}$ with

$$\frac{1}{4}\frac{\delta^2 (z_2^{(k+1)})^2}{\left(h_2/(\sqrt{3}r_p) - z_2^{(k+1)}\right)^2} = \frac{1}{r_p^4} + \frac{r_p^2 - 1}{r_p^2}(z_2^{(k)})^2 = \ell^{(k)} \,, \tag{H.7a}$$

or

$$z_2^{(k+1)} = \frac{h_2/(\sqrt{3}r_p)}{1 + \delta/(2\sqrt{\ell^{(k)}})} \,. \tag{H.7b}$$

From $z_2$, it is trivial to calculate $z_3$ and $h_3$.

From Fig. 4.23a, it is apparent that the lattice is invariant under a set of coordinate transformations. These symmetry elements imply a certain structure for its material properties. Consider for instance a fourth rank tensor $\mathbf{Y}$, which is a function of the particle configuration only, and denote $\mathbf{Y} \odot^4 \mathbf{e}_l\mathbf{e}_k\mathbf{e}_j\mathbf{e}_i$ by $Y_{ijkl}$. The reflection symmetry about the origin then stipulates that $Y_{ijkl} = 0$ whenever an odd number of the coordinate labels 1, 2, or 3 appear in the indices $ijkl$. Assuming that $\mathbf{Y}$ is symmetric in its first and last two indices and that $Y_{ijkl} = Y_{klij}$ (a consequence of Lorentz' reciprocal theorem in the case of $\mathbf{R}_{\Sigma E}$), this reduces the number of independent coefficients characterizing the material property to 9. The invariance of the crystal structure under a rotation by $\frac{\pi}{3}$ in the $\mathbf{e}_1\,\mathbf{e}_2$ plane imposes the additional relations

$$Y_{1133} = Y_{2233} \qquad Y_{1313} = Y_{2323} \qquad Y_{1111} = Y_{2222} \tag{H.8a}$$

$$Y_{1111} = Y_{1122} + 2Y_{1212} \,. \tag{H.8b}$$

These can be shown by standard techniques to hold for every geometry which is indifferent to a rotation in the $\mathbf{e}_1\,\mathbf{e}_2$ plane, except if it concerns 90° turns (or the special cases 0° and 180°). The fourth rank tensor $\mathbf{Y}$ is now fully determined by only 5 components. If furthermore we require tracelessness in its first and last two indices, only 3 independent elements remain. In $\mathbf{R}_{\Sigma E}$, we called these 3 coefficients $\eta_T$, $\eta_\parallel$ and $\eta_\perp$ (see (4.43)). For *cubic* face-centered crystals, one more invariance relation exists, and the number of independent coefficients drops to 2

(Nunan & Keller, 1984). Both the *efc* and the *smc*-lattices satisfy the symmetries used in this paragraph and their stress/rate-of-strain coupling is consequently characterized by 3 constants. The *ebc*, *esc* and *isc*-dispersions however, must be rotated by $\frac{\pi}{2}$ rather than $\frac{\pi}{3}$ to return to the same orientation. This invalidates (H.8b) so that 4 components are needed to specify $\mathbf{R}_{\Sigma E}$ for these configurations.

The construction of the five lattices defined in §4.6 is fairly simple (see Fig.4.10), and an appropriate set of basis vectors can easily be found. Yet it may not be obvious how to expand a *body-centered* cubic crystal of spheres so as to satisfy the criteria proposed above for the reference geometries. The first step of the procedure is to identify three pairs of touching particles in the close packed configuration whose centre-to-centre vectors are linearly independent. Referring to the standard description of the "*bcc*" unit cell for spheres (Fig. 4.24a), these vectors might be $\sqrt{2/3}(1,1,1)$, $\sqrt{2/3}(1,-1,1)$ and $\sqrt{2/3}(-1,1,1)$. Any two define a "close-packed" plane. For *bcc*-lattices, the mesh formed by the particle centres in this plane is diamond shaped, with an inscribed angle of $\arccos(1/3)$ ($\simeq 70°$) (Fig. 4.24b). In order to retain as many invariance relations as possible in the crystal of spheroids, it is best to stretch the unit cell for spheres in the direction perpendicular to this close-packed grid (so as to preserve the mirror symmetry across that plane). The resulting structure consists of parallel stacks of spheroids arranged on a pattern of isosceles triangles in the plane perpendicular to their direction of alignment. Adjacent layers are staggered so as to fit in each other's interstices (Fig. 4.24b). Unfortunately, the only symmetry element in the close-packed plane is a rotation by $\pi$. Six independent components are therefore needed to fully characterize $\mathbf{R}_{\Sigma E}$, which is why this crystal was not considered in §4.6.

# APPENDIX J

## Coefficients $\alpha$ and $\gamma$ characterizing the material properties of isolated prolate spheroids

Following the notation of Kim (1985)

$$\alpha_1 = e^2\left\{-2e + (1+e^2)\log\left(\frac{1+e}{1-e}\right)\right\}^{-1} \tag{J.1}$$

$$\alpha_2 = 2e^2\left\{2e + (3e^2-1)\log\left(\frac{1+e}{1-e}\right)\right\}^{-1} \tag{J.2}$$

$$\gamma = (1-e^2)\left\{2e + (1-e^2)\log\left(\frac{1+e}{1-e}\right)\right\}^{-1} \tag{J.3}$$

$$\gamma' = (2-e^2)\left\{-2e + (1+e^2)\log\left(\frac{1+e}{1-e}\right)\right\}^{-1} \tag{J.4}$$

$$\gamma_3' = \left\{-2e + (1+e^2)\log\left(\frac{1+e}{1-e}\right)\right\}^{-1} \tag{J.5}$$

$$\alpha^* = e^2\gamma_3'\left\{2e(2e^2-1) + (1-e^2)\log\left(\frac{1+e}{1-e}\right)\right\}\cdot \cdot\left\{2e(2e^2-3) + 3(1-e^2)\log\left(\frac{1+e}{1-e}\right)\right\}^{-1} \tag{J.6}$$

$$\alpha_5 = e^2\left\{6e - (3-e^2)\log\left(\frac{1+e}{1-e}\right)\right\}^{-1} \tag{J.7}$$

$$\alpha_4 = 2e^2(1-e^2)\left\{2e(3-5e^2) - 3(1-e^2)^2\log\left(\frac{1+e}{1-e}\right)\right\}^{-1}. \tag{J.8}$$

The results for spherical particles can be recovered by noting that

$$\lim_{e\to 0}\alpha_1 = \lim_{e\to 0}\alpha_2 = \frac{3}{8}e^{-1} \tag{J.9}$$

$$\lim_{e\to 0}\gamma = \lim_{e\to 0}\gamma' = \frac{3}{4}e^{-3} \tag{J.10}$$

$$\lim_{e\to 0}\alpha_4 = -\frac{5}{8}e^{-3} \qquad \lim_{e\to 0}\alpha_5 = -\frac{15}{8}e^{-3} \qquad \lim_{e\to 0}\alpha^* = -\frac{5}{4}e^{-3}. \tag{J.11}$$

**References**

Abramowitz, M. & Stegun, I.A. (1970) *Handbook of mathematical functions.* Dover Publications, Inc.

Adler, P.M. (1985) Spatially periodic suspensions, *J. Theor. Appl. Mech.,* Special volume, 73-100.

Allen, M.P. (1990) Diffusion coefficient increases with density in hard ellipsoid liquid crystals, *Phys. Rev. Lett.* **65**, 2881-2884.

Allen, M.P., Frenkel, D. & Talbot, J. (1989) Molecular dynamics simulation using hard particles, *Comp. Phys. Reports* **9**, 301-353.

Batchelor, G.K. (1970a) Slender body theory for particles of arbitrary cross-section in Stokes flow, *J. Fluid Mech.* **44**, 419-440.

Batchelor, G.K. (1970b) The stress in a suspension of force-free particles, *J. Fluid Mech.* **41**, 545-570.

Batchelor, G.K. (1971) The stress generated in a non-dilute suspension of elongated particles by pure straining motion, *J. Fluid Mech.* **46**, 813-829.

Batchelor, G.K. (1972) Sedimentation in a dilute suspension of spheres, *J. Fluid Mech.* **52**, 245-268.

Batchelor, G.K. (1976) Brownian diffusion of particles with hydrodynamic interactions, *J. Fluid Mech.* **74**, 1-29.

Batchelor, G.K. & Green, J.T. (1972) The determination of the bulk stress in a suspension of spherical particles to order $c^2$, *J. Fluid Mech.* **56**, 401-427.

Beenakker, C.W.J. (1986) Ewald sum of the Rotne-Prager tensor, *J. Chem. Phys.* **85**, 1581-1582.

Bibbo, M.A., Dinh, S.M. & Armstrong, R.C. (1985) Shear flow properties of semi-concentrated fiber suspensions, *J. Rheol.* **29**, 905-929.

Bitsanis, I., Davis, H.T. & Tirrell, M. (1988) Brownian dynamics of nondilute solutions of rodlike polymers. I. Low concentrations, *Macromol.* **21**, 2824-2835.

Bitsanis, I., Davis, H.T. & Tirrell, M. (1988) Brownian dynamics of nondilute solutions of rodlike polymers. II. High concentrations, *Macromol.* **23**, 1157-1165.

Bohlin, T. (1960) On the drag on a rigid sphere moving in a viscous liquid inside a cylindrical tube, *Trans. R. Inst. Tech. (Stockholm)* **155**, 1-63.

Bonnecaze, R.T. (1991) *Macroscopic properties of electrically interacting suspensions.*, Ph.D. thesis, California Institute of Technology.

Bossis, G. & Brady, J.F. (1989) The rheology of Brownian suspensions, *J. Chem. Phys.* **91**, 1866-1874.

Brady, J.F. & Bossis, G. (1988) Stokesian dynamics, *Ann. Rev. Fluid Mech.* **20**, 111-157.

Brady, J.F., Phillips, R.J., Lester, J.C. & Bossis, G. (1988) Dynamic simulation of hydrodynamically interacting suspensions, *J. Fluid Mech.* **195**, 257-280.

Brenner, H. (1966) The Stokes resistance of an arbitrary particle—Part V. Symbolic operator representation of intrinsic resistance, *Chem. Eng. Sci.* **21**, 97-109.

Brenner, H. (1964) The Stokes resistance of an arbitrary particle—III. Shear fields, *Chem. Eng. Sci.* **19**, 631-651.

Brenner, H. (1974) Rheology of a dilute suspension of axisymmetric Brownian particles, *Int. J. Multiph. Flow* **1**, 195-341.

Brinkman, H.C. (1947) A calculation of the viscous force exerted by a flowing fluid on a dense swarm of particles, *Appl. Sci. Res.* **A1**, 27-34.

Chwang, A.T. & Wu, T.Y.-T. (1974) Hydromechanics of low-Reynolds-number flow. Part 1. Rotation of axisymmetric prolate bodies, *J. Fluid Mech.* **63**, 607-622.

Chwang, A.T. & Wu, T.Y.-T. (1975) Hydromechanics of low-Reynolds-number flow. Part 2. Singularity method for Stokes flows, *J. Fluid Mech.* **67**, 787-815.

Claeys, I.L. & Brady, J.F. (1989) Lubrication singularities of the grand resistance tensor for two arbitrary particles, *PhysicoChem. Hydrodyn.* **11**, 261-293.

Cuckier, R.I. (1983) Diffusion of Brownian spheres in semidilute polymer solutions, *Macromol.* **17**, 252-255.

de Gennes, P.G. (1971) Reptation of a polymer chain in the presence of fixed obstacles, *J. Chem. Phys.* **55**, 572-579.

Doi, M. & Edwards, S.F. (1986) *The theory of polymer dynamics*, Clarendon Press, Oxford.

Durlofsky, L. & Brady, J.F. (1987) Analysis of the Brinkman equation as a model for flow in porous media, *Phys. Fluids* **30**, 3329-3341.

Durlofsky, L., Brady, J.F. & Bossis, G. (1987) Dynamic simulation of hydrodynamically interacting particles, *J. Fluid Mech.* **180**, 21-49.

Ewald, P.P. (1921) Die berechnung optischer und elektrostatischer Gitterpotentiale, *Ann. Phys.* **64**, 253-287.

Frenkel, D. (1987) Computer simulation of hard-core models for liquid crystals, *Mol. Phys.* **60**, 1-20.

Frenkel, D. & Mulder, B.M. (1985) The hard ellipsoid-of-revolution fluid I. Monte-Carlo simulations, *Mol. Phys.* **55**, 1171-1192.

Frenkel, D., Mulder, B.M. & McTague, J.P. (1984) Phase diagram of a system of hard ellipsoids, *Phys. Rev. Lett.* **52**, 287-290.

Glendinning, A.B. & Russel, W.B. (1982) A pairwise additive description of sedimentation and diffusion in concentrated suspensions of hard spheres, *J. Colloid Interface Sci.* **89**, 124-143.

Gruber, P.M. & Lekkerkerker, C.G. (1987) *Geometry of numbers.* North-Holland.

Haber, S. & Brenner, H. (1984) Rheological properties of dilute centrally symmetric Brownian particles at small shear-rates, *J. Colloid Interface Sci.* **97**, 496-514.

Happel, J. & Brenner, H. (1973) *Low Reynolds Number Hydrodynamics.* Martinus Nijhoff.

Hasimoto, H. (1959) On the periodic fundamental solution of the Stokes equations

and their application to viscous flow past a cubic array of spheres, *J. Fluid Mech.* **5**, 317-328.

Hinch, E.J. (1972) Note on the symmetries of certain material tensors for a particle in Stokes flow, *J. Fluid Mech.* **54**, 423-425.

Hinch, E.J. (1977) An averaged-equation approach to particle interactions in a fluid suspension, *J. Fluid Mech.* **83**, 695-720.

Jeffrey, D.J. (1973) Conduction through a random suspension of spheres, *Proc. R. Soc. Lond. A* **335**, 355-367.

Kahaner, D.K. & Rechard, O.W. (1987) TWODQD, an adaptive routine for two-dimensional integration, *J. Comp. Appl. Math.* **17**, 215-234.

Kim, S. (1985) A note on Faxen laws for nonspherical particles, *Int. J. Multiph. Flow* **5**, 713-719.

Kim, S. (1986) Singularity solutions for ellipsoids in low-Reynolds-number flows: with applications to the calculation of hydrodynamic interactions in suspensions of ellipsoids, *Int. J. Multiph. Flow* **12**, 469-491.

Kim, S. & Arunachalam, P.V. (1987) The general solution for ellipsoids in low-Reynolds-number flow, *J. Fluid Mech.* **178**, 535-547.

Koch, D.L. & Shaqfeh, E.S.G. (1989) The instability of a dispersion of sedimenting spheroids, *J. Fluid Mech.* **209**, 521-542.

Ladd, A.J.C. (1988) Hydrodynamic interactions in a suspension of spherical particles, *J. Chem. Phys.* **88**, 5051-5063.

Ladd, A.J.C. (1990) Hydrodynamic transport coefficients of random dispersions of hard spheres, *J. Chem. Phys.* **93**, 3484-3494.

Ladyzhenskaya, O.A. (1963) *The Mathematical Theory of Viscous Incompressible Flow.* Gordon & Breach.

Lam, J. (1990) Effective longitudinal dielectric constant of a rectangular lattice of parallel conducting prolate spheroids, *J. Appl. Phys.* **68**, 392-403.

Metropolis, N., Rosenbluth, A.W., Rosenbluth, M.N., Teller, A.H. & Teller, E. (1953) Equation of state calculations by fast computing machines, J. Chem. Phys. **21**, 1087-1092.

Mewis, J. & Metzner, A.B. (1974) The rheological properties of suspensions of fibres in Newtonian fluids subjected to extesional deformations, *J. Fluid Mech.* **62**, 593-600.

Milliken, W.J., Gottlieb, M., Graham, A.L., Mondy, L.A. & Powell, R.L. (1989) The viscosity-volume fraction relation for suspensions of rod-like particles by falling-ball rheometry, *J. Fluid Mech.* **202**, 217-232.

Nijboer, B.R.A. & De Wette, F.W. (1957) On the calculation of lattice sums, *Physica* **23**, 309-321.

Nunan, K.C. & Keller, J.B. (1984) Effective viscosity of a periodic suspension, *J. Fluid Mech.* **142**, 269-287.

O'Brien, R.W. (1979) A method for the calculation of the effective transport properties of suspensions of interacting particles, *J. Fluid Mech.* **91**, 17-39.

Onsager, L. (1949) The effects of shape on the interaction of colloidal particles, *Ann. N.Y. Acad. Sci.* **51**, 627-659.

Ottewill, R.H. & Williams, N.St.J. (1987) Study of particle motion in concentrated dispersions by tracer diffusion, *Nature* **325**, 232-234.

Perram, J.W. & Wertheim, M.S. (1985) Statistical mechanics of hard ellipsoids. I. Overlap algorithm and the contact function, *J. Comput. Phys.* **58**, 409-416.

Perry, P. & Throop, G.J. (1972) Decay of pair correlations in hard sphere fluids, *J. Chem. Phys.* **57**, 1827-1829.

Phan-Thien, N. & Graham, A.L. (1991) A new constitutive model for fibre suspensions: flow past a sphere, *Rheol. Acta* **30**, 44-57.

Phan-Thien, N., Zheng, R. & Graham, A.L. (1991) The flow of a model suspension fluid past a sphere, *J. Stat. Phys.* **62**, 1173-1195.

Phillies, G.D.J. (1987) Dynamics of polymers in concentrated solutions: the universal scaling equation derived, *Macromol.* **20**, 558-564.

Phillips, R.J., Brady, J.F. & Bossis, G. (1988) Hydrodynamic transport properties of hard-sphere dispersions, I. Suspensions of freely mobile particles, *Phys. Fluids* **31**, 3462-3472.

Phillips, R.J., Brady, J.F. & Bossis, G. (1988) Hydrodynamic transport properties of hard-sphere dispersions, II. Porous media, *Phys. Fluids* **31**, 3473-3479.

Pittman, J.F.T. & Bayram, J. (1990) Extensional flow of polydisperse fibre suspensions in free-falling liquid jets, *Int. J. Multiph. Flow* **16**, 545-559.

Powell, R.L. (1991) Rheology of suspensions of rod-like particles, *J. Stat. Phys.* **62**, 1073-1094.

Powell, R.L., Mondy, L.A., Stoker, G.G., Milliken, W.J. & Graham, A.L. (1989) Development of a falling ball rheometer with applications to opaque systems: measurements of the rheology of suspensions of rods, *J. Rheol.* **33**, 1173-1188.

Pusey, P.N. & van Megen, W. (1983) Measurement of the short-time self-mobility of particles in concentrated suspensions. Evidence for many-particle hydrodynamic interactions, *J. Chem. Phys.* **44**, 285-291.

Reinelt, D. & Kraynik, A.M. (1990) *Existence of strain periodic solutions for extensional flow*, personal communication.

Salinas, A. & Pittman, J.F.T. (1981) Bending and breaking fibers in sheared suspensions, *Polym. Eng. Sci.* **21**, 23-31.

See, H., Doi, M. & Larson, R. (1990) The effect of steady flow fields on the isotropic-nematic transition of rigid rod-like polymers, *J. Chem. Phys.* **92**, 792-800.

Shaqfeh, E.S.G. (1988) A non local theory for the heat transport in composites containing highly conducting fibrous inclusions, *Phys. Fluids* **31**, 2405-2425.

Shaqfeh, E.S.G. & Fredrickson, G.H. (1990) The hydrodynamic stress in a suspension of rods, *Phys. Fluids A* **2**, 7-24.

Smith, W.R. & Henderson, D. (1970) Analytical representation of the Percus-Yevick hard sphere radial distribution function, *Mol. Phys.* **19**, 411-415.

Spielman, L. & Goren, S.L. (1968) Model for predicting pressure drop and filtration efficiency in fibrous media, *Env. Sci. Tech.* **2**, 279-287.

Talbot, J., Kivelson, D., Allen, M.P., Evans, G.T. & Frenkel, D. (1990) Structure of the hard-ellipsoid fluid, *J. Chem. Phys.* **92**, 3048-3057.

Thirumalai, D. (1986) Effect of elongational flow on the isotropic-to-nematic phase transition of rod-like systems, *J. Chem. Phys.* **84**, 5869-5873.

van der Werff, J.C., de Kruiff, C.G., Blom, C. & Mellema, J. (1989) Linear viscoelastic behavior of dense hard-sphere dispersions, *Phys. Rev. A* **39**, 795-807.

van Megen, W. & Underwood, S.M. (1989) Tracer diffusion in concentrated colloidal dispersions III. Mean squared displacements and self-diffusion coefficients, *J. Chem. Phys.* **91**, 552-559.

Verlet, L. & Weiss, J.J. (1972) Equilibrium theory of simple liquids, *Phys. Rev. A* **5**, 939-952.

Vieillard-Baron, J. (1970) Phase transitions of the classical hard-ellipse system, *J. Chem. Phys.* **56**, 4729-4744.

Weinbaum, S., Ganatos, P. & Yan, Z.Y. (1990) Numerical multipole and boundary integral techniques in Stokes flow, *Ann. Rev. Fluid Mech.* **22**, 275-316.

Wheeler, L.M., Lodge, T.P., Hanley, B. & Tirrell, M. (1987) Translational diffusion of linear polystyrenes in dilute and semidilute solutions of poly(vinyl methyl ether), *Macromol.* **20**, 1120-1129.

White, M.L. & Dorion, G.H. (1961) Diffusion in a crosslinked acrylamide polymer gel, *J. Polym. Sci.* **55**, 731-740.

Zick, A.A. & Homsy, G.M. (1982) Stokes flow through periodic arrays of spheres, *J. Fluid Mech.* **115**, 13-26.

Zuzovsky, M., Adler, P.M. & Brenner, H. (1983) Spatially periodic suspensions of

convex particles in linear shear flows. III. Dilute arrays of spheres suspended in Newtonian fluids, *Phys. Fluids* **26**, 1714-1723.

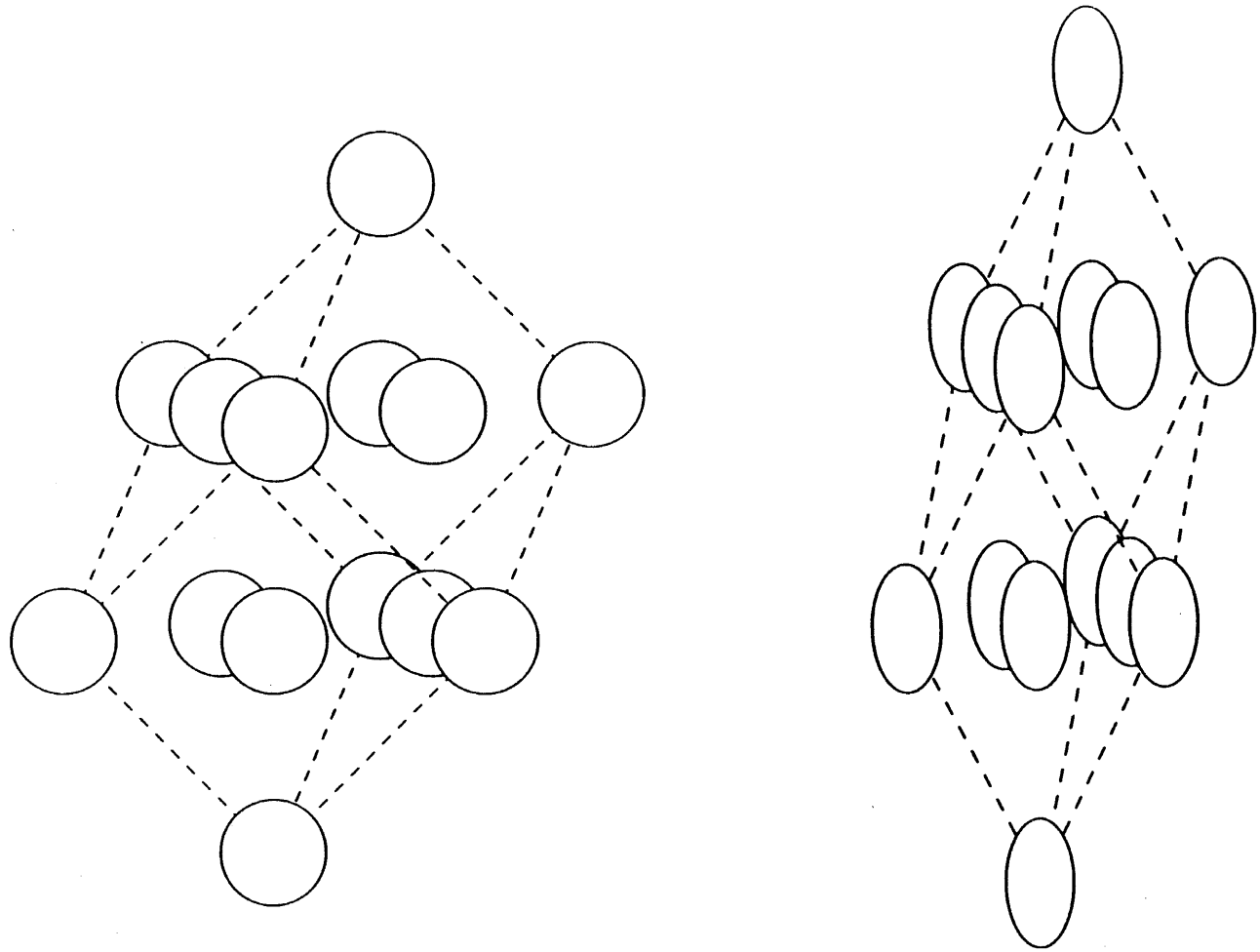

**Fig.4.1** : Expansion of a face-centered cubic lattice of spheres into an *efc* lattice of spheroids. The particles are not drawn as touching for the sake of clarity. The direction of stretch is perpendicular to the hexagonally packed plane.

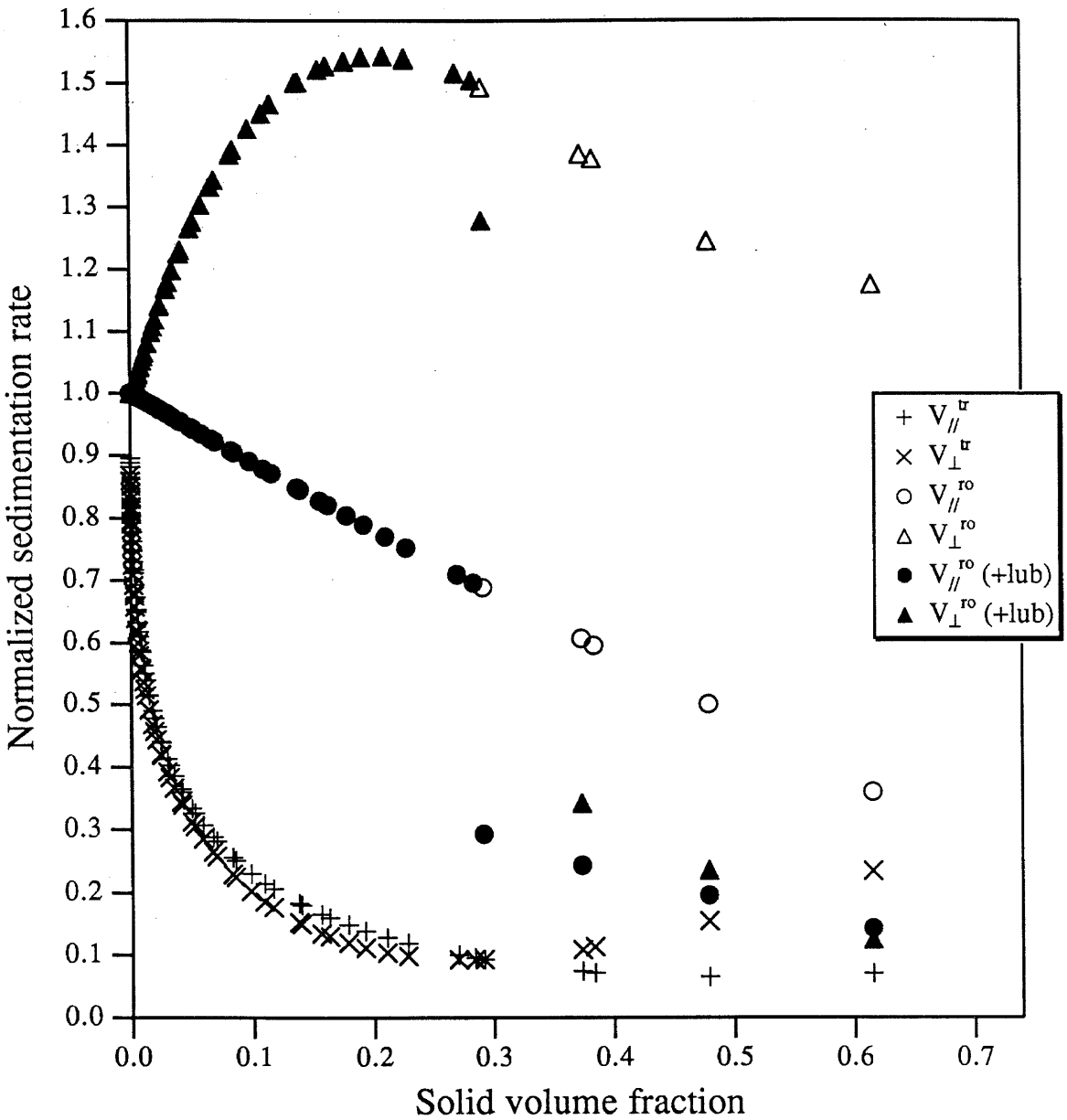


**Fig.4.2**: Sedimentation rates of *efc* lattices of spheroids of aspect ratio 6. The sedimentation rates are normalized by their value at infinite dilution . The maximum packing fraction compatible with the mutual impenetrability of the particles is 74.05%.

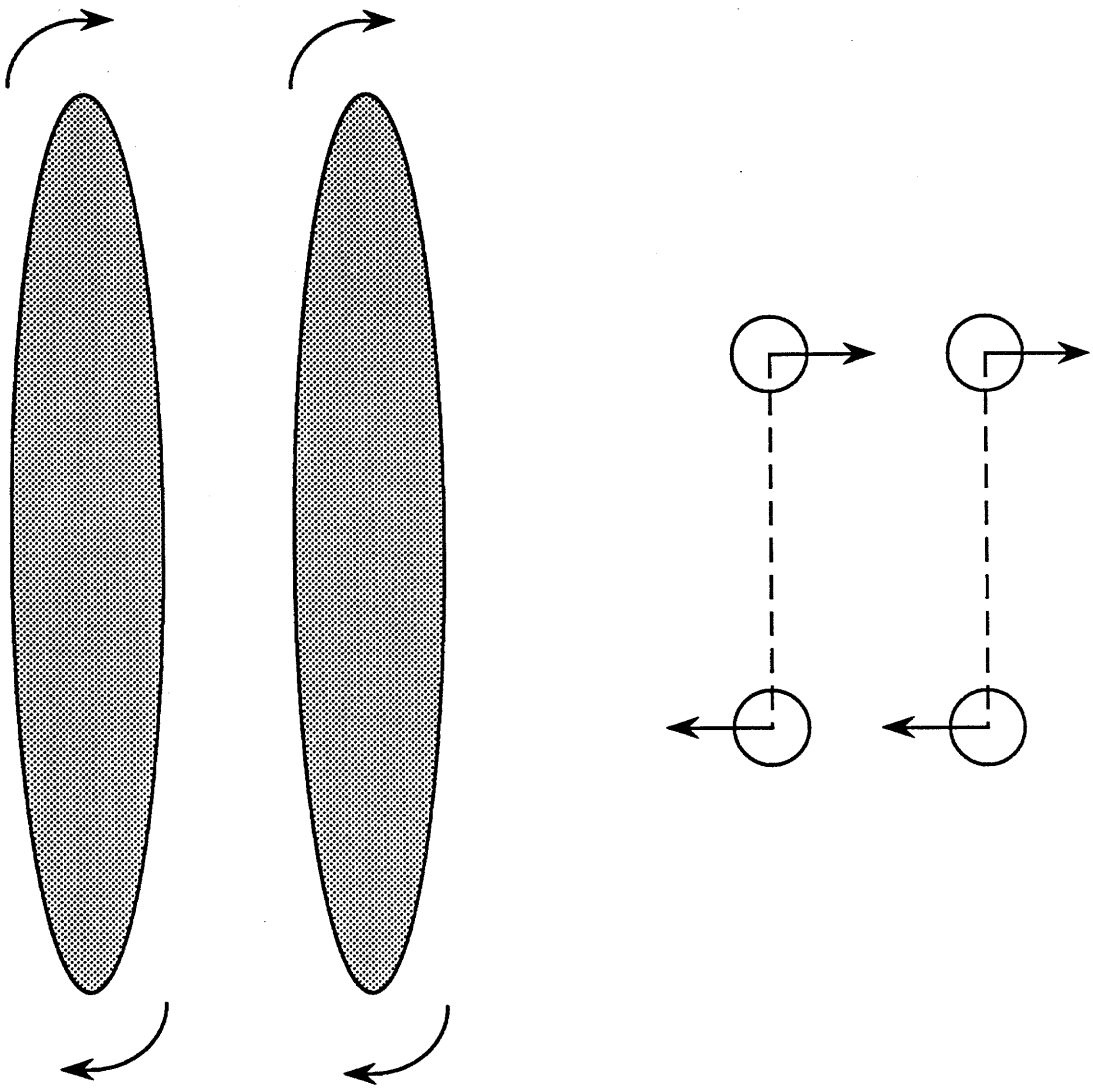

**Fig.4.3** : Illustration of the mechanism leading to enhanced rotational diffusivities perpendicular to the spheroidal axis in *efc*-crystals of ellipsoids.

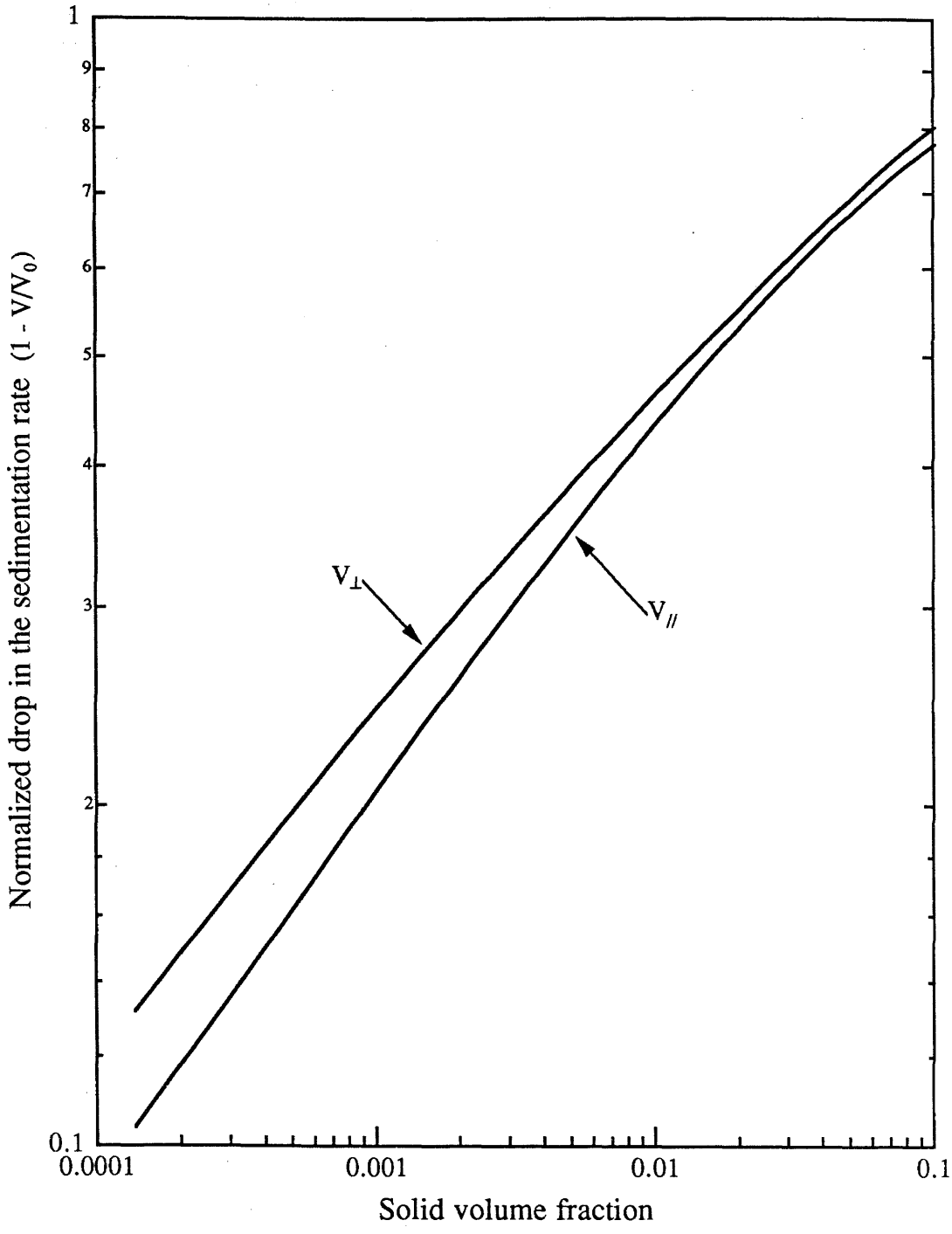


**Fig.4.4**: Asymptotic dependence of the sedimentation rate of *efc* crystals on the volume fraction of particles.
The aspect ratio of the spheroids is 6. For reference, note that the diagonal of the graph has a slope of 1/3.

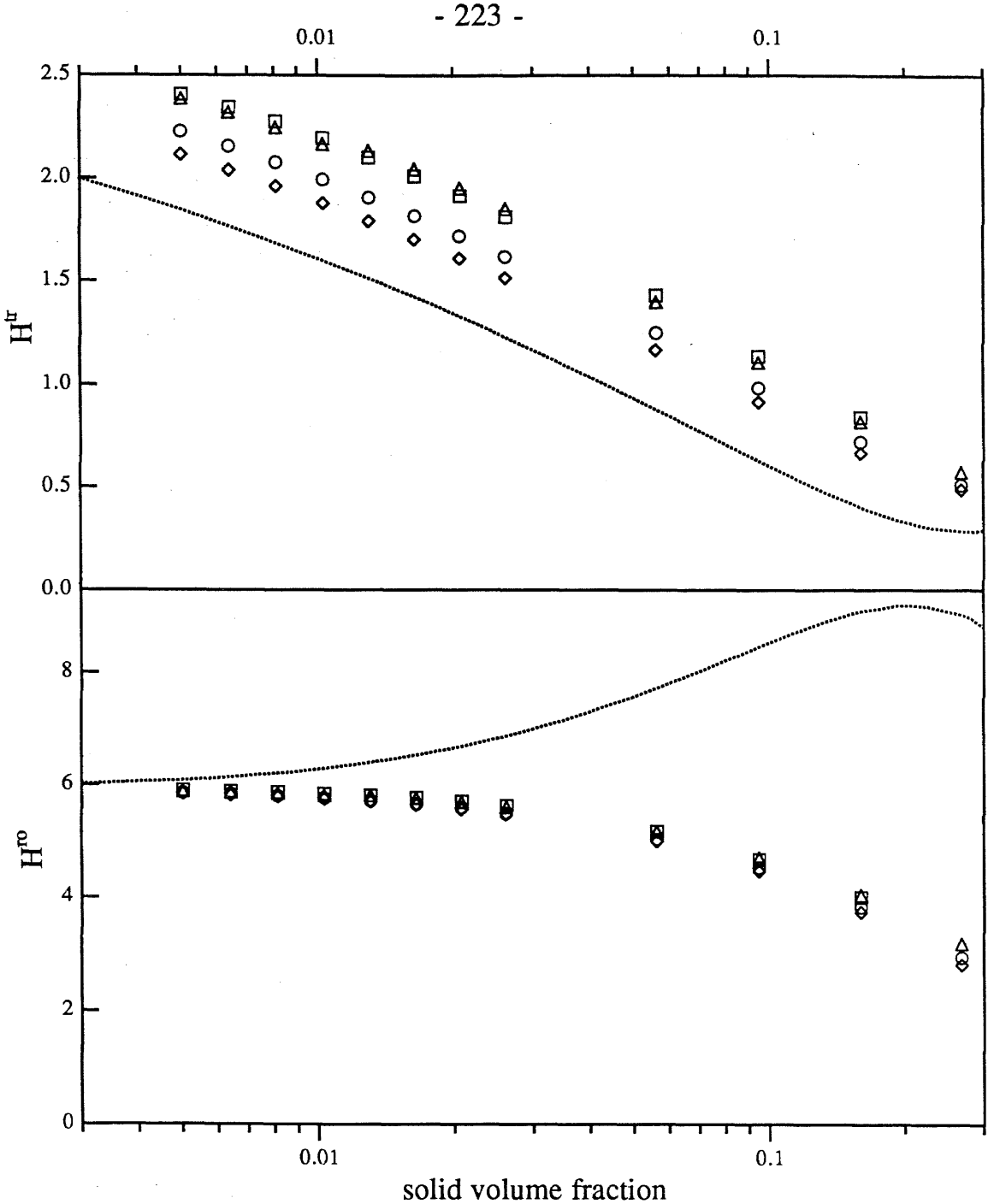


**Fig.4.5**: Hindered diffusivity *vs*. volume fraction for *efc* crystals of prolate spheroids of aspect ratio 6.

(normalized by $kT / 8\pi\mu a^n$, with n=1 for $H^{tr}$ and n=2 for $H^{ro}$)
Only the results for the diffusivity perpendicular to the rod axis are shown. The dotted lines represent data for one particle per unit cell and correspond to the sedimentation rate and its rotational analog. The unit cell for $N = 4$ ( ◇ ) was constructed by including the images closest to the origin in the hexagonally packed plane. These were then replicated one basis vector away to build a unit cell with 8 particles ( ○ ). This procedure was repeated to obtain $N = 16$ ( △ ) and 32 ( □ ).

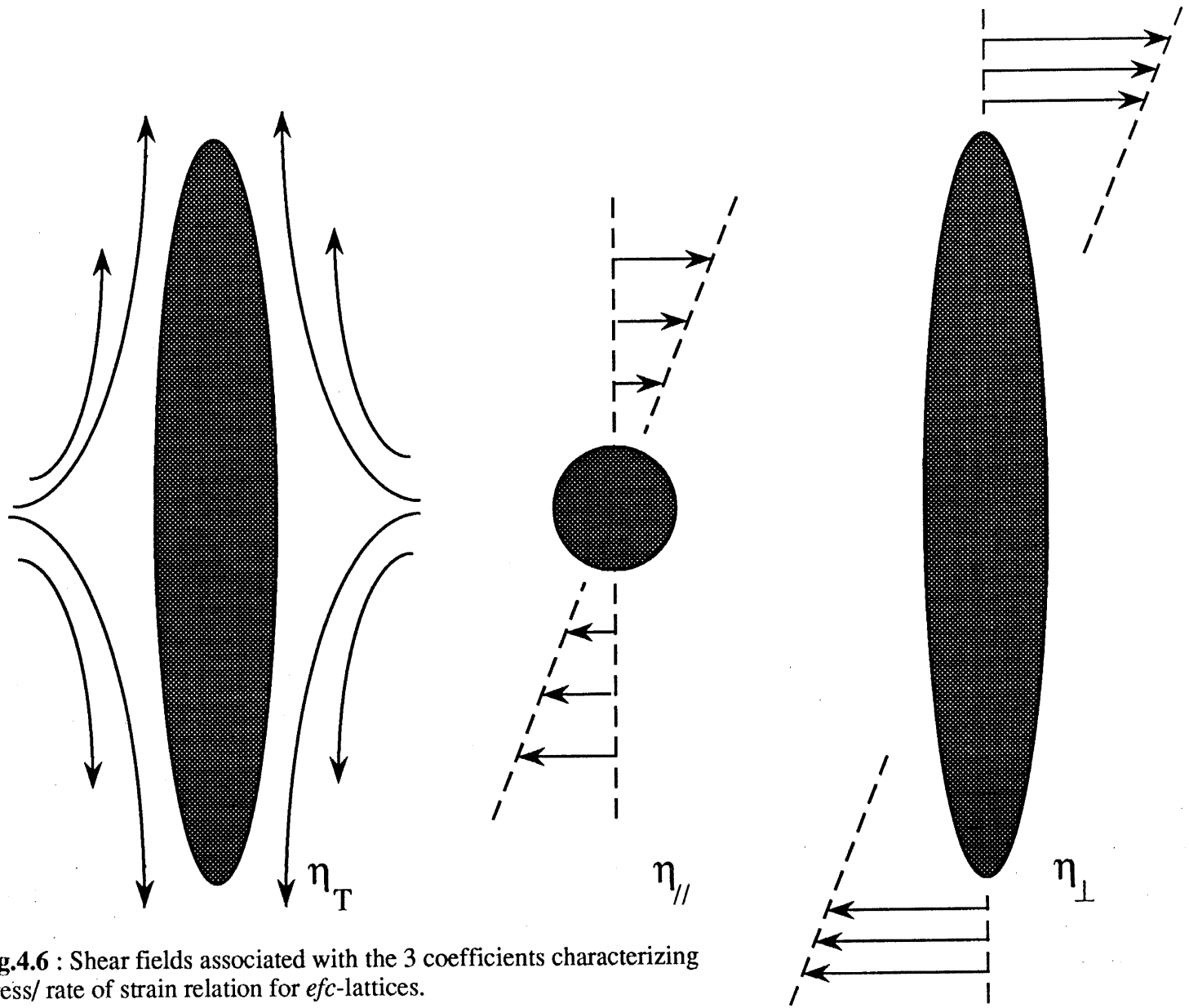


**Fig.4.6** : Shear fields associated with the 3 coefficients characterizing stress/ rate of strain relation for *efc*-lattices.

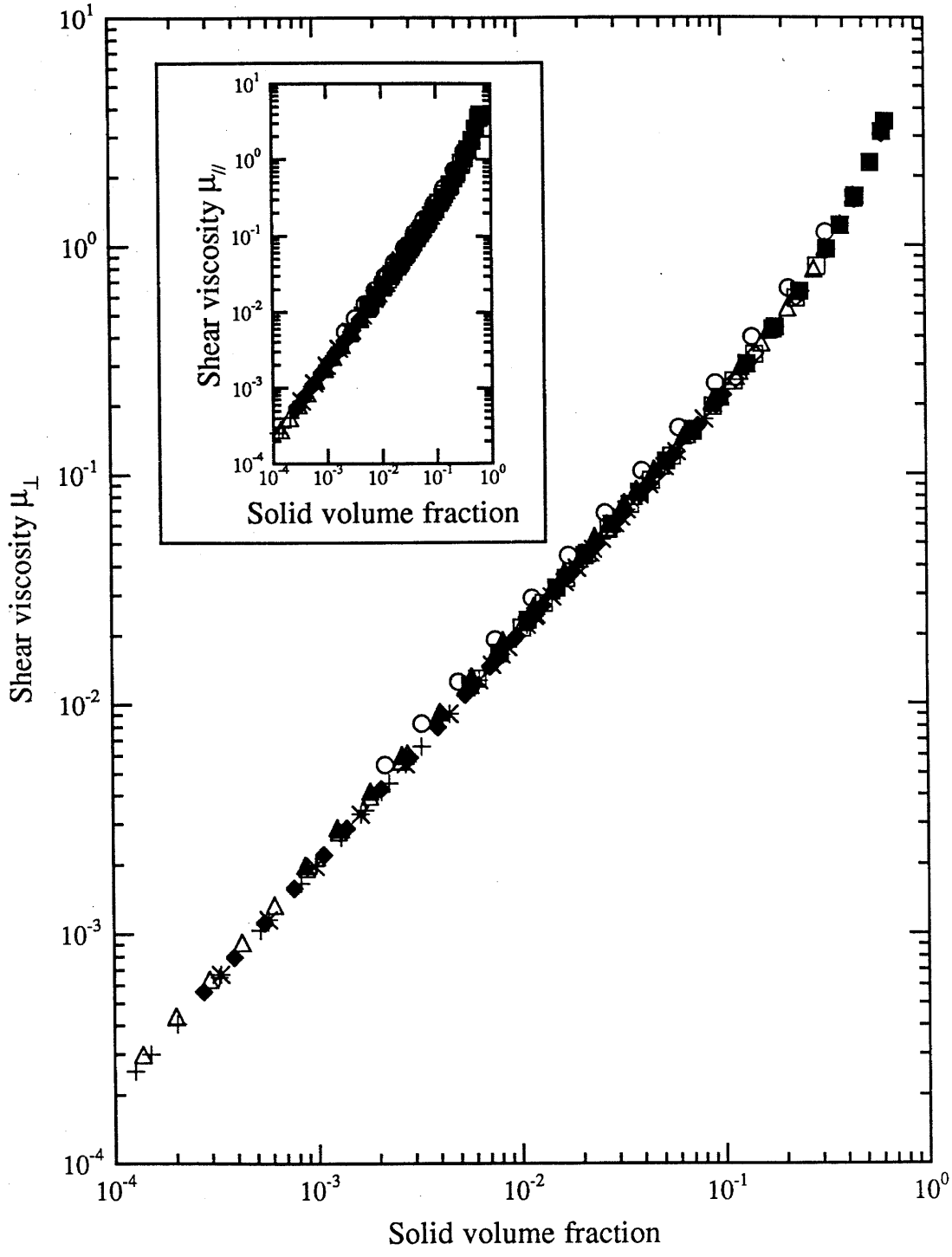


**Fig.4.7**: Apparent shear viscosities $\mu_\perp$ and $\mu_{//}$ of *efc*-lattices of spheroids.

The symbols are explained in the legend of the next figure. Lubrication interactions have been suppressed. The data for both viscosities are almost indistinguishable.

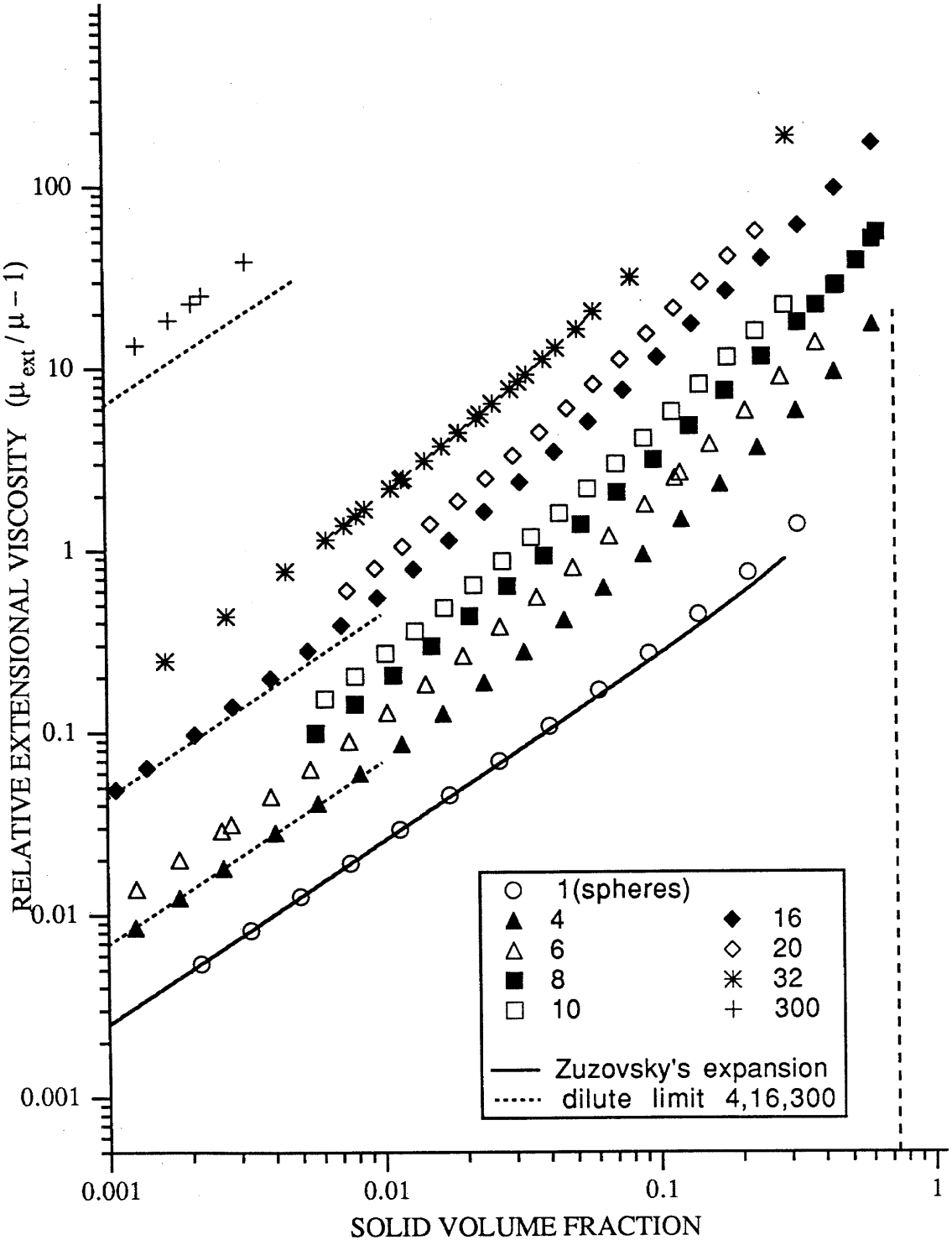


**Fig.4.8**: Extensional viscosity of *efc*-lattices of prolate spheroids. Lubrication interactions have been suppressed. The aspect ratio of the particles is mentioned in the legend. The solid line represents the expansion due to Zuzovsky *et al.* (1983). The dilute limit expansions for $r_p$ = 4, 16 and 300 are shown as dotted lines.

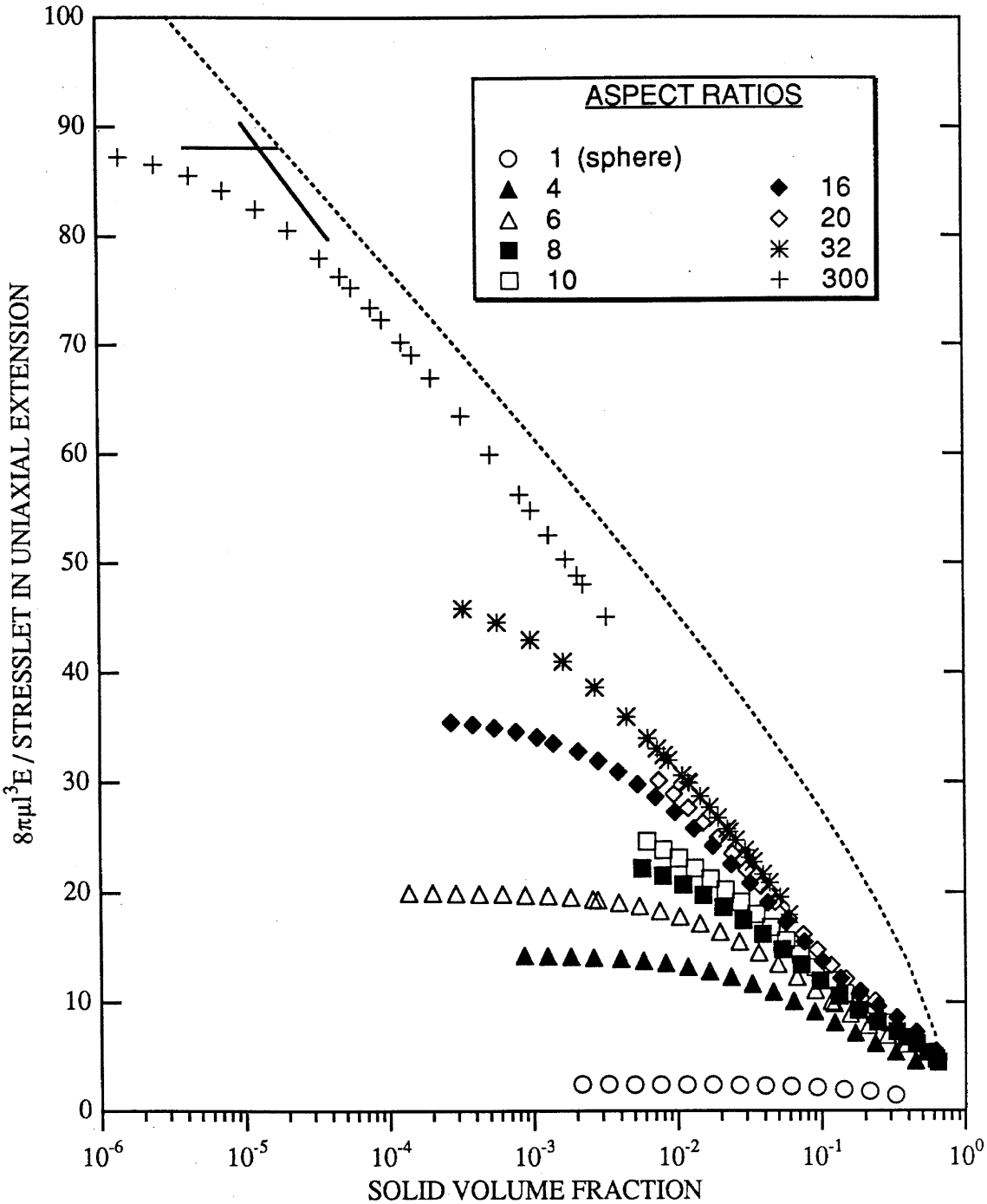


**Fig.4.9**: Verification of hydrodynamic screening in *efc* suspensions of spheroids (plot of the inverse of the stresslet *vs*. the logarithm of the volume fraction). See text for details. The dotted line represents eq.(4.46) multiplied by 3/2 to account for the perfect correlation of the centres of mass in this system.

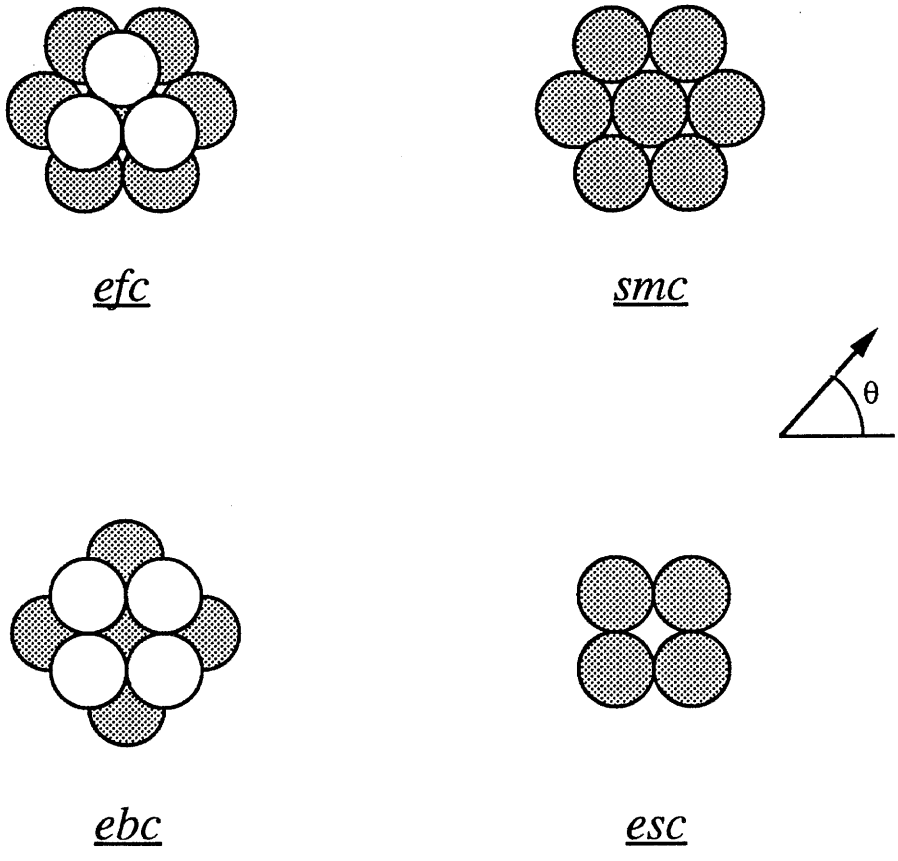


**Fig.4.10** : Projection of the lattice geometry onto the close packed planes (i.e., along the spheroidal axis). The white and shaded particles are in different layers.

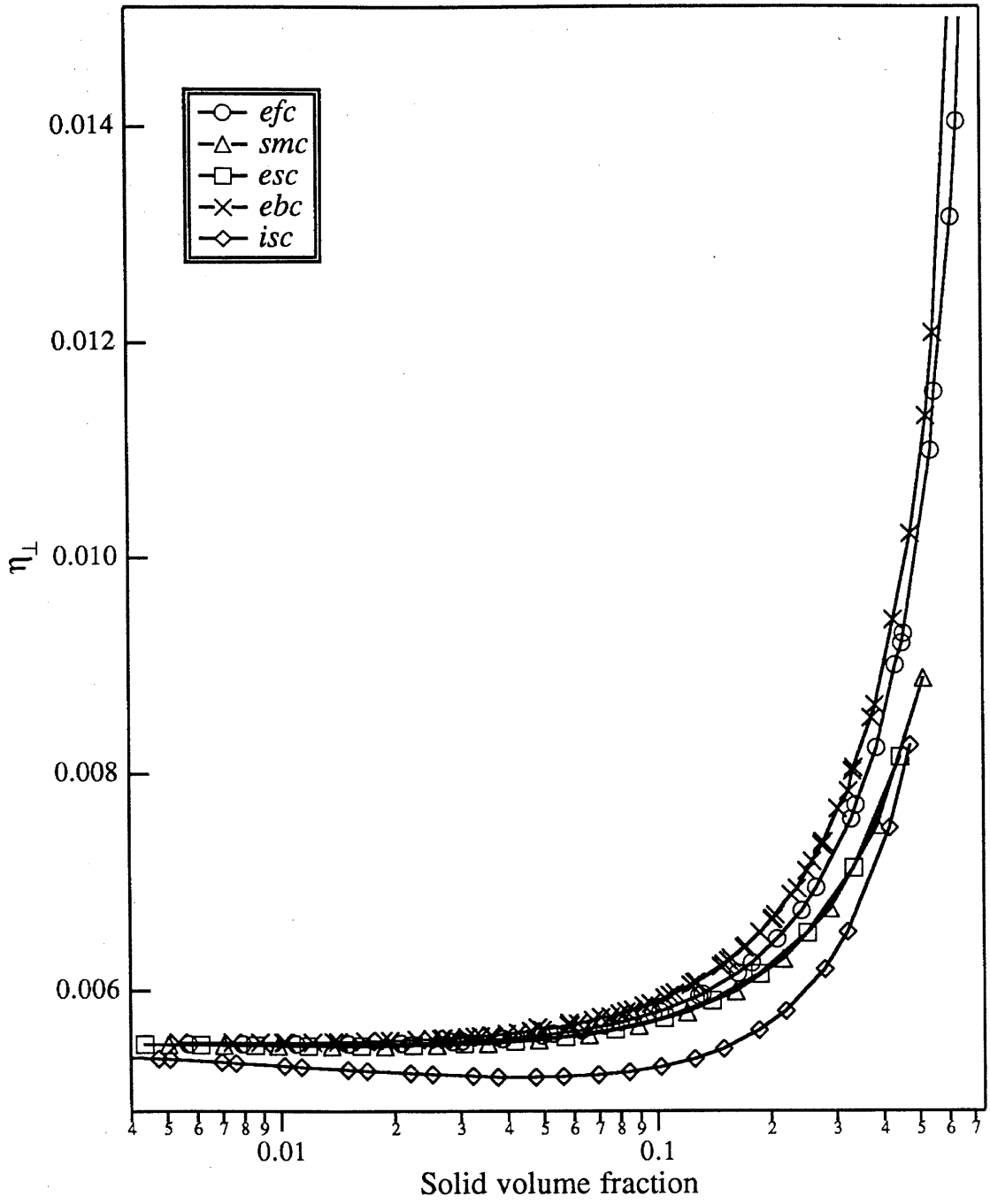


**Fig.4.11a**: Coefficient $\eta_\perp$ of the stress / rate of strain relation for a variety of crystalline configurations of spheroids of aspect ratio 8.

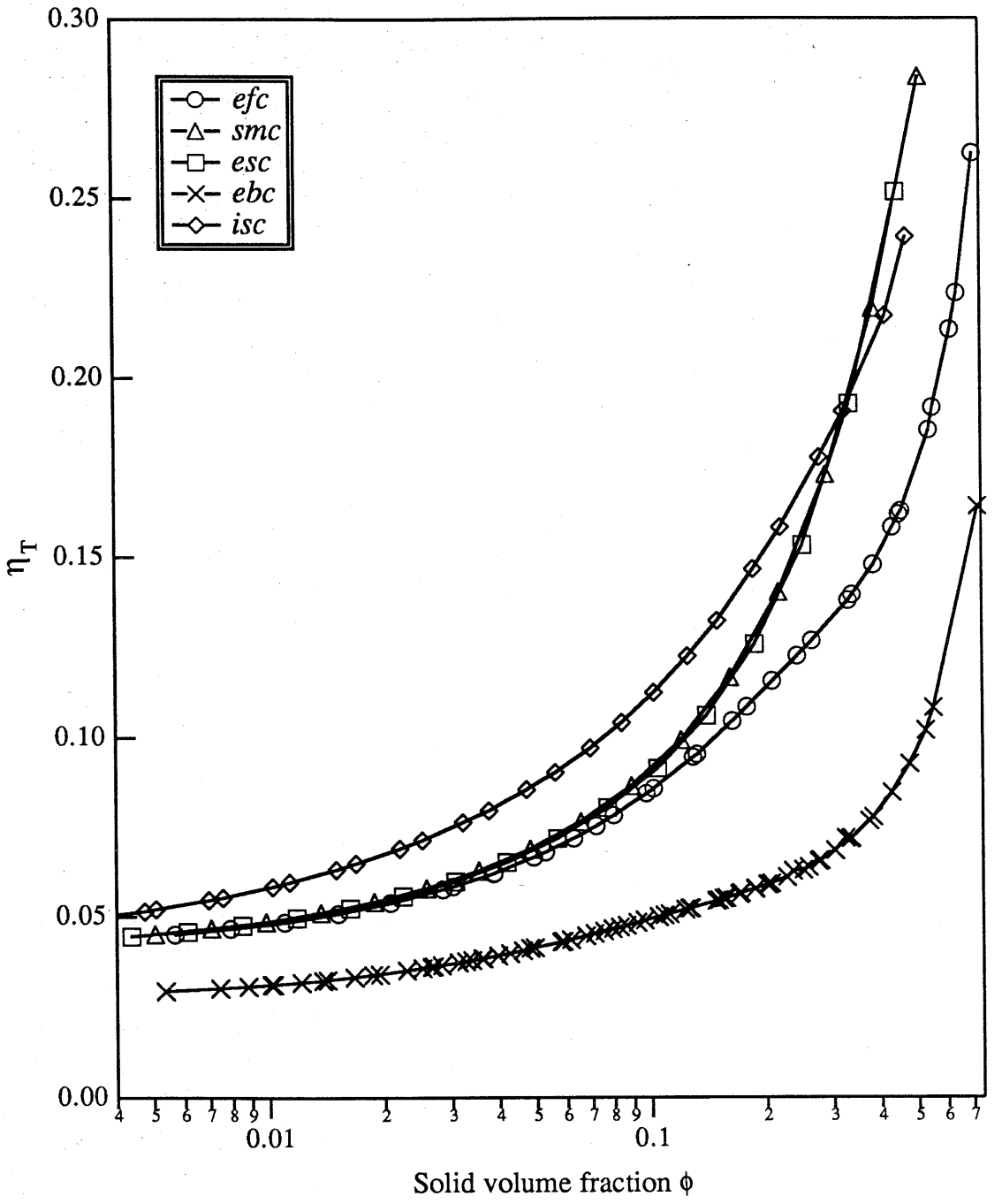


**Fig.4.11b**: Coefficient $\eta_T$ of the relation between the hydrodynamic stress and the rate of strain for various lattices of freely suspended spheroids with $r_p = 8$.

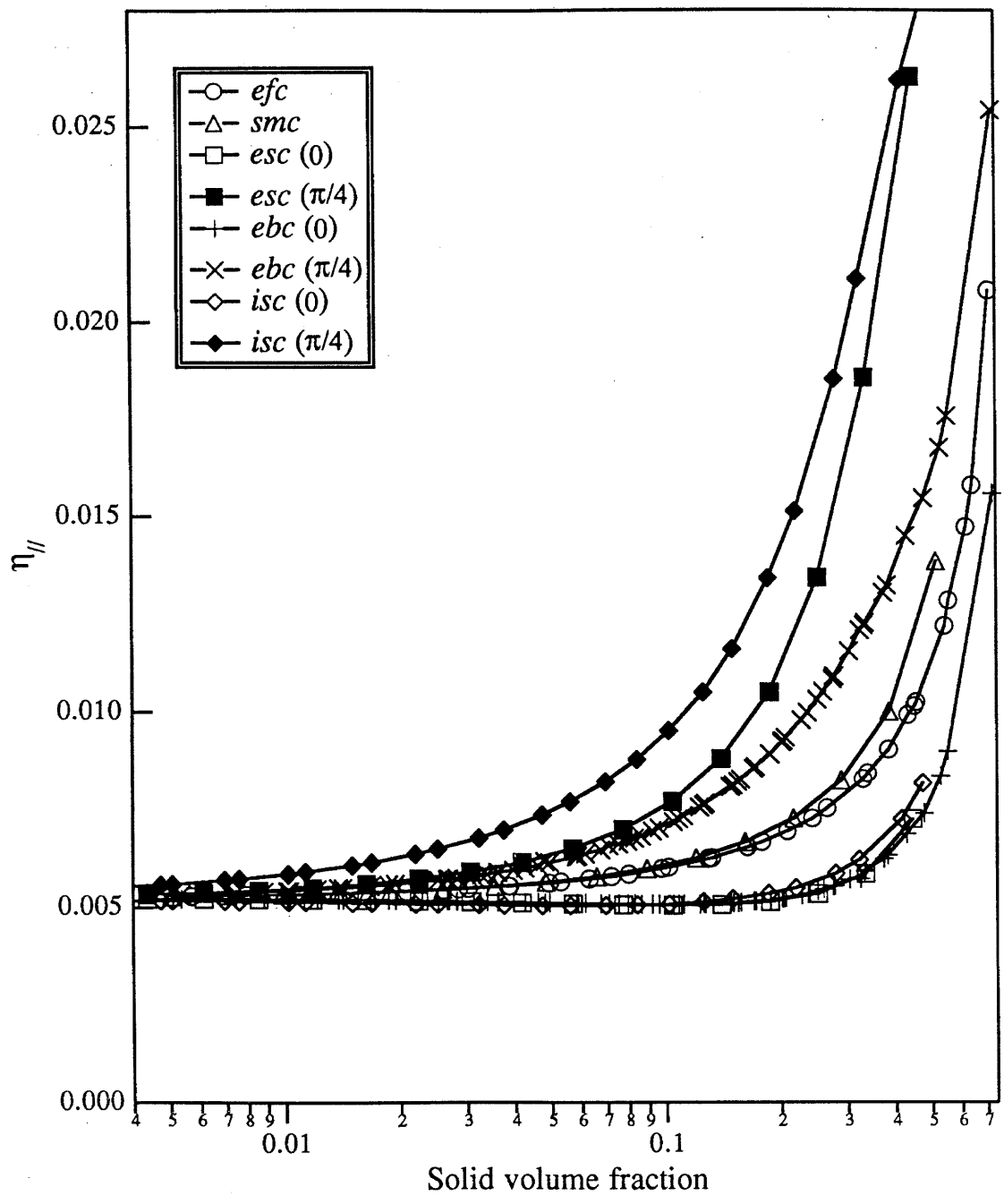


**Fig.4.11c**: Coefficient $\eta_{//}$ of $\mathbf{R}_{\Sigma E}$ for lattices of spheroids of aspect ratio 8.

The number in parentheses indicates the angle θ between the shortest basis vector of the lattice and the direction of the shear flow (see Fig.4.10).

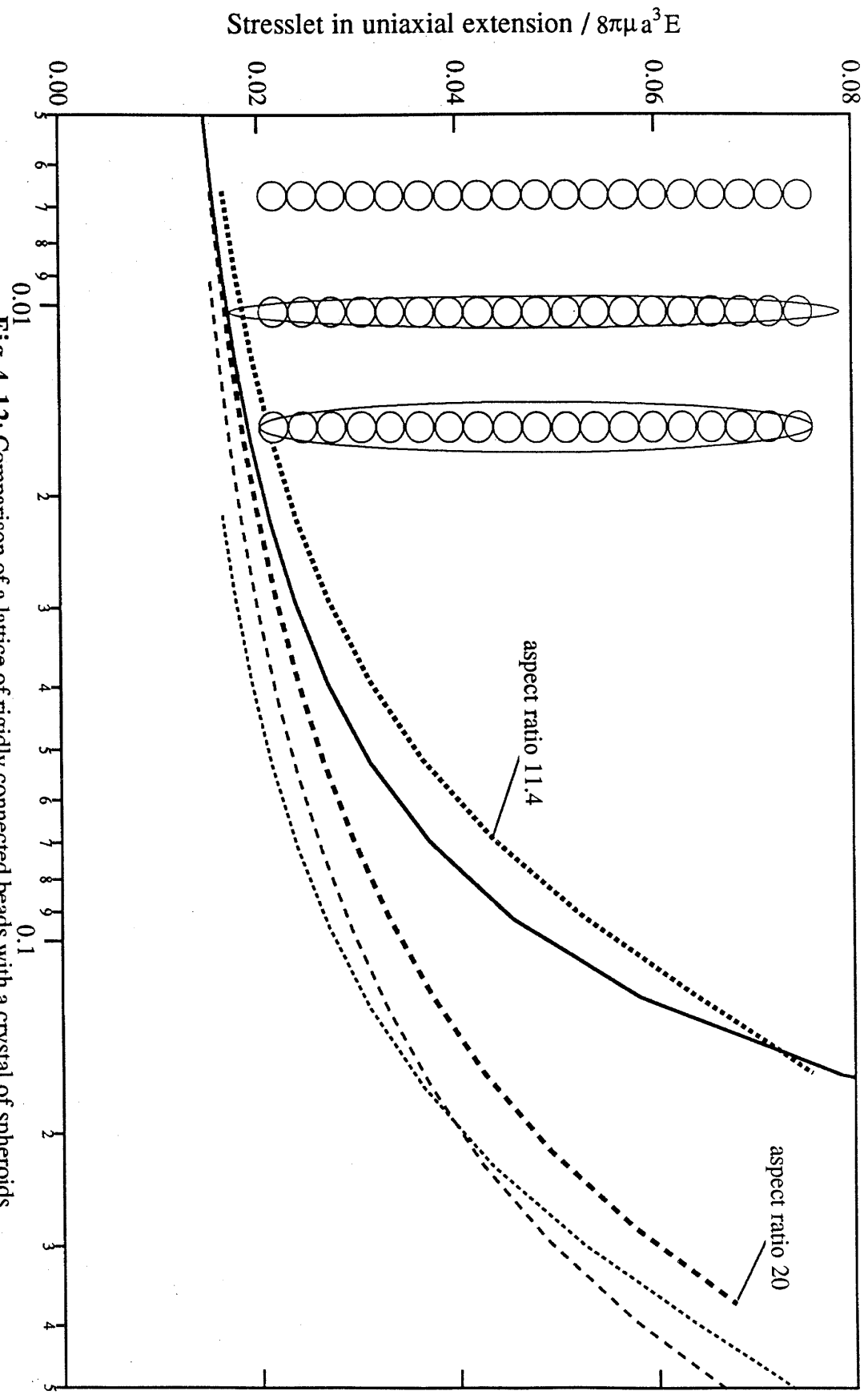


**Fig.4.12**: Comparison of a lattice of rigidly connected beads with a crystal of spheroids. The bold dashed lines show $\eta_T$ for *smc*-lattices of spheroids vs. the volume fraction of equivalent strings. The other lines are plotted vs. the actual concentration.

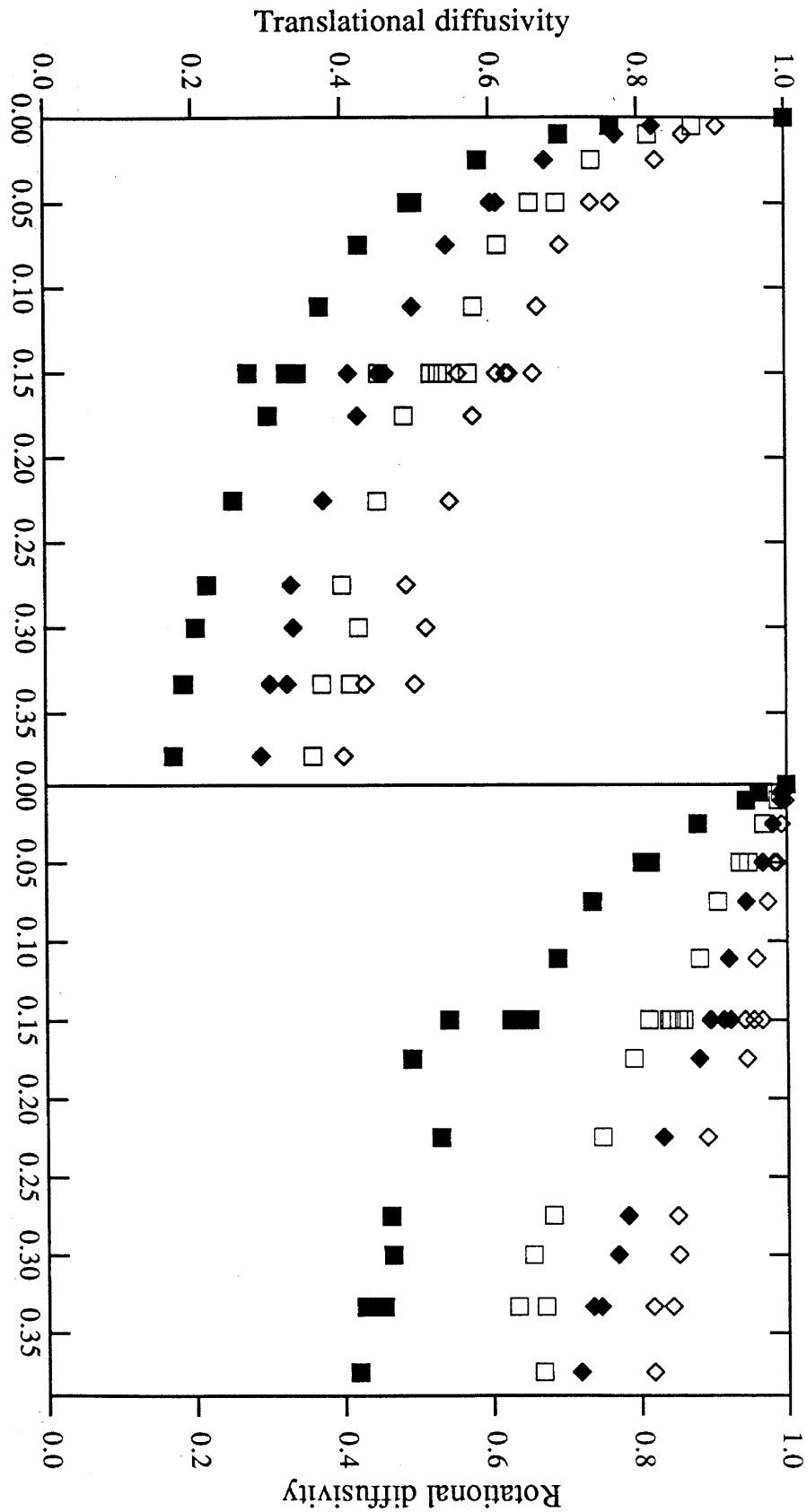


**Fig.4.13:** Translational and rotational diffusivities of equilibrium dispersions of prolate spheroids of aspect ratio 6

Self-diffusion coefficients: ◇ $D_{//}$ □ $D_{\perp}$

Hindered diffusivities: ◆ $H_{//}$ ■ $H_{\perp}$

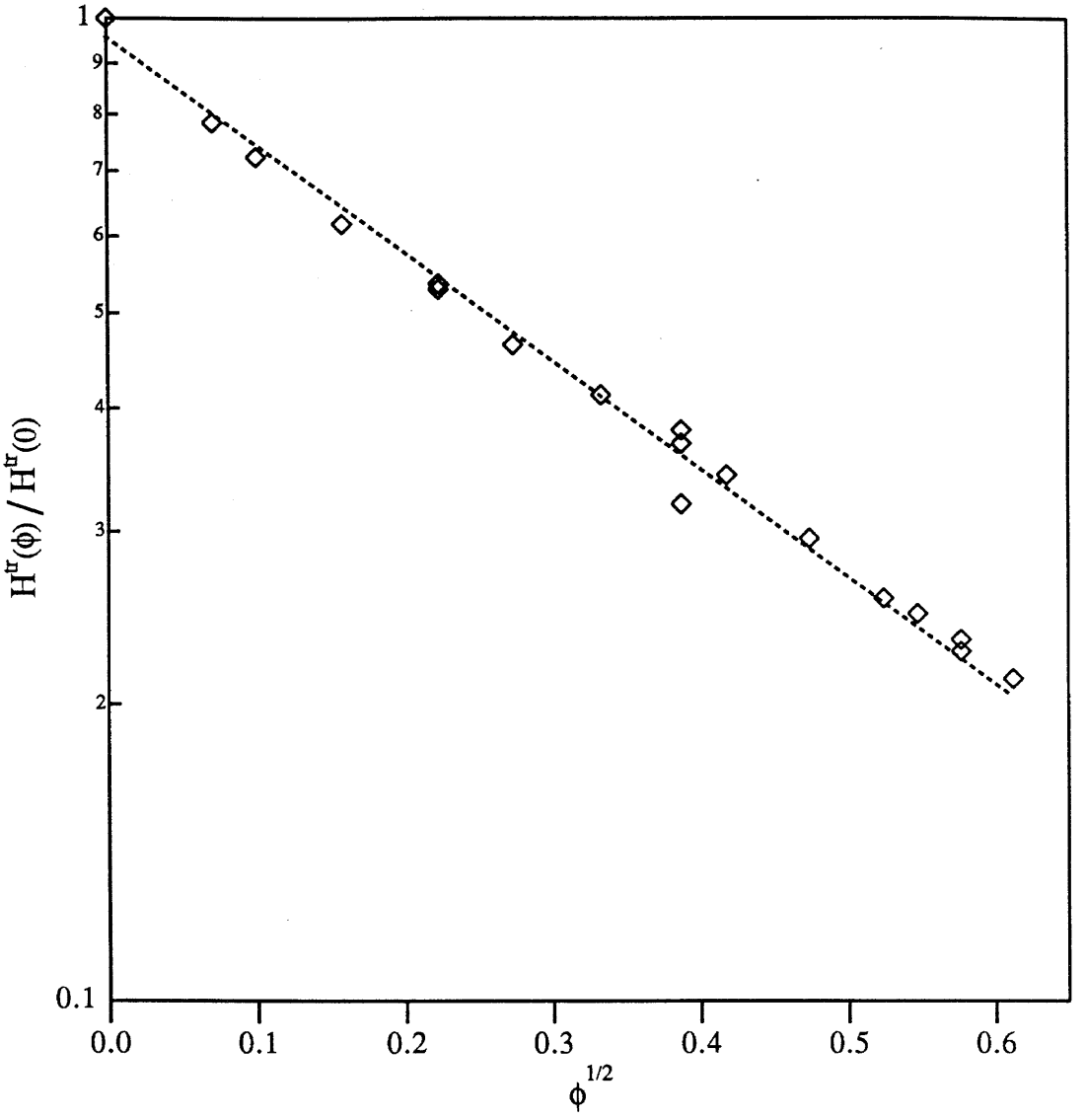


**Fig.4.14**: Semi-logarithmic plot of the hindered translational diffusivity in equilibrium dispersions of spheroids of aspect ratio 6 *vs*. the square root of concentration. The diffusion coefficient is normalized by its value at infinite dilution.

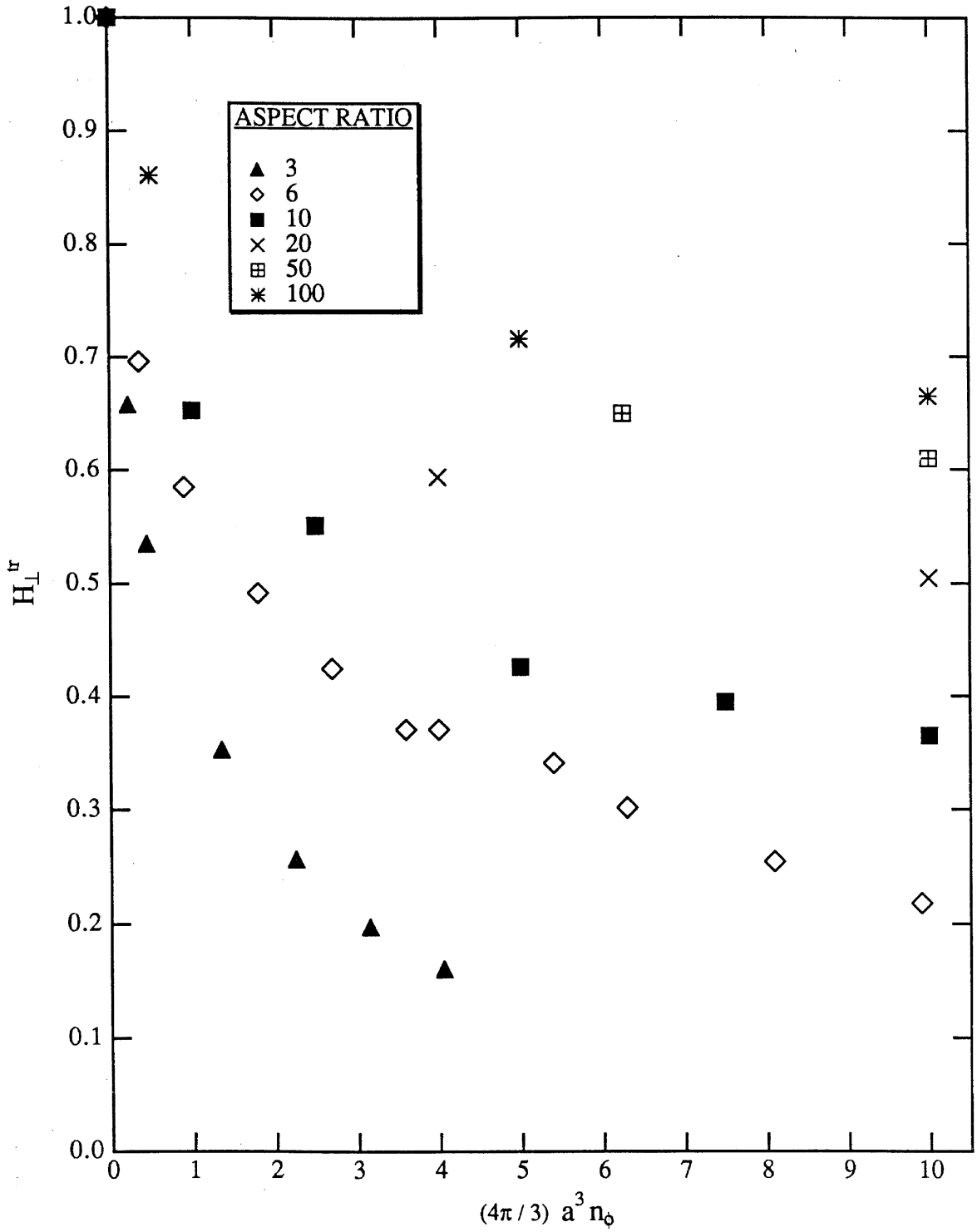


**Fig.4.15**: Hindered diffusion coefficient *vs*. number density of particles for equilibrium dispersions of spheroids of various aspect ratios.
The hindered diffusivity is normalized by its value at infinite dilution.
Each simulation typically used 60 particles per unit cell.

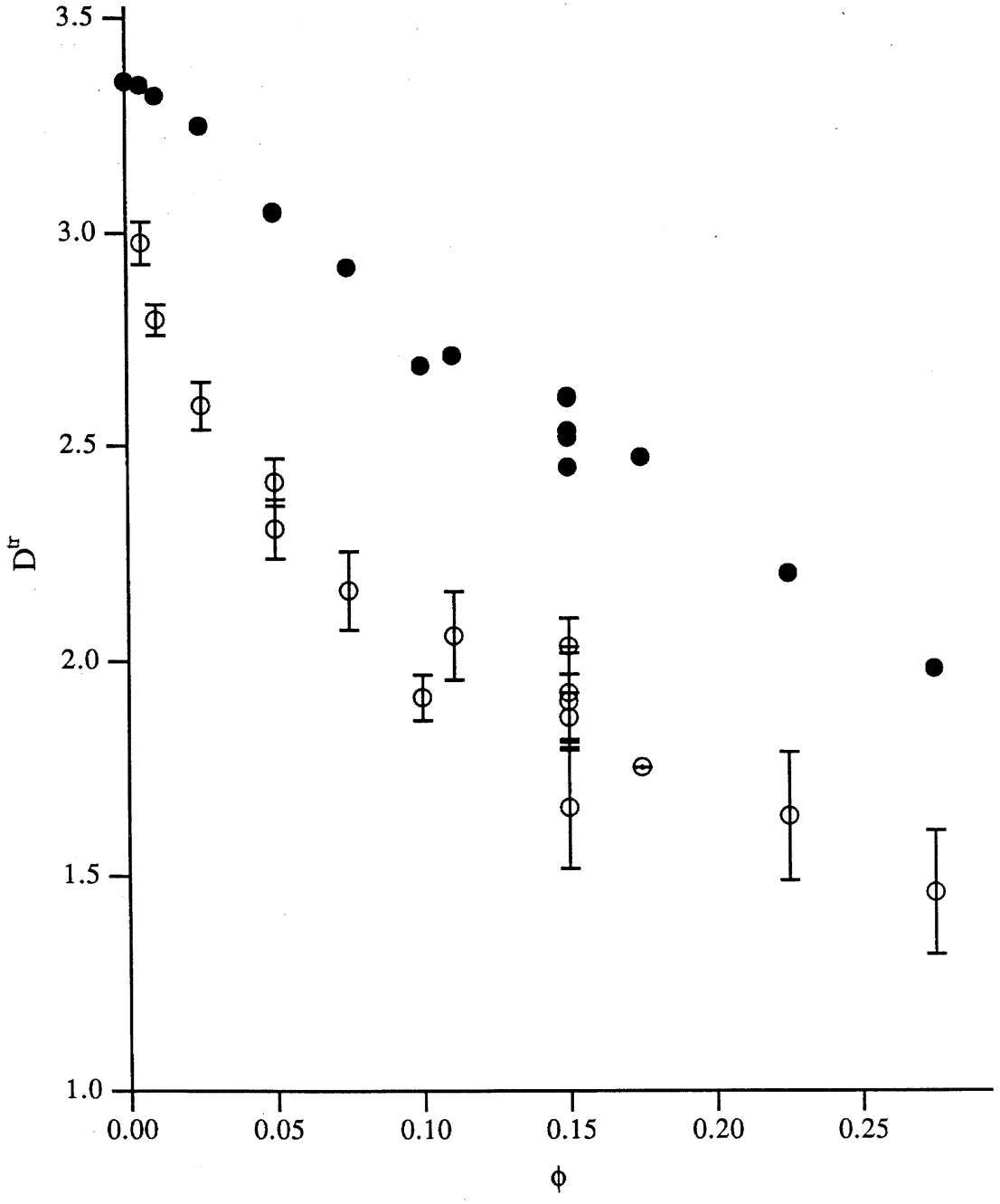


**Fig.4.16**: Corrected values of the translational self-mobility of spheroids of aspect ratio 6 in equilibrium dispersions.

The diffusion coefficient is normalized by $kT / 8\pi\mu a$. The open circles show the data from the simulations. The results, extrapolated to the thermodynamic limit by means of eq.(4.49), are given by the solid symbols.

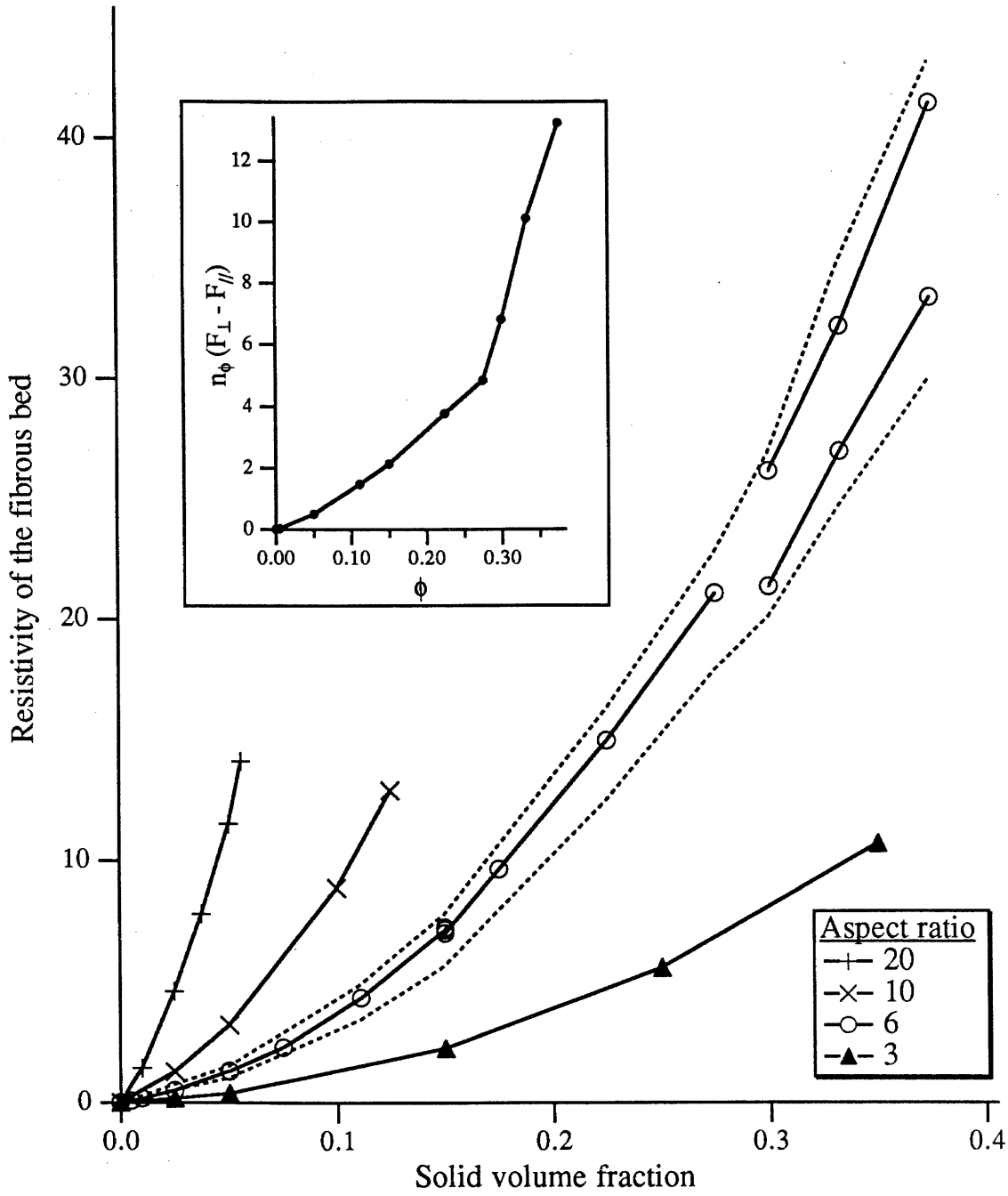


**Fig.4.17**: Resistivity of fibrous media.

The resistivity (normalized by $6\mu / a^2$) is plotted for equilibrium dispersions of spheroids. The insert, for aspect ratio 6, clearly shows that the difference between the average component of the force supported by the rods along their axis and perpendicular to it is emphasized past the isotropic to nematic phase transition (at 29%).

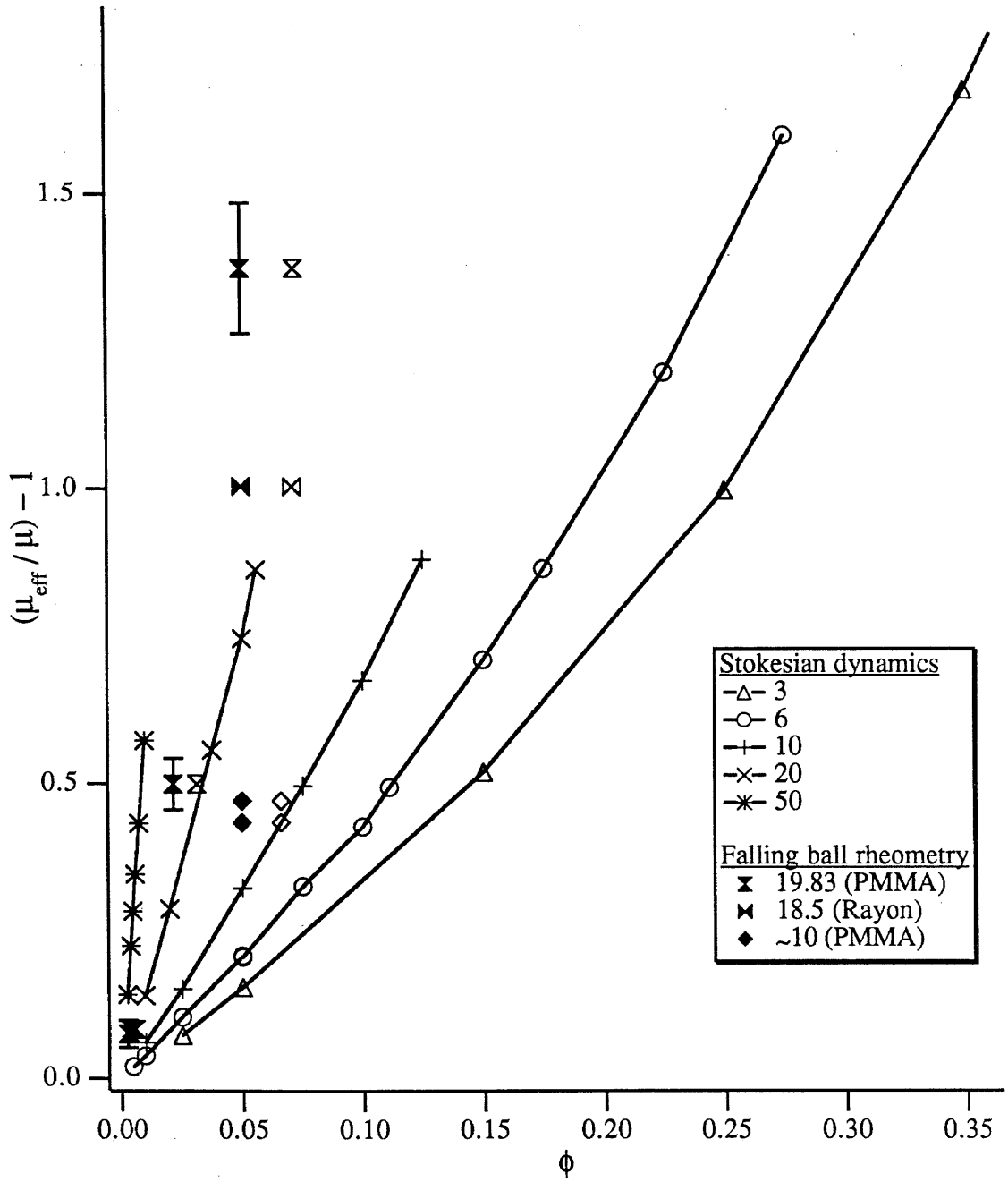


**Fig.4.18**: Viscosity of equilibrium dispersions of spheroids.
The experimental measurements reported are from Milliken *et al.* (1989) and Powell *et al.* (1989). The solid symbols are their raw data; the ones in outline have been adjusted to fit the "equivalent" spheroid.

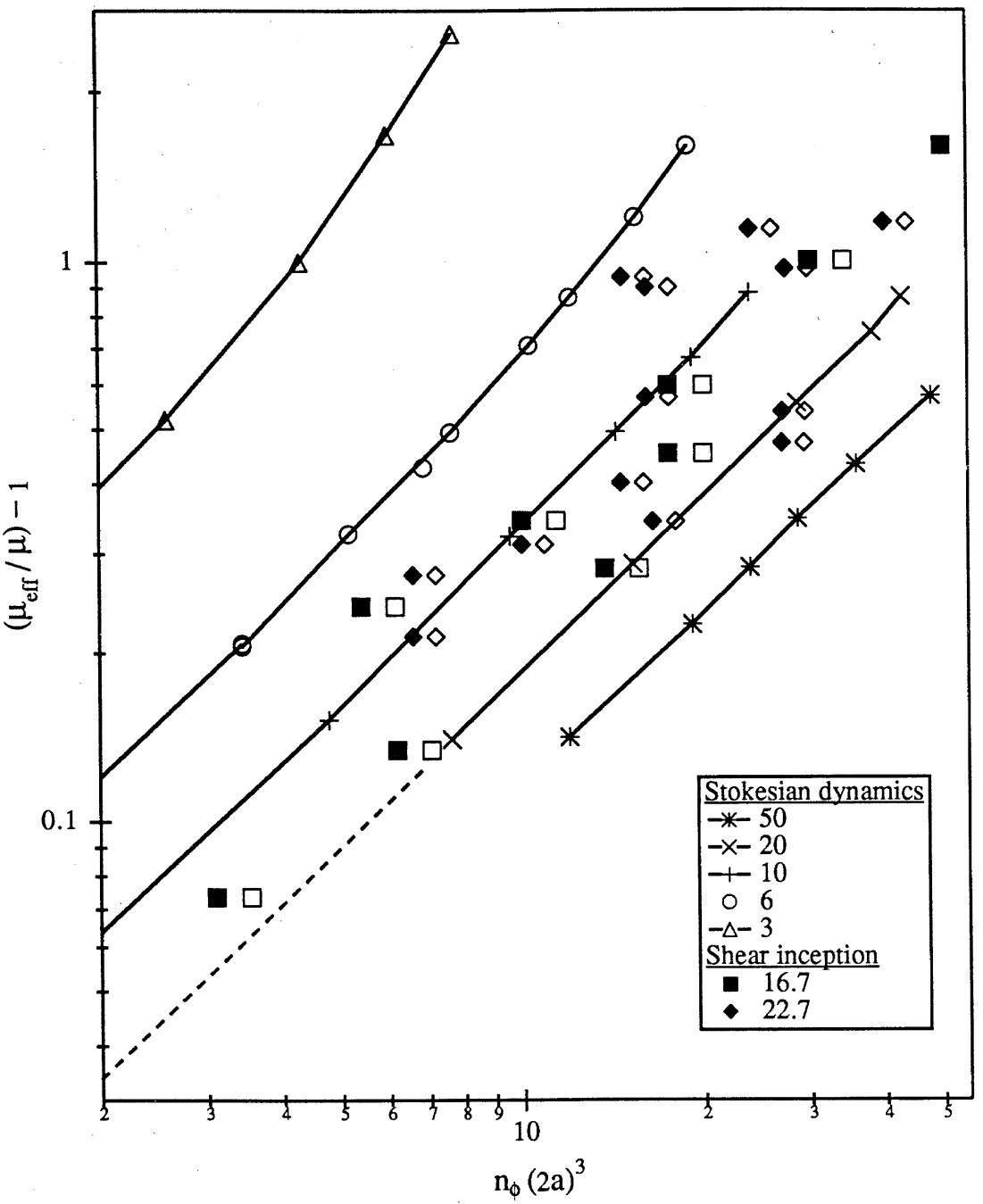


**Fig.4.19**: Double logarithmic plot of the viscosity of isotropic dispersions of spheroids *vs*. volume fraction for various aspect ratios.
Also included are the viscosity increments relative to pure solvent measured at the inception of shear by Bibbo *et al.* (1985). The filled symbols represent the data from their Fig.2. The open symbols account for the presumed cylindrical shape of the rods.

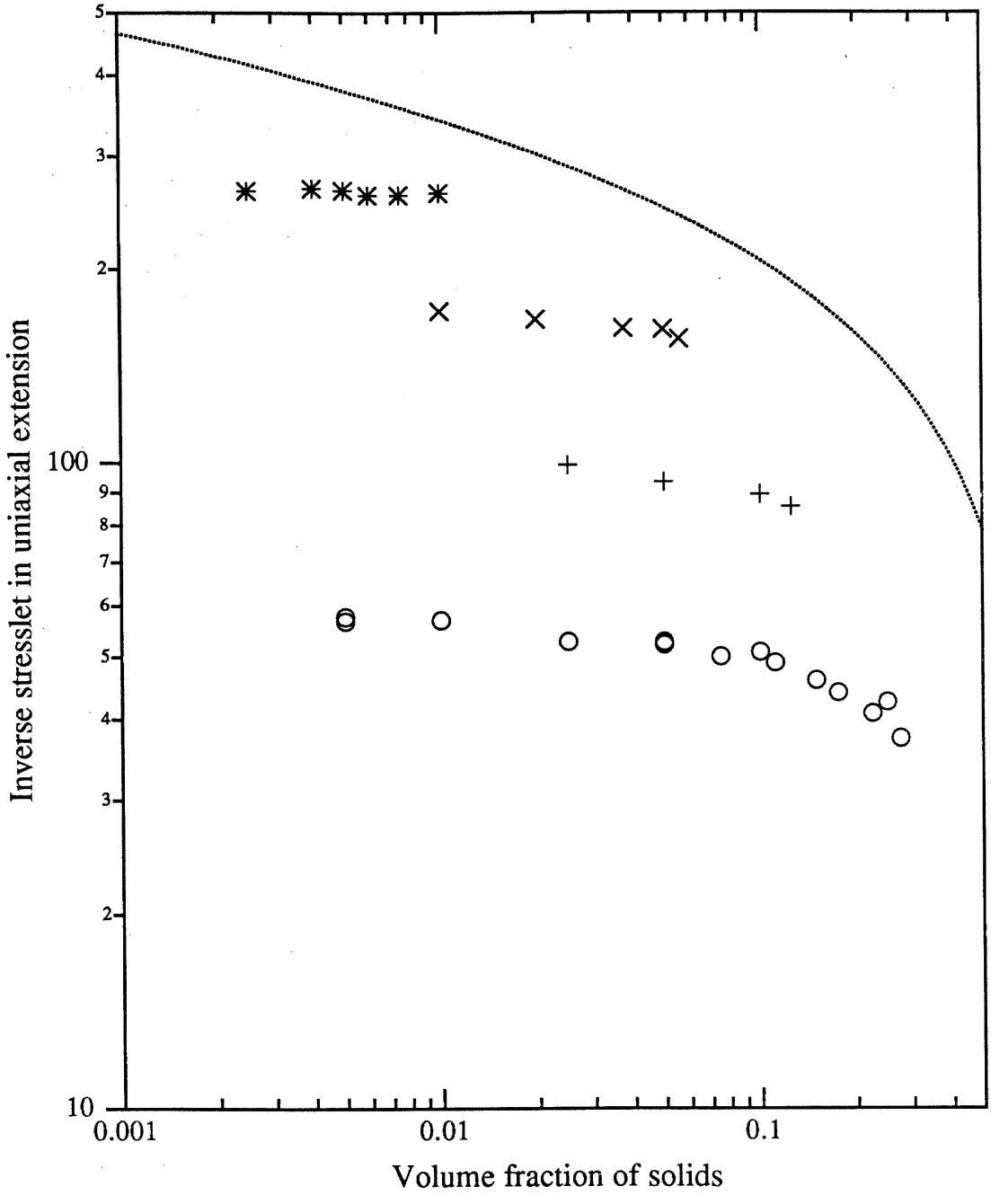


**Fig.4.20**: Transition from dilute to semidilute behavior in isotropic dispersions. The stresslet in the principal direction of strain (normalized by $8\pi\mu a^3 E$, with "E" the rate of uniaxial extension and "a" the particle half-length) gradually increases with volume fraction as the suspension deviates from the dilute limit. The symbols are as in the two previous figures. Also shown is the theoretical prediction due to Shaqfeh & Fredrickson (1990) (dotted line).

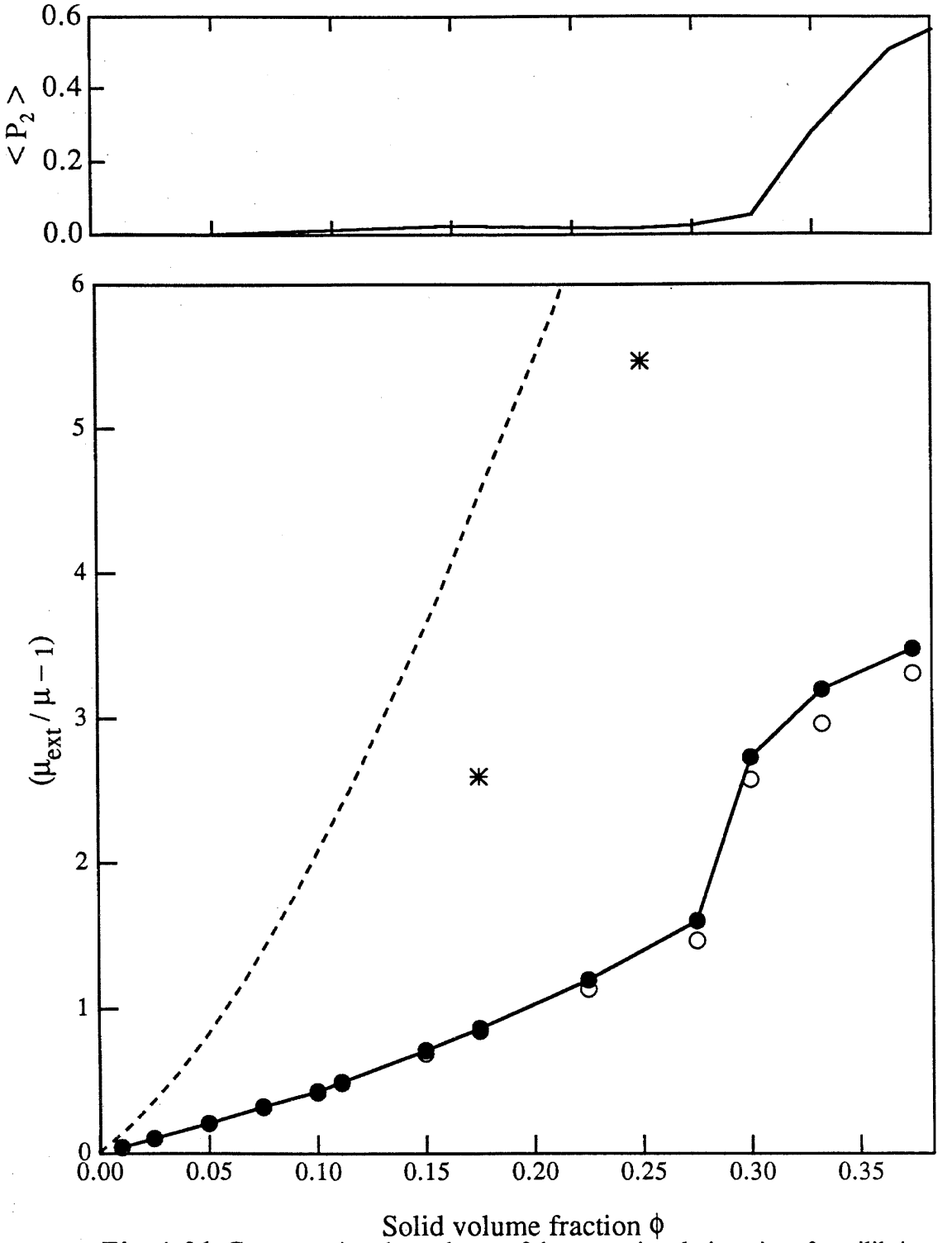


**Fig.4.21**: Concentration dependence of the extensional viscosity of equilibrium dispersions of spheroids of aspect ratio 6.
In the nematic region, the principal axis of strain lies along the director of the liquid crystal. The asterisks are results for random microstructures of parallel ellipsoids. The dotted line shows data for *efc*-lattices. Lubrication interactions have been suppressed for the open symbols.

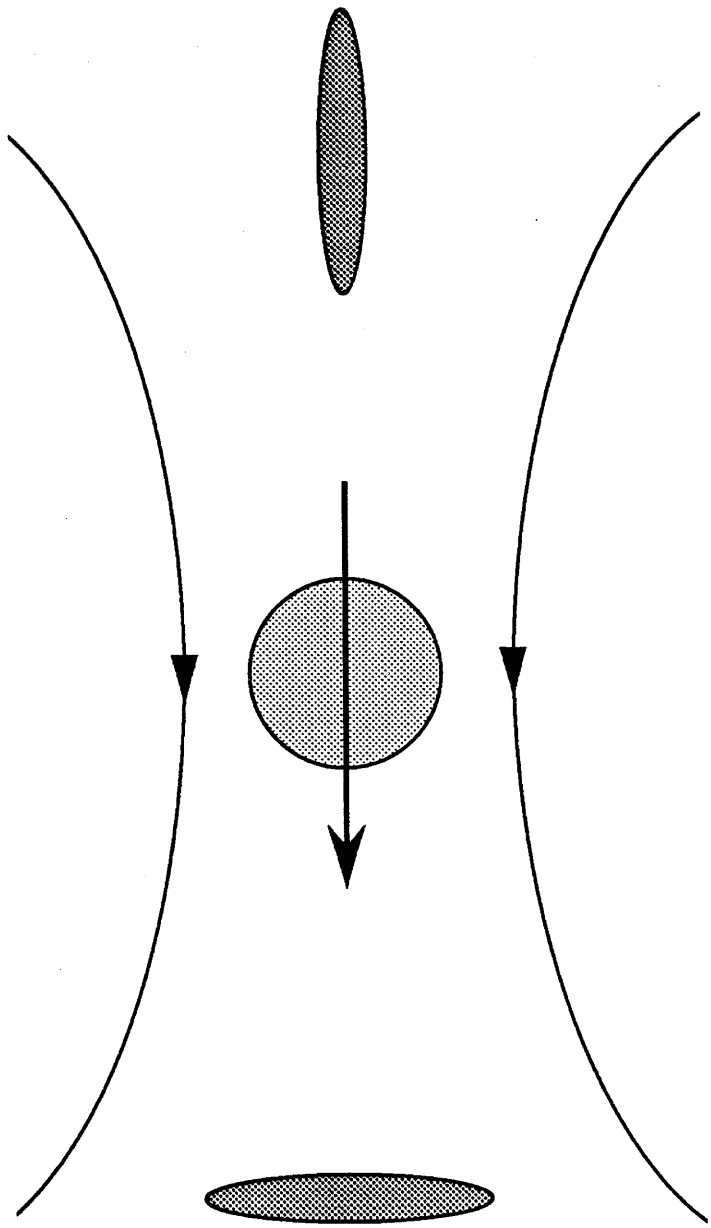

**Fig.4.22** : Influence of the velocity field caused by a sedimenting sphere on the microstructure of a dispersion of spheroids.
This schematic drawing illustrates the partial order induced in a suspension of rods by the extensional components of the disturbance velocity. The spheroids are drawn in their preferred orientation.

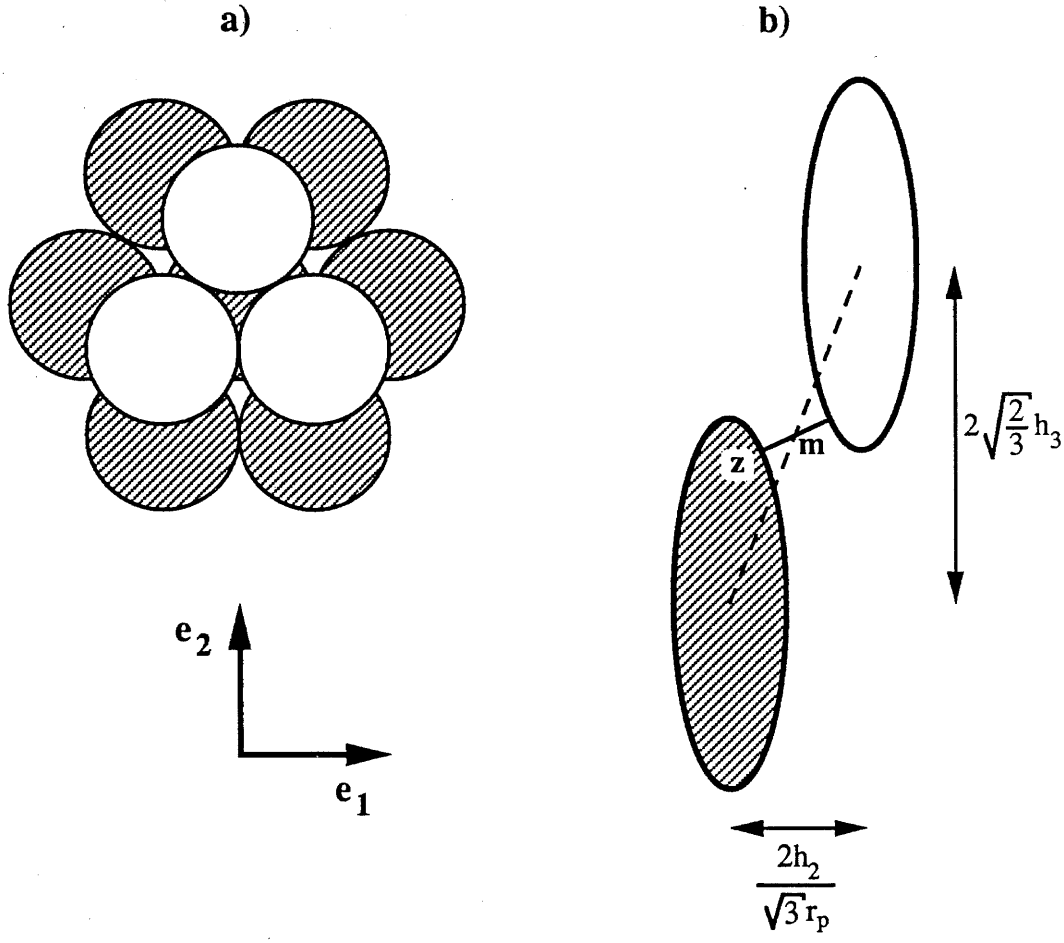


**Fig.4.23** : Definition of an *efc*-crystal of spheroids.
**a)** Projection onto the "1-2" plane. The spheroidal axis (in the "3" direction) points out of the paper. The white particles are stacked on top of the shaded ones. The layer below is staggered with respect to both of the sheets shown, in the customary "ABCABC" repeat structure of face-centered crystals.
**b)** Cross section of the dispersion in the "2-3" plane.

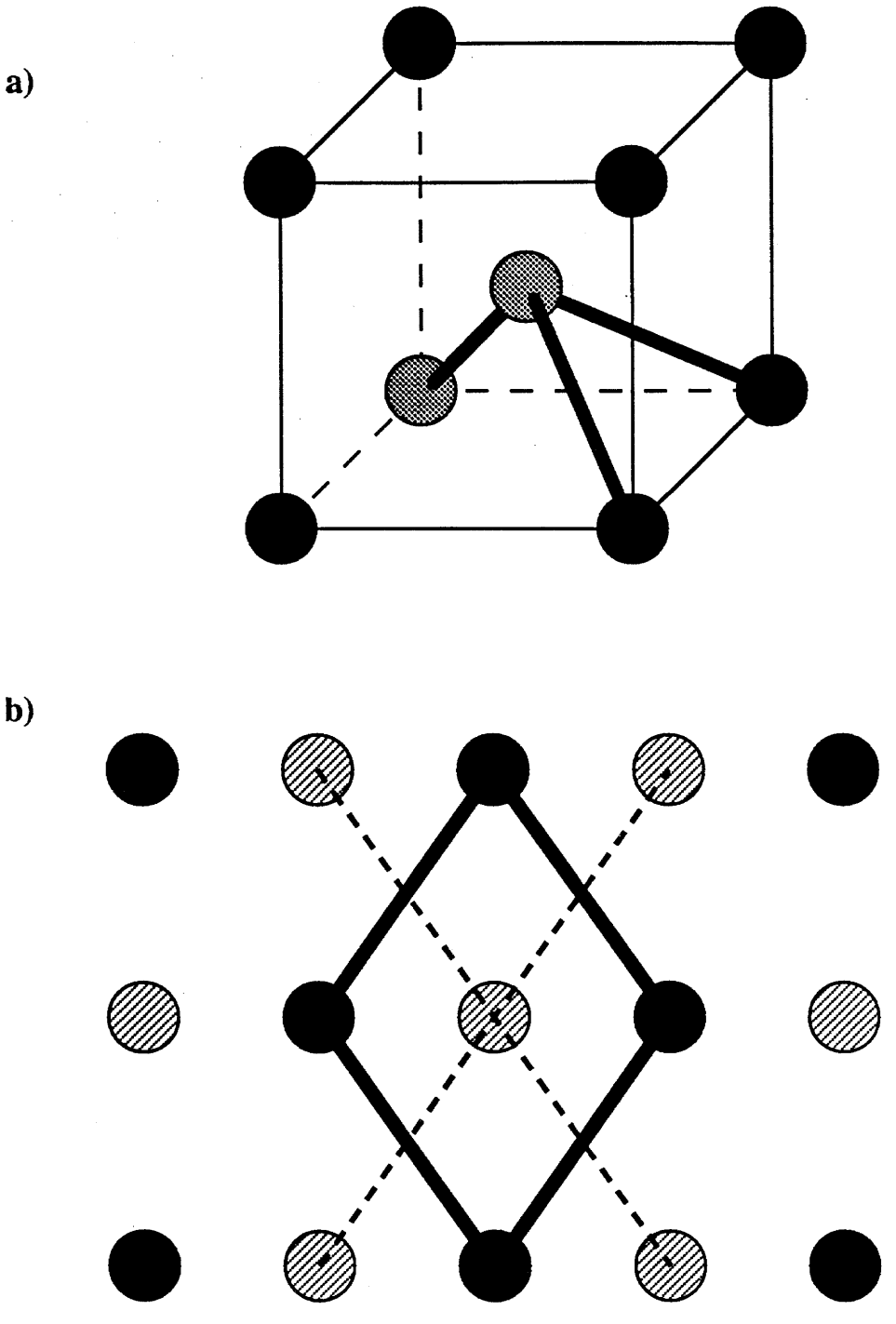


**Fig.4.24** : Expansion of a *bcc*-cell into a configuration satisfying the criteria proposed in appendix H.
**a)** Standard body centered cubic cell of spheres. Touching pairs are indicated by bold lines.
**b)** Close packed plane orthogonal to the direction of stretch.

# Chapter V
# Towards dynamic simulations: the unit cell

## 5.1 Introduction

In the previous chapters, we have focussed primarily on developing an accurate representation of hydrodynamic interactions between prolate spheroids in Stokes flow, and illustrated the effectiveness of the computational scheme by calculating the short-time limit of various transport properties in unbounded dispersions. Dynamic simulations, which track the evolution of the microstructure in time, are not more complicated conceptually, since they only involve one additional step, namely the temporal integration of the velocities $\boldsymbol{U}$ and rotation rates $\boldsymbol{\Omega}$ calculated via the grand resistance tensor $\boldsymbol{\mathcal{R}}$ for the instantaneous configuration of the particles from the imposed forces $\boldsymbol{F}$, torques $\boldsymbol{L}$ and the straining field $\boldsymbol{E}_\infty$:

$$\begin{pmatrix} \boldsymbol{F} \\ \boldsymbol{L} \\ \boldsymbol{S} \end{pmatrix} = \boldsymbol{\mathcal{R}} \otimes \begin{pmatrix} \boldsymbol{U} - \boldsymbol{U}_\infty \\ \boldsymbol{\Omega} - \boldsymbol{\Omega}_\infty \\ -\boldsymbol{E}_\infty \end{pmatrix} = \begin{pmatrix} \boldsymbol{R}_{FU} & \boldsymbol{R}_{LU} & \boldsymbol{R}_{SU} \\ \boldsymbol{R}_{F\Omega} & \boldsymbol{R}_{L\Omega} & \boldsymbol{R}_{S\Omega} \\ \boldsymbol{R}_{FE} & \boldsymbol{R}_{LE} & \boldsymbol{R}_{SE} \end{pmatrix} \otimes \begin{pmatrix} \boldsymbol{U} - \boldsymbol{U}_\infty \\ \boldsymbol{\Omega} - \boldsymbol{\Omega}_\infty \\ -\boldsymbol{E}_\infty \end{pmatrix} . \quad (5.1)$$

The tensors $\mathbf{U}_\infty$,‡ $\boldsymbol{\Omega}_\infty$ and $\boldsymbol{E}_\infty$ fully characterize the macroscopic rate of deformation by specifying the impressed uniform velocity, the bulk vorticity and the rate of strain respectively. Since it is inconsistent in unbounded, statistically homogeneous suspensions to consider any global motions other than plug flows or linear shear flows, higher derivatives of the ambient velocity field vanish. In periodic systems (such as the ones generated by periodic boundary conditions on a unit cell sufficiently large to imitate the randomness of a "real" dispersion), the lattice must, by symmetry, deform affinely with the flow. As discussed by Adler and Brenner for regular crystals of spheres (Adler & Brenner, 1985; Adler, 1984, 1985), purely

‡ The vector $\boldsymbol{U}_\infty$ in (5.1) groups the ambient fluid velocity at the locator points $\mathbf{x}_q$ of all the particles (see Ch. III and IV).

kinematic considerations therefore imply the existence of a maximum packing fraction compatible with each deformation; beyond this density, particles collide and eventually interpenetrate (or deform). In addition, only few lattices accept the limiting concentration, and many cannot accommodate *any* solid material under certain flow conditions. These considerations are important during the set-up of dynamic simulations, and we briefly touched upon this issue in §4.1. We return to it here, and derive unit cells compatible with various types of velocity fields in §5.3. First, however, we comment on a basis (or "box") standardization algorithm, and illustrate its advantages for search operations which recur frequently in the course of a simulation.

## 5.2 Box standardization algorithm

A microstructure is spatially periodic if, $\forall \mathbf{z} \in \mathcal{Z}^3$,

$$\mathbf{x} \in \partial V \iff \mathbf{x} + \boldsymbol{x}_{\{z\}} \in \partial V \ , \qquad \text{with} \quad \boldsymbol{x}_{\{z\}} = \mathbf{B} \cdot \mathbf{z} \ . \tag{5.2}$$

$\partial V$ denotes the union of all solid boundaries in the system (i.e., the ensemble of all particle surfaces in the dispersion); $\mathcal{Z}^3$ is the space of all ordered sets of three integers, and $\mathbf{B}$ contains the basis vectors of the unit cell (see Ch.IV, equation (4.3)). The collection of all points $\boldsymbol{x}_{\{z\}}$ constitutes a lattice $\mathcal{L}$; the vector $\mathbf{z}$ holds the three coordinates of $\boldsymbol{x}_{\{z\}}$ in the reference frame defined by the columns $\mathbf{b}_i$ of $\mathbf{B}$. Evidently, $\mathbf{B}$ is not unique, and many unit cells exist for a given microstructure. Each of them, however, can be derived from the basis vectors $\{\mathbf{b}_i\}$ by a set of integer linear combinations. We shall focus in particular on transformations of the type $\mathbf{b}'_i = \mathbf{b}_i \pm \mathbf{b}_j$, or

$$\mathbf{B}' = \mathbf{B} \cdot \mathbf{A} \ , \tag{5.3}$$

where the matrix $\mathbf{A}$ consists of 1's on the diagonal and one non-zero off-diagonal element equal to $\pm 1$ (the element $ji$ in the example above). A change of basis from $\mathbf{B}$ to $\mathbf{B}'$ preserves the volume of the simulation box since $|\mathbf{A}| = 1$, and hence the number $N$ of particles used to describe the system is unaltered. Furthermore,

every combination of basis vectors which conserves $N$ can be derived by successive applications of (5.3). Thus we do not restrict our analysis in any way by considering these transformations only.

Consider two arbitrary vectors $\mathbf{b}_i$ and $\mathbf{b}_j$, for which we assume $|\mathbf{b}_i| > |\mathbf{b}_j|$, and examine

$$|\mathbf{b}'_i| = |\mathbf{b}_i \pm \mathbf{b}_j| = (\mathbf{b}_i^2 \pm 2\mathbf{b}_i \cdot \mathbf{b}_j + \mathbf{b}_j^2)^{1/2} = (|\mathbf{b}_i|^2 \pm 2|\mathbf{b}_i||\mathbf{b}_j| \cos\theta + |\mathbf{b}_j|^2)^{1/2} \ . \quad (5.4)$$

It is apparent that $\mathbf{b}'_i$ can be made smaller than $\mathbf{b}_i$ if $|\cos\theta| > \frac{1}{2}|\mathbf{b}_j|/|\mathbf{b}_i|$, i.e., if the angle $\theta$ inscribed between the two vectors deviates sufficiently from $\frac{\pi}{2}$. We define as "standard" or "minimal" any basis cell for which this is impossible; i.e., for every pair of indices $(i, j)$, with $i \neq j$, the basis vectors $\mathbf{b}_i^s$ and $\mathbf{b}_j^s$ must satisfy

$$|\mathbf{b}_i^s \cdot \mathbf{b}_j^s| \leq \tfrac{1}{2}|\mathbf{b}_j^s|^2 \qquad \text{or} \quad |\cos\theta_{ij}| \leq \tfrac{1}{2}\min\Big(\frac{|\mathbf{b}_j|}{|\mathbf{b}_i|}, \frac{|\mathbf{b}_i|}{|\mathbf{b}_j|}\Big) \ . \quad (5.5)$$

This definition guarantees that the basis vectors are as short as possible, and that the angles inscribed between any two of them lie between $\frac{\pi}{3}$ and $\frac{2\pi}{3}$. In other words, the simulation box is as compact and as "straight" as possible. Moreover, the more anisometric it is, the less skewed. For a given lattice, the standard unit cell is unique,‡ except in the degenerate case that two (or all three) of its basis vectors are of equal length and make an angle of 60° or 120° with each other. We have assumed in the coded version of Stokesian dynamics for prolate spheroids (Claeys, 1991) that the working cell always satisfies (5.5). (If it deforms with the flow, it needs to be "reset" consistently during the simulation.) This does not impose any restriction on the type of microstructure which can be examined, but offers the advantage that the anisotropy of the unit cell is always minimal. As explained in the next paragraph, the standardization of the simulation box facilitates "geometric" operations such as the search for nearest neighbors. In addition, its "nearly cubic" shape (within the

‡ This can most easily be proven by the geometric argument that there always exist three non-planar points in a lattice which are closest to the origin.

constraints of the imposed periodicity) minimizes any numerical artifacts brought about by the boundary conditions, even if distorted cells are perfectly equivalent in theory.

During a typical simulation, one frequently needs to find all pairs of particles whose centre-to-centre separation is smaller than a specified distance $R$. This might be to detect overlap, to extract structural information about the dispersion (such as pair correlation functions), or to calculate hydrodynamic interactions (recall from Ch. IV, App. G, that the construction of the grand mobility tensor involves lattice summations which only take into account spheroids within an optimally calculated cutoff distance from one another). This may seem an easy problem, yet the solution is quite complicated if the lattice geometry is specified in terms of non-orthogonal basis vectors of unequal length. Suppose for instance that one wishes to determine whether lubrication interactions occur between a particle $p$ and images of another body $q$. In a first step, one considers $p$ embedded in a lattice of spheroids $q$ and searches for all images of $q$ with centre $\mathbf{x}_{q+\{z\}}$ within $R = a_p + a_q + \epsilon$ of $\mathbf{x}_p$. (The distance $\epsilon$ is the maximum gap width for which lubrication interactions need to be taken into account, and $a_p$, $a_q$ represent the length of the major semi-axes of the ellipsoids.) Denoting by $\mathbf{r}_{pq}$ the vector connecting $\mathbf{x}_p$ to the centre of a "reference" particle $q$, we must minimize $(\mathbf{r}_{pq} + \sum_{i=1}^{3} z_i \mathbf{b}_i)^2 = (\mathbf{r}_{pq} + \mathbf{B} \cdot \mathbf{z})^2$ with respect to the integers $\{z_i\}$ to find the image of $q$ closest to $p$. Suppressing for a moment the restriction to $\mathcal{Z}^3$, the solution is readily found as $\mathbf{z}^r = -\mathbf{B}^{-1} \cdot \mathbf{r}_{pq}$. The coordinates $\{z_i^r\}$, however, are not all integers, since the centre $\mathbf{x}_p$ of $p$ would otherwise coincide with an image of $q$. At first glance, it may seem that picking

$$z_i = \lfloor z_i^r + \tfrac{1}{2} \rfloor = z_i^c \ . \tag{5.6}$$

(i.e., rounding off to the nearest integer) gives the correct answer, since it is the element of $\mathcal{Z}^3$ nearest to the solution $\mathbf{z}^r$. (The notation $\lfloor x \rfloor$ means the largest integer smaller than or equal to $x$.) However, as illustrated for two dimensions in Fig. 5.1, $\mathbf{x}_{q+\{z^c\}}$ may not be the lattice point closest to $\mathbf{x}_p$ if the basis vectors are not

orthogonal. In other words, the metric in $\mathcal{Z}^3$ does not define a distance in real space, and the simple search algorithm offered by (5.6) can lead to incorrect conclusions. This is inconsequential, however, if all locations $\mathbf{x}_p$ which give erroneous answers (the shaded region of Fig. 5.1) lie farther than $R$ from the most proximate point on the lattice. In order to derive a criterion to decide when the "misallocation" of nearest neighbors by use of (5.6) is insignificant, we consider the geometric puzzle of Fig. 5.1. For all intents and purposes, the search in $\mathcal{Z}^2$ is adequate if the radius $R_c$ of the tangent circle is larger than the maximal distance of interest $R$. Also, $R_c$ is smallest (relative to $|\mathbf{b}_i|$) for the most slanted unit cells. The box standardization algorithm described earlier guarantees that the angle between any two basis vectors is always at least $\frac{\pi}{3}$. The worst scenario is thus depicted in Fig. 5.1. Elementary trigonometry shows in two dimensions that the search (5.6) detects all sought pairs if $R < \sqrt{3}/4\, b_{\min}$, with $b_{\min}$ the length of the shortest basis vector in the standard cell. In three dimensions, a similar calculation involving a sphere tangent to a plane demonstrates that the search in $\mathcal{Z}^3$ is satisfactory if $R < b_{\min}/\sqrt{6}$. We must thus consider three cases depending on the relative size of the unit cell and the distance of interest:

a) $[R < b_{\min}/\sqrt{6}]$ the nearest neighbor can be taken to be located at $\mathbf{x}_{q+\{z^c\}}$ without adverse effects;

b) $[b_{\min}/\sqrt{6} < R < b_{\min}/2]$ the simple scheme given by (5.6) may be inappropriate, but there certainly is not more than one pair of particles within $R$ of each other;

c) $[b_{\min}/2 < R]$; if the pertinent separation $R$ is very large, many images of $q$ may interact simultaneously with $p$, and it is advisable to step along the lattice in all directions (from $\mathbf{x}_{q+\{z^c\}}$) in order to find the relevant pairs of particles.

In case (b), the easiest procedure consists in checking the distance from $\mathbf{x}_p$ to each of the four lattice points corresponding to the quadrant of $\mathcal{Z}^3$ in which $\mathbf{z}^r$ lies (i.e., $\mathbf{x}_{q+\{z^c\}}$ and the three points adjacent to it and closest to $\mathbf{x}_p$), and to stop the search as soon as one of them is smaller than $R$. The appropriate direction in

which to step can be deduced from the sense in which $z_i^r$ has been rounded off to $z_i^c$. Stricter bounds than the ones given above may be derived by taking into account other characteristics of the unit cell. The concomitant increase in complexity makes them less suited for computer programming, however. Simplicity is the key.

It will be clear that the standardization of the box size and shape significantly reduces the geometric complications associated with the type of searches described above. Since these occur repeatedly in normal simulations, it is imperative to always use the minimal unit cell.

## 5.3 Compatibility of unit cells with imposed deformations

We now return to the problem mentioned in the introduction of this chapter, the compatibility of the unit cell with an imposed macroscopic velocity field. This question was first addressed in a slightly different context by Adler & Brenner (1985) for two-dimensional deformations, and by Adler (1984) for three dimensional flows. Relying on concepts borrowed from the geometry of numbers (Gruber & Lekkerkerker, 1987), they calculated the maximum volume fraction of spheres that is kinematically allowed for all types of steady linear isochoric motions. In general, the imposition of a macroscopic deformation decreases the admissible density below the tight packing possible in the absence of flow because the spheres sweap a region of space larger than their own volume and therefore come into contact at lower concentrations. While the lower bound on $\phi_{\max}$ calculated by Adler & Brenner (1985) for flows with open streamlines is correct, they wrongly concluded that self-reproducing lattices do not exist in such cases.‡ (Self-reproducing or strain-periodic lattices are defined (see below) as lattices which are mapped onto themselves in a finite time

‡ Their wording is somewhat ambiguous as they distinguish the strain-periodicity of the lattice from that of its basis; in other words, they consider different representations of the same structure as separate. This distinction unnecessarily obscures the geometric interpretation of their conclusions, since the particles are not labeled and therefore interchangeable.

by the deformation.) Indeed, Kraynik & Hansen (1986) later found strain-periodic networks in two-dimensional extensional flows, contradicting Adler & Brenner's statement (1985). Their analysis, which was restricted to hexagonal grids parallel to the plane of shear, is generalized below. We then demonstrate rigorously that there are no self-reproducing lattices in uniaxial stretching flows, and discuss their existence in more general pure straining fields (three-dimensional but not axisymmetric). We also derive the basis vectors of a lattice accepting the maximum packing fraction compatible with biaxial extension, as calculated by Adler (1985). This opens new avenues for dynamic simulations of axisymmetric extensional flows in unbounded suspensions by providing a suitable unit cell. We shall draw on some notions of the mathematical field of the geometry of numbers in the latter portions of this chapter (related to the solution of Diophantine equations), and refer to the paper by Adler & Brenner (1985) and the treatise by Cassels (1959) for an elementary introduction to the concepts needed. A more thorough discussion, and a state-of-the-art survey of the existing knowledge in this matter, can be found in the excellent book by Gruber & Lekkerkerker (1987).

**5.3.1 Strain-periodicity in linear incompressible flows: problem definition**

Consider a linear incompressible flow characterized by a constant tensor $\mathbf{G}$ specifying the velocity field $\mathbf{u}$ as

$$\mathbf{u}(\mathbf{x}) = \mathbf{G} \cdot \mathbf{x} \ . \tag{5.7}$$

(Uniform flows $\mathbf{U}_\infty$ do not need to be studied since they only induce a translation "in the bulk" of the dispersion, and are therefore compatible with all particle configurations.) The matrix $\mathbf{G}$ is traceless as a consequence of incompressibility. Also consider a lattice $\mathcal{L}$ constructed from a set of linearly independent basis vectors $\{\mathbf{b}_i\}$ such that each point $\boldsymbol{x}_{\{z\}}$ belonging to $\mathcal{L}$ can be written uniquely as

$$\boldsymbol{x}_{\{z\}} = \sum_{i=1}^{D} z_i \mathbf{b}_i = \mathbf{B} \cdot \mathbf{z} \ , \tag{5.8}$$

with $D$ the dimensionality of the network, $\mathbf{z}$ the column vector of integer coordi-

nates $\{z_i\}$, and $\mathbf{B} = (\{\mathbf{b}_i\})$ the matrix of basis vectors (see Ch. IV, equation (4.3)). By symmetry, $\mathcal{L}$ deforms affinely with the flow, i.e., $\forall\{z_i\}$,

$$\dot{\boldsymbol{x}}_{\{z\}} = \mathbf{G} \cdot \boldsymbol{x}_{\{z\}} \tag{5.9a}$$

or, integrating,

$$\boldsymbol{x}_{\{z\}}(t) = \exp(\mathbf{G}t) \cdot \boldsymbol{x}_{\{z\}}(0) = \exp(\mathbf{G}t) \cdot \mathbf{B} \cdot \mathbf{z} \ . \tag{5.9b}$$

The lattice $\mathcal{L}$ is called strain-periodic or self-reproducing for the flow $\mathbf{u}$ if $\mathcal{L}(t) = \mathcal{L}(0)$ at some finite time $t$. Each point $\boldsymbol{x}_{\{z\}}(t)$ of the deformed network must therefore be mapped onto an integer linear combination of the basis vectors $\{\mathbf{b}_i(0)\}$ of the original lattice. This is clearly satisfied if and only if there exists a finite time $t > 0$ and an integer matrix $\mathbf{M} \in \mathcal{Z}^D \times \mathcal{Z}^D$ such that

$$\exp(\mathbf{G}t) \cdot \mathbf{B} = \mathbf{B} \cdot \mathbf{M} \ . \tag{5.10}$$

Our goal is therefore to find a set of basis vectors $\mathbf{B}$ such that (5.10) can be satisfied for a specified velocity gradient $\mathbf{G}$.

We focus mainly on flows for which $\nabla\mathbf{u} = \mathbf{G}$ has real eigenvalues, so that

$$\mathbf{G} = \mathbf{P} \cdot \mathbf{\Lambda} \cdot \mathbf{P}^{-1} \ . \tag{5.11}$$

The columns of $\mathbf{P}$ are the eigenvectors of $\mathbf{G}$ (the principal directions of the strain) and $\mathbf{\Lambda}$ is the corresponding diagonal matrix of eigenvalues. All forms of planar and uniaxial extension belong to this class of flows. Obviously,

$$\exp(\mathbf{G}t) = \mathbf{P} \cdot \exp(\mathbf{\Lambda}t) \cdot \mathbf{P}^{-1} \ . \tag{5.12a}$$

Since $\mathbf{G}$ is traceless, and since the trace is invariant for equivalent matrices, the sum of the diagonal elements of $\mathbf{\Lambda}$ must be zero. Hence

$$\exp(\mathbf{\Lambda}t) = \begin{pmatrix} e^{\lambda_1 t} & 0 & 0 \\ 0 & e^{\lambda_2 t} & 0 \\ 0 & 0 & e^{-(\lambda_1+\lambda_2)t} \end{pmatrix} = \begin{pmatrix} S & 0 & 0 \\ 0 & S^{\nu} & 0 \\ 0 & 0 & S^{-(1+\nu)} \end{pmatrix} \ , \tag{5.12b}$$

with $\nu = \lambda_2/\lambda_1$ the ratio of eigenvalues. Without loss of generality, we shall assume that $\lambda_1 > 0$, so that $S = \exp(\lambda_1 t) > 1$. Obviously, any lattice which is self-reproducing for $\mathbf{\Lambda}$ (i.e., for the velocity field $\mathbf{\Lambda}\cdot\mathbf{x}$) is also strain-periodic for $-\mathbf{\Lambda}$, since time-reversal does not affect this property. Also, we may confine $\nu$ to the range [0,1] by labeling $\lambda_1$ and $\lambda_2$ appropriately. The limits $\nu = 0$ and $\nu = 1$ represent planar and uniaxial extension respectively.

Evidently, if $\mathbf{B}$ is strain-periodic for $\mathbf{u} = \mathbf{\Lambda}\cdot\mathbf{x}$ then $\mathbf{P}\cdot\mathbf{B}$ is self-reproducing for $\mathbf{G}$. Thus we may restrict ourselves to the study of flows for which $\nabla\mathbf{u}$ is diagonal. In summary, the problem consists in finding $\mathbf{B}$, $S$ and $\mathbf{M}$ for a given $\nu$ such that

$$\begin{pmatrix} S & 0 & 0 \\ 0 & S^{\nu} & 0 \\ 0 & 0 & S^{-(1+\nu)} \end{pmatrix} \cdot \mathbf{B} = \mathbf{B} \cdot \mathbf{M} \tag{5.13}$$

Note that $\mathbf{M} = \mathbf{B}^{-1} \cdot \exp(\mathbf{\Lambda} t)\cdot\mathbf{B}$. One must thus identify an integer matrix $\mathbf{M}$ whose left-eigenvalues $\mu_i$ are exponentials of the right-eigenvalues $\lambda_i$ of the velocity gradient tensor $\mathbf{G}$, i.e., $\mu_i = \tau^{\lambda_i}$ with $\tau = e^t$. The basis vectors $\mathbf{b}_i$ of the self-reproducing lattice are then given by the columns of the matrix $\mathbf{B}$, whose rows are the left-eigenvectors of $\mathbf{M}$.

Before proceeding with the solution of (5.13), we briefly indicate the correspondence between strain-periodicity and compatibility with the flow. (For a more elaborate discussion of this issue, see Adler (1985).) This is most easily explained in terms of the crystalline configurations considered by Adler & Brenner (1985), who imagined an orderly dispersion constructed by placing a sphere at each point of a three-dimensional lattice. Such a suspension is said to be kinematically incompatible with a specified deformation if the imposed motion causes particles to overlap in a finite time. If this happens regardless of the spheres' dimension (i.e., independently of the concentration), the lattice is incompatible with the prescribed velocity field. Clearly, if a streamline carries a node of the network arbitrarily close to the origin, incompatibility ensues; conversely, if all lattice points remain at a finite distance from the origin at all times, a dispersion with non-zero density can

be constructed which deforms affinely with the flow. [Note from (5.9a) that the origin is stationary. However, in view of the spatial periodicity of the lattice and the linearity of the flow, all nodes are equivalent —apart from a translation and a superimposed uniform flow— and there is no loss of generality in considering the origin in this argument.] Because the velocity decays linearly as the saddle point at the origin is approached, it is impossible for a point to reach the origin in a finite amount of time. Consequently, the nodes of a self-reproducing lattice remain at a finite separation from the origin during each period, and hence forever. Strain-periodicity thus implies compatibility with the flow, even though the reverse is not necessarily true.

### 5.3.2 Planar extensional flows ($\nu = 0$)

In order to simplify the analysis, we can reduce the dimensionality of the problem to $D = 2$ in this case:†

$$\boldsymbol{\mathcal{S}} \cdot \mathbf{B} = \begin{pmatrix} S & 0 \\ 0 & 1/S \end{pmatrix} \cdot \mathbf{B} = \mathbf{B} \cdot \mathbf{M} \ . \tag{5.14}$$

Since $\boldsymbol{\mathcal{S}}$ and $\mathbf{M}$ are equivalent matrices, they must have the same invariants. We thus immediately deduce that

$$\mathrm{tr}(\mathbf{M}) = M_{11} + M_{22} = S + S^{-1} = \mathrm{tr}(\boldsymbol{\mathcal{S}}) \ , \tag{5.15a}$$

† Even though the flow is two-dimensional, the restriction to $D = 2$ is substantial, as self-reproducing lattices may exist which do not possess a pair of basis vectors in the plane of shear. It is thus conceivable that our approach cannot detect the lattice accepting the maximum density compatible with planar extension. Also, even though the lower bound on $\phi_{\max}$ calculated by Adler & Brenner (1985) for these hyperbolic flows was derived assuming $D = 2$, there is no guarantee that the corresponding "critical" lattice is strain-periodic. Again, we may therefore not be able to retrieve it. The two-dimensional analysis, however, provides quite a few solutions to (5.13) (infinitely many, as a matter of fact), and is tractable without recourse to detailed knowledge of Diophantine equations.

$$\det(\mathbf{M}) = M_{11}M_{22} - M_{12}M_{21} = 1 = \det(\boldsymbol{\mathcal{S}}) \ . \tag{5.15b}$$

It follows from (5.15a) that the trace of $\mathbf{M}$ is at least 2, since it has to be an integer larger than 1. Furthermore, $\mathrm{tr}(\mathbf{M}) = 2$ is only possible for the trivial case $S = 1$ (no motion). We thus conclude that $\mathrm{tr}(\mathbf{M}) \geq 3$. Of course, if $\mathbf{M}$ is known, equation (5.15a) is a simple quadratic equation in $S$ which can be solved straightforwardly.

We now proceed to determine the lattice geometry. Let

$$\mathbf{B} = \begin{pmatrix} A\cos\theta_1 & \cos\theta_2 \\ A\sin\theta_1 & \sin\theta_2 \end{pmatrix} \ . \tag{5.16}$$

Solving the eigenvalue problem then yields (making use of (5.15 a)):

$$\frac{\cos\theta_1}{\cos\theta_2} = \frac{S - M_{22}}{AM_{12}} \ , \tag{5.17a}$$

$$\frac{\sin\theta_1}{\sin\theta_2} = \frac{M_{11} - S}{AM_{12}} \ . \tag{5.17b}$$

Again these equations are easy to solve for $\theta_1, \theta_2$ and $A$. Since any $\mathbf{M}$ satisfying (5.15) yields a solution, there exist infinitely many self-reproducing networks in planar stretching flows.

As an example, we calculate a square strain-periodic lattice for planar extensional flows. For a square, $\theta_1 = \theta_2 + \pi/2$ and $A = 1$. Thus

$$\tan\theta_1 = \frac{M_{12}}{M_{22} - S} = \frac{M_{11} - S}{M_{12}} \ . \tag{5.18}$$

Using (5.15a) to simplify (5.18), we get $M_{11}M_{22} - 1 = M_{12}^2$, which, from (5.15b) requires $M_{12} = M_{21}$. The simplest choice for $M_{12}$ is $M_{12} = 1$, which yields $M_{11} = M_{12} = M_{21} = 1$, $M_{22} = 2$, $S = 2.618...$ and $\theta_1 = -58°16'57''$. The choice $M_{12} = 0$ would, from (5.15b), only give the trivial solutions $\mathbf{M} = \pm\boldsymbol{\delta}$ and $S = 1$.

This treatment generalizes the results obtained by Kraynik & Hansen (1986), who limited their search to those solutions with $\theta_2 - \theta_1 = \frac{\pi}{3}$ because of the application they had in mind. As an aside, we also note that the set of basis vectors

$$\mathbf{B} = \begin{pmatrix} 1 & \frac{1}{2} - \frac{\sqrt{5}}{2} \\ 1 & \frac{1}{2} + \frac{\sqrt{5}}{2} \end{pmatrix} \ , \tag{5.19}$$

which generate a "critical" lattice accepting the maximum density compatible with planar extensional flows in two dimensions (Gruber & Lekkerkerker, 1987), can be found in Adler & Brenner (1985). They apparently overlooked the fact that this represents a self-reproducing lattice.

### 5.3.3 Non-existence of strain-periodic lattices in uniaxial extension ($\nu = 1$)

We have just shown by example that infinitely many lattices can be found which are compatible with planar extension. We now prove that none exist for axisymmetric straining flows.‡ Two eigenvalues are equal in this case. However, since $\{\mathbf{b}_i\}$ forms a basis in three dimensional space, two linearly independent eigenvectors must be associated with the double eigenvalue. The problem (5.13) now reads

$$\boldsymbol{\mathcal{S}} \cdot \mathbf{B} = \begin{pmatrix} S & 0 & 0 \\ 0 & S & 0 \\ 0 & 0 & 1/S^2 \end{pmatrix} \cdot \mathbf{B} = \mathbf{B} \cdot \mathbf{M} \ . \tag{5.20}$$

Note that $\boldsymbol{\Lambda}$ describes uniaxial compression rather than extension due to our convention for the sign of $\lambda_1 = \lambda_2$. However, the two problems are interchangeable. The equivalence of $\boldsymbol{\mathcal{S}}$ and $\mathbf{M}$ again allows us to equate their invariants:

$$\det(\mathbf{M}) = 1 \tag{5.21a}$$

$$M_{11}M_{22} + M_{22}M_{33} + M_{33}M_{11} - M_{12}M_{21} - M_{23}M_{32} - M_{31}M_{13} = 2/S + S^2 \tag{5.21b}$$

$$M_{11} + M_{22} + M_{33} = 2S + 1/S^2 \ . \tag{5.21c}$$

The first relation merely states the fact that the volume of the unit cell is conserved, a direct consequence of the isochoric nature of the deformation. We now express

‡ An alternative proof of this assertion was independently developed by Reinelt & Kraynik (1990) somewhat prior to ours. We shall reproduce a version of their derivation, which they kindly communicated to us, in the next section.

the basis vectors in spherical coordinates measuring the azimuth about the axis of compression:

$$\mathbf{B} = \begin{pmatrix} A_1 \sin\theta_1 \cos\phi_1 & A_2 \sin\theta_2 \cos\phi_2 & \sin\theta_3 \cos\phi_3 \\ A_1 \sin\theta_1 \sin\phi_1 & A_2 \sin\theta_2 \sin\phi_2 & \sin\theta_3 \sin\phi_3 \\ A_1 \cos\theta_1 & A_2 \cos\theta_2 & \cos\theta_3 \end{pmatrix} . \tag{5.22}$$

As should be expected from the axisymmetry of the flow, the eigenvalue problems involving the angles $\phi_i$ can be rewritten in terms of the relative positions $\phi_1 - \phi_2$ and $\phi_2 - \phi_3$. Eliminating $S$ and $\phi_1 - \phi_3$ from these equations yields

$$M_{12} A_1 \sin\theta_1 \sin(\phi_1 - \phi_2) + M_{32} \sin\theta_3 \sin(\phi_3 - \phi_2) = 0 \tag{5.23a}$$

$$M_{13} M_{21} A_1 \sin\theta_1 \sin(\phi_1 - \phi_2) + M_{23} M_{31} \sin\theta_3 \sin(\phi_3 - \phi_2) = 0 \ , \tag{5.23b}$$

which is soluble only if

$$M_{12} M_{23} M_{31} = M_{13} M_{32} M_{21} \ . \tag{5.24}$$

We shall occasionally refer to this relation as the "symmetry requirement", since symmetric matrices obviously satisfy it. (One can prove that the exceptional cases $\theta_i = 0$ or $\phi_i = \phi_j$ in (5.23) are either incompatible with the strain-periodicity, with the linear independence of the basis vectors, or agree with (5.24).) One obtains three additional solvability conditions by eliminating, successively, terms involving $\sin\theta_1, \sin\theta_2$ and $\sin\theta_3$. Elementary algebra then shows that solutions can exist only if

$$M_{23} M_{31} = M_{21} (M_{33} - S) \ , \tag{5.25a}$$

$$M_{31} M_{12} = M_{32} (M_{11} - S) \ , \tag{5.25b}$$

$$M_{12} M_{23} = M_{13} (M_{22} - S) \ . \tag{5.25c}$$

One can eliminate $S$ from (5.25) to get

$$M_{23} (M_{12} M_{21} - M_{13} M_{31}) = M_{13} M_{21} (M_{22} - M_{33}) \ , \tag{5.26a}$$

$$M_{31}(M_{12}M_{21} - M_{23}M_{32}) = M_{32}M_{21}(M_{11} - M_{33}) \ , \tag{5.26b}$$

and

$$S = (M_{21}M_{33} - M_{23}M_{31})/M_{21} \ . \tag{5.26c}$$

The remaining equations are the analog of (5.23a),

$$M_{21}A_2 \sin\theta_2 \sin(\phi_1 - \phi_2) + M_{31} \sin\theta_3 \sin(\phi_1 - \phi_3) = 0 \ , \tag{5.27}$$

and the relations obtained from the eigenvalue problem with root $1/S^2$:

$$(1/S^2)A_1 \cos\theta_1 = M_{11}A_1 \cos\theta_1 + M_{21}A_2 \cos\theta_2 + M_{31} \cos\theta_3 \ , \tag{5.28a}$$

$$(1/S^2)A_2 \cos\theta_2 = M_{12}A_2 \cos\theta_1 + M_{22}A_2 \cos\theta_2 + M_{32} \cos\theta_3 \ . \tag{5.28b}$$

Finally, (5.21) is required to solve the entire set of equations. One will note that (5.21), (5.23a), (5.24), (5.26), (5.27) and (5.28) determine 11 relations, while the original eigenvalue problem (5.20) only specified 9. We shall show later that (5.21b-c) are redundant with (5.24), (5.26a-b) and (5.21a).

Using (5.26a-b), we can eliminate $M_{11}$ and $M_{22}$ from the expansion of the determinant in terms of the elements of $\mathbf{M}$, and after a little algebra, making occasional use of the symmetry requirement (5.24), we arrive at the following factorization:

$$\det(\mathbf{M}) = \Big(M_{33} - \frac{M_{23}M_{31}}{M_{21}}\Big) \times \tag{5.29a}$$
$$\Big(M_{33}^2 + \big[\frac{M_{12}M_{31}}{M_{32}} + \frac{M_{12}M_{23}}{M_{13}} - \frac{M_{23}M_{31}}{M_{21}}\big]M_{33} - M_{13}M_{31} - M_{23}M_{32}\Big) \ .$$

The first expression between parentheses on the right hand side is $S$ (see (5.26c)). The second expression, with the help of (5.26a-b), can be written as

$$M_{33}^2 + \big[M_{22} + M_{11} - 2M_{33} + \frac{M_{23}M_{31}}{M_{21}}\big]M_{33} - M_{13}M_{31} - M_{23}M_{32} \ . \tag{5.29b}$$

Since $\det(\mathbf{M}) = 1$, the preceding expression must equal $1/S$. This can be shown to imply the solvability condition (5.21b-c). Hence a few equations are redundant, as alluded to earlier.

We now show that $S$ cannot be integer. Suppose it is. Then, since $S = M_{33} - M_{23}M_{31}/M_{21}$ (eq. (5.26c)), the fraction $F = M_{23}M_{31}/M_{21}$ must be integer.

It follows that $1/S$ must also be integer, since (5.29b) involves integers only. Excluding the trivial case $S = 1$, this leads to a contradiction; therefore $S$ cannot be integer, and $F$ is a non-integer rational.

We also know that $S$ can be written in two other ways:

$$S = M_{22} - \frac{M_{12}M_{23}}{M_{13}} = M_{11} - \frac{M_{31}M_{12}}{M_{32}} \ . \tag{5.30}$$

If $S$ is purely rational, the two fractions occurring in (5.30) must also be non-integer rational. We first show by means of an example that 6 integers can be found such that the "symmetry requirement" (5.24) is satisfied, but none of the ratios implicated are integer. Indeed, choose $M_{13} = 3 \times 7$, $M_{32} = 2 \times 11$, $M_{21} = 5 \times 13$, $M_{31} = 2 \times 7$, $M_{23} = 11 \times 5$ and $M_{12} = 3 \times 13$.

We now show that there are no solutions to the problem, hence that there exist no strain-periodic lattices for uniaxial compression or extension. Indeed, since $F = M_{23}M_{31}/M_{21}$ is non-integer, but $M_{23}M_{31}M_{12}/M_{21} = M_{13}M_{32}$ (see the symmetry requirement) is, the decomposition of $M_{12}$ and $M_{21}$ into their prime factors must have at least one prime in common. Call it $K_{12}$. (In the numerical example above, $K_{12} = 13$.) Obviously, $K_{12}$ and $M_{23}M_{31}$ are coprime since $F$ is purely fractional. By rearranging (5.26a) as

$$\frac{M_{13}M_{31}M_{23}}{M_{21}} = M_{13}(M_{33} - M_{22}) + M_{12}M_{23} \ , \tag{5.31}$$

it is clear that the fraction on the left hand side is integer. Thus since $M_{31}M_{23}$ and $K_{12}$ are coprime, $K_{12}$ must divide $M_{13}$. However, by the symmetry requirement, we can write $F = M_{32}M_{13}/M_{12}$, so that $K_{12}$ and $M_{32}M_{13}$ must be coprime. Hence there is a contradiction. We can therefore conclude that there is no solution to (5.20), and thus that strain-periodic lattices in axisymmetric straining fields do not exist.

### 5.3.4 Arbitrary flow with real eigenvalues ($\nu \in (0, 1)$)

We now consider the general problem formulation (5.13), with $\nu$ specified by the imposed flow. Supposing that we can find an integer matrix $\mathbf{M}$ whose left-

eigenvalues can be parametrized by a scalar $S > 1$ such that $\mu_1 = S$, $\mu_2 = S^\nu$, and $\mu_3 = S^{-(1+\nu)}$, one can solve the three problems

$$\mathbf{x}_i \cdot \mathbf{M} = \mu_i \mathbf{x}_i \tag{5.32}$$

for the eigenvectors $\mathbf{x}_i$, with $i = 1, 2$, and 3, and can associate these with the row vectors of the characteristic matrix $\mathbf{B}$ of the network. Writing the basis vectors in spherical coordinates as in (5.22), it easily follows that

$$\tan \phi_i = (\mathbf{x}_2)_i / (\mathbf{x}_1)_i \ , \tag{5.33a}$$

$$\tan \theta_i = \sqrt{[(\mathbf{x}_1)_i^2 + (\mathbf{x}_2)_i^2]} / (\mathbf{x}_3)_i \ , \tag{5.33b}$$

$$A_i = \sqrt{(\mathbf{x}_1)_i^2 + (\mathbf{x}_2)_i^2 + (\mathbf{x}_3)_i^2} \ . \tag{5.33c}$$

Therefore the lattice geometry can be resolved if $\mathbf{M}$ can be found. We now focus on that problem.

The characteristic equation for the eigenvalues of $\mathbf{M}$ has to be satisfied by $S$, $S^\nu$ and $S^{-(1+\nu)}$. Thus we need to find a cubic equation of the form

$$\mu^3 - I_1 \mu^2 + I_2 \mu - 1 = 0 \tag{5.34}$$

which has $S$ and $S^\nu$ as roots. (Setting the last term equal to 1 guarantees that $S^{-(1+\nu)}$ will be a root then.) $I_1$ is the trace of the matrix $\mathbf{M}$ and $I_2$ is the invariant on the left hand side of (5.21b). Since $I_1 = \mathrm{tr}(\mathbf{M}) = S + S^\nu + S^{-(1+\nu)}$ is an integer larger than 2, and since $I_1 = 3$ only admits the solution $S = 1$, we may conclude that $I_1 > 3$. Also, the three roots of the cubic are positive, and two of them must be greater than 1. Hence, the value of (5.34) at $\mu = 1$ must be positive and $I_2 > I_1$. Finally, from the fact that the cubic must have real extrema, we deduce that $3I_2 \leq I_1^2$. In summary, we need to find an integer matrix $\mathbf{M}$ which simultaneously satisfies

$$\det(\mathbf{M}) = 1 \ , \tag{5.35a}$$

$$\mathrm{tr}(\mathbf{M}) = I_1 > 3 \ , \tag{5.35b}$$

$$I_1 < I_2 = M_{11}M_{22} + M_{22}M_{33} + M_{33}M_{11} - M_{12}M_{21} - M_{23}M_{32} - M_{31}M_{13} \leq I_1^2/3 \ . \tag{5.35c}$$

These are necessary conditions for a solution to exist. Sufficient conditions will be derived below. An example of such a matrix is

$$\mathbf{M} = \begin{pmatrix} 2 & 3 & 0 \\ 1 & 2 & 1 \\ 1 & 2 & 2 \end{pmatrix} \ , \tag{5.36a}$$

whose characteristic equation has the roots

$$S^{\nu} = 1.343379570... \qquad \text{and} \qquad S = 4.490863615... \tag{5.36b}$$

Thus $\mathbf{M}$ determines the structure of a lattice which is mapped onto itself by an affine transformation along the streamlines of an incompressible flow characterized by $\nu = .1965...$, such as

$$\mathbf{\Lambda} = \begin{pmatrix} .8358 & 0 & 0 \\ 0 & .1642 & 0 \\ 0 & 0 & -1 \end{pmatrix} \ . \tag{5.36c}$$

The geometry of the unit cell can be calculated by computing the left eigenvectors of $\mathbf{M}$, as explained above.

This proves that strain-periodic solutions exist for at least some values of $\nu$. Extending an analysis of the cubic (5.34) due to Reinelt & Kraynik (1990), it is possible to demonstrate that solutions to (5.13) exist for an infinite number of values $\nu$ in the interval (0,1). Furthermore, their procedure indicates how to calculate $\mathbf{M}$, and hence a strain-periodic lattice, for any permissible $\nu$ (i.e., for a specified flow field), rather than "working backwards" as in the example (5.36). We shall also show based on their work that uniaxial extension can be approximated arbitrarily closely by flows having self-reproducing lattices. (In other words, for any $\varepsilon > 0$, one can find values of $\nu \in (1-\varepsilon, 1)$ for which solutions to (5.13) exist.) However, the strain period of these networks (defined as the amount of stretch $S$ after which the lattice returns to its original configuration) becomes increasingly long, tending to $\infty$ as $\nu \to 1$.

Although their monograph on the existence of strain-periodic lattices in extensional flows (Reinelt & Kraynik, 1990) has not yet been published, Reinelt & Kraynik kindly granted me permission to reproduce their proof in my dissertation. Their approach centers around the conditions which the integers $I_1$ and $I_2$ must satisfy in order for the characteristic equation (5.34) to have three real and positive solutions. The crux of their reasoning is that each set of three such roots corresponds to a pure straining flow. One can therefore determine all the deformations which possess compatible lattices by finding all pairs of integers $(I_1, I_2)$ such that the cubic (5.34) has three positive roots. Both problems are equivalent. We report the main points of their derivation in what follows.

The roots $S, S^\nu$, and $S^{-(1+\nu)}$ of the polynomial (5.34) are related to its coefficients by†

$$I_1 = S + S^\nu + S^{-(1+\nu)} \tag{5.37a}$$

$$I_2 = S^{1+\nu} + S^{-\nu} + S^{-1} \ . \tag{5.37b}$$

Observe that if $S$ satisfies the cubic for a pair of integers $(I_1, I_2)$, then $S^{-1}$ is a solution when $I_1$ and $I_2$ are interchanged. (This is another manifestation of the fact that strain-periodicity is unaffected by time reversal.) The domain of allowable integers (i.e., those which give three positive roots for the cubic) is thus symmetric about the line $I_1 = I_2$. We can therefore restrict ourselves to $I_1 < I_2$. (The special case $I_1 = I_2$ corresponds to planar extensional flow and was discussed in §5.3.2, where we found infinitely many solutions.)

The polynomial (5.34), which we shall denote by $p(\mu) = 0$, has a local minimum at

$$\mu_0 = \frac{I_1 + \sqrt{I_1^2 - 3I_2}}{3} \ , \tag{5.38a}$$

where it reaches the value

$$p(\mu_0) = \frac{I_1 I_2}{9} - \frac{2}{27}(I_1^2 - 3I_2)\left[I_1 + \sqrt{I_1^2 - 3I_2}\right] - 1 \ . \tag{5.38b}$$

† Alternatively, one may state that the equivalent matrices $\boldsymbol{\mathcal{S}}$ and $M$ possess the same invariants.

If $p(\mu_0) < 0$, the cubic crosses the $\mu$-axis in three points, and the set $(I_1, I_2)$ defines a self-reproducing lattice. If $p(\mu_0) = 0$, the characteristic equation possesses a simple and a double root. This is the situation for biaxial extensional flow. Hence axisymmetric deformations lie on the boundary between allowable and inadmissible pairs of integers $(I_1, I_2)$. By examining (5.38b) for large $I_1$, we find that $I_2$ must be proportional to $I_1^2/4$ in order that $p(\mu_0) \simeq 0$. In fact, if we substitute $I_2 = I_1^2/4$ into (5.38b), we get exactly $p(\mu_0) = -1$. Setting

$$I_2 = \frac{I_1^2}{4} + j \ , \tag{5.39}$$

equation (5.38b) for the minimum becomes

$$p(\mu_0) = \frac{I_1^3}{36}\left\{\left(1 + \frac{4j}{I_1^2}\right) + \left(\frac{12j}{I_1^2} - 1\right)\left[\frac{2}{3} + \frac{1}{3}\sqrt{1 - \frac{12j}{I_1^2}}\,\right]\right\} - 1 \ . \tag{5.40}$$

For $j = 0$, the right hand side equals $-1$, as discussed above. Since both terms within the braces of (5.40) decrease with decreasing $j$, the minimum $p(\mu_0)$ of the cubic is also negative for $j < 0$, and there are then three positive roots to the characteristic equation. If $j > 0$, we note that the factor between brackets in (5.40) is always less than 1 and that the second term in the brace is negative, so that

$$p(\mu_0) > \frac{I_1^3}{36}\left\{\left(1 + \frac{4j}{I_1^2}\right) + \left(\frac{12j}{I_1^2} - 1\right)\right\} - 1 = \frac{4}{9} I_1 j - 1 \geq 0 \ . \tag{5.41}$$

The last equality follows from the observation that $I_1 \geq 3$ and that the smallest strictly positive value of $j$ allowed by the integer equation (5.39) is $3/4$. We conclude that, in order for the polynomial (5.34) to have three positive roots, $j$ must be zero or negative. Thus, from (5.39), the relations $I_2 = I_1^2/4$ and, by symmetry, $I_1 = I_2^2/4$ define the boundaries between the integer pairs $(I_1, I_2)$ that are allowed and those that are not (Fig. 5.2). This constraint provides a tighter upper bound for $I_2$ than the one given as a necessary condition in (5.35c). Also, remark that the fact that $p(\mu_0) \neq 0$ for all $(I_1, I_2) \in \mathcal{Z}^2$ furnishes an alternative proof of the non-existence of strain-periodic lattices in axisymmetric extensional flows (see §5.3.3).

Reinelt & Kraynik (1990) further point out that many integer matrices with invariants $I_1$ and $I_2$ can be constructed for each allowable pair. They cite the example

$$\mathbf{M} = \begin{pmatrix} 1 & 0 & 1 \\ I_1 - I_2 & 1 & I_1 - I_2 \\ I_1 - 3 & 1 & I_1 - 2 \end{pmatrix} . \tag{5.42}$$

This implies that the conditions $I_2 \leq I_1^2/4$ and $I_1 \leq I_2^2/4$ are necessary and sufficient conditions to insure the existence of strain-periodic lattices. This concludes the proof by Reinelt & Kraynik (1990).

The elegant treatment of the issue of self-reproducibility in extensional flows by Reinelt & Kraynik (1990) confirms the conclusions of §5.3.2-3, and can be used to demonstrate that flows exist which approach uniaxial extension arbitrarily closely, yet possess strain-periodic lattices. To investigate this further, we note that the condition

$$S^3 - I_1 S^2 + I_2 S - 1 = 0 \tag{5.43}$$

defines a straight line in an $(I_1, I_2)$ diagram (Fig. 5.2). Recall that $S = \exp(\lambda_1 t)$. The root $S$ is therefore a direct measure of the period $t_s$ in which the lattice returns to its starting configuration.‡ The region of $\mathcal{Z}^2$ between the limiting curves $4I_1 = I_2^2$ and $4I_2 = I_1^2$ then constitutes all points through which three lines (5.43) with $S > 0$ pass. This is illustrated for our example (5.36) in Fig. 5.2. In the half-domain delimited by $4I_2 = I_1^2$ and the symmetry axis $I_1 = I_2$, two roots are positive, and $\nu$ can be determined from the ratio of their logarithms. Also, although we did not derive a closed form expression for curves of constant $\nu$,† it is obvious that they

‡ $S$ is actually a measure of strain, but one can non-dimensionalize time by $\lambda_1^{-1}$, the amplitude of the largest elongational component of the rate of strain, to obtain a one-to-one correspondence between the amount of deformation and the time necessary to achieve it.

† The curve for $\nu = 1$, of course, is given by the implicit relation $I_1 I_2/9 - \frac{2}{27}(I_1^2 - 3I_2)\left[I_1 + \sqrt{I_1^2 - 3I_2}\right] = 1$, as can be seen from (5.38b).

are continuous and cannot cross except at the trivial point $I_1 = I_2 = 3$. They must therefore fan out, away from the diagonal, as $\nu$ goes from 0 to 1. The limit of biaxial extension can consequently be approached arbitrarily closely by picking an allowable pair of suitably large integers along the curve $I_2 = I_1^2/4$. This geometric argument becomes more clear perhaps if one calculates the roots of (5.34) for large $I_1 = 2\sqrt{I_2}$. We find, asymptotically, that

$$S = \frac{I_1}{2} + \sqrt{\frac{2}{I_1}} - \frac{2}{I_1^2} + O(I_1^{-7/2}) \tag{5.44a}$$

$$S^{\nu} = \frac{I_1}{2} - \sqrt{\frac{2}{I_1}} - \frac{2}{I_1^2} + O(I_1^{-7/2}) \ , \tag{5.44b}$$

$$S^{-(1+\nu)} = \frac{4}{I_1^2} + \frac{64}{I_1^5} + O(I_1^{-8}) \ . \tag{5.44c}$$

Thus, by choosing $I_1$ sufficiently large, $S^{\nu}$ can be made to approach $S$ arbitrarily closely; i.e., $\nu \to 1$ as $I_1 \to \infty$ keeping $I_2 = I_1^2/4$. (Note that $I_1$ must be even to ensure that $I_2$ is integer). Since however $S \simeq I_1/2$, the corresponding straining period $t_s = \ln(S)/\lambda_1 \simeq \ln(I_1/2)/\lambda_1$ also increases. Self-reproducing lattices can thus be found in nearly axisymmetric pure straining flows, but at the expense of long periods of replication.

Finally, let us point out that although we have just shown that there exist infinitely many values of $\nu$ for which solutions to (5.13) exist, it is not yet clear whether these constitute a discrete or a continuous spectrum in the interval [0,1). This, we believe, remains an open question.

### 5.3.5 Self-reproducibility in flows possessing vorticity

We now briefly mention flow types for which the eigenvalues of $\nabla \mathbf{u}$ (see (5.11)) are all zero or have imaginary components. This case is fully understood for planar deformations (Adler & Brenner, 1985). A zero eigenvalue corresponds to simple shear, for which infinitely many strain-periodic lattices exist. When eigenvalues are complex in two dimensions, they must be purely imaginary and the flow is a simple

rotation. Any lattice is self-reproducing under these circumstances. The three-dimensional problem has been investigated by Adler (1984) to deduce the maximal density of suspensions kinematically compatible with the deformations, but the analysis was not complete and did not address the issue of strain-periodicity.

### 5.3.6 Non-self-reproducing compatible lattices and "adequate" unit cells

Although we have demonstrated in §5.3.3-4 that strain-periodicity is impossible under uniaxial or biaxial extension, Adler (1984) calculated a non-zero maximum packing fraction for crystalline dispersions subject to axisymmetric stretch. Hence non-self-reproducing compatible lattices exist. We now derive basis vectors for such a network.

Recall from (5.9) that the trajectory of a point $\mathbf{x}_o$ is given by $\mathbf{x}(t) = \exp(\mathbf{G}t) \cdot \mathbf{x}_o$, with, for biaxial extension,

$$\mathbf{G} = \begin{pmatrix} \frac{1}{2} & 0 & 0 \\ 0 & \frac{1}{2} & 0 \\ 0 & 0 & -1 \end{pmatrix} \qquad \text{and} \qquad \exp(\mathbf{G}t) = \begin{pmatrix} S & 0 & 0 \\ 0 & S & 0 \\ 0 & 0 & S^{-2} \end{pmatrix} . \tag{5.45}$$

The length $|\mathbf{x}(t)|$ becomes minimal when $S = \left(2x_3^2/(x_1^2+x_2^2)\right)^{1/6}$ where it reaches the value

$$|\mathbf{x}(t)|^2_{\min} = \left\{ \sqrt[3]{2} + \frac{1}{\sqrt[3]{4}} \right\} \sqrt[3]{x_3^2(x_1^2+x_2^2)^2} \, . \tag{5.46}$$

[$(x_1, x_2, x_3)$ represent the coordinates of $\mathbf{x}_o$, the "3" axis being coincident with the axis of compression of the flow.] The minimum (5.46) can be made non-zero for all points $\boldsymbol{x}_{\{z\}}$ of a three-dimensional grid by finding a lattice $\mathcal{L}$ admitting the star-body $\mathcal{B}$ defined by $|x_3(x_1^2+x_2^2)| \leq 1$ (or some other appropriate constant). (A lattice is called admissible for $\mathcal{B}$ if none of its nodes, except the origin, lie within $\mathcal{B}$.) A critical lattice for $\mathcal{B}$ exists (Davenport & Rogers, 1950; Cassels, 1959; Gruber & Lekkerkerker, 1987), with basis vectors

$$\mathbf{L} = \begin{pmatrix} 1 & \theta_R & \theta_R^2 - \theta_I^2 \\ 0 & \theta_I & 2\theta_R\theta_I \\ 1 & \phi & \phi^2 \end{pmatrix} , \tag{5.47a}$$

where $\phi$ and $\theta_\pm = \theta_R \pm i\theta_I$ are the roots of $\xi^3 - \xi = 1$. Numerically,

$$\phi = 1.324... \qquad \text{and} \quad \theta_+ = -0.662... + i0.562... \tag{5.47b}$$

The volume of this basis cell is $\det(\mathbf{L}) = \sqrt{23}/2$. By construction, the points of this lattice never approach the origin any closer than $(\sqrt[3]{2} + 1/\sqrt[3]{4})^{\frac{1}{2}}$. The maximum packing fraction of spheres which this network can accommodate under uniaxial extension is therefore

$$\phi_{\max} = \frac{\frac{\pi}{6}(\sqrt[3]{2} + \frac{1}{\sqrt[3]{4}})^{\frac{3}{2}}}{\sqrt{23}/2} = \frac{\pi\sqrt{3}}{2\sqrt{23}}\,, \tag{5.48}$$

in agreement with Adler's result (1984). He did not, however, give the basis vectors. A few of the lattice points lying on the star body $\mathcal{B}$, and which will therefore pass closest to the origin, are $\mathbf{b}_2 + \mathbf{b}_3$, $-4\mathbf{b}_2 + 3\mathbf{b}_3$, $\mathbf{b}_1 - \mathbf{b}_2$, $\mathbf{b}_1 - \mathbf{b}_3$, $\mathbf{b}_1 + \mathbf{b}_2 + \mathbf{b}_3$, $7\mathbf{b}_1 - 49\mathbf{b}_2 + 33\mathbf{b}_3$, etc. [These were generated by a computer program, and are not given in any special order. Many more exist which are not reported here (an infinite number, actually, since $\mathcal{B}$ is fully automorphic according to the definition of Davenport & Rogers (1950)).] The notation $\mathbf{b_i}$ refers to the column vectors of $\mathbf{L}$, numbered sequentially from left to right. For our purposes, the vectors $\mathbf{b}_i$ define the edges of a unit cell suited for dynamic simulations of uniaxial extensional flows. (Of course, repeated application of the box standardization algorithm discussed in §5.2 will be necessary.)

Finally, if $\mathbf{L}$ proves to be impractical, it should be noted that the discussion in this chapter assumed that $t \to \infty$ to derive criteria for compatibility. Any real simulation, however, ends after a limited time, during which the unit cell can only have deformed a finite amount. It may therefore be possible to find "adequate" unit cells which are not, strictly speaking, compatible with the studied flow, but suffice for the simulation objectives.

**References**

Adler, P.M. (1984) Spatially periodic suspensions of convex particles in linear shear flow. IV. Three-dimensional flows, *J. Theor. Appl. Mech.* **3**, 725-746.

Adler, P.M. (1985) Spatially periodic suspensions, *J. Theor. Appl. Mech.*, Special volume, 73-100.

Adler, P.M. & Brenner, H. (1985) Spatially periodic suspensions of convex particles in linear shear flows. I. Description and kinematics, *Int. J. Multiph. Flow* **11**, 361-385.

Cassels, J.W.S. (1959) *An introduction to the geometry of numbers*, Springer Verlag.

Claeys, I.L. (1991) *SDPS, A package of subroutines to simulate systems of hydrodynamically interacting prolate spheroids*, FORTRAN program, California Institute of Technology 210-41.

Davenport, H. & Rogers, C.A. (1950) Diophantine equations with an infinity of solutions, *Phil. Trans. Roy. Soc. Lond.* **A 242**, 311-344.

Gruber, P.M. & Lekkerkerker, C.G. (1987) *Geometry of numbers*, North Holland.

Kraynik, A.M. & Hansen, M.G. (1986) Foam and emulsion rheology: a quasistatic model for large deformations of spatially-periodic cells, *J. Rheol.* **30**, 409-439.

Reinelt, D. & Kraynik, A.M. (1990) Existence of strain-periodic solution for extensional flow, personal communication.

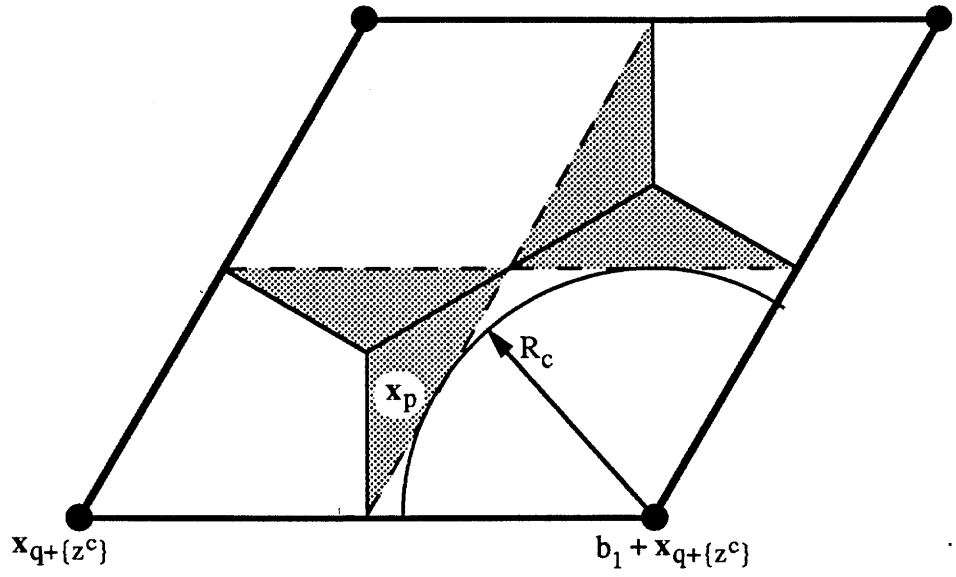


**Fig. 5.1.**: Misallocation of the nearest lattice point.
The solid lines within the unit cell bissect the vectors connecting the lattice points, and thus define the points for which both corners are equidistant. The dashed lines connect the points halfway between the lattice points. Both criteria give different results if $x_p$ is within the shaded region (as shown). For instance, $x_p$ is closer to $b_1 + x_{q+\{z^c\}}$ than to $x_{q+\{z^c\}}$ in this figure.

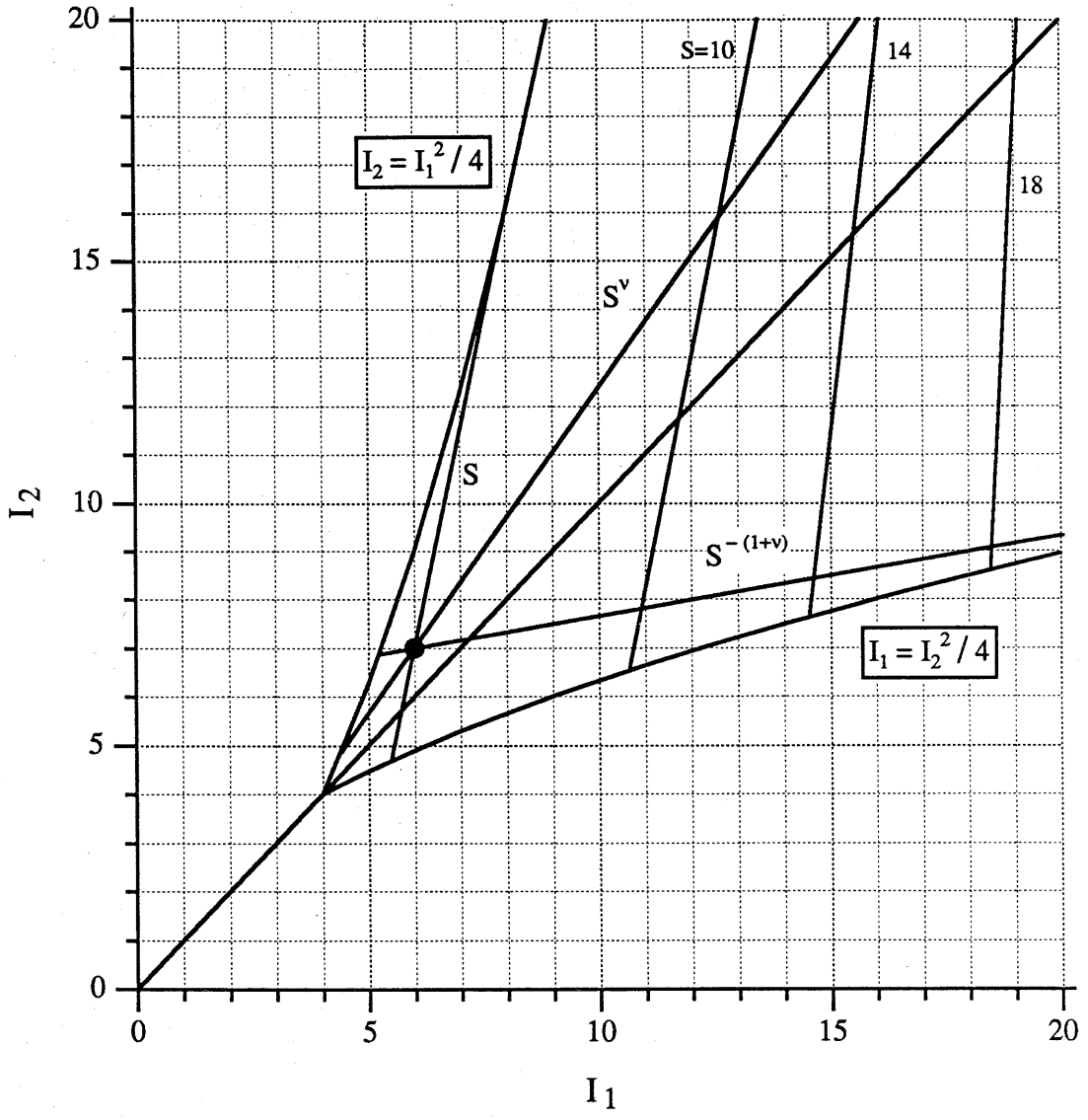


**Fig.5.2**: Graphical representation of the allowable pairs of integers $(I_1, I_2)$. The two parabolae delimit the domain of allowable integers. The diagonal corresponds to planar extensional flows. The solid lines are curves of constant straining periods S. Note that S increases as one follows the lower bound to the right. The straight lines denoted by S, $S^\nu$ and $S^{-(1+\nu)}$ are drawn for the numerical example (5.36) from the text. Notice that they intersect at (6,7).

# APPENDIX K

## Some hydrodynamic transport coefficients for crystals of spheroids

As explained in Appendix H, crystals of spheroids are useful reference configurations whose properties serve as benchmarks to test the accuracy of present and future simulation methods. We therefore collected a few results on the hydrodynamic transport properties of orderly arrangements of spheroids in this appendix. Some of the tables contain the numerical values used for the figures of Chapter IV, but others consist of new information.

We first discuss the relation $\mathbf{R}_{\Sigma E}$ between the hydrodynamic stress and the rate of strain. Due to the tracelessness and symmetry of $\mathbf{E}$ and $\mathbf{S}$, this tensor is indeterminate. Following the usual convention, we define $\mathbf{R}_{\Sigma E}$ uniquely by specifying that it, too, must be traceless and symmetric in its first and last two indices. This allows one to compact it into a $5 \times 5$ matrix $\mathbf{Y}$ such that

$$\begin{pmatrix} \Sigma_{11} \\ \Sigma_{22} \\ \Sigma_{12} \\ \Sigma_{23} \\ \Sigma_{31} \end{pmatrix} = 8\pi a^3 \mu \mathbf{Y} \cdot \begin{pmatrix} E_{11} - E_{33} \\ E_{22} - E_{33} \\ 2E_{12} \\ 2E_{23} \\ 2E_{31} \end{pmatrix} , \tag{K.1}$$

with $\mu$ the viscosity of the suspending fluid and $a$ the length of the spheroidal semi-axis. It follows from Lorentz' reciprocal theorem that $\mathbf{Y}$ is symmetric. It thus contains only 15 independent elements, which we label as shown below.

$$\mathbf{Y} = \begin{pmatrix} Y_{1111} & Y_{1122} & Y_{1112} & Y_{1123} & Y_{1131} \\ Y_{1122} & Y_{2222} & Y_{2212} & Y_{2223} & Y_{2231} \\ Y_{1112} & Y_{2212} & Y_{1212} & Y_{1223} & Y_{1231} \\ Y_{1123} & Y_{2223} & Y_{1223} & Y_{2323} & Y_{2331} \\ Y_{1131} & Y_{2231} & Y_{1231} & Y_{2331} & Y_{3131} \end{pmatrix} . \tag{K.2}$$

For dispersions possessing a 6-fold axis of symmetry $\mathbf{d}$, invariance laws imply that 3 components suffice to characterize $\mathbf{Y}$ (App. H). In terms of the coefficients $\eta$

introduced in Ch. IV (eq. (4.43)), and assuming that **d** lies along the "3" axis, it is easy to find in this case that

$$\mathbf{Y} = \begin{pmatrix} \eta_T/3 + \eta_\parallel & \eta_T/3 - \eta_\parallel & 0 & 0 & 0 \\ \eta_T/3 - \eta_\parallel & \eta_T/3 + \eta_\parallel & 0 & 0 & 0 \\ 0 & 0 & \eta_\parallel & 0 & 0 \\ 0 & 0 & 0 & \eta_\perp & 0 \\ 0 & 0 & 0 & 0 & \eta_\perp \end{pmatrix}, \qquad \text{(K.3)}$$

By analogy, we set $\eta_T = \frac{3}{2}(Y_{1111} + Y_{1122})$, $\eta_\parallel = Y_{1212}$ and $\eta_\perp = Y_{3131}$ for all configurations in Fig. 4.11, even though (4.43) does not hold in general. This definition of $\eta_\parallel$ makes it equal to one third of the Trouton viscosity in uniaxial extensional flows along the "3" axis. For isotropic suspensions, one sees from (K.3) that **Y** has 7 non-zero elements, two of which are identical because of symmetry. The 6 remaining components were averaged appropriately to obtain the values reported in Ch. IV.

Lubrication interactions were suppressed in all calculations concerning crystalline dispersions for reasons explained in Ch. IV. The non-dimensionalization used in this appendix is consistent with the remainder of this work: diffusion coefficients scale with $kT/8\pi\mu a^n$ ($n = 1$ for translational components, $n = 2$ for rotary diffusivities), sedimentation rates with $|\mathbf{F}|/8\pi\mu a$ and their rotational analogs with $|\mathbf{T}|/8\pi\mu a^2$. [**F** and **T** represent the uniformly applied force or torque respectively. "k" is Boltzmann's constant, and "T" the absolute temperature.]

*Table* K.1: Rheological data for *efc*-crystals of spheroids with $r_p = 8$.‡

| $\phi$ | $Y_{1111}$ | $Y_{1212}$ | $Y_{3131}$ |
|---|---|---|---|
| 0.00568 | 2.03E-02 | 5.288E-03 | 5.506E-03 |
| 0.00791 | 2.08E-02 | 5.304E-03 | 5.504E-03 |
| 0.01096 | 2.15E-02 | 5.327E-03 | 5.503E-03 |
| 0.01513 | 2.23E-02 | 5.357E-03 | 5.505E-03 |
| 0.02080 | 2.33E-02 | 5.398E-03 | 5.511E-03 |
| 0.02850 | 2.46E-02 | 5.454E-03 | 5.526E-03 |
| 0.03025 | 2.48E-02 | 5.466E-03 | 5.530E-03 |
| 0.03866 | 2.61E-02 | 5.527E-03 | 5.552E-03 |
| 0.03890 | 2.62E-02 | 5.529E-03 | 5.552E-03 |
| 0.04931 | 2.77E-02 | 5.604E-03 | 5.585E-03 |
| 0.05294 | 2.82E-02 | 5.630E-03 | 5.597E-03 |
| 0.06279 | 2.95E-02 | 5.699E-03 | 5.630E-03 |
| 0.07185 | 3.07E-02 | 5.769E-03 | 5.669E-03 |
| 0.07985 | 3.18E-02 | 5.826E-03 | 5.700E-03 |
| 0.09735 | 3.39E-02 | 5.962E-03 | 5.783E-03 |
| 0.10145 | 3.44E-02 | 5.992E-03 | 5.801E-03 |
| 0.12884 | 3.76E-02 | 6.210E-03 | 5.945E-03 |
| 0.13180 | 3.79E-02 | 6.235E-03 | 5.962E-03 |
| 0.16367 | 4.12E-02 | 6.505E-03 | 6.155E-03 |
| 0.17854 | 4.27E-02 | 6.632E-03 | 6.249E-03 |
| 0.20815 | 4.53E-02 | 6.912E-03 | 6.466E-03 |
| 0.24236 | 4.80E-02 | 7.237E-03 | 6.727E-03 |
| 0.26515 | 4.97E-02 | 7.496E-03 | 6.941E-03 |
| 0.32999 | 5.41E-02 | 8.234E-03 | 7.568E-03 |

‡ We demonstrated in App. H that $Y_{1111} = Y_{1122} + 2Y_{1212}$ for this type of lattice.

| | | | |
|---|---|---|---|
| 0.33841 | 5.48E-02 | 8.388E-03 | 7.699E-03 |
| 0.38474 | 5.81E-02 | 8.994E-03 | 8.227E-03 |
| 0.43279 | 6.25E-02 | 9.883E-03 | 8.997E-03 |
| 0.45074 | 6.39E-02 | 1.011E-02 | 9.201E-03 |
| 0.45600 | 6.43E-02 | 1.021E-02 | 9.289E-03 |
| 0.54094 | 7.39E-02 | 1.217E-02 | 1.099E-02 |
| 0.55455 | 7.66E-02 | 1.282E-02 | 1.153E-02 |
| 0.61755 | 8.57E-02 | 1.470E-02 | 1.315E-02 |
| 0.64225 | 9.01E-02 | 1.576E-02 | 1.405E-02 |
| 0.71180 | 1.08E-01 | 2.078E-02 | 1.813E-02 |

*Table* K.2: Rheological data for *ebc*-crystals of spheroids with $r_p = 8$.

| $\phi$ | $Y_{1111}$ | $Y_{1122}$ | $Y_{1212}$ | $Y_{3131}$ |
|---|---|---|---|---|
| 0.00535 | 2.94E-02 | 5.23E-03 | 5.334E-03 | 5.517E-03 |
| 0.00743 | 3.02E-02 | 5.22E-03 | 5.371E-03 | 5.518E-03 |
| 0.00879 | 3.07E-02 | 5.22E-03 | 5.394E-03 | 5.518E-03 |
| 0.01013 | 3.12E-02 | 5.21E-03 | 5.418E-03 | 5.520E-03 |
| 0.01027 | 3.12E-02 | 5.21E-03 | 5.420E-03 | 5.520E-03 |
| 0.01213 | 3.18E-02 | 5.20E-03 | 5.454E-03 | 5.522E-03 |
| 0.01376 | 3.23E-02 | 5.20E-03 | 5.482E-03 | 5.524E-03 |
| 0.01414 | 3.25E-02 | 5.20E-03 | 5.489E-03 | 5.525E-03 |
| 0.01667 | 3.32E-02 | 5.19E-03 | 5.533E-03 | 5.529E-03 |
| 0.01864 | 3.38E-02 | 5.18E-03 | 5.568E-03 | 5.533E-03 |
| 0.01941 | 3.40E-02 | 5.18E-03 | 5.582E-03 | 5.535E-03 |
| 0.02284 | 3.50E-02 | 5.17E-03 | 5.642E-03 | 5.543E-03 |
| 0.02518 | 3.57E-02 | 5.17E-03 | 5.684E-03 | 5.549E-03 |
| 0.02656 | 3.60E-02 | 5.16E-03 | 5.708E-03 | 5.553E-03 |
| 0.02688 | 3.61E-02 | 5.16E-03 | 5.714E-03 | 5.554E-03 |
| 0.02819 | 3.64E-02 | 5.16E-03 | 5.737E-03 | 5.558E-03 |
| 0.03122 | 3.72E-02 | 5.15E-03 | 5.791E-03 | 5.567E-03 |
| 0.03265 | 3.75E-02 | 5.15E-03 | 5.816E-03 | 5.572E-03 |
| 0.03394 | 3.79E-02 | 5.14E-03 | 5.840E-03 | 5.576E-03 |
| 0.03604 | 3.83E-02 | 5.14E-03 | 5.877E-03 | 5.584E-03 |
| 0.03626 | 3.84E-02 | 5.14E-03 | 5.881E-03 | 5.585E-03 |
| 0.03964 | 3.92E-02 | 5.13E-03 | 5.942E-03 | 5.597E-03 |
| 0.04259 | 3.98E-02 | 5.12E-03 | 5.995E-03 | 5.608E-03 |
| 0.04567 | 2.77E-02 | 5.12E-03 | 1.244E-02 | 5.621E-03 |
| 0.04603 | 4.06E-02 | 5.12E-03 | 6.058E-03 | 5.622E-03 |

| | | | | |
|---|---|---|---|---|
| 0.04810 | 4.11E-02 | 5.11E-03 | 6.156E-03 | 5.656E-03 |
| 0.04944 | 4.13E-02 | 5.11E-03 | 6.120E-03 | 5.636E-03 |
| 0.05803 | 4.29E-02 | 5.10E-03 | 6.278E-03 | 5.675E-03 |
| 0.05835 | 4.30E-02 | 5.09E-03 | 6.332E-03 | 5.694E-03 |
| 0.05875 | 4.30E-02 | 5.09E-03 | 6.288E-03 | 5.675E-03 |
| 0.06141 | 4.35E-02 | 5.09E-03 | 6.341E-03 | 5.691E-03 |
| 0.06736 | 4.46E-02 | 5.09E-03 | 6.452E-03 | 5.720E-03 |
| 0.07078 | 4.52E-02 | 5.08E-03 | 6.555E-03 | 5.750E-03 |
| 0.07500 | 4.58E-02 | 5.07E-03 | 6.593E-03 | 5.756E-03 |
| 0.07908 | 4.64E-02 | 5.07E-03 | 6.673E-03 | 5.781E-03 |
| 0.08260 | 4.70E-02 | 5.07E-03 | 6.742E-03 | 5.800E-03 |
| 0.08589 | 4.74E-02 | 5.07E-03 | 6.802E-03 | 5.816E-03 |
| 0.09183 | 4.82E-02 | 5.07E-03 | 6.920E-03 | 5.852E-03 |
| 0.09580 | 4.88E-02 | 5.06E-03 | 6.994E-03 | 5.874E-03 |
| 0.10429 | 4.98E-02 | 5.06E-03 | 7.160E-03 | 5.925E-03 |
| 0.10789 | 5.02E-02 | 5.06E-03 | 7.236E-03 | 5.949E-03 |
| 0.01112 | 5.06E-02 | 5.06E-03 | 7.302E-03 | 5.971E-03 |
| 0.12250 | 5.18E-02 | 5.07E-03 | 7.528E-03 | 6.043E-03 |
| 0.12540 | 5.20E-02 | 5.07E-03 | 7.588E-03 | 6.063E-03 |
| 0.12672 | 5.22E-02 | 5.07E-03 | 7.620E-03 | 6.073E-03 |
| 0.14749 | 5.41E-02 | 5.09E-03 | 8.044E-03 | 6.218E-03 |
| 0.01501 | 5.43E-02 | 5.09E-03 | 8.098E-03 | 6.237E-03 |
| 0.15410 | 5.47E-02 | 5.10E-03 | 8.186E-03 | 6.268E-03 |
| 0.15685 | 5.49E-02 | 5.11E-03 | 8.244E-03 | 6.289E-03 |
| 0.16965 | 5.60E-02 | 5.13E-03 | 8.519E-03 | 6.388E-03 |
| 0.17161 | 5.62E-02 | 5.14E-03 | 8.552E-03 | 6.399E-03 |
| 0.18681 | 5.74E-02 | 5.17E-03 | 8.891E-03 | 6.527E-03 |
| 0.18758 | 5.75E-02 | 5.17E-03 | 8.875E-03 | 6.525E-03 |
| 0.20113 | 5.85E-02 | 5.21E-03 | 9.205E-03 | 6.648E-03 |

| | | | | |
|---|---|---|---|---|
| 0.20209 | 5.86E-02 | 5.21E-03 | 9.211E-03 | 6.648E-03 |
| 0.02029 | 5.87E-02 | 5.21E-03 | 9.229E-03 | 6.655E-03 |
| 0.20575 | 5.89E-02 | 5.22E-03 | 9.307E-03 | 6.688E-03 |
| 0.22666 | 6.07E-02 | 5.30E-03 | 9.773E-03 | 6.876E-03 |
| 0.23539 | 6.24E-02 | 5.33E-03 | 9.955E-03 | 6.933E-03 |
| 0.24975 | 6.27E-02 | 5.40E-03 | 1.029E-02 | 7.097E-03 |
| 0.25828 | 6.35E-02 | 5.44E-03 | 1.049E-02 | 7.182E-03 |
| 0.27487 | 6.51E-02 | 5.51E-03 | 1.082E-02 | 7.332E-03 |
| 0.27525 | 6.51E-02 | 5.53E-03 | 1.087E-02 | 7.357E-03 |
| 0.27753 | 6.53E-02 | 5.53E-03 | 1.088E-02 | 7.360E-03 |
| 0.30341 | 6.80E-02 | 5.70E-03 | 1.152E-02 | 7.668E-03 |
| 0.32362 | 7.14E-02 | 5.71E-03 | 1.206E-02 | 7.828E-03 |
| 0.33213 | 7.12E-02 | 5.90E-03 | 1.219E-02 | 8.013E-03 |
| 0.33452 | 7.15E-02 | 5.92E-03 | 1.225E-02 | 8.044E-03 |
| 0.37315 | 7.62E-02 | 6.22E-03 | 1.302E-02 | 8.507E-03 |
| 0.38197 | 7.74E-02 | 6.30E-03 | 1.322E-02 | 8.631E-03 |
| 0.42763 | 8.42E-02 | 6.84E-03 | 1.448E-02 | 9.420E-03 |
| 0.47655 | 9.22E-02 | 7.36E-03 | 1.544E-02 | 1.021E-02 |
| 0.52672 | 1.02E-01 | 8.31E-03 | 1.673E-02 | 1.131E-02 |
| 0.55122 | 1.08E-01 | 8.95E-03 | 1.755E-02 | 1.208E-02 |
| 0.72754 | 1.64E-01 | 1.55E-02 | 2.543E-02 | 1.969E-02 |

*Table* K.3: Rheological data for *esc*-crystals of spheroids with $r_p = 8$.

| $\phi$ | $Y_{1111}$ | $Y_{1122}$ | $Y_{1212}$ | $Y_{3131}$ |
|---|---|---|---|---|
| 0.00436 | 2.02E-02 | 9.54E-03 | 5.227E-03 | 5.501E-03 |
| 0.00611 | 2.07E-02 | 9.92E-03 | 5.219E-03 | 5.497E-03 |
| 0.00851 | 2.13E-02 | 1.04E-02 | 5.209E-03 | 5.493E-03 |
| 0.01180 | 2.20E-02 | 1.10E-02 | 5.196E-03 | 5.491E-03 |
| 0.01629 | 2.30E-02 | 1.18E-02 | 5.179E-03 | 5.491E-03 |
| 0.02241 | 2.42E-02 | 1.28E-02 | 5.159E-03 | 5.496E-03 |
| 0.03068 | 2.58E-02 | 1.40E-02 | 5.134E-03 | 5.508E-03 |
| 0.04185 | 2.77E-02 | 1.55E-02 | 5.106E-03 | 5.532E-03 |
| 0.05686 | 3.03E-02 | 1.73E-02 | 5.076E-03 | 5.574E-03 |
| 0.07698 | 3.36E-02 | 1.97E-02 | 5.048E-03 | 5.641E-03 |
| 0.10387 | 3.80E-02 | 2.27E-02 | 5.032E-03 | 5.745E-03 |
| 0.13970 | 4.40E-02 | 2.65E-02 | 5.045E-03 | 5.904E-03 |
| 0.18735 | 5.23E-02 | 3.13E-02 | 5.119E-03 | 6.146E-03 |
| 0.25056 | 6.44E-02 | 3.76E-02 | 5.326E-03 | 6.521E-03 |
| 0.33426 | 8.27E-02 | 4.56E-02 | 5.838E-03 | 7.120E-03 |
| 0.44492 | 1.10E-01 | 5.75E-02 | 7.215E-03 | 8.142E-03 |

*Table* K.4: Rheological data for *smc*-crystals of spheroids with $r_p = 8$.

| $\phi$ | $Y_{1111}$ | $Y_{1122}$ | $Y_{1212}$ | $Y_{3131}$ |
|---|---|---|---|---|
| 0.00504 | 2.04E-02 | 9.79E-03 | 5.288E-03 | 5.497E-03 |
| 0.00705 | 2.09E-02 | 1.03E-02 | 5.305E-03 | 5.492E-03 |
| 0.00982 | 2.15E-02 | 1.09E-02 | 5.327E-03 | 5.488E-03 |
| 0.01362 | 2.23E-02 | 1.16E-02 | 5.358E-03 | 5.485E-03 |
| 0.01882 | 2.34E-02 | 1.26E-02 | 5.399E-03 | 5.486E-03 |
| 0.02587 | 2.47E-02 | 1.38E-02 | 5.454E-03 | 5.493E-03 |
| 0.03543 | 2.64E-02 | 1.53E-02 | 5.529E-03 | 5.509E-03 |
| 0.04832 | 2.85E-02 | 1.72E-02 | 5.631E-03 | 5.539E-03 |
| 0.06566 | 3.12E-02 | 1.96E-02 | 5.770E-03 | 5.590E-03 |
| 0.08889 | 3.46E-02 | 2.27E-02 | 5.963E-03 | 5.671E-03 |
| 0.11994 | 3.92E-02 | 2.68E-02 | 6.236E-03 | 5.796E-03 |
| 0.16131 | 4.54E-02 | 3.22E-02 | 6.633E-03 | 5.988E-03 |
| 0.21633 | 5.39E-02 | 3.94E-02 | 7.236E-03 | 6.283E-03 |
| 0.28932 | 6.58E-02 | 4.94E-02 | 8.211E-03 | 6.747E-03 |
| 0.38597 | 8.30E-02 | 6.30E-02 | 9.967E-03 | 7.510E-03 |
| 0.51375 | 1.08E-01 | 8.08E-02 | 1.383E-02 | 8.878E-03 |

One can verify the relation $Y_{1111} = Y_{1122} + 2Y_{1212}$ predicted for structures with cylindrical symmetry.

*Table* K.5: Rheological data for *isc*-crystals of spheroids with $r_p = 8$.

| $\phi$ | $Y_{1111}$ | $Y_{1122}$ | $Y_{1212}$ | $Y_{3131}$ |
|---|---|---|---|---|
| 0.00102 | 2.02E-02 | 9.51E-03 | 5.227E-03 | 5.464E-03 |
| 0.00150 | 2.06E-02 | 9.87E-03 | 5.219E-03 | 5.446E-03 |
| 0.00220 | 2.12E-02 | 1.03E-02 | 5.210E-03 | 5.425E-03 |
| 0.00323 | 2.19E-02 | 1.09E-02 | 5.198E-03 | 5.400E-03 |
| 0.00474 | 2.27E-02 | 1.16E-02 | 5.182E-03 | 5.371E-03 |
| 0.00508 | 2.29E-02 | 1.18E-02 | 5.179E-03 | 5.365E-03 |
| 0.00696 | 2.39E-02 | 1.25E-02 | 5.163E-03 | 5.338E-03 |
| 0.00758 | 2.41E-02 | 1.27E-02 | 5.159E-03 | 5.330E-03 |
| 0.01021 | 2.53E-02 | 1.36E-02 | 5.141E-03 | 5.302E-03 |
| 0.01131 | 2.57E-02 | 1.39E-02 | 5.134E-03 | 5.292E-03 |
| 0.01498 | 2.70E-02 | 1.49E-02 | 5.115E-03 | 5.266E-03 |
| 0.01689 | 2.76E-02 | 1.54E-02 | 5.106E-03 | 5.255E-03 |
| 0.02199 | 2.92E-02 | 1.65E-02 | 5.086E-03 | 5.232E-03 |
| 0.02521 | 3.01E-02 | 1.72E-02 | 5.076E-03 | 5.222E-03 |
| 0.03226 | 3.20E-02 | 1.85E-02 | 5.058E-03 | 5.206E-03 |
| 0.03763 | 3.34E-02 | 1.95E-02 | 5.049E-03 | 5.200E-03 |
| 0.04734 | 3.57E-02 | 2.10E-02 | 5.037E-03 | 5.196E-03 |
| 0.05617 | 3.77E-02 | 2.23E-02 | 5.032E-03 | 5.200E-03 |
| 0.06947 | 4.05E-02 | 2.41E-02 | 5.034E-03 | 5.216E-03 |
| 0.08384 | 4.34E-02 | 2.59E-02 | 5.045E-03 | 5.243E-03 |
| 0.10194 | 4.69E-02 | 2.79E-02 | 5.070E-03 | 5.289E-03 |
| 0.12515 | 5.12E-02 | 3.03E-02 | 5.119E-03 | 5.363E-03 |
| 0.14959 | 5.56E-02 | 3.25E-02 | 5.189E-03 | 5.457E-03 |
| 0.18582 | 6.22E-02 | 3.54E-02 | 5.326E-03 | 5.629E-03 |
| 0.21951 | 6.78E-02 | 3.75E-02 | 5.480E-03 | 5.806E-03 |

| | | | | |
|---|---|---|---|---|
| 0.27886 | 7.77E-02 | 4.07E-02 | 5.839E-03 | 6.193E-03 |
| 0.32211 | 8.45E-02 | 4.24E-02 | 6.178E-03 | 6.534E-03 |
| 0.41626 | 9.85E-02 | 4.61E-02 | 7.218E-03 | 7.492E-03 |
| 0.47267 | 1.08E-01 | 5.15E-02 | 8.139E-03 | 8.252E-03 |

*Table* K.6: Rheological data for *efc*-crystals of spheroids with $r_p = 4$.

| $\phi$ | $Y_{1111}$ | $Y_{1212}$ | $Y_{3131}$ |
|---|---|---|---|
| 0.00087 | 4.49E-02 | 2.141E-02 | 2.376E-02 |
| 0.00126 | 4.49E-02 | 2.142E-02 | 2.375E-02 |
| 0.00182 | 4.50E-02 | 2.143E-02 | 2.375E-02 |
| 0.00262 | 4.52E-02 | 2.145E-02 | 2.374E-02 |
| 0.03773 | 4.54E-02 | 2.463E-02 | 2.374E-02 |
| 0.00404 | 4.55E-02 | 2.149E-02 | 2.373E-02 |
| 0.00579 | 4.58E-02 | 2.154E-02 | 2.372E-02 |
| 0.00825 | 4.63E-02 | 2.161E-02 | 2.370E-02 |
| 0.01173 | 4.70E-02 | 2.171E-02 | 2.369E-02 |
| 0.01659 | 4.80E-02 | 2.185E-02 | 2.367E-02 |
| 0.02339 | 4.93E-02 | 2.204E-02 | 2.366E-02 |
| 0.03284 | 5.10E-02 | 2.232E-02 | 2.368E-02 |
| 0.04592 | 5.34E-02 | 2.270E-02 | 2.375E-02 |
| 0.06398 | 5.65E-02 | 2.324E-02 | 2.392E-02 |
| 0.08886 | 6.07E-02 | 2.399E-02 | 2.425E-02 |
| 0.12305 | 6.62E-02 | 2.507E-02 | 2.485E-02 |
| 0.17003 | 7.35E-02 | 2.665E-02 | 2.592E-02 |
| 0.23461 | 8.28E-02 | 2.907E-02 | 2.781E-02 |
| 0.32350 | 9.49E-02 | 3.309E-02 | 3.129E-02 |
| 0.44610 | 1.14E-01 | 4.068E-02 | 3.829E-02 |
| 0.61555 | 1.55E-01 | 5.947E-02 | 5.559E-02 |

*Table* K.7: Rheological data for *efc*-crystals of spheroids with $r_p = 16$.

| $\phi$ | $Y_{1111}$ | $Y_{1212}$ | $Y_{3131}$ |
|---|---|---|---|
| 0.00027 | 1.07E-02 | 1.305E-03 | 1.331E-03 |
| 0.00055 | 1.09E-02 | 1.306E-03 | 1.330E-03 |
| 0.00077 | 1.10E-02 | 1.306E-03 | 1.330E-03 |
| 0.00107 | 1.11E-02 | 1.307E-03 | 1.330E-03 |
| 0.00139 | 1.13E-02 | 1.307E-03 | 1.330E-03 |
| 0.00207 | 1.15E-02 | 1.308E-03 | 1.329E-03 |
| 0.00286 | 1.18E-02 | 1.310E-03 | 1.329E-03 |
| 0.00393 | 1.21E-02 | 1.312E-03 | 1.312E-03 |
| 0.00538 | 1.25E-02 | 1.315E-03 | 1.329E-03 |
| 0.00710 | 1.30E-02 | 1.318E-03 | 1.330E-03 |
| 0.00965 | 1.36E-02 | 1.322E-03 | 1.331E-03 |
| 0.01306 | 1.43E-02 | 1.328E-03 | 1.333E-03 |
| 0.01763 | 1.51E-02 | 1.336E-03 | 1.336E-03 |
| 0.02373 | 1.62E-02 | 1.347E-03 | 1.341E-03 |
| 0.03184 | 1.74E-02 | 1.361E-03 | 1.348E-03 |
| 0.04263 | 1.89E-02 | 1.380E-03 | 1.358E-03 |
| 0.05697 | 2.07E-02 | 1.406E-03 | 1.373E-03 |
| 0.07602 | 2.30E-02 | 1.441E-03 | 1.394E-03 |
| 0.10141 | 2.58E-02 | 1.489E-03 | 1.425E-03 |
| 0.13544 | 2.91E-02 | 1.557E-03 | 1.471E-03 |
| 0.18158 | 3.29E-02 | 1.657E-03 | 1.543E-03 |
| 0.24480 | 3.66E-02 | 1.808E-03 | 1.661E-03 |
| 0.33185 | 4.12E-02 | 2.057E-03 | 1.866E-03 |
| 0.45200 | 4.87E-02 | 2.525E-03 | 2.263E-03 |
| 0.61807 | 6.43E-02 | 3.666E-03 | 3.220E-03 |

*Table* K.8: Rheological data for *efc*-crystals of spheroids with $r_p = 300$.

| $\phi$ | $Y_{1111}$ | $Y_{1212}$ | $Y_{3131}$ |
|---|---|---|---|
| 0.21430E-09 | 0.3785E-02 | 0.3704E-05 | 0.3704E-05 |
| 0.13384E-06 | 0.3789E-02 | 0.3704E-05 | 0.3704E-05 |
| 0.25001E-05 | 0.3854E-02 | 0.3704E-05 | 0.3704E-05 |
| 0.12536E-04 | 0.4043E-02 | 0.3704E-05 | 0.3704E-05 |
| 0.20971E-04 | 0.4142E-02 | 0.3704E-05 | 0.3704E-05 |
| 0.34729E-04 | 0.4280E-02 | 0.3704E-05 | 0.3704E-05 |
| 0.47678E-04 | 0.4377E-02 | 0.3704E-05 | 0.3704E-05 |
| 0.56996E-04 | 0.4437E-02 | 0.3704E-05 | 0.3704E-05 |
| 0.77839E-04 | 0.4550E-02 | 0.3704E-05 | 0.3704E-05 |
| 0.89568E-04 | 0.4606E-02 | 0.3704E-05 | 0.3704E-05 |
| 0.92792E-04 | 0.4620E-02 | 0.3704E-05 | 0.3704E-05 |
| 0.12615E-03 | 0.4753E-02 | 0.3704E-05 | 0.3704E-05 |
| 0.15002E-03 | 0.4834E-02 | 0.3704E-05 | 0.3704E-05 |
| 0.20316E-03 | 0.4987E-02 | 0.3705E-05 | 0.3705E-05 |
| 0.23294E-03 | 0.5065E-02 | 0.3705E-05 | 0.3705E-05 |
| 0.32543E-03 | 0.5257E-02 | 0.3705E-05 | 0.3705E-05 |
| 0.37261E-03 | 0.5336E-02 | 0.3705E-05 | 0.3705E-05 |
| 0.51893E-03 | 0.5569E-02 | 0.3706E-05 | 0.3705E-05 |
| 0.59348E-03 | 0.5676E-02 | 0.3707E-05 | 0.3706E-05 |
| 0.82439E-03 | 0.5929E-02 | 0.3708E-05 | 0.3706E-05 |
| 0.98912E-03 | 0.6088E-02 | 0.3708E-05 | 0.3707E-05 |
| 0.13019E-02 | 0.6346E-02 | 0.3710E-05 | 0.3708E-05 |
| 0.14905E-02 | 0.6494E-02 | 0.3711E-05 | 0.3708E-05 |
| 0.17121E-02 | 0.6630E-02 | 0.3712E-05 | 0.3709E-05 |
| 0.20624E-02 | 0.6833E-02 | 0.3713E-05 | 0.3710E-05 |

| | | | |
|---|---|---|---|
| 0.22497E-02 | 0.6943E-02 | 0.3714E-05 | 0.3710E-05 |
| 0.23529E-02 | 0.6983E-02 | 0.3715E-05 | 0.3711E-05 |
| 0.29834E-02 | 0.7286E-02 | 0.3718E-05 | 0.3712E-05 |
| 0.32510E-02 | 0.7404E-02 | 0.3719E-05 | 0.3713E-05 |
| 0.39148E-02 | 0.7712E-02 | 0.3722E-05 | 0.3715E-05 |
| 0.51341E-02 | 0.8102E-02 | 0.3727E-05 | 0.3719E-05 |
| 0.67298E-02 | 0.8599E-02 | 0.3735E-05 | 0.3723E-05 |
| 0.77450E-02 | 0.8840E-02 | 0.3739E-05 | 0.3726E-05 |
| 0.88177E-02 | 0.9085E-02 | 0.3744E-05 | 0.3729E-05 |
| 0.10146E-01 | 0.9500E-02 | 0.3750E-05 | 0.3734E-05 |
| 0.13286E-01 | 0.1015E-01 | 0.3765E-05 | 0.3743E-05 |
| 0.17393E-01 | 0.1095E-01 | 0.3784E-05 | 0.3755E-05 |
| 0.22763E-01 | 0.1162E-01 | 0.3809E-05 | 0.3772E-05 |
| 0.29785E-01 | 0.1225E-01 | 0.3842E-05 | 0.3793E-05 |
| 0.38966E-01 | 0.1267E-01 | 0.3887E-05 | 0.3822E-05 |
| 0.50967E-01 | 0.1419E-01 | 0.3946E-05 | 0.3860E-05 |

*Table* K.9: Sedimentation rates for *efc*-crystals of spheroids with $r_p = 8$.

| $\phi$ | $V_{\parallel}^{\mathrm{tr}}$ | $V_{\perp}^{\mathrm{tr}}$ | $V_{\parallel}^{\mathrm{ro}}$ | $V_{\perp}^{\mathrm{ro}}$ |
|---|---|---|---|---|
| 0.00000 | 0.4610E+01 | 0.3276E+01 | 0.9327E+02 | 0.6808E+01 |
| 0.03025 | 0.1783E+01 | 0.1221E+01 | 0.9004E+02 | 0.9141E+01 |
| 0.03866 | 0.1619E+01 | 0.1100E+01 | 0.8912E+02 | 0.9682E+01 |
| 0.04931 | 0.1455E+01 | 0.9773E+00 | 0.8797E+02 | 0.1030E+02 |
| 0.06279 | 0.1293E+01 | 0.8524E+00 | 0.8657E+02 | 0.1100E+02 |
| 0.07985 | 0.1135E+01 | 0.7273E+00 | 0.8475E+02 | 0.1176E+02 |
| 0.10145 | 0.9803E+00 | 0.6050E+00 | 0.8247E+02 | 0.1256E+02 |
| 0.12884 | 0.8321E+00 | 0.4909E+00 | 0.7963E+02 | 0.1334E+02 |
| 0.16367 | 0.6914E+00 | 0.3939E+00 | 0.7607E+02 | 0.1401E+02 |
| 0.20815 | 0.5602E+00 | 0.3303E+00 | 0.7162E+02 | 0.1443E+02 |
| 0.26515 | 0.4419E+00 | 0.3219E+00 | 0.6605E+02 | 0.1445E+02 |
| 0.33841 | 0.3446E+00 | 0.3976E+00 | 0.5903E+02 | 0.1389E+02 |
| 0.43279 | 0.2836E+00 | 0.5909E+00 | 0.5011E+02 | 0.1263E+02 |
| 0.55455 | 0.2762E+00 | 0.9183E+00 | 0.3867E+02 | 0.1070E+02 |
| 0.71180 | 0.3404E+00 | 0.1392E+01 | 0.2385E+02 | 0.8134E+01 |

*Table* K.10: Sedimentation rates for *smc*-crystals of spheroids with $r_p = 8$.

| $\phi$ | $V_{\parallel}^{\mathrm{tr}}$ | $V_{\perp}^{\mathrm{tr}}$ | $V_{\parallel}^{\mathrm{ro}}$ | $V_{\perp}^{\mathrm{ro}}$ |
|---|---|---|---|---|
| 0.00000 | 0.4610E+01 | 0.3276E+01 | 0.9327E+02 | 0.6808E+01 |
| 0.00538 | 0.2819E+01 | 0.2086E+01 | 0.9271E+02 | 0.7454E+01 |
| 0.00705 | 0.2633E+01 | 0.1982E+01 | 0.9247E+02 | 0.7728E+01 |
| 0.00982 | 0.2440E+01 | 0.1872E+01 | 0.9214E+02 | 0.8094E+01 |
| 0.01362 | 0.2240E+01 | 0.1755E+01 | 0.9169E+02 | 0.8572E+01 |
| 0.01882 | 0.2036E+01 | 0.1631E+01 | 0.9107E+02 | 0.9186E+01 |
| 0.02587 | 0.1829E+01 | 0.1500E+01 | 0.9023E+02 | 0.9960E+01 |
| 0.03543 | 0.1621E+01 | 0.1361E+01 | 0.8910E+02 | 0.1092E+02 |
| 0.04832 | 0.1416E+01 | 0.1214E+01 | 0.8758E+02 | 0.1210E+02 |
| 0.06566 | 0.1214E+01 | 0.1065E+01 | 0.8556E+02 | 0.1352E+02 |
| 0.08889 | 0.1020E+01 | 0.9096E+00 | 0.8288E+02 | 0.1521E+02 |
| 0.11994 | 0.8384E+00 | 0.7535E+00 | 0.7934E+02 | 0.1719E+02 |
| 0.16132 | 0.6736E+00 | 0.6008E+00 | 0.7466E+02 | 0.1945E+02 |
| 0.21633 | 0.5326E+00 | 0.4580E+00 | 0.6850E+02 | 0.2194E+02 |
| 0.28932 | 0.4239E+00 | 0.3340E+00 | 0.6041E+02 | 0.2449E+02 |
| 0.38597 | 0.3592E+00 | 0.2414E+00 | 0.4979E+02 | 0.2662E+02 |
| 0.51375 | 0.3533E+00 | 0.1988E+00 | 0.3587E+02 | 0.2695E+02 |

*Table* K.11: Hindered diffusivities for *efc*-crystals of spheroids with $r_p = 6$ constructed using 32 particles per unit cell.

| $\phi$ | $H_{\parallel}^{tr}$ | $H_{\perp}^{tr}$ | $H_{\parallel}^{ro}$ | $H_{\perp}^{ro}$ |
|---|---|---|---|---|
| 0.0000E00 | 0.4099E+1 | 0.2991E+1 | 0.5167E+2 | 0.5939E+1 |
| 0.5007E-2 | 0.3539E+1 | 0.2406E+1 | 0.5164E+2 | 0.5898E+1 |
| 0.6379E-2 | 0.3486E+1 | 0.2343E+1 | 0.5162E+2 | 0.5882E+1 |
| 0.8111E-2 | 0.3428E+1 | 0.2273E+1 | 0.5161E+2 | 0.5861E+1 |
| 0.1029E-1 | 0.3363E+1 | 0.2196E+1 | 0.5159E+2 | 0.5832E+1 |
| 0.1303E-1 | 0.3307E+1 | 0.2104E+1 | 0.5156E+2 | 0.5808E+1 |
| 0.1646E-1 | 0.3225E+1 | 0.2015E+1 | 0.5152E+2 | 0.5761E+1 |
| 0.2075E-1 | 0.3135E+1 | 0.1919E+1 | 0.5146E+2 | 0.5700E+1 |
| 0.2611E-1 | 0.3037E+1 | 0.1817E+1 | 0.5139E+2 | 0.5621E+1 |
| 0.5626E-1 | 0.2630E+1 | 0.1433E+1 | 0.5089E+2 | 0.5171E+1 |
| 0.9500E-1 | 0.2284E+1 | 0.1135E+1 | 0.5013E+2 | 0.4673E+1 |
| 0.1597E00 | 0.1879E+1 | 0.8356E00 | 0.4865E+2 | 0.4000E+1 |

The basis vectors for this lattice at $\phi = 0.056259$ are given by the column vectors of

$$\mathbf{B} = \begin{pmatrix} 2 & -2 & 4 \\ -2/\sqrt{3} & \sqrt{12} & 0 \\ -4.77631 & 0 & 0 \end{pmatrix} .$$

The spheroids are aligned with the "3" axis and are arranged in two stacks of 4 by 4. For comparison, at the same concentration,

| $D_{\parallel}^{tr}$ | $D_{\perp}^{tr}$ | $D_{\parallel}^{ro}$ | $D_{\perp}^{ro}$ |
|---|---|---|---|
| 2.9792 | 2.0210 | 51.394 | 5.8188 |
| $V_{\parallel}^{tr}$ | $V_{\perp}^{tr}$ | $V_{\parallel}^{ro}$ | $V_{\perp}^{ro}$ |
| 1.2797 | 0.87518 | 48.415 | 7.6835 |

These properties have not been corrected for the periodicity effect.

# APPENDIX L

## A sample of simulation results for unbounded equilibrium dispersions of spheroids

This appendix groups a few of the numerical results obtained for "random" configurations of prolate spheroids of aspect ratio 6 and 20. The list is by no means exhaustive, and perhaps not even fully representative of the capabilities of our simulation method. (Polydisperse systems for instance are not discussed.) We hope, however, that this information will be useful for comparison with experiments or with data obtained by different techniques.

Entries in parentheses indicate the variance on the single-particle data. This spread is caused mainly by the difference in the local environments of the spheroids in the dispersion, and is usually much larger than the uncertainty about the mean values. Variables are non-dimensionalized as in Appendix K. The data are not corrected for periodicity effects brought about by the finite number $N$ of particles in the unit cell. Lubrication interactions were included below a threshold gap width $\epsilon_{max} = 0.08$ (made dimensionless using the harmonic mean of the radii of curvature at the points of closest approach). The number of accepted moves between data acquisition in the Monte-Carlo procedure depended on the concentration and on the aspect ratio of the spheroids. The magnitude of the translational and rotational displacements was adapted to achieve a mean rejection ratio of 35%. At a volume fraction $\phi = 0.05$, for $r_p = 6$, the step size was nearly $a/2$, i.e., one quarter of a particle length; each spheroid was moved successfully 1000 times on average to generate each new configuration; 4000 displacements per particle were used to randomize the system initially. At $\phi = 0.275$, 3600 and 21000 moves/particle were employed respectively, but the step size had to be reduced to about $0.03\,a$ to achieve the same rejection rate. The number of configurations over which the data has been averaged is denoted by $N_R$ in the following tables.

## Spheroids of aspect ratio 6

*Table* L.1: Simulation parameters

| $\phi$ | $N$ | $N_R$ |
|---|---|---|
| .005e0 | 50 | 5 |
| .050e0 | 50 | 5 |
| .111e0 | 50 | 5 |
| .150e0 | 60 | 4 |
| .225e0 | 50 | 3 |
| .275e0 | 50 | 4 |
| .300e0 | 50 | 4 |
| .333e0 | 60 | 4 |
| .333e0 | 63 | 3 |
| .375e0 | 60 | 5 |

*Table* L.2: Self-diffusivities

| $\phi$ | $D_{\parallel}^{tr}$ | | $D_{\perp}^{tr}$ | |
|---|---|---|---|---|
| 0.005E+00 | 0.369E+01 | (0.80E-01) | 0.262E+01 | (0.30E-01) |
| 0.050E+00 | 0.311E+01 | (0.70E-01) | 0.207E+01 | (0.40E-01) |
| 0.111E+00 | 0.271E+01 | (0.15E+00) | 0.173E+01 | (0.80E-01) |
| 0.150E+00 | 0.255E+01 | (0.16E+00) | 0.161E+01 | (0.80E-01) |
| 0.225E+00 | 0.222E+01 | (0.21E+00) | 0.134E+01 | (0.12E+00) |
| 0.275E+00 | 0.198E+01 | (0.21E+00) | 0.120E+01 | (0.11E+00) |
| 0.300E+00 | 0.209E+01 | (0.22E+00) | 0.127E+01 | (0.10E+00) |
| 0.333E+00 | 0.175E+01 | (0.21E+00) | 0.112E+01 | (0.12E+00) |
| 0.333E+00 | 0.203E+01 | (0.19E+00) | 0.123E+01 | (0.90E-01) |
| 0.375E+00 | 0.164E+01 | (0.16E+00) | 0.108E+01 | (0.80E-01) |

| $\phi$ | $D_{\parallel}^{ro}$ | | $D_{\perp}^{ro}$ | |
|---|---|---|---|---|
| 0.500E-02 | 0.515E+02 | (0.10E+01) | 0.589E+01 | (0.15E+00) |
| 0.500E-01 | 0.510E+02 | (0.14E+01) | 0.563E+01 | (0.10E+00) |
| 0.111E+00 | 0.495E+02 | (0.28E+01) | 0.523E+01 | (0.24E+00) |
| 0.150E+00 | 0.487E+02 | (0.31E+01) | 0.498E+01 | (0.30E+00) |
| 0.225E+00 | 0.460E+02 | (0.48E+01) | 0.445E+01 | (0.41E+00) |
| 0.275E+00 | 0.439E+02 | (0.49E+01) | 0.405E+01 | (0.48E+00) |
| 0.300E+00 | 0.440E+02 | (0.46E+01) | 0.389E+01 | (0.46E+00) |
| 0.333E+00 | 0.422E+02 | (0.61E+01) | 0.398E+01 | (0.48E+00) |
| 0.333E+00 | 0.435E+02 | (0.49E+01) | 0.377E+01 | (0.42E+00) |
| 0.375E+00 | 0.422E+02 | (0.53E+01) | 0.397E+01 | (0.40E+00) |
| 0.375E+00 | 0.422E+02 | (0.53E+01) | 0.397E+01 | (0.40E+00) |

*Table* L.3: Hindered diffusivities

| $\phi$ | $H_{\parallel}^{\mathrm{tr}}$ | | $H_{\perp}^{\mathrm{tr}}$ | |
|---|---|---|---|---|
| 0.50000E-02 | 0.334E+01 | (0.30E+00) | 0.229E+01 | (0.21E+00) |
| 0.50000E-01 | 0.248E+01 | (0.19E+00) | 0.149E+01 | (0.14E+00) |
| 0.11100E+00 | 0.202E+01 | (0.22E+00) | 0.111E+01 | (0.15E+00) |
| 0.15000E+00 | 0.183E+01 | (0.21E+00) | 0.982E+00 | (0.14E+00) |
| 0.22500E+00 | 0.153E+01 | (0.23E+00) | 0.762E+00 | (0.16E+00) |
| 0.27500E+00 | 0.135E+01 | (0.21E+00) | 0.653E+00 | (0.13E+00) |
| 0.30000E+00 | 0.136E+01 | (0.20E+00) | 0.607E+00 | (0.12E+00) |
| 0.33300E+00 | 0.124E+01 | (0.20E+00) | 0.560E+00 | (0.14E+00) |
| 0.33300E+00 | 0.133E+01 | (0.19E+00) | 0.554E+00 | (0.10E+00) |

| $\phi$ | $H_{\parallel}^{\mathrm{ro}}$ | | $H_{\perp}^{\mathrm{ro}}$ | |
|---|---|---|---|---|
| 0.500E-02 | 0.513E+02 | (0.13E+01) | 0.572E+01 | (0.34E+00) |
| 0.500E-01 | 0.500E+02 | (0.17E+01) | 0.484E+01 | (0.29E+00) |
| 0.111E+00 | 0.475E+02 | (0.33E+01) | 0.409E+01 | (0.39E+00) |
| 0.150E+00 | 0.462E+02 | (0.36E+01) | 0.372E+01 | (0.44E+00) |
| 0.225E+00 | 0.429E+02 | (0.53E+01) | 0.315E+01 | (0.53E+00) |
| 0.275E+00 | 0.405E+02 | (0.52E+01) | 0.275E+01 | (0.57E+00) |
| 0.300E+00 | 0.397E+02 | (0.48E+01) | 0.276E+01 | (0.44E+00) |
| 0.333E+00 | 0.380E+02 | (0.62E+01) | 0.254E+01 | (0.51E+00) |
| 0.333E+00 | 0.385E+02 | (0.48E+01) | 0.269E+01 | (0.39E+00) |

*Table* L.4: Sedimentation rates

| $\phi$ | $V^{tr}$ | |
|---|---|---|
| .005E+00 | .284E+01 | (.55E+00) |
| .050E+00 | .176E+01 | (.48E+00) |
| .111E+00 | .117E+01 | (.37E+00) |
| .150E+00 | .962E+00 | (.30E+00) |
| .225E+00 | .685E+00 | (.21E+00) |
| .275E+00 | .554E+00 | (.17E+00) |

| $\phi$ | $V_{\perp}^{tr}$ | | $V_{\parallel}^{tr}$ | |
|---|---|---|---|---|
| .300E+00 | .527E+00 | (.35E+00) | .626E+00 | (.16E+00) |
| .333E+00 | .458E+00 | (.15E+00) | .502E+00 | (.12E+00) |
| .333E+00 | .428E+00 | (.26E+00) | .559E+00 | (.11E+00) |
| .375E+00 | .389E+00 | (.14E+00) | .463E+00 | (.12E+00) |

$V_{\perp}^{tr}$ refers to the sedimentation rate when gravity acts perpendicular to the director of the nematic phase. The corresponding velocity when the spheroidal axes are approximately aligned vertically is $V_{\parallel}^{tr}$.

*Table* L.5: Relation between the stress and the rate of strain

| $\phi$ | $Y_{1111}$ | $Y_{1122}$ | $Y_{1212}$ |
|---|---|---|---|
| .005E+00 | .232E-01 | .870E-01 | .180E-01 |
| .050E+00 | .254E-01 | -.138E-01 | .190E-01 |
| .111E+00 | .274E-01 | -.169E-01 | .204E-01 |
| .150E+00 | .294E-01 | -.214E-01 | .217E-01 |
| .225E+00 | .328E-01 | -.243E-01 | .247E-01 |
| .250E+00 | .327E-01 | -.126E-01 | .230E-01 |
| .275E+00 | .372E-01 | -.254E-01 | .263E-01 |

| $\phi$ | $Y_{1111}$ | $Y_{1122}$ | $Y_{2323}$ | $Y_{1212}$ |
|---|---|---|---|---|
| .300E+00 | .334E-01 | -.795E-02 | .276E-01 | .194E-01 |
| .333E+00 | .354E-01 | -.230E-01 | .300E-01 | .206E-01 |
| .333E+00 | .346E-01 | -.884E-02 | .278E-01 | .176E-01 |
| .375E+00 | .346E-01 | -.199E-01 | .335E-01 | .204E-01 |

For the isotropic samples (top table), the column labeled $Y_{1111}$ contains the average of $Y_{1111}$ and $Y_{2222}$, and the column $Y_{1212}$ gives the mean of the three other diagonal elements of $\mathbf{Y}$ (see App. K). In the nematic phase (with director aligned in the "3" direction), $Y_{1212}$ is distinct from $Y_{2323}$ and $Y_{3131}$, and is tabulated separately. Note that $Y_{1212} \simeq \frac{3}{4} Y_{1111}$ in the isotropic dispersions, as required by rotational invariance. The data for $Y_{1122}$ are subject to large fluctuations, and their variance (not shown) suggests that they are not very reliable.

## Spheroids of aspect ratio 20

*Table* L.6: Simulation parameters

| $\phi$ | $N$ | $N_R$ |
|---|---|---|
| .0100e0 | 60 | 8 |
| .0250e0 | 64 | 7 |
| .0375e0 | 64 | 4 |
| .0500e0 | 64 | 6 |
| .0560e0 | 64 | 6 |

*Table* L.7: Self-diffusivities

| $\phi$ | $D_{\parallel}^{\mathrm{tr}}$ | | $D_{\perp}^{\mathrm{tr}}$ | |
|---|---|---|---|---|
| 0.100E-01 | 0.532E+01 | (0.14E+00) | 0.318E+01 | (0.67E-01) |
| 0.250E-01 | 0.492E+01 | (0.20E+00) | 0.285E+01 | (0.86E-01) |
| 0.375E-01 | 0.462E+01 | (0.19E+00) | 0.263E+01 | (0.95E-01) |
| 0.500E-01 | 0.440E+01 | (0.24E+00) | 0.246E+01 | (0.12E+00) |
| 0.560E-01 | 0.432E+01 | (0.22E+00) | 0.239E+01 | (0.12E+00) |

| $\phi$ | $D_{\parallel}^{\mathrm{ro}}$ | | $D_{\perp}^{\mathrm{ro}}$ | |
|---|---|---|---|---|
| 0.100E-01 | 0.594E+03 | (0.91E+01) | 0.922E+01 | (0.22E+00) |
| 0.250E-01 | 0.592E+03 | (0.94E+01) | 0.882E+01 | (0.32E+00) |
| 0.375E-01 | 0.590E+03 | (0.11E+02) | 0.852E+01 | (0.39E+00) |
| 0.500E-01 | 0.585E+03 | (0.27E+02) | 0.822E+01 | (0.40E+00) |
| 0.560E-01 | 0.586E+03 | (0.16E+02) | 0.805E+01 | (0.50E+00) |

*Table* L.8: Hindered diffusivities

| $\phi$ | $H_{\parallel}^{\mathrm{tr}}$ | | $H_{\perp}^{\mathrm{tr}}$ | |
|---|---|---|---|---|
| 0.100E-01 | 0.446E+01 | (0.31E+00) | 0.249E+01 | (0.19E+00) |
| 0.250E-01 | 0.396E+01 | (0.28E+00) | 0.211E+01 | (0.16E+00) |
| 0.375E-01 | 0.369E+01 | (0.27E+00) | 0.193E+01 | (0.17E+00) |
| 0.500E-01 | 0.346E+01 | (0.35E+00) | 0.178E+01 | (0.22E+00) |
| 0.560E-01 | 0.342E+01 | (0.28E+00) | 0.175E+01 | (0.19E+00) |

| $\phi$ | $H_{\parallel}^{\mathrm{ro}}$ | | $H_{\perp}^{\mathrm{ro}}$ | |
|---|---|---|---|---|
| 0.100E-01 | 0.591E+03 | (0.10E+02) | 0.802E+01 | (0.50E+00) |
| 0.250E-01 | 0.587E+03 | (0.11E+02) | 0.719E+01 | (0.49E+00) |
| 0.375E-01 | 0.583E+03 | (0.12E+02) | 0.670E+01 | (0.57E+00) |
| 0.500E-01 | 0.575E+03 | (0.31E+02) | 0.633E+01 | (0.58E+00) |
| 0.560E-01 | 0.577E+03 | (0.17E+02) | 0.619E+01 | (0.64E+00) |

*Table* L.9: Sedimentation rates

| $\phi$ | $V^{\mathrm{tr}}$ | |
|---|---|---|
| 0.0100E+00 | 0.3578E+01 | (0.89E+00) |
| 0.0250E+00 | 0.2742E+01 | (0.78E+00) |
| 0.0375E+00 | 0.2452E+01 | (0.72E+00) |
| 0.0500E+00 | 0.2196E+01 | (0.64E+00) |
| 0.0560E+00 | 0.1943E+01 | (0.57E+00) |

*Table* L.10: Relation between the stress and the rate of strain

| $\phi$ | $Y_{1111}$ | $Y_{1122}$ | $Y_{1212}$ |
|---|---|---|---|
| 0.0100E+00 | 0.748E-02 | -0.386E-02 | 0.599E-02 |
| 0.0200E+00 | 0.798E-02 | -0.413E-02 | 0.597E-02 |
| 0.0375E+00 | 0.853E-02 | -0.653E-02 | 0.602E-02 |
| 0.0500E+00 | 0.780E-02 | -0.571E-02 | 0.643E-02 |
| 0.0560E+00 | 0.832E-02 | -0.558E-02 | 0.653E-02 |

The column labeled $Y_{1111}$ contains the average of $Y_{1111}$ and $Y_{2222}$, and the column $Y_{1212}$ gives the mean of the three other diagonal elements of $\mathbf{Y}$ (see App. K). The data for $Y_{1122}$ are subject to large fluctuations, and their variance (not shown) suggests that they are not very reliable.